Phenomenological and formal aspects of scattering amplitudes in Quantum Chromodynamics

By

DAVID GORDO GÓMEZ

Facultad de Física Teórica
UNIVERSIDAD AUTÓNOMA DE MADRID

Instituto de Física Teórica
IFT UAM-CSIC

Memoria de Tesis Doctoral presentada por David Gordo Gómez para optar al título de Doctor en Física por la Universidad Autónoma de Madrid. Tesis Doctoral dirigida por **Dr. Agustín Sabio Vera** y **Dr. Paolo Benincasa**.

SEPTIEMBRE 2018

AUTHOR'S DECLARATION

I declare that this thesis is the result of my own original work and that it has not been submitted for any other degree or academic award. In cases where the work of others is presented, appropriate citations are used. Chapter 1 serves as an introduction to the research topics presented in the first part of the thesis, consisting of the original work organized in Chapers 2 [1], 3 [2], 4 [3], 5 [4], 6 [5]. In Part II, Chapter 8 serves as an introduction , and the original work is presented in Chapters 9 [6] and 10 [7]. Our main results have been published in:

[5] F. G. Celiberto, D. Gordo Gómez, and A. Sabio Vera, "Forward Drell-Yan production at the LHC in the BFKL formalism with collinear corrections," arXiv:1808.09511 [hep-ph].

[1] F. Caporale, F. Celiberto, G. Chachamis, D. Gordo Gómez, and A. S. Vera, "Inclusive dijet hadroproduction with a rapidity veto constraint," *Nuclear Physics B* (2018) , 1806.06309 [hep-ph]. http://www.sciencedirect.com/science/article/pii/S0550321318302499.

[3] F. Caporale, F. G. Celiberto, G. Chachamis, D. Gordo Gómez, and A. Sabio Vera, "Stability of Azimuthal-angle Observables under Higher Order Corrections in Inclusive Three-jet Production," *Phys. Rev.* **D95** no. 7, (2017) 074007, arXiv:1612.05428 [hep-ph].

[7] P. Benincasa and D. Gordo Gómez, "On-shell diagrams and the geometry of planar $\mathcal{N} < 4$ SYM theories," *JHEP* **11** (2017) 192, arXiv:1609.01923 [hep-th].

[4] F. Caporale, F. G. Celiberto, G. Chachamis, D. Gordo Gómez, and A. Sabio Vera, "Inclusive Four-jet Production at 7 and 13 TeV: Azimuthal Profile in Multi-Regge Kinematics," *Eur. Phys. J.* **C77** no. 1, (2017) 5, arXiv:1606.00574 [hep-ph].

[2] F. Caporale, F. G. Celiberto, G. Chachamis, D. Gordo Gómez, and A. Sabio Vera, "BFKL Azimuthal Imprints in Inclusive Three-jet Production at 7 and 13 TeV," *Nucl. Phys.* **B910** (2016) 374–386, arXiv:1603.07785 [hep-ph].

[6] P. Benincasa, E. Conde, and D. Gordo Gómez, "On the Regularization of On-Shell Diagrams," arXiv:1411.7987 [hep-th].

Also, the publications previously cited have been presented in the following conferences [8–15]:

[8] F. Caporale, F. G. Celiberto, D. Gordo Gómez, A. Sabio Vera, and G. Chachamis, "Multi-jet production in the high energy limit at LHC," in *25th Low-x Meeting (Low-x 2017) Bari, Italy, June 13-17, 2017*. arXiv:1801.00014 [hep-ph].

[9] F. Deganutti, D. Gordo Gómez, T. Raben, and C. Royon, "Pomeron Physics at the LHC," *EPJ Web Conf.* **172** (2018) 06006, arXiv:1711.07514 [hep-ph].

[10] G. Chachamis, F. Caporale, F. G. Celiberto, D. Gordo Gómez, and A. Sabio Vera, "Azimuthal-angle Observables in Inclusive Three-jet Production," *PoS* **DIS2017** (2018) 067, arXiv:1709.02649 [hep-ph].

[11] F. Caporale, F. G. Celiberto, G. Chachamis, D. Gordo Gómez, and A. Sabio Vera, "Probing the BFKL dynamics in inclusive three jet production at the LHC," *EPJ Web Conf.* **164** (2017) 07027, arXiv:1612.02771 [hep-ph].

[12] F. Caporale, F. G. Celiberto, G. Chachamis, D. Gordo Gómez, and A. Sabio Vera, "Inclusive three- and four-jet production in multi-Regge kinematics at the LHC," *AIP Conf. Proc.* **1819** no. 1, (2017) 060009, arXiv:1611.04813 [hep-ph].

[13] G. Chachamis, F. Caporale, F. Celiberto, D. Gordo Gómez, and A. Sabio Vera, "Inclusive three jet production at the LHC for 7 and 13 TeV collision energies," *PoS* **DIS2016** (2016) 178.

[14] F. Caporale, F. G. Celiberto, G. Chachamis, D. Gordo Gómez, B. Murdaca, and A. Sabio Vera, "High energy effects in multi-jet production at LHC," in *24th Low-x Meeting (Low-x 2016) Gyongyos, Hungary, June 6-10, 2016*. arXiv:1610.04765 [hep-ph].

[15] G. Chachamis, F. Caporale, F. G. Celiberto, D. Gordo Gómez, and A. Sabio Vera, "Inclusive three jet production at the LHC at 7 and 13 TeV collision energies," arXiv:1610.01342 [hep-ph].

SIGNED: ..... DATE: .....

RESUMEN

A través del estudio de las Amplitudes de Dispersión hemos explorado diversos aspectos de la teoría de la interacción fuerte, Cromodinámica Cuántica (QCD), abarcando desde la física de los colisionadores de partículas y su fenomenología, hasta cuestiones más fundamentales, que apuntan hacia un entendimiento más profundo de la Teoría Cuántica de Campos. El cálculo de Amplitudes de Dispersión sirve como una herramienta para describir las interacciones entre partículas en experimentos de física de altas energías. Sin embargo en las últimas décadas se ha convertido en un campo propio debido a su importancia – no solo por la necesidad de predicciones más precisas para el Gran Colisionador de Hadrones (LHC), sino también por permitir desvelar nuevas estructuras matemáticas que permiten una descripción de estos procesos sin referencia alguna al concepto de espacio-tiempo.

El límite de altas energías es aún un gran reto en el estudio de la Cromodinámica Cuántica. Este régimen, caracterizado por la colisión a energías del centro de masas mayores que cualquier otra escala participando en el proceso, ofrece una descripción de dispersiones en colisiones de partículas de tipo difractivo o muy cercanas al eje del choque. Además, es un candidato sólido para el estudio de los constituyentes fundamentales de los hadrones cuando las densidades son altas. Si todas las escalas involucradas en el proceso son suficientemente altas, la fuerza de la interacción se hace más débil y se pueden describir mediante técnicas de teoría de perturbaciones. En este límite, se producen simplificaciones notables en las Amplitudes de Dispersión, permitiendo resumar los grandes logaritmos que dominan la expansión perturbativa usando la ecuación de Balitsky-Fadin-Kuraev-Lipatov (BFKL).

La primera parte de la tesis está dedicada a la aplicación del formalismo BFKL a la predicción y entendimiento de diferentes procesos en el LHC. Empezamos con la interpretación de los datos experimentales de Mueller-Navelet *jets* usando un procedimiento no estándar para controlar las correcciones a la expansión BFKL, conocido como veto en rapidez. El resultado de nuestras investigaciones nos permite determinar, por primera vez, el valor apropiado del nuevo parámetro de la teoría para aplicaciones fenomenológicas, así como sentar base para futuras predicciones de otros observables.

Dado el éxito del formalismo BFKL en la descripción fenomenológica de eventos tipo Mueller-Navelet *jets*, es de suma importancia proponer nuevos observables a un nivel más exclusivo para un estudio más conciso de las características del estado final de la colisión. Este trabajo nos permitirá fijar incertidumbres teóricas que siguen presentes cuando

se aplican correcciones a segundo orden perturbativo en el marco BFKL. Proponemos el estudio de procesos *multi-jet* inclusivos, que nos permiten definir una generalización de los observables basados en el ángulo azimutal. Definimos las herramientas que nos permiten calcular eventos con tres *jets* en las aproximaciones de *leading logarithmic accuracy* (LLA) y *next-to-leading logarithmic accuracy* (NLLA), con cortes cinemáticos realistas, y demostrando que los observables son estables y que se llega a un régimen en el cual éstos no cambian al elevar la energía de 7 a 14 TeV. En el caso de cuatro *jets*, sólo realizamos las predicciones en la aproximación LLA para motivar análisis experimentales y posponemos un análisis más preciso para el futuro. Al contrario que en el caso de tres *jets*, en este estudio no se llega a una región de estabilidad cuando se aumenta la energía.

Para concluir esta parte, exploramos una reacción diferente, la producción de pares Drell-Yan muy cerca del eje de colisión en el LHC. Este proceso cuenta con la ventaja de haber sido medido experimentalmente, con lo que nos permite comprobar la idea de factorización a altas energías. En este marco, la ecuación BFKL describe la estructura partónica del protón cuando la fracción de momento longitudinal de éste es pequeña, conocido como régimen de *small-x*. Usando un ajuste de datos de otro colisionador de partículas, HERA, y de otro proceso, Difracción Profundamente Inelástica (DIS), somos capaces de describir la producción de pares Drell-Yan a energías mucho más altas, confirmando que la ecuación BFKL en la aproximación NLLA puede dar una buena descripción de la evolución de la estructura del protón.

En la segunda parte de la tesis, nos sumergimos en aspectos más formales, investigando novedosos marcos para describir las Amplitudes de Dispersión que se centran en grados de libertad *on-shell*. La descripción habitual del régimen perturbativo se basa en el uso de diagramas de Feynman, con los que resulta realmente complicado calcular procesos en los que la multiplicidad es alta o en los que se requiere un gran número de correcciones cuánticas. Una de las características básicas de los diagramas de Feynman es que hacen uso de partículas virtuales, que no son físicas, y, por lo tanto, requieren la introducción de nuevos grados de libertad que eliminen las redundancias *gauge*. El hacer uso de esta descripción redundante, que usa grados de libertad no físicos, hace que el marco sea computacionalmente engorroso y no óptimo desde un punto de vista teórico. Una descripción alternativa, centrada en el uso de información *on-shell*, puede ofrecer un mayor entendimiento de la teoría y nuevas y poderosas herramientas. Esta forma de abordar el problema ha sido muy fructífera para la extensión máximamente supersimétrica de QCD, la teoría $\mathcal{N}$=4 Yang-Mills Supersimétrica (SYM), que puede considerarse un modelo simplificado de QCD. Por ejemplo, toda la información del sector gluónico de QCD a nivel de árbol se puede extraer de $\mathcal{N}$=4 SYM. La idea principal de enfoque *on-shell* parte de describir las Amplitudes de Dispersión sin referencia alguna a diagramas de Feynman o al Lagrangiano, usando solamente estados físicos. Los procesos de dispersión más simples, que involucran tres partículas, están fijados por las simetrías de la teoría, y sirven de ladrillos para amplitudes de mayor multiplicidad. Un hecho sorprendente, que en principio está sólo asociado al sector *planar* de $\mathcal{N}$=4 SYM, es que el marco permite construir el integrando de la Amplitud de Dispersión a todos los órdenes de un modo recursivo. Entonces, es

natural intentar extender estos métodos a teorías más generales, y nos centramos en el sector *planar* de teorías Yang-Mills con una cantidad arbitraria de supersimetría. Aquí es importante recalcar que el caso no supersimétrico corresponde exactamente al sector gluónico de QCD.

El siguiente paso de nuestro proyecto es la propuesta de un procedimiento para convertir los integrandos dados por diagramas *on-shell* en las Amplitudes. Comenzamos con la presentación de un esquema de regularización, que permite dar sentido a las divergencias que plagan las Teorías Cuánticas de Campos. El marco usado trabaja en cuatro dimensiones y la introducción de masas rompería simetrías importantes, con lo que las regularizaciones habituales como pueden ser regularización dimensional o Pauli-Villars no se pueden aplicar. Nuestra propuesta consiste en un esquema de regularización perfectamente ajustado al marco y, lo que es muy importante, no depende de la teoría específica bajo estudio. La formulación *on-shell* se caracteriza por el hecho de que, en general, una sola forma *on-shell* rompe localidad, *i.e.*, aparecen polos que no afectan al resultado final, y por lo tanto son espurios. De esta manera, es natural pensar en una prescripción de regularización que rompe localidad de una manera controlada, con la idea de recuperarla con la eliminación del parámetro de regularización, y de forma que todas las cantidades no locales corresponderán a términos del resultado final que dependen del esquema usado. Conseguimos esto mediante la deformación controlada del espacio de helicidades. Sin embargo, una procedimiento general para definir el contorno de integración desde principios primeros no se conoce aún.

El capítulo final está dedicado a la descripción de las Amplitudes de Dispersión en términos del Grassmanniano, una estructura matemática objeto de investigación en Combinatoria. Fue desarrollado inicialmente para el estudio de $\mathcal{N}$=4 SYM y nuestro trabajo consiste en extenderlo al sector gluónico de QCD. Para las teorías tenidas en cuenta, hemos estudiado la estructura de los diagramas *on-shell*, que es muy diferente a la del modelo máximamente supersimétrico, y el consecuente impacto en la geometría del Grassmanniano. Para ello, hemos llevado a cabo una primera exploración de la combinatoria asociada a dicha descripción y los nuevos diagramas que aparecen, destapando una relación entre los diagramas de teorías con poco o ningún grado de supersimetría y teorías no *planares*. De manera general, esta tesis ofrece una contribución fundamental a la idea de que cualquier Teoría de Campos puede ser descrita en términos de observables y cantidades físicas, sin tener que introducir grados de libertad no físicos y las consecuentes redundancias. A pesar de que en la literatura la mayor parte del progreso, especialmente a nivel de *loop*, se ha realizado en $\mathcal{N}$=4 SYM (que es una teoría muy especial), en esta tesis se han prolongado estas ideas a teorías más realistas.

Para concluir, en esta tesis hemos trabajado en la frontera de la Teoría Cuántica de Campos perturbativa. Tanto investigando fenómenos de dispersión en colisionadores de hadrones modernos, como buscando un entendimiento más profundo de la teoría misma.

Abstract

By studying Scattering Amplitudes we have explored several aspects in the theory for the strong interaction, Quantum Chromodynamics (QCD), ranging from the physics of particle colliders and its phenomenology, to more fundamental questions, which points, more generally, towards a deeper understanding of Quantum Field Theory. The calculation of Scattering Amplitudes serves as a tool to describe particle interactions in high-energy physics experiments, whereas in the past decades it has been raised as a field by its own importance – not only from the need of more accurate predictions for the Large Hadron Collider (LHC) but also from the unveiling of novel mathematical structures which provide a description of these processes without any reference to space-time.

The dynamics of the high-energy limit still offers a major challenge in the study of Quantum Chromodynamics. This regime, characterized by the scattering at center-of-mass energies larger than any other of the participating scales in the process, offers a description of forward and diffractive scattering in particle collisions, and it is a solid candidate for the study of the fundamental constituents of hadrons at large densities. When all scales in the scattering event are high enough, the strength of the interaction weakens and perturbative techniques are applicable. In this limit, noteworthy simplifications occur in the Scattering Amplitudes, allowing us to resum large logarithms dominating the perturbative expansion using the Balitsky-Fadin-Kuraev-Lipatov (BFKL) equation.

The first part of the thesis is devoted to the application of the BFKL framework to the prediction and understanding of different processes at the LHC. We start with the interpretation of Mueller-Navelet jets' experimental data using a non-standard procedure to tame the higher order corrections of the BFKL expansion, the rapidity veto. The outcome of our investigations allows us to determine the newly introduced parameter in phenomenological applications for the first time, and to set the ground for future predictions of other observables.

Given the successful BFKL phenomenology in Mueller-Navelet jet events it is important to propose new observables at more exclusive level to further study its associated final-state features. This is done in the subsequent three chapters. This work will allow us to fix some of the theoretical uncertainties still present at next-to-leading order (NLO) level in the framework. We introduce inclusive multi-jet production processes that allow us to define generalized azimuthal angle observables.We define the framework to calculate the three-jet observables at leading logarithmic accuracy (LLA) and next-to-leading logarithmic accuracy (NLLA) with realistic kinematical cuts, being able to show the stability of the

observables and realizing that we have entered an stability region in which the observables do not change when raising the energy from 7 to 14 TeV. In the four-jets case, we only perform the predictions at LLA to motivate experimental analysis, postponing a more accurate analysis for the future. Contrary to the former case, no stability region is observed when raising the energy.

To conclude this part, we move into a totally different reaction, forward production of Drell-Yan pairs at the LHC. The advantage of this process is that it has been already measured, serving as a playground to test the idea of high-energy factorization. In this setup, the BFKL equation describes the partonic structure of the proton at small longitudinal momentum fraction, or small-x. Using a fit to data from another particle collider, HERA, and process, Deep Inelastic Scattering (DIS), we are able to describe the Drell-Yan production at much larger energies, confirming that the BFKL at NLLA can provide a good description of the evolution of the proton structure.

In the second part of the thesis, we dive into more formal aspects, investigating new frameworks to describe Scattering Amplitudes focusing only on on-shell degrees of freedom. The general description of the perturbative regime relies on the Feynman diagrammatics, in which it is notably complicated to compute processes if the multiplicity is high or we require a larger number of quantum corrections. One of the basic features of Feynman diagrams is the fact that they encode virtual unphysical particles and, therefore, they require the introduction of new degrees of freedom that need to be eliminated via gauge redundancies. It is really uncomfortable, and computationally expensive, that our understanding depends on such a redundant description which makes use of unphysical degrees of freedom. An alternative description, based on the use of on-shell physical information, would offer both a deeper understanding of the theory itself and a new and powerful collection of tools. This approach has been pushed forward for the maximally sypersymmetric extension of QCD, the $\mathcal{N} = 4$ Supersymmetric Yand-Mills (SYM) theory, which can be considered a toy model for QCD – for example, it is possible to extract the tree-level amplitudes of the gluonic sector from it. The main idea of the on-shell approach is to describe Scattering Amplitudes with no reference whatsoever to Feynman diagrams and the Lagrangian, and in terms of physical states only. The simplest scattering processes, involving three particles, are fixed by the symmetries of the theory, and serve as the building blocks of higher multiplicity amplitudes. An impressive fact, in principle attached to the planar sector of $\mathcal{N} = 4$ SYM, is that this framework allows us to construct the all-loop integrand of the theory in a recursive way. Then, it is natural to attempt to extend these methods to more general theories, and we focus on the planar sector of Yang-Mills theories with an arbitrary amount of supersymmetry – where it is important to remark that the non-supersymmetric case is exactly the gluonic sector of QCD.

The next step in our work is to propose a procedure to convert the integrands given by on-shell diagrams into the integrated amplitudes. Such a step begins with the introduction of a regularization procedure, which allows us to make sense of the divergences that plague Quantum Field Theories. The framework used is purely four-dimensional and the introduction of masses will break important symmetries, thus the typical approaches such

as dimensional regularization or Pauli-Villars cannot be used. We provide a regularization proposal which is perfectly suited to the framework and, more importantly, is not theory dependent. The on-shell formulation is characterized by the fact that, in general, a single on-shell form breaks locality, *i.e.*, it presents poles which are not present in the final amplitudes and thus are spurious. Thus, it can be natural to think of a regularization prescription which breaks locality in a controlled way, with the idea to recover it upon removal of the regularization parameter, with the remaining non-local quantities reorganizing themselves into the scheme-dependent terms of the integrated object. We do this by introducing a controlled deformation of the helicity-space. However, a general procedure to define the integration contour from first principles it is not known yet, and a generic prescription is still lacking..

The final Chapter is dedicated to extend the Grassmannian – a mathematical structure which is a subject of frontier research in combinatorics – description for scattering processes, originally developed for planar $\mathcal{N} = 4$ SYM to the gluonic sector of QCD. For the class of theories under consideration, we studied the structure of on-shell diagrams, which are rather different to those in the maximally supersymmetric model, and its impact on the geometry of the Grassmannian. In doing so, we made a first exploration of the combinatorics tied to such a description and new diagrams related to it, uncovering a relation between less/non-supersymmetric theories and non-planar ones. More broadly, this thesis offers a fundamental contribution to the idea that any field theory can be described directly in terms of observables and in terms of physical data only, without the need of introducing unphysical degrees of freedom and redundancies to get rid of them. In the current literature, most of the progress, especially at loop level, was carried out for $\mathcal{N} = 4$ SYM – a theory with very distinct properties. This thesis further develops these ideas for more realistic theories.

To conclude, in this thesis have worked at the frontier of perturbative Quantum Field Theory, both investigating phenomena scattering phenomena at modern hadron colliders and searching for a deeper understanding of the theory itself.

Agradecimientos

A mis padres, que han sabido guiarnos y enseñarnos a pesar de todo.

CONVENTIONS

Natural units ($\hbar = c = 1$) are used throughout the text. Our convention for Minkowski metric is $g_{\mu\nu} = g^{\mu\nu}$ =diag$(+1,-1,-1,-1)$. The Levi-Civita density is defined with the convention $\varepsilon^{01234} = +1$ (this implies $\varepsilon_{01234} = -1$). Generic 4-vectors are written in Cartesian components as $V^\mu = (A^0, A^1, A^2, A^3) = (A^0, \vec{A}_T, A^3)$.

e and g will be employed, respectively, for the electromagnetic and strong couplings, with $\alpha \equiv \frac{e^2}{4\pi}$ and $\alpha_s \equiv \frac{g^2}{4\pi}$. We will also introduce the shorthand notation for the effective coupling constant $\bar{\alpha}_s \equiv \frac{\alpha_s N_c}{\pi}$, where N_c is the number of colors in QCD.

The Balitsky-Fadin-Kuraev-Lipatov (BFKL) Gluon Green Function (GGF) is normalized such that $\varphi(\vec{k}_A, \vec{k}_B, Y = 0) = \delta^2(\vec{k}_A - \vec{k}_B)$.

Useful color-algebra objects include the Casimir $C_F = \frac{N_C^2 - 1}{2N_C} = \frac{4}{3}$, the color factor associated with the gluon emission from a quark; $C_A = N_C = 3$ is the color factor associated with the gluon emission from a gluon and $T_R = \frac{1}{2}$ is the color factor for a gluon to split into a quark-antiquark pair. It will be convenient to write the one-loop beta function of the strong coupling as $\beta_2 \equiv \frac{\beta_0}{4N_C} = \frac{11N_C - 2N_F}{12N_C}$.

We will use extensively the following effective parton distribution function (PDF), defined as $f^\star\left(x_J, \mu_F\right) \equiv \frac{N_C}{C_F} f_g(x_J, \mu_F) + \sum_{i=q,\bar{q}} f_i(x_J, \mu_F)$.

We denote with caligraphic letters the amplitudes including the momentum-conserving delta function $\mathscr{M}$; being them related to the momentum-conservation stripped amplitude $\mathscr{M}(\varepsilon, p) = \delta^4\left(\sum_i p^{(i)}\right) \times M(\varepsilon, p)$.

The spinor-helicity formalism has the following conventions $p_\mu \to p_{a\dot{b}} = \sigma^\mu_{a\dot{b}} p_\mu$, where $\sigma^\mu_{a\dot{b}} = \left(\mathbb{1}_{a\dot{b}}, \vec{\sigma}_{a\dot{b}}\right)$ are the Pauli matrices. The angle and square brackets are defined as

$$\left\langle \lambda, \lambda' \right\rangle \equiv \epsilon^{ab} \lambda_a \lambda'_b = \lambda_a \lambda'^a \ , \ [\tilde{\lambda}, \tilde{\lambda}'] \equiv \epsilon^{\dot{a}\dot{b}} \tilde{\lambda}_{\dot{a}} \tilde{\lambda}'_{\dot{b}} = \tilde{\lambda}_{\dot{a}} \tilde{\lambda}'^{\dot{a}} , \tag{1}$$

using the Levi-Civita symbols ϵ_{ab} and $\epsilon_{\dot{a}\dot{b}}$, for which we take the convention $\epsilon_{12} = 1 = \epsilon_{\dot{1}\dot{2}}$ and $\epsilon^{12} = -1 = \epsilon^{\dot{1}\dot{2}}$. We raise and lower indices as $\lambda^a \equiv \epsilon^{ab} \lambda_b \Leftrightarrow \lambda_a \equiv \epsilon_{ab} \lambda^b$, using the same convention for the dotted indices.

Acronyms

$\overline{\text{MS}}$/MS (Modified) Minimal Subtraction Scheme.

(N)LLA (Next-to-) Leading Log Accuracy.

(N)LO (Next-to-) Leading Order.

(S)YM (Supersymmetric) Yang-Mills.

(p)QCD (Perturbative) Quantum ChromoDynamics.

BCFW Britto-Cachazo-Feng-Witten.

BFKL Balitsky-Fadin-Kuraev-Lipatov.

BK Balitsky-Kovchegov.

BLM Brodsky-Lepage-Mackenzie.

CCFM Ciafaloni-Catani-Fiorani-Marchesini.

CGC Color Glass Condensate.

DGLAP Dokshitzer-Gribov-Lipatov-Altarelli-Parisi.

DIS Deep Inelastic Scattering.

DLLA Double Leading Logarithmic Approximation.

IR Infra Red.

LHC Large Hadron Collider.

MN Mueller-Navelet.

MOM MOMentum (Subtraction Scheme).

MRK Multi-Regge kinematics.

PDF Parton Distribution Function.

QFT Quantum Field Theory.

uPDF Unintegrated Parton Distribution Function.

UV Ultra Violet.

Overview of the thesis

This thesis is divided in two parts, both of them explore several aspects of the Quantum Chromodynamics physics, ranging from its phenomenological aspects at hadron colliders to more formal questions related to the deeper structure of Quantum Field Theory.

Part I is devoted to the study of phenomenological aspects of QCD in the high energy limit. Our final goal is to find distinct signals of BFKL effects at present collider energies.

We start by introducing the notation, the formalism and the context of Part I in Chapter 1. After this we present our own work.

The presentation of our original work begins in Chapter 2, where we investigate a new form of controlling the higher order corrections in the BFKL perturbative expansion, using a so-called rapidity veto. The theoretical ideas are confronted with the experiment, by finding the best fit values of the proposed parameters. Based on [1].

Then, in Chapter 3, we start our journey into exclusive observables, generalizing Mueller-Navelet jets events introducing the tagging of a central, third jet. We propose new observables designed to enhance BFKL features and calculate some of them for LHC kinematics. Based on [2].

We extend this formalism in Chapter 4 to take into account NLLA corrections. In this study, we demonstrate that the previously proposed observables enjoy good perturbative stability and we quantify the different possible sources of theoretical uncertainty. In addition to that, we perform phase space integrations which are needed to make comparisons with the experimental data in a more direct way. Based on [3].

In Chapter 5, we consider processes in which four tagged jets are required in the final state, bringing us the possibility of exploring even more exclusive observables, and of comparing our predictions with double parton scattering experiments. Based on [4].

In Chapter 6 we investigate forward production of Drell-Yan pairs at the LHC. That allows us to test the idea of high-energy factorization, describing observables at the LHC using unintegrated gluon densities obtained from global fits to HERA data. Based on [5].

To conclude this part, we summarize our main results and describe future related work

in Chapter 7.

The focus in Part II shifts towards more formal aspects of QCD and the realm of scattering amplitudes in general.

In Chapter 8 we give an overview on Scattering Amplitudes methods that are not standard in most Quantum Field Theory textbook literature, mostly concerning on-shell methods in $d = 4$ space-time dimensions.

We give in Chapter 9 a regularization scheme suitable for on-shell forms, not restricting ourselves to any particular theory. We also give some ideas about how to integrate amplitudes in this scheme without making use of the usual momentum space. Based on [6].

In Chapter 10, for first time, we extend the ideas of on-shell diagrams and the Grassmannian formalism to theories with less supersymmetry than $\mathcal{N} = 4$ SYM. Based on [7]

In Chapter 11, we summarize the results of this last part and give some hints about future related projects.

Finally, in Part III the final conclusions are given in Spanish. Some computations and important notation are given in the Appendices: A, B and C.

Table of Contents

List of Figures

Figure **Page**

Part I

Phenomenological Aspects

CHAPTER 1

PRELIMINARIES

Quantum Chromodynamics (QCD), the Quantum Field Theory of quarks and gluons, was originally formulated in 1973 [16–18], and it is nowadays well established as the correct theory describing strong interactions. At present colliders, it is probably the part of the Standard Model with the most complicated phenomenology, since the asymptotic states measured at the experiments, hadrons, are not straightforwardly connected to the fundamental fields appearing in the Lagrangian. The theory evolves from having quarks and gluons as the best suited degrees of freedom at very short distances, to a confining theory of hadrons at large distances. The path towards QCD was illuminated with the discovery of a new quantum number, the color. Historically this new degree of freedom was a theoretical idea to resolve the spin-statistics paradox of the Δ^{++} baryon, which has a wave function symmetric in space, spin and $SU(3)$ flavor. However, as the constituents of the baryon, the quarks, are fermions, the wave function must be antisymmetric, to agree with the spin-statistics theorem. The solution to the paradox [19–21] was to add the color degree of freedom to the quarks, and make the wave function antisymmetric in it. As colored states are not detected in experiments we need to add an extra constraint, confinement, which states that only color singlet states can be isolated in nature.

QCD is a non-abelian gauge theory with color gauge group $SU(3)$, and this idea has been repeatedly checked experimentally. For example, in the measurement of the cross sections in $e^+e^- \to$ hadrons or $\pi^0 \to \gamma\gamma$ reactions. Another experimental hint for the correct theory to be a non-abelian Yang-Mills theory is the confirmation of Bjorken scaling [22], discovered in Deep Inelastic Scattering (DIS) experiments at SLAC, which pointed towards

the existence of point-like constituents inside the hadrons and the parton model and, what is crucial, to asymptotic freedom.

The use of Yang-Mills (YM) theories to describe nuclear interactions was thought incompatible for a long time, and there were important alternatives, as the S-matrix program [23–25]. This difficulty was overcome with the discovery of spontaneous symmetry breaking in the early 60's, with the discovery of asymptotic freedom in non-abelian YM theories [18, 26, 27] and, finally, the proof of renormalizability of non-abelian YM theories [28] in 1972-1973.

We would like to point out some of the key properties of the theory, as confinement and asymptotic freedom. In spite of the simple form of its Lagrangian, this interplay of perturbative versus nonperturbative physics makes QCD a challenging theory with a very rich phenomenology. For the long distance phenomena we have to rely on purely phenomenological models, QCD sum rules or on lattice calculations. Nonetheless, asymptotic freedom allows us to make sense of a perturbative treatment of short distance phenomena. However, every hard scale process is accompanied by nonperturbative effects associated to energy scales where the coupling constant is big. It is possible to disentangle these parts using factorization theorems, justified by Wilson's operator product expansion, which allow to describe the hard part within perturbative QCD by a fixed order expansion in the coupling. These theorems are strictly proven for a limited number of processes, but have shown its usability in a large number of processes.

1.1 Evolution equations and resummations

1.1.1 Renormalization group

The bare parameters entering the Lagrangian in a QFT are not, in general, physical values. When we want to compute observables beyond the leading order approximation, loop level diagrams appear in the Feynman diagrammatics. In a QFT, the Lorentz invariant generalization of the uncertainty principle allows for quantum fluctuations of arbitrary high energies, arising when the loop momenta go to infinity, and one often obtains divergent results. Then, we first need to regularize the theory in order to make sense of it. In renormalizable theories (all couplings have non-negative dimensions), there is a systematic procedure to obtain meaningful results from these divergent integrals. The key lies in the difference between the bare parameters of the theory and the renormalized ones, which can be linked to physical quantities.

Firstly, we need to suppress the high energy modes generating these ultraviolet (UV)

divergences, this is called regularization procedure. The most intuitive way is by means of the introduction of a cutoff scale Λ, parameterizing our ignorance on physics at scales above it. In practice, the physical results do not depend on the regularization procedure, so it is computationally convenient to break as few symmetries as possible to keep the simplicity at intermediate steps. Among them, dimensional regularization [28, 29], based on the observation that UV divergences are milder when reducing the number of space-time dimensions, and which allows to treat IR divergences as well, while respecting gauge invariance, is the most extended one.

Then we perform the transition from the bare quantities to the renormalized ones, being the latter free of divergences. We can redefine the fields and couplings in the Lagrangian as $\phi(\Lambda) = Z_\phi(\Lambda)\phi_R$, or equivalently add counterterms, where all the divergences of the bare quantities are absorbed in the $Z(\Lambda)$ factors. This procedure can be applied in a consistent way in perturbation theory, as can be studied in many QFT textbooks [30, 31].

After one regularization procedure is applied, we have introduced ambiguities in the way the finite parts of the counterterms are defined, and also an spurious dependence on the regularization parameter, Λ in this case. We need all observables at physical scales $\mu_R << \Lambda$ to be independent of the regularization parameters before safely taking the limit that removes the regularization, $\Lambda \to \infty$. The procedure that allows us to remove the regularization parameter leaving meaningful quantities is the renormalization group flow, pioneered by Wilson. It leads to two important observations. Firstly, we can describe low energy physics without knowledge of the true theory at really high energies, they are decoupled in that sense. Secondly, the coupling "constants" and masses are not constant anymore, but depend on the scale at which the processes are conducted.

Within the philosophy described before, we relate the renormalized n-point functions at the renormalization scale μ_R as

$$\Gamma_R^{(n)}\left(p^{(i)}, g_R, \mu_R\right) = Z^{-n/2}\left(g(\Lambda), \Lambda/\mu_R\right)\Gamma^{(n)}\left(p^{(i)}, g(\Lambda), \Lambda\right). \tag{1.1}$$

Imposing that the renormalized quantities at the scale μ_R do not depend on the regularization parameter Λ leads to the renormalization group equation

$$\left\{\frac{\partial}{\partial \log\Lambda} + \beta(g)\frac{\partial}{\partial g} - n\eta(g)\right\}\Gamma\left(p^{(i)}, g(\Lambda), \Lambda\right) = 0, \tag{1.2}$$

where we have defined the beta function $\beta(g) \equiv \frac{\mathrm{d}g}{\mathrm{d}\log\Lambda}$ and $\eta(g) \equiv \frac{1}{2}\frac{\mathrm{d}\log Z}{\mathrm{d}\log\Lambda}$. Equivalently, we derive the Callan-Symanzik equation for the renormalized quantities demanding the bare quantities to be independent of the renormalization scale μ_R at which we define the

physical quantities. It states the following

$$\left\{\frac{\partial}{\partial \log \mu_R}+\beta(g_R)\frac{\partial}{\partial g_R}+n\gamma(g_R)\right\}\Gamma_R^{(n)}\left(p^{(i)},g_R,\mu_R\right)=0\,, \tag{1.3}$$

where now we have that $\beta(g_R)\equiv\frac{\mathrm{d}g_R}{\mathrm{d}\log\mu_R}$ and the anomalous dimension of the field is $\gamma(g_R)\equiv\frac{1}{2}\frac{\mathrm{d}\log Z}{\mathrm{d}\log\mu_R}$. The equation can be solved as [32]

$$\Gamma_R^{(n)}\left(\lambda p^{(i)},g_R,\mu_R\right)=\lambda^{d_\Gamma}e^{\left[n\int_0^{\log\lambda}\mathrm{d}\log\lambda'\gamma(g_R(\lambda'\mu_R))\right]}\Gamma_R^{(n)}\left(p^{(i)},g_R(\lambda\mu_R),\mu_R\right), \tag{1.4}$$

where d_Γ is the mass dimension of the n-point function $\Gamma_R^{(n)}$, we have also defined the running coupling constant $g_R(\lambda\mu_R)$ as the solution to $\int_{g_R}^{g_R(\lambda\mu_R)}\frac{\mathrm{d}g'_R}{\beta(g'_R)}=\int_{\mu_R}^{\lambda\mu_R}\mathrm{d}log\mu'=\log\lambda$. From Eq. (1.4) we see that the rescaling of energies, in the limit in which we have neglected the couplings associated with masses, is driven by two effects. Observables do not scale simply as the mass dimension indicates, naive dimensional analysis breaks, since the presence of infinities forced us to introduce new dimensional scales (Λ or μ_R). Instead of having only the intuitive λ^{d_Γ} factor, we have an extra piece driven by the anomalous dimension γ. Also, the couplings have to run when calculated at different scales, according to the definition of the β function.

1.1.2 Asymptotic freedom

We will devote the next part to briefly explain the crucial concept of asymptotic freedom. Let us begin introducing the QCD lagrangian

$$\mathscr{L}=\bar{\psi}(i\not{D}-m)\psi-\frac{1}{4}F^a_{\mu\nu}F^{a,\mu\nu}+\mathscr{L}_{\text{gauge-fixing}}+\mathscr{L}_{\text{ghost}}\,, \tag{1.5}$$

The fields of quarks and gluons are represented by ψ and A respectively, F is the field strength tensor. The field strength tensor and the covariant derivative are defined as

$$F^a_{\mu\nu}=\partial_\mu A^a_\mu-\partial_\nu A^a_\mu+gf^{abc}A^b_\mu A^c_\nu\,, \tag{1.6}$$

$$D^\mu=\partial^\mu-igA^{a,\mu}T(R)^a\,, \tag{1.7}$$

where $T(R)$ depends on the representation of the field to which the operator acts. $a=1,\ldots,N_C^2-1$ is the color index, f^{abc} are the $SU(N_C)$ structure constants and N_C the number of colors in the theory. We do not need to discuss the gauge-fixing and ghost parts of the theory, introduced to remove the unphysical degrees of freedom associated with gauge redundancies of the theory.

Once we have the Lagrangian, we can obtain the Feynman rules and start computing observables, until we go to loop level and hit ultraviolet (UV) divergences. In order to keep gauge invariance manifest, it is more convenient to regularize the theory using dimensional regularization, in which the number of space-time dimensions is analytically continued from 4 to $D = 4 - 2\epsilon$. Now, the divergences are transformed into poles in the variable ϵ, Then, when the requisite of renormalizability is satisfied the potentially divergent terms are of the form of the most general terms in the Lagrangian compatible with the original field content, the true symmetries of the theory and renormalizability, with couplings dependent on ϵ. These divergent terms can be eliminated by adding counterterms to the Lagrangian [30]. Equivalently, this can be done redefining the fields and couplings in the Lagrangian

$$\begin{aligned} \psi &= Z_2^{1/2}(\epsilon)\psi_R \\ A^\mu &= Z_3^{1/2}(\epsilon)A_R^\mu \\ g &= Z_g(\epsilon)\mu_R^\epsilon g_R \\ m &= Z_m(\epsilon)m_R\,, \end{aligned} \tag{1.8}$$

where the renormalization scale μ_R has been introduced to keep the renormalized coupling dimensionless, but we have to remember that the bare fields do not depend on this new scale. And it is useful to define $Z_1 \equiv Z_g Z_2 Z_3^{1/2}$.

In the $\overline{\text{MS}}$ scheme, we choose the Z's to cancel off the poles in ϵ, and nothing more, so they have the following form

$$Z = 1 + \sum_{n=1}^{\infty} \frac{a_n(\alpha_s)}{\epsilon^n} \tag{1.9}$$

with $\alpha_s = \frac{g_R^2}{4\pi}$ is the coupling constant in the $\overline{\text{MS}}$ scheme. We are interested in the renormalization of the coupling constant, so we focus on Z_g. At one loop order the calculation can be done by hand, but we refer to [33] for a detailed computation. The final result is

$$Z_g = \frac{Z_1}{Z_2 Z_3^{1/2}} = 1 - \frac{b_0 \alpha_s}{2\epsilon} \tag{1.10}$$

where b_0 defined as

$$b_0 \equiv \frac{1}{2\pi}\left[\frac{11}{6}C_A - \frac{2}{3}N_F T_R\right] \tag{1.11}$$

where we have that N_F is the number of quark favors, $C_A = N_C$ and $T_R = \frac{1}{2}$ are Casimir operators of $SU(N_C)$.

The renormalization group equations are obtained imposing that the bare quantities do not depend on the scale μ_R. In particular, for the coupling we have

$$\frac{\mathrm{d}g}{\mathrm{d}\mu_R} = 0 = \frac{\mathrm{d}}{\mathrm{d}\mu_R}\left(Z_g \mu_R^{\epsilon} g\right) \Rightarrow \frac{\mathrm{d}}{\mathrm{d}\log\mu_R^2}\left(\log\left(\alpha_s \mu_R^{2\epsilon} Z_g^2\right)\right), \tag{1.12}$$

Performing the derivative and expanding in ϵ we obtain

$$\frac{\mathrm{d}\log\alpha_s}{\mathrm{d}\log\mu_R^2} = -b_0\alpha_s\,. \tag{1.13}$$

We obtain the renormalization of the coupling at one loop as

$$\alpha_s(\mu_R) = \frac{\alpha_s(\mu_0)}{1 + b_0\alpha_s(\mu_0)\log\left(\frac{\mu_R^2}{\mu_0^2}\right)}\,. \tag{1.14}$$

In terms of the position of the infrared pole Λ_{QCD}, where the coupling goes to infinity, we get the expression

$$\alpha_s(\mu_R) = \frac{1}{b_0\log\left(\frac{\mu_R^2}{\Lambda_{\mathrm{QCD}}^2}\right)}\,. \tag{1.15}$$

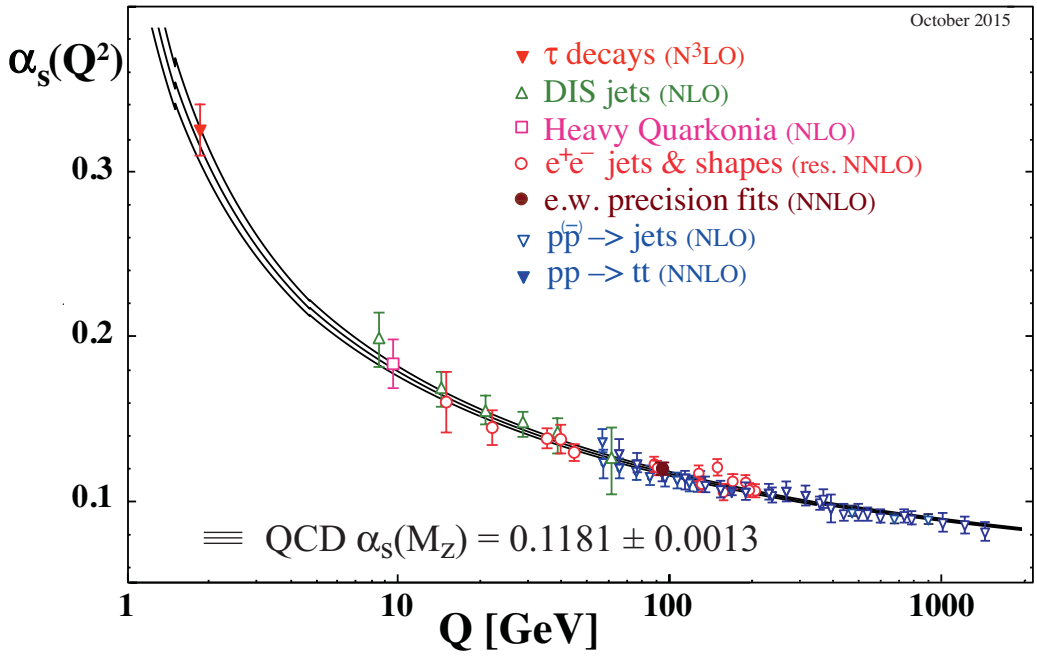

Figure 1.1: Summary of measurements of α_s as a function of the energy scale Q. The respective degree of QCD perturbation theory used in the extraction of α_s is indicated in brackets (NLO: next-to-leading order; NNLO: next-to-next-to leading order; res. NNLO: NNLO matched with resummed next-to-leading logs; N3LO: next-to-NNLO). Extracted from [34].

This result is known as the running of the coupling and it indicates that, at high energies, the coupling tends to zero. Quarks and gluons can be considered as asymptotically free at very small distances, we have the important signature of asymptotic freedom. It is crucial that b_0 is positive, something that cannot be obtained in abelian YM theories, as Quantum Electrodynamics. It is a direct consequence of this that we can trust perturbative calculations at high momentum transfer, since the coupling is small at these scales. For example, the coupling in the $\overline{\text{MS}}$ scheme at energies of the order of the Z boson mass is equal to $\alpha_s(M_Z) = 0.1181(11)$, as given by the Particle Data Group Collaboration [34]. However, at low energies, the same equation dictates that α_s becomes large. At some point the strong coupling becomes large enough to invalidate perturbation theory and the very same calculation leading to Eq. (1.15). Considering that the typical factor of loop calculations is $\frac{\alpha_s}{4\pi}$, we may estimate that perturbation theory is expected to fail at scales around the mass of the strange quark $\mu_R \approx 200$ MeV, that is of the order of Λ_{QCD}. To conclude, we see that asymptotic freedom in closely tied to infrared slavery.

In general, the coupling constant α_s is follwing renormalization group equation in the $\overline{\text{MS}}$ scheme

$$\frac{\mathrm{d}\alpha_s}{\mathrm{d}\log\mu_R^2} = \beta(\alpha_s) = -\left(b_0\alpha_s^2 + b_1\alpha_s^3 + b_2\alpha_s^4 + b_3\alpha_s^4 + \cdots\right) \tag{1.16}$$

where $b_0 = \frac{11C_A - 4N_F T_R}{12\pi}$ is the one loop β function coefficient, that we derived earlier. The two loops coefficient is $b_1 = \frac{17C_A^2 - N_F T_R(10C_A + 6C_F)}{24\pi^2}$ and the three loops one $b_2 = \frac{2857 - \frac{5033}{9}N_F + \frac{325}{27}N_F^2}{128\pi^3}$ [34]. The four loops coefficient was computed in Refs. [35, 36] and, recently, the five loops one was calculated in Ref. [37]. Only the first two terms are independent of the renormalization scheme for negligible masses or mass independent schemes[1] as $\overline{\text{MS}}$, something that we will discuss later in Section 1.1.3.

1.1.3 Renormalization scale invariance at perturbative level

Now that we have reviewed the basics of the renormalization group, let us apply it to an observable which has been calculated perturbatively, as it is usual at practice. A pedagogical explanation of the concept of renormalization group and its implications in perturbation theory can be found in Ref. [40], where some of the arguments applied in this section can be found with a more detailed explanation. To be concrete, we consider the expansion of an observable which is dimensionless and only depends on one energy scale, Q, the observable have a perturbative expansion given by

$$R(Q) = R\left(\alpha_s(\mu_R), \frac{Q}{\mu_R}\right) = \sum_{n=0}^{\infty} r^{(n)}\left(\frac{Q}{\mu_R}\right)\alpha_s^n(\mu_R). \tag{1.17}$$

As we saw before, the structure of the r_n functions is constrained by the renormalization group equations, which imposes that physical observables do not depend on the choice of the renormalization scheme, but this only holds exactly if we calculate them to all orders. In practice we deal with an n-th order truncated expansion $R^{(n)}$ of the observable, and we can only state that

$$\frac{\mathrm{d}R^{(n)}}{\mathrm{d}\log\mu_R^2} = \mathcal{O}\left(\alpha_s^n\right). \tag{1.18}$$

[1] For mass dependent schemes, even the first coefficients depend on the masses. In mass independent schemes, the β and γ functions do not depend on the masses of the particles, which is in contradiction with the Appelquist-Carazzone decoupling theorem [38]. Usually, we introduce the notion of active flavors by hand, where we only consider flavors with mass less than the scale in the evolution equations, see the lecture notes of effective field theories in [39].

Looking at Eq. (1.16), the running of α_s starts at α_s^2, *i.e.*, $\beta(\alpha_s) = -b_0\alpha_s^2 + \mathcal{O}\left(\alpha_s^3\right)$. Taking that into account we can expand Eq. (1.18) up to α_s^2 order as

$$\left\{\frac{\partial}{\partial \log \mu_R^2} + \beta(\alpha_s)\frac{\partial}{\partial \alpha_s}\right\} R^{(2)} \simeq \frac{\partial r^{(0)}}{\partial \log \mu_R^2} + \alpha_s\left(\frac{\partial r^{(1)}}{\partial \log \mu_R^2}\right) + \alpha_s^2\left(\frac{\partial r^{(2)}}{\partial \log \mu_R^2} - b_0 r^{(1)}\right) + \cdots \simeq 0\,. \tag{1.19}$$

That result implies that the first two coefficients do not depend on the ratio of scales $\frac{Q}{\mu_R}$, and that the second coefficient satisfies the differential equation

$$\frac{\partial r^{(2)}}{\partial \log \mu_R^2} - b_0 r^{(1)} = 0 \tag{1.20}$$

that we can easily solve in term of constant terms $C^{(n)}$ as

$$r^{(2)}\left(\frac{Q}{\mu_R}\right) = b_0 C^{(1)} \log \frac{\mu_R^2}{Q^2} + C^{(2)}\ ,\ r^{(1)} = C^{(1)}\,. \tag{1.21}$$

We have unveiled the scale dependence of the truncated observable as

$$R^{(2)}\left(\alpha_s\left(\mu_R\right), \frac{Q}{\mu_R}\right) = C^{(0)} + \alpha_s(\mu_R)C^{(1)} + \alpha_s^2(\mu_R)C^{(1)} \log \frac{\mu_R^2}{Q^2} + \alpha_s^2(\mu_R)C^{(2)} + \cdots\,. \tag{1.22}$$

The important lesson to take home is that we can establish the scale dependent term of the two loops calculation without having to carry out the calculation itself. It can be the case that the scales μ_R and Q differ largely and it compensates for the smallness of the coupling, that makes a piece of the order two contribution to be effectively order one, numerically breaking the condition from Eq. 1.18. To recover the renormalization scale invariance, we should be able to resum all these logarithms to all orders, in particular we have that the n-th coefficient satisfies

$$r^{(n)}\left(\frac{Q}{\mu_R}\right) = C^{(1)}\left(b_0 \log\left(\frac{\mu_R^2}{Q^2}\right)\right)^{n-1} + \text{terms subleading in} \log\left(\frac{\mu_R^2}{Q^2}\right), \tag{1.23}$$

which allow us to rewrite Eq. (1.22) as

$$R^{(2)}\left(\alpha_s\left(\mu_R\right), \frac{Q}{\mu_R}\right) = C^{(0)} + \frac{\alpha_s(\mu_R)}{1 - b\,\alpha_s(\mu_R)\log\frac{\mu_R^2}{Q^2}} C^{(1)} + \alpha_s^2(\mu_R)C^{(2)} + \cdots\,, \tag{1.24}$$

that we should compare with the running of the coupling constant calculated in Eq. (1.14). The argument can be extended to all orders in the perturbative calculation to resum all the higher orders by setting the scale of the coupling to Q

$$R\left(\alpha_s(\mu_R), \frac{Q}{\mu_R}\right) = R(Q) = \sum_{n=0}^{\infty} C^{(n)} \alpha_s^n(Q)\,. \tag{1.25}$$

The coefficients $C^{(n)}$ must be calculated for each observable through explicit calculation, and now the truncation at a given order is effectively neglecting $\mathcal{O}\left(\alpha_s^{n+1}\right)$ terms, since the higher order terms are not larger than the leading order ones. To conclude, a wrong choice of the renormalization scale leads to a bad convergence of the perturbative expansion, and therefore a large deviation of the truncated expression from the exact one, which we are able to compute in exceptional cases in QFT.

Given the importance of choosing the most suitable renormalization scheme for comparing to data, we should know how to transform our results from one scheme to another. This will be specially relevant when using Momentum Substraction (MOM) schemes [41]. Let us consider we start with a given renormalization scheme (RS), and we want to transform observables to a new one $\overline{\text{RS}}$, whose variable we will denote by bars. We will have a relationship among the couplings[2]

$$\bar{\alpha}(\bar{\mu}) = \alpha(\mu)\left\{1 + \sum_{n=1}^{\infty} \rho_n\left(\frac{\bar{\mu}}{\mu}\right)\alpha^n(\mu)\right\} \tag{1.26}$$

To simplify the calculations, we are considering results to next-to-leading order in the coupling α

$$R^{(2)}\left(\alpha\left(\mu\right), \frac{Q}{\mu}\right) = r^{(0)} + \alpha_s(\mu) r^{(1)} + \alpha_s^2(\mu) r^{(2)} + \cdots, \tag{1.27}$$

where $\alpha(\mu)$ is the running coupling using the truncated renormalization group equation

$$\frac{\mathrm{d}\,\alpha(\mu)}{\mathrm{d}\log\mu^2} = -b_0\alpha^2 - b_1\alpha^3\,. \tag{1.28}$$

At this order Eq. (1.28) is invariant under the following transformation [41]:

$$\mu \to \bar{\mu}\ ,\ \alpha \to \bar{\alpha} = \alpha(1 + C\,\alpha)\,, \tag{1.29}$$

with the factor $C = -b_0 \log\frac{\bar{\mu}^2}{\mu^2}$. As a direct consequence, we can implement any change in the renormalization scheme as a rescaling of the renormalization scale μ, or making the opposite rescaling to the QCD scale $\bar{\Lambda}_{\text{QCD}} = \Lambda_{\text{QCD}} e^{\frac{C}{2b_0}} = \Lambda_{\text{QCD}}\frac{\mu}{\bar{\mu}}$. This result only hold at second order, for a detailed derivation we refer to [42] and to Ref. [41], where the MOM schemes are studied.

1.1.4 Factorization

There are only a few observables, like hadron production cross section in e^+e^- annihilation or the total width of the Z boson, which are independent of nonperturbative effects and can

[2] In the following we omit the index R to denote renormalized quantities.

be calculated in perturbation theory[3]. In QCD, the presence of jets makes the entanglement of perturbative and nonperturbative physics omnipresent, and the importance of separating them has been realized since the conception of the parton model.

The main assumption of the parton model, which considers hadrons as a collection of pointlike constituents called partons is that we can neglect parton interactions during the time they are probed. This is possible because we are dealing with two very different scales. A short distance region, or equivalently a hard scale Q, of the order of the jet transverse energy ~ 10 GeV, which describes the primary scattering between the partons. We also have a long distance region, characterized by the hadroninization or QCD scale Λ_{QCD}, which describes how the scattering partons splits from the parent hadrons and how the scattered partons hadronize.

To have an intuitive picture of how this factorization shows up in the parton model picture, let us apply it to a hadron scattering. If we are situated in the center-of-mass frame, and we have a very high energy scattering process there are some kinematical effects that apply. Each hadron is highly boosted, being Lorentz contracted in the collision axis and therefore looking like a pancake. Accordingly, the time it takes a parton within one hadron to pass though the other hadron will be Lorentz contracted. Parton interactions within each hadron are time dilated, making the time scale of the interaction of two partons within the same hadron much longer than the time scale of going through the other hadron. Therefore, each parton sees the other hadron as a frozen distribution of noninteracting partons. Also, the momentum transfer Q is large, so each parton probes a region of size $\sim \frac{1}{Q}$ on the other hadron, so it will probe only one parton unless we are reaching the saturation regime.

Then we can describe the scattering process of two hadrons as the convolution of two contributions separating the two scales, as it is detailed in Ref. [43], with the following formula

$$\sigma = \sum_{ab} \int_{\zeta_A}^{1} \mathrm{d}x_A \int_{\zeta_B}^{1} \mathrm{d}x_B \, f_{a/A}\left(x_A, \mu_F^2\right) f_{b/B}\left(x_B, \mu_F^2\right) \hat{\sigma}_{ab}\left(\frac{\zeta_A}{x_A}, \frac{\zeta_B}{x_B}, \alpha_s(\mu_F^2), \frac{Q^2}{\mu_F^2}\right), \tag{1.30}$$

where a, b are summed over the parton species and flavors, ζ_A, ζ_B are parameterized by the kinematical variables of the produced hadrons or jets, $\hat{\sigma}$ is the cross section of the hard process, which can be computed through perturbation theory, $f_{a/A}\left(x_A, \mu_F^2\right)$ is the probability that a parton a is found in hadron A carrying a fraction x_A of its longitudinal momentum. The quantities $f_{a/A}\left(x_A, \mu_F^2\right)$ are called parton distribution functions (PDFs), and they are

[3] And this is true when we neglect terms suppressed by powers of energy.

universal, *i.e.*, they do not depend on the particular hard process considered, encode all the nonperturbative physics and must be inferred from the experiments.

The separation between low momentum and high momentum physics is done through the factorization scale μ_F, which is only constrained by the fact that we need a small parameter in the perturbative expansion. This role is played by the strong coupling constant $\alpha_s(\mu_F^2)$, and therefore the factorization scale must be hard, *i.e.*, $\mu_F >> \Lambda_{\rm QCD}$, to ensure that the truncation of the expansion makes sense.

The factorization formula in Eq. (1.30) is valid in the limit $Q^2 \to \infty$, keeping $x_{A|B}$ fixed. For finite values of Q, the cross section is expanded in powers of $\frac{\Lambda_{\rm QCD}}{Q}$, being Eq. (1.30) the leading term. In the language of the operator product expansion, the leading term is called the leading twist contribution, which factorizes. The remainder of the expansion, called the higher twist, does not usually factorize.

Then we proceed to calculate the partonic cross section $\hat{\sigma}$, where we can neglect the masses and transverse momenta of the partons, since they are of order $\frac{\Lambda_{\rm QCD}}{Q}$, belonging to the higher twist corrections. As we discussed in Sec. 1.1.1, we encounter UV divergences that are subtracted away by the renormalization prescription, introducing the renormalization scale μ_R. In addition to that, we have the infrared (IR) divergences [4] , which origin can be from collinear (generated when we produce collinear masssless particles in a vertex) and soft (appearing when a particle momentum vanishes). After including all the real and virtual radiative corrections to a given order in the perturbative expansion, the soft divergences cancel out. We still have the collinear divergences, but they can be shown to be universal, *i.e.*, independent of the hard process $\hat{\sigma}$ we are calculating. They are produced by the collinear emissions from each parton on its evolution towards the hard scattering, which increase the absolute value of the parton virtuality, being the evolution space-like. Since these collinear parton evolutions are universal we factorize them into the PDFs.

We have now that the PDFs and the partonic cross section depend on the renormal-

[4] In any observed process there is an indefinite emission of soft photons and gluons, which experimentally cannot be separated from the accompanying charged particles. In QED the Bloch-Nordsieck [44] ensures that the IR divergences cancel out when summing over all the degenerate final states. In QCD the situation is more complicated due to the self-interacting nature of the gluon. In that case, we need to sum over all the initial and final degenerate states in order to obtain a IR divergences free answer, as ensure the Kinoshita-Lee-Nauenberg (KLN) theorem [45, 46]. This theorem ensures that one gets finite answers for completely inclusive processes, i.e. those in which one does not register the momenta of partons in the initial or final state, like the total hadronic cross section for e^+e^- annihilation, the jet cross section with fixed resolution in angle and energy, etc. But one has to ensure that we are dealing with IR-safe observables. When one or several partons are identified by measuring their momenta, the KLN theorem no longer applies, and the perturbative calculation presents large logarithms due to the collinear singularities. However, these logarithms can be resummed. In this kind of processes, soft singularities coming from virtual corrections and real emissions still cancel. This last class of processes includes Deep Inelastic Scattering (where the active parton momenta is known from the measurement of the lepton), or the cross section for jets with fixed invariant mass of the observed particles.

ization and factoriztion scales [5] , but their convolution, which is observable, does not. We argued that for the renormalization scale μ_R in Sec. 1.1.1. In the case of the factorization scale μ_F, this is an artificial variable describing the virtuality at which we stop the collinear parton evolution at. Applying this condition to Eq. (1.30), we obtain Renormalization Group equations for the partonic cross section and for the PDFs [43]. In particular, for the PDFs we obtain

$$\frac{\mathrm{d}f_{a/A}\left(x,\mu_F^2\right)}{\mathrm{d}\log\mu_F^2} = \frac{\alpha_s(\mu_F^2)}{2\pi}\sum_c\int_x^1\frac{\mathrm{d}\zeta}{\zeta}P_{ac}\left(\zeta,\alpha_s(\mu_F^2)\right)f_{c/A}\left(\frac{x}{\zeta},\mu_F^2\right), \tag{1.31}$$

the Dokshitzer-Grivob-Lipatov-Altarelli-Parisi (DGLAP) evolution equations, firstly derived in Refs. [47–50]. These equations determine the scale dependence of the PDFs, allowing us to determine how they evolve as the scale varies, once they have been obtained experimentally at a given scale. The DGLAP equation also describes the evolution of the parton c of fraction ζ of the longitudinal momentum of the parent hadron and transverse size less than $1/\mu_F$, within the parton a of momentum fraction x and transverse momentum and mass equal to zero. The functions P_{ac} are the splitting functions, and should be computed in perturbation theory in QCD.

The DGLAP equations resum the collinear logarithms in the evolution at a given accuracy, determined by the order at which the splitting functions are calculated. At LO (or one loop), the resolution of the DGLAP equations leads to the leading logarithmic accuracy (LLA) evolution of the PDFs, and so on. To be consistent, the running of the coupling constant α_s must be determined at the same accuracy. As we studied in Sec. 1.1.3, if we truncate the perturbative expansion for the observable, its independence with respect to variations of the scale no longer holds. Therefore, in a fixed order expansion of the observable to order $\mathcal{O}\left(\alpha_s^n\right)$, we will have $\mathcal{O}\left(\alpha_s^{n+1}\right)$ terms depending on the unphysical scale μ_F.

[5] The factorization scale separates grosso modo the perturbative and non-perturbative regimes. The same way it happened with renormalization, the factorization scale dependence of the PDFs should cancel exactly with that of the coupling, as it is not a physical scale. However, without having computed corrections to all orders, it is necessary to take an specific choice for μ_F To avoid the appearance of large logarithms it is usual to set both the factorization and renormalization scales to $\mu_F = \mu_R \equiv \mu$, though one should remember that the two scales are not conceptually the same.

1.2 Deep inelastic scattering

A perfect scenario to test the idea of factorization discussed above, and to make a connection to small-x physics is via the study of deep inelastic scattering (DIS). Since collinear divergences are universal, we can study them in that process to determine the PDFs, and afterwards use them in other processes. If we consider electron-proton scattering at center-of-mass energies above the mass of the proton, the proton can start to break apart. For example, at high enough energies, we can have the reaction $e^- p^+ \to e^- p^+ \pi^0$. At very high energies, the proton breaks apart completely, but the physics simplifies in this deeply inelastic regime. Although the hadronic nature of the scattering introduce nonperturbative physics, we can derive relations between what will be measured in different experiments.

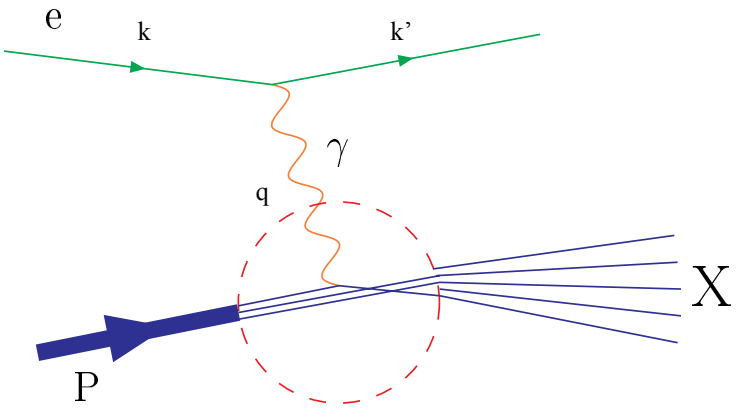

Figure 1.2: Kinematics of electron-proton DIS process, where the pronton completely breaks up. k and P are known from the experimental setup, and k' is obtained by measuring the deflected lepton.

It is standard to express the kinematical variables in terms of the following Lorentz invariant quantities

$$
\begin{aligned}
& s \equiv (P+k)^2 && \text{center-of-mass energy squared;} \\
& Q^2 \equiv -q^2 = -(k-k')^2 && \text{virtuality of the photon;} \\
& W^2 \equiv (P+q)^2 = m_P^2 + 2\nu - Q^2 && \text{invariant mass of the hadronic state } X; \\
& \nu \equiv \frac{P\cdot q}{m_P} && e^- \text{ energy loss in the proton } P \text{ rest frame;} \\
& x \equiv \frac{Q^2}{2P\cdot q} = \frac{Q^2}{2m_P\nu} && \text{Bjorken-x variable;} \\
& y \equiv \frac{P\cdot q}{P\cdot k} && \text{fractional energy transferred in } P \text{ rest frame.}
\end{aligned}
\tag{1.32}
$$

In the deep inelastic electron-proton scattering, the interaction can be mediated via a very energetic virtual photon or Z boson, with large transverse momentum. For simplicity, we are going to neglect the Z boson contribution, which is not needed in order to explain the importance of the collinear factorization, and it is a safe approximation for in the case $Q^2 << M_Z^2$. When $Q^2 >> m_P^2$, the virtual photon does not fluctuate through strong interactions (*e.g.*, into a ρ meson) and it probes the hadron through the electromagnetic coupling. The fact that in DIS $W^2 \geq m_P^2$ implies that $0 \leq x \leq 1$, being the limit $x = 1$ the elastic scattering. We also have, if we neglect the mass of the electron, the following relationship

$$xy = \frac{Q^2}{s - m_P^2} \simeq \frac{Q^2}{s} \ , \ 0 \leq y \leq 1 \, . \tag{1.33}$$

The inclusive cross section, in which we sum over all the possible hadronic final states, is given by

$$E' \frac{\mathrm{d}\sigma}{\mathrm{d}^3 \vec{k}'} = \sum_{\{X\}} \int \frac{\mathrm{d}\Pi_X}{32\pi^3 (s - m_P^2)} (2\pi)^4 \delta^4 \left(p + k - k' - p_X\right) \left\langle |\mathscr{A}_X|^2 \right\rangle \tag{1.34}$$

where Π_X denotes the phase space of the hadronic state X, and the squared amplitude is averaged over spin polarization of the initial state and summed over those in the final state. The amplitude is decomposed into an electromagnetic and a hadronic parts as

$$\mathscr{A}_X = \frac{ie}{q^2} \left[\bar{u}\left(\vec{k}'\right) \gamma^\mu u\left(\vec{k}\right) \right] \left\langle X \right| J_\mu(0) \left| P(P) \right\rangle \, , \tag{1.35}$$

where $\bar{u}\left(\vec{k}'\right)$, $u\left(\vec{k}\right)$ are the electron spinor states, J_μ is the hadron electromagnetic current coupling to the photon and $|P(P)\rangle$ denotes the state of the proton. We can separate the leptonic and the hadronic parts in the differential cross section as

$$E' \frac{\mathrm{d}\sigma}{\mathrm{d}^3 \vec{k}'} = \frac{1}{32\pi^3 (s - m_P^2)} \frac{e^2}{Q^4} 4\pi L^{\mu\nu} W_{\mu\nu} \, , \tag{1.36}$$

where the leptonic tensor is[6]

$$L^{\mu\nu} \equiv \frac{1}{2} \mathrm{Tr}\left[\not{k}' \gamma^\mu \not{k} \gamma^\nu \right] = 2\left(k'^\mu k^\nu + k'^\nu k^\mu - k \cdot k' g^{\mu\nu} \right) \tag{1.37}$$

, where the factor 1/2 comes from averaging over the initial electron spin, and it is evident that $L_{\mu\nu} = L_{\nu\mu}$.

[6] We have neglectec the electron mass.

The hadronic tensor $W^{\mu\nu}$ its the rate for the$\gamma^\star + P \to$ anything, given by the amplitude squared $\left|\mathscr{A}\left(\gamma^\star + P \to X\right)\right|^2$, integrated over all the phase space for all final state particles X:

$$\begin{aligned} 4\pi W^{\mu\nu} &\equiv \sum_{\{X\}} \int \mathrm{d}\Pi_X \, (2\pi)^4 \delta^4(p+q-p_X) \left\langle \left\langle P(P) \middle| J^{\dagger\mu}(0) \middle| X \right\rangle \left\langle X \middle| J^{\mu}(0) \middle| P(P) \right\rangle \right\rangle \\ &= \int \mathrm{d}^4 z \, e^{iq\cdot z} \left\langle \left\langle P(P) \middle| J^{\dagger\mu}(z) J^{\mu}(0) \middle| P(P) \right\rangle \right\rangle . \end{aligned} \tag{1.38}$$

Since final states are integrated over, $W^{\mu\nu}$ can depend only on P and q, and the invariants we can form from them, Q^2 and x. In unpolarized scattering, it must be symmetric [7] . By the Ward identity imposing gauge invariance, it should satisfy $q_\mu W^{\mu\nu} = 0$. Thus, we can parametrize the hadronic tensor in terms of two scalar structure functions as

$$W^{\mu\nu}\left(x, Q^2\right) = \left(-g^{\mu\nu} + \frac{q^\mu q^\nu}{q^2}\right) F_1\left(x, Q^2\right) + \frac{\tilde{P}^\mu \tilde{P}^\nu}{P\cdot q} F_2\left(x, Q^2\right) \;;\; \tilde{P} \equiv P + \frac{q}{2x} . \tag{1.39}$$

Contracting the two tensors the differential cross section reads

$$\frac{\mathrm{d}\sigma}{\mathrm{d}x\,\mathrm{d}y} = \frac{4\pi\alpha_{\mathrm{e}}^2 s}{Q^4} \left[xy^2 F_1\left(x, Q^2\right) + \left(1 - y - \frac{xym_P^2}{s}\right) F_2\left(x, Q^2\right) \right] . \tag{1.40}$$

Given that expression, we only need to know the momenta of the incoming and outgoing electrons, and not anything about the final hadronic state X. We can completely determine the structure functions $F_i\left(x, Q^2\right)$ by measuring the energy and angular dependence of the outgoing electron. Notice that in the lab frame, in which the proton is at rest, $y = 1 - \frac{E'}{E}$ and $x = \frac{Q^2}{2m_P(E-E')}$ and $Q^2 = 2\left(EE' - \vec{k}\cdot\vec{k}'\right)$.

[7] Also, only the symmetric part contributes because it is contracted with $L^{\mu\nu}$.

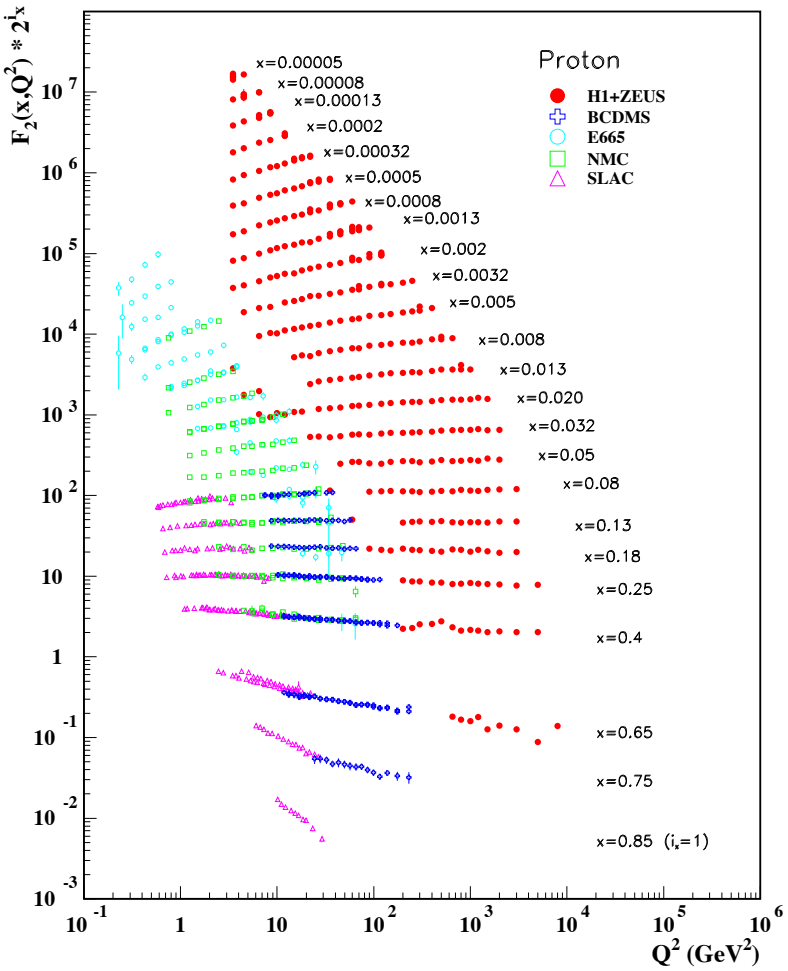

Figure 1.3: The proton structure function F_2 measured in electromagnetic scattering of electrons and positrons on protons (collider experiments H1 and ZEUS for $Q^2 \geq 2\text{GeV}^2$), in the kinematic domain of the HERA data, and for electrons (SLAC) and muons (BCDMS, E665, NMC) on a fixed target. For the purpose of plotting, F_2 has been multiplied by 2^{i_x}, where i_x is the number of the x bin. Figure extracted from [51].

The parton model proposed by Bjorken and Feynman [52, 53] was born to explain the results of the DIS at SLAC (see Fig. 1.3). As was pointed out in Ref. [54], electrons were scattered with large transfers of momentum more frequently than anticipated, what suggested that the proton contained discrete scattering centers within. Moreover, the structure functions $F_{1,2}\left(x,Q^2\right)$ exhibited the phenomenon of Bjorken scaling, which demands that in the limit of $Q^2 \to \infty$ with x fixed, only depend on the dimensionless variable x. The physical interpretation is that the constituents of the proton have no scale associated, and

hence are pointlike.

As we described when we discussed factorization in Sec. 1.1.4, the main assumption of the parton model is that we can treat the constituents of the proton as essentially free during the time they are probed. Let us call p_i (p_f) the initial (final) momentum of the parton in the $p_i\gamma^\star \to p_f$ scattering. Squaring the conservation of momentum we have

$$m_p^2 + 2p_i\cdot q - Q^2 = m_p^2 \quad \Rightarrow \quad \frac{Q^2}{2p_i\cdot q} = 1\,. \tag{1.41}$$

If we neglect the momentum of the parton in the transverse plane, we can assume that the parton's momentum is proportional to the parent hadron's one, $p_i = \zeta P$, then we have a suggestive interpretation of the Bjorken-x variable, since

$$x = \zeta = \frac{p_i}{P}\,, \tag{1.42}$$

as the momentum fraction of the parent hadron carried by the parton, and it can be determined in DIS by measuring the deflected lepton.

The idea that interactions of partons within the same hadron can be neglected requires that QCD is an asymptotically free theory, where interactions are switched off logarithmically at asymptotically high momenta. The hierarchy of scales $Q^2 \gg \Lambda_{\rm QCD}$ allows us to treat the parton wavefunctions withing the hadron as being decoherent, giving a probabilistic interpretation. For a formal proof of this decoherence a rigorous proof of factorization is needed, we refer to [55] for a detailed explanation. We then introduce the classical probabilities $f_i(\zeta)\mathrm{d}\zeta$ of the photon interacting with the parton species i which has a fraction of the parent hadron momentum ζ. These are the PDFs we introduced in Sec. 1.1.4. The cross section for the reaction $e^- P \to e^- X$ is given by the incoherent sum of the different $e^- p_i \to e^- X$ scatterings, which reads

$$\sigma(e^- P \to e^- X) = \sum_i \int_0^1 \mathrm{d}\zeta\, f_i(\zeta)\hat{\sigma}(e^- p_i \to e^- X)\,. \tag{1.43}$$

Assuming that the only partons which interact with the photon are charged spin $\frac{1}{2}$ particles, the quarks, we can compute the hadronic tensor though the amplitude $\left|\mathscr{A}\left(p_i + \gamma^\star \to p_f\right)\right|^2$ integrated over final states. The structure functions are given by[8]

$$\frac{F_2(x)}{x} = 2F_1(x) = -g^{\mu\nu}W_{\mu\nu} = \sum_i \int \mathrm{d}\zeta\, Q_i^2 f_i(\zeta)\delta(\zeta - x) = \sum_i Q_i^2 f_i(x)\,. \tag{1.44}$$

[8] The trace of the hadronic tensor is given by $W^{(0)}(x,Q^2) \equiv -g_{\mu\nu}W^{\mu\nu} = 3F_1 - \frac{F_2}{2x}\left(1 + \frac{m_P^2 4x^2}{Q^2}\right)$, which in the limit $Q^2 \gg m_P^2$ simplifies to $w_0 = 3F_1 - \frac{F_2}{2x}$.

The relation $F_L = F_2 - 2xF_1 = 0$ is the Callan-Gross relation [56], which is a consequence of assuming that the partons are pointlike fermions with spin $\frac{1}{2}$. At SLAC, the relation was experimentally observed, showing that the partons were, in principle, quarks. But even taking into account the sea of virtual quark-antiquark pairs, the predicted cross section was found to be too small [52], and then that there must be also electrically neutral partons: the gluons.

In spite of all the successes, we can see already in Fig. 1.3 that Bjorken scaling does not quite hold, since there is some weak dependence on Q^2. This can be understand once we combine the parton model with the quantum properties of QCD, studying higher order corrections to the processes described below.

1.2.1 The Dokshitzer-Gribov-Lipatov-Altarelli-Parisi evolution equations

In this section we will explain how the presence of quantum corrections, driven by gluon radiation at the NLO, determines the patter of violation of Bjorken scaling. Since the PDFs are not observables, in order to apply the renormalization prescription is convenient to relate them to an observable, we have just seen in Eq. (1.44) that at LO, with $Q^2 \gg m_P^2$, we have

$$W^{(0)}\left(x,Q^2\right) \equiv -g_{\mu\nu}W^{\mu\nu} = \sum_i Q_i^2 f_i(x), \tag{1.45}$$

and this is what we will use as the equation defining the PDFs beyond the leading order. Notice that $W^{(0)}\left(x,Q^2\right)$ is convenient because it is the unpolarized cross section[9] for the reaction $\gamma^\star + P \to X$. The renormalization condition for the PDFs reads

$$W^{(0)}\left(x,Q^2\right) \equiv \sum_i Q_i^2 f_{R,i}\left(x,Q^2\right), \tag{1.46}$$

It is convenient to work with the partonic version of the hadronic tensor. We have that the differential cross section can be written in terms of the leptonic tensor $L^{\mu\nu}$ and the hadronic tensor $W^{\mu\nu}\left(x,Q^2\right)$, with the latter given by the squared amplitude $\left|\mathscr{A}\left(\gamma^\star + P \to X\right)\right|^2$ integrated over all final states, as in Eq. (1.38). Let us define the partonic hadronic tensor $\hat{W}_i^{\mu\nu}\left(z,Q^2\right)$, related to the squared amplitude $\left|\mathscr{A}\left(\gamma^\star + p_i \to X\right)\right|^2$, integrated over all final states. The partonic version of the Bjorken-x variable is defined as

$$z \equiv \frac{Q^2}{2p_i \cdot q} \tag{1.47}$$

[9] The use of this cross section as the observable is convenient because it allows us to consider only amputated diagrams, as dictated by the Lehmann-Symanzik-Zimmermann (LSZ) reduction formula [57].

that is related to the momentum fraction ζ of the parton model. Since we the probability of the parton of having momentum $p_i = \zeta P$ if given by $f_i(\zeta)$, then the relation $x = z\zeta$ holds. This leads to

$$W^{\mu\nu}\left(x,Q^2\right) = \sum_i \int_0^1 \mathrm{d}z \int_0^1 \mathrm{d}\zeta\, f_i(\zeta)\delta\left(x - z\zeta\right)\hat{W}_i^{\mu\nu}\left(z,Q^2\right) = \\ = \sum_i \int_x^1 \frac{\mathrm{d}\zeta}{\zeta} f_i(\zeta)\hat{W}_i^{\mu\nu}\left(\frac{x}{\zeta},Q^2\right) \tag{1.48}$$

which allows us to transform Eq. (1.44) into partonic variables at LO as

$$\frac{\hat{F}_{2,i}\left(z,Q^2\right)}{z} = 2\hat{F}_{1,i}\left(z,Q^2\right) = \hat{W}_i^{(0)}\left(z,Q^2\right) = Q_i^2\delta(1-z). \tag{1.49}$$

At NLO in the parton model in QCD we have three diagrams to consider, one virtual (see Fig. 1.4) for a $\gamma^\star + q \to q$ reaction (q denotes a quark and g a gluon), and two real radiative corrections (see Fig. 1.5), a s-channel and a t-channel $\gamma^\star + q \to q + g$ processes. To describe the kinematics let us denote the momenta as p_i for the initial quark found in the hadron, p_f for the final state quark, and k to the momentum of the gluon.

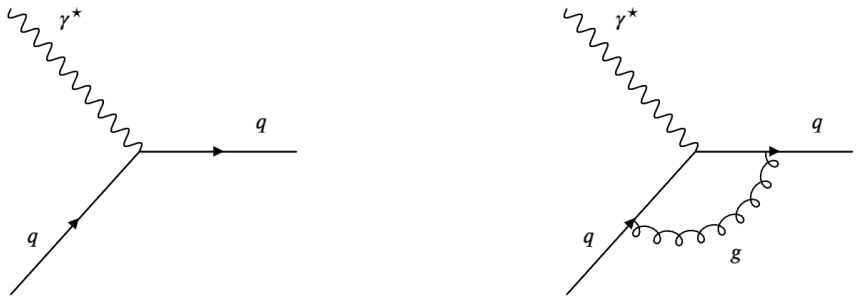

Figure 1.4: LO diagram (left) and NLO virtual radiative corrections (right) to the $\gamma^\star + q \to q$ process.

The radiative corrections to the Born level process develop two types of IR singularities:

- The soft divergences appear when the gluon momentum k is very soft, *i.e.*, $k \to 0$, and are present in theories which contain massless gauge fields. In our case, they appear both, virtual and real corrections, and cancel out among them.

- Collinear singularities appear when the quark emits a collinear gluon while remaining on-shell, these divergences take place when we have massless fields coupled to other massless fields, like in the case of massless quarks in QCD or massless gauge bosons in non-abelian theories, through the trilinear and quadrilinear self-couplings.

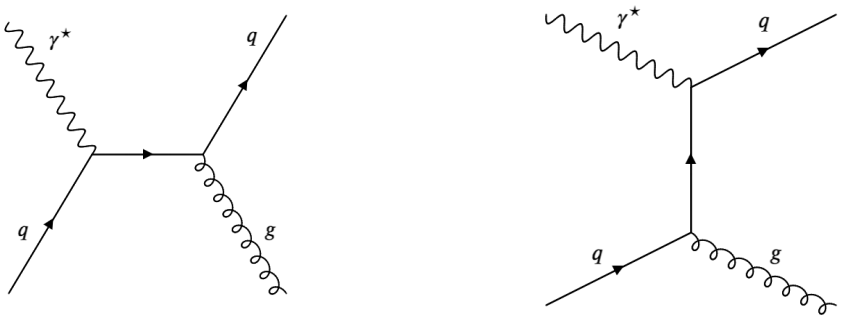

Figure 1.5: NLO real radiate corrections to the leading order $\gamma^\star + q \to q$ process. We have the s-channel diagram (left) and the t-channel diagram (right) contributions.

In the t-channel diagram, the gluon can be emitted collinear to the final state quark, but this divergence turns out to be harmless, since we are summing over all possible final states. Whether the final state quark keeps all its energy, or shares it with a gluon emitted collinearly does not in inclusive measurements. The s-channel diagram is more problematic, since it is the initial parton the one which can emit a collinear gluon, but the photon does differentiate between the two possibilities, since it only couples to electrically charged particles. This means that no cancellation between the real and virtual diagrams is possible in that case.

To summarize, there will remain a collinear singularity related to the initial state radiation once we compute the NLO corrections. As we will see, these divergences will be absorbed in the definition of the bare PDFs, and the Kinoshita-Lee-Nauemberg (KLN) theorem will apply, since we are summing over all possible initial and final states, in addition to the virtual corrections. Let us now state the contributions to $\hat{W}_i^{(0)}\left(z,Q^2\right)$ coming from the virtual and real diagrams, while the full calculation can be found in Ref. [58].

The interference between the leading diagram and the virtual one in Fig. 1.4, once we have removed the UV singularities[10], gives

$$\hat{W}_i^{(0),V}\left(z,Q^2\right) = Q_i^2 \frac{\alpha_s(Q^2)}{2\pi} C_F \left(\frac{4\pi\mu^2}{Q^2}\right)^{\epsilon} \frac{\Gamma(1-\epsilon)}{\Gamma(1-2\epsilon)} \left(-\frac{2}{\epsilon^2} - \frac{3}{\epsilon} - 8 - \frac{\pi^2}{3}\right) \delta(1-z) \tag{1.50}$$

up to terms that do not contribute in the limit $\epsilon \to 0$. For the real emission graph we have

[10]The UV singularities are taking into account via the renormalization of the coupling, and using the scale Q^2 in the running coupling as it is explained in Sec. 1.1.3. Since we are only showing the IR divergences, have that the space-time dimension is $D = 4 - 2\epsilon$, but we have to understand ϵ as the infrared regulator $\epsilon_{\rm IR}$, which is negative.

the following result

$$\begin{aligned}\hat{W}_i^{(0),R}\left(z,Q^2\right) =& Q_i^2\frac{\alpha_s(Q^2)}{2\pi}C_F\left(\frac{4\pi\mu^2}{Q^2}\right)^{\epsilon}\frac{\Gamma(1-\epsilon)}{\Gamma(1-2\epsilon)}\times \\ &\times\left[3z+z^{\epsilon}(1-z)^{-\epsilon}\left(-\frac{1}{\epsilon}\frac{1+z^2}{1-z}+3-z-\frac{3}{2}\frac{1}{1-z}-\epsilon\frac{7}{4}\frac{1}{1-z}\right)\right].\end{aligned} \tag{1.51}$$

Now, we have to treat with caution the term $(1-z)^{-1-\epsilon}$, since they develop an extra singularity when we integrate z in a region containing $z\to 1$, *i.e.*, we cannot naively Laurent expand in ϵ and then integrate. The usual solution is to treat it as a distribution, to anticipate what will happen when we integrate afterwards, the relevant identity is

$$\frac{1}{(1-z)^{1+\epsilon}} = -\frac{1}{\epsilon}\delta(1-z)+\frac{1}{[1-z]_+}-\epsilon\left[\frac{\log(1-z)}{1-z}\right]_+ +\sum_{n=2}^{\infty}\frac{(-\epsilon)^n}{n!}\left[\frac{\log^n(1-z)}{1-z}\right]_+, \tag{1.52}$$

where the plus distribution is defined so that

$$\int_0^1 \mathrm{d}z\,[g(z)]_+ f(z) \equiv \int_0^1 \mathrm{d}z\, g(z)(f(z)-f(1)) \;;\; [g(z)]_+ = g(z) \text{ for } z\neq 1. \tag{1.53}$$

Finally we have

$$\begin{aligned}\hat{W}_i^{(0),R}\left(z,Q^2\right) =& Q_i^2\frac{\alpha_s(Q^2)}{2\pi}C_F\left(\frac{4\pi\mu^2}{Q^2}\right)^{\epsilon}\frac{\Gamma(1-\epsilon)}{\Gamma(1-2\epsilon)}\times \\ &\times\left\{3+2z-\frac{1+z^2}{1-z}\log z+\left(\frac{2}{\epsilon^2}+\frac{3}{2\epsilon}+\frac{7}{2}\right)\delta(1-z)-\right. \\ &\left.-\left(\frac{1+z^2}{\epsilon}+\frac{3}{2}\right)\left[\frac{1}{1-z}\right]_+ +\left(1+z^2\right)\left[\frac{\log(1-z)}{1-z}\right]_+\right\}.\end{aligned} \tag{1.54}$$

The total contribution to NLO order is

$$\begin{aligned}\hat{W}_i^{(0)}\left(z,Q^2\right) =& \hat{W}_i^{(0),LO}+\hat{W}_i^{(0),V}+\hat{W}_i^{(0),R} = \\ =& Q_i^2\left\{\delta(1-z)-\frac{2\alpha_s\left(Q^2\right)}{\epsilon\pi}P_{qq}(z)\left(\frac{4\pi\mu^2}{Q^2}\right)^{\epsilon}\frac{\Gamma(1-\epsilon)}{\Gamma(1-2\epsilon)}+\mathscr{F}(z)\right\},\end{aligned} \tag{1.55}$$

where the function $\mathscr{F}(z)$ contains terms which are Q^2-independent and regular in ϵ and z. The distribution $P_{qq}(z)$ is known as DGLAP splitting function

$$P_{qq}(z) = C_F\left\{(1+z^2)\left[\frac{1}{1-z}\right]_+ +\frac{3}{2}\delta(1-z)\right\}. \tag{1.56}$$

Now we have that all double poles have cancelled, but we still have the simple pole in ϵ associated to the initial collinear singularity. This is not a problem, as long as it disappears

in physical predictions, we can obtain the observable we are using as the renormalization condition plugging Eq. (1.55) into Eq. (1.48) to get

$$W^{(0)}\left(x,Q^2\right)=\sum_i Q_i^2\int_x^1\frac{\mathrm{d}\zeta}{\zeta}f_i(\zeta)\left\{\delta\left(1-\frac{x}{\zeta}\right)-\frac{\alpha_s\left(Q^2\right)}{2\pi}P_{qq}\left(\frac{x}{\zeta}\right)\left(\frac{1}{\epsilon}+\log\frac{\tilde{\mu}^2}{Q^2}\right)+\mathscr{F}\left(\frac{x}{\zeta}\right)\right\}. \tag{1.57}$$

Now, if we integrate $W^{(0)}\left(x,Q^2\right)$ over x, which is equivalent to integrating over all possible initial states, to get the total DIS cross section at a given Q^2, the pole in ϵ cancels out due to the property

$$\int_0^1 \mathrm{d}z\,P_{qq}(z)=0\,. \tag{1.58}$$

At fixed x the quantity differential cross section is divergent, but following the Renormaliztion Group philosophy, we can compare the observable at two different scales[11]

$$W^{(0)}\left(x,Q^2\right)-W^{(0)}\left(x,Q_0^2\right)=\sum_i Q_i^2\int_x^1\frac{\mathrm{d}\zeta}{\zeta}f_i(\zeta)\frac{\alpha_s\left(Q^2\right)}{2\pi}P_{qq}\left(\frac{x}{\zeta}\right)\log\frac{Q^2}{Q_0^2}, \tag{1.59}$$

which is a finite integral. We see that the ϵ pole in the parton level cross section leads to a logarithmic dependence on the scale Q^2 of the hadronic cross section. There is a reason of why we cannot calculate $W^{(0)}\left(x,Q^2\right)$ without an addition renormalization. In the full QCD theory, we would have to cut off the IR divergences with physical scales as the mass of the quarks, and also the nonpertubative scale Λ_{QCD}, since we are integrating over regions of the phase space which are purely nonperturbative. In that case, we would have obtained really large logarithms, $\log\frac{Q^2}{m_q^2}$ and $\log\frac{Q^2}{\Lambda_{\mathrm{QCD}}^2}$. Using differences, or the renormalization group, we avoid the presence of these large logarithms comparing similar scales.

Instead of calculating differences of observables, let us define renormalized PDFs through the physical observable, so we impose

$$W^{(0)}\left(x,Q^2\right)\equiv\sum_i Q_i^2 f_i^R\left(x,Q^2\right) \tag{1.60}$$

at any arbitrary scale Q^2. Comparing with Eq. (1.57) we obtain the definition of the renormalized PDFs in terms of the bare ones. Taking the derivarive w.r.t. $\log Q^2$ we obtain the RGE

$$\frac{\mathrm{d}f_i^R\left(x,Q^2\right)}{\mathrm{d}\log Q^2}=\frac{\alpha_s\left(Q^2\right)}{2\pi}\int_x^1\frac{\mathrm{d}\zeta}{\zeta}f_i^R\left(\zeta,Q^2\right)P_{qq}\left(\frac{x}{\zeta}\right). \tag{1.61}$$

[11] We are neglecting subleading terms proportional to $\alpha_s^2\left(Q^2\right)\log\frac{Q^2}{Q_0^2}$ when using the same coupling for both terms when taking the difference. However, that approximation is in accordance with the accuracy we are working at.

This is the DGLAP equation, which considers the case when the photon interacts with a quark coming from a quark parent with momentum fraction $\zeta \geq x$. This differential equation effectively resums a full tower of ladder diagrams giving the leading logarithms in Q^2, see Fig. 1.6. To see that, we can iterate the DGLAP equation to obtain an expansion of the form[12]

$$f\left(x,Q^2\right) = f\left(x,Q_0^2\right) + \sum_{n=1}^{\infty} \frac{1}{n!} \left(\frac{\alpha_s\left(Q^2\right)}{2\pi} \log \frac{Q^2}{Q_0^2} \right)^n \left[\prod_{i=1}^{n} \int_{\zeta_{i-1}}^{1} \frac{\mathrm{d}\zeta_i}{\zeta_i} P_{qq}\left(\frac{\zeta_{i-1}}{\zeta_i} \right) \right] f\left(\zeta_n, Q_0^2\right), \tag{1.62}$$

where we have an ordering in the momentum fraction of the quarks w.r.t. the parent hadron after each collinear gluon emission, $x = \zeta_0 \leq \zeta_1 \leq \cdots \leq \zeta_n \leq 1$, being x the momentum fraction of the quark that interacts with the photon.

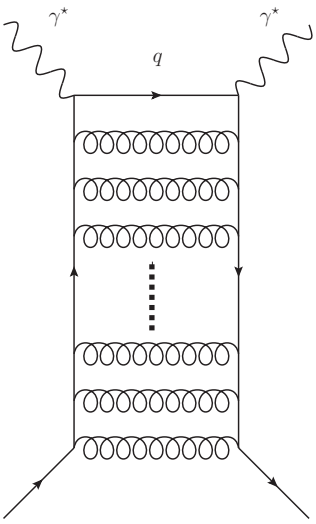

Figure 1.6: Quark-quark ladder diagrams resumming the contributions to the quark PDF coming from the emission of n collinear gluons, as dictatedby the DGLAP equation involving $P_{qq}(z)$. The connection to the Feynman diagrams of the splitting functions is done via the optical theorem.

So far we have only considered quarks in the initial state, in the NLO there are also precesses such as $\gamma^\star g \to q\bar{q}$ with gluons in the initial state. Since there is a possibility of finding antiquarks and gluons in the proton, we have PDFs associated with them, and they all mix among the DGLAP renormalization group equations. The various splitting functions $P_{ab}(z)$ (see Fig. 1.7) can be derived from the processes $g \to gg$, $g \to q\bar{q}$, $q \to gq$, and the charge conjugated ones. Note that at NLO there is no flavor mixing $q_i \to q_j X$ or

[12] From now on we are always assuming that we deal with renormalized PDFs, so we don't write the index R.

quark-antiquark mixing, $q \to \bar{q}X$. At leading order they are

$$
\begin{aligned}
P_{qq}(z) &= C_F \left\{ \frac{1+z^2}{[1-z]_+} + \frac{3}{2}\delta(1-z) \right\}, \\
P_{qg}(z) &= T_R \left(z^2 + (1-z)^2 \right), \\
P_{gq}(z) &= C_F \frac{1+(1-z)^2}{z}, \\
P_{gg}(z) &= 2C_A \left\{ \frac{z}{[1-z]_+} + \frac{1-z}{z} + z(1-z) \right\} + \frac{\beta_0}{2}\delta(1-z)
\end{aligned}
\tag{1.63}
$$

where $\beta_0 = \frac{11}{3}C_A - \frac{4}{3}T_R N_F$. Where they can be found, for example, in Ref. [59].

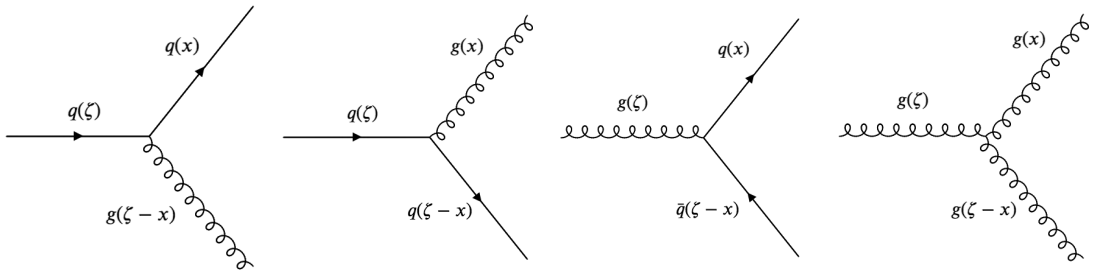

$P_{qq}\left(\frac{x}{\zeta}\right)$ $P_{gq}\left(\frac{x}{\zeta}\right)$ $P_{qg}\left(\frac{x}{\zeta}\right)$ $P_{gg}\left(\frac{x}{\zeta}\right)$

Figure 1.7: NLO DGLAP splitting functions.

The splitting functions $P_{ab}(z)$ have an attractive physical interpretation as the probability of finding a parton of type a in another parton of type b, with a fraction z of the longitudinal momentum of the parent parent parton. The probabilistic interpretation of the splitting functions implies that are positive definite for $z < 1$, and that satisfy the sum rules

$$
\begin{aligned}
\int_0^1 \mathrm{d}z \sum_i \left(P_{q_i q_j}(z) - P_{\bar{q}_i q_j}(z) \right) &= 0, \\
\int_0^1 \mathrm{d}z\, z \left\{ \sum_i \left(P_{q_i q_j}(z) + P_{\bar{q}_i q_j}(z) \right) + P_{g q_j}(z) \right\} &= 0, \\
\int_0^1 \mathrm{d}z\, z \left\{ \sum_i \left(P_{q_i g}(z) + P_{\bar{q}_i g}(z) \right) + P_{gg}(z) \right\} &= 0,
\end{aligned}
\tag{1.64}
$$

which correspond to quark number conservation and momentum conservation in the splittings of quarks and gluons respectively.

To conclude, the full set of DGLAP renormalization equations is really a system of integro-differential equations, for quarks and gluons, that in general can be written in the

form

$$\frac{\mathrm{d}}{\mathrm{d}\log Q^2}\begin{pmatrix} f_{q_i}(x,Q^2) \\ f_g(x,Q^2)\end{pmatrix} = \frac{\alpha_s(Q^2)}{2\pi}\sum_j \int_x^1 \frac{\mathrm{d}\zeta}{\zeta} \times \\ \times \begin{pmatrix} P_{q_i q_j}\left(\frac{x}{\zeta},\alpha_s(Q^2)\right) & P_{q_i g}\left(\frac{x}{\zeta},\alpha_s(Q^2)\right) \\ P_{g q_j}\left(\frac{x}{\zeta},\alpha_s(Q^2)\right) & P_{gg}\left(\frac{x}{\zeta},\alpha_s(Q^2)\right)\end{pmatrix}\begin{pmatrix} f_{q_j}(\zeta,Q^2) \\ f_g(\zeta,Q^2)\end{pmatrix}, \tag{1.65}$$

which can be solved in terms of Mellin moments of the distribution functions [59]. We recall that solving the DGLAP equations have collected all the contributions proportional to $\left(\alpha_s(Q^2)\log\frac{Q^2}{Q_0^2}\right)^n$, corresponding to the leading logarithmic approximation (LLA) valid in the limit

$$\alpha_s(Q^2)\log\frac{1}{x} \ll \alpha_s(Q^2)\log\frac{Q^2}{Q_0^2} < 1. \tag{1.66}$$

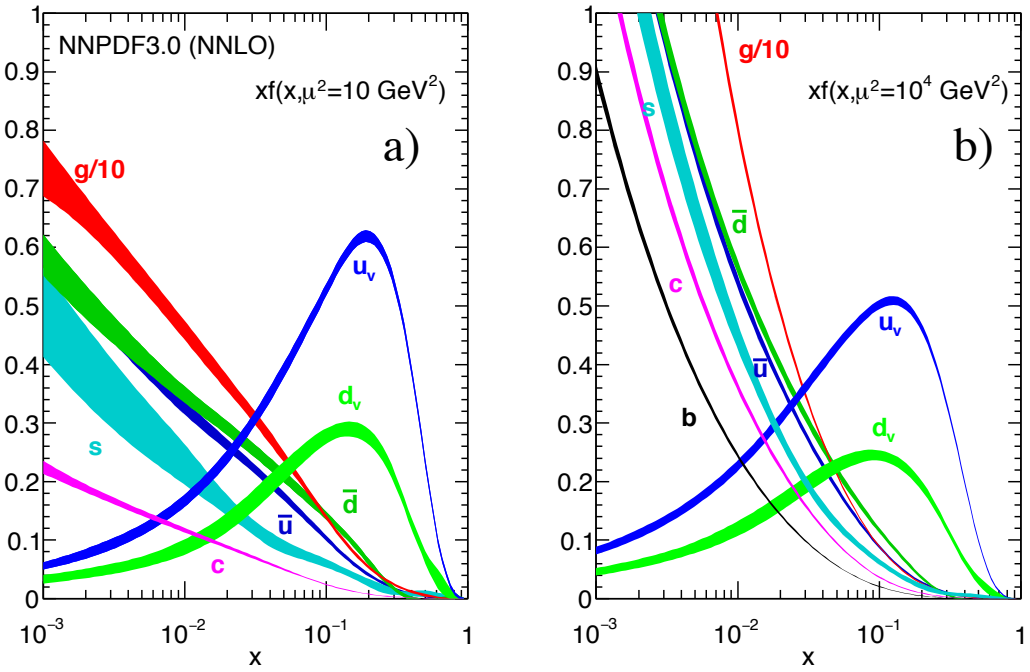

Figure 1.8: Momentum distributions (x times the unpolarized PDF $f(x)$) using the NNPDF3.0 parameterization. They are represented at scales $\mu^2 = 10\ \mathrm{GeV}^2$ (left) and $\mu^2 = 10^4\ \mathrm{GeV}^2$ (right). Extracted from [34].

1.2.2 DGLAP equations at small-x

In this Part I of the thesis, we are gonna study extensively small-x dynamics, which remains one of the most interesting open problems in QCD. In DIS we can investigate the PDFs in the small-x region, and we can also study the transition between perturbative and nonperturbative regimes. Using the DGLAP equations we obtained a good description of the structure function $F_2\left(x,Q^2\right)$ w.r.t to the scale Q^2, the scaling violations. But we have always assumed that we do not need to resum the $\log\frac{1}{x}$ terms, so it is important to test up to which x the DGLAP picture remains a good description. Looking at Fig. 1.9 we can see that the structure function $F_2(x,Q^2)$ rises when $x\to 0$, and this rise is steeper as we increase Q^2.

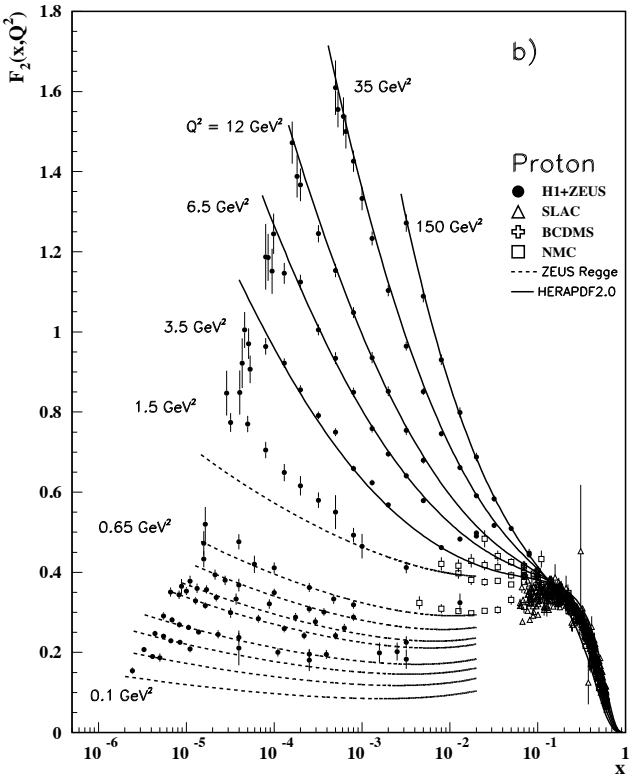

Figure 1.9: Proton structure function $F_2\left(x,Q^2\right)$ at small-x and Q^2. A turn-over is visible in the low-x points at medium Q^2 (3.5 GeV^2 and 6 GeV^2) for the H1+ZEUS combined values. In order to obtain F_2 from the measured reduced cross-section, F_L must be estimated; for the points shown, this estimate is obtained from HERAPDF2.0. No F_L value consistent with the HERA data can eliminate the turn-over. This may indicate that at low-x and Q^2 there are contributions to the structure functions that cannot be described in standard DGLAP evolution. Extracted from [34].

In the small-x regime the dominant partonic contribution is the gluonic one, $f_g\left(x,Q^2\right)$, since the production of gluons in the splitting functions, driven by P_{gg} and P_{gq} (see Eq. (1.63)), diverges in the limit $x \to 0$. This tells us that in the small-x, gluon ladders as depicted in Fig. 1.10 with repeated iterations of $P_{gg}(z)$, each one with $z \ll 1$ will dominate, *i.e.*, we have a strong ordering in the logitudinal momentum fraction x of the gluons going up through the ladder[13].

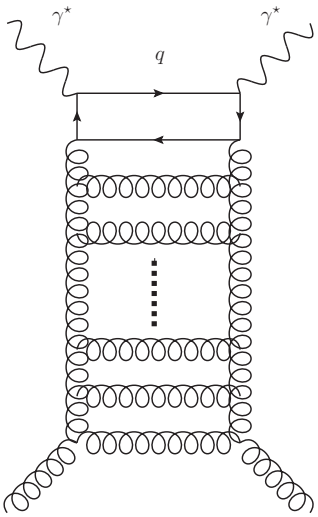

Figure 1.10: Gluonic ladder diagrams contribution to the DIS process at small-x. It is built through the repeated iteration of P_{gg} , resumming the contributions to the quark PDF coming from the emission of n collinear gluons from an initial partonic gluon. The connection to the Feynman diagrams of the splitting functions is done via the optical theorem.

Let us solve the DGLAP equations in Eq. (1.65) for the gluonic PDF using the LO splitting functions. In order to diagonalize the convolution, it is convenient to take Mellin of the function involved

$$\begin{aligned} f_i\left(N,Q^2\right) &\equiv \int_0^1 \mathrm{d}z\, z^{N-1} f_i\left(z,Q^2\right), \\ \gamma_{a,b}(N) &\equiv \int_0^1 \mathrm{d}z\, z^{N-1} P_{ab}(z), \end{aligned} \tag{1.67}$$

where the $\gamma_{a,b}(N)$ are known as anomalous dimensions. We have that in the low-x limit

[13] In addition to the strong ordering in transverse momentum, which corresponds to the leading logarithms in Q^2 of the DGLAP evolution. We are dealing with a double logarithmic approximation in here.

the equation for f_g is

$$\frac{\mathrm{d}f_g\left(N,Q^2\right)}{\mathrm{d}\log Q^2} = \frac{\alpha_s(Q^2)}{2\pi}\gamma_{gg}(N) f_g\left(N,Q^2\right). \tag{1.68}$$

The divergence of $P_{gg}(z)$ at $z \to 0$ is translated into a pole when $N \to 1$, the leading behavior is

$$\gamma_{gg}(N) \xrightarrow{N=1} \frac{2N_C}{N-1}, \tag{1.69}$$

which allows us to solve the equation as

$$g\left(N,Q^2\right) = g\left(N,Q_0^2\right) e^{\frac{\gamma_{gg}}{2\pi}\int_{Q_0^2}^{Q^2}\mathrm{d}\log Q'^2\,\alpha_s(Q'^2)}. \tag{1.70}$$

We go back to the x space through the inverse Mellin transform,

$$f_g\left(x,Q^2\right) = \int \frac{\mathrm{d}N}{2\pi i} z^{-N} f_g\left(N,Q^2\right) = \int \frac{\mathrm{d}N}{2\pi i} f_g\left(N,Q_0^2\right) e^{N\log\frac{1}{x}+\frac{N_C}{\pi}\frac{\eta(Q^2)}{N-1}}, \tag{1.71}$$

where the evolution of the coupling is encoded in

$$\eta(Q^2) \equiv \int_{Q_0^2}^{Q^2} \mathrm{d}\log Q'^2\,\alpha_s\left(Q'^2\right) = \frac{1}{b_0}\log\frac{\log\frac{Q^2}{\Lambda_{\mathrm{QCD}}}}{\log\frac{Q_0^2}{\Lambda_{\mathrm{QCD}}}}. \tag{1.72}$$

In the double limit $\log\frac{1}{x} \gg 1$ and $\log\frac{Q^2}{Q_0^2} \gg 1$, the exponent is large and we can approximate the integral with its saddle point, with $N_{\mathrm{saddle}} = 1 + \sqrt{\frac{N_c}{\pi}\frac{\eta(Q^2)}{\log\frac{1}{x}}}$. The final solution using the LLA for the running of the coupling, and first obtained in Ref. [60], is given by

$$f_g\left(x,Q^2\right) \sim \frac{1}{x}\exp\sqrt{\frac{4N_C}{\pi b_0}\log\frac{\log\frac{Q^2}{\Lambda_{\mathrm{QCD}}}}{\log\frac{Q_0^2}{\Lambda_{\mathrm{QCD}}}}\log\frac{1}{x}}. \tag{1.73}$$

This result correspond to the double leading logarithmic approximation (DLLA). To connect this result to the interpretation in terms of ladder diagrams in scattering amplitudes, it can also be obtained through the calculation of the gluonic ladder depicted in Fig. 1.10. The dominant contribution in the DLLA is obtained assuming strong ordering in transverse momentum $Q^2 \gg k_n^2 \gg \cdots \gg k_1^2 \gg Q_0^2$ and longitudinal momentum fraction $x \ll x_n \ll \cdots \ll x_1 \ll 1$. The probability of gluon bremsstrahlung, *i.e.*, the probability of emitting a gluon with modulus of the transverse momentum k and momentum fraction x is proportional to

$$P \sim \frac{N_C\alpha_s\left(k^2\right)}{\pi}\frac{\mathrm{d}x}{x}\frac{\mathrm{d}k^2}{k^2}, \tag{1.74}$$

where the factor $\frac{\mathrm{d}x}{x}\mathrm{d}k^2$ is nothing more than the invariant volume for the emission $\mathrm{d}^3\vec{k}/E$, and the extra $1/k^2$ comes from the gluon propagator. Also, this is the only possible dimensionless combination, and QCD is a dimensionless theory (except for quantum corrections).

Applying the strong ordering condition to the phase space integration of each emission times the corresponding splitting function we obtain[14]

$$\int_{Q_0^2}^{Q^2}\frac{\alpha_s\left(k_n^2\right)\mathrm{d}k_n^2}{k_n^2}\int_{Q_0^2}^{k_n^2}\frac{\alpha_s\left(k_{n-1}^2\right)\mathrm{d}k_{n-1}^2}{k_{n-1}^2}\cdots\int_{Q_0^2}^{k_2^2}\frac{\alpha_s\left(k_1^2\right)\mathrm{d}k_1^2}{k_1^2}=\frac{1}{n!}\left(\frac{1}{b_0}\log\frac{\log\frac{Q^2}{\Lambda_{\mathrm{QCD}}}}{\log\frac{Q_0^2}{\Lambda_{\mathrm{QCD}}}}\right)^n, \tag{1.75}$$
$$\int_x^1\frac{\mathrm{d}x_n}{x_n}\int_{x_n}^1\frac{\mathrm{d}x_{n-1}}{x_{n-1}}\cdots\int_{x_2}^1\frac{\mathrm{d}x_1}{x_1}=\frac{1}{n!}\log^n\frac{1}{x},$$

which gives us an alternative calculation[15] of the gluon PDF dependence at small-x

$$xf_g\left(x,Q^2\right)\sim\sum_n\frac{1}{(n!)^2}\left(\frac{1}{b_0}\log\frac{\log\frac{Q^2}{\Lambda_{\mathrm{QCD}}}}{\log\frac{Q_0^2}{\Lambda_{\mathrm{QCD}}}}\log\frac{1}{x}\right)^n\sim \tag{1.76}$$
$$\sim\exp\sqrt{\frac{4N_C}{\pi}\frac{1}{b_0}\log\frac{\log\frac{Q^2}{\Lambda_{\mathrm{QCD}}}}{\log\frac{Q_0^2}{\Lambda_{\mathrm{QCD}}}}\log\frac{1}{x}},$$

which can be compared with the more formal derivation in Eq. (1.73).

The more formal solution in Eq. (1.73) is valid when we assume an initial distribution which does not depend on x, since we have neglected the $f_g\left(N,Q_0^2\right)$ when performing the saddle point approximation. If we choose a more realistic option, as can be a steep dependence that we model with a power law

$$f_g\left(x,Q_0^2\right)=\mathcal{N}x^{-N_0}\quad\Leftrightarrow\quad f_g\left(N,Q_0^2\right)=\frac{\mathcal{N}}{N-N_0}, \tag{1.77}$$

[14] Taking the running of the coupling into account in the transverse momentum integration is equivalent to considering the running in the calculation of $\eta\left(Q^2\right)$ in Eq. (1.72). If we neglect it we would have obtained $\eta\left(Q^2\right)=\alpha_s\log\left(Q^2/Q_0^2\right)$ instead of $\eta\left(Q^2\right)=\frac{1}{b_0}\log\frac{\log\frac{Q^2}{\Lambda_{\mathrm{QCD}}}}{\log\frac{Q_0^2}{\Lambda_{\mathrm{QCD}}}}$. Therefore, we would have a series in $\left(\alpha_s\log\frac{Q^2}{Q_0^2}\log\frac{1}{x}\right)^n$, which is the way the DLLA is usually presented. Here we see that the sum we obtain is really the DLLA, but considering the running of the coupling.

[15] The sum can be solved in terms of the modified Bessel function $I_0(2\sqrt{z})=\sum_n\frac{z^n}{(n!)^2}$, and then using the asymptotic approximation $I_0(z)\sim\frac{e^z}{\sqrt{2\pi z}}$.

that can be easily evolved and transformed back to the x-space in the small-x limit taking the residue of the pole. The solution is

$$f_g\left(x,Q^2\right) = \mathcal{N} x^{-N_0} \exp^{\frac{N_C}{N_0-1}\frac{1}{b_0}\log\frac{\log\frac{Q^2}{\Lambda_{\rm QCD}}}{\log\frac{Q_0^2}{\Lambda_{\rm QCD}}}} = \mathcal{N} x^{-N_0}\left(\frac{\log\frac{Q^2}{\Lambda_{\rm QCD}}}{\log\frac{Q_0^2}{\Lambda_{\rm QCD}}}\right)^{\frac{N_C}{(N_0-1)b_0}}, \tag{1.78}$$

which keeps the same x dependence we proposed in the initial condition, and depends on the non-perturbative parameter N_0. If the initial distribution of gluons is too steep, the evolution described by perturbative effects is suppressed because we do not have enough fast gluons that will emit the collinear low-x ones, which fuel the gluonic ladder.

1.2.3 Small-x resummation and $k_\perp$-factorization

Up to this moment, we have payed special attention to collinear factorization, and how we resum the large logarithms in the transverse scale Q^2 by means of the DGLAP renormalization group equations. Previously, in Section 1.2.2, we also considered a further small-x limit on top of the DGLAP evolution, the DLLA, resumming $\left(\alpha\log\frac{1}{x}\log\frac{Q^2}{Q_0^2}\right)^n$ terms. But when moving to kinematic regions in where an additional hierarchy of two scales appears, there will appear large logarithms of the ratio of these two scales in the computation of amplitudes [31], in the same way we encounter then when studying the renormalization group (Sec. 1.1.3) and factorization (Sec. 1.1.4).

In the so-called semi-hard processes, we work in the high energy limit, or Regge limit, in which the center-of-mass-energy squared s is much larger than the momentum transfer $|t|$ or the typical transverse scales Q^2. When computing quantum corrections to the amplitude large logarithms of the form $\left(\alpha_s\log\frac{s}{Q^2}\right)^n$ appear, and we have to resum then to all orders to have a reliable perturbative expansion. In DIS, this high energy limit is equivalent to the small-x limit, and we have to deal with the following hierarchy

$$\alpha_s\left(Q^2\right)\log\frac{Q^2}{Q_0^2} \ll \alpha_s\left(Q^2\right)\log\frac{1}{x} < 1 \tag{1.79}$$

so we need to resum terms of the following form

$$\left(\alpha_s\left(Q^2\right)\log\frac{1}{x}\right)^n, \tag{1.80}$$

which is done through the Balitsky-Fadin-Kuraev-Lipatov (BFKL) equation [61–63] at LLA.

In order to clarify the differences among the resummations, let us describe each one with more detail, that are schematized in Fig. 1.11. In the LLA DGLAP, at each perturbative

order only the highest power in $\log \frac{Q^2}{Q_0^2}$ is retained. We have a sum of terms, omitting the coefficients, of the form

$$\text{LLA DGLAP: } \sum_n \left(\alpha_s \log \frac{Q^2}{Q_0^2}\right)^n \left\{\log^n \frac{1}{x} + \log^{n-1} \frac{1}{x} + \cdots\right\}, \tag{1.81}$$

which diagrammatically is equivalent to consider ladder diagrams with a strong ordering in the transverse momenta of the partons going down through the ladder $Q^2 \gg k_1^2 \gg \cdots \gg k_2^2 \gg Q_0^2$, while the longitudinal momentum fractions are normally ordered $x < x_1 < \cdots < x_n < 1$..

In the LLA BFKL resummation, only the leading terms in $\log \frac{1}{x}$ are considered at each order. We have then

$$\text{LLA BFKL: } \sum_n \left(\alpha_s \log \frac{1}{x}\right)^n \left\{\log^n \frac{Q^2}{Q_0^2} + \log^{n-1} \frac{Q^2}{Q_0^2} + \cdots\right\}, \tag{1.82}$$

that in terms of ladders, it is resumming gluon ladders with strong ordering in the logitudinal momentum fractions, while no ordering in the transverse momenta $k_1^2 \simeq \cdots \simeq k_n^2$.

Finally, in the DLLA one, which can be considered a special case of both resummations considered before, we have a strong ordering in both the transverse momenta and the longitudinal momentum fractions. In terms of the expansion, we only retain the highest order of each logarithm, this is

$$\text{DLLA: } \sum_n \left(\alpha_s \log \frac{1}{x} \log \frac{Q^2}{Q_0^2}\right)^n. \tag{1.83}$$

In Sec. 1.1.4 we saw that collinear factorization allows us to describe the observables of hadrons by the convolution of some non-perturbative, but universal, quantities (the PDFs), with the perturbatively calculable partonic level observable. At large energies, or small-x, the evolution of the PDFs proceeds over a large $\log \frac{1}{x}$ region and effects of finite transverse momenta of the partons may become increasingly important. In this limit a new form of factorization is more suitable, known as $k_\perp$-factorization [65, 66]. Cross sections can then be factorized as the convolution of an off-shell ($k_\perp$ dependent partonic cross section and a $k_\perp$-unintegrated parton distribution function $\mathcal{G}\left(x, k^2\right)$ as

$$\sigma = \int \frac{\mathrm{d}\zeta}{\zeta} \mathrm{d}^2\vec{k}\, \mathcal{G}\left(\zeta, k^2\right) \hat{\sigma}\left(\frac{x}{\zeta}, k^2\right). \tag{1.84}$$

The main motivation to define and study distributions with transverse momentum dependence, and their respective factorization theorems, is to extend the scope of the factorization approach described in the previous section to be able to include processes

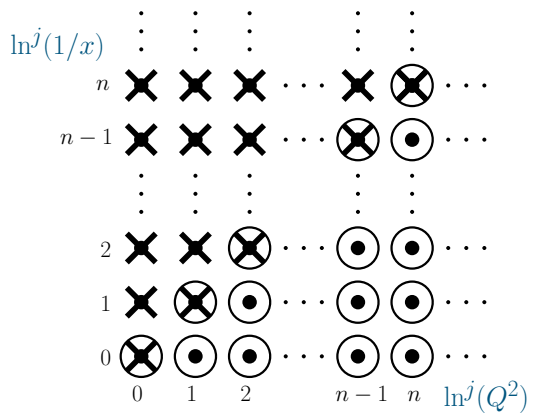

Figure 1.11: Terms in $\log\left(Q^2/Q_0^2\right)$ and $\log(1/x)$ included in the different resummations in semi-hard processes. The terms resummed by LLA DGLAP (circles), LLA BFKL (crosses) and the DLLA (circles and crosses). Adapted from [64].

that, in a partonic picture, would be sensitive to the transverse momentum of the incoming partons. Accounting for transverse momentum dependence implies relaxing the assumption that all energy scales in the problem are of the same order. In particular when the new energy scale is much smaller than the hard scale, this formalism allows one to calculate only the leading term in a series expansion in terms of the ratio of the two energy scales, which is exactly what we are looking for in the small-x region. The unintegrated PDF (uPDF) of the gluon, $\mathcal{G}\left(x,k^2\right)$, is the probability density to find a gluon with longitudinal momentum fraction x and transverse momentum squared k^2. It is evolved by the BFKL evolution equation in the small-x region and related to the usual gluon PDF by means of

$$xf_g\left(x,Q^2\right) \equiv \int_0^{Q^2} \frac{\mathrm{d}k^2}{k^2}\mathcal{G}\left(x,k^2\right) \quad \Leftrightarrow \quad \mathcal{G}\left(x,k^2\right) = \frac{\partial\left[xf_g\left(x,k^2\right)\right]}{\partial \log k^2}\,. \tag{1.85}$$

By explicitly carrying out the $\vec{k}$ integration in Eq. (1.84) one can obtain a form fully consistent with collinear factorization. However, in the new approach the partonic cross section and the DGLAP splitting functions leading to the $f_i\left(x,Q^2\right)$ evolution are no longer evaluated in fixed order perturbation theory, but supplemented with the all-orders resummation of the $\left(\alpha_s \log\frac{1}{x}\right)^n$ terms at small-x.

The BFKL equation can be used to obtain the unintegrated gluon density at low x, once a starting distribution at some x_0 value is assumed. The applicability of the leading order BFKL equation does not extend to very large Q^2, since the subdominant contributions in $\log\frac{1}{x}$, that can also be accompanied by large $\log\frac{Q^2}{Q_0^2}$ terms, are neglected. One can improve the LLA approximation going to the next order in accuracy, *i.e.*, to next-to-leading

logarithmic accuracy (NLLA), which was presented after long *tour de force* by Fadin and Lipatov in Ref. [67]. There is another description, appropriate for both small and large x, described by the Ciafaloni-Catani-Fiorani-Marchesini (CCFM) evolution equation, we will comment on it in Sec. 1.2.4.

The BFKL equation describing the unintegrated gluon density, that we will discuss in detail later, reads

$$\frac{\partial \mathcal{G}\left(x,k^2\right)}{\partial \log \frac{1}{x}} = \bar{\alpha}_s \int_0^\infty \frac{\mathrm{d}q^2\, k^2}{q^2} \left\{ \frac{\mathcal{G}\left(x,q^2\right) - \mathcal{G}\left(x,k^2\right)}{\left|q^2-k^2\right|} + \frac{\mathcal{G}\left(x,k^2\right)}{\sqrt{4q^4+k^4}} \right\}, \tag{1.86}$$

with $\bar{\alpha}_s \equiv \frac{N_C \alpha_s}{\pi}$.

The solution for fixed α_s can be solved analytically, and a detailed calculation can be found in Ref. [64], it reads

$$\mathcal{G}\left(x,k^2\right) \sim \left(\frac{x}{x_0}\right)^{-\lambda}, \tag{1.87}$$

with $\lambda = 4\log 2\bar{\alpha}_s \simeq 0.5$, for $N_C = 3$ and $\alpha_s = 0.19$. Which gives a prediction for the rise of the gluon PDF faster than the DLLA of Eq. (1.73), in this case we obtain

$$f_g\left(x,Q^2\right) \sim x^{-\lambda-1} \sim x^{-1.5}. \tag{1.88}$$

In order to make contact with the impact factor formalism of BFKL high energy factorization (see Fig. 1.12), that we will extensively use later, let us establish the connection of the uPDF with the BGKL Gluon Green's Function (GGF) φ. This factorization is based on the separation of the cross section into process dependent impact factors Φ and the BFKL kernel, which is supposed to be independent of the external probes. This factorization is based on two key properties: 1) the dominance of the exchange of gluons in the t-channel; and 2) the reggeization of the gluon propagator. This factorization formula has been proven at one loop in Ref. [68] and two loops in Ref. [69].

Let us apply it to the case of DIS, *i.e.*, the $\gamma^\star P$ cross section is given by [64] [16]

$$\sigma_\lambda^{\gamma^\star P}\left(x,Q^2\right) = \int \frac{\mathrm{d}k^2}{k^2} \mathcal{G}\left(x,k^2\right) \int_x^1 \frac{\mathrm{d}z}{z} \hat{\sigma}_\lambda^{\gamma^\star g}\left(z,k^2,Q^2\right) \tag{1.89}$$

, where we have defined the partonic gluon cross section, using the high energy factorization it can be rewritten as

$$\sigma_\lambda^{\gamma^\star P}\left(x,Q^2\right) = \frac{1}{(2\pi)^4} \int \frac{\mathrm{d}^2\vec{k}_1}{k_1^2} \int \frac{\mathrm{d}^2\vec{k}_2}{k_2^2} \Phi_\lambda\left(k_1^2,Q^2\right) \Phi_P\left(k_2^2\right) \varphi\left(\vec{k}_1,\vec{k}_2,x\right), \tag{1.90}$$

[16] This result is described in Section 9.5.4 of [64]. Where they have neglected NLLA terms in $\log(1/x)$ setting $\mathcal{G}\left(x/z,k^2\right) \simeq \mathcal{G}\left(x,k^2\right)$.

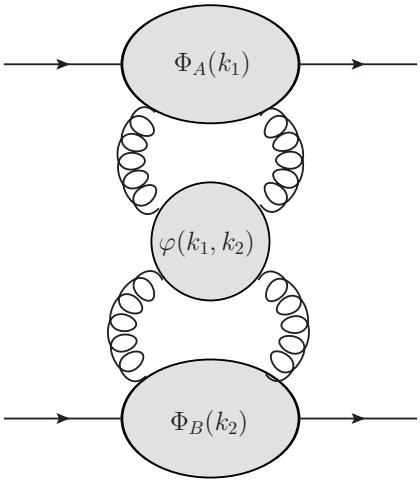

Figure 1.12: Schematic elements for BFKL high energy factorization, used to describe hadron-hadron or photon-hadron scattering in the Regge limit.

where $\Phi_{\lambda,P}$ are the photon and proton impact factors. Defining the relationship between the unintegrated gluon distribution and the BFKL GGF by

$$\mathcal{G}\left(x,k^2\right) = \frac{1}{(2\pi)^3}\int \frac{\mathrm{d}\vec{q}}{q^2}\Phi_P\left(q^2\right)\varphi\left(\vec{k},\vec{q},x\right), \tag{1.91}$$

leads to a definition of the photon impact factor

$$\Phi_\lambda\left(k^2,Q^2\right) = 2k^2\int_0^1 \frac{\mathrm{d}z}{z}\hat{\sigma}_\lambda^{\gamma^\star g}\left(z,k^2,Q^2\right), \tag{1.92}$$

and the cross section is finally

$$\sigma_\lambda^{\gamma^\star P}\left(x,Q^2\right) = \frac{1}{2\pi}\int \frac{\mathrm{d}^2\vec{k}}{k^4}\mathcal{G}\left(x,k^2\right)\Phi_\lambda\left(k^2,Q^2\right). \tag{1.93}$$

Although the photonic impact factor Φ_λ can be computed perturbatively by a one loop calculation of photon-gluon diagrams, the proton one, Φ_P encodes the non-perturbative information of its structure. The perturbative evaluation of the BFKL GGF allows us to evolve the unintegrated gluon distribution $\mathcal{G}\left(x,k^2\right)$ from a given distribution $\mathcal{G}\left(x_0,k^2\right)$, *i.e.*, an ansatz for Φ_P is usually assumed and fitted to experimental data. In Ref. [70] some available parameterizations are described, where they are divided into three groups

- Obtained from DGLAP parameterizations, simply by taking the derivative as in Eq. (1.85).
- Derived through the use of the BFKL approach, famous examples are the Golec-Biernat-Wüsthoff (GBW) model [71, 72] (based on the color-dipole approach), the

Ryskin-Shabelski (RS) [73] one and the Kwiecinski-Martin-Stasto (KMS) [74]. In Chapter 6, we will use a model proposed by Hentschinski-Sabio Vera-Salas [75, 76] based on the NLLA BFKL equation, using collinear improvement [77], and fitted to combined HERA data at small values of x.

- Unintegrated PDFs derived in the CCFM formalism. We have for example the models proposed by J. Blumlein (JB) [78], Kimber-Martin-Ryskin (KMR) [79] and Jung-Salam (JS) [80, 81].

1.2.4 Other approaches

Even if the predictions we obtained using the LLA BFKL equation and the LO splitting functions for the DGLAP equations are different , both approaches to describe the evolution of the gluon PDF don't contradict each other. They are simply organizing the double power expansion in logarithms in a different way (see Fig. 1.11) and, as we increase the accuracy of each approach, the predictions should approach each other. At small-x and $Q^2 \simeq Q_0^2$, for example, the logarithmic terms taken into account in the BFKL formalism should be important, and they affect the perturbative expansion of the splitting functions. Depending on the region of the kinematical space we want to describe, it can be that one type of logarithms is enhanced, and we can use one of the previous approaches. A general map of the available descriptions is given in Fig. 1.13.

The BFKL equation has a limited region of validity determined by the size of the logarithms it resums, for the LLA equation we have that $\alpha_s \log \frac{1}{x} \sim 1$, while $\alpha_s \log \frac{Q^2}{\Lambda^2_{\text{QCD}}} \ll 1$. On the other hand, the DGLAP equation, which resums $\left(\alpha_s \log \frac{Q^2}{\Lambda^2_{\text{QCD}}}\right)^n$ terms is not expected to hold at very small values of x. For the cases in which both type of logarithms become sizable, it is important to have an unified way of evolving the DIS structure functions throughout the x-Q^2 plane. A theoretical framework which provides such a treatment has been developed by Ciafaloni-Catani-Fiorani-Marchesini (CCFM) in Refs [83–85]. It leads to an evolution equation, usually called the CCFM equation, which reduces to the BFKL equation in the leading $\log \frac{1}{x}$ approximation, and is equivalent to the DGLAP equation at moderate x (solutions of the CCFM equation can be found in [86]).

The CCFM equation is based on the coherent branching of gluons along a ladder like that shown in Fig. 1.10. The emissions are coherent in the sense that there is an angular ordering $\theta_1 < \cdots < \theta_n$ going downwards along the tower, where θ_i is the angle that the i-th gluon forms with the original direction, the one of the first parton emitted by the parent hadron. Outside this kinematic region there is a destructive interference such

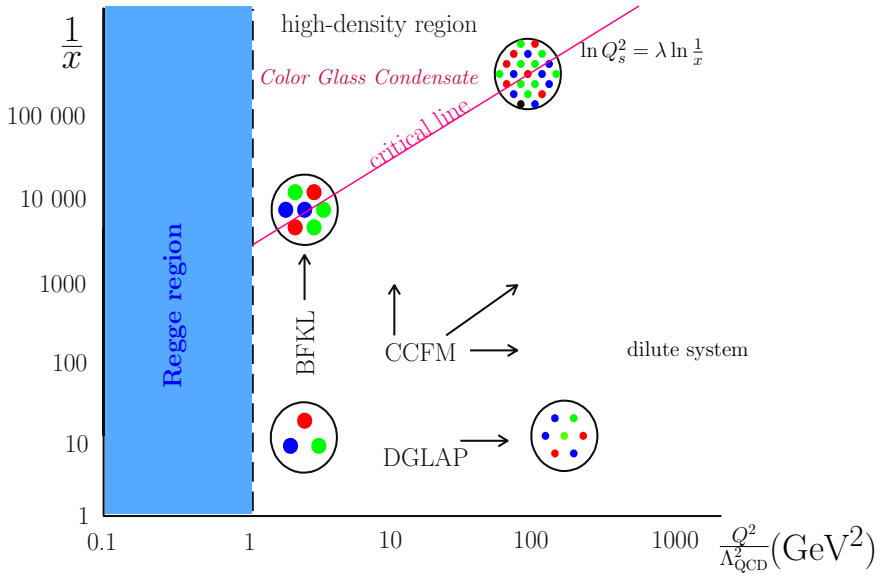

Figure 1.13: Schematic map of the different regimes in the $\frac{1}{x}$- $\frac{Q^2}{\Lambda^2_{\rm QCD}}$ space with the respective evolution equations expected to describe them. The critical line marks the appearance of saturation effects. The transverse *size* of the partons is indicated in the different regions. Adapted from [82].

that the multigluon contributions vanish to leading order. Here, we simply recall that the CCFM equation is an integral equation for the Q^2-dependent unintegrated gluon density $f\left(x,k^2,Q^2\right)$. The additional scale Q^2 arises from the angular ordering and specifies the maximum angle of gluon emission. At small x, the angular ordering does not provide any constraint on the transverse momenta along the gluon ladder, so that $f\left(x,k^2,Q^2\right)$ becomes independent of Q^2, and one recovers the BFKL equation for $\mathcal{G}\left(x,k^2\right)$. At larger x, the angular ordering becomes an ordering in the gluon transverse momenta and, by integrating over k^2, one recovers the DGLAP evolution for $f_g\left(x,Q^2\right)$.

In the upper region of the Q^2-$\frac{1}{x}$ plane of Fig. 1.13 we encounter the high-density region. As we discussed in Sec. 1.2.2 the gluon density grows at low-x, and this result is confirmed by the BFKL approach. But there must be a limit to this growing to respect the unitarity of the DIS cross section. The Froissart bound states that at asymptotically high energies the total cross section must approach a constant (the geometrical size of the hadron) up to $\log(s)$ corrections. Therefore, we can state the following unitarity bound on the structure function and, using the factorization formula and that at low-x the gluon PFD dominates [87]

$$F_2\left(x,Q^2\right) \simeq \alpha_s f_g\left(x,Q^2\right) \lesssim \pi R_p^2 Q^2, \tag{1.94}$$

where R_p is the radius of the proton. As we saw in the DLLA, this condition is violate in both BFKL and DGLAP equations at small-x, The physical reason is that in the leading twist approximation the partons within the hadron are considered free, but it is clear that when the number of partons is too large their wavefunctions start to overlap and recombination effects will take place. These phenomena, known as *saturation effects* should limit the growth of the gluonic PDF.

Then, we find there must be a scale at which the hadron is heavily packed and recombination effects are important, the saturation scale $Q_s(x)$. That the saturation scale is greater than Λ_{QCD} ensures that it can be understood within perturbative methods. Balitsky and Kovchegov [88, 89] showed from an effective Lagrangian and from Mueller dipole formalism [90] respectively, that in the large N_C limit, there is a non-linear generalization of the BFKL equation, the BK that reads [91]

$$\frac{\partial \mathscr{G}\left(x,k^2\right)}{\partial \log \frac{1}{x}} = \bar{\alpha}_s \int_0^\infty \frac{\mathrm{d}q^2\, k^2}{q^2} \left\{ \frac{\mathscr{G}\left(x,q^2\right) - \mathscr{G}\left(x,k^2\right)}{\left|q^2-k^2\right|} + \frac{\mathscr{G}\left(x,k^2\right)}{\sqrt{4q^4+k^4}} \right\} - \bar{\alpha}_s^2 \frac{\mathscr{G}\left(x,k^2\right)}{k^4}, \tag{1.95}$$

to be compared with Eq. (1.86). The BK equation is a central tool for understanding the initial conditions in hadronic collisions in situations where gluon density approaches unitarity limits. Among its important properties is that it has solutions explicitly exhibiting geometric scaling [92], i.e. the property that in DIS collisions, $\sigma_{\gamma^\star P}\left(x,Q^2\right) = 4\pi^2\alpha_s F_2\left(x,Q^2\right)/Q^2$ only depends on the two independent kinematic invariants Q^2 and W^2 through the specific combination $\tau = Q^2/Q_s^2(x)$, where the saturation scale is $Q_s^2(x) \sim Q_0^2 (x/x_0)^{-\lambda}$ [71]. However, there are a number of contributions not considered and, in general, the scattering of two dilute systems remains still essentially an open problem.

We can go further in the $\frac{1}{x}$ direction, and cross the saturation line, where the system is not dilute anymore. When the parton density increases, processes involving many parton interactions become sizable and must be considered. When the gluon occupation number is of order $1/\alpha_s$, the problem becomes non-perturbative in the sense that there is an infinite number of graphs contributing to each order, despite the smallness of the coupling. Moreover, this situation requires the knowledge of the complete wavefunction of the hadron, and not only the single-parton densities. A common approach in this situation is to use an effective theory, the color glass condensate [93, 94]. It is based on two ideas: 1) large occupation number or large charges give rise to classical fields, giving rise to the term *condensate*; and 2) there is a natural separation of scales in the x variable, *glass*. To conclude, the distribution of charges in that formalism is given by the BK/JIMWLK equation described in Refs. [88, 89, 95–97]. For weak fields, or low density, the BK/JIMWLK equation reduces to the BFKL one, and the BK equation is recovered in the large N_C limit.

1.3 The BFKL equation

The formulation of the Balitsky-Fadin-Kuraev-Lipatov (BFKL) equation [61–63] equation is considered as one of the most important steps in the development of small-x physics. Despite the possible problems it may have at very high energies, it remains a very good approximation with many phenomenological applications, and also an extremely useful tool in the field of Scattering Amplitudes. This section is devoted to show the main ingredients to build the BFKL equation which, at leading logarithmic accuracy, resums the leading $\left(\alpha_s \log \frac{s}{|t|}\right)^n$ to all orders in perturbation theory, where s and t are the Mandelstam variables. The resummation of these large logarithms is mandatory if we want to describe the Regge limit, in which the center-of-mass energy is much larger that any transverse scale in the scattering process. As we have already discuss, this is especially relevant for the small-x description of DIS. A didactic derivation of the BFKL equation in momentum space, as was originally demonstrated, can be found in the textbooks [64, 98]. A simpler derivation in transverse coordinate space is done through the dipole model picture of Mueller [90], which is formulated in the large N_C limit. The next-to-leading logarithmic accuracy (NLLA) calculation was performed in Refs. [67, 69].

1.3.1 Gluon Reggeization

The BFKL approach relies on gluon reggeization, which can be described as the appearance of an effective particle, the reggeon, with modified propagator of the form (in the Feynman gauge)[17]

$$D_{\mu\nu}\left(\underline{q},t\right) = -i\frac{g_{\mu\nu}}{\underline{q}^2}\left(\frac{s}{s_0}\right)^{\alpha(t)-1} \tag{1.96}$$

or equivalently, by if the amplitude has the following power-like behaviour

$$\mathscr{A} \sim s^{\alpha(t)} \tag{1.97}$$

when its quantum numbers are exchanged in the t-channel. The factor in the exponent, $\alpha(t)$ is the gluon Regge trajectory. The concept of reggeization of an elementary particle was introduced in [99–102], in the study of backward Compton scattering in QED. In contrast to QED, where the electron reggeizes and the photon remains elementary [103]; in QCD both the gluon reggeizes [61, 104–107] and the quark [108–111]. Therefore, in QCD all elementary degrees of freedom reggeize.

[17] Four vectors are denoted by an underlined letter, while non-underlined letters denote the modulus of a transverse vector.

In order to obtain the derivation of the reggeization property at LLA, we need to keep only the leading $\log(s)$ term at each order. In order to do so, we need to select diagrams in which the quantum numbers interchanged in the t-channel are spin 1 and color octet, which corresponds to a reggeized gluon exchange and are the relevant ones in the Regge limit.

1.3.1.1 Born level

Let us consider the scattering of two different quarks in the Regge limit, Fig. 1.14. Instead of taking the limit at the level of the amplitude squared, it is more convenient to take it already at the level of the amplitude, using the so-called eikonal approximation. Consider the qqg vertex in the gluon exchange diagram. In the Regge limit the colliding particles are slightly deflected, and we have that the gluon is soft compared to the quarks

$$ig\bar{u}\left(\underline{p}_1+\underline{q}\right)\gamma^\mu u\left(\underline{p}_1\right)\simeq ig\bar{u}\left(\underline{p}_1\right)\gamma^\mu u\left(\underline{p}_1\right)=2ig\underline{p}_1^\mu. \tag{1.98}$$

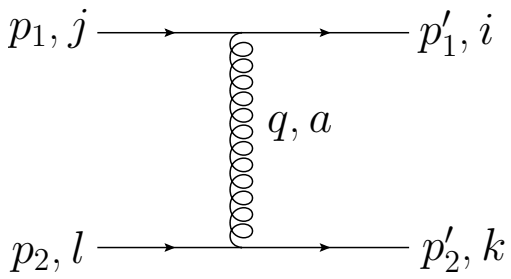

Figure 1.14: Born level diagram for the quark-quark scattering through the interchange of a gluon in the t-channel.

Applying the same approximation to both vertices, we obtain that the Born level amplitude in qq' scattering is given in the Regge limit by

$$A_{qq'}^{(0)}=g^2t_{ij}^at_{kl}^a\frac{4\underline{p}_1\cdot\underline{p}_2}{\underline{q}^2}=8\pi\alpha_st_{ij}^at_{kl}^a\frac{s}{t}\Rightarrow\left|A_{qq'}^{(0)}\right|^2=\frac{8}{9}g^4\left(\frac{s}{t}\right)^2. \tag{1.99}$$

In the case of the scattering of two gluons we obtain, in the same approximation

$$\left|A_{gg}^{(0)}\right|^2=\left(\frac{C_A}{C_F}\right)^2\left|A_{qq'}^{(0)}\right|^2. \tag{1.100}$$

1.3.1.2 One loop

Now we want to compute the one loop correction to the Born level $qq'\to qq'$ amplitude. At the LLA level, self energy insertions and vertex corrections are not relevant, since they

are subleading in $\log(s)$: they have an extra α_s factor w.r.t. the Born level graph, but no $\log(s)$ enhancement, since the vertex or bubble subdiagrams cannot depend on s, since they depend only on external legs squared (which are on-shell) or their product with $\underline{k}$, which gives order $\sqrt{-t}$ contributions. Using the Cutkosky rules [112], based on unitarity, we can recycle tree diagrams into loops, at the expense of adding on-shell phase space integrations. With them we can obtain the imaginary part of the box amplitude in Fig

$$\mathrm{Im}\, A^{(1)}_{(a)} = 4\alpha_s^2 \left(t^a t^b\right)_{ij} \left(t^a t^b\right)_{kl} s \int \frac{\mathrm{d}^2\vec{k}}{k^2\left(\vec{k}-\vec{q}\right)^2}\,. \tag{1.101}$$

Taking into account that we are looking for the leading $\log\frac{s}{t}$ in the amplitude, and that t is negative we have that the amplitude will have the following form $A = C\log^n(s/t) + \cdots = C\log^n(s/|t|) - in\pi C\log^{n-1}(s/|t|)$. This lets us extract the real part from the imaginary one easily, so we have the complete amplitude for diagram (a)

$$A^{(1)}_{(a)} = -\frac{16\pi\alpha_s}{N_C}\left(t^a t^b\right)_{ij}\left(t^a t^b\right)_{kl}\frac{s}{t}\log\frac{s}{t}\omega(t)\ ,\ \omega(t) \equiv \frac{\bar{\alpha}_s}{4\pi}\int \frac{\mathrm{d}^2\vec{k}\,\left(-q^2\right)}{k^2\left(\vec{k}-\vec{q}\right)^2}\,, \tag{1.102}$$

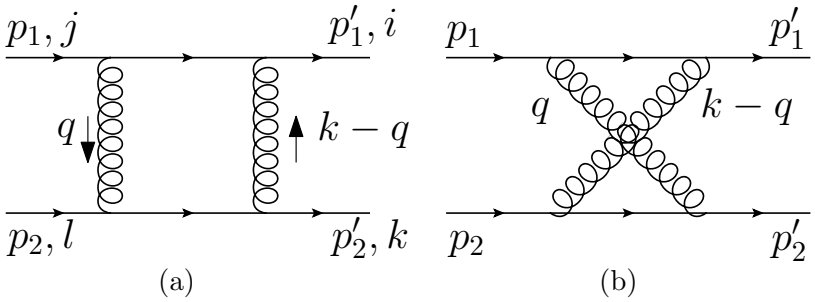

Figure 1.15: One loop level diagrams for the quark-quark scattering through the interchange of two gluons in the t-channel. Box diagram (a) and the crossed diagram (b).

In the Regge limit, since $\log\frac{s}{t} = \log\left(\frac{s}{|t|}\right) - i\pi$, the amplitude is real. The quantity $\omega(t)$ is IR divergent, but this singularity appears because we have considered the external quarks massless and on-shell. However, since they are confined inside hadrons they will have some virtuality giving an infrared cutoff. Adding the contribution of the crossed diagram (b), we obtain

$$A^{(1)} = A^{(1)}_{(a)} + A^{(1)}_{(b)} = -\frac{16\pi\alpha_s}{N_C}\left(t^{a t^b}\right)_{ij}\frac{s}{t}\left[\left[t^a, t^b\right]_{kl}\log\left(\frac{s}{|t|}\right) - i\pi\left(t^a t^b\right)_{kl}\right]w(t)\,. \tag{1.103}$$

We can apply the projectors to the singlet and *octet* representations of $SU(N_c)$ to the amplitude to decompose it into

$$A_8^{(1)}(s,t) = 8\pi\alpha_s t^a_{ij} t^a_{kl} \frac{s}{t} \log\left(\frac{s}{|t|}\right) w(t) \;\;,\;\; A_1^{(1)}(s,t) = 4i\pi^2 \alpha_s \delta_{ij}\delta_{kl} \frac{N_C^2 - 1}{N_C^2} \frac{s}{t} w(t) \tag{1.104}$$

where we see that the color-singlet part, also called as pomeron, is subleading in $\log(s)$. Finally we can write the one loop leading contribution as

$$A^{(1)}(s,t) = w(t) \log\left(\frac{s}{|t|}\right) A^{(0)}(s,t)\,. \tag{1.105}$$

1.3.1.3 Two loops

Going to two loops, we can still avoid the corrections to vertices and self-energy bubbles. There are two types of contributions when we apply the Cutosky rules. Diagrams in which there is one internal gluon cutted (Fig. 1.16, (a) for example), so we put it on-shell, are called "real" emissions, since once we integrate over the phase space of the on-shell gluon the amplitude is related to a real gluon emission in a quark-quark scattering. We also have "virtual" corrections, in which one part of the cutted diagram has a virtual correction on it, see Fig. 1.18.

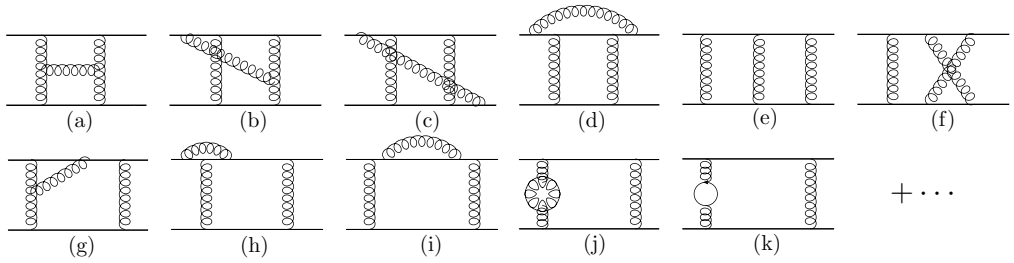

Figure 1.16: Some of the two-loop order diagrams contributing to the quark-quark scattering at LLA.

All the real contributions can be written in the really simple form with the help of an effective vertex, defined by Lipatov, from whom it receives its name. Then the leading part of the real emissions is encoded in the Lipatov's effective vertex of Fig. 1.17. Introducing the Sudakov parametrization for the exchanged gluons

$$\underline{k}_i = \alpha_i \underline{p}_1 + \beta_i \underline{p}_2 + \vec{k}_i\,, \tag{1.106}$$

the effective vertex is given by

$$\Gamma^{\rho}_{\mu\nu}(\underline{k}_1, \underline{k}_2) = \frac{2\underline{p}_{2\mu}\underline{p}_{1\nu}}{s} C^{\rho} \;\;,\;\; C^{\rho} = \left(\alpha_1 + \frac{2k_1^2}{\beta_2 s}\right)\underline{p}_1^{\rho} + \left(\beta_2 + \frac{2k_2^2}{\alpha_1 s}\right)\underline{p}_2^{\rho} - \left(\vec{k}_1^{\rho} + \vec{k}_2^{\rho}\right). \tag{1.107}$$

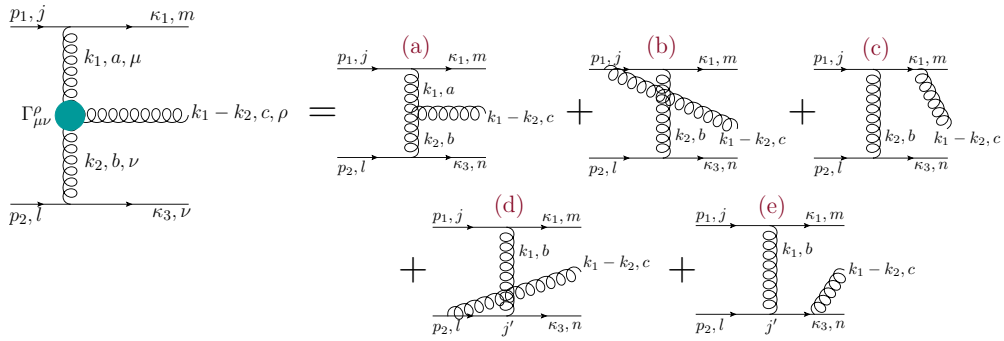

Figure 1.17: Diagrammatic definition of Lipatov's effective vertex. The blob gives a factor $g f_{abc} \Gamma^{\rho}_{\mu\nu}(\underline{k}_1, \underline{k}_2)$.

Then we have that the real corrections are simply a cut diagram where each side is the diagram of Fig. 1.17, this gives a $gg \to ggg$ amplitude

$$A^{\rho}_{2\to 3} = 4ig^3 \frac{p_1^{\mu} p_2^{\nu}}{k_1^2 k_2^2} t^a_{mj} t^b_{nl} f_{abc} \Gamma^{\rho}_{\mu\nu} . \tag{1.108}$$

Having computed all the parts (the u-channel contribution, integration over the phase space, color factors) we obtain the imaginary part of the octed representation coming from the real emissions

$$\begin{aligned} \mathrm{Im} A_8^{(2),R}(s,t) = \frac{\alpha_s^3 N_C^2}{2\pi^2} t^a_{ij} t^b_{kl} s \log\left(\frac{s}{|t|}\right) \int\int \mathrm{d}^2\vec{k}_1 \, \mathrm{d}^2\vec{k}_2 \times \left[\frac{q^2}{k_1^2 k_2^2 \left(\vec{k}_1 - \vec{q}\right)^2 \left(\vec{k}_2 - \vec{q}\right)^2} - \right. \\ \left. - \frac{1}{k_2^2 \left(\vec{k}_1 - \vec{q}\right)^2 \left(\vec{k}_1 - \vec{k}_2\right)^2} - \frac{1}{k_1^2 \left(\vec{k}_2 - \vec{q}\right)^2 \left(\vec{k}_1 - \vec{k}_2\right)^2} \right] . \end{aligned} \tag{1.109}$$

The computation of the virtual corrections (Fig. 1.18) can be simplified using that we have already calculated the one-loop amplitude, which is part of the cutted diagram, the final result is

$$\begin{aligned} \mathrm{Im} A_8^{(2),V}(s,t) = \frac{\alpha_s^3 N_C^2}{2\pi^2} t^a_{ij} t^b_{kl} s \log\left(\frac{s}{|t|}\right) \int\int \mathrm{d}^2\vec{k}_1 \, \mathrm{d}^2\vec{k}_2 \times \\ \left[\frac{1}{k_2^2 \left(\vec{k}_1 - \vec{q}\right)^2 \left(\vec{k}_1 - \vec{k}_2\right)^2} + \frac{1}{k_1^2 \left(\vec{k}_2 - \vec{q}\right)^2 \left(\vec{k}_1 - \vec{k}_2\right)^2} \right] . \end{aligned} \tag{1.110}$$

Combining both the real and virtual contributions we have a great simplification in the octet case, leading to

$$A_8^{(2)}(s,t) = \frac{\alpha_s^3 N_C^2}{2\pi^2} t^a_{ij} t^b_{kl} s \log\left(\frac{s}{|t|}\right) \int\int \mathrm{d}^2\vec{k}_1 \, \mathrm{d}^2\vec{k}_2 \left[\frac{q^2}{k_1^2 k_2^2 \left(\vec{k}_1 - \vec{q}\right)^2 \left(\vec{k}_2 - \vec{q}\right)^2}\right] = \tag{1.111}$$

$$= 8\pi^2 \alpha_s t^a_{ij} t^b_{kl} \frac{s}{|t|} \log\left(\frac{s}{|t|}\right) \omega^2(t) .$$

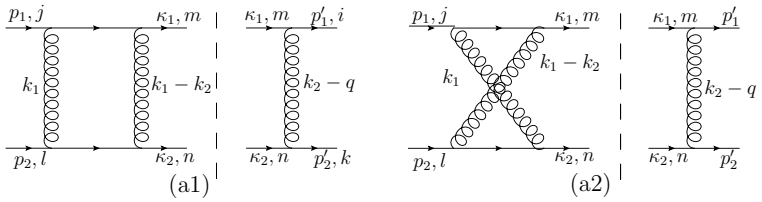

Figure 1.18: Some of the two-loop “virtual" corrections to qq' scattering at LLA. We need also to add the topologies related by mirroring.

We obtain a really simple solution for the complete amplitude, once we derive the real part as in the previous case. The reason of that miraculous cancellation of terms is reggeization, as we will see.

$$A_8^{(2)}(s,t) = \frac{1}{2}\left(\log\left(\frac{s}{|t|}\right)\omega(t)\right)^2 A^{(0)}(s,t) . \tag{1.112}$$

which gives the appealing form to the total amplitude

$$A_8(s,t) = A^{(0)}\left(1 + \omega(t)\log\left(\frac{s}{|t|}\right) + \frac{1}{2}\left(\omega(t)\log\left(\frac{s}{|t|}\right)\right)^2 + \cdots\right) . \tag{1.113}$$

1.3.1.4 All loops

The previous result looks like the first three terms of a reggeized particle, and it suggests us to make the following guess for the amplitude

$$A_8(s,t) = A^{(0)}\left(\frac{s}{s_0}\right)^{\omega(t)} , \tag{1.114}$$

which is nothing but the Born level result amplitude with a modified propagator. We are gonna give a partial demonstration, but all the technical details can be found in, for example Ref. [98]. As we have seen before, the real part contribution at arbitrary order will be the emission of n gluons, where the use of the Lipatov's effective vertex enormously

simplifies the number and topology of the diagrams involved. The diagram in Fig. 1.19 (a) will be expressed as

(1.115)

$$A_{2\to 2+n}^{\rho_1\cdots\rho_n} = 2is g_s t_{ij}^{a_1} \frac{i}{k_1^2}\left[-gf_{a_1a_2b_1}C^{\rho_1}\left(\underline{k}_1,\underline{k}_2\right)\frac{i}{k_2^2}\right]\cdots\left[-gf_{a_na_{n+1}b_n}C^{\rho_n}\left(\underline{k}_n,\underline{k}_{n+1}\right)\frac{i}{k_{n+1}^2}\right] g t_{kl}^{a_{n+1}}.$$

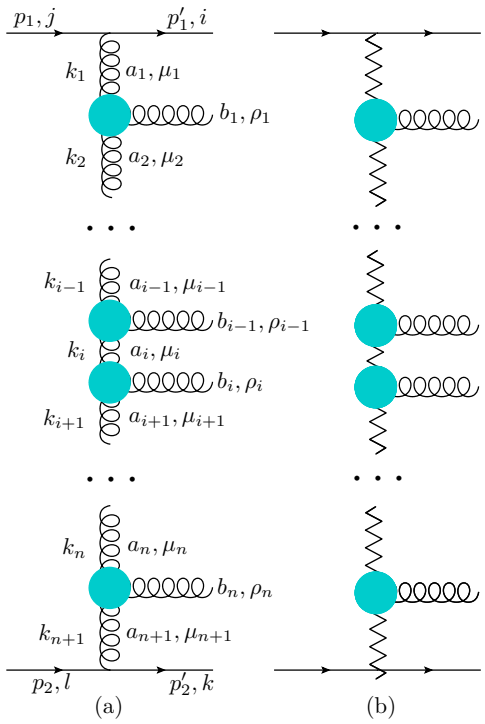

Figure 1.19: Diagram for the process $qq \to qq + n \times g$. The blobs represent the Lipatov's effective vertex. We have the diagram at tree level (a), and assuming the reggeization of the t-channel gluons (b).

In order to apply the Cutosky rules to obtain the imaginary part of the amplitude of the $qq' \to qq'$ scattering, we have to take the amplitude given in Eq. (1.115), multiply it by its hermitian conjugate and integrate over the on-shell phase space of the real emissions. But then, we would need the virtual corrections. Looking at Fig. 1.18 we notice that they are equivalent to consider already the the amplitude of $qq' \to qq'$ scattering at the previous order, so we will proceed by induction and assume that the reggeization hypothesis is valid. This procedure is known as *bootstrap* method, and we will have to check the consistency of it at the end. Then, virtual corrections are taken into account by the modification of the

t-channel gluons in the following way

$$\frac{ig_{\mu\nu}}{k_i^2} \to \frac{ig_{\mu\nu}}{k_i^2}\left(\frac{\alpha_{i-1}}{\alpha_i}\right)^{\alpha(-k_i^2)}, \tag{1.116}$$

since $s_i = \left(\underline{k}_{i-1} + \underline{k}_i\right)^2 \simeq \frac{\alpha_{i-1}}{\alpha_i} k_i^2$, where the gluon Regge trajectory is defined as $\alpha\left(q^2\right) = 1 + \omega\left(q^2\right)$.

We obtain the following ansatz for the amplitude

$$A_{2\to 2+n}^{\rho_1\cdots\rho_n} = 2isg_s^2 t_{ij}^{a_1} t_{kl}^{a_{n+1}} \frac{i}{k_1^2} e^{y_1\omega(-k_1^2)} \prod_{i=1}^{n}\left[-gf_{a_i a_{i+1} b_i} C^{\rho_i}\left(\underline{k}_i, \underline{k}_{i+1}\right) \frac{i}{k_{i+1}^2} e^{(y_i - y_{i+1})\omega(-k_{i+1}^2)}\right], \tag{1.117}$$

where we have defined the rapidity variable as $\alpha_i \equiv e^{y_i}$.

Now, once we have assumed reggeization for the gluon, we can obtain the imaginary part of the amplitude in each representation, multiplying by the hermitian conjugate and integrating over the phase space, it follows that

$$\begin{aligned}\mathrm{Im}\, A_R(s,t) = \frac{1}{2}\sum_{n=0}^{\infty} 4s^2 g_s^4 \mathscr{G}_R \int \mathrm{d}\Pi_{n+2} \frac{1}{k_1^2\left(\vec{k}_1 - \vec{q}\right)^2} e^{-y_i\left(\omega(-k_1^2) + \omega\left((\vec{k}_1 - \vec{q})^2\right)\right)} \times \\ \times \left[\prod_{i=1}^{n} \frac{-2\eta_R g_s^2}{k_{i+1}^2\left(\vec{k}_{i+1} - \vec{q}\right)^2} K\left(\vec{k}_i, \vec{k}_{i+1}\right) e^{(y_i - y_{i+1})\left(\omega(-k_{i+1}^2) + \omega\left((\vec{k}_{i+1} - \vec{q})^2\right)\right)}\right],\end{aligned} \tag{1.118}$$

where the kernel is given by the contraction of Lipatov's effective vectices

$$\begin{aligned}K\left(\vec{k}_i, \vec{k}_{i+1}\right) \equiv q^2 - \frac{k_i^2\left(\vec{k}_{i+1} - \vec{q}\right)^2}{\left(\vec{k}_i - \vec{k}_{i+1}\right)^2} - \frac{k_{i+1}^2\left(\vec{k}_i - \vec{q}\right)^2}{\left(\vec{k}_i - \vec{k}_{i+1}\right)^2} = \\ = -\frac{1}{2} C^{\rho_i}\left(\underline{k}_i, \underline{k}_{i+1}\right) C_{\rho_i}\left(-\underline{k}_i + \underline{q}, -\underline{k}_{i+1} + \underline{q}\right).\end{aligned} \tag{1.119}$$

And the color factors that appear are given by

$$\mathscr{G}_1 = \frac{N_C^2 - 1}{4N_C}, \eta_1 = N_C \;;\; \mathscr{G}_8 = -\frac{N_C}{8}, \eta_8 = \frac{N_C}{2}. \tag{1.120}$$

In order to disentangle the nested integrations occurring in the phase space integration, it is better to work in Mellin space, conjugating the s variable. We define

$$f_R(\omega,t) = \int_1^{\infty} \mathrm{d}\left(\frac{s}{|t|}\right)\left(\frac{s}{|t|}\right)^{-\omega-1} \frac{\mathrm{Im}\, A_R(s,t)}{s} \Leftrightarrow \frac{\mathrm{Im}\, A_R(s,t)}{s} = \int \frac{\mathrm{d}\omega}{2\pi i}\left(\frac{s}{|t|}\right)^{\omega} f_R(\omega,t). \tag{1.121}$$

Also, the u-channel contribution must be added to the previous part, it can be done through the introduction of the signature

$$\mathrm{Im}\, A_R(u,t) = \mathrm{Im}\, A_R(-s,t) = -\xi_R A_R(s,t) \;,\; \xi_1 = 1 \,,\, \xi_8 = -1. \tag{1.122}$$

The crossed contribution is added in Mellin space with the substitution $f_R(\omega,t) \to \left(1-\xi_R e^{-i\pi\omega}\right) f_R(\omega,t)$. Applying a dispersion relation we finally obtain the full amplitude

$$A_R(s,t) = -\frac{1}{2}\int \frac{\mathrm{d}\omega}{2\pi i}\left(\frac{s}{|t|}\right)^{\omega+1} \frac{\xi_R - e^{-i\omega\pi}}{\sin\pi\omega} f_R(\omega,t)\,. \tag{1.123}$$

The great observation is that introducing the auxiliary function $\mathscr{F}_R\left(\omega,\vec{k},\vec{q}\right)$ we can cast the equation in terms of an integral equation

$$f_R\left(\omega,q^2\right) = (4\pi\alpha_s)^2 \mathscr{G}_R \int \frac{\mathrm{d}^2\vec{k}}{(2\pi)^2} \frac{\mathscr{F}_R\left(\omega,\vec{k},\vec{q}\right)}{k^2(\vec{k}-\vec{q})^2}\,, \tag{1.124}$$

where the equation for the GGF is

$$\left(\omega - \omega\left(-k^2\right) - \omega\left(-(\vec{k}-\vec{q})^2\right)\right)\mathscr{F}_R\left(\omega,\vec{k},\vec{q}\right) = 1 - \frac{2\alpha_s\xi_R}{(2\pi)^2}\int \mathrm{d}^2\vec{l}\,\frac{K\left(\vec{k},\vec{l}\right)}{l^2\left(\vec{l}-\vec{q}\right)^2}\mathscr{F}_R\left(\omega,\vec{l},\vec{q}\right). \tag{1.125}$$

For the case of the octet solution the equation dramatically simplifies, and it admits a $\vec{k}$-independent solution leading to

$$A_8(s,t) = -4\pi\alpha_s t^a_{ij} t^a_{kl}\left(1-e^{-i\pi\alpha(t)}\right)\left(\frac{s}{|t|}\right)^{\alpha(t)} \tag{1.126}$$

where we have defined $\alpha(t) = 1+\omega(t)$. That finally demonstrates that the reggeization hypothesis was correct.

For the singlet case (the pomeron) the form of the equation is cumbersome

$$\left(\omega - \omega\left(-k^2\right) - \omega\left(-(\vec{k}-\vec{q})^2\right)\right)\mathscr{F}_1\left(\omega,\vec{k},\vec{q}\right) = 1 - \frac{\bar{\alpha}_s}{2\pi}\int \mathrm{d}^2\vec{l}\,\frac{K\left(\vec{k},\vec{l}\right)}{l^2\left(\vec{l}-\vec{q}\right)^2}\mathscr{F}_1\left(\omega,\vec{l},\vec{q}\right), \tag{1.127}$$

and it is usually written in terms of the BFKL Green's function, or Gluon Green's Function (GGF) defined as

$$\mathscr{F}_1\left(\omega,\vec{k},\vec{q}\right) = \int \frac{\mathrm{d}^2\vec{l}}{l^2} k^2 \varphi\left(\omega,\vec{k},\vec{l},\vec{q}\right), \tag{1.128}$$

in which the BFKL equation reads

$$\left(\omega - \omega\left(-k^2\right) - \omega\left(-(\vec{k}-\vec{q})^2\right)\right)\varphi\left(\omega,\vec{k},\vec{l},\vec{q}\right) = \delta^2\left(\vec{k}-\vec{l}\right) - \frac{\bar{\alpha}_s}{2\pi}\int \mathrm{d}^2\vec{p}\,\frac{K\left(\vec{k},\vec{p}\right)}{k^2\left(\vec{p}-\vec{q}\right)^2}\varphi\left(\omega,\vec{p},\vec{l},\vec{q}\right). \tag{1.129}$$

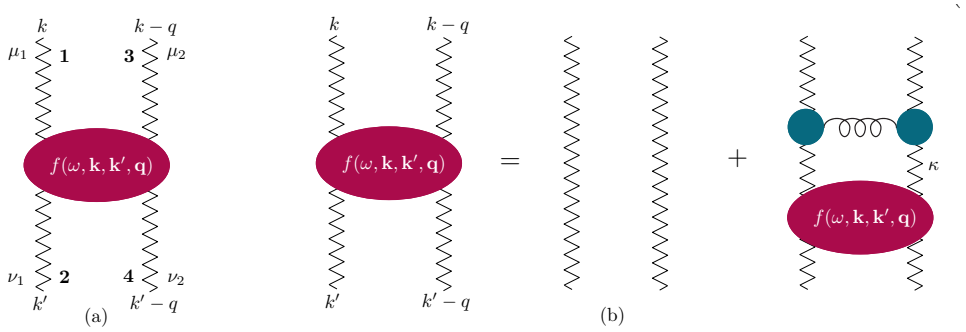

Figure 1.20: The BFKL GGF (a) and the diagrammatic representation of the iterative BFKL equation (b) for the GGF. Adapted from [98].

Although the expression above is complicated, it greatly simplifies in the zero momentum transfer case, $\vec{q} = 0$, that is the relevant one for the forward scattering amplitude and the total cross section, defining $\varphi\left(\omega, \vec{k}_1, \vec{k}_2\right) \equiv \varphi\left(\omega, \vec{k}_1, \vec{k}_2, 0\right)$ we have

$$\begin{aligned} \omega\varphi\left(\omega, \vec{k}_1, \vec{k}_2\right) = \delta^2\left(\vec{k}_1 - \vec{k}_2\right) + \frac{\bar{\alpha}_s}{\pi} \int \times \frac{\mathrm{d}^2\vec{q}}{\left(\vec{q} - \vec{k}_1\right)^2} \\ \times \left(\varphi\left(\omega, \vec{q}, \vec{k}_2\right) - \frac{k_1^2}{q^2 + \left(\vec{k}_1 - \vec{q}\right)^2} \varphi\left(\omega, \vec{k}_1, \vec{k}_2\right) \right). \end{aligned} \tag{1.130}$$

The total cross section for inclusive processes is directly related to the imaginary part of the forward scattering amplitude we just computed, via the optical theorem. The cross section can be expressed as

$$\sigma = \frac{\mathrm{Im}\, A}{s}, \tag{1.131}$$

that will be crucial, in combination with collinear factorization and high-energy factorization to compute observables for the Mueller-Navelet jets. The solution of the BFKL equation for the GGF will be described at LLA and NLLA in Sec. 1.4.2.

1.4 Mueller-Navelet Jets

At hadronic colliders and in particular at the LHC, a phenomenologically interesting process is Mueller-Navelet (MN) jet production. It was originally proposed by Mueller and Navelet in Ref. [113], as a reaction in which one could disentangle the high-energy behavior of the partonic cross section while removing most of the parton distribution functions (PDFs) dependence, making the observable a suitable probe for BFKL dynamics. Note that, contrary to the DIS case, in MN jet production where are interested in a kinematical regime where the presence of the BFKL resummation is relevant only in the partonic scattering, not in the PDFs. Another aspect of this type of events is that, as one measures higher energy reactions, the amount of jet production increases rapidly and it is desirable to obtain a good theoretical description of these high multiplicity events. Originally, MN were interested in giving a precise quantitative prediction for these phenomena, and therefore they focused on the growth with the center-of-mass energy squared s of the inclusive minijet cross section. MN jets (dijet production) are inclusive final states where two jets with transverse momenta of similar sizes, $k_{A,B}$ are tagged to have a large rapidity separation Y.

The presence of two hard but similar in size scales (k_A and k_B) ensures in principle the applicability of a BFKL-based approach. A number of works in the literature [114–129] generalized the original MN work by studying the azimuthal angle (θ) behaviour of the two jets, instead of only only its cross section. This behavior is driven by the presence of decisive minijet activity in the rapidity space between the two outermost jets which in BFKL based studies is accounted for by a BFKL gluon Green's function connecting the two jets, $\varphi(k_A, k_B, Y)$. The comparison of different NLLA calculations for these correlations [130–134] against LHC experimental data [135, 136] has been promising so far, but the debate for the data presenting BFKL or DGLAP features has not been settled yet.

1.4.1 Notation and Conventions

In collisions of two hadrons (protons at the LHC) MN jets is the final state characterized by two tagged jets well separated in rapidity

$$p(p_A) + p(p_B) \to J_A(k_A) + J_B(k_B) + X\,. \tag{1.132}$$

The relevant kinematical configuration is given by[18]

$$s \equiv \left(\underline{p}_A + \underline{p}_B\right)^2 \gg Q^2 \sim k_A^2 \sim k_B^2 \gg \Lambda_{QCD}^2 \tag{1.133}$$

[18] All transverse two-momenta will be denoted by vector variables. We will use underline latin letters to denote 4-vectors, in contrast to plain latin letters, denoting the modulus of a transverse momentum.

where Q is some typical hard transverse scale that guarantees the applicability of perturbation theory. Using Sudakov decomposition with $p_{A,B}$ as a basis[19], we have

$$\underline{k}_A = x_{J_A}\underline{p}_A + \frac{k_A^2}{x_{J_A}s}\underline{p}_B + \underline{k}_{A,\perp}\,,\ \underline{k}_B = x_{J_B}\underline{p}_B + \frac{k_B^2}{x_{J_B}s}\underline{p}_A + \underline{k}_{B,\perp}\,,\ \underline{k}_{A,B,\perp}^2 = -k_{A,B}^2\,, \tag{1.134}$$

where $x_{J_{A,B}}$ are the longitudinal momentum fractions of the jets. The rapidities $y_{A,B}$ of the two tagged jets are related to the Sudakov parameters in the following way

$$y_A = \frac{1}{2}\log\left(\frac{x_{J_A}^2 s}{k_A^2}\right),\ y_B = -\frac{1}{2}\log\left(\frac{x_{J_B}^2 s}{k_B^2}\right), \tag{1.135}$$

while the rapidity difference Y is

$$Y \equiv y_A - y_B = \log\frac{x_{J_A}x_{J_B}s}{k_A k_B}\,. \tag{1.136}$$

MN jets is a semi-hard process, in order to study it properly we need to combine both collinear factorization and BFKL dynamics. Initially the two partons, before their hard partonic interaction which is described by BFKL, are following the standard DGLAP evolution [47, 49, 50]. In collinear factorization, the leading twist approximation allows us to write the cross section as a convolution of the parton distribution functions (PDFs) $f_i\left(x,\mu_F\right)$ and the partonic cross section $\hat{\sigma}$

$$\frac{\mathrm{d}\sigma\left(s\right)}{\mathrm{d}y_A\,\mathrm{d}y_B\,\mathrm{d}^2\vec{k}_A\,\mathrm{d}^2\vec{k}_B} = \sum_{i,j}\int_0^1 f_i\left(x_A,\mu_F\right) f_j\left(x_B,\mu_F\right)\frac{\mathrm{d}\hat{\sigma}_{ij}\left(x_A x_B s,\mu_F\right)}{\mathrm{d}y_A\,\mathrm{d}y_B\,\mathrm{d}^2\vec{k}_A\,\mathrm{d}^2\vec{k}_B} \tag{1.137}$$

where the indices i,j specify the parton type ($i,j = q,\bar{q},g$), μ_F is the factorization scale and $x_{A,B}$ represent the longitudinal momentum fractions of the partons. Note that these are different from the jet momentum fractions and that $x_{J_{A,B}} \le x_{A,B}$.

As mentioned earlier, within the BFKL framework, we can perform the resummation either at LLA or NLLA accuracy, however for both cases there is one additional important fact to keep in mind, namely, in the high-energy limit we are considering, the partonic cross-section itself also factorizes into a convolution of process-dependent jet vertices V and a universal part which is accounted for by the gluon Green's function φ

$$\begin{aligned}\frac{\mathrm{d}\hat{\sigma}_{ij}\left(x_A x_B s,\mu_F\right)}{\mathrm{d}y_A\,\mathrm{d}y_B\,\mathrm{d}^2\vec{k}_A\,\mathrm{d}^2\vec{k}_B} = \frac{x_{J_A}x_{J_B}}{(2\pi)^2}\int\frac{\mathrm{d}^2\vec{q}_A}{\vec{q}_A^{\,2}}V_i\left(\vec{q}_A,x_A,s_0,\vec{k}_A,x_{J_A},\mu_F,\mu_R\right)\\ \int\frac{\mathrm{d}^2\vec{q}_B}{\vec{q}_B^{\,2}}V_j\left(-\vec{q}_B,x_B,s_0,\vec{k}_B,x_{J_B},\mu_F,\mu_R\right)\int_C\frac{\mathrm{d}\omega}{2\pi i}\left(\frac{x_A x_B s}{s_0}\right)^{\omega}\varphi_\omega(\vec{q}_A,\vec{q}_B)\,.\end{aligned} \tag{1.138}$$

[19] The mass of the jets is neglected.

Each jet vertex $V_{i(j)}$ describes the transition from the parton with longitudinal fraction $x_{A(B)}$ to the jet $A(B)$ after exchanging a t-channel Reggeized gluon with momentum $\vec{q}_{A(B)}$. The jet vertices depend on the factorization scale μ_F, the renormalisation scale μ_R, an arbitrary energy scale s_0 that is introduced when taking the inverse Mellin transform in the calculation of the gluon Green's function and on the jet algorithm definition, whereas they have no s dependence. It is important to note that the total cross section does not depend on s_0 within NLLA accuracy although s_0 affects higher order terms.

The integration contour C is a vertical line such that all poles in ω are to the left of the contour and the gluon Green's function satisfies the forward BFKL equation

$$\omega\varphi_\omega(\vec{q}_A,\vec{q}_B) = \delta^2(\vec{q}_A-\vec{q}_B) + \int \mathrm{d}^2\vec{q}\, K(\vec{q}_A,\vec{q})\varphi_\omega(\vec{q},\vec{q}_B)\,. \tag{1.139}$$

We will work with a combination of the jet vertex (impact factor)[20] together with its respective contribution from of the PDFs, that is, with the inclusive impact factor:

$$\Phi\left(\vec{q},\vec{k},x_J,\omega,s_0,\mu_F,\mu_R\right) \equiv \sum_i \int_0^1 \mathrm{d}x\, f_i\left(x,\mu_F\right) V_i\left(\vec{q},x,s_0,\vec{k},x_J,\mu_F,\mu_R\right)\left(\frac{x}{x_J}\right)^\omega, \tag{1.140}$$

where the last factor $\left(\frac{x}{x_J}\right)^\omega$ is not conventional. It has been taken from the gluon Green's function to the impact factor to let us perform the integration over the parton momentum fraction x before integrating over the rest of the variables, see [122]. This change does not affect the leading order (LO) part of the impact factor, since at this order we have $x = x_J$.

After using the inclusive impact factors Φ, we write the differential cross section as

$$\begin{aligned}\frac{\mathrm{d}\sigma\,(s)}{\mathrm{d}y_A\,\mathrm{d}y_B\,\mathrm{d}^2\vec{k}_A\,\mathrm{d}^2\vec{k}_B} = \frac{x_{J_A}x_{J_B}}{(2\pi)^2}\int_C\frac{\mathrm{d}\omega}{2\pi i}\int\frac{\mathrm{d}^2\vec{q}_A}{\vec{q}_A^{\,2}}\Phi\left(\vec{q}_A,\vec{k}_A,x_{J_A},\omega,s_0,\mu_F,\mu_R\right)\\ \int\frac{\mathrm{d}^2\vec{q}_B}{\vec{q}_B^{\,2}}\Phi\left(-\vec{q}_B,\vec{k}_B,x_{J_B},\omega,s_0,\mu_F,\mu_R\right)e^{\omega(Y-Y_0)}\varphi_\omega(\vec{q}_A,\vec{q}_B)\,,\end{aligned} \tag{1.141}$$

where the relation between Y_0 and s_0 is given by $Y_0 = \log\frac{s_0}{k_A k_B}$, that we will set to $Y_0 = 0$ in phenomenological applications.

1.4.2 Solution of the gluon Green's function at LLA and NLLA

In order to study the gluon Green's function it is convenient to use the Dirac's braket notation as in [137] and to introduce eigenfunctions of the integral kernel, allowing us to solve the BFKL equation in a simple way. In this section we will give a quick overview of the methods used to solve the BFKL equation for the singlet at vanishing momentum transfer,

[20] Hereafter, the terms "impact factor" and "jet vertex" will be used interchangeably.

the BFKL gluon Green's function (GGF). The explicit normalization and relationships of the eigenfunctions are found in Section A.1. In operator notation, Eq. (1.139) reads

$$\omega\varphi_\omega = \mathbb{1} + \mathcal{K}\,\varphi_w \tag{1.142}$$

and the total cross section (1.141) can be written as[21]

$$\frac{\mathrm{d}\sigma\,(s)}{\mathrm{d}y_A\,\mathrm{d}y_B\,\mathrm{d}^2\vec{k}_A\,\mathrm{d}^2\vec{k}_B} = \frac{x_{J_A}x_{J_B}}{(2\pi)^2}\int_C \frac{\mathrm{d}\omega}{2\pi i}e^{\omega(Y-Y_0)}\left\langle \Phi(J_A)\right| \frac{\mathbb{1}}{\omega\mathbb{1}-\mathcal{K}} \left|\Phi(J_B)\right\rangle . \tag{1.143}$$

Since the BFKL kernel is known to NLLA accuracy, we can write

$$\mathcal{K} = \bar{\alpha}_{\mu_R}\mathcal{K}_0 + \bar{\alpha}^2_{\mu_R}\mathcal{K}_1 + \mathcal{O}\left(\bar{\alpha}^3_{\mu_R}\right), \tag{1.144}$$

where

$$\bar{\alpha}_{\mu_R} = \frac{N_C\,\alpha_S(\mu_R^2)}{\pi} \tag{1.145}$$

is the renormalized strong coupling constant evaluated at the renormalization scale μ_R, while N_C is the number of colors in QCD. $\mathcal{K}_0$ and $\mathcal{K}_1$ are the leading order (LO) [61–63, 104, 105] and next-to-leading order (NLO) [67, 69] contributions to the BFKL kernel, which resum the leading and next-to-leading logarithms respectively.

At LLA the kernel enjoys conformal invariance and the eigenvectors can be found to be $|n,\nu\rangle$ (see Appendix A.1) manifesting conformal symmetry [138]. At NLLA this basis is no longer diagonal due to the breaking of conformal invariance by the running of the strong coupling and its action on the LLA eigenvectors is given by [139]

$$\langle\vec{q}\,|\,\mathcal{K}_0\,|n,\nu\rangle = \chi_0(n,\nu)\,\langle\vec{q}\,|\,n,\nu\rangle\,, \tag{1.146}$$

$$\langle\vec{q}\,|\,\mathcal{K}_1\,|n,\nu\rangle = \chi_1(n,\nu)\,\langle\vec{q}\,|\,n,\nu\rangle + \beta_2\left(\frac{i}{2}\frac{\partial\chi_0(n,\nu)}{\partial\nu} - \chi_0(n,\nu)\log\frac{\vec{q}^{\,2}}{\mu_R^2}\right)\langle\vec{q}\,|\,n,\nu\rangle\,, \tag{1.147}$$

where $\beta_2 \equiv \frac{\beta_0}{4N_C} = \frac{11N_C-2N_F}{12N_C}$ is the one-loop beta function of the strong coupling and N_F is the number of active quark flavors. Note that the second term in the r.h.s. of Eq. (1.147) is proportional to β_0 and it is either purely imaginary or $\vec{q}^{\,2}$ dependent.

The LO kernel eigenvalue $\chi_0(n,\nu)$ is given by

$$\chi_0(n,\nu) = 2\psi(1) - \psi\left(\frac{1+|n|}{2}+i\nu\right) - \psi\left(\frac{1+|n|}{2}-i\nu\right), \tag{1.148}$$

[21] From now on, the input J in the impact factor Φ stands for all the variables associated with the jet J: $\vec{k}_J, x_J, \mu_F, \mu_R, R$, being R the radius associated with the jet reconstruction algorithm.

with $\psi(z) = \frac{\mathrm{d}}{\mathrm{d}z}\log\Gamma(z)$ the digamma function.

The remaining term $\chi_1(n,\nu)$ is given by [139]

$$\chi_1(n,\nu) = \gamma_K^{(2)}\chi_0(n,\nu) + \frac{3}{2}\zeta(3) - \frac{\beta_2}{2}\chi_0^2(n,\nu) + \frac{1}{4}\chi_0''(n,\nu) - \frac{1}{2}\left(\Phi(|n|,\nu)+\Phi(|n|,-\nu)\right) + \\ + \frac{\pi^2\sinh\pi\nu}{8\nu\cosh^2\pi\nu}\left\{-\delta_{n0}\left[3+\left(1+\frac{N_F}{N_C^3}\right)\frac{11+12\nu^2}{16\left(1+\nu^2\right)}\right] + \delta_{|n|2}\left(1+\frac{N_F}{N_C^3}\right)\frac{1+4\nu^2}{32\left(1+\nu^2\right)}\right\}. \tag{1.149}$$

In Eq. (1.149) $\Phi(n,\nu)$ is defined as

$$\Phi(n,\nu) = \sum_{k=0}^{\infty}\frac{(-1)^{k+1}}{k+i\nu+\frac{1+n}{2}}\Big\{\psi'(k+n+1)-\psi'(k+1)+ \\ +(-1)^{k+1}\left(\beta'(k+n+1)+\beta'(k+1)\right)+\frac{\psi(k+1)-\psi(k+n+1)}{k+i\nu+\frac{1+n}{2}}\Big\}, \tag{1.150}$$

where

$$\beta(z) = \frac{1}{2}\left(\psi\left(\frac{1+z}{2}\right)-\psi\left(\frac{z}{2}\right)\right), \tag{1.151}$$

while the accents on $\chi_0(n,\nu)$ indicate derivatives with respect to ν. The two-loop QCD cusp anomalous dimension in the dimensional reduction scheme is

$$\gamma_K^{(2)} = \frac{1}{3}\left(5\beta_2+1\right) - \frac{\zeta(2)}{2} = \frac{1}{4}\left(\frac{67}{9}-\frac{10N_F}{9N_C}-2\zeta(2)\right). \tag{1.152}$$

In [140, 141], Chirilli and Kovchegov built the eigenvectors of the NLLA kernel perturbatively, expanding around the LLA (conformal) ones. Their detailed properties are given in Appendix A.1. Here we will only note that they satisfy

$$\mathcal{K}\left|H_{n,\nu}\right\rangle = \left(\bar{\alpha}_{\mu_R}\chi_0(n,\nu)+\bar{\alpha}_{\mu_R}^2\chi_1(n,\nu)\right)\left|H_{n,\nu}\right\rangle \equiv \chi(n,\nu)\left|H_{n,\nu}\right\rangle . \tag{1.153}$$

The remaining necessary ingredient to compute the cross section is the impact factor which was calculated at NLO in [142, 143] and was later confirmed in [144]. We will be using the small-cone approximation (SCA), where the jet cone aperture R in the rapidity-azimuthal angle plane is considered small, neglecting powers in R. The impact factor was calculated in Ref. [145] directly in $|n,\nu\rangle$ space where the result can be expressed in a simple analytical form. A comparison between different jet algorithms (the Furman algorithm [146], the k_T algorithm [147] and the cone algorithm [148]) can be found in [149].

The expressions for the LO and NLO impact factor can be directly extracted from Ref. [145] after taking into account some slight changes in normalization and notation. They respectively read

$$\left\langle \Phi^{(LO)}(J)\right| n,\nu\Big\rangle = \frac{\mathcal{N}}{k_J^2}f^\star(x_J)\frac{1}{\pi\sqrt{2}}\left(k_J^2\right)^{i\nu-\frac{1}{2}}e^{in\theta_J} = \frac{\mathcal{N}}{k_J^2}f^\star(x_J)\left\langle\vec{k}\right| n,\nu\Big\rangle \tag{1.154}$$

and

$$\left\langle \Phi^{(NLO)}(J) \middle| n,\nu \right\rangle = \frac{\mathcal{N}}{\vec{k}_J^2} f^\star(x_J) \left\langle \vec{k} \middle| n,\nu \right\rangle \left(1+\bar{\alpha}_{\mu_R}\phi_1(n,\nu,\omega,J)\right). \tag{1.155}$$

The normalization factor is $\mathcal{N} = 2\pi^2\bar{\alpha}_{\mu_R}\sqrt{\frac{2C_F}{N_C^3}}$ and the NLO correction to the impact factor, $\phi_1(n,\nu,J)$, can be found in Appendix A.2. We have also defined the effective PDF [150]

$$f^\star(x_J) \equiv \frac{N_C}{C_F} f_g(x_J) + \sum_{i=q,\bar{q}} f_i(x_J). \tag{1.156}$$

The LO and NLO impact factor in the $|H_{n,\nu}\rangle$ basis can be easily computed, resulting in

$$\left\langle \Phi^{(LO)}(J) \middle| H_{n,\nu} \right\rangle = \frac{\mathcal{N}}{k_J^2} f^\star(x_J) \left\langle \vec{k} \middle| H_{n,\nu} \right\rangle \tag{1.157}$$

and

$$\left\langle \Phi^{(NLO)}(J) \middle| H_{n,\nu} \right\rangle = \frac{\mathcal{N}}{k_J^2} f^\star(x_J) \left\langle \vec{k} \middle| H_{n,\nu} \right\rangle \left(1+\bar{\alpha}_{\mu_R}\phi_1(n,\nu,\omega,J)\right) \tag{1.158}$$

respectively.

The cross section after using the NLLA kernel and the LO impact factors reads

$$\begin{aligned}
&\frac{\mathrm{d}\sigma^{(LO,NLLA)}(s)}{\mathrm{d}y_A\,\mathrm{d}y_B\,\mathrm{d}^2\vec{k}_A\,\mathrm{d}^2\vec{k}_B} = \\
&= \frac{x_{J_A}x_{J_B}}{2\pi}\sum_n \int \frac{\mathrm{d}\nu}{2\pi} e^{\chi(n,\nu)(Y-Y_0)} \left\langle \Phi^{(LO)}(J_A) \middle| H_{n,\nu} \right\rangle \left\langle H_{n,\nu} \middle| \Phi^{(LO)}(J_B) \right\rangle = \\
&= \frac{\mathcal{N}^2 x_{J_A}x_{J_B}}{2\pi k_A^2 k_B^2} f^\star(x_{J_A}) f^\star(x_{J_B}) \sum_n \int \frac{\mathrm{d}\nu}{2\pi} e^{\chi(n,\nu)(Y-Y_0)} \left\langle \vec{k}_A \middle| H_{n,\nu} \right\rangle \left\langle H_{n,\nu} \middle| -\vec{k}_B \right\rangle = \\
&= \frac{4\pi^2 C_F \bar{\alpha}_{\mu_R}^2}{N_C^3 k_A^3 k_B^3} x_{J_A} f^\star(x_{J_A}) x_{J_B} f^\star(x_{J_B}) \sum_n \frac{e^{in\theta}}{2\pi} \int \frac{\mathrm{d}\nu}{2\pi} e^{\tilde{\chi}(n,\nu)(Y-Y_0)} \left(\frac{k_A^2}{k_B^2}\right)^{i\nu},
\end{aligned} \tag{1.159}$$

where the azimuthal angle difference[22] θ is given by $\theta \equiv \theta_A - \theta_B - \pi$ and we have also inserted the term $|H_{n,\nu}\rangle\langle H_{n,\nu}|$. Following Ref. [140], we have placed the terms originated by the NLO eigenfunctions in the exponential, thus modifying the eigenvalue to

$$\tilde{\chi}(n,\nu) \equiv \bar{\alpha}_{\mu_R}\chi_0(n,\nu)\left(1-\bar{\alpha}_{\mu_R}\beta_2 \log\frac{k_A k_B}{\mu_R^2}\right) + \bar{\alpha}_{\mu_R}^2\chi_1(n,\nu). \tag{1.160}$$

If we neglect higher order terms beyond NLO, we can interpret the modification of the eigenfunctions as a change of the renormalization scale from μ_R to $\mu_N = \sqrt{k_A k_B}$ (natural

[22] When $\theta = 0$ the two jets are back to back in transverse space.

scale) and therefore, we can use the LO eigenfunctions instead of the NLO ones after setting the renormalization scale in the kernel to be equal to the natural scale μ_N. Following the same steps for the case of the NLO impact factor, we finally obtain the equations at LLA with LO impact factors

$$\frac{\mathrm{d}\sigma^{(LO,LLA)}(s)}{\mathrm{d}y_A\,\mathrm{d}y_B\,\mathrm{d}^2\vec{k}_A\,\mathrm{d}^2\vec{k}_B} = \frac{4\pi^2 C_F\,\bar{\alpha}_{\mu_R}^2}{N_C^3 k_A^3 k_B^3} x_{J_A} f^\star(x_{J_A}) x_{J_B} f^\star(x_{J_B}) \times \\ \times \sum_n \frac{e^{in\theta}}{2\pi} \int \frac{\mathrm{d}\nu}{2\pi} \left(\frac{k_A^2}{k_B^2}\right)^{i\nu} e^{\bar{\alpha}_{\mu_R}\chi_0(n,\nu)(Y-Y_0)}. \tag{1.161}$$

If we include the NLLA kernel and the NLO impact factors, which is , as of today, the most accurate description we obtain

$$\frac{\mathrm{d}\sigma^{(NLO,NLLA)}(s)}{\mathrm{d}y_A\,\mathrm{d}y_B\,\mathrm{d}^2\vec{k}_A\,\mathrm{d}^2\vec{k}_B} = \frac{4\pi^2 C_F\,\bar{\alpha}_{\mu_R}^2}{N_C^3 k_A^3 k_B^3} x_{J_A} f^\star(x_{J_A}) x_{J_B} f^\star(x_{J_B}) \times \\ \times \sum_n \frac{e^{in\theta}}{2\pi} \int \frac{\mathrm{d}\nu}{2\pi} \left(\frac{k_A^2}{k_B^2}\right)^{i\nu} \left(1+\bar{\alpha}_{\mu_R}\phi_1(n,\nu,\chi,J_A)\right)\left(1+\bar{\alpha}_{\mu_R}\bar{\phi}_1(n,\nu,\chi,J_B)\right) e^{\tilde{\chi}(n,\nu)(Y-Y_0)}. \tag{1.162}$$

As a technical detail, when solving the equation numerically it is often convenient to deform the contour in Mellin space. We are performing the inverse Mellin Transform using a straight line parameterization of the contour $\gamma = \frac{1}{2} + i\nu$, but we can deform it without changing the result (being cautious with the analytical structures of the funcions involved to don't cross poles) into a parabolic path $\gamma = \frac{1}{2} + i\nu \pm a\nu^2$, where $a > 0$ is a parameter to optimize for numerical efficiency purposes.

1.4.3 Azimuthal angle correlations

The original proposal by Mueller and Navelet [113] was to study the dependence of the cross section on the increasing rapidity difference Y, however, it proved more advantageous to study the azimuthal decorrelation of the two jets as was proposed in [114, 115]. The total cross section receives large corrections after including the NLLA terms to the gluon Green's function largely increasing the theoretical uncertainty. This can, to a major degree, be avoided by studying ratios of azimuthal decorrelation coefficients [151] which essentially means removing the contribution with conformal spin $n = 0$. This leads to theoretical computations with much better perturbative stability. In this work, since we are interested in investigating the fundamental character of the rapidity veto we will include observables that depend on the zeroth conformal spin and study the influence they show on the veto.

The Fourier expansion in the azimuthal angle difference θ of the differential cross section is

$$\frac{\mathrm{d}\sigma(s)}{\mathrm{d}y_A\,\mathrm{d}y_B\,\mathrm{d}k_A\,\mathrm{d}k_B\,\mathrm{d}\theta_A\,\mathrm{d}\theta_B} = \frac{1}{(2\pi)^2}\left(\mathscr{C}_0 + \sum_{n=1}^{\infty} 2\cos(n\theta)\,\mathscr{C}_n\right), \tag{1.163}$$

and therefore the azimuthal decorrelation is directly related to the coefficients $\frac{\mathscr{C}_n}{\mathscr{C}_0} = \langle\cos(n\theta)\rangle$.

The physical intuition about the decorrelation coefficients is the following. If there are only the two tagged jets in the final state, they will be totally correlated due to momentum conservation, making all $\frac{\mathscr{C}_n}{\mathscr{C}_0} = 1$. Due to the extra radiation, the distribution in θ is not a delta, and its moments are fully characterized by the coefficients, providing information about the importance of the minijet radiation that we have not tagged. In the BFKL approach, an increase in Y will lead to an increase in the amount of radiation[23], generating more decorrelation on the tagged jets.

These observables are, however, strongly affected by collinear effects [151, 152], stemming from the $n = 0$ Fourier component in ϕ of the BFKL kernel. This dependence is removed if instead the ratios of projections on azimuthal-angle observables $\mathscr{R}_n^m = \langle\cos(m\phi)\rangle/\langle\cos(n\phi)\rangle$ [151, 152] (where m,n are integers and ϕ the azimuthal angle between the two tagged jets) are introduced. In particular, these also offer a more clear signal of BFKL effects than the standard predictions for the growth of hadron structure functions $F_{2,L}$ (well fitted within NLLA approaches [75, 76]).

[23] This argument is not valid at the boundary of the phase space, when there is no more available energy to produce extra radiation.

CHAPTER 2

RAPIDITY VETO

In this chapter we study an alternative procedure to tame the perturbative series of the NLLA BFKL equation, the rapidity veto. To test it, we analyze ratios of azimuthal-angle distributions in Mueller-Navelet jets. When imposing a rapidity veto constraint, the minijet radiation activity is restricted to only allow final-state partons separated at least a distance in rapidity b. It is well-known that the asymptotic growth with the rapidity separation of the two tagged jets of the NLLA BFKL Green's function requires a value of $b \simeq \mathcal{O}(2)$ in order to avoid unphysical cross sections. We further investigate this point from a phenomenological point of view and work out those values of b which best fit angular distributions measured at the LHC in a realistic set-up where impact factors and parton distribution effects are also taken into account.

At hadronic colliders and in particular at the LHC, a phenomenologically interesting process is Mueller-Navelet (MN) jet production, described in Sec. 1.4. MN jets are inclusive final states where two jets with transverse momenta of similar sizes, $k_{A,B}$ are tagged to have a large rapidity separation Y.

The azimuthal angle (θ) behavior of the two jets have received a lot of attention not only from theorists, but also from experimentalists. This behavior is driven by the presence of decisive minijet activity in the rapidity space between the two outermost jets which in BFKL based studies is accounted for by a BFKL gluon Green's function connecting the two jets, $\varphi(k_A, k_B, Y)$. It was shown by Schwennsen and Savio Vera in Ref. [151, 152], that

ratios of projections on azimuthal angle observables

$$\mathscr{R}_N^M = \langle \cos(M\theta)\rangle / \langle \cos(N\theta)\rangle \,, \tag{2.1}$$

(where m,n are integers) are the more favourable quantities in the search for a clear signal of BFKL effects. There is already a comparison of different NLLA calculations for these ratios $\mathscr{R}_N^M$ [130–134] against LHC experimental data, which makes these observable a perfect candidate to test new theoretical ideas.

Alternatively, a generalization of the azimuthal ratios in Eq. (2.1) was proposed for processes that have three and four final state jets, that we will describe in Chapters 3 and 4, and Chapter 5 respectively. These can be seen as special MN cases since the outermost jets still need to have a large rapidity distance and any other tagged jet is to be found in more central regions of the detector. Moreover, these new observables present additional advantages to the MN jets in the effort to disentangle a BFKL signal. However, there are no experimental analyses to compare to yet and hereafter we will restrict our discussion to MN jets.

In Refs. [135, 136] one can find a comparison between experimental data and theoretical predictions for a number of MN azimuthal ratios. The theoretical predictions are obtained from the usual collinear Monte-Carlo tools and from a BFKL based approach. The latter is to NLLA accuracy computed in the so-called Brodsky-Lepage-Mackenzie (BLM) scheme , introduced in Ref.[153]. It turns out that working in the BLM scheme is only essential in having a good description of the data when one studies $\mathscr{R}_N^M$ with either $M = 0$ or $N = 0$.

Another essential point is that higher order corrections to the BFKL equation (corrections beyond the LLA) are very important for both theoretical and phenomenological studies of QCD at high energies. So far, there is no unique approach on how to properly account for the corrections beyond the NLLA and for every process. It is known, however, that the largest portion of the NLLA corrections are due to effects related to the running of α_s and to collinear contributions, while it has been argued that the NLLA kernel induces large and negative logarithms in the ratio k_A/k_B at NNLLA and beyond. Although these logarithms lie formally beyond the boundary of the NLLA approach, they can induce spurious large effects. For consistency with the DGLAP approach we know that they must be resummed to all orders. In Ref. [77] it was shown how to extend the NLLA kernel so as to guarantee exactly that resummation, however, the prescription for modifying the kernel is not unique. Schmidt, in Ref. [154], pointed out that a significant reduction in the resultant Green's function occurs if one only considers diagrams in which emitted gluons (minijets) have a minimum rapidity distance, b, relative to the preceding emitted gluon or,

in other words, if one imposes a rapidity veto[1] on the minimal rapidity distance between two subsequent minijet emissions. Furthermore, in Ref. [155] it was shown that the large effect of imposing such a restriction accounts for the same regions of phase space in the NLLA corrections to the BFKL Green's function as the collinear summation as proposed in Ref. [77]. Recently, in Ref. [156], the effect of a rapidity veto on the discrete BFKL Pomeron was studied whereas there were works in which a rapidity veto was applied to non linear evolution equations in Refs. [157, 158].

In this Chapter, we want to address the following questions: is it possible to obtain a good theoretical description of the ratios $\mathscr{R}_N^M$ including the ones with either $M = 0$ or $N = 0$ without necessarily using the BLM scheme? Is it possible to achieve that by employing a single global scale, such as the rapidity veto? If indeed employing a rapidity veto allows in principle for a fit of the data, at what values of b this happens? Do the optimal b values tell us how far from asymptotia we are at LHC energies?

Here, we remind the reader of a key conclusion from previous studies in Ref. [155]. It was shown that the rapidity veto samples the region of phase space corresponding to collinear emissions already at a typical value that is somewhat larger than two units of rapidity, *i.e.*, $b \approx 2$. However, that work focused on very high colliding energies, that is, well into the asymptotia region. On the contrary, the key aspect of this work is that we contrast out results with experimental data at collider energies.

The Chapter is structured as follows. In Section 2.1 we make use of the concepts introduced in Chapter 1 regarding the description of MN jets and important formulas for the NLLA gluon Green's function to impose the rapidity veto on the azimuthal angle correlations and their ratios. In Sections 2.2 and 2.3, we study numerically the functional dependence of the ratios $\mathscr{R}_N^M$ on the rapidity veto b after imposing the same kinematical cuts as the ones used for the experimental analysis in Refs. [135, 136]. Finally, we sum up the Chapter in Section 2.4.

2.1 Hadronic observables after imposing a rapidity veto

Mueller-Navelet jets were proposed as a process in hadron colliders for which one could disentangle the high-energy behavior of the partonic cross section after removing most of the PDFs dependence. In collisions of two protons at the LHC, MN jets is described by the following process

$$p(p_A) + p(p_B) \to J_A(k_A) + J_B(k_B) + X\,. \tag{2.2}$$

[1]The original presentation of this idea was by L. N. Lipatov at a talk presented at the 4th Workshop on Small-x and Diffractive Physics, Fermi National Accelerator Laboratory, Sept. 17-20, 1998.

The relevant kinematical configuration is given by[2]

$$s \gg Q^2 \sim k_A^2 \sim k_B^2 \gg \Lambda_{QCD}^2 \tag{2.3}$$

where s is the center-of-mass energy squared and Q is some typical hard transverse scale that guarantees the applicability of perturbation theory.

The rapidity difference Y is related to the rest of kinematical variables as

$$Y \equiv Y_A - Y_B = \log \frac{x_{J_A} x_{J_B} s}{k_A k_B} . \tag{2.4}$$

where $x_{J_{A,B}}$ are the longitudinal momentum fractions of the jets.

Since we are describing a semi-hard process, in order to study it properly we need to combine both collinear factorization and BFKL dynamics. In collinear factorization we write the cross section as a convolution of the PDFs and the partonic cross section. In the high-energy limit we are considering, the partonic cross-section itself also factorizes into a convolution of process-dependent jet vertices and a universal part which is accounted for by the gluon Green's function φ. Mixing all the ingredients, while the details can be found in Chapter 1, the differential cross section is given by

$$\begin{aligned} \frac{\mathrm{d}\sigma(s)}{\mathrm{d}Y_A\,\mathrm{d}Y_B\,\mathrm{d}^2\vec{k}_A\,\mathrm{d}^2\vec{k}_B} = \frac{x_{J_A} x_{J_B}}{(2\pi)^2} \int_C \frac{\mathrm{d}\omega}{2\pi i} \int \frac{\mathrm{d}^2\vec{q}_A}{\vec{q}_A^{\,2}} \Phi\left(\vec{q}_A, \vec{k}_A, x_{J_A}, \omega, s_0, \mu_F, \mu_R\right) \\ \int \frac{\mathrm{d}^2\vec{q}_B}{\vec{q}_B^{\,2}} \Phi\left(-\vec{q}_B, \vec{k}_B, x_{J_B}, \omega, s_0, \mu_F, \mu_R\right) e^{\omega(Y-Y_0)} \varphi_\omega(\vec{q}_A, \vec{q}_B) , \end{aligned} \tag{2.5}$$

where Φ denotes the inclusive impact factors defined in Eq. (1.140), and in the following we will set Y_0 to 0. It is useful to write the previous equation in Dirac's notation[3]

$$\frac{\mathrm{d}\sigma(s)}{\mathrm{d}Y_A\,\mathrm{d}Y_B\,\mathrm{d}^2\vec{k}_A\,\mathrm{d}^2\vec{k}_B} = \frac{x_{J_A} x_{J_B}}{(2\pi)^2} \int_C \frac{\mathrm{d}\omega}{2\pi i} e^{\omega(Y-Y_0)} \left\langle \Phi(J_A) \middle| \frac{\mathbb{1}}{\omega\mathbb{1} - \mathscr{K}} \middle| \Phi(J_B) \right\rangle . \tag{2.6}$$

Where the BFKL kernel $\mathscr{K}$ is known up to next-to-leading order (NLO)

$$\mathscr{K} = \bar{\alpha}_s \mathscr{K}_0 + \bar{\alpha}_s^2 \mathscr{K}_1 + \mathscr{O}\left(\bar{\alpha}_s^3\right) , \tag{2.7}$$

where $\mathscr{K}_0$ and $\mathscr{K}_1$ are the LO [61–63, 104, 105] and NLO [67, 69] contributions to the BFKL kernel, which resum the leading and next-to-leading logarithms respectively.

At LLA the kernel enjoys conformal invariance and we can use the LO eigenvectors $|n,\nu\rangle$ (see Appendix A.1 and Sec. 1.4.2 for a detailed explanation)

$$\langle \vec{q} | \mathscr{K}_0 | n,\nu \rangle = \chi_0(n,\nu) \langle \vec{q} | n,\nu \rangle . \tag{2.8}$$

[2] All transverse two-momenta will be denoted by vector variables and their modulus by the letter itself.

[3] From now on, the input J in the impact factor Φ stands for all the variables associated with the jet J: $\vec{k}_J, x_J, \mu_F, \mu_R, R$, being R the radius associated with the jet reconstruction algorithm.

Following the Chirilli-Kovchegov procedured described in Ref. [140, 141], we use the NLO eigenfunctions $|H_{n,\nu}\rangle$ when dealing with the NLLA GGF. In Appendix A.1 they are described in detail. Here we will only note that they satisfy

$$\mathscr{K}\left|H_{n,\nu}\right\rangle = \left(\bar{\alpha}_s\chi_0(n,\nu)+\bar{\alpha}_s^2\chi_1(n,\nu)\right)\left|H_{n,\nu}\right\rangle \equiv \chi(n,\nu)\left|H_{n,\nu}\right\rangle\,, \tag{2.9}$$

where the NLO part of the kernel, $\chi_1(n,\nu)$ was calculated in Ref. [139] and its expression is given in Eq. (1.149).

The remaining necessary ingredient to compute the cross section is the impact factor at NLO. We will be using the small-cone approximation (SCA), where the jet cone aperture R in the rapidity-azimuthal angle plane is considered small, neglecting powers in R. The expressions for the LO and NLO impact factor can be directly extracted from Ref. [145] after taking into account how the act on the NLO eigenfunctions we obtain

$$\left\langle \Phi^{(LO)}(J)\right| H_{n,\nu}\Big\rangle = \frac{\mathscr{N}}{k_J^2} f^\star(x_J)\left\langle \vec{k}\right| H_{n,\nu}\Big\rangle\,, \tag{2.10}$$

$$\left\langle \Phi^{(NLO)}(J)\right| H_{n,\nu}\Big\rangle = \frac{\mathscr{N}}{k_J^2} f^\star(x_J)\left\langle \vec{k}\right| H_{n,\nu}\Big\rangle\left(1+\bar{\alpha}_s\phi_1(n,\nu,\omega,J)\right). \tag{2.11}$$

The normalization factor is $\mathscr{N} = 2\pi^2\bar{\alpha}_s\sqrt{\frac{2C_F}{N_C^3}}$ and the NLO correction to the impact factor, $\phi_1(n,\nu,J)$, can be found in Appendix A.2. We have also defined the effective PDF, introduced in Ref. [150], as $f^\star(x_J)\equiv\frac{N_C}{C_F}f_g(x_J)+\sum_{i=q,\bar{q}}f_i(x_J)$. .

After some manipulations, the cross section at NLLA and using LO impact factors reads

$$\begin{aligned}&\frac{\mathrm{d}\sigma^{(LO,NLLA)}(s)}{\mathrm{d}Y_A\,\mathrm{d}Y_B\,\mathrm{d}^2\vec{k}_A\,\mathrm{d}^2\vec{k}_B} = \\ &=\frac{4\pi^2C_F\bar{\alpha}_s^2}{N_C^3k_A^3k_B^3}x_{J_A}f^\star(x_{J_A})x_{J_B}f^\star(x_{J_B})\sum_n\frac{e^{in\theta}}{2\pi}\int\frac{\mathrm{d}\nu}{2\pi}e^{\tilde{\chi}(n,\nu)(Y-Y_0)}\left(\frac{k_A^2}{k_B^2}\right)^{i\nu}\,,\end{aligned} \tag{2.12}$$

where the azimuthal angle difference[4] θ is given by $\theta\equiv\theta_A-\theta_B-\pi$.

Where the effective eigenvalue at NLLA is

$$\tilde{\chi}(n,\nu)\equiv\bar{\alpha}_s\chi_0(n,\nu)\left(1-\bar{\alpha}_s\beta_2\log\frac{k_Ak_B}{\mu_R^2}\right)+\bar{\alpha}_s^2\chi_1(n,\nu)\,. \tag{2.13}$$

[4]When $\theta=0$ the two jets are back to back in transverse space.

Following the same steps for the case of the NLO impact factor, we finally obtain

$$\frac{\mathrm{d}\sigma^{(NLO,NLLA)}(s)}{\mathrm{d}Y_A\,\mathrm{d}Y_B\,\mathrm{d}^2\vec{k}_A\,\mathrm{d}^2\vec{k}_B} = \frac{4\pi^2 C_F\bar{\alpha}_s^2}{N_C^3 k_A^3 k_B^3} x_{J_A} f^\star(x_{J_A}) x_{J_B} f^\star(x_{J_B}) \times \\ \times \sum_n \frac{e^{in\theta}}{2\pi}\int\frac{\mathrm{d}\nu}{2\pi}\left(\frac{k_A^2}{k_B^2}\right)^{i\nu}\left(1+\bar{\alpha}_s\phi_1(n,\nu,\chi,J_A)\right)\left(1+\bar{\alpha}_s\bar{\phi}_1(n,\nu,\chi,J_B)\right)e^{\tilde{\chi}(n,\nu)(Y-Y_0)}. \tag{2.14}$$

In all the cases, since the impact factors and the GGF are both invariant under the inversion of the conformal spin $n \leftrightarrow -n$, the Fourier expansion of the cross section contains cosines only, it is given by

$$\frac{\mathrm{d}\sigma(s)}{\mathrm{d}Y_A\,\mathrm{d}Y_B\,\mathrm{d}k_A\,\mathrm{d}k_B\,\mathrm{d}\theta_A\,\mathrm{d}\theta_B} = \frac{1}{(2\pi)^2}\left(\mathscr{C}_0 + \sum_{M=1}^{\infty} 2\cos(M\theta)\,\mathscr{C}_M\right), \tag{2.15}$$

and therefore the azimuthal correlations are directly related to the coefficients

$$\frac{\mathscr{C}_M}{\mathscr{C}_0} = \langle\cos(M\theta)\rangle\,. \tag{2.16}$$

From a more theoretical perspective, it is important to have as good as possible perturbative stability in our predictions, but the total cross section receives large corrections after including the NLLA terms. This can, to a major degree, be avoided by studying ratios of azimuthal correlation coefficients, as was discussed in Ref. [151]. This is equivalent to the removal of the contribution with conformal spin $n = 0$. In this work, since we are interested in investigating the fundamental character of the rapidity veto we will include observables that depend on the zeroth conformal spin and study the influence they show on the veto, investigating the ratios defined in Eq. (2.1) for all the experimentally measured values of M,N.

2.1.1 The basics of the rapidity veto

Now that we have set the notation and all the basic ingredients, we have to add on top of it a new physical constraint, the rapidity veto. Imposing that subsequent minijet emissions must have a rapidity difference greater than a fixed value b leads to the following modification of the BFKL kernel at LLA, which was demonstrated by Schmidt in Ref. [154], and only affects terms beyond LLA accuracy:

$$\varphi(\vec{q}_A,\vec{q}_B,Y) \to \varphi(\vec{q}_A,\vec{q}_B,Y,b) = \int_{\mathscr{C}}\frac{\mathrm{d}\omega}{2\pi i}e^{\omega(Y-Y_0-b)}\left\langle\vec{q}_A\right|\frac{\mathbb{1}}{\omega\mathbb{1}-e^{-\omega b}\mathscr{K}}\left|\vec{q}_B\right\rangle, \tag{2.17}$$

and the integral over ω can be computed via residues to give

$$\varphi(\vec{q}_A,\vec{q}_B,Y,b)=\frac{2}{q_A q_B}\sum_n \frac{e^{in(\theta_{q_A}-\theta_{q_B})}}{2\pi}\int \frac{\mathrm{d}\nu}{2\pi}\left(\frac{k_A^2}{k_B^2}\right)^{i\nu}\frac{e^{\tilde{\omega}(Y-Y_0-b)}}{1+b\tilde{\omega}}. \tag{2.18}$$

Where we have the presence of $\tilde{\omega}$, which is the solution to the following transcendental equation

$$\tilde{\omega}=e^{-b\tilde{\omega}}\bar{\alpha}_s\chi_0(n,\nu)\leftrightarrow\tilde{\omega}=\frac{\mathcal{W}\left(b\,\bar{\alpha}_s\chi_0(n,\nu)\right)}{b}, \tag{2.19}$$

where $\mathcal{W}$ is Lambert's W function. As pointed out in Ref. [155], the solution of (2.19) develops unphysical branch points at $\pm\nu_0$ that satisfy

$$\bar{\alpha}_s\chi_0(n,\nu_0)=-\frac{e^{-1}}{b} \tag{2.20}$$

because we have summed over an arbitrarily large number of gluon emissions, something that is inconsistent with the rapidity veto constraint. We can expand the gluon Green's function as a power series in the kernel and truncate the sum to limit the number of emissions

$$\frac{e^{\tilde{\omega}(Y-Y_0-b)}}{1+b\tilde{\omega}}=\sum_k\frac{(Y-Y_0-(k+1)b)^k\left(\bar{\alpha}_s\chi_0(n,\nu)\right)^k}{k!}. \tag{2.21}$$

The power series converges only asymptotically, as was rigorously studied in Ref. [154], and the best approximation is obtained by the truncated series at the largest value of k that satisfies $(Y-Y_0-(k+1)b)>0$. This is in accordance with the physical intuition, that only a fixed number of emissions should be allowed if the rapidity constrained is to be respected. In our numerical computations and the results we will present in the next section, we have used the truncated expansion.

The modification of the BFKL equation after imposing a rapidity veto at NLLA was also carried out by Schmidt in Ref. [154]. The b dependence can be set requiring that the total cross section only depends on b through NNLLA terms, *i.e.*, the corrections to the cross section of order $(\bar{\alpha}_s Y)^n$ and $\bar{\alpha}_s(\bar{\alpha}_s Y)^n$ should be independent on the veto. In that way, the influence of the veto at NLLA is reduced considerably compared to the LLA case. The veto dependence is found after performing the following modifications to the kernel and to the impact factors

$$\mathcal{K}\rightarrow\mathcal{K}_b=\mathcal{K}+b\mathcal{K}_0\mathcal{K}_0+\mathcal{O}(\bar{\alpha}_s^3) \tag{2.22}$$

$$|\Phi(J)\rangle\rightarrow|\Phi_b(J)\rangle=|\Phi(J)\rangle+b\mathcal{K}_0\left|\Phi^{(LO)}(J)\right\rangle+\mathcal{O}(\bar{\alpha}_s^3) \tag{2.23}$$

and the total cross section can be written as

$$\frac{\mathrm{d}\sigma\left(s\right)}{\mathrm{d}Y_A\,\mathrm{d}Y_B\,\mathrm{d}^2\vec{k}_A\,\mathrm{d}^2\vec{k}_B}=\frac{x_{J_A}x_{J_B}}{(2\pi)^2}\int_C\frac{\mathrm{d}\omega}{2\pi i}e^{\omega(Y-Y_0-b)}\left\langle\Phi_b(J_A)\right|\frac{\mathbb{1}}{\omega\mathbb{1}-e^{-b\omega}\mathcal{K}_b}\left|\Phi_b(J_B)\right\rangle. \tag{2.24}$$

Using the completeness relation for $\left|H_{n,\nu}\right\rangle$, we can solve the equation as previously resulting in

$$\begin{aligned}&\frac{\mathrm{d}\sigma^{(NLO,NLLA)}\left(s\right)}{\mathrm{d}Y_A\,\mathrm{d}Y_B\,\mathrm{d}^2\vec{k}_A\,\mathrm{d}^2\vec{k}_B}=\\&=\frac{4\pi^2C_F\bar{\alpha}_s^2}{N_C^3k_A^3k_B^3}x_{J_A}f^\star(x_{J_A})x_{J_B}f^\star(x_{J_B})\sum_n\frac{e^{in\theta}}{2\pi}\int\frac{\mathrm{d}\nu}{2\pi}\left(\frac{k_A^2}{k_B^2}\right)^{i\nu}\frac{e^{\tilde{\omega}'(Y-Y_0-b)}}{1+b\tilde{\omega}'}\times\\&\times\left(1+\bar{\alpha}_s\phi_1(n,\nu,\chi,J_A)+\bar{\alpha}_sb\chi_0(n,\nu)\right)\left(1+\bar{\alpha}_s\bar{\phi}_1(n,\nu,\chi,J_B)+\bar{\alpha}_sb\chi_0(n,\nu)\right),\end{aligned} \tag{2.25}$$

where now

$$\tilde{\omega}'=e^{-b\tilde{\omega}'}\tilde{\chi}_b(n,\nu)\leftrightarrow\tilde{\omega}'=\frac{\mathcal{W}\left(b\tilde{\chi}_b(n,\nu)\right)}{b} \tag{2.26}$$

and

$$\tilde{\chi}_b(n,\nu)=\bar{\alpha}_s\chi_0(n,\nu)\left(1+\bar{\alpha}_sb\chi_0(n,\nu)-\bar{\alpha}_s\beta_2\log\frac{k_Ak_B}{\mu_R^2}\right)+\bar{\alpha}_s^2\chi_1(n,\nu). \tag{2.27}$$

Repeating the procedure we followed in the LLA case, we expand to get the asymptotic sum

$$\frac{e^{\tilde{\omega}'(Y-Y_0-b)}}{1+b\tilde{\omega}'}=\sum_k\frac{(Y-Y_0-(k+1)b)^k\left(\tilde{\chi}_b(n,\nu)\right)^k}{k!}. \tag{2.28}$$

The final expression we use for our numerical computations is (2.25) combined with (2.28) and integrated over the appropriate phase space.

2.2 Kinematics and details of the nurmerical analysis

In order to compare against experimental data, a phase space integration over $\vec{k}_A$ and $\vec{k}_B$ is needed. The measurement of Mueller-Navelet azimuthal decorrelation has been performed by the CMS collaboration in Refs. [135, 136], and by ATLAS in Ref. [159]. We will use the kinematical cuts of the CMS analysis, in particular for our numerical study we use

$$35\ \text{GeV} \leq k_A, k_B \leq 60\ \text{GeV}\ ,\ |k_A - k_B| \geq 2\ \text{GeV}\ ,\ 0 \leq Y_A, |Y_B| \leq 4.7\,, \tag{2.29}$$

whereas the initial observables we are computing are the following

$$C_M(Y,b) = \int \mathrm{d}^2\vec{k}_A\, \mathrm{d}^2\vec{k}_B\, \mathrm{d}Y_A\, \mathrm{d}Y_B\, \delta(Y_A - Y_B - Y)\cos(M\theta)\frac{\mathrm{d}\sigma}{\mathrm{d}Y_A\, \mathrm{d}Y_B\, \mathrm{d}^2\vec{k}_A\, \mathrm{d}^2\vec{k}_B} \tag{2.30}$$

in order to compute the final ratios

$$R_N^M(Y,b) \equiv \frac{C_M(Y,b)}{C_N(Y,b)}\,. \tag{2.31}$$

Some remarks are in order at this point:

- In the CMS analysis performed in Ref. [135, 136], in the relevant plots, what is shown is not $R_m^n(Y,0)$ but rather $R_m^n(Y,0)$ integrated over a bin in the rapidity difference centered at Y. The latter would be preferable in the theoretical analysis of this study for a one to one comparison, however, such a computation requires one further integration and the accompanying computational cost. We have decided to avoid this extra integration since the purpose of the current investigation is to understand the influence of the veto on the azimuthal decorrelations rather than performing a proper fitting to the experimental points. Moreover, we should note that since the total cross section decreases quickly with the rapidity difference, the result from integrating over any given rapidity bin will be biased toward the value at the smaller limit of the rapidity bin.

- There is no upper transverse momenta cutoff in the experimental selection. This is done for numerical reasons, but the dependence of the observable on this parameter is negligible, since the cross section is rapidly decreasing with increasing transverse momenta as was demonstrated in Ref. [125].

- The phase space region considered in our analysis has a lower cutoff in the difference of the transverse momenta $|k_A - k_B|$. This reduces the influence of collinear contamination effects on the observables. Actually, it has been suggested in Ref. [131] that eliminating the "back to back" region will enhance the BFKL effects with respect to fixed order calculations.

- The jet algorithm used in the experimental analysis in Ref. [135, 136] was the anti-k_T clustering algorithm with a radius value $R = 0.5$, while here we have used the Furman algorithm with $R = 0.5$ as we have already discussed in Section 1.4.2 (see discussion in Ref. [149]).

- There is a mismatch in the event selection procedure from the experimental and the theoretical side as was originally pointed out in Ref. [131]. To make that clear, let us suppose that we have three jets satisfying the transverse momenta conditions, two of them in the very forward region with rapidities y_1,y_2 ($y_1 > y_2$) while the third one is very backward with a rapidity y_3. In the CMS study this would be counted as one MN event with tagged jets the ones with rapidities y_1 and y_3. However, another MN configuration is possible here formed by the jets with rapidities y_2 and y_3. The effect from this discrepancy has been computed in Ref. [160], and it is below the 4% level with a peak at rapidity difference $Y \simeq 4$.

Finally, in order to compare against the experimental values, a center-of-mass energy of $\sqrt{s} = 7$ TeV was used while the rapidity scale Y_0 was set to zero. The NLO MSTW 2008 PDF [5] sets described in Ref. [161] were used, while for the strong coupling α_s we chose a two-loop running coupling setup with $\alpha_s(M_Z) = 0.11707$ setting the number of active flavors to $N_F = 5$. The renormalization scale was chosen to be the natural one, $\mu_R = \mu_N = \sqrt{k_A k_B}$. The factorization scales have been set to $\mu_{F_{A,B}} = |\vec{k}_{A,B}|$ for each impact factor respectively. The influence of using such a choice instead of $\mu_{F_{A,B}} = \mu_R$ was investigated in Ref. [131]. Finally, the multivariable integrations have been performed using the numerical integration packages in `MATHEMATICA`.

2.3 Results and comparison to experimental data

In this Section we present our results in Figs. 1 – 8. In each figure, we plot the dependence of some of the ratios defined in 2.31 on the veto b for a fixed value of the rapidity difference Y. In particular, we show results for $R_0^1(Y,b)$, $R_0^2(Y,b)$, $R_0^3(Y,b)$, $R_1^2(Y,b)$ and $R_2^3(Y,b)$. In each plot we include the experimental value along with its systematic uncertainty (reddish fixed-width band) for the rapidity bin centered at the given rapidity point. The experimental values have been obtained from the 2013 analysis in Ref. [135], since the 2016 data in Ref. [136] are not yet publicly available. This has special impact on the $Y = 5.75$ data, since this point shows an increase on the value of $R_0^3(Y,b)$ and $R_2^3(Y,b)$ that

[5] Changing from MSTW08 to MMHT14 has a very small impact on our numerical results, typically, less than 1‰.

is not shown in the 2016 analysis. The theoretical uncertainty from the variation of the renormalization scale[6] is represented by a bluish band the limits of which are obtained for $\mu_R = \mu_R^{\text{centr}}/2$ and $\mu_R = 2\mu_R^{\text{centr}}$, where μ_R^{centr} is the renormalisation scale used for the computation of the central blue dashed line within the bluish uncertainty band.

[6]The numerical uncertainty of our computations is negligible compared to the scale variation uncertainty.

There are several features that are common to all plots. In the regions with larger veto values the coefficients become negative since they are more affected by collinear contributions. This effect is more pronounced when we reduce the renormalization scale (since we approach the non-perturbative regime). Except for the large rapidity region ($Y = 7.5$ and 8.7) for which our expansion breaks down and for which we will not show any plots, there is always an interval of the veto where not only the ratios of correlation functions ($R_1^2(Y,b)$ and $R_2^3(Y,b)$) but also the correlation functions themselves ($R_0^1(Y,b)$, $R_0^2(Y,b)$, $R_0^3(Y,b)$) are well described. Interestingly, this happens for values of the veto in the region where the asymptotic series we are using reaches its boundary of convergence ($b \gtrsim 1$). A natural explanation for the unfavourable behaviour of the veto approach at large Y and for the present setup should be sought at the influence of the PDFs in that regions. More concretely, we are in a region where the PDFs tend very fast to zero and introduce extra energy-momentum conservation effects beyond those present in the BFKL Green's function. This is the reason why the idea of a simple constant rapidity veto is not viable at larger Y.

Fig. 2.8 shows the values of the rapidity veto that fit best the experimental values for the correlation functions (left) and the ratios of correlation functions (right) in the rapidity range $3.25 \leq Y \leq 6.5$. We find that the optimal value of the veto fitting the data slightly grows monotonically with the rapidity difference Y.

Returning to the questions we have listed in the introduction, it is safe to claim that is it possible to obtain a good theoretical description of the ratios $\mathscr{R}_N^M$ including the ones with either $M = 0$ or $N = 0$ without necessarily using the BLM scheme. Moreover, a rapidity veto allows in principle for a fit of the data –excluding the larger Y ones as explained previously– assuming that $b \gtrsim 1$. Regarding the question on whether the optimal b values tell us how far from asymptotia we are at LHC energies, one can only make qualitative statements. Clearly, at LHC energies we are not in asymptotia, however, a value of b close to unity suggests that pre-asymptotic BFKL effects are already present and possibly important.

2.4 Summary

There are different methods to stabilize the perturbative expansion in the Multi-Regge kinematics regime. Here we have explored the possibility of introducing a rough constant cut-off in the rapidity differences among emitted mini jets in the final state. By comparing to current LHC data we have found that it is possible to get a reasonable global description of many different azimuthal angle correlations in dijet cross sections with a rapidity veto $b \gtrsim 1$. This value is far from previous formal studies based on the asymptotic behavior of the gluon Green's function alone and it depends on the actual rapidity difference.

The effect of introducing jet vertices and parton distribution functions at realistic energies such as those proved at the LHC is to drastically reduce the value of the veto from $b \gtrsim 2$ to half of this value. This encodes different types of information. It shows how far we are in this observable from the asymptotic region where power-suppressed with energy terms are negligible. It also indicates the size of the collinear regions of phase space which need to be taken into account in order to get a good description of the data. The success of renormalization schemes such as the BLM approach when applied to the class of observables here described can be also understood since they essentially absorb the effect of the veto using a redefinition of the position of the Landau pole which numerically generates similar values of the cross sections.

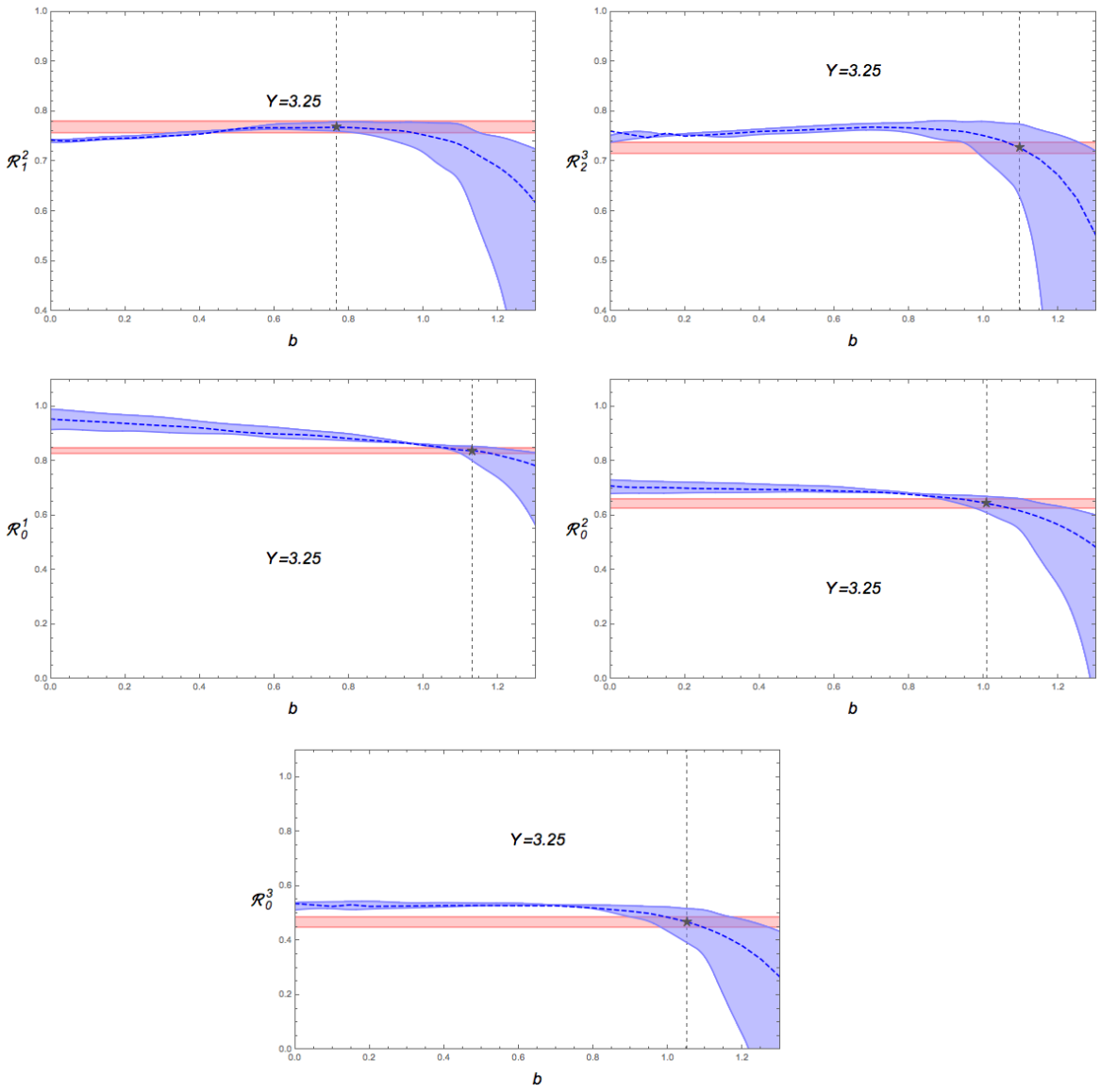

Figure 2.1: Functional dependence of the different R_m^n functions on the veto b at $Y = 3.25$. The reddish band denotes the experimental uncertainty while the blueish band denotes the theoretical uncertainty from the renormalisation scale variation.

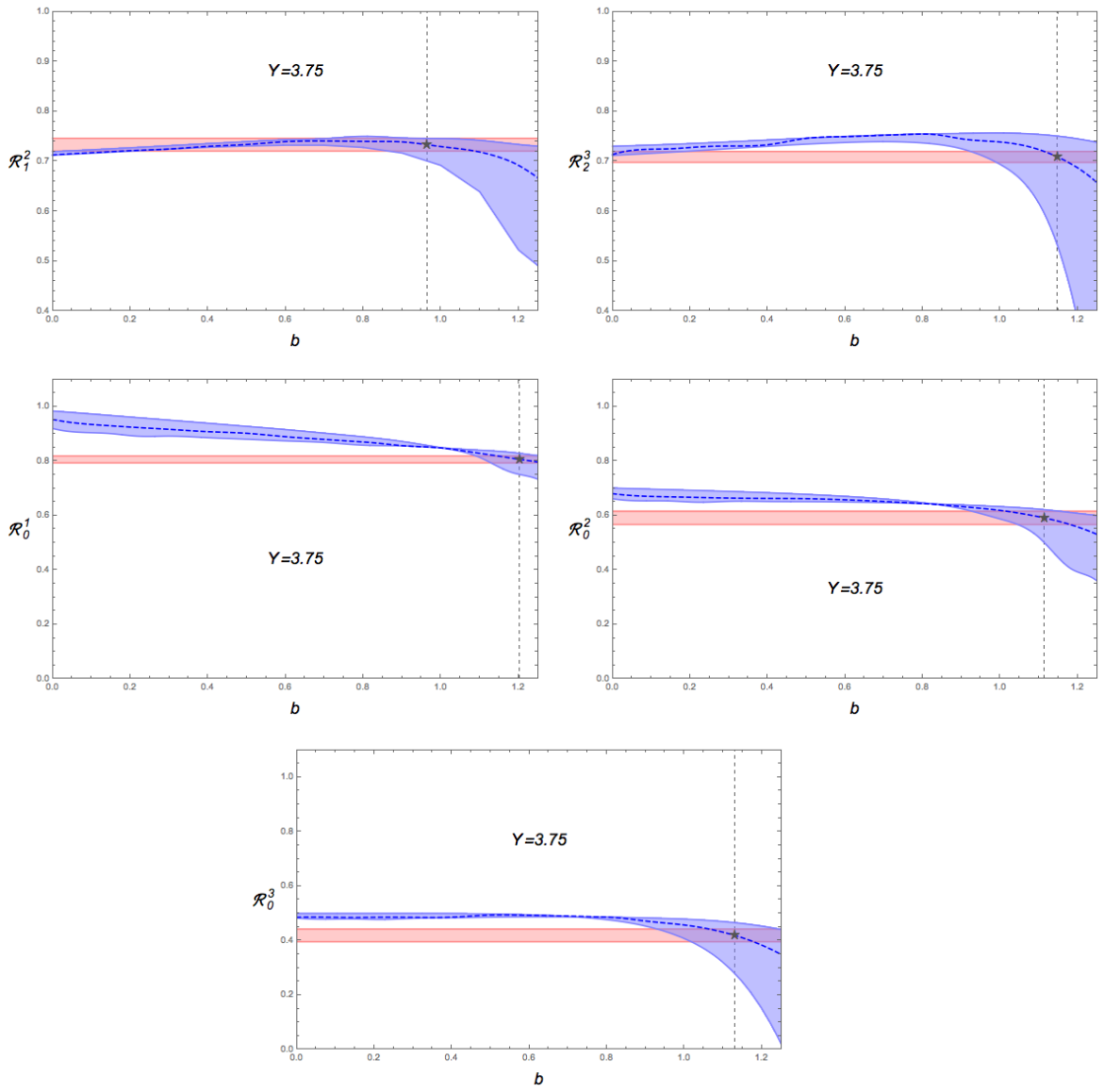

Figure 2.2: Functional dependence of the different R_m^n functions on the veto b at $Y = 3.75$. The reddish band denotes the experimental uncertainty while the blueish band denotes the theoretical uncertainty from the renormalisation scale variation.

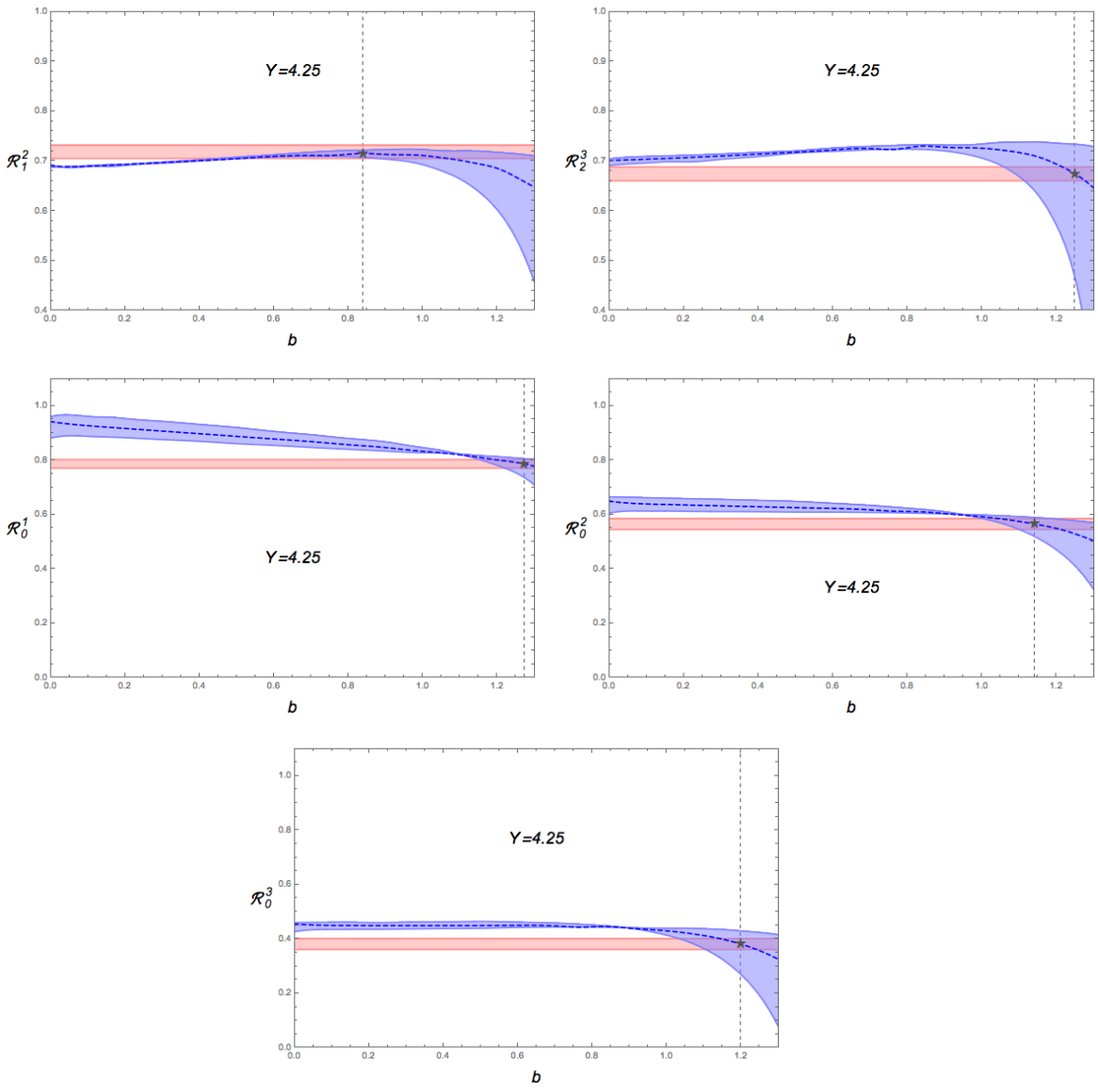

Figure 2.3: Functional dependence of the different R_m^n functions on the veto b at $Y = 4.25$. The reddish band denotes the experimental uncertainty while the blueish band denotes the theoretical uncertainty from the renormalisation scale variation.

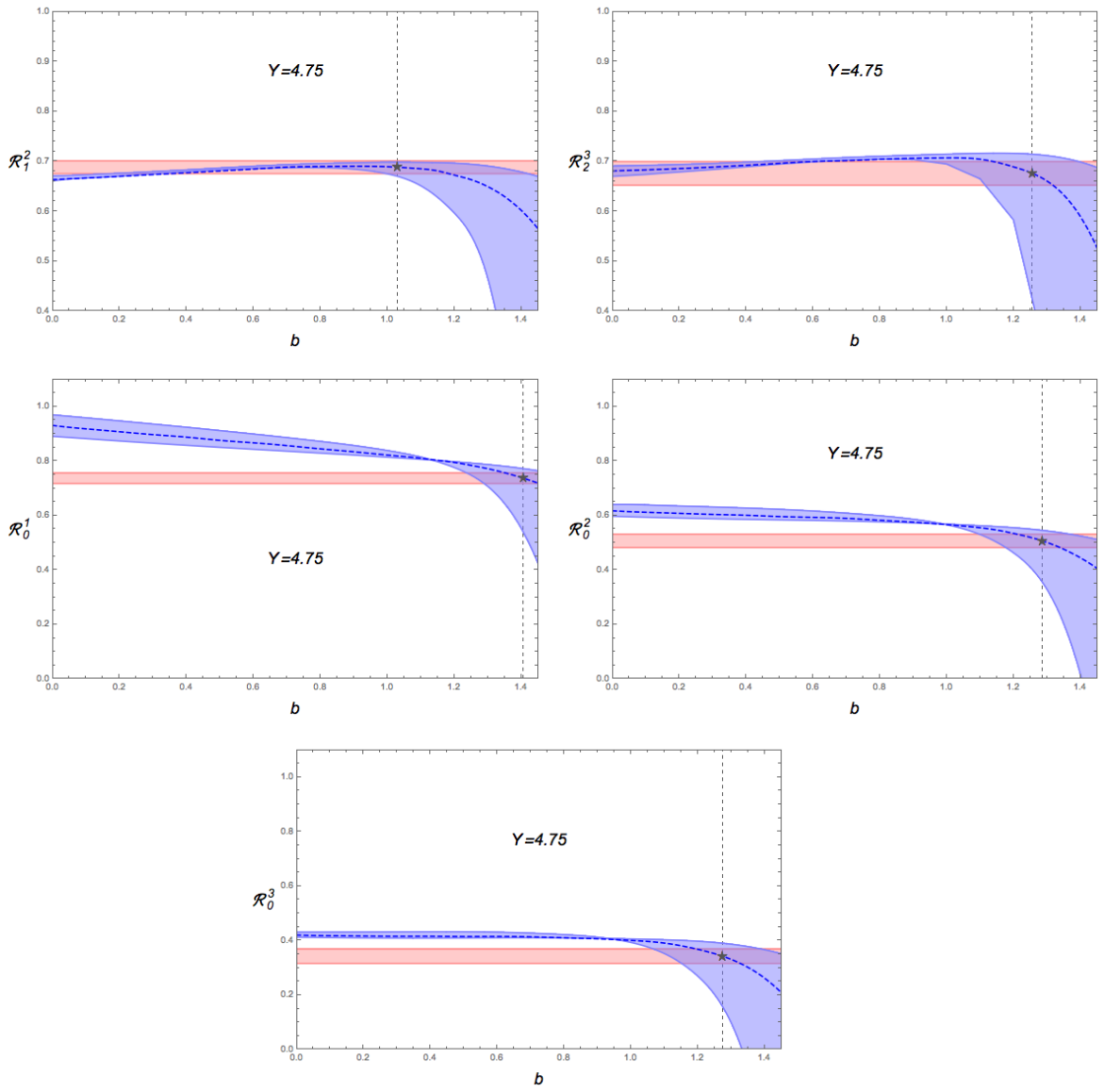

Figure 2.4: Functional dependence of the different R_m^n functions on the veto b at $Y = 4.75$. The reddish band denotes the experimental uncertainty while the blueish band denotes the theoretical uncertainty from the renormalisation scale variation.

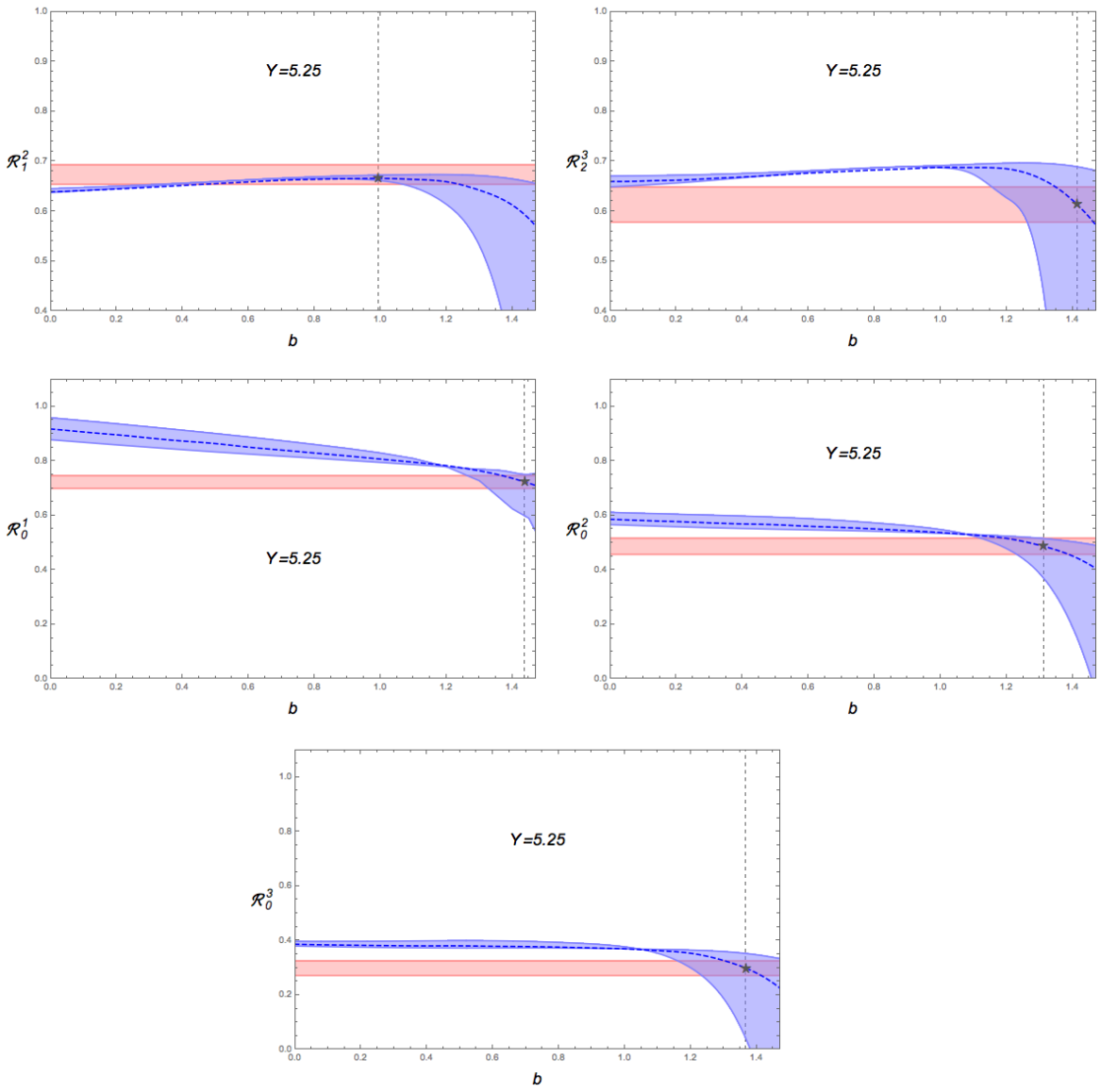

Figure 2.5: Functional dependence of the different R_m^n functions on the veto b at $Y = 5.25$. The reddish band denotes the experimental uncertainty while the blueish band denotes the theoretical uncertainty from the renormalisation scale variation.

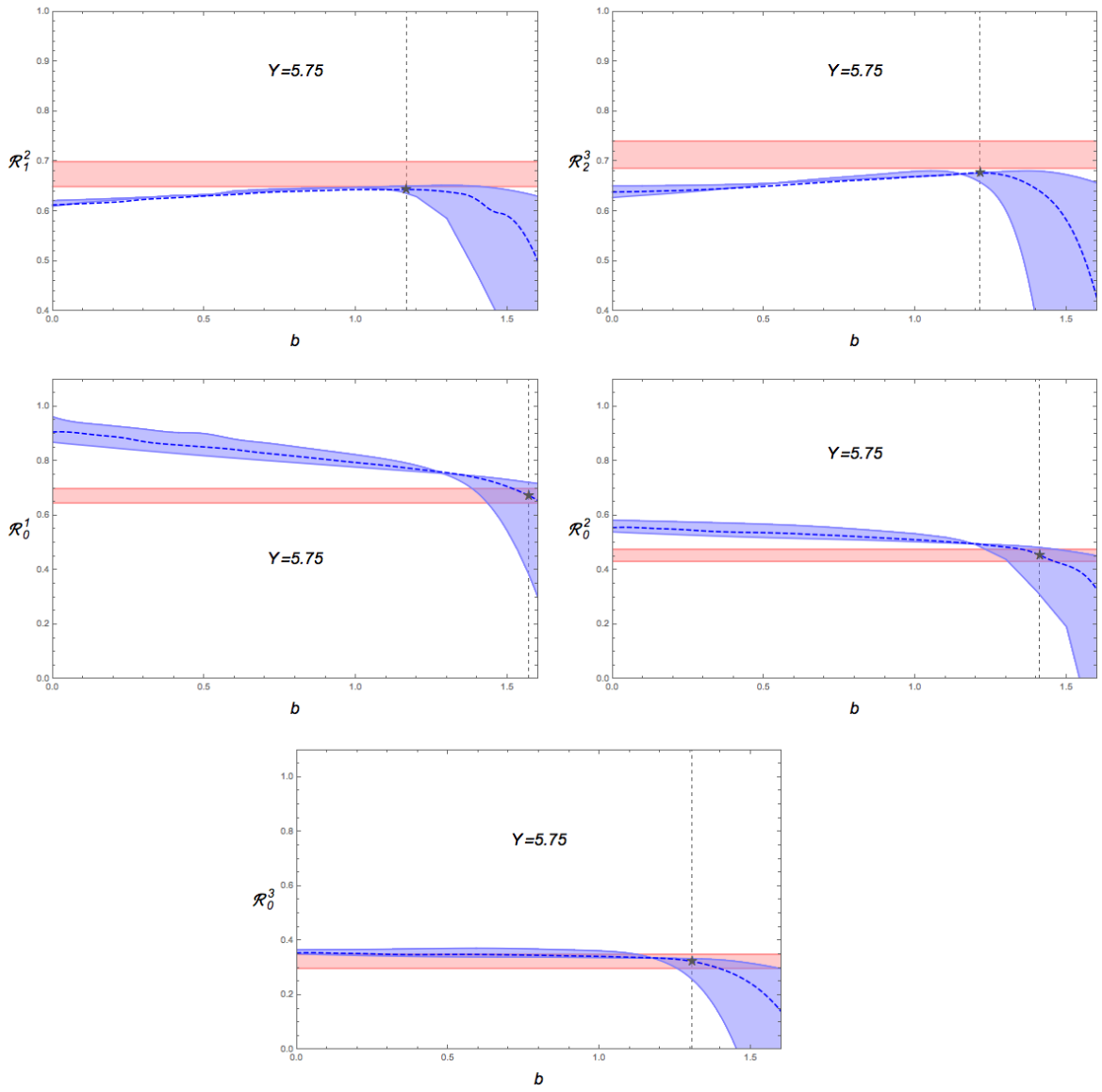

Figure 2.6: Functional dependence of the different R_m^n functions on the veto b at $Y = 5.75$. The reddish band denotes the experimental uncertainty while the blueish band denotes the theoretical uncertainty from the renormalisation scale variation.

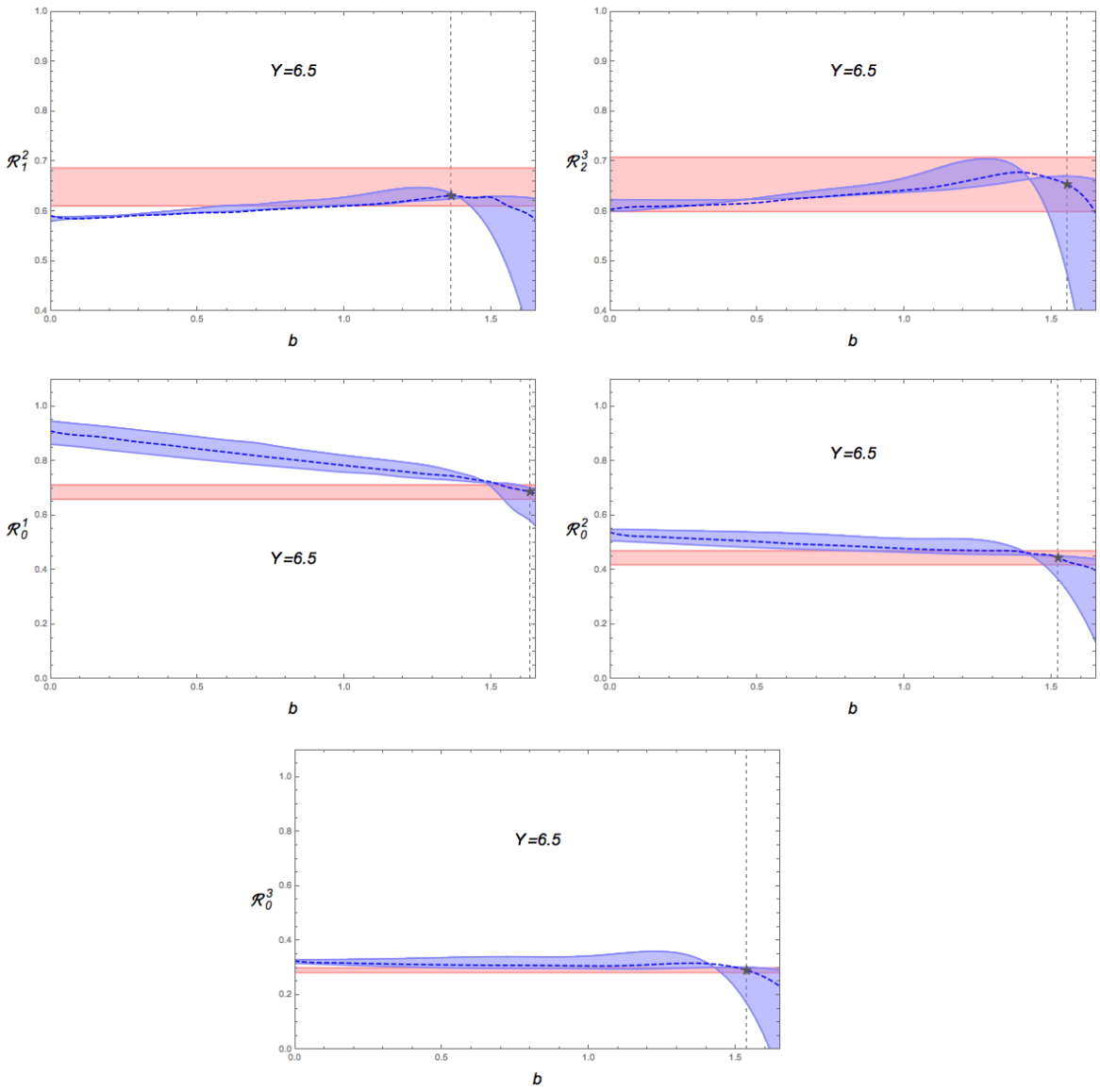

Figure 2.7: Functional dependence of the different R_m^n functions on the veto b at $Y = 6.5$. The reddish band denotes the experimental uncertainty while the blueish band denotes the theoretical uncertainty from the renormalisation scale variation.

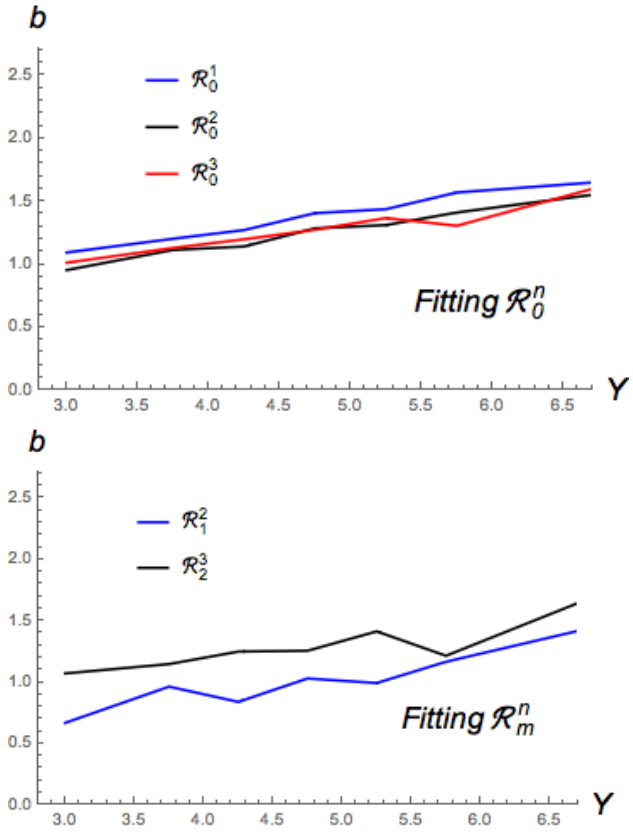

Figure 2.8: Dependence of the rapidity veto best-fit values on the rapidity Y for the different R_m^n functions.

CHAPTER 3

THREE-JET PRODUCTION

In the introduction, Chapter 1, we presented the basics of the BFKL resummation, and described some past attempts to measure its predictions. In Chapter 2, we modified the BFKL equation introducing a new physical assumption, the rapidity veto, and tested it against the experimental data in Mueller-Navelet jets. So far, the search for BFKL effects has had the drawback of involving collisions with too low center-of-mass energies or rapidity differences among the tagged particles, which the main assumption of the Regge limit. An additional problem has been to study observables which are too inclusive as to be able to claim that events under study could only be described by BFKL events, as we discussed in 1.4. The purpose of this section is to introduce other, less inclusive, observables to test where these resummation effects need to be taken into account.

Bearing that in mind, the LHC looks promising since the available energies are much higher than in older colliders as Tevatron or HERA, and since it provides enough statistics to allow for the study of more exclusive quantities, even with strong kinematical cuts. Needless to say, the experimental challenges to tackle these problems are remarkable, since it is needed large rapidity differences among the final tagged particles. Also, it is needed enough resolution in the other degrees of freedom involved, the azimuthal angles and the transverse momenta of the final states. In the following studies, we will separate even further from the usual "growth with energy" of the cross section, associated with the exchange of a hard pomeron, to focus on footprints related to the energy flow through the BFKL ladder and azimuthal angle differences.

After the arrival of the LHC data it has been seen that the NLLA predictions, when

including the NLO forward jet vertices, for the ratios of azimuthal angle correlations are in agreement with the experiment, see Ref. [135]. These predictions completely failed in describing the azimuthal angle correlations itself, which can be directly related to the presence of the zeroth conformal spin of the BFKL kernel and the influence of the collinear regions on it. In Ref. [136] one can find the most recent comparison between experimental data and theoretical prediction, in which the theoretical predictions from Ref. [130] also adequately described the the azimuthal angle correlations. The main change in this new prediction was to include the BLM scheme for setting the renormalization scale, which shows that the ratios are quite stable under changes in the renormalization scale, and that the BLM scheme is only essential in having a good description of the data when one studies observables where the zeroth conformal spin is involved. An important aspect is that, as of today, the only experimental analysis of Mueller-Navelet jets carried out with LHC data were done at 7 TeV.

In the pursuit of finding a clear signal of BFKL dynamics, which cannot be explained without the introduction of these resummation effects, there are two viable ways to proceed: going to higher center-of-mass energies and exploring less inclusive observables. Moreover, there exists many theoretical questions to be answered within the framework itself. Some of these include to determine the most accurate way to implement the running of the coupling constant, if there is any appearance of saturation effects in proton-proton collisions, how to isolate BFKL dynamics from the multiple interaction effects, etc.

In order to address these issues, we proposed to study multi-jet production, as a generalization of Mueller-Navelet jets. Inclusive multi-jet production opens up the study of BFKL dynamics in a novel and much more exclusive way. Investigating more exclusive final states (with more than two jets) although more challenging on a technical level, allows for more complex observables to be defined so that one can finally choose those that encapsulate the essence of these features of MRK that are distinct in the BFKL dynamics only. In the remaining of Part I, we will focus only on inclusive three-jet (Chapters 3 and 4) and four-jet (Chapter 5) production.

3.1 Unfolding the ladder

In going from the two-body to the n-body case we need to generalize the formalism to account for the extra tagging of jets in more central regions of rapidity, keeping the large rapidity differences among tagged emissions. In this section, we will describe an intuitive way of obtaining the expression at LLA.

Starting from the Monte-Carlo solution of the BFKL GGF, first obtained in Ref. [162]. Let us denote λ the cutoff introduced to tame IR divergences, and μ the resolution scale which satisfies $\mu > \lambda$.

The GGF can be expressed as a series solution, where the nth term is the contribution from the emission of n real gluons having a transverse momentum greater than λ. Each contribution can be expressed as the product of integrals over the phase space of each gluon in the BFKl ladder as

$$\varphi^{(n)}\left(\vec{k}_A,\vec{k}_B,Y_A-Y_B\right)=\int\left[\prod_{i=0}^{n}\mathscr{D}k_i\,e^{\omega(q_{i-1})(y_{i-1}-y_i)}\right]\times \times e^{\omega(q_n)(y_n-y_{n+1})}\delta^2\left(\vec{q}_n-\vec{k}_{n+1}\right), \tag{3.1}$$

where the rapidity ordering $Y_A = y_0 > y_1 > \cdots > y_n > y_{n+1} = Y_B$ is understood, and $\vec{k}_0 = \vec{k}_A$, $\vec{k}_{n+1} = \vec{k}_B$. Also, we have defined $\vec{q}_i \equiv \vec{k}_A + \sum_{j=1}^{i}\vec{k}_j$, the momentum running through the ladder and the measure is defined as

$$\mathscr{D}k \equiv \frac{\bar{\alpha}_s \mathrm{d}^2\vec{k}\,\mathrm{d}y}{\pi}\theta(k-\lambda). \tag{3.2}$$

Now, in order to have at least[1] one resolved emission, we will impose that one of the transverse momenta satisfy that $k_j > \mu$. So the nth order contribution to the GGF with at least with resolved emission is

$$\begin{aligned}\varphi^{(1R,n)}\left(\vec{k}_A,\vec{k}_B,Y_A-Y_B\right)=\sum_{j=1}^{n}\int\left[\prod_{i=0}^{j-1}\mathscr{D}k_i\,e^{\omega(q_{i-1})(y_{i-1}-y_i)}\right]\times\\ \times\mathscr{D}k_j\,\theta(k_j-\mu)e^{\omega(q_{j-1})(y_{j-1}-y_j)}\left[\prod_{i=j+1}^{n}\mathscr{D}k_i\,e^{\omega(q_{i-1})(y_{i-1}-y_i)}\right]\times\\ \times e^{\omega(q_n)(y_n-y_{n+1})}\delta^2\left(\vec{q}_n-\vec{k}_{n+1}\right).\end{aligned} \tag{3.3}$$

Now, to have a clearer notation, we introduce two vectors $\vec{p}_B = \vec{q}_j$, $\vec{p}_A = \vec{q}_{j-1}$,that are the two momenta flowing in(out)to the vertex producing the tagged emission j. Adding the

[1] Notice that we are considering inclusive cross sections.

required delta functions we transform Eq. (3.3) into

$$\begin{aligned}\varphi^{(1R,n)}\left(\vec{k}_A,\vec{k}_B,Y_A-Y_B\right) &= \int \mathrm{d}^2\vec{p}_A\,\mathrm{d}^2\vec{p}_B \sum_{j=1}^{n}\mathscr{D}k_j\,\theta(k_j-\mu)\delta^2\left(\vec{q}_j-\vec{p}_B\right)\times \\ &\times\left[\prod_{i=0}^{j-1}\mathscr{D}k_i\,e^{\omega(q_{i-1})(y_{i-1}-y_i)}\right]e^{\omega(q_{j-1})(y_{j-1}-y_j)}\delta^2\left(\vec{q}_{j-1}-\vec{p}_A\right)\times \\ &\times\left[\prod_{i=j+1}^{n}\mathscr{D}k_i\,e^{\omega(q_{i-1})(y_{i-1}-y_i)}\right]e^{\omega(q_n)(y_n-y_{n+1})}\delta^2\left(\vec{q}_n-\vec{k}_{n+1}\right).\end{aligned} \tag{3.4}$$

From here we can clearly identify the expressions of two GGFs and write the previous equation as

$$\begin{aligned}\varphi^{(1R,n)}\left(\vec{k}_A,\vec{k}_B,Y_A-Y_B\right) &= \int \mathrm{d}^2\vec{p}_A\,\mathrm{d}^2\vec{p}_B\sum_{j=1}^{n}\mathscr{D}k_j\,\theta(k_j-\mu)\times \\ \times\delta^2\left(\vec{p}_A+\vec{k}_j-\vec{p}_B\right)\varphi^{(j-1)}\left(\vec{k}_A,\vec{p}_A,Y_A-y_j\right)&\varphi^{(n-j)}\left(\vec{p}_B,\vec{k}_B,y_j-Y_B\right).\end{aligned} \tag{3.5}$$

Summing over the index n we obtain the inclusive cross section for one resolved gluon, which is independent of the cutoff λ

$$\begin{aligned}\frac{\mathrm{d}\sigma^{(1R)}\left(\vec{k}_A,\vec{k}_B,\vec{k}_j,Y_A,y_J,Y_B\right)}{\mathrm{d}^2\vec{k}_J\,\mathrm{d}y_J} &= \frac{\bar{\alpha}_s\theta(k_j-\mu)}{\pi k_J^2}\int \mathrm{d}^2\vec{p}_A\,\mathrm{d}^2\vec{p}_B\times \\ \times\delta^2\left(\vec{p}_A+\vec{k}_J-\vec{p}_B\right)\sum_{n=1}^{\infty}\sum_{j=1}^{n}&\varphi^{(j-1)}\left(\vec{k}_A,\vec{p}_A,Y_A-y_J\right)\varphi^{(n-j)}\left(\vec{p}_B,\vec{k}_B,y_J-Y_B\right),\end{aligned} \tag{3.6}$$

and the double sum is nothing but the product of two GGF, leading us to our final expression[2]

$$\begin{aligned}\frac{\mathrm{d}\sigma^{(1R)}\left(\vec{k}_A,\vec{k}_B,\vec{k}_J,Y_A,y_J,Y_B\right)}{\mathrm{d}^2\vec{k}_J\,\mathrm{d}y_J} &= \frac{\bar{\alpha}_s\theta(k_J-\mu)}{\pi k_J^2}\int \mathrm{d}^2\vec{p}_A\,\mathrm{d}^2\vec{p}_B\times \\ \times\delta^2\left(\vec{p}_A+\vec{k}_J-\vec{p}_B\right)&\varphi\left(\vec{k}_A,\vec{p}_A,Y_A-y_J\right)\varphi\left(\vec{p}_B,\vec{k}_B,y_J-Y_B\right),\end{aligned} \tag{3.7}$$

which describes the tagging of a single gluon with rapidity y_J and transverse momentum $\vec{k}_J$. An important feature of this expression is that there is a clear factorization among the radiation produced by the GGFs, which we do not tag, and the tagged jets.

The same procedure can be carried out to have two or more additional tagged jets, leading to the following expression for the two additional jets case[3], which will be used in

[2] We are omitting the step functions imposing the rapidity order constraints, *i.e.*, $\theta(Y_A-y_J)\theta(y_J-Y_B)$.

[3] We are omitting the step functions imposing the rapidity order constraints, *i.e.*, $\theta(Y_A-y_{J_1})\theta(y_{J_2}-Y_B)$.

Chapter 5,

$$\begin{aligned}\frac{\mathrm{d}\sigma^{(2R)}\left(\vec{k}_A,\vec{k}_B,\vec{k}_{J_1},\vec{k}_{J_2},Y_A,y_{J_1},y_{J_2},Y_B\right)}{\mathrm{d}^2\vec{k}_{J_1}\,\mathrm{d}y_{J_1}\,\mathrm{d}^2\vec{k}_{J_2}\,\mathrm{d}y_{J_2}} &= \theta(y_{J_1}-y_{J_2})\frac{\bar{\alpha}_s\theta(k_{J_1}-\mu)}{\pi k_{J_1}^2}\frac{\bar{\alpha}_s\theta(k_{J_2}-\mu)}{\pi k_{J_2}^2}\times \\ &\times\int \mathrm{d}^2\vec{p}_A\,\mathrm{d}^2\vec{p}_B\int \mathrm{d}^2\vec{p}_C\,\mathrm{d}^2\vec{p}_D\,\delta^2\left(\vec{p}_A+\vec{k}_{J_1}-\vec{p}_B\right)\delta^2\left(\vec{p}_C+\vec{k}_{J_2}-\vec{p}_D\right)\times \\ &\times\varphi\left(\vec{k}_A,\vec{p}_A,Y_A-y_{J_1}\right)\varphi\left(\vec{p}_B,\vec{p}_C,y_{J_1}-y_{J_2}\right)\varphi\left(\vec{p}_D,\vec{k}_B,y_{J_2}-Y_B\right),\end{aligned} \tag{3.8}$$

3.2 Warming up: Observables at partonic level

In order to introduce the concepts in a pedagogical way, we are going to develop first the machinery at partonic level. This prevents us from considering the difficulties all the difficulties that appear when we want to confront the observables with the experiment: phase space integrations, the inclusion of the PDFs, etc. We are especially interested in azimuthal angle correlations, since the BFKL framework makes the analytic computation of them convenient, and to continue building on the traditional of Mueller-Navelet jets studies.

At both, LLA and NLLA, the Fourier coefficients of the GGF can be easily extracted, since they correspond to a fixed conformal spin, we recall that

$$\varphi(\vec{k}_A,\vec{k}_B,Y)=\sum_{n=-\infty}^{\infty}\frac{e^{i(\theta_A-\theta_B)n}}{2\pi}\varphi_n\left(k_A^2,k_B^2,Y\right) \tag{3.9}$$

where the back-to-back configuration is given by $\theta_A=\theta_B$. Since there are no more vectors involved, the GGF can only depend on $\vec{k}_A,\vec{k}_B$ through their moduli and their product $\vec{k}_A\cdot\vec{k}_B=k_Ak_B\cos(\theta_A-\theta_B)$. That makes obvious the symmetry $n\leftrightarrow -n$ in the components φ_n, which will be important.

Let us massage Eq. (3.7) using one of the delta functions to get rid of one of the integrations[4]

$$\begin{aligned}\frac{\mathrm{d}\sigma}{\mathrm{d}^2\vec{k}_J\,\mathrm{d}y_J}\left(\vec{k}_A,\vec{k}_B,Y_A-Y_B\right)&=\frac{\bar{\alpha}_s}{2\pi k_J^2}\int\mathrm{d}p^2\,\mathrm{d}\theta\,\varphi(\vec{k}_A,\vec{p},Y_A-y_J)\varphi(\vec{p}+\vec{k}_J,\vec{k}_B,y_J-Y_B)=\\&=\frac{\bar{\alpha}_s}{(2\pi)^3k_J^2}\int dp^2d\theta\sum_{n,m}e^{im(\theta_A-\theta)}e^{in(\theta_{p+k_J}-\theta_B)}\varphi_m\left(k_A^2,p^2,Y_A-y_J\right)\varphi_n\left((\vec{p}+\vec{k}_J)^2,k_B^2,y_J-Y_B\right),\end{aligned} \tag{3.10}$$

where the angle θ_{p+k_J} is the azimuthal angle of the vector $\vec{p}+\vec{k}_J$. The second GGF depends on the angle difference $\theta-\theta_J$ through $(\vec{p}+\vec{k}_J)^2$, something easy to avoid through a change of variables $\theta\to\theta+\theta_J$. But first, let us simplify the $\exp(in\theta_{p+k_J})$ factor. The following trigonometric formulae will be useful

$$\tan\theta_{p+k_J}=\frac{p\sin\theta+k_J\sin\theta_J}{p\cos\theta+k_J\cos\theta_J},\ \arctan z=\frac{i}{2}(\log(1-iz)-\log(1+iz)), \tag{3.11}$$

which allow us to write[5]

$$e^{in\theta_{p+k_J}}=\left(\frac{1+iz}{1-iz}\right)^{n/2}=\left(\frac{pe^{i\theta}+k_Je^{i\theta_J}}{pe^{-i\theta}+k_Je^{-i\theta_J}}\right)^{n/2}=e^{in\theta_J}\frac{(pe^{i(\theta-\theta_J)}+k_J)^n}{(p^2+k_J^2+2k_Jp\cos(\theta-\theta_J))^{n/2}}. \tag{3.12}$$

[4] The notation has been simplified to not clutter the following formulae.

[5] It is important to remember that $(ab)^c\neq a^cb^c$, which makes nontrivial to factor out $e^{in\theta_J}$. For example, $e^{in\theta_J}(\frac{pe^{i(\theta-\theta_J)}+k_J}{pe^{-i(\theta-\theta_J)}+k_J})^{n/2}$, is not correct.

After these intermediate steps, and performing a translation in the integration variable $\theta \to \theta + \theta_J$, the differential cross section reads

$$\frac{\mathrm{d}\sigma}{\mathrm{d}^2\vec{k}_J\,\mathrm{d}y_J}\left(\vec{k}_A,\vec{k}_B,Y_A-Y_B\right) = \frac{\bar{\alpha}_s}{(2\pi)^3 k_J^2}\sum_{n,m} e^{im\theta_A}e^{-in\theta_B}e^{i(n-m)\theta_J}\int dp^2 d\theta e^{-im\theta}e^{in\alpha}\times \\ \times\varphi_m\left(k_A^2,p^2,Y_A-y_J\right)\varphi_n\left(p^2+k_J^2+2pk_J\cos\theta,k_B^2,y_J-Y_B\right), \tag{3.13}$$

where the angle α does not depend on the tagged azimuthal angles, it is more intuitive, and simplifies considerably the notation. We have that

$$e^{in\alpha} \equiv \frac{(pe^{i\theta}+k_J)^n}{(p^2+k_J^2+2k_Jp\cos\theta)^{n/2}}. \tag{3.14}$$

In order to simplify the expression it is convenient to write the differential cross section obtained in Eq. (3.13) as

$$\frac{\mathrm{d}\sigma}{\mathrm{d}^2\vec{k}_J\,\mathrm{d}y_J}\left(\vec{k}_A,\vec{k}_B,Y_A-Y_B\right) = \frac{\bar{\alpha}_s}{(2\pi)^3 k_J^2}\sum_{n,m} e^{im\theta_A}e^{-in\theta_B}e^{i(n-m)\theta_J}\Omega_{mn}, \tag{3.15}$$

where we have defined

$$\Omega_{mn} \equiv \int \mathrm{d}p^2\,\mathrm{d}\theta\, e^{-im\theta}e^{in\alpha}\times \\ \times\varphi_m\left(k_A^2,p^2,Y_A-y_J\right)\varphi_n\left(p^2+k_J^2+2pk_J\cos\theta,k_B^2,y_J-Y_B\right), \tag{3.16}$$

This way of expressing the partonic differential cross section allows us to obtain azimuthal correlations in an easy way, since now the dependence on the angles of the tagged particles is trivial.

Let us start with the typical MN observables, the azimuthal angle correlations among the two external jets. Note that this observable is not exactly the same, since we are asking for the presence of at least one additional hard jet, and also it depends on the kinematical configuration of the former

$$\mathscr{C}_M \equiv \langle\cos(M(\theta_A-\theta_B))\rangle = \mathscr{N}\int \mathrm{d}\theta_A\,\mathrm{d}\theta_B\,\mathrm{d}\theta_J\cos(M(\theta_A-\theta_B))\frac{\mathrm{d}\sigma}{\mathrm{d}^2\vec{k}\,\mathrm{d}y_J}, \tag{3.17}$$

where the normalization constant is

$$\mathscr{N}^{-1} = \int \mathrm{d}\theta_A\,\mathrm{d}\theta_B\,\mathrm{d}\theta_J\,\frac{\mathrm{d}\sigma}{\mathrm{d}^2\vec{k}\,\mathrm{d}y_J} = \frac{\bar{\alpha}_s}{k_J^2}\Omega_{00}, \tag{3.18}$$

which is nothing else than the total cross section. It is important to draw attention to the presence of the zeroth conformal spin in this factor, which is very sensitive to collinear dynamics well beyond the multi-Regge kinematics approximation [151, 152].

Performing the angular integrations is straightforward now and gives

$$\langle \cos(M(\theta_A - \theta_B)) \rangle = \mathcal{N} \frac{\bar{\alpha}_s}{k_J^2} \frac{1}{2} \left(\Omega_{MM} + \Omega_{-M,-M} \right), \tag{3.19}$$

where we have that

$$\begin{aligned} \Omega_{mm} \equiv \int \mathrm{d}p^2 \, \mathrm{d}\theta \, \frac{\left(p + k_J e^{-i\theta}\right)^m}{\left(p^2 + k_J^2 + 2k_J p \cos\theta\right)^{m/2}} \times \\ \times \varphi_m \left(k_A^2, p^2, Y_A - y_J\right) \varphi_m \left(p^2 + k_J^2 + 2pk_J \cos\theta, k_B^2, y_J - Y_B\right). \end{aligned} \tag{3.20}$$

Finally, using the fact that the GGF, φ_n, is left invariant under $n \leftrightarrow -n$, and that it is a real quantity, it can be easily shown that

$$\Omega_{MM} = \Omega_{-M,-M} = \Omega_{M,M}^* = \mathrm{Re}(\Omega_{M,M}), \tag{3.21}$$

this property can be used to simplify the numerical calculations, and also it serves to demonstrate that the sine observables $\langle \sin(M(\theta_A - \theta_B)) \rangle$ vanish.

Up to this point, we have not used the third available azimuthal angle, θ_J, but this new ingredient (in addition to the scale k_J) offers a richer phase space that we can explore defining generalized azimuthal correlations. These new observables are defined using the projections on the two relative azumuthal angles formed by each of the forward jets with the central jet, $\phi_A \equiv \theta_A - \theta_J - \pi$ and $\phi_B \equiv \theta_J - \theta_B - \pi$, in the form[6]

$$\mathscr{C}_{MN} \equiv \langle \cos\left(M\phi_A\right) \cos\left(N\phi_B\right) \rangle = \mathcal{N} \int \mathrm{d}\theta_A \, \mathrm{d}\theta_B \, \mathrm{d}\theta_J \, \cos\left(M\phi_A\right) \cos\left(N\phi_B\right) \frac{\mathrm{d}\sigma}{\mathrm{d}^2\vec{k} \, \mathrm{d}y_J}. \tag{3.22}$$

As before, using that the GGF is real and that it is left invariant under $n \leftrightarrow -n$, we obtain the relationship

$$\Omega_{mn} = \Omega_{-m,-n} = \Omega_{mn}^* = \mathrm{Re}(\Omega_{mn}), \tag{3.23}$$

which generalizes Eq. (3.21). In this case, a direct consequence is that the correlation functions involving only one sine will vanish. From a kinematical perspective, this is equivalent to say that the differential cross section is invariant under the discrete transformation

[6] There is an important subtlety regarding ϕ_B. Although the kinematical configuration $\phi_A = 0$ corresponds to the jets A and J being back to back in the transverse space, this is not the case for $\phi_B = 0$, where it corresponds to the jets J and B sharing the same direction. The origin of this asymmetry is related to the convention chosen for the flow of transverse momentum through the BFKL ladder, where $\vec{k}_B$ has been chosen to be ingoing, but the rest to be outgoing. A straightforward check of this can be done taking the $Y \to 0$ limit in all the GGFs. Nevertheless, the only effect of this convention is the appearance of a $(-1)^N$ factor in the $\mathscr{C}_{MN}$ observable.

$(\theta_A,\theta_J,\theta_B)\to(-\theta_A,-\theta_J,-\theta_B)$, or an inversion with respect to a plane containing the beam axis.

The differential cross section in Eq (3.15) can be rewritten using the former symmetry as

$$\begin{aligned}\frac{\mathrm{d}\sigma}{\mathrm{d}^2\vec{k}_J\,\mathrm{d}y_J}\left(\vec{k}_A,\vec{k}_B,Y_A-Y_B\right)&=\frac{\bar{\alpha}_s}{(2\pi)^3k_J^2}\left[\Omega_{00}+\right.\\ +2\sum_{m,n>0}(-1)^{m+n}&\left\{\cos\left(m\phi_A\right)\cos\left(n\phi_B\right)\left(\Omega_{mn}+\Omega_{m,-n}\right)+\right.\\ &\left.\left.+\sin\left(m\phi_A\right)\sin\left(n\phi_B\right)\left(\Omega_{m,-n}-\Omega_{mn}\right)\right\}\right],\end{aligned}\tag{3.24}$$

Now we can easily simplify the generalized azimuthal correlations $\mathscr{C}_{MN}$ defined at Eq. (3.22), and using the relationships from Eq. (3.23) we obtain the final expression

$$\begin{aligned}\mathscr{C}_{MN}&=\mathscr{N}\frac{\bar{\alpha}_s}{k_J^2}(-1)^{M+N}\frac{1}{2}\left(\Omega_{M,N}+\Omega_{M,-N}\right)=\\ &=\mathscr{N}\frac{\bar{\alpha}_s}{k_J^2}(-1)^{M+N}\int\mathrm{d}p^2\,\mathrm{d}\theta\,\cos(M\theta)\cos(N\alpha)\times\\ &\times\varphi_M\left(k_A^2,p^2,Y_A-y_J\right)\varphi_N\left(p^2+k_J^2+2pk_J\cos\theta,k_B^2,y_J-Y_B\right),\end{aligned}\tag{3.25}$$

which is explicitly real.

In the case of the generalized azimuthal correlations, we can define additional observables involving the rest of trigonometric functions, but not all of them are different from zero because of the relationships stated at Eq. (3.23), they trivially imply that

$$\langle\sin\left(M\phi_A\right)\cos\left(N\phi_B\right)\rangle=\langle\cos\left(M\phi_A\right)\sin\left(N\phi_B\right)\rangle=0\,.\tag{3.26}$$

However, the observable involving two sines respects the $(\theta_A,\theta_J,\theta_B)\to(-\theta_A,-\theta_J,-\theta_B)$ symmetry, and it is given by

$$\begin{aligned}\mathscr{S}_{MN}\equiv\langle\sin\left(M\phi_A\right)\sin\left(N\phi_B\right)\rangle&=\mathscr{N}\frac{\bar{\alpha}_s}{k_J^2}(-1)^{M+N}\frac{1}{2}\left(\Omega_{M,-N}-\Omega_{M,N}\right)=\\ &=\mathscr{N}\frac{\bar{\alpha}_s}{k_J^2}(-1)^{M+N}\int\mathrm{d}p^2\,\mathrm{d}\theta\,\sin(M\theta)\sin(N\alpha)\times\\ &\times\varphi_M\left(k_A^2,p^2,Y_A-y_J\right)\varphi_N\left(p^2+k_J^2+2pk_J\cos\theta,k_B^2,y_J-Y_B\right).\end{aligned}\tag{3.27}$$

This last observable, although it is not explored in the following sections, deserves the same attention and, for example, it is involved in the difference between $\langle\cos(M(\theta_A-\theta_B))\rangle$ and $\langle\cos(M(\theta_A+\theta_B-2\theta_J))\rangle$, two observables that will differ in general.

Finally, let us investigate how the observables relate under parity, which relates the kinematical configurations

$$(k_A,k_B,k_J,\theta_A,\theta_B,\theta_J,Y_A-y_J,y_J-Y_B)\leftrightarrow(k_B,k_A,k_J,\theta_B,\theta_A,\theta_J+\pi,y_J-Y_B,Y_A-y_J)\,.\tag{3.28}$$

Using the delta function to solve for $\vec{p}_A$ in Eq. (3.7), we obtain an equivalent expression for Ω_{mn}

$$\Omega_{mn}(k_A,k_B,k_J,Y_A-y_J,y_J-Y_B)=(-1)^{n+m}\int \mathrm{d}p^2\,\mathrm{d}\theta\,\frac{\left(pe^{i\theta}+k_J\right)^m}{\left(p^2+k_J^2+2k_Jp\cos\theta\right)^{m/2}}\times \\ \times e^{-in\theta}\varphi_n\left(p^2+k_J^2+2pk_J\cos\theta,k_B^2,y_J-Y_B\right)\varphi_m\left(k_A^2,p^2,Y_A-y_J\right), \tag{3.29}$$

comparing with Eqs. (3.16, 3.14) and using that $\varphi_n\left(k_A^2,k_B^2,Y\right)=\varphi_n\left(k_B^2,k_A^2,Y\right)$ we can establish the following relationship

$$\Omega_{mn}(k_A,k_B,k_J,Y_A-y_J,y_J-Y_B)=(-1)^{n+m}\Omega_{nm}(k_B,k_A,k_J,y_J-Y_B,Y_A-y_J), \tag{3.30}$$

that directly translates into[7]

$$\begin{aligned}\mathscr{C}_{MN}(k_A,k_B,k_J,Y_A-y_J,y_J-Y_B)&=(-1)^{M+N}\mathscr{C}_{NM}(k_B,k_A,k_J,y_J-Y_B,Y_A-y_J)\\ \mathscr{S}_{MN}(k_A,k_B,k_J,Y_A-y_J,y_J-Y_B)&=(-1)^{M+N}\mathscr{S}_{NM}(k_B,k_A,k_J,y_J-Y_B,Y_A-y_J),\end{aligned} \tag{3.31}$$

which is something you expect of QCD, since both of the observables transform this way under parity, that is preserved in the theory.

This property may seem to have a really limited range of applicability. Nevertheless, it is usual in experimental studies to apply parity invariant kinematical cuts. For example, it can be used in the case of symmetrical phase space cuts for k_A and k_B, which is the configuration that was experimentally measured by the CMS Collaboration in Refs. [135, 136]. In addition to that, it is required that the variation of y_J is symmetrical with respect to its distance from Y_A and Y_B. On the other hand, it can be used to speed up the numerical integration of the phase space when performing theoretical predictions.

[7] If we had used the opposite convention for the sign of $\vec{k}_B$, as explained in Footnote (6), we would have obtained $\mathscr{C}_{MN}\left(k_A,k_B,k_J,Y_A-y_J,y_J-Y_B\right)=\mathscr{C}_{NM}\left(k_B,k_A,k_J,y_J-Y_B,Y_A-y_J\right)$, which is more intuitive. Also, the parity transformation would act as $\left(k_A,k_B,k_J,\theta_A,\theta_B,\theta_J,Y_A-y_J,y_J-Y_B\right)\leftrightarrow\left(k_B,k_A,k_J,\theta_B+\pi,\theta_A+\pi,\theta_J+\pi,y_J-Y_B,Y_A-y_J\right)$.

3.3 Hadronic observables

Here we advance in this direction by proposing new observables associated with the inclusive production of three jets: two of them are the original Mueller-Navelet jets and the third one is a tagged jet in central regions of rapidity (see Fig. 3.1). Experimentally, they have the advantage to belong to the already recorded Mueller-Navelet events, it only requires of further binning in the internal jets. Theoretically, they will allow us to better understand distinct features of the BFKL ladder, in other words, to find out which ones of its predictions cannot be reproduced by other approaches such as low order exact perturbation theory or general-purpose Monte-Carlo event generators. Parton-level studies have been already presented in [163] while here we focus on calculating realistic cross-sections at the LHC.

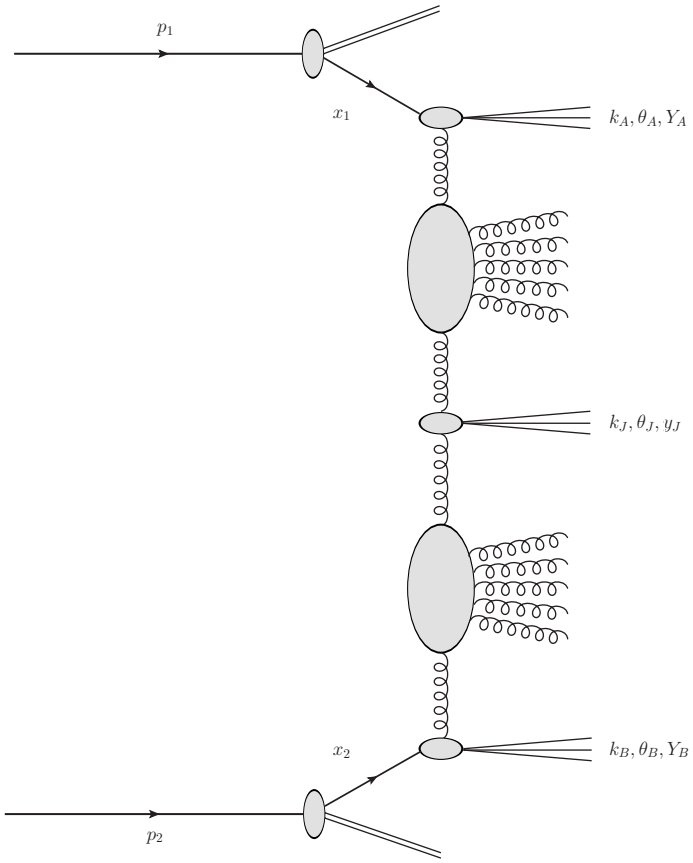

Figure 3.1: Inclusive three-jet production process in multi-Regge kinematics.

In order to focus our discussion, we will present results for the above mentioned $\mathscr{R}_n^m$ ratios but now with a further dependence on the p_t and rapidity of the central jet. As a

novel result, we will also present predictions for the new ratios

$$\mathscr{R}^{MN}_{PQ} = \frac{\langle \cos(M\phi_1)\cos(N\phi_2)\rangle}{\langle \cos(P\phi_1)\cos(Q\phi_2)\rangle}, \tag{3.32}$$

where ϕ_1 and ϕ_2 are, respectively, the azimuthal angle difference between the first and the second (central) jet and between this one and the third jet (see Fig. 3.2).

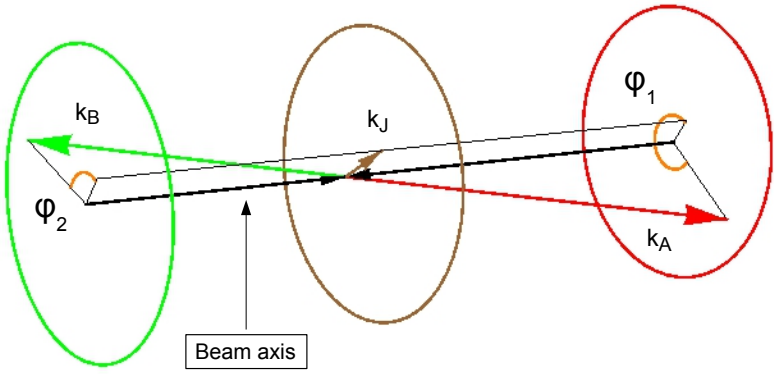

Figure 3.2: Representation of a three-jet event in a generic detector. All three circles are perpendicular to the beam axis.

A further natural development in this direction has been the extension of these observables to the case of four-jet production in multi-Regge kinematics with a second tagged jet being produced in the central region of rapidity [4, 164], that we will present in Chapter 5. This allows for the study of even more differential distributions in the transverse momenta, azimuthal angles and rapidities of the two central jets, for fixed values of the four momenta of the two forward (originally Mueller-Navelet) jets. The main observable $\mathscr{R}^{MNL}_{PQR}$ proposed at parton level in [164] is the extension of the one in Eq. (3.32), using three cosines instead of two in numerator and denominator. This observable also paves the way for detailed studies of multiple parton scattering [165–169] although we should point out that in Ref. [170] there is a claim that multiple parton interactions (MPI) are negligible in the present LHC kinematics for the values of transverse momenta used in the following.

In the next two Sections, we focus on the case of inclusive three-jet production performing a realistic study beyond the parton level calculation. This will allow for a comparison of our observables with forthcoming analysis of the LHC experimental data. Cross-sections are calculated using collinear factorization to produce the two most for-

ward/backward jets, convoluting the “hard" differential cross section, which follows the BFKL dynamics, with collinear parton distribution functions included in the forward “jet vertex" [68, 142, 143, 171–174]. We link these two Mueller-Navelet jet-vertices with the centrally produced jet via two BFKL gluon Green functions. To simplify our predictions, we integrate over the momenta of all produced jets, using current LHC experimental cuts, only fixing the rapidity of the central jet to lie in the middle of the two most forward/backward tagged jets. In the following Section we will show the main formulas, in Section 3.5 we will present our numerical predictions to finally end with our Summary 3.6.

3.4 Hadronic inclusive three-jet production in multi-Regge kinematics

The process under investigation (see Figs. 3.1, 3.2 and 3.3) is the production of two forward/backward jets, both characterized by high transverse momenta $\vec{k}_{A,B}$ and well separated in rapidity, together with a third jet produced in the central rapidity region and with possible associated mini-jet production. This corresponds to

$$\text{proton}(p_1)+\text{proton}(p_2)\to\text{jet}(k_A)+\text{jet}(k_J)+\text{jet}(k_B)+\text{minijets}\,. \tag{3.33}$$

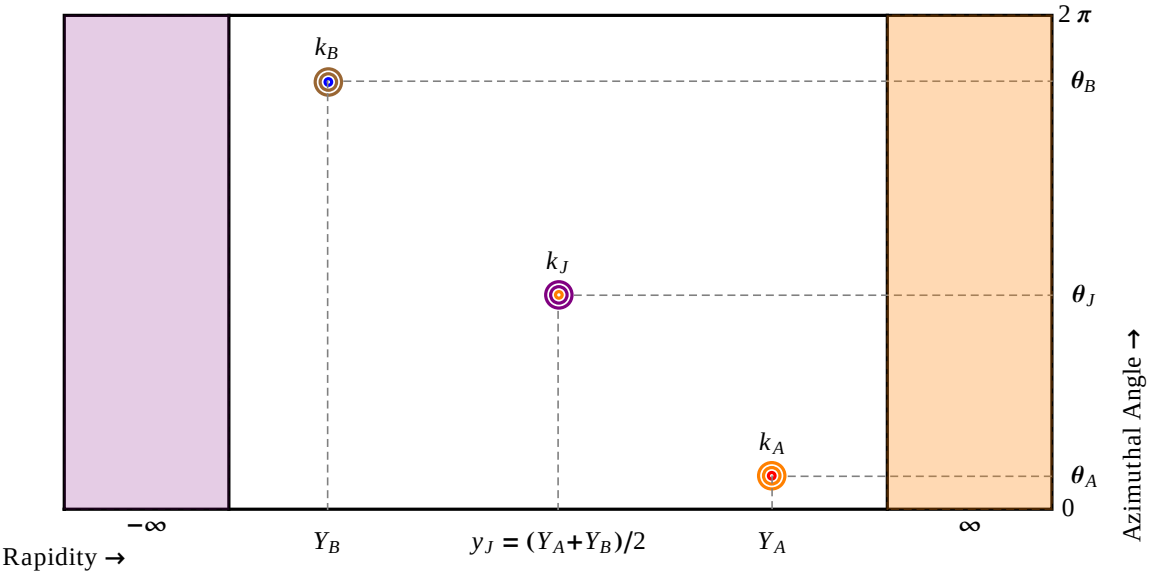

Figure 3.3: A primitive lego plot depicting a three jet event. k_A is a forward jet with large positive rapidity Y_A and azimuthal angle θ_A, k_B is a forward jet with large negative rapidity Y_B and azimuthal angle θ_B and k_J is a central jet with rapidity y_J and azimuthal angle θ_J.

In collinear factorization the cross section for the process (3.33) reads

$$\frac{d\sigma^{3-\text{jet}}}{dk_A\,dY_A\,d\theta_A\,dk_B\,dY_B\,d\theta_B\,dk_J\,dy_J d\theta_J} = \sum_{r,s=q,\bar{q},g}\int_0^1 dx_1\int_0^1 dx_2\, f_r\left(x_1,\mu_F\right)\, f_s\left(x_2,\mu_F\right)\, d\hat{\sigma}_{r,s}\left(\hat{s},\mu_F\right)\,, \tag{3.34}$$

where the r,s indices specify the parton types (quarks $q = u,d,s,c,b$; antiquarks $\bar{q} = \bar{u},\bar{d},\bar{s},\bar{c},\bar{b}$; or gluon g), $f_{r,s}\left(x,\mu_F\right)$ are the initial proton PDFs; $x_{1,2}$ represent the longitudinal fractions of the partons involved in the hard subprocess; $d\hat{\sigma}_{r,s}\left(\hat{s},\mu_F\right)$ is the partonic

cross section for the production of jets and $\hat{s} \equiv x_1 x_2 s$ is the squared center-of-mass energy of the hard subprocess (see Fig. 3.1). The BFKL dynamics enters in the cross-section for the partonic hard subprocess $d\hat{\sigma}_{r,s}$ in the form of two forward gluon Green functions φ to be described below.

Using the definition of the jet vertex in the leading order approximation [171], we can present the cross section for the process as

$$\begin{aligned}
&\frac{d\sigma^{3-\text{jet}}}{dk_A\, dY_A\, d\theta_A\, dk_B\, dY_B\, d\theta_B\, dk_J\, dy_J d\theta_J} = \\
&= \frac{8\pi^3 C_F\, \bar{\alpha}_s^3}{N_C^3}\, \frac{x_{J_A} x_{J_B}}{k_A\, k_B\, k_J} f^\star\left(x_{J_A}, \mu_F\right) f^\star\left(x_{J_B}, \mu_F\right) \times \\
&\times \int d^2\vec{p}_A \int d^2\vec{p}_B\, \delta^{(2)}\left(\vec{p}_A + \vec{k}_J - \vec{p}_B\right) \times \\
&\times \varphi\left(\vec{k}_A, \vec{p}_A, Y_A - y_J\right) \varphi\left(\vec{p}_B, \vec{k}_B, y_J - Y_B\right),
\end{aligned} \tag{3.35}$$

where the effective PDF is defined as $f^\star\left(x_J, \mu_F\right) \equiv \frac{N_C}{C_F} f_g(x_J, \mu_F) + \sum_{i=q,\bar{q}} f_i(x_J, \mu_F)$. In order to lie within multi-Regge kinematics, we have considered the ordering in the rapidity of the produced particles $Y_A > y_J > Y_B$, while k_J^2 is always above the experimental resolution scale. $x_{J_{A,B}}$ are the longitudinal momentum fractions of the two external jets, linked to the respective rapidities $Y_{J_{A,B}}$ by the relation $x_{J_{A,B}} = k_{A,B}\, e^{\pm Y_{J_{A,B}}}/\sqrt{s}$. φ are BFKL gluon Green functions normalized to $\varphi(\vec{p}, \vec{q}, 0) = \delta^{(2)}(\vec{p} - \vec{q})$ and $\bar{\alpha}_s = N_c/\pi\, \alpha_s\left(\mu_R\right)$.

Building up on the work in Ref. [163, 164], we study observables for which the BFKL approach will be distinct from other formalisms and also rather insensitive to possible higher order corrections. We focus on new quantities whose associated distributions are different from the ones which characterize the Mueller-Navelet case, though still related to the azimuthal-angle correlations by projecting the differential cross section on the two relative azimuthal angles between each external jet and the central one $\phi_A = \theta_A - \theta_J - \pi$ and $\phi_B = \theta_J - \theta_B - \pi$ (see Fig. 3.3). Taking into account the factors coming from the jet vertices, it is possible to write the generalized azimuthal correlations at hadronic level in

the following form

$$
\begin{aligned}
&\int_0^{2\pi} \mathrm{d}\theta_A\,\mathrm{d}\theta_J\,\mathrm{d}\theta_B\,\cos\left(M\phi_A\right)\cos\left(N\phi_B\right)\times \\
&\qquad\times\frac{d\sigma^{3-\mathrm{jet}}}{\mathrm{d}k_A\,\mathrm{d}Y_A\,\mathrm{d}\theta_A\,\mathrm{d}k_J\,\mathrm{d}Y_J\,\mathrm{d}\theta_J\,\mathrm{d}k_B\,\mathrm{d}Y_B\,\mathrm{d}\theta_B} = \\
&= \frac{8\pi^4 C_F\bar{\alpha}_s^3}{N_C^3}\frac{x_{J_A}x_{J_B}}{k_A k_J k_B} f^\star\left(x_{J_A},\mu_F\right) f^\star\left(x_{J_B},\mu_F\right)\times \\
&\qquad\times(-1)^{M+N}\int_0^\infty \mathrm{d}p^2\int_0^{2\pi}\mathrm{d}\theta\,\cos(M\theta)\frac{\mathrm{Re}\left[\left(pe^{i\theta}+k_J\right)^N\right]}{\sqrt{\left(p^2+k_J^2+2pk_J\cos\theta\right)^N}}\times \\
&\qquad\times\varphi_M\left(k_A^2,p^2,Y_A-y_J\right)\varphi_N\left(p^2+k_J^2+2pk_J\cos\theta,k_B^2,y_J-Y_B\right),
\end{aligned}
\tag{3.36}
$$

where

$$
\varphi_n\left(k^2,q^2,Y\right) = \frac{2}{\pi\,k\,q}\int_0^\infty d\nu\cos\left(\nu\ln\frac{k^2}{q^2}\right)e^{\bar{\alpha}_s\chi_0(n,\nu)(Y-Y_0)},
\tag{3.37}
$$

$$
\chi_0(n,\nu) = 2\psi(1)-\psi\left(\frac{1+n}{2}+i\nu\right)-\psi\left(\frac{1+n}{2}-i\nu\right) = 2\mathrm{Re}\left[\psi(1)-\psi\left(\frac{1+n}{2}+i\nu\right)\right],
\tag{3.38}
$$

and ψ is the logarithmic derivative of Euler's gamma function.

The related experimental observable we propose corresponds to the mean value (with M,N being positive integers)

$$
\begin{aligned}
\mathscr{C}_{MN} &= \langle\cos\left(M\phi_A\right)\cos\left(N\phi_B\right)\rangle = \\
&= \frac{\int_0^{2\pi} d\theta_A d\theta_B d\theta_J\cos\left(M\phi_A\right)\cos\left(N\phi_B\right)d\sigma^{3-\mathrm{jet}}}{\int_0^{2\pi} d\theta_A d\theta_B d\theta_J d\sigma^{3-\mathrm{jet}}}.
\end{aligned}
\tag{3.39}
$$

From a phenomenological point of view, since our main target is to provide testable predictions compatible with the current and future experimental data, we now introduce those kinematical cuts already in place at the LHC. For this purpose, we have to take the average that defines $\mathscr{C}_{M,N}$ integrating over the momenta and rapidity of the tagged jets in the form

$$
C_{MN} \equiv \frac{\int\mathscr{D}\mathrm{PS}\,\cos\left(M\phi_A\right)\cos\left(N\phi_B\right)d\sigma^{3-\mathrm{jet}}}{\int\mathscr{D}\mathrm{PS}\,d\sigma^{3-\mathrm{jet}}},
\tag{3.40}
$$

where the integration measure is defined as

$$
\begin{aligned}
\int\mathscr{D}\mathrm{PS} \equiv &\int_{Y_A^{\min}}^{Y_A^{\max}}\mathrm{d}Y_A\int_{Y_B^{\min}}^{Y_B^{\max}}\mathrm{d}Y_B\int_{k_A^{\min}}^{k_A^{\max}}\mathrm{d}k_A\int_{k_B^{\min}}^{k_B^{\max}}\mathrm{d}k_B\int_{k_J^{\min}}^{k_J^{\max}}\mathrm{d}k_J\times \\
&\times\delta(Y_A-Y_B-Y)\int_0^{2\pi}\mathrm{d}\theta_A\int_0^{2\pi}\mathrm{d}\theta_B\int_0^{2\pi}\mathrm{d}\theta_J\,.
\end{aligned}
\tag{3.41}
$$

The forward/backward jet rapidities are taken in the range delimited by $Y_A^{\min} = Y_B^{\min} = -4.7$ and $Y_A^{\max} = Y_B^{\max} = 4.7$, keeping their difference $Y \equiv Y_A - Y_B$ fixed at definite values in the range $5 < Y < 9$.

From a more theoretical perspective, it is important to have as good as possible perturbative stability in our predictions (see [121] for a related discussion). This can be achieved by removing the contribution stemming from the zero conformal spin, which corresponds to the index $n = 0$ in Eq. (3.37). We, therefore, introduce the ratios where the observable have been integrate over the whole phase space as

$$R_{PQ}^{MN} = \frac{C_{MN}}{C_{PQ}} \tag{3.42}$$

which are free from any $n = 0$ dependence for $M, N, P, Q > 0$. We proceed now to present our numerical results for a number of different kinematic configurations.

3.5 Numerical results for azimuthal-angle dependences

We now study the ratios $R_{PQ}^{MN}(Y)$ in Eq. (4.12) as functions of the rapidity difference Y between the most forward and the most backward jets for a set of characteristic values of M,N,P,Q and for two different center-of-mass energies: $\sqrt{s} = 7$ and $\sqrt{s} = 13$ TeV. Since we are integrating over k_A and k_B, we have the opportunity to impose either symmetric or asymmetric cuts, as it has been previously done in the Mueller-Navelet case [125, 133]. To be more precise, we study the two kinematical configurations:

1. $k_A^{\min} = 35$ GeV, $k_B^{\min} = 35$ GeV, $k_A^{\max} = k_B^{\max} = 60$ GeV (symmetric);

2. $k_A^{\min} = 35$ GeV, $k_B^{\min} = 50$ GeV, $k_A^{\max} = k_B^{\max} = 60$ GeV (asymmetric).

In order to be as close as possible to the rapidity ordering characteristic of multi-Regge kinematics, we set the value of the central jet rapidity such that it is equidistant to Y_A and Y_B by imposing the condition $y_J = \frac{Y_A+Y_B}{2}$. Moreover, since by tagging a central jet we are able to extract more exclusive information from our observables, we allow three possibilities for the transverse momentum k_J, that is, $20\,\text{GeV} < k_J < 35\,\text{GeV}$ (bin-1), $35\,\text{GeV} < k_J < 60\,\text{GeV}$ (bin-2) and $60\,\text{GeV} < k_J < 120\,\text{GeV}$ (bin-3). Keeping in mind that the forward/backward jets have transverse momenta in the range $[35\,\text{GeV}, 60\,\text{GeV}]$, restricting the value of k_J within these three bins allows us to see how the ratio $R_{PQ}^{MN}(Y)$ changes behaviour depending on the relative size of the central jet when compared to the forward/backward ones. Bin-1, bin-2 and bin-3 correspond to k_J being smaller than, similar to and larger than k_A, k_B, respectively.

Before we proceed to present our numerical results, we should note that we performed the numerical computation of the ratios $\mathscr{R}_{PQ}^{MN}$ both in FORTRAN and in MATHEMATICA (mainly for cross-checks). We set the scale s_0 such that $Y_0 = 0$. The NLO MSTW 2008 PDF sets [161] were used and for the strong coupling α_s we chose a two-loop running coupling setup with $\alpha_s(M_Z) = 0.11707$. We made extensive use of the integration routine `Vegas` [175] as implemented in the `Cuba` library [176, 177]. Furthermore, we used the `Quadpack` library [178] and a slightly modified version of the `Psi` [179] routine.

In the following, we present our results collectively in four figures. In Figs. 3.4 and 3.6 different ratios are shown for $\sqrt{s} = 7$ TeV and in Figs. 3.5 and 3.7 we see the same ratios for $\sqrt{s} = 13$ TeV. In all four figures, in the left column we place the plots for the symmetric kinematic cut ($k_B^{\min} = 35$ GeV) and in the right column the plots for the asymmetric one ($k_B^{\min} = 50$ GeV). The red dot-dashed curve corresponds to k_J bounded in bin-1, the green dashed curve to k_J bounded in bin-2 and finally the blue continuous one to k_J bounded in

bin-3. In total, we show the results for six different observables: R_{22}^{11}, R_{12}^{13}, R_{12}^{22}, R_{12}^{23}, R_{12}^{33} and R_{22}^{33}.

The first observation that becomes apparent from a preliminary view to the four figures is that the dependence of the different observables on the rapidity difference between k_A and k_B is rather smooth. This is more pronounced when we consider k_J being larger than the forward/backward jets (blue line). Indeed, the blue curve, which corresponds to large values of the transverse momentum in the central jet, is mostly linear. The other two curves (red and green) follow generally the same smooth with Y behavior although they tend to be less linear than the blue curve.

The slope of the three curves, in absolute values, depends on the particular observable. For example, in Fig. 3.4, the blue curve in the top left drops from ~ 3.5 at $Y = 5$ to ~ 4.5 at $Y = 9$, whereas in bottom left it drops from ~ 0.7 to ~ 0.6.

Another interesting observation is that there are ratios for which changing from the symmetric to the asymmetric cut makes no real difference and other ratios for which the picture changes radically. A characteristic example of the former case is the observable R_{12}^{22} in Fig. 3.4 bottom line, where we see practically no big differences between the left and right plots. If instead we focus on R_{12}^{13} in Fig. 3.4 middle line, we see that going from the symmetric cut (left) to the asymmetric one (right) brings forward a big change.

The main conclusion we would like to draw after comparing Fig. 3.4 to Fig. 3.5 and Fig. 3.6 to Fig. 3.7 is that, in general, for most of the observables there are no significant changes when we increase the colliding energy from 7 to 13 TeV. This is indeed remarkable since it indicates that a sort of asymptotic regime has been reached for the kinematical configurations included in our analysis. It also tells us that our observables are really as insensitive as possible to effects which have their origin outside the BFKL dynamics and which normally cannot be isolated (*e.g.* influence from the PDFs).

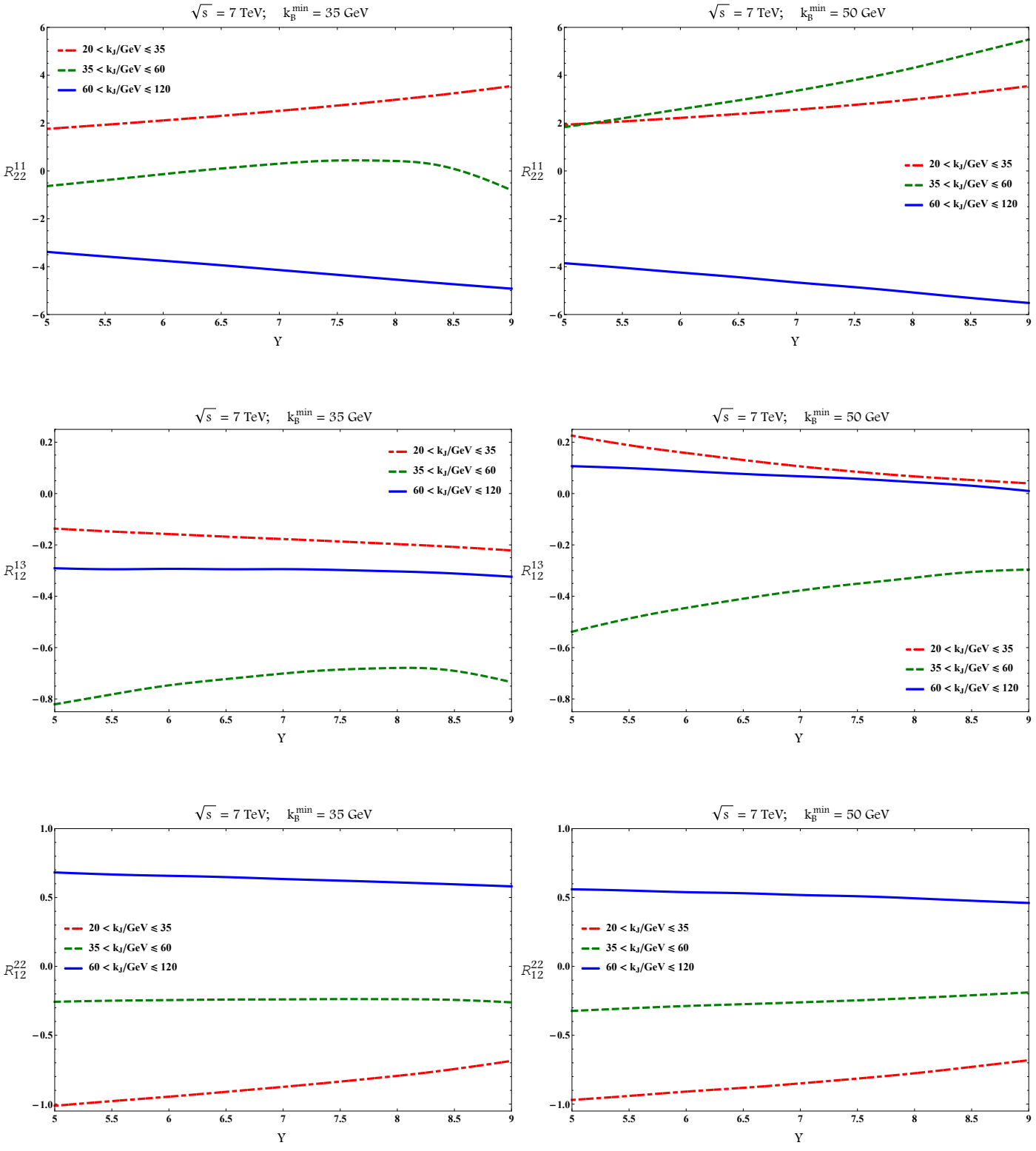

Figure 3.4: Y-dependence of R_{22}^{11}, R_{12}^{13} and R_{12}^{22} for $\sqrt{s} = 7$ TeV and $k_B^{\min} = 35$ GeV (left column) and $k_B^{\min} = 50$ GeV (right column).

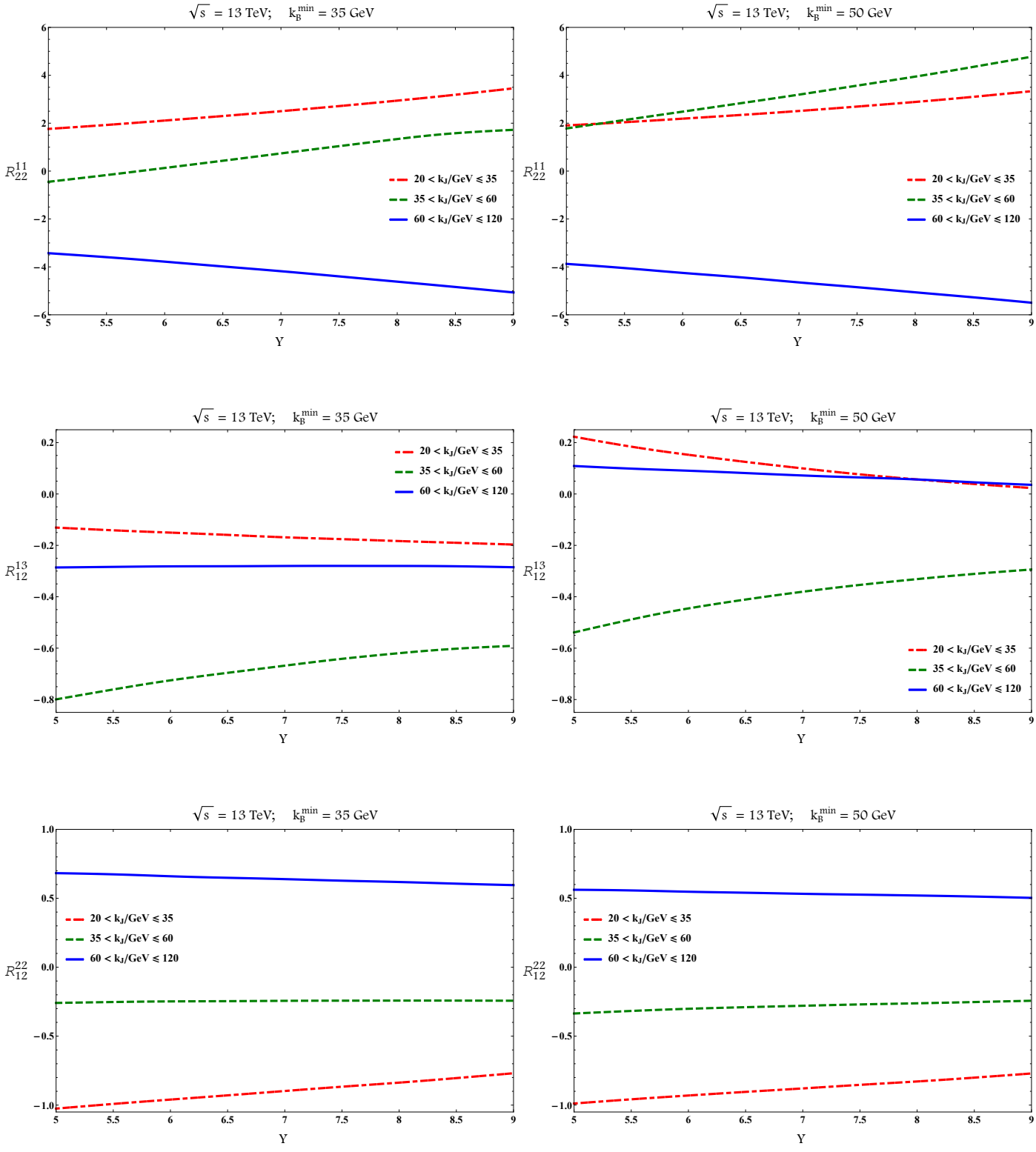

Figure 3.5: Y-dependence of R_{22}^{11}, R_{12}^{13} and R_{12}^{22} for $\sqrt{s} = 13$ TeV and $k_B^{\min} = 35$ GeV (left column) and $k_B^{\min} = 50$ GeV (right column).

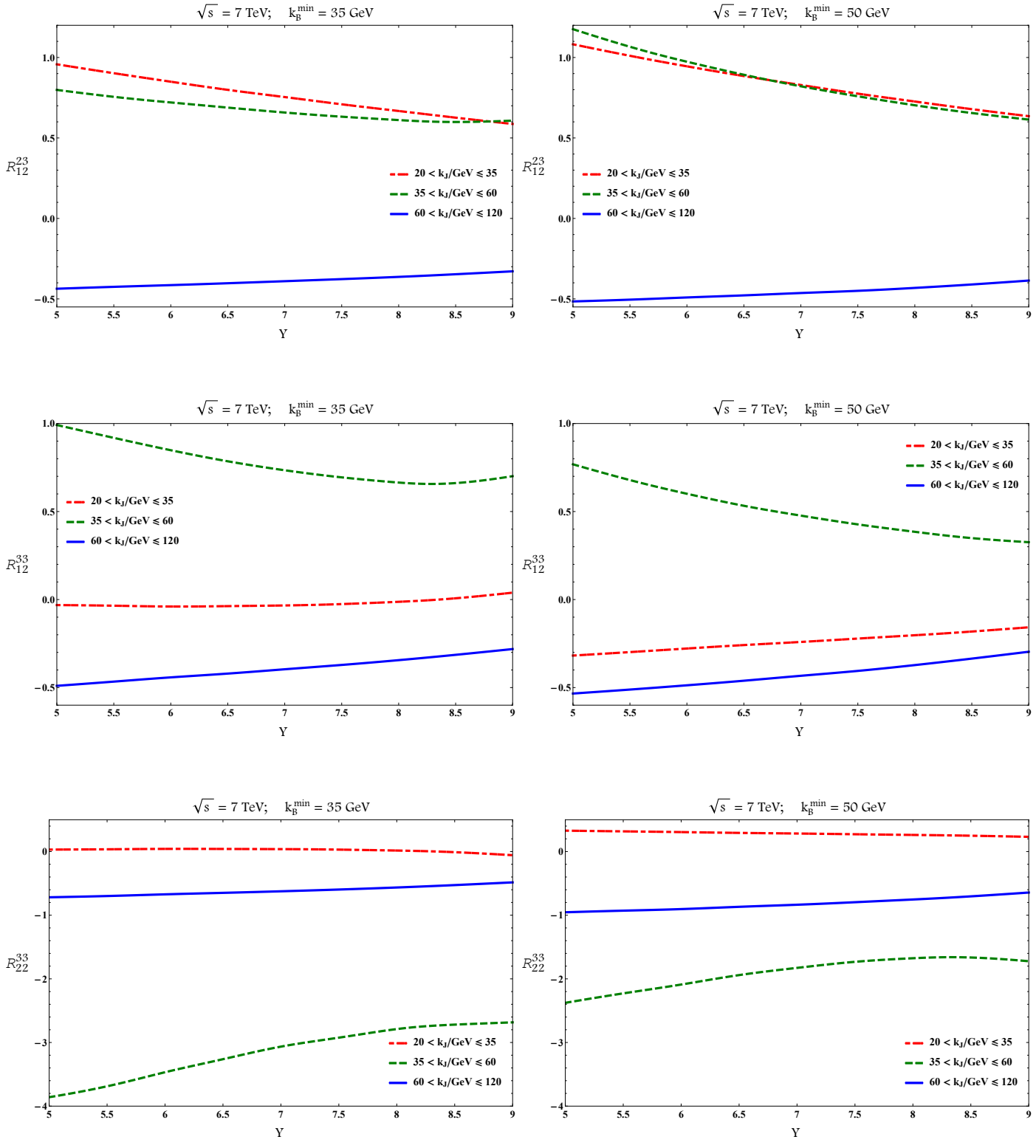

Figure 3.6: Y-dependence of R_{12}^{23}, R_{12}^{33} and R_{22}^{33} for $\sqrt{s} = 7$ TeV and $k_B^{\min} = 35$ GeV (left column) and $k_B^{\min} = 50$ GeV (right column).

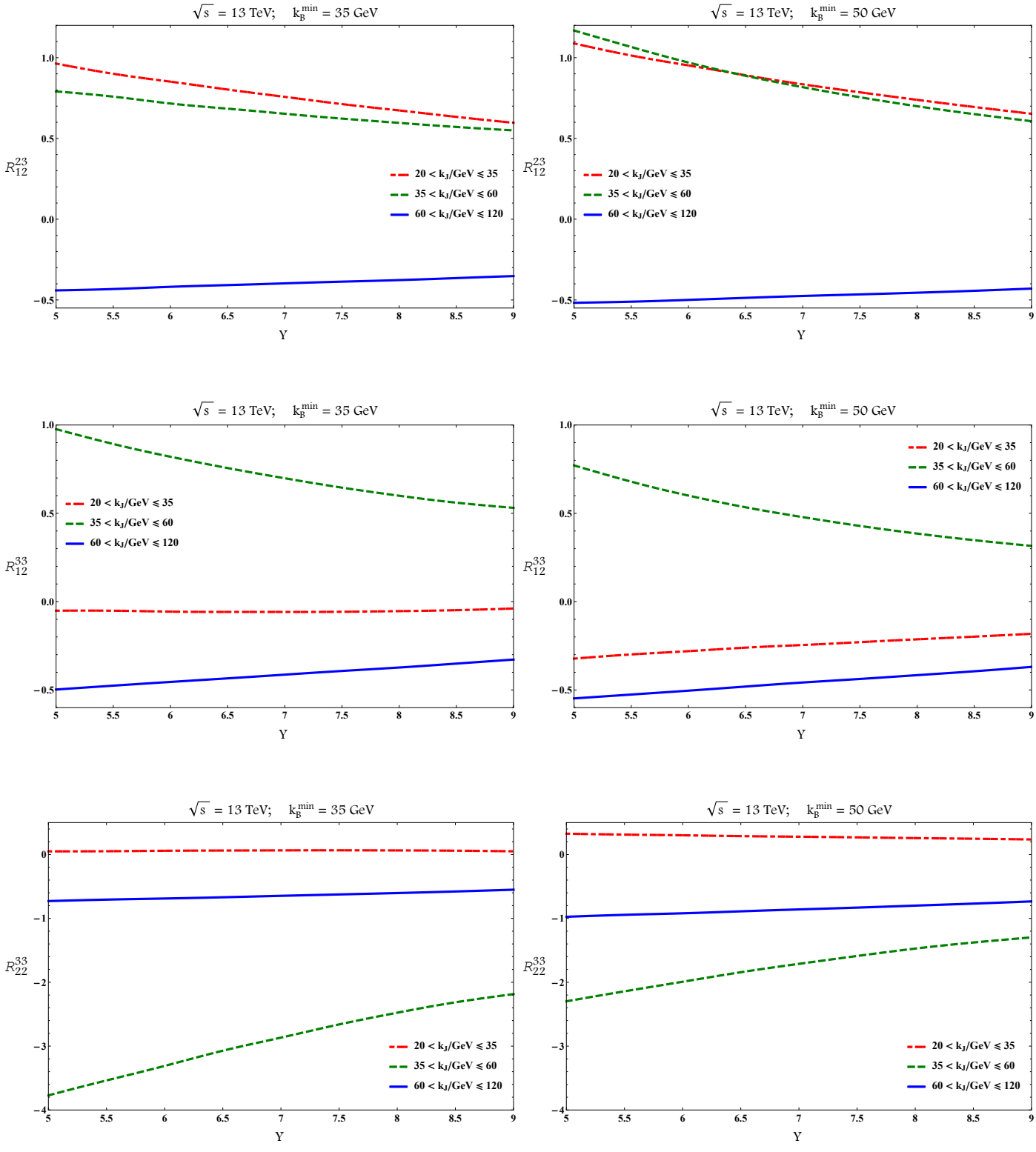

Figure 3.7: Y-dependence of R_{12}^{23}, R_{12}^{33} and R_{22}^{33} for $\sqrt{s} = 13$ TeV and $k_B^{\min} = 35$ GeV (left column) and $k_B^{\min} = 50$ GeV (right column).

3.6 Summary

In this chapter we have presented a first full phenomenological study of inclusive three-jet production at the LHC within the BFKL framework, focussing on the study of azimuthal-angle dependent observables. Following the work done in Ref. [163] where a new family of observables was proposed to probe the window of applicability of BFKL at the LHC, we have studied here a selection of these observables at a hadronic level (with PDFs) at two different colliding energies, $\sqrt{s} = 7, 13$ TeV, and imposing kinematical cuts compatibles with the experimental studies performed so far by CMS in [135, 136]. We have considered a symmetric and an asymmetric kinematic cut with respect to the transverse momentum of the forward (k_A) and backward (k_B) jets. In addition, we have chosen to impose an extra condition on the value of the transverse momentum k_J of the central jet, dividing the allowed region for k_J into three sub-regions: k_J smaller than $k_{A,B}$, k_J similar to $k_{A,B}$ and k_J larger than $k_{A,B}$.

We have shown how our observables R_{22}^{11}, R_{12}^{13}, R_{12}^{22}, R_{12}^{23}, R_{12}^{33} and R_{22}^{33} change when we vary the rapidity difference Y between k_A and k_B from 5 to 9 units. We notice a generally smooth functional dependence of the ratios on Y. These observables do not considerably change when we increase the colliding energy from 7 to 13 TeV which assures us that they capture the essence of what the BFKL dynamics dictates regarding the azimuthal behavior of the hard jets in inclusive three-jet production. It will be very interesting to compare with possible predictions for these observables from fixed order analyses as well as from the BFKL inspired Monte-Carlo `BFKLex` [180–186]. Predictions from general-purpose Monte-Carlos should also be put forward.

Most importantly though, it would be extremely interesting to see an experimental analysis for these observables using the existing and future LHC data. We would like to motivate our experimental colleagues to proceed to such an analysis since we believe it will help address the question of how phenomenologically relevant the BFKL dynamics is at present energies. It would also serve as a very good test of models describing multiple interactions and to gauge how important those effects can be.

CHAPTER 4

THREE-JET PRODUCTION AT NLLA

Previously, in Chapter 3, a new family of observables consisting of azimuthal-angle generalized ratios was proposed in a kinematical setup that resembles the usual Mueller-Navelet jets but with an additional tagged jet in the central region of rapidity. These were obtained after using collinear factorization to produce the two most forward/backward jets and convoluting the partonic differential cross section, which follows the BFKL dynamics, with collinear parton distribution functions included in the forward "jet vertex" [68, 142, 143, 171–174]. In addition, the two Mueller-Navelet jet-vertices were linked with the centrally produced jet via two BFKL gluon Green functions. Finally, we integrated over the momenta of all produced jets, using actual LHC experimental cuts.

Non-tagged minijet activity between the three jets can affect significantly the azimuthal angle orientation of the jets and is accounted for by the introduction of two BFKL gluon Green functions, as was demonstrated in Section 3.1. Here, we calculate the, presumably, most relevant higher order corrections to the observables by now convoluting the three LO jet vertices with two GGFs at NLLA. The corrections appear to be mostly moderate giving us confidence that the recently proposed observables are actually an excellent way to probe the BFKL dynamics at the LHC.

Furthermore, we allow for the jets to take values in different rapidity bins in various configurations such that a comparison between our predictions and the experimental data is simpler..

The main idea behind all this effort is that we need more exclusive final states in order to be able to address a number of theoretical issues, *e.g.* what is the optimal way to

implement the running of the strong coupling or could one speak about saturation effects at present energies, etc.

Despite the fact that the LLA analysis presented in Chapter 3, and published in Ref. [2], may in principle be directly compared to experimental data once these are available, do not resolve three issues:

I. They do not offer any estimate of the theoretical uncertainty that comes into play once higher order corrections are considered.

II. They do not include the running of the coupling constant, therefore they are unable to solve what is the optimal way to set the renormalization scale.

III. Since we restricted the central jet to be produced in the middle of the rapidity interval between the outermost jets, one could possibly raise concerns of whether a experimental analysis following the kinematical setup used in the previous Chapter is possible at all.

Equally important is that the use of NLLA GGFs has already been successful in describing similar type of processes at the LHC, as was shown by the CMS group in Ref. [136].

Here, we address the three of these issues. To that end, regarding issues (I) and (II), one needs to calculate higher order corrections for the ratios at partonic-level. This comprises of two steps: considering NLLA corrections to the BFKL kernel and NLO corrections to the jet vertices. However, although the corrections to the jet vertices may be in general significant, we expect them not to affect much the azimuthal angle characteristics of the jets which are driven mostly by the minijet activity in the rapidity intervals between the jets.[1] Demanding three tagged jets along with central minijets leaves little room for higher order real emission activity near the jet vertices. We expect that the higher order virtual corrections to the vertices may be interpreted as K-factor corrections which would cancel out in our observables since we consider ratios. We have argued in Sec. 3.1 that the minijet activity is accounted for by the introduction of the two gluon Green functions. Large corrections from LLA to NLLA for the gluon Green function, which is actually a usual outcome in many BFKL-based calculations, could potentially have a strong impact on the ratios and this at any rate needs to be assessed. Therefore, in this work we work with NLLA[2] gluon Green functions and LO jet vertices.

[1] This argument is not valid at the boundary of the phase space, when and the inclusion of NLO impact factors have a big impact in imposing energy-momentum conservation.

[2] Note that from now on, we will refer to the results with NLLA gluon Green functions and LO vertices as NLLA results.

The answer to issue (III) is, naturally, positive since allowing for the central jet to live in a rapidity range instead of a single point, as long as this range is located generally in the middle of the rapidity interval between the outermost jets, does not affect the values of the generalized ratios in Eq (4.14), as was shown in [163]. Nevertheless, to avoid any confusion and to have a complete study, in Sec. 4.4 we are also considering cases in which the central jet lives in a rapidity bin of unit width, while the central value of the bin may vary. The calculations show that the observable is robust under this displacement, which suggest that the width of the bin can be enlarged to capture more events in an experimental analysis.

Other potential sources of uncertainty could be due to the particular PDF sets one uses. One can still argue though that the uncertainty due to different PDF sets does not need to be ascertained before one has gauged how large are the full beyond the LLA corrections to the partonic-level ratios, since it will be overshadowed by the latter. Indeed, from first tries we see no significant difference in the results when we work with different PDFs sets and therefore we do not offer any dedicated analysis on that here[3].

In the bulk of the Chapter we present theoretical predictions for the ratios R_{PQ}^{MN} at NLLA and we compare these to the LLA ones. In particular, in Section 4.1 we define the computational framework and our notation for the LLA and NLLA calculations. Building on the results of Chapters 1 and 3. In Section 4.2 we present results for R_{22}^{12}, R_{33}^{12} and R_{33}^{22} as a function of the rapidity distance Y between the outermost jets while the central jet is fixed at the middle of this distance, for both $\sqrt{s} = 7$ and $\sqrt{s} = 13$ TeV colliding energies. In Section 4.3, we present the LLA and NLLA results for R_{22}^{12}, R_{33}^{12} and R_{33}^{22} while the central jet is allowed to take values in the rapidity bin $[-0.5, 0.5]$. The results are plotted again as functions of the rapidity interval Y between the outermost jets for $\sqrt{s} = 7$ and $\sqrt{s} = 13$ TeV. In Section 4.4, we do not keep Y fixed at any certain value, instead, we allow for the forward jet to be in the rapidity interval $[3, 4.7]$, for the backward one to be in the symmetric rapidity interval $[-4.7, -3]$ while the rapidity of the central jet takes again values in a bin of unit 1. The central value of the bin though, may now take five different values, namely, $\{-1, -0.5, 0, 0.5, 1\}$ and we plot both the LLA and NLLA results for R_{22}^{12}, R_{33}^{12} and R_{33}^{22} as a function of that central value, again for $\sqrt{s} = 7$ and $\sqrt{s} = 13$ TeV. We finish Chapter 4 with a Summary of the results in Section 4.5.

[3]For further information regarding this aspect, an analysis of the uncertainty from the use of different PDFs sets was carried out in Ref. [134] for Mueller-Navelet jets, in Ref. [187] for dihadron production, and in Ref. [188] for hadron-jet production. They all confirm that this uncertainty in negligible compared to the numerical integration and renormalization scale uncertainties.

4.1 Hadronic inclusive three-jet production in multi-Regge kinematics

The process under investigation is the same we described in Chapter 3 (see Figs. 3.1 and 3.1). For sake of clarity, we will describe it again. We are working with the production of two forward/backward jets, both characterized by high transverse momenta $k_{A,B}$ and well separated in rapidity. Additionally, there is third jet is tagged in the central rapidity region and with possible associated minijet production driven by the BFKL GGFs.

Taking into account the factors coming from the jet vertices, it is possible to rewrite the projection of the differential cross section on the azimuthal angle differences (that we recycle from Eq. (3.36)) in the form

$$\begin{aligned}
&\int_0^{2\pi} \mathrm{d}\theta_A\, \mathrm{d}\theta_J\, \mathrm{d}\theta_B \cos\left(M\phi_A\right) \cos\left(N\phi_B\right) \times \\
&\quad \times \frac{d\sigma^{3-\mathrm{jet}}}{\mathrm{d}k_A\, \mathrm{d}Y_A\, \mathrm{d}\theta_A\, \mathrm{d}k_J\, \mathrm{d}Y_J\, \mathrm{d}\theta_J\, \mathrm{d}k_B\, \mathrm{d}Y_B\, \mathrm{d}\theta_B} = \\
&= \frac{8\pi^4 C_F \bar{\alpha}_s^3}{N_C^3} \frac{x_{J_A} x_{J_B}}{k_A k_J k_B} f^\star\left(x_{J_A}, \mu_F\right) f^\star\left(x_{J_B}, \mu_F\right) \times \\
&\quad \times (-1)^{M+N} \int_0^\infty \mathrm{d}p^2 \int_0^{2\pi} \mathrm{d}\theta \cos(M\theta) \frac{\mathrm{Re}\left[\left(pe^{i\theta} + k_J\right)^N\right]}{\sqrt{\left(p^2 + k_J^2 + 2pk_J\cos\theta\right)^N}} \times \\
&\quad \times \varphi_M\left(k_A^2, p^2, Y_A - y_J\right) \varphi_N\left(p^2 + k_J^2 + 2pk_J\cos\theta, k_B^2, y_J - Y_B\right),
\end{aligned} \tag{4.1}$$

In this expression the gluon Green function φ is either at LLA ($\varphi^{(LLA)}$) or at NLLA ($\varphi^{(NLLA)}$) accuracy. In particular, at LLA we have

$$\varphi_n^{(LLA)}\left(k^2, q^2, Y\right) = \frac{2}{\pi k q} \int_0^\infty d\nu \cos\left(\nu \ln \frac{k^2}{q^2}\right) e^{\bar{\alpha}_s \chi_0(n,\nu)(Y - Y_0)}, \tag{4.2}$$

while the LLA BFKL kernel $\chi_n(\nu)$ reads

$$\chi_0(n,\nu) = 2\psi(1) - \psi\left(\frac{1+n}{2} + i\nu\right) - \psi\left(\frac{1+n}{2} - i\nu\right) = 2\mathrm{Re}\left[\psi(1) - \psi\left(\frac{1+n}{2} + i\nu\right)\right] \tag{4.3}$$

and ψ is the logarithmic derivative of Euler's gamma function.

In order to treat the NLLA case, we have already developed all the machinery in Sec. 1.4.2. Using Dirac's notation, the GGF is given by

$$\varphi^{(NLLA)}\left(\vec{k}_A, \vec{k}_B, Y\right) = \int \frac{\mathrm{d}\omega}{2\pi i} e^{\omega(Y - Y_0)} \left\langle \vec{k}_A \middle| \varphi_\omega^{(NLLA)} \middle| \vec{k}_B \right\rangle, \tag{4.4}$$

inserting the basis of NLO eigenfunctions and using that $\varphi_\omega = \frac{\mathbb{1}}{\omega\mathbb{1}-\mathcal{K}^{(NLLA)}}$ we get

$$\begin{aligned}\varphi^{(NLLA)}\left(\vec{k}_A,\vec{k}_B,Y\right) &= \sum_n \int \mathrm{d}\nu\, e^{\chi(n,\nu)(Y-Y_0)} \left\langle \vec{k}_A \middle| H_{n,\nu}\right\rangle \left\langle H_{n,\nu}\middle| \vec{k}_B\right\rangle = \\ &= \frac{2}{k_A k_B}\sum_n \frac{e^{in(\theta_A-\theta_B)}}{2\pi}\int_{-\infty}^{\infty}\frac{\mathrm{d}\nu}{2\pi}\cos\left(\nu\log\frac{k_A^2}{k_B^2}\right)e^{\tilde{\chi}(n,\nu)(Y-Y_0)},\end{aligned} \tag{4.5}$$

where final kernel associated with the NLLA GGF is given by Eq. (1.160). For the sake of clarity, we will repeat it here

$$\tilde{\chi}(n,\nu) \equiv \bar{\alpha}_s\chi_0(n,\nu)\left(1-\bar{\alpha}_s\beta_2\log\frac{k_A k_B}{\mu_R^2}\right)+\bar{\alpha}_s^2\chi_1(n,\nu). \tag{4.6}$$

Taking everything into account, the n-th component of the GGF at NLLA is given by

$$\varphi_n^{(NLLA)}(k_A,k_B,Y) = \frac{2}{\pi k_A k_B}\int_0^\infty \mathrm{d}\nu\cos\left(\nu\log\frac{k_A^2}{k_B^2}\right)e^{\tilde{\chi}(n,\nu)(Y-Y_0)}. \tag{4.7}$$

In order to make an appropriate choice of the renormalization scale μ_R, we used the Brodsky-Lepage-Mackenzie (BLM) prescription [153] which is proven a very successful choice for fitting the data in Mueller-Navelet studies [130, 131]. However, the BLM procedure is more conveniently applied in a physical renormalization scheme. So, following Refs. [130, 131], we first perform the transition from the $\overline{\text{MS}}$ scheme to the MOM scheme, as described in Ref. [41] this is done through the following substitution

$$\bar{\alpha}_s^{\left(\overline{\text{MS}}\right)}\left(\mu_R\right) = \bar{\alpha}_s^{(\text{MOM})}\left(\mu_R\right)\left(1+\bar{\alpha}_s^{(\text{MOM})}\left(\mu_R\right)\frac{T}{N_C}\right) \tag{4.8}$$

where

$$\begin{aligned} T &= T^\beta + T^{\text{conf}}, \\ T^\beta &= -2N_C\beta_2\left(1+\frac{2}{3}I\right), \\ T^{conf} &= \frac{C_A}{8}\left[\frac{17}{2}I+\frac{3}{2}(I-1)\xi+\left(1-\frac{1}{3}I\right)\xi^2-\frac{1}{6}\xi^3\right]. \end{aligned}$$

Here $I = -2\int_0^1 dx\frac{\ln(x)}{x^2-x+1} \simeq 2.3439$ and ξ is a gauge parameter, fixed at zero.

The change to the MOM scheme affects to the kernel in Eq. (4.6) transforming it into

$$\tilde{\chi}(n,\nu)\xrightarrow{\text{MOM}}\tilde{\chi}(n,\nu) = \bar{\alpha}_s\chi_0(n,\nu)\left(1+\bar{\alpha}_s\beta_2\log\frac{\mu_R^2}{k_A k_B}+\bar{\alpha}_s\frac{T}{N_C}\right)+\bar{\alpha}_s^2\chi_1(n,\nu). \tag{4.9}$$

Applying the BLM prescription implies choosing the scale μ_R such that the β_2-dependence of a given observable vanishes. Imposing that the NLLA GGF is β_2-independent leads to the renormalization scale μ_R to be fixed at the value

$$(\mu_R^{\text{BLM}})^2 = k_A k_B\ \exp\left[\frac{1+4I}{3}+\frac{1}{2}\chi_0(n,\nu)\right]. \tag{4.10}$$

In our numerical analysis we consider two cases. In one, we set $\mu_R = \mu_R^{\rm BLM}$ only in the exponential factor of the gluon Green function φ_n, while we let the argument of the $\bar{\alpha}_s^3$ in Eq. (4.1) to be at the 'natural' scale $\sqrt{k_A k_B}$, that is, $\bar{\alpha}_s^3(\sqrt{k_A k_B})$. In the second case, we fix $\mu_R = \mu_R^{\rm BLM}$ everywhere in Eq. (4.1). These two cases lead in general to two different but similar values for our NLLA predictions and wherever we present plots we fill the space in between so that we end up having a band instead of a single curve for the NLLA observables. The band represents the uncertainty that comes into play after using the BLM prescription since there is no unambiguous way to apply it.

The experimental observables we initially proposed are based on the partonic-level average values (with M,N being positive integers)

$$\begin{aligned} \mathscr{C}_{MN} &= \langle \cos(M(\theta_A - \theta_J - \pi)) \cos(N(\theta_J - \theta_B - \pi)) \rangle = \\ &= \frac{\int_0^{2\pi} d\theta_A d\theta_B d\theta_J \cos(M(\theta_A - \theta_J - \pi)) \cos(N(\theta_J - \theta_B - \pi)) d\sigma^{3-\rm jet}}{\int_0^{2\pi} d\theta_A d\theta_B d\theta_J d\sigma^{3-\rm jet}}. \end{aligned} \tag{4.11}$$

whereas, in order to provide testable predictions for the current and future experimental data, we will introduce the hadronic-level values C_{MN} after generalizing $\mathscr{C}_{M,N}$ integrating also over the momenta of the tagged jets, as we will see in the following sections.

From a more theoretical perspective, it is important to have as good as possible perturbative stability in our predictions (see [121] for a related discussion). This can be achieved by removing the contribution stemming from the zero conformal spin, which corresponds to the index $n = 0$ in Eqs. (4.2) and (4.7).

We improve the observables we computed in the previous section, the generalized azimuthal correlation ratios, going to NLLA. As we stated previously, these observables are characterized by being rather insensitive to possible higher order corrections and their BFKL description will differ from other formalisms. They are defined as

$$R_{PQ}^{MN} = \frac{C_{MN}}{C_{PQ}}. \tag{4.12}$$

The C_{MN} coefficients are merely the following correlations among azimuthal angle differences

$$C_{MN} \equiv \langle \cos\left(M\phi_A\right) \cos\left(N\phi_B\right) \rangle_{\rm PS} = \frac{\int \mathscr{D}{\rm PS}\, \cos\left(M\phi_A\right) \cos\left(N\phi_B\right) d\sigma^{3-\rm jet}}{\int \mathscr{D}{\rm PS}\, d\sigma^{3-\rm jet}}, \tag{4.13}$$

where we defined the azimuthal angle differences as $\phi_A = \theta_A - \theta_J - \pi$ and $\phi_B = \theta_J - \theta_B - \pi$ (see Fig. 3.2). The integration measure $\int \mathscr{D}{\rm PS}$ will be different in each one of the Sections of this Chapter.

We, therefore, introduce the ratios

$$R_{PQ}^{MN} = \frac{C_{MN}}{C_{PQ}} \tag{4.14}$$

which are free from any $n = 0$ dependence, as long as $M,N,P,Q > 0$. The postulate that Eq. (4.14) generally describes observables with good perturbative stability is under scrutiny in Sections 4.2, 4.3 and 4.4 where we compare LLA and NLLA results.

Before we proceed to our numerical results in the next sections, we should give a few details with regard to our numerical computations. From all the possible ratios, we have chosen to study the following three: R_{22}^{12}, R_{33}^{12} and R_{33}^{22}. These are enough to have an adequate view of how the generic R_{PQ}^{MN} behaves. We computed R_{22}^{12}, R_{33}^{12} and R_{33}^{22} in all cases almost exclusively in FORTRAN whereas MATHEMATICA was used mainly for cross-checks. We set the scale s_0 such that $Y_0 = 0$. The NLO MSTW 2008 PDF sets [161] were used and for the strong coupling α_s we chose a two-loop running coupling setup with $\alpha_s(M_Z) = 0.11707$ and five quark flavours. We made extensive use of the integration routine `Vegas` [175] as implemented in the `Cuba` library [176, 177]. Furthermore, we used the `Quadpack` library [178] and a slightly modified version of the `Psi` [179] routine.

4.2 R_{22}^{12}, R_{33}^{12} and R_{33}^{22} with the central jet fixed in rapidity

In this section, we will present results for three generalized ratios, R_{22}^{12}, R_{33}^{12} and R_{33}^{22}, assuming that the central jet is fixed in rapidity at $y_J = (Y_A + Y_B)/2$ (see Fig. 4.1).

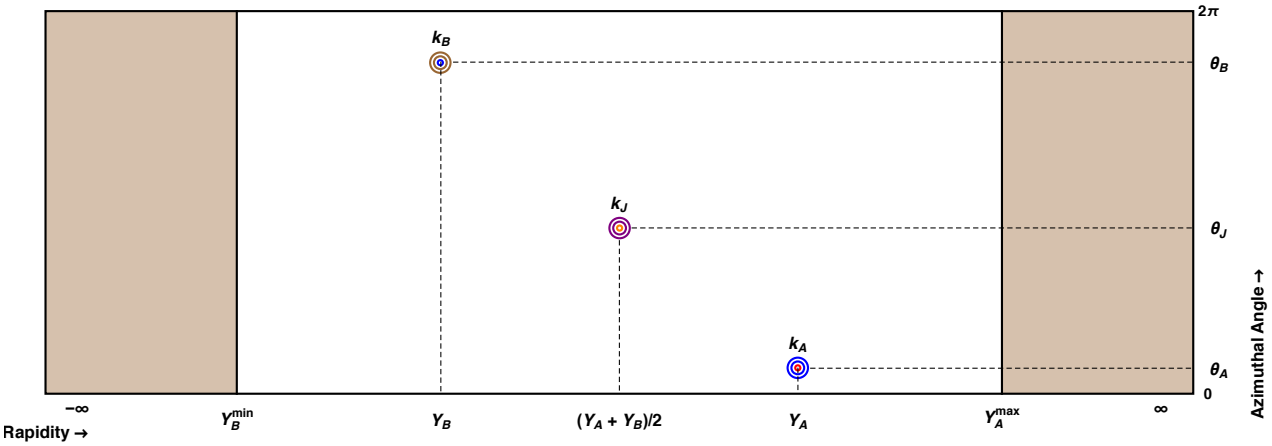

Figure 4.1: A primitive lego plot depicting a three-jet event. k_A is a forward jet with large positive rapidity Y_A and azimuthal angle θ_A, k_B is a forward jet with large negative rapidity Y_B and azimuthal angle θ_B and k_J is a central jet with rapidity y_J and azimuthal angle θ_J. The fade-brown areas to the left and right highlight the regions in rapidity that are not covered by the standard detectors.

In particular,

$$C_{MN} \equiv \frac{\int \mathscr{D}\mathrm{PS}\, \cos\left(M\phi_A\right)\cos\left(N\phi_B\right) d\sigma^{3-\mathrm{jet}}}{\int \mathscr{D}\mathrm{PS}\, d\sigma^{3-\mathrm{jet}}}, \tag{4.15}$$

where the integration measure is defined as

$$\begin{aligned}\int \mathscr{D}\mathrm{PS} \equiv \int_{Y_A^{\min}}^{Y_A^{\max}} \mathrm{d}Y_A \int_{Y_B^{\min}}^{Y_B^{\max}} \mathrm{d}Y_B \int_{k_A^{\min}}^{k_A^{\max}} \mathrm{d}k_A \int_{k_B^{\min}}^{k_B^{\max}} \mathrm{d}k_B \int_{k_J^{\min}}^{k_J^{\max}} \mathrm{d}k_J \times \\ \times \delta(Y_A - Y_B - Y) \int_0^{2\pi} \mathrm{d}\theta_A \int_0^{2\pi} \mathrm{d}\theta_B \int_0^{2\pi} \mathrm{d}\theta_J\,.\end{aligned} \tag{4.16}$$

In this case there are slight differences compared to the phase space in Eq. (3.41). The forward jet rapidity is taken in the range delimited by $0 < Y_A < 4.7$, the backward jet rapidity in the range $-4.7 < Y_B < 0$, while their difference $Y \equiv Y_A - Y_B$ is kept fixed at definite values in the range $5.5 < Y < 9$.

We can now study the ratios $R_{PQ}^{MN}(Y)$ in Eq. (4.14) as functions of the rapidity difference Y between the most forward and the most backward jets for a set of characteristic values

of M,N,P,Q and for two different center-of-mass energies: $\sqrt{s}=7$ and $\sqrt{s}=13$ TeV. Since we are integrating over k_A and k_B, we have the opportunity to impose either symmetric or asymmetric kinematic cuts, as it has been previously done in Mueller-Navelet studies. Here, and for the rest of the paper, we choose to study the asymmetric cut which presents certain advantages over the symmetric one (see Refs. [125, 133]). To be more precise, we set $k_A^{\min}=35$ GeV, $k_B^{\min}=50$ GeV, $k_A^{\max}=k_B^{\max}=60$ GeV throughout the paper.

In order to be as close as possible to the characteristic rapidity ordering of the multi-Regge kinematics, we set the value of the central jet rapidity such that it is equidistant to Y_A and Y_B by imposing the condition $y_J=(Y_A+Y_B)/2$. Moreover, since the tagging of a central jet permits us to extract more exclusive information from our observables, we allow three possibilities for the transverse momentum k_J, that is, $20\,\text{GeV}<k_J<35\,\text{GeV}$ (bin-1), $35\,\text{GeV}<k_J<60\,\text{GeV}$ (bin-2) and $60\,\text{GeV}<k_J<120\,\text{GeV}$ (bin-3). Keeping in mind that the forward/backward jets have transverse momenta in the range $[35\,\text{GeV},60\,\text{GeV}]$, restricting the value of k_J within these three bins allows us to see how the ratio $R_{PQ}^{MN}(Y)$ changes its behaviour depending on the relative size of the central jet momentum when compared to the forward/backward ones. Throughout the paper, we will keep the same setup regarding bin-1, bin-2 and bin-3 which roughly correspond to the cases of k_J being 'smaller' than, 'similar' to and 'larger' than k_A, k_B, respectively.

Finally, apart from the functional dependence of the ratios on Y we will also show the relative corrections when we go from LLA to NLLA. To be more precise, we define

$$\delta x(\%)=\left(\text{res}^{\text{LLA}}-\frac{\text{res}^{\text{(BLM-1)}}+\text{res}^{\text{(BLM-2)}}}{2}\right)\frac{1}{\text{res}^{\text{LLA}}}\,. \tag{4.17}$$

$\text{res}^{\text{BLM-1}}$ is the BLM NLLA result for $\mu_R=\mu_R^{\text{BLM}}$ only in the gluon Green function while the cubed term of the strong coupling in Eq. (4.1) actually reads $\bar{\alpha}_s^3=\bar{\alpha}_s^3(\sqrt{k_A k_B})$. $\text{res}^{\text{(BLM-2)}}$ is the BLM NLLA result for $\mu_R=\mu_R^{\text{BLM}}$ everywhere in Eq. (4.1), therefore, $\bar{\alpha}_s^3=\bar{\alpha}_s^3(\mu_R^{\text{BLM}})$, as was previously discussed in Section 2.

In the following, we present our results for R_{22}^{12}, R_{33}^{12} and R_{33}^{22}, with $y_J=(Y_A+Y_B)/2$, collectively in Fig. 4.2 ($\sqrt{s}=7$ TeV) and Fig. 4.3 ($\sqrt{s}=13$ TeV), In the left column we are showing plots for $R_{PQ}^{MN}(Y)$ whereas to the right we are showing the corresponding $\delta x(\%)$ between LLA and NLLA corrections. The LLA results are represented with dashed lines whereas the NLLA ones with a continuous band. The boundaries of the band are the two different curves we obtain by the two different approaches in applying the BLM prescription. Since there is no definite way to choose one in favour of the other, we allow for any possible value in between and hence we end up with a band. In many cases, as we will see in the following, the two boundaries are so close that the band almost degenerates into a single curve. The red curve (band) corresponds to k_J bounded in bin-1, the green curve

(band) to k_J bounded in bin-2 and finally the blue curve (band) to k_J bounded in bin-3. For the $\delta x(\%)$ plots we only have three curves, one for each of the three different bins of k_J.

A first observation from inspecting Figs. 4.2 and 4.3 is that the dependence of the different observables on the rapidity difference between k_A and k_B is rather smooth. R_{22}^{12} (top row in Figs. 4.2 and 4.3) at $\sqrt{s} = 7$ TeV and for k_J in bin-1 and bin-3 exhibits an almost linear behaviour with Y both at LLA and NLLA, whereas at $\sqrt{s} = 13$ TeV the linear behaviour is extended also for k_J in bin-2. The difference between the NLLA BLM-1 and BLM-2 values is small, to the point that the blue and the red bands collapse into a single line which in addition lies very close to the LLA results. When k_J is restricted in bin-2 (green curve/band), the uncertainty from applying the BLM prescription in two different ways seems to be larger. The relative NLLA corrections at both colliding energies are very modest ranging from close to 1% for k_J in bin-3 to less than 10% for k_J in the other two bins.

R_{33}^{12} (middle row in Figs. 4.2 and 4.3) compared to R_{22}^{12}, shows a larger difference between BLM-1 and BLM-2 values for k_J in bin-1 and bin-2. The 'green' corrections lower the LLA estimate whereas the 'red' ones make the corresponding LLA estimate less negative. The corrections are generally below 20%, in particular, 'blue' $\sim 5\%$, 'red' $\sim 10\%$ and 'green' $\sim 20\%$.

Finally, R_{33}^{22} (bottom row in Figs. 4.2 and 4.3) also shows a larger difference between BLM-1 and BLM-2 values for k_J in bin-1 and less so for k_J in bin-2. Here, the 'red' corrections lower the LLA estimate whereas the 'green' ones make the corresponding LLA estimate less negative. The corrections are smaller than the ones for R_{33}^{12} and somehow larger than the corrections for R_{22}^{12}, specifically, 'blue' $\sim 5\%$, 'red' $\sim 5\%$ and 'green' $\sim 15\%$. Noticeably, while for R_{22}^{12} and R_{33}^{12} the corrections are very similar at $\sqrt{s} = 7$ and $\sqrt{s} = 13$ TeV, the 'green' R_{33}^{22} receives larger corrections at $\sqrt{s} = 7$ TeV.

One important conclusion we would like to draw after comparing Figs. 4.2 and 4.3 is that, in general, for most of the observables there are no striking changes when we increase the colliding energy from 7 to 13 TeV. This indicates that a sort of asymptotic regime has been approached for the kinematical configurations included in our analysis. It also tells us that our observables are really as insensitive as possible to effects which have their origin outside the BFKL dynamics and which normally cannot be isolated (*e.g.* influence from the PDFs) with a possible exclusion at the higher end of the plots, when $Y \sim 8.5 - 9$. There, some of the observables and by that we mean the 'red', 'green' or 'blue' cases of R_{22}^{12}, R_{33}^{12} and R_{33}^{22}, exhibit a more curved rather than linear behaviour with Y at $\sqrt{s} = 7$ TeV.

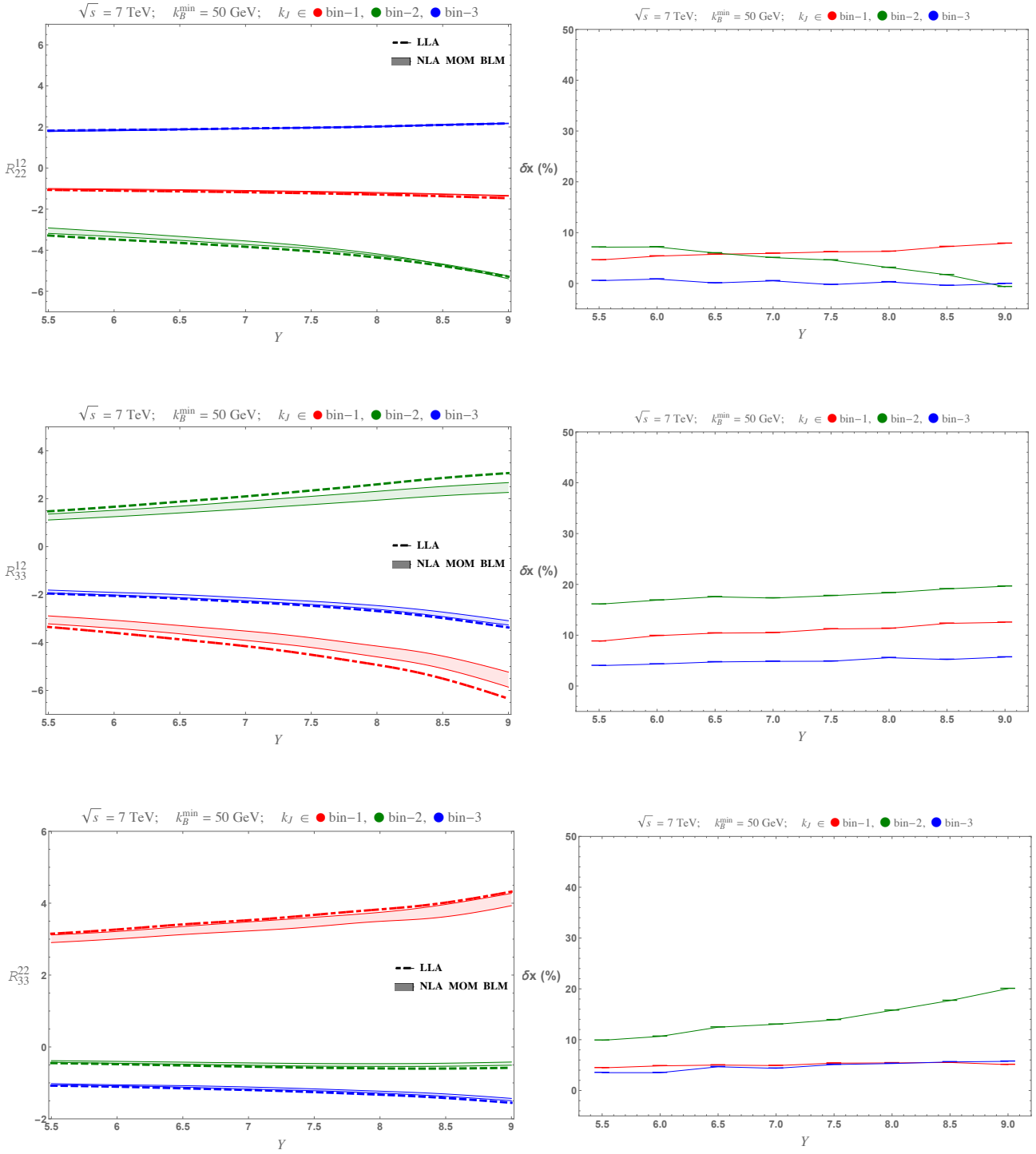

Figure 4.2: Y-dependence of the LLA and NLLA R_{22}^{12}, R_{33}^{12} and R_{33}^{22} at $\sqrt{s} = 7$ TeV with y_J fixed (left) and the relative NLLA to LLA corrections (right).

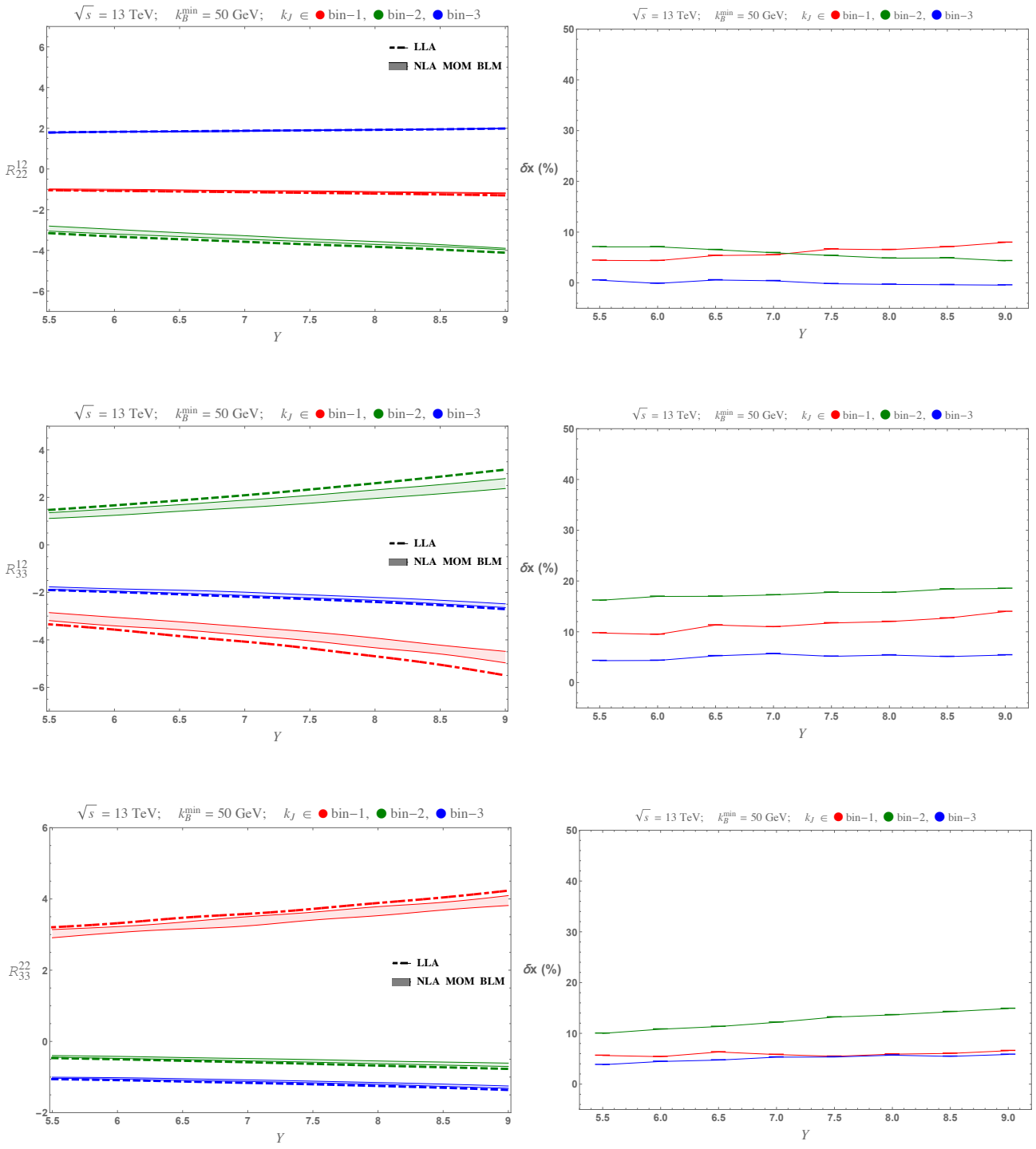

Figure 4.3: Y-dependence of the LLA and NLLA R_{22}^{12}, R_{33}^{12} and R_{33}^{22} at $\sqrt{s} = 13$ TeV with y_J fixed (left) and the relative NLLA to LLA corrections (right).

4.3 R_{22}^{12}, R_{33}^{12} and R_{33}^{22} after integration over a central jet rapidity bin

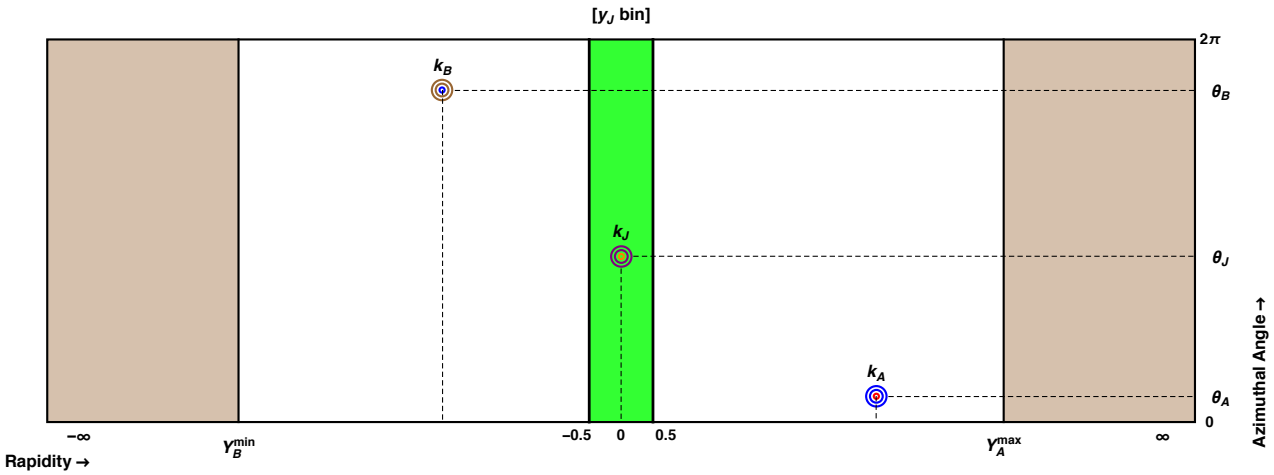

Figure 4.4: A primitive lego plot depicting a three-jet event similar to Fig. 4.4. Here, however, the central jet can take any value in the rapidity range $-0.5 < y_J < 0.5$.

In this section, everything is kept the same as in Section 3 with the exemption of the allowed values for y_J (see Fig. 4.4). While in the previous section $y_J = (Y_A + Y_B)/2$, here y_J is not anymore dependent on the rapidity difference between the outermost jets, Y, and is allowed to take values in a rapidity bin around $y_J = 0$. In particular, $-0.5 < y_J < 0.5$, which in turn means that an additional integration over y_J needs to be considered in Eq. (4.13) with $y_J^{\min} = -0.5$ and $y_J^{\max} = 0.5$:

$$C_{MN}^{\text{integ}} = \\ = \int_{y_J^{\min}}^{y_J^{\max}} dy_J \int_{Y_A^{\min}}^{Y_A^{\max}} dY_A \int_{Y_B^{\min}}^{Y_B^{\max}} dY_B \int_{k_A^{\min}}^{k_A^{\max}} dk_A \int_{k_B^{\min}}^{k_B^{\max}} dk_B \int_{k_J^{\min}}^{k_J^{\max}} dk_J \delta(Y_A - Y_B - Y) \mathscr{C}_{MN}, \tag{4.18}$$

With a slight abuse of notation, we will keep denoting our observables R_{PQ}^{MN}:

$$R_{PQ}^{MN} = \frac{C_{MN}^{\text{integ}}}{C_{PQ}^{\text{integ}}}. \tag{4.19}$$

Therefore, in Figs. 4.5 and 4.6 we still have R_{22}^{12}, R_{33}^{12} and R_{33}^{22} although here they do contain the extra integration over y_J.

We notice immediately that Fig. 4.2 is very similar to the integrated over y_J observables in Fig. 4.5 and the same holds for Figs. 4.3 and 4.6. Therefore, we will not discuss here the

individual behaviours of R_{22}^{12}, R_{33}^{12} and R_{33}^{22} with Y, neither the $\delta x(\%)$ corrections, since this would only mean to repeat the discussion of the previous section. We would like only to note that the striking similarity between Fig. 4.2 and Fig. 4.5 and between Fig. 4.3 and Fig. 4.6 was to be expected if we remember that the partonic-level quantities $\mathscr{R}_{PQ}^{MN}$ do not change noticeably if we vary the position in rapidity of the central jet, as long as the position remains “sufficiently" central (see Ref. [163]). This property is very important and we will discuss it more in the next section. Here, we should stress that the observables as presented in this section can be readily compared to experimental data.

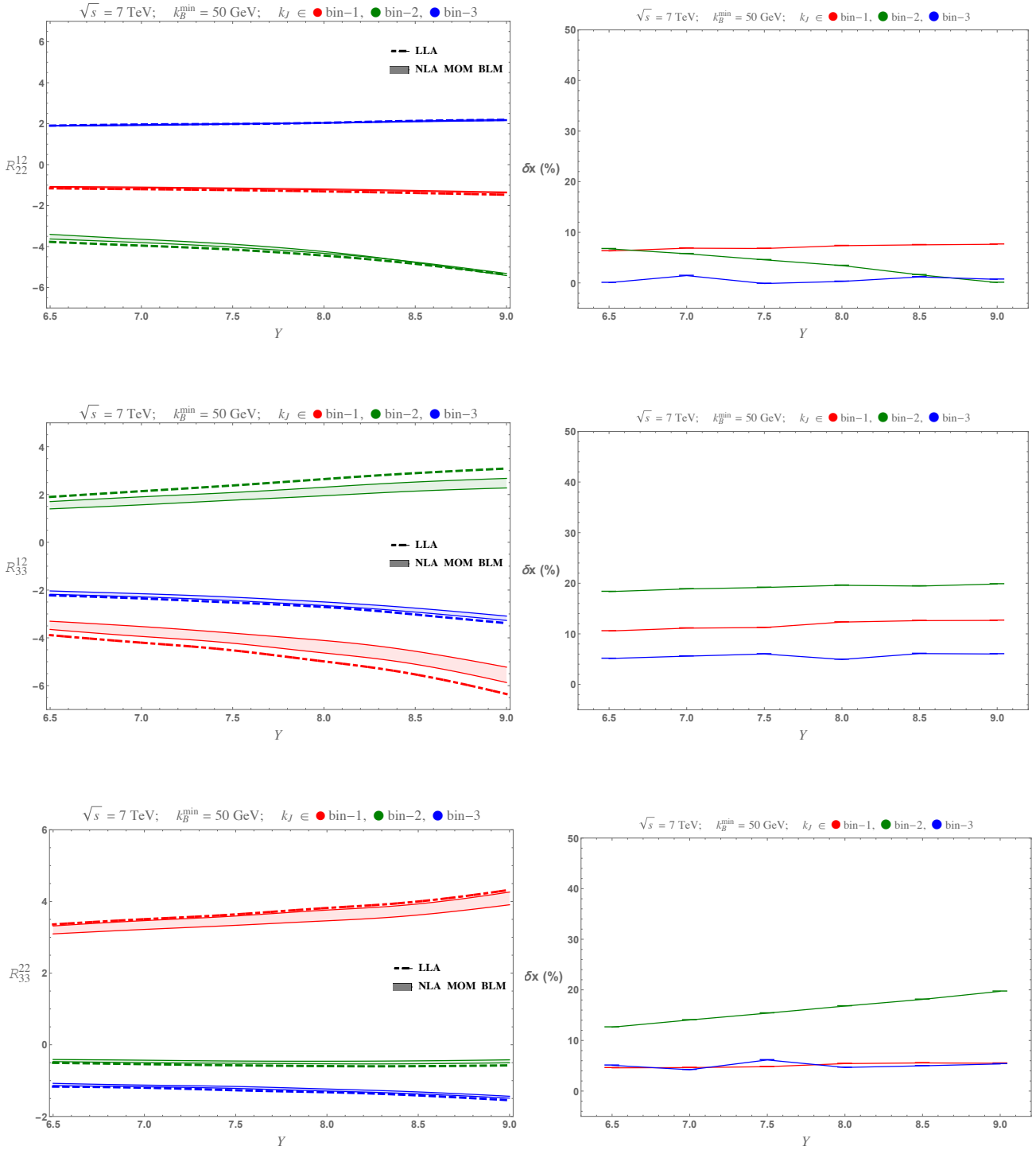

Figure 4.5: Y-dependence of the LLA and NLLA R_{22}^{12}, R_{33}^{12} and R_{33}^{22} at $\sqrt{s} = 7$ TeV with y_J integrated over a central rapidity bin (left) and the relative NLLA to LLA corrections (right).

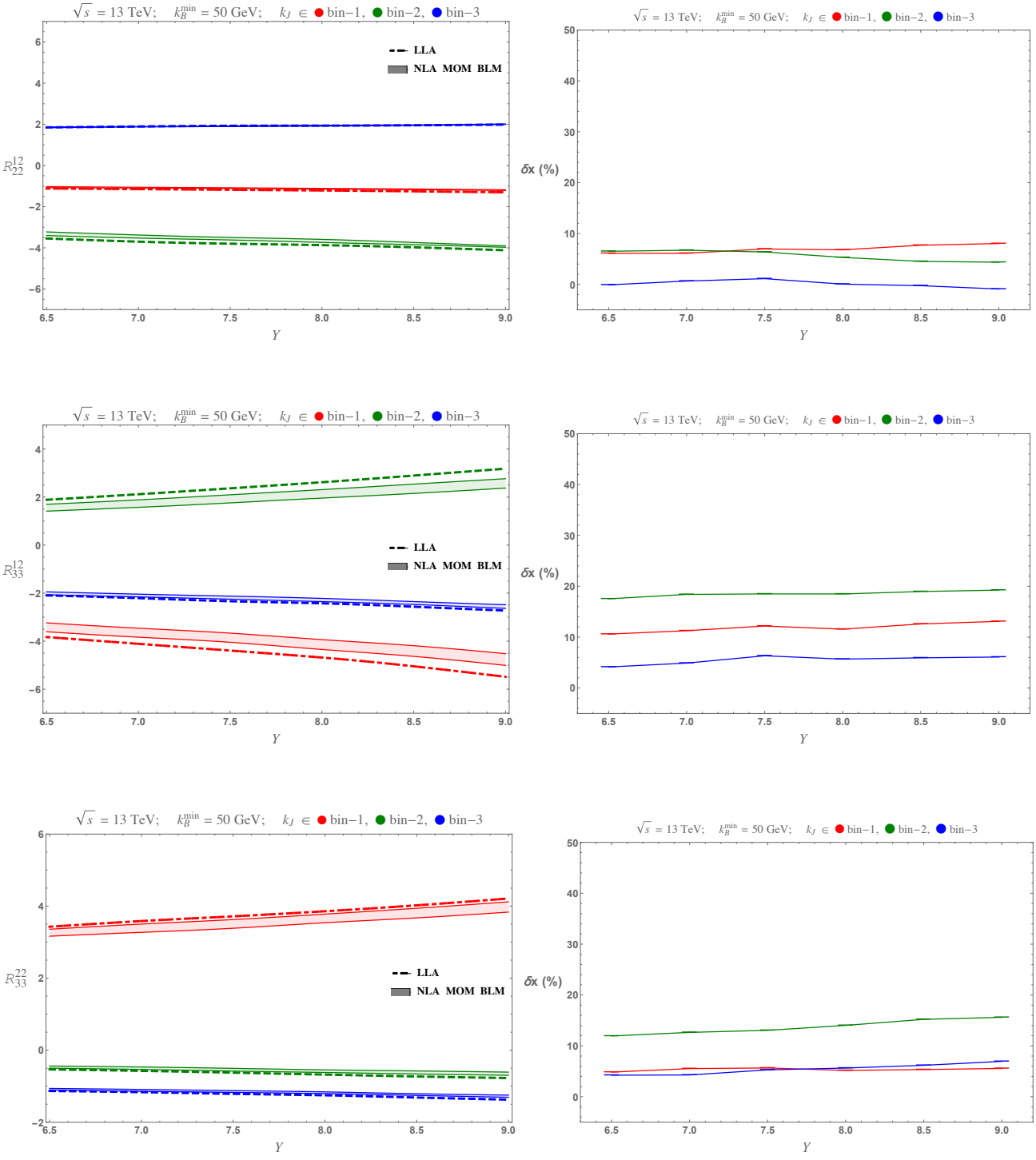

Figure 4.6: Y-dependence of the LLA and NLLA R_{22}^{12}, R_{33}^{12} and R_{33}^{22} at $\sqrt{s} = 13$ TeV with y_J integrated over a central rapidity bin (left) and the relative NLLA to LLA corrections (right).

4.4 R_{22}^{12}, R_{33}^{12} and R_{33}^{22} after integration over a forward, backward and central rapidity bin

In this section, we present an alternative kinematical configuration (see Fig. 4.7) for the generalized ratios R_{PQ}^{MN}. We do this for two reasons. Firstly, to offer a different setup for which the comparison between theoretical predictions and experimental data might be easier, compared to the previous section. Secondly, to demonstrate that the generalized ratios do capture the Bethe-Salpeter characteristics of the BFKL radiation. The latter needs a detailed explanation.

Let us assume that we have a gluonic ladder exchanged in the t-channel between a forward jet (at rapidity Y_A) and a backward jet (at rapidity Y_B) accounting for minijet activity between the two jets. By gluonic ladder here we mean the gluon Green function $\varphi(\vec{p}_A,\vec{p}_B,Y_A-Y_B)$, where $\vec{p}_A$ and $\vec{p}_B$ are the reggeized momenta connected to the forward and backward jet vertex respectively. The following relation for the gluon Green function, that we demonstrate in Appendix B, holds:

$$\varphi(\vec{p}_A,\vec{p}_B,Y_A-Y_B) = \int d^2\vec{k}\,\varphi\left(\vec{p}_A,\vec{k},Y_A-y\right)\varphi\left(\vec{k},\vec{p}_B,y-Y_B\right). \tag{4.20}$$

In other words, one may 'cut' the gluonic ladder at any rapidity y between Y_A and Y_B and then integrate over the reggeized momentum $\vec{k}$ that flows in the t-channel, to recover the initial ladder. Which value of y one chooses to 'cut' the ladder at is irrelevant. Therefore, observables directly connected to a realisation of the r.h.s of Eq. (4.20) should display this y-independence.

In our study actually, we have a very similar picture as the one described in the r.h.s of Eq. (4.20). The additional element is that we do not only 'cut' the gluonic ladder but we also 'insert' a jet vertex for the central jet. This means that the y-independence we discussed above should be present in one form or another. To be precise, we do see the y-independence behaviour but now we have to consider the additional constraint that y cannot take any extreme values, that is, it cannot be close to Y_A or Y_B. For a more detailed discussion of Eq. (4.20), we refer the reader to Appendix B, here we will proceed to present our numerical results.

The kinematic setup now is different than in the previous sections. We allow Y_A and Y_B to take values such that $(Y_A^{\min}=3)<Y_A<(Y_A^{\max}=4.7)$ and $(Y_B^{\min}=-4.7)<Y_B<(Y_B^{\max}=-3)$. Moreover, we allow for the rapidity of the central jet to take values in five distinct rapidity bins of unit width, that is, $y_i-0.5<y_J<y_i+0.5$, with $y_i=\{-1,-0.5,0,0.5,1\}$ and

we define the coefficients $C_{MN}^{\text{integ}}(y_i)$ as function of y_i:

$$C_{MN}^{\text{integ}}(y_i) = \\ = \int_{y_i-0.5}^{y_i+0.5} dy_J \int_{Y_A^{\min}}^{Y_A^{\max}} dY_A \int_{Y_B^{\min}}^{Y_B^{\max}} dY_B \int_{k_A^{\min}}^{k_A^{\max}} dk_A \int_{k_B^{\min}}^{k_B^{\max}} dk_B \int_{k_J^{\min}}^{k_J^{\max}} dk_J \, \mathscr{C}_{MN}. \tag{4.21}$$

Again, keeping our notation with regard to the ratios uniform, we continue denoting our observables by R_{PQ}^{MN} but now the ratios are functions of y_i instead of Y:

$$R_{PQ}^{MN}(y_i) = \frac{C_{MN}^{\text{integ}}(y_i)}{C_{PQ}^{\text{integ}}(y_i)}. \tag{4.22}$$

We present our results in Figs. 4.8 and 4.9. We see that indeed, the y_i-dependence of the three ratios is very weak. Moreover, the similarity between the $\sqrt{s} = 7$ TeV and $\sqrt{s} = 13$ TeV plots is more striking that in the previous sections. The relative NLLA to LLA corrections seem to be slightly larger here than in the previous sections. We would like to stress once more that the results in this section are readily comparable to the experimental data once the same cuts are applied in the experimental analysis.

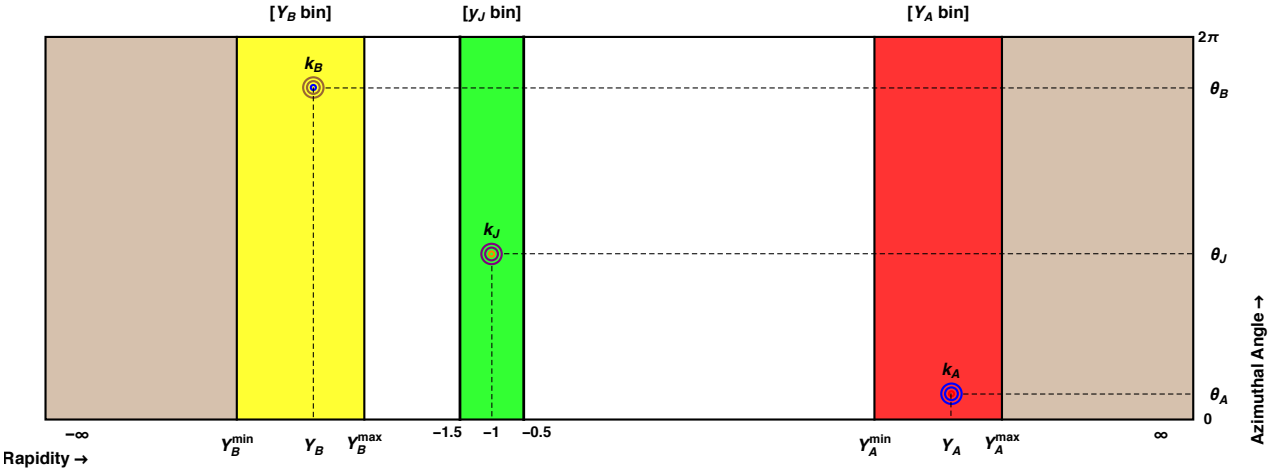

Figure 4.7: A primitive lego plot depicting a three-jet event similar to Fig. 4.4. Here, however, the rapidity of the central jet can take any value in the distinct ranges $y_i - 0.5 < y_J < y_i + 0.5$, where y_i is the central value of the rapidity bin with $y_i = \{-1, -0.5, 0, 0.5, 1\}$. In this figure, $y_i = -1$. Moreover, $Y = Y_A - Y_B$ is not anymore fixed. Instead, the forward jet has a rapidity restricted in the red bin whereas the backward jet in the yellow bin.

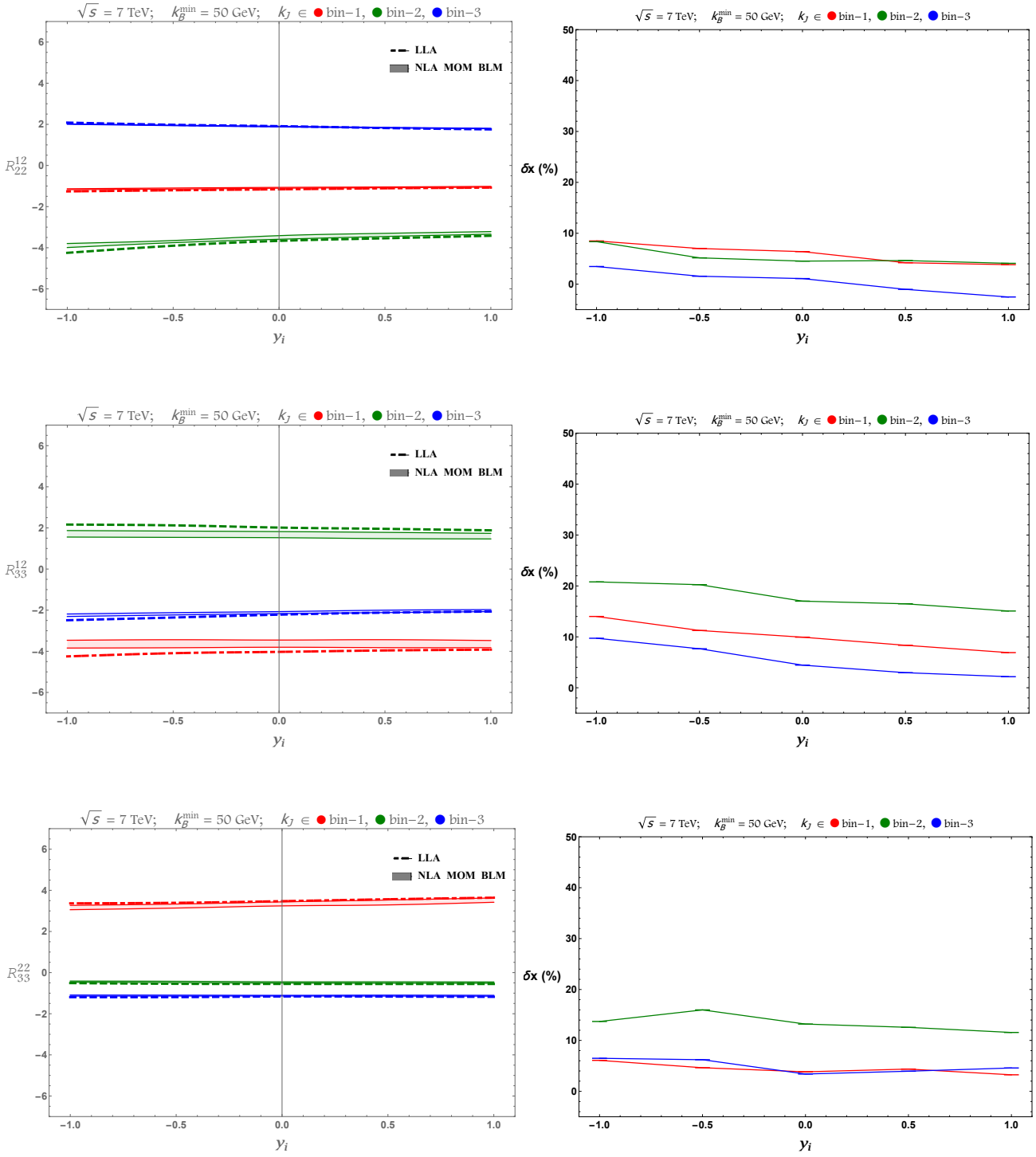

Figure 4.8: y_i-dependence of the LLA and NLLA R_{22}^{12}, R_{33}^{12} and R_{33}^{22} at $\sqrt{s} = 7$ TeV (left) and the relative NLLA to LLA corrections (right).

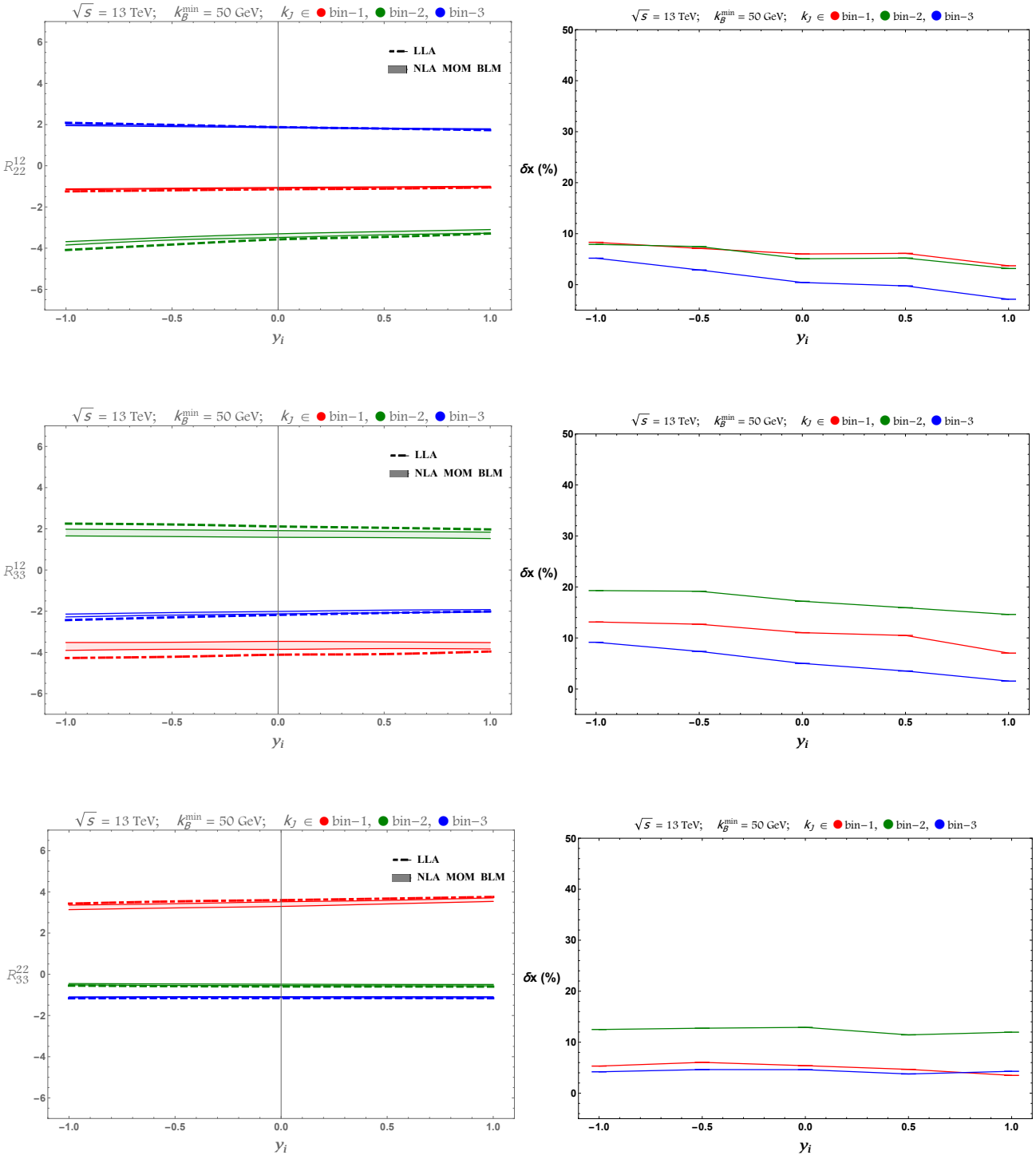

Figure 4.9: y_i-dependence of the LLA and NLLA R_{22}^{12}, R_{33}^{12} and R_{33}^{22} at $\sqrt{s} = 13$ TeV (left) and the relative NLLA to LLA corrections (right).

4.5 Summary

We have presented a first complete phenomenological study beyond the LLA of inclusive three-jet production at the LHC within the BFKL framework, focussing on azimuthal-angle dependent observables. We considered two colliding energies, $\sqrt{s} = 7, 13$ TeV and an asymmetric kinematic cut with respect to the transverse momentum of the forward (k_A) and backward (k_B) jets. In addition, we have chosen to consider an extra condition regarding the value of the transverse momentum k_J of the central jet, dividing the allowed region for k_J into three sub-regions: k_J smaller than $k_{A,B}$, k_J similar to $k_{A,B}$ and k_J larger than $k_{A,B}$.

For a proper study at full NLLA, one needs to consider the NLO jet vertices and the NLLA gluon Green functions. We have argued that we expect the latter to be of higher relevance and we proceed to calculate them using the BLM prescription which has been successful in previous phenomenological analyses. We have shown how our observables R_{22}^{12}, R_{33}^{12} and R_{33}^{22} change when we vary the rapidity difference Y between k_A and k_B from 5.5 to 9 units for a fixed y_J and from 6.5 to 9 units for $-0.5 < y_J < 0.5$. We have presented both the LLA and NLLA results along with plots that show the relative size of the NLLA corrections compared to the LLA ones. We have also presented an alternative kinematical setup where we allow for Y_A and Y_B to take values such that $3 < Y_A < 4.7$ and $-4.7 < Y_B < -3$, while the rapidity of the central jet takes values in five distinct rapidity bins of unit width, that is, $y_i - 0.5 < y_J < y_i + 0.5$, with $y_i = \{-1, -0.5, 0, 0.5, 1\}$. In this alternative setup, we presented our results for R_{12}^{22}, R_{12}^{33} and R_{22}^{33} as functions of y_i.

The general conclusion is that the NLLA corrections are moderate and our proposed observables exhibit a good perturbative stability. Furthermore, we see that for a wide range of rapidities, the changes we notice when going from 7 TeV to 13 TeV are small which makes us confident that these generalized ratios pinpoint the crucial characteristics of the BFKL dynamics regarding the azimuthal behavior of the hard jets in inclusive three-jet production. It will be very interesting to compare with possible predictions for these observables from fixed order analyses as well as from the BFKL inspired Monte-Carlo `BFKLex` [180–186, 189]. Predictions from general-purpose Monte-Carlos tools should also be welcome. It would be extremely interesting to pursue an experimental analysis for these observables using LHC data.

CHAPTER 5

FOUR-JETS OBSERVABLES

In Chapters 3 and 4, new observables in LHC inclusive events with three tagged jets were proposed. Here, we extend our discussion to the case of four-jet events (different experimental analyses can be found in Refs. [190–192]). For the present study, we need to have one jet in the forward direction with rapidity Y_A, one in the backward direction with rapidity Y_B and both well-separated in rapidity from the each other so that $Y_A - Y_B$ is large, along with two extra jets tagged in more central regions of the detector. Additionally, the relative rapidity separation between any two neighboring jets cannot be very different than one third of $Y_A - Y_B$ so that the kinematical configurations of the events actually follow the multi-Regge kinematics. In our setup, non-tagged associated mini-jet multiplicity is present and needs to be accounted for by the inclusion of BFKL gluon Green functions. The projection of the cross section on azimuthal-angle components opens up the opportunity for defining new ratios of correlation functions of the azimuthal angle differences among the tagged jets that can be used as probes of the BFKL dynamics.

We already studied the tagging of two extra emissions in the BFKL ladder in Section 3.1, where we derived Eq. (3.8), the differential cross section for the emission of four jets in the MRK limit. Extending the generalized azimuthal correlations of the previous sections to the partonic four-jet production, it was studied in [164] different ratios of three cosines in numerator and denominator:

$$\mathscr{R}^{MNL}_{PQR} = \frac{\langle \cos(M\,\phi_1)\cos(N\,\phi_2)\cos(L\,\phi_3)\rangle}{\langle \cos(P\,\phi_1)\cos(Q\,\phi_2)\cos(R\,\phi_3)\rangle}, \tag{5.1}$$

where ϕ_1, ϕ_2 and ϕ_3 are the azimuthal angle differences between neighbouring in rapidity jets. These ratios allow for the study of even more differential distributions in the transverse momenta, azimuthal angles and rapidities of the two central jets as well as for detailed work in connection to multiple parton scattering [165–170, 193].

In this paper, we define and study ratios of three cosines in numerator and denominator beyond the partonic level. We make use of the collinear factorization scheme to produce the two uttermost jets and we convolute the partonic differential cross section, which is described by the BFKL dynamics, with collinear parton distribution functions. We also include in our computation the forward “jet vertex" [142, 143, 171–173]. Three BFKL gluon Green functions link the outermost (Mueller-Navelet-like) jets with the more centrally produced ones. We integrate over the momenta of the four produced jets, using LHC kinematical cuts so that a comparison of our predictions with forthcoming experimental analyses of LHC data is possible. In the following sections we will overview the main formulas at partonic and hadronic level and present our numerical results. We conclude with our Summary 5.3.

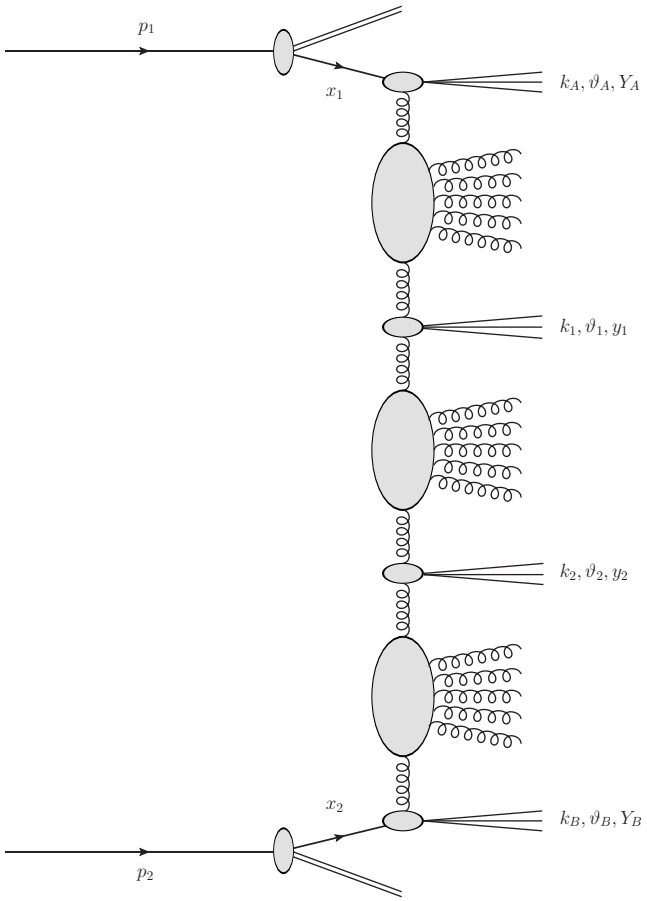

Figure 5.1: Inclusive four-jet production process in multi-Regge kinematics.

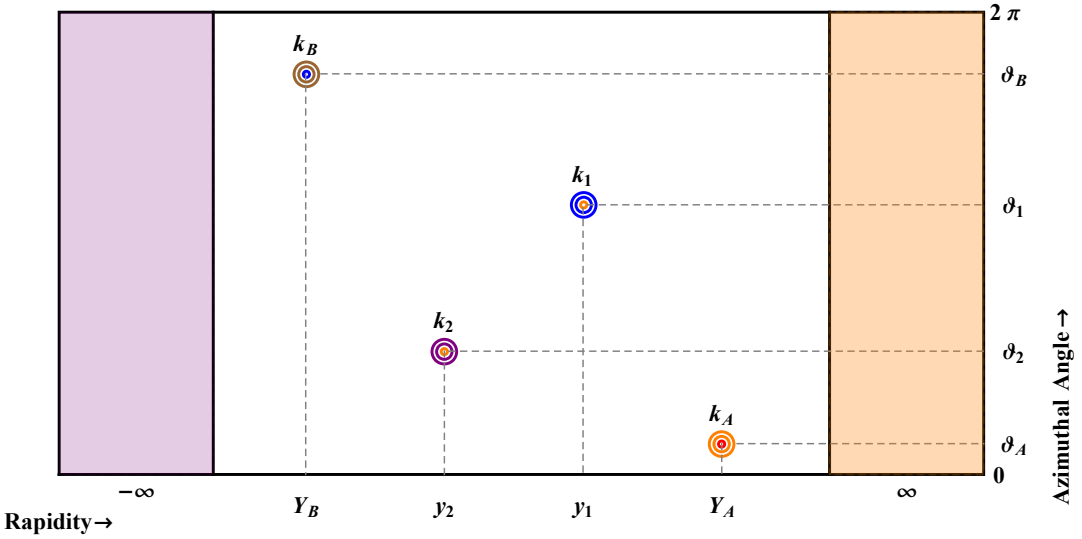

Figure 5.2: A primitive lego plot depicting a four-jet event. k_A is a forward jet with large positive rapidity Y_A and azimuthal angle ϑ_A, k_B is a backward jet with large negative rapidity Y_B and azimuthal angle ϑ_B and k_1 and k_2 are two jets with azimuthal angles ϑ_1 and ϑ_2 respectively and rapidities y_1 and y_2 such that $Y_A - y_1 \sim y_1 - y_2 \sim y_2 - Y_B$.

5.1 Partonic level inclusive four-jet production in multi-Regge kinematics

For the sake of clarity, we will first introduce the partonic level formulae, since it is the best way of exploring their symmetries and their possible simplifications. As in Section 3.2, this path provides more concise expressions and keeps away extra difficulties only related to the hadronic upgrade. Since our main goal are azimuthal angle correlations, we will need to extract the Fourier coefficients of the differential cross section.

Let us recall the differential cross section for the tagging of two extra jets in the MRK limit, Eq. (3.8), with a slight notational change

$$\begin{aligned}\frac{\mathrm{d}\sigma}{\mathrm{d}^3J_1\,\mathrm{d}^3J_2}\left(\vec{k}_A,\vec{k}_B,\vec{k}_1,\vec{k}_2,Y_A,y_1,y_2,Y_B\right) &= \frac{\bar{\alpha}_s}{\pi k_1^2}\frac{\bar{\alpha}_s}{\pi k_2^2}\times\\ \times\int \mathrm{d}^2\vec{p}_A\,\mathrm{d}^2\vec{p}_B\,\mathrm{d}^2\vec{p}_1\,\mathrm{d}^2\vec{p}_2\,\delta^2\left(\vec{p}_A+\vec{k}_{J_1}-\vec{p}_1\right)\delta^2\left(\vec{p}_B+\vec{k}_{J_2}-\vec{p}_2\right)\times\\ \times\varphi\left(\vec{k}_A,\vec{p}_A,Y_A-y_{J_1}\right)\varphi\left(\vec{p}_1,\vec{p}_2,y_{J_1}-y_{J_2}\right)\varphi\left(\vec{p}_B,\vec{k}_B,y_{J_2}-Y_B\right),\end{aligned} \tag{5.2}$$

where now the measure $\mathrm{d}^3J \equiv \mathrm{d}^2\vec{k}\,\mathrm{d}y = \frac{1}{2}\mathrm{d}p^2\,\mathrm{d}^\theta\,\mathrm{d}\,y$, and we always assume that the following rapidity ordering holds $Y_A > y_1 > y_2 > Y_B$. We also denote as $\psi_{A|B}$ the angles associated with $\vec{p}_{A|B}$. Solving for the deltas we have

$$\begin{aligned}\frac{\mathrm{d}\sigma}{\mathrm{d}^3J_1\,\mathrm{d}^3J_2} &= \frac{\bar{\alpha}_s^2}{\pi^2k_1^2k_2^2}\int \mathrm{d}^2\vec{p}_A\,\mathrm{d}^2\vec{p}_B\times\\ \times\varphi\left(\vec{k}_A,\vec{p}_A,Y_A-y_1\right)\varphi\left(\vec{p}_A+\vec{k}_1,\vec{p}_B-\vec{k}_2,y_1-y_2\right)\varphi\left(\vec{p}_B,\vec{k}_B,y_2-Y_B\right).\end{aligned} \tag{5.3}$$

In order to simplify the Fourier expansion of the GGFs, we first simplify the angles associated with the vectors $\vec{p}_A+\vec{k}_1$ and $\vec{p}_B-\vec{k}_2$

$$\begin{aligned}e^{i\theta_{p_A+k_1}} &= e^{i\theta_1}\frac{p_Ae^{i(\psi_A-\theta_1)}+k_1}{(p_A^2+k_1^2+2k_Ap_1\cos(\psi_A-\theta_1))^{1/2}};\\ e^{i\theta_{p_B-k_2}} &= e^{i(\theta_2+\pi)}\frac{p_Be^{i(\psi_B-\theta_2-\pi)}+k_2}{(p_B^2+k_2^2+2k_Bp_2\cos(\psi_B-\theta_2-\pi))^{1/2}}.\end{aligned} \tag{5.4}$$

We factor out the external angular dependence through the change of variables $\psi_A \to \psi_A+\theta_1, \psi_B \to \psi_B+\theta_2+\pi$ and obtain

$$\begin{aligned}\frac{\mathrm{d}\sigma}{\mathrm{d}^3J_1\,\mathrm{d}^3J_2} &= \frac{\bar{\alpha}_s^2}{(2\pi)^5k_1^2k_2^2}\sum_{m,n,l}(-1)^{n+l}e^{im\theta_A}e^{-i\theta_1(m-n)}e^{-i\theta_2(n-l)}e^{-il\theta_B}\times\\ \times\int \mathrm{d}p_A^2\,\mathrm{d}\psi_A\,\mathrm{d}p_B^2\,\mathrm{d}\psi_B\,e^{-im\psi_A}e^{in\alpha}e^{il\psi_B}\varphi_m\left(k_A^2,p_A^2,Y_A-y_1\right)\times\\ \times\varphi_n\left(p_A^2+k_1^2+2p_Ak_1\cos\psi_A,p_B^2+k_2^2+2p_Bk_2\cos\psi_B,y_1-y_2\right)\varphi_l\left(p_B^2,k_B^2,y_2-Y_B\right),\end{aligned} \tag{5.5}$$

where we have defined the angles α and $\alpha_{1|2}$ as

$$\begin{aligned}&\alpha \equiv \alpha_1 - \alpha_2;\\ &e^{i\alpha_1} \equiv \frac{p_A e^{i\psi_A} + k_1}{(p_A^2 + k_1^2 + 2k_A p_1 \cos\psi_A)^{1/2}}\,;\, e^{i\alpha_2} \equiv \frac{p_B e^{i\psi_B} + k_2}{(p_B^2 + k_2^2 + 2k_B p_2 \cos\psi_B)^{1/2}}\,.\end{aligned} \tag{5.6}$$

which both of them satisfy that $\alpha_{1|2} \to -\alpha_{1|2}$ when $\psi_{A|B} \to -\psi_{A|B}$.

As a generalization of the 3-jets case Ω_{mn} we define here

$$\begin{aligned}\Omega_{mnl} \equiv \int \mathrm{d}p_A^2\,\mathrm{d}\psi_A\,\mathrm{d}p_B^2\,\mathrm{d}\psi_B\, e^{-im\psi_A} e^{in\alpha} e^{il\psi_B} \varphi_m\left(k_A^2, p_A^2, Y_A - y_1\right) \times\\ \times\varphi_n\left(p_A^2 + k_1^2 + 2p_A k_1 \cos\psi_A, p_B^2 + k_2^2 + 2p_B k_2 \cos\psi_B, y_1 - y_2\right)\varphi_l\left(p_B^2, k_B^2, y_2 - Y_B\right),\end{aligned} \tag{5.7}$$

which satisfy an equivalent relationship

$$\Omega_{mnl} = \Omega_{-m,-n,-l} = \Omega^*_{mnl} = \mathrm{Re}(\Omega_{mnl}). \tag{5.8}$$

This last symmetry encodes the invariance of the cross section under the following discrete symmetry $(\theta_A, \theta_1, \theta_2, \theta_B) \to -(\theta_A, \theta_1, \theta_2, \theta_B)$, which imposes strong constraints on the number of correlation functions that are non-vanishing.

If we are only interested in the usual Mueller-Navelet correlation functions, *i.e.*, the ones involving the azimuthal angle differences among the two outermost jets, we need to compute

$$\begin{aligned}\int_0^{2\pi} \mathrm{d}\theta_1\,\mathrm{d}\theta_2\,\frac{\mathrm{d}\sigma}{\mathrm{d}^3J_1\,\mathrm{d}^3J_2} = \frac{\bar{\alpha}_s^2}{(2\pi)^3 k_1^2 k_2^2}\sum_m e^{im(\theta_A - \theta_B)}\Omega_{mmm} =\\ \frac{\bar{\alpha}_s^2}{(2\pi)^3 k_1^2 k_2^2}\sum_{m=0}^{\infty}(2 - \delta_{m0})\cos(m(\theta_A - \theta_B))\mathrm{Re}(\Omega_{mmm})\end{aligned} \tag{5.9}$$

showing that only the cosines survive. Indeed, we have that

$$\begin{aligned}\mathscr{C}_M \equiv \langle\cos(M(\theta_A - \theta_B))\rangle = \mathscr{N}\int \mathrm{d}\theta_A\,\mathrm{d}\theta_B\,\mathrm{d}\theta_1\,\mathrm{d}\theta_2\cos(M(\theta_A - \theta_B))\frac{\mathrm{d}\sigma}{\mathrm{d}^3J_1\,\mathrm{d}^3J_2} =\\ = \mathscr{N}\frac{\bar{\alpha}_s^2}{2\pi k_1^2 k_2^2}\mathrm{Re}(\Omega_{MMM}) = \mathscr{N}\frac{\bar{\alpha}_s^2}{2\pi k_1^2 k_2^2}\int \mathrm{d}p_A^2\,\mathrm{d}\psi_A\,\mathrm{d}p_B^2\,\mathrm{d}\psi_B \times\\ \times\cos M\left(\psi_A - \alpha - \psi_B\right)\varphi_M\left(k_A^2, p_A^2, Y_A - y_1\right)\varphi_M\left(p_B^2, k_B^2, y_2 - Y_B\right)\times\\ \times\varphi_M\left(p_A^2 + k_1^2 + 2p_A k_1\cos\psi_A, p_B^2 + k_2^2 + 2p_B k_2\cos\psi_B, y_1 - y_2\right).\end{aligned} \tag{5.10}$$

In addition to that, we can define observables consisting in two azimuthal angle differences, like in Chapters 3 and 4. But to exploit all the kinematical possibilities that the four jets bring us, we are going to focus on the three azimuthal angle differences defined as

$$\phi_1 \equiv \theta_A - \theta_1 - \pi\,;\, \phi_1 \equiv \theta_1 - \theta_2 - \pi\,;\, \phi_3 \equiv \theta_2 - \theta_B - \pi\,, \tag{5.11}$$

what allows us to express the differential cross section as

$$\frac{\mathrm{d}\sigma}{\mathrm{d}^3J_1\,\mathrm{d}^3J_2} = \frac{\bar{\alpha}_s^2}{(2\pi)^5 k_1^2 k_2^2} \sum_{m,n,l} (-1)^m e^{im\phi_1} e^{in\phi_2} e^{il\phi_3} \Omega_{mnl}\,, \tag{5.12}$$

and obtain the correlation functions as

$$\begin{aligned} \mathscr{C}_{MNL} &\equiv \langle \cos\left(M\phi_1\right) \cos\left(N\phi_2\right) \cos\left(L\phi_3\right) \rangle = \\ &= \mathscr{N} \frac{\bar{\alpha}_s^2}{2\pi k_1^2 k_2^2} \int \mathrm{d}p_A^2\,\mathrm{d}\psi_A\,\mathrm{d}p_B^2\,\mathrm{d}\psi_B\,(-1)^M \times \\ &\times \cos\left(M\psi_A\right) \cos(N\alpha) \cos\left(L\psi_B\right) \varphi_M\left(k_A^2, p_A^2, Y_A - y_1\right) \varphi_L\left(p_B^2, k_B^2, y_2 - Y_B\right) \times \\ &\times \varphi_N\left(p_A^2 + k_1^2 + 2p_A k_1 \cos\psi_A, p_B^2 + k_2^2 + 2p_B k_2 \cos\psi_B, y_1 - y_2\right)\,, \end{aligned} \tag{5.13}$$

$$\begin{aligned} \mathscr{S}^{(1)}_{MNL} &\equiv \langle \cos\left(M\phi_1\right) \sin\left(N\phi_2\right) \sin\left(L\phi_3\right) \rangle = \\ &= \mathscr{N} \frac{\bar{\alpha}_s^2}{2\pi k_1^2 k_2^2} \int \mathrm{d}p_A^2\,\mathrm{d}\psi_A\,\mathrm{d}p_B^2\,\mathrm{d}\psi_B\,(-1)^M \times \\ &\times \cos\left(M\psi_A\right) \sin(N\alpha) \sin\left(L\psi_B\right) \varphi_M\left(k_A^2, p_A^2, Y_A - y_1\right) \varphi_L\left(p_B^2, k_B^2, y_2 - Y_B\right) \times \\ &\times \varphi_N\left(p_A^2 + k_1^2 + 2p_A k_1 \cos\psi_A, p_B^2 + k_2^2 + 2p_B k_2 \cos\psi_B, y_1 - y_2\right)\,, \end{aligned} \tag{5.14}$$

$$\begin{aligned} \mathscr{S}^{(2)}_{MNL} &\equiv \langle \sin\left(M\phi_1\right) \cos\left(N\phi_2\right) \sin\left(L\phi_3\right) \rangle = \\ &= \mathscr{N} \frac{\bar{\alpha}_s^2}{2\pi k_1^2 k_2^2} \int \mathrm{d}p_A^2\,\mathrm{d}\psi_A\,\mathrm{d}p_B^2\,\mathrm{d}\psi_B\,(-1)^{M+1} \times \\ &\times \sin\left(M\psi_A\right) \cos(N\alpha) \sin\left(L\psi_B\right) \varphi_M\left(k_A^2, p_A^2, Y_A - y_1\right) \varphi_L\left(p_B^2, k_B^2, y_2 - Y_B\right) \times \\ &\times \varphi_N\left(p_A^2 + k_1^2 + 2p_A k_1 \cos\psi_A, p_B^2 + k_2^2 + 2p_B k_2 \cos\psi_B, y_1 - y_2\right)\,, \end{aligned} \tag{5.15}$$

$$\begin{aligned} \mathscr{S}^{(3)}_{MNL} &\equiv \langle \sin\left(M\phi_1\right) \sin\left(N\phi_2\right) \cos\left(L\phi_3\right) \rangle = \\ &= \mathscr{N} \frac{\bar{\alpha}_s^2}{2\pi k_1^2 k_2^2} \int \mathrm{d}p_A^2\,\mathrm{d}\psi_A\,\mathrm{d}p_B^2\,\mathrm{d}\psi_B\,(-1)^{M+1} \times \\ &\times \sin\left(M\psi_A\right) \sin(N\alpha) \cos\left(L\psi_B\right) \varphi_M\left(k_A^2, p_A^2, Y_A - y_1\right) \varphi_L\left(p_B^2, k_B^2, y_2 - Y_B\right) \times \\ &\times \varphi_N\left(p_A^2 + k_1^2 + 2p_A k_1 \cos\psi_A, p_B^2 + k_2^2 + 2p_B k_2 \cos\psi_B, y_1 - y_2\right)\,, \end{aligned} \tag{5.16}$$

whereas the rest of combinations are zero.

The differential cross section is left invariant under parity, which is represented in our system of coordinates as

$$\begin{aligned} &(k_A, k_1, k_2, k_B, \theta_A, \theta_1, \theta_2, \theta_B, Y_A, y_1, y_2, Y_B) \Leftrightarrow \\ &\Leftrightarrow (k_B, k_2, k_1, k_A, \theta_B, \theta_2 + \pi, \theta_1 + \pi, \theta_A, -Y_B, -y_2, -y_1, -Y_A)\,, \end{aligned} \tag{5.17}$$

or equivalently[1]

$$\begin{aligned}(5.18)\qquad &\left(k_A,k_1,k_2,k_B,\phi_1,\phi_2,\phi_3,Y_{A1},y_{12},Y_{2B}\right)\Leftrightarrow\\ \Leftrightarrow &\left(k_B,k_2,k_1,k_A,-\phi_3+\pi,-\phi_2,-\phi_1+\pi,Y_{2B},y_{12},Y_{A1}\right),\end{aligned}$$

which translates into the following equalities among the correlation functions[2]

$$\begin{aligned}&\mathscr{C}_{MNL}(k_A,k_1,k_2,k_B,Y_{A1},y_{12},Y_{2B})=(-1)^{M+L}\mathscr{C}_{LNM}(k_B,k_2,k_1,k_A,Y_{2B},y_{12},Y_{A1})\\ (5.19)\qquad &\mathscr{S}^{(1)}_{MNL}(k_A,k_1,k_2,k_B,Y_{A1},y_{12},Y_{2B})=(-1)^{M+L}\mathscr{S}^{(3)}_{LNM}(k_B,k_2,k_1,k_A,Y_{2B},y_{12},Y_{A1})\\ &\mathscr{S}^{(2)}_{MNL}(k_A,k_1,k_2,k_B,Y_{A1},y_{12},Y_{2B})=(-1)^{M+L}\mathscr{S}^{(2)}_{LNM}(k_B,k_2,k_1,k_A,Y_{2B},y_{12},Y_{A1})\end{aligned}$$

For a discussion regarding the applicability of these symmetries, we refer to the last part of Sec. 3.2.

[1] We have defined the rapidities with two indices as the difference between them, *i.e.*, $Y_{AB}\equiv Y_A-Y_B$.

[2] If we had used the opposite convention for the sign of $\vec{k}_B$, as explained in Footnote (6) in Sec. 3.2, we would have obtained all the relationships without the factor $(-1)^{M+L}$, which is more intuitive. This is related to the fact that the parity transformation is defined in a different way.

5.2 Hadronic level inclusive four-jet production in multi-Regge kinematics

We study (see Figs. 5.1 and 5.2) the production of one forward and one backward jet, both characterized by high transverse momenta $\vec{k}_{A,B}$ and well separated in rapidity, together with two more jets produced in the central rapidity region and with possible associated mini-jet production:

$$\text{proton}(p_1) + \text{proton}(p_2) \to \text{jet}(k_A) + \text{jet}(k_1) + \text{jet}(k_2) + \text{jet}(k_B) + \text{minijets} \tag{5.20}$$

The cross section for the inclusive four-jet production process (5.20) reads in collinear factorization

$$\begin{aligned} &\frac{d\sigma^{4-\text{jet}}}{dk_A\, dY_A\, d\vartheta_A\, dk_B\, dY_B\, d\vartheta_B\, dk_1\, dy_1 d\vartheta_1\, dk_2\, dy_2 d\vartheta_2} = \\ &= \sum_{\alpha,\beta=q,\bar{q},g} \int_0^1 dx_1 \int_0^1 dx_2\, f_\alpha\left(x_1,\mu_F\right)\, f_\beta\left(x_2,\mu_F\right)\, d\hat{\sigma}_{\alpha,\beta}\left(\hat{s},\mu_F\right), \end{aligned} \tag{5.21}$$

where α,β characterise the partons (gluon g; quarks $q = u,d,s,c,b$; antiquarks $\bar{q} = \bar{u},\bar{d},\bar{s},\bar{c},\bar{b}$), $f_{\alpha,\beta}\left(x,\mu_F\right)$ are the parton distribution functions of the protons; $x_{1,2}$ represent the longitudinal fractions of the partons involved in the hard subprocess; $d\hat{\sigma}_{\alpha,\beta}\left(\hat{s},\mu_F\right)$ is the partonic cross section for the production of jets and $\hat{s} \equiv x_1 x_2 s$ is the partonic squared center-of-mass energy (see Fig. 5.1). The cross-section for the partonic hard subprocess $d\hat{\sigma}_{\alpha,\beta}$ features a dependence on BFKL dynamics keeping in mind that the emissions of mini-jet in the rapidity span between any two subsequent-in-rapidity jets can be described by a forward gluon Green function φ.

Making use of the leading order approximation of the jet vertex [171], the cross section for the process (5.20) reads

$$\begin{aligned} &\frac{d\sigma^{4-\text{jet}}}{dk_A\, dY_A\, d\vartheta_A\, dk_B\, dY_B\, d\vartheta_B\, dk_1\, dy_1 d\vartheta_1\, dk_2\, dy_2 d\vartheta_2} = \\ &= \frac{16\pi^4 C_F\, \bar{\alpha}_s^4}{N_C^3} \frac{x_{J_A}\, x_{J_B}}{k_A\, k_B\, k_1\, k_2} f^\star\left(x_{J_A},\mu_F\right) f^\star\left(x_{J_B},\mu_F\right) \times \\ &\times \int d^2\vec{p}_A \int d^2\vec{p}_B \int d^2\vec{p}_1 \int d^2\vec{p}_2\, \delta^{(2)}\left(\vec{p}_A + \vec{k}_1 - \vec{p}_1\right) \delta^{(2)}\left(\vec{p}_B - \vec{k}_2 - \vec{p}_2\right) \times \\ &\times \varphi\left(\vec{k}_A, \vec{p}_A, Y_A - y_1\right) \varphi\left(\vec{p}_1, \vec{p}_2, y_1 - y_2\right) \varphi\left(\vec{p}_B, \vec{k}_B, y_2 - Y_B\right). \end{aligned} \tag{5.22}$$

In order to follow a multi-Regge kinematics setup, we demand that the rapidities of the produced particles obey $Y_A > y_1 > y_2 > Y_B$, while k_1^2 and k_2^2 are well above the resolution scale of the detectors. $x_{J_{A,B}}$ are the longitudinal momentum fractions of the two external

jets, connected to the respective rapidities $Y_{A,B}$ by the relation $x_{J_{A,B}} = k_{A,B}\, e^{\pm Y_{A,B}}/\sqrt{s}$. The strong coupling is $\bar{\alpha}_s = \alpha_s\left(\mu_R\right) N_c/\pi$ and φ are BFKL gluon Green functions following the normalization $\varphi(\vec{p},\vec{q},0) = \delta^{(2)}(\vec{p}-\vec{q})$.

As we mentioned previously, we would like to consider quantities that are easily measured experimentally and moreover we want to eliminate as much as possible any dependence on higher order corrections. Thus, we need to consider ratios[3] of the $\mathscr{C}_{MNL}$ coefficients defined in Eq. (5.13), but defined on a hadronic level though. Therefore, in order to provide testable theoretical predictions against any current and forthcoming experimental data, we proceed in two steps. Firstly, we impose LHC kinematical cuts by averaging the azimuthal angle correlations over the momenta of the tagged jets. More precisely[4],

$$C_{MNL} \equiv \frac{\int \mathscr{D}\mathrm{PS}\, \cos\left(M\phi_1\right)\cos\left(N\phi_2\right)\cos\left(L\phi_3\right) d\sigma^{4-\mathrm{jet}}}{\int \mathscr{D}\mathrm{PS}\, d\sigma^{4-\mathrm{jet}}}\,, \tag{5.23}$$

where the integration measure is defined as

$$\begin{aligned}\int \mathscr{D}\mathrm{PS} \equiv \int_{Y_A^{\min}}^{Y_A^{\max}} \mathrm{d}Y_A \int_{Y_B^{\min}}^{Y_B^{\max}} \mathrm{d}Y_B \int_{k_A^{\min}}^{k_A^{\max}} \mathrm{d}k_A \int_{k_B^{\min}}^{k_B^{\max}} \mathrm{d}k_B \int_{k_1^{\min}}^{k_1^{\max}} dk_1 \int_{k_2^{\min}}^{k_2^{\max}} dk_2 \times \\ \times \delta(Y_A - Y_B - Y) \int_0^{2\pi} \mathrm{d}\theta_A \int_0^{2\pi} \mathrm{d}\theta_B \int_0^{2\pi} \mathrm{d}\theta_1 \int_0^{2\pi} \mathrm{d}\theta_2\,.\end{aligned} \tag{5.24}$$

where the rapidity Y_A of the most forward jet k_A is restricted to $0 < Y_A < 4.7$ and the rapidity Y_B of the most backward jet k_B is restricted to $-4.7 < Y_B < 0$ while their difference $Y \equiv Y_A - Y_B$ is kept fixed at definite values within the range $6.5 < Y < 9$. Obviously, the last condition on the allowed values of Y makes both the integration ranges over Y_A and Y_B smaller than 4.7 units of rapidity. Secondly, we remove the zeroth conformal spin contribution responsible for any collinear contamination (contributions that originate at φ_0) and we minimise possible higher order effects by introducing the ratios

$$R^{MNL}_{PQR} = \frac{C_{MNL}}{C_{PQR}} \tag{5.25}$$

where M,N,L,P,Q,R are positive definite integers.

[3] See discussion in Refs. [151, 152].

[4] In this work we have not considered the rest of the observables that we can define, but they are equally important and they will need to be studied if experimental data are available.

The numerator in Eq. (5.23) is proportional to

$$
\begin{aligned}
&\int_0^{2\pi} d\vartheta_A \int_0^{2\pi} d\vartheta_B \int_0^{2\pi} d\vartheta_1 \int_0^{2\pi} d\vartheta_2 \cos(M\phi_1)\cos(N\phi_2)\cos(L\phi_3) \\
&\times \frac{d\sigma^{4-\text{jet}}}{dk_A\, dY_A\, d\vartheta_A\, dk_B\, dY_B\, d\vartheta_B\, dk_1\, dy_1 d\vartheta_1\, dk_2\, dy_2 d\vartheta_2} = \\
&= \frac{8\pi^5 C_F\, \bar{\alpha}_s^4}{N_C^3} \frac{x_{J_A}\, x_{J_B}}{k_A\, k_B\, k_1\, k_2} f^\star\left(x_{J_A}, \mu_F\right) f^\star\left(x_{J_B}, \mu_F\right) \times \\
&\times \int \mathrm{d}p_A^2\, \mathrm{d}\psi_A\, \mathrm{d}p_B^2\, \mathrm{d}\psi_B\, (-1)^M \cos\left(M\psi_A\right) \cos(N\alpha) \cos\left(L\psi_B\right) \times \\
&\times \varphi_M\left(k_A^2, p_A^2, Y_A - y_1\right) \varphi_L\left(p_B^2, k_B^2, y_2 - Y_B\right) \times \\
&\times \varphi_N\left(p_A^2 + k_1^2 + 2p_A k_1 \cos\psi_A, p_B^2 + k_2^2 + 2p_B k_2 \cos\psi_B, y_1 - y_2\right).
\end{aligned}
\tag{5.26}
$$

where

$$
\varphi_n\left(k^2, q^2, Y\right) = \frac{2}{\pi\, k\, q} \int_0^\infty d\nu \cos\left(\nu \ln\frac{k^2}{q^2}\right) e^{\bar{\alpha}_s \chi_0(n,\nu)(Y - Y_0)},
\tag{5.27}
$$

$$
\chi_0(n,\nu) = 2\psi(1) - \psi\left(\frac{1+n}{2} + i\nu\right) - \psi\left(\frac{1+n}{2} - i\nu\right) = 2\mathrm{Re}\left[\psi(1) - \psi\left(\frac{1+n}{2} + i\nu\right)\right]
\tag{5.28}
$$

and ψ is the logarithmic derivative of Euler's gamma function.

Let us proceed now and present results for the ratios $R^{MNL}_{PQR}(Y)$ in Eq. (5.25) as functions of the rapidity difference Y between the outermost jets for different momenta configurations and for two center-of-mass energies: $\sqrt{s} = 7$ and $\sqrt{s} = 13$ TeV. For the transverse momenta k_A, k_B, k_1 and k_2 we impose the following cuts:

1.

$$
\begin{aligned}
k_A^{min} &= 35\,\text{GeV},\ k_A^{max} = 60\,\text{GeV}, \\
k_B^{min} &= 45\,\text{GeV},\ k_B^{max} = 60\,\text{GeV}, \\
k_1^{min} &= 20\,\text{GeV},\ k_1^{max} = 35\,\text{GeV}, \\
k_2^{min} &= 60\,\text{GeV},\ k_2^{max} = 90\,\text{GeV}.
\end{aligned}
\tag{5.29}
$$

2.

$$
\begin{aligned}
k_A^{min} &= 35\,\text{GeV},\ k_A^{max} = 60\,\text{GeV}, \\
k_B^{min} &= 45\,\text{GeV},\ k_B^{max} = 60\,\text{GeV}, \\
k_1^{min} &= 25\,\text{GeV},\ k_1^{max} = 50\,\text{GeV}, \\
k_2^{min} &= 60\,\text{GeV},\ k_2^{max} = 90\,\text{GeV}.
\end{aligned}
\tag{5.30}
$$

To keep things simple, in both cuts, we set k_2 to be larger than all the other three jet momenta and we only vary the range of k_1. In the cut defined in Eq. (5.29), k_1 is smaller that all the other three jet momenta whereas in the cut defined in Eq. (5.30), the allowed k_1 values overlap with the ranges of k_A and k_B. In the plots to follow, we plot the ratios for the cut defined in Eq. (5.29) with a red dot-dashed line and the ratios for the cut defined in Eq. (5.30) with a blue dashed line.

The numerical computation of the observables to be shown was done in FORTRAN. MATHEMATICA was used for various cross-checks. We used the NLO MSTW 2008 PDF sets [161] whereas, regarding the strong coupling α_s, a two-loop running coupling setup with $\alpha_s(M_Z) = 0.11707$ was used. We set the energy scale s_0 in the GGF in such a way that $Y_0 = 0$. `Vegas` [175] as implemented in the `Cuba` library [176, 177] was our main integration routine. We also made use of the library `Quadpack` [178] as well as of a modified version of the `Psi` [179] routine.

In the following, we present our results for the ratios $R^{111}_{221}, R^{112}_{111}, R^{112}_{211}, R^{212}_{111}, R^{122}_{221}, R^{221}_{112}$ in Figs. 5.3–5.8. We place the $\sqrt{s} = 7$ TeV results on the top of each figure and the $\sqrt{s} = 13$ TeV results at the bottom.

The functional dependence of the ratios R^{MNL}_{PQR} on the rapidity difference between k_A and k_B is rather smooth. We can further notice that there are ratios with an almost linear behaviour with Y and with a rather small slope. To be specific, the ratios represented by the blue curve in Fig. 5.3 and the red curve in Figs. 5.4, 5.5 and 5.6 demonstrate this linear behaviour in a striking fashion. Furthermore, whenever a ratio exhibits a linear dependence on Y (for a certain kinematical cut of k_1) at colliding energy 7 TeV, we observe that the ratio maintains almost the exact same linear behaviour –with very similar actual values– at 13 TeV as well.

On the other hand, there are configurations for which the functional dependence on Y is much stronger and far from linear. In Fig. 5.4, the blue curve on the top rises from ~ 1.2 at $Y = 6.5$ to ~ 6.8 at $Y = 9$, whereas in Fig. 5.6 on the top it drops from $\sim(-1.5)$ to $\sim(-4.8)$ for the same variation in Y. Generally, if for some ratio there is a strong functional dependence on Y for a k_1 of intermediate size (blue curve), this dependence is 'softened' at higher colliding energy (see plots in Figs. 5.4, 5.5, 5.6 and 5.8). However, for a k_1 of smaller size (red curve), we see that the functional dependence on Y gets stronger at 13 TeV (Figs. 5.3, 5.7 and 5.8), unless of course it exhibits a linear behaviour as was discussed in the previous paragraph.

In all plots presented in Figs. 5.3–5.8, there is no red or blue curve that changes sign in the interval $6.5 < Y < 9$. Moreover, if a ratio R^{MNL}_{PQR} is positive (negative) at 7 TeV, it will continue being positive (negative) at 13 TeV, disregarding the specific functional behaviour

on Y.

In contrast to our main observation in Chapter 3 (published in Ref. [2]) where in general, for most of the observables R_{PQ}^{MN} there were no significant changes after increasing the colliding energy from 7 to 13 TeV, here we notice that, depending on the kinematical cut, an increase in the colliding energy may lead to a noticeable change to the shape of the functional Y dependence, e.g. red curve in Fig. 5.3, blue and red curve in Fig. 5.8. This is a very interesting point for the following reason. If a BFKL-based analysis for an observable dictates that the latter does not change much when the energy increases, this fact actually indicates that a kind of asymptotia has been reached, e.g. the slope of the gluon Green function plotted as a function of the rapidity for very large rapidities. In asymptotia, the dynamics is driven by pure BFKL effects whereas pre-asymptotic effects are negligible. In the present study, we have a mixed picture. We have ratios that do not really change when the energy increases and other ratios for which a higher colliding energy changes their functional dependence on Y. A crucial point that allows us to speak about pre-asymptotic effects, which in itself infers that BFKL is still the relevant dynamics, was outlined previously in this section: despite the fact that for some cases we see a different functional dependence on Y after raising the colliding energy, it is important to note that we observe no change of sign for any ratio R_{PQR}^{MNL}. Therefore, the four-jet ratio observables we are studying here are more sensitive to pre-asymptotic effects than the related three-jet ratio observables studied in Ref. [2]. Nevertheless, by imposing different kinematical cuts one can change the degree of importance of these effects.

To conclude with, carefully combined choice of cuts for the R_{PQR}^{MNL} observables and a detailed confrontation between theoretical predictions and data may turn out to be an excellent way to probe deeper into the BFKL dynamics.

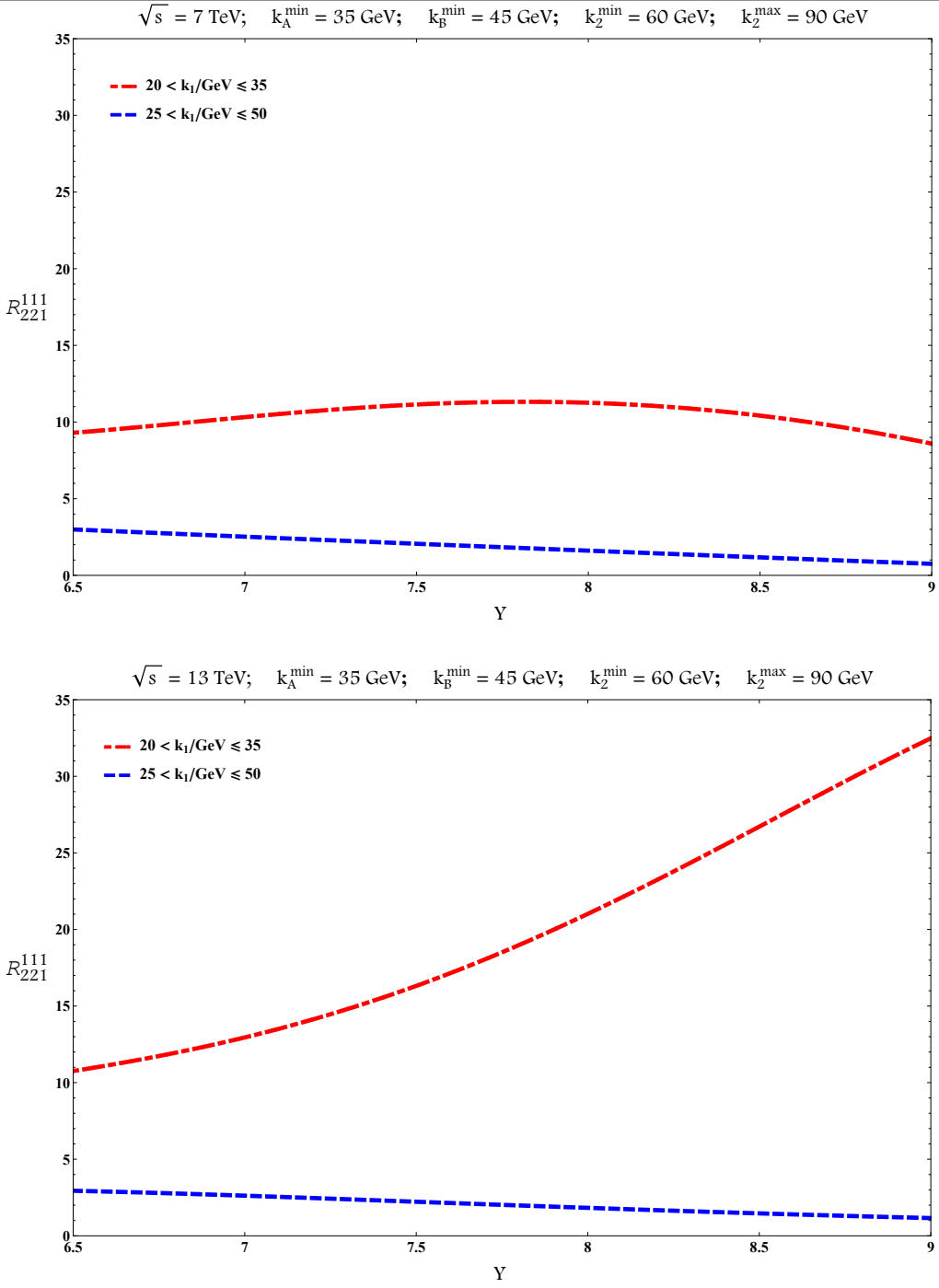

Figure 5.3: Y-dependence of R^{111}_{221} for $\sqrt{s} = 7$ TeV (top) and for $\sqrt{s} = 13$ TeV (bottom).

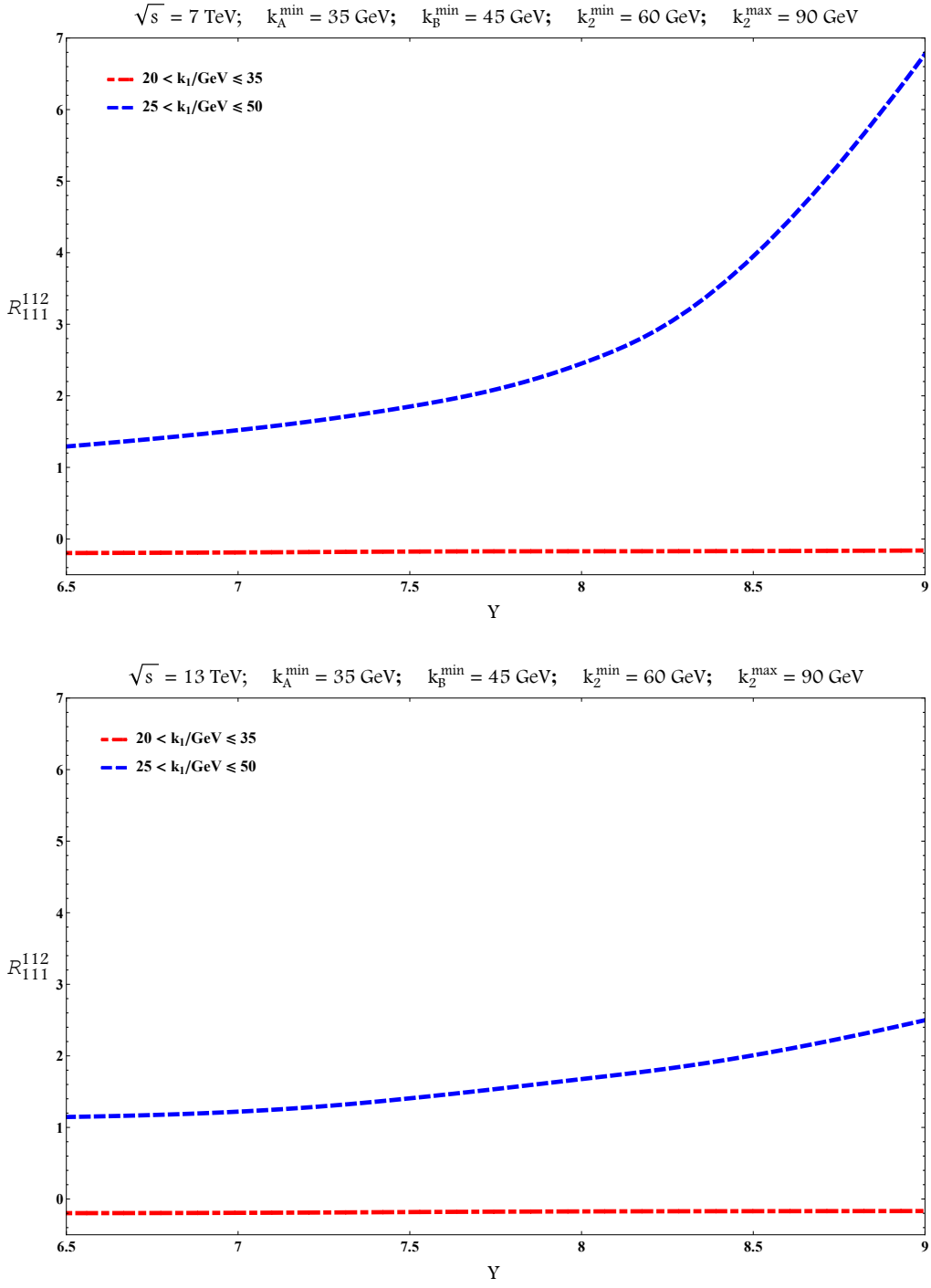

Figure 5.4: Y-dependence of R_{111}^{112} for $\sqrt{s} = 7$ TeV (top) and for $\sqrt{s} = 13$ TeV (bottom).

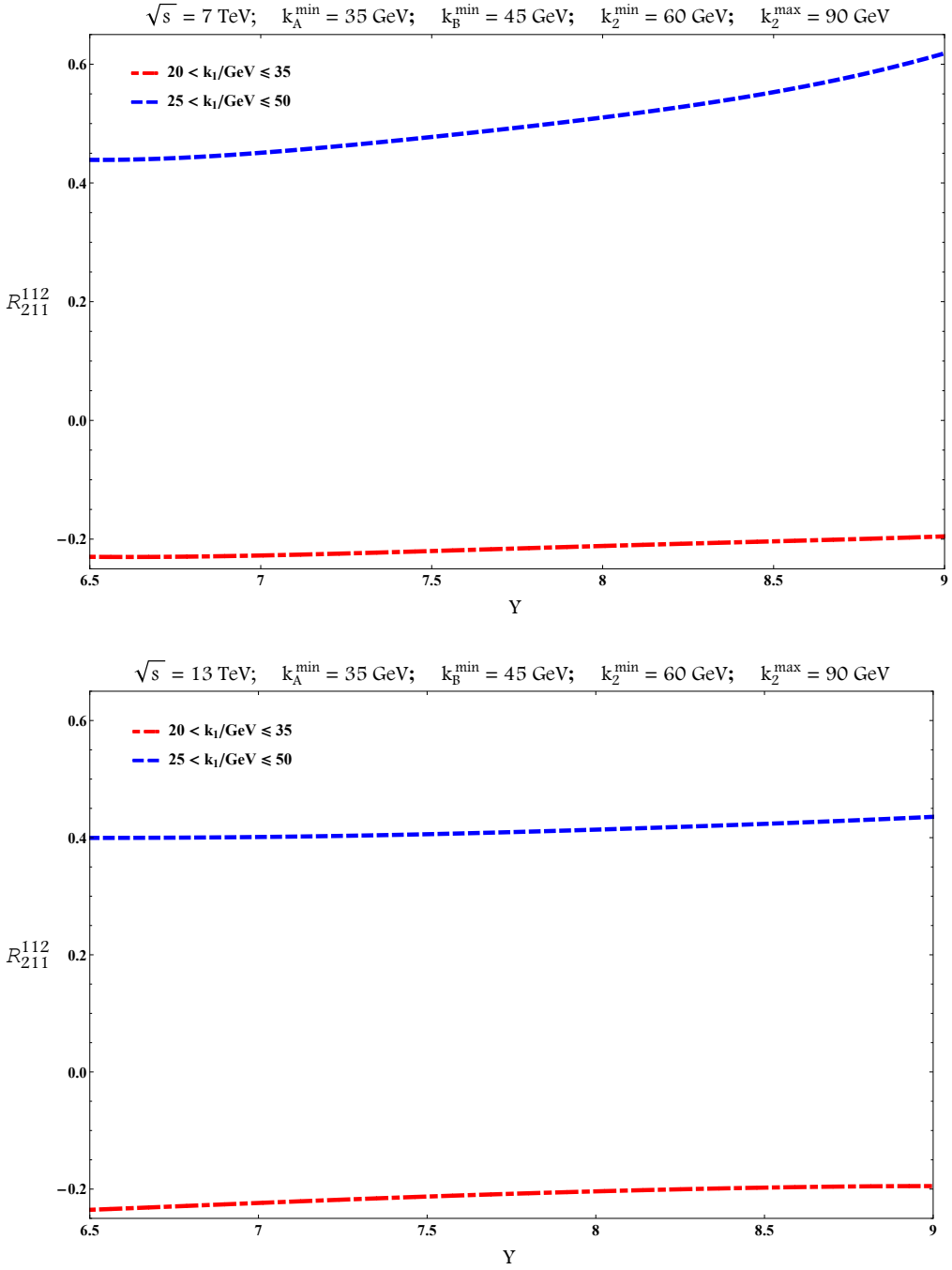

Figure 5.5: Y-dependence of R_{211}^{112} for $\sqrt{s} = 7$ TeV (top) and for $\sqrt{s} = 13$ TeV (bottom).

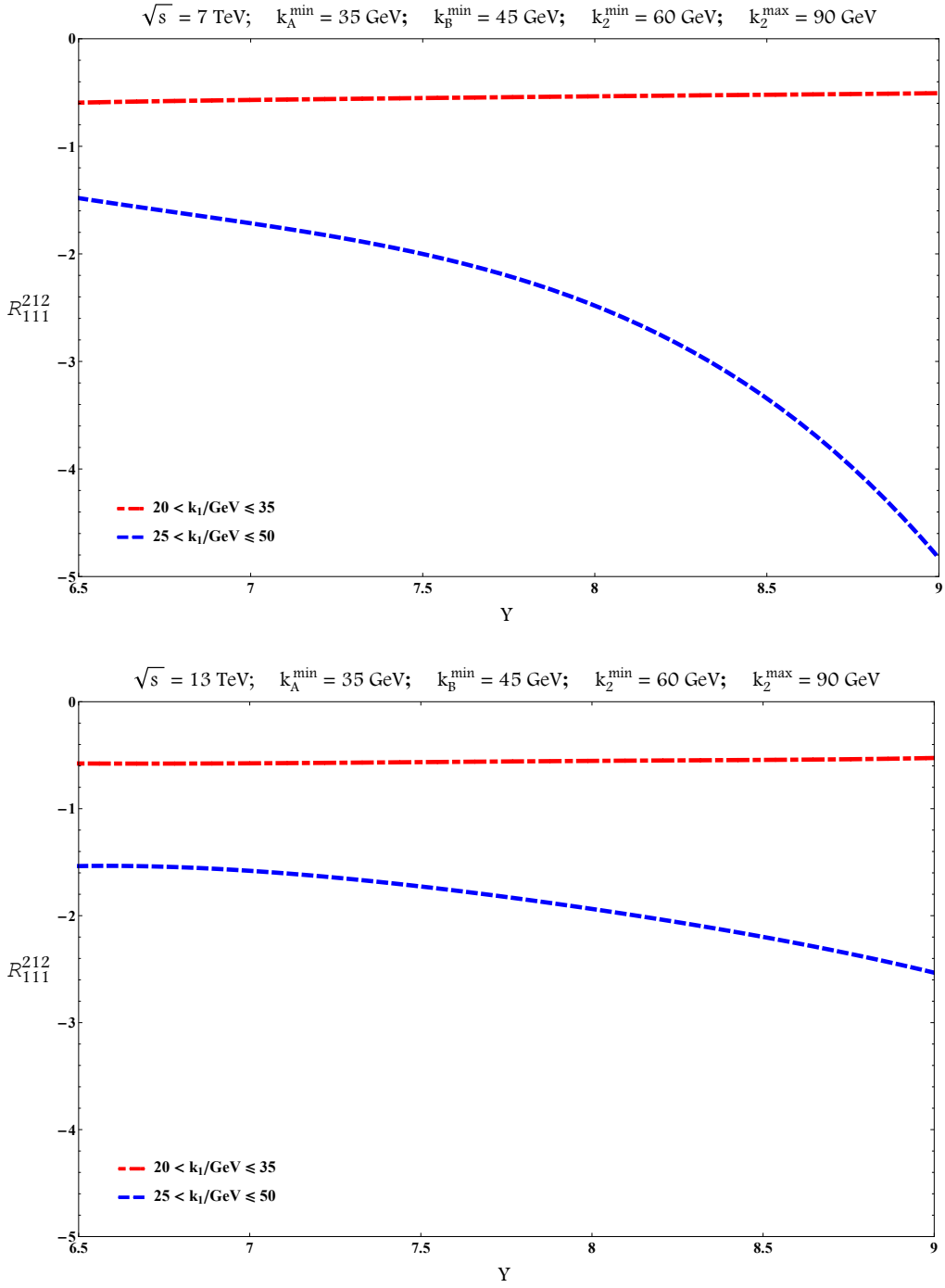

Figure 5.6: Y-dependence of R^{212}_{111} for $\sqrt{s} = 7$ TeV (top) and for $\sqrt{s} = 13$ TeV (bottom).

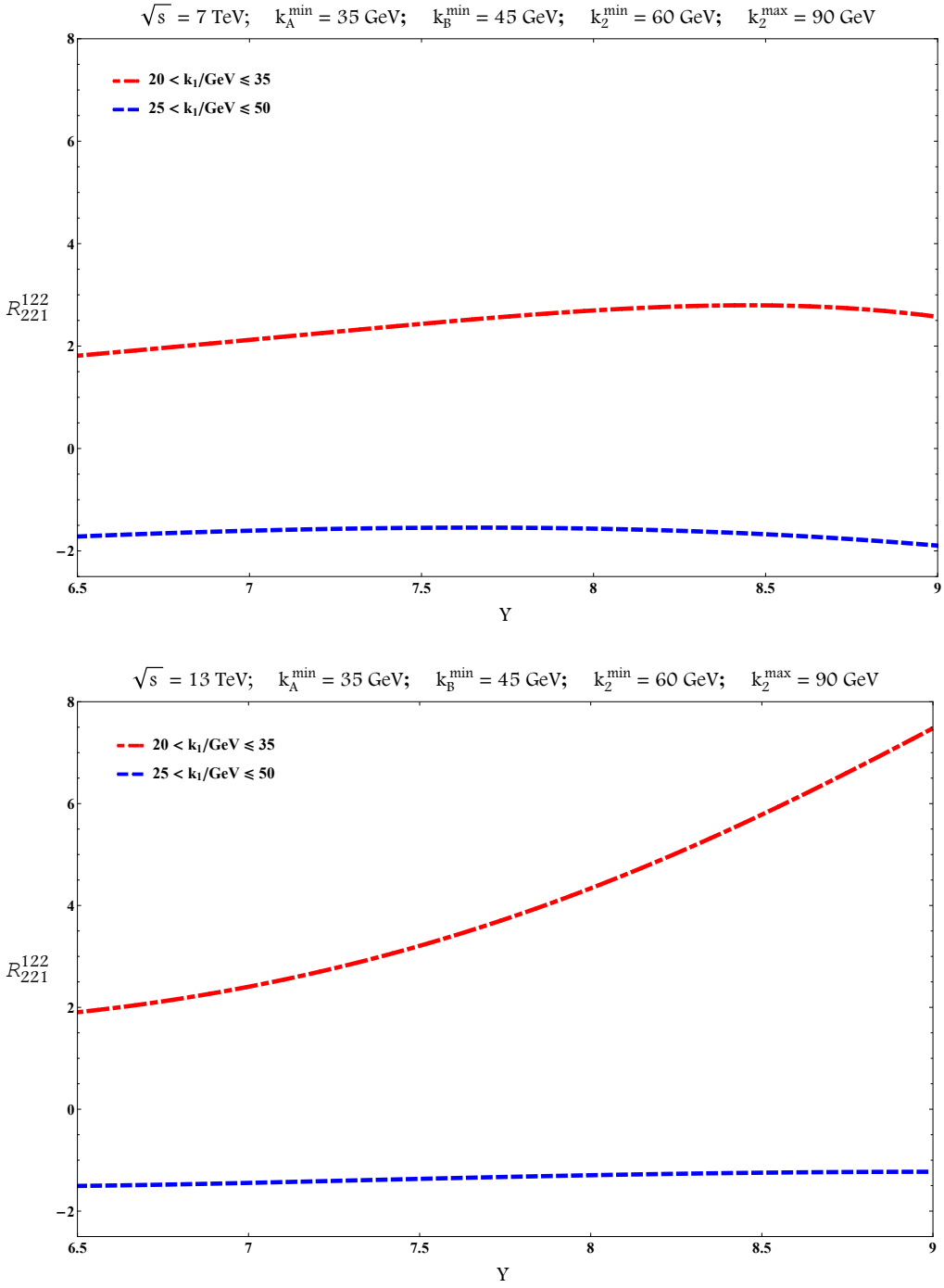

Figure 5.7: Y-dependence of R_{221}^{122} for $\sqrt{s} = 7$ TeV (top) and for $\sqrt{s} = 13$ TeV (bottom).

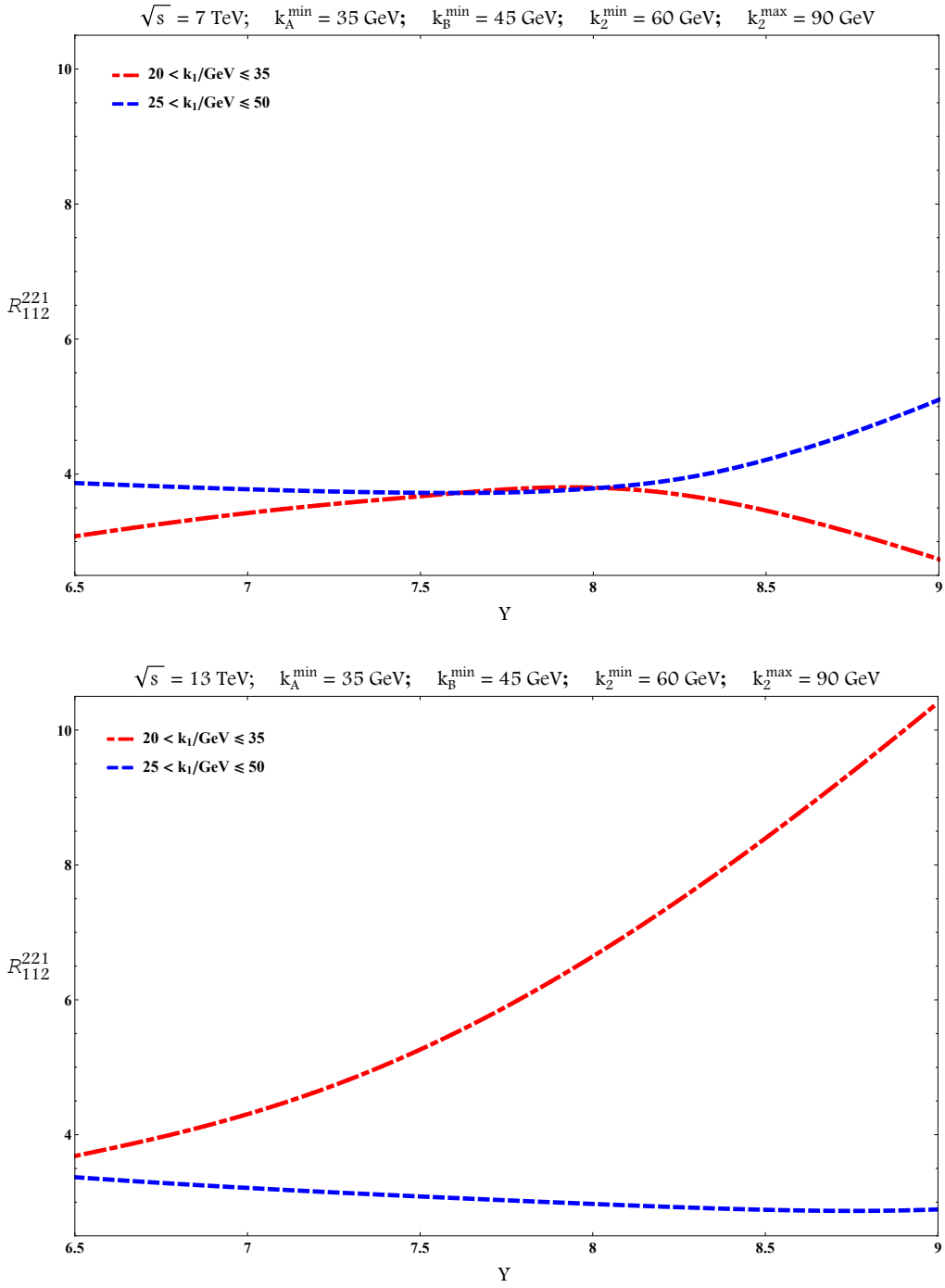

Figure 5.8: Y-dependence of R^{221}_{112} for $\sqrt{s} = 7$ TeV (top) and for $\sqrt{s} = 13$ TeV (bottom).

5.3 Summary

In this Chapter we have described a first phenomenological study for some aspects of the jets' azimuthal profile in LHC inclusive four-jet production within the BFKL resummation framework. Following up the work in Ref. [164], where a new set of BFKL probes was proposed for the LHC based on a partonic level study, we have calculated some of these observables here, after convoluting the previous results with parton distribution functions and imposing LHC kinematical cuts, at two different center-of-mass energies, $\sqrt{s} = 7, 13$ TeV.

We have chosen an asymmetric kinematical cut with respect to the transverse momenta of the most forward (k_A) and most backward (k_B) jet which is arguably a more interesting kinematical configuration that a symmetric cut since it allows for an easier distinction between BFKL and fixed order predictions [125, 133]. The asymmetry was realised by imposing different lower limits to k_A and k_B ($k_A^{min} = 35$ GeV and $k_B^{min} = 45$ GeV). Additionally, we demanded for k_2 to be larger than both k_A and k_B whereas the value of the transverse momentum k_1 was allowed to be either smaller than both k_A and k_B or overlapping the k_A and k_B range of values.

We have plotted six generalised-azimuthal-ratio observables, R^{111}_{221}, R^{112}_{111}, R^{112}_{211}, R^{212}_{111}, R^{122}_{221}, R^{221}_{112}, as a function of the rapidity distance Y between k_A and k_B for $6.5 < Y < 9$. A smooth functional dependence of the ratios on Y appears to be the rule. It is noteworthy that the plots for ratios we presented exhibit in some cases considerable change when the colliding energy increases from 7 to 13 TeV. This tells us that pre-asymptotic effects do play a role for the azimuthal ratios in inclusive four-jet production. A comparison with predictions for these observables from fixed order analyses as well as from the BFKL inspired Monte-Carlo `BFKLex` [180–186] seems to be the logical next step. Predictions from multi-purpose Monte-Carlos tools should also be pursued.

We will conclude our discussion by stressing that it would be very interesting to have an experimental analysis for these observables using existing and future LHC data. We have the strong belief that such an analysis will be a big step forward to the direction of gauging the applicability, at present energies, of the BFKL dynamics in phenomenological studies.

CHAPTER 6

FORWARD DRELL-YAN PRODUCTION AT THE LHC IN THE BFKL FORMALISM WITH COLLINEAR CORRECTIONS

In this chapter, we conclude Part I slightly deviating from the main guideline followed so far. As we discussed in Sec. 1.2.3, there is a factorization scheme more suited for the small-x regime, the so-called $k_\perp$ factorization. In this scheme, we make use an unintegrated PDF (uPDF) for the gluoninc partons, which evolution in $\log(1/x)$ is described by the BFKL equation. Since the uPDF, $\mathcal{G}(x_g, \kappa_T^2)$, describes the transverse momentum of the partonic gluon in addition to the longitudinal momentum fraction, the theoretical modeling program is not as mature as for the usual collinear PDFs.

Motivated by the recent work of Brzemiński, Motyka, Sadzikowski and Stebel in [194], where forward Drell-Yan production is studied in proton-proton collisions at the LHC, we improve their calculation by introducing an unintegrated gluon density obtained in [75, 76] from a fit to combined HERA data at small values of Bjorken x. This gluon density was calculated within the BFKL formalism at next-to-leading order with collinear corrections. We show that it generates a good description of the forward Drell-Yan cross section dependence on the invariant mass of the lepton pair both for LHCb and ATLAS data.

For many years forward Drell-Yan (DY) production at hadron colliders [195–203] has been proposed as an interesting observable to prove the unintegrated gluon density in the proton at very small values of Bjorken-x [204, 205]. In the recent work of Brzemiński, Motyka, Sadzikowski and Stebel in [194] this observable has been studied in the context

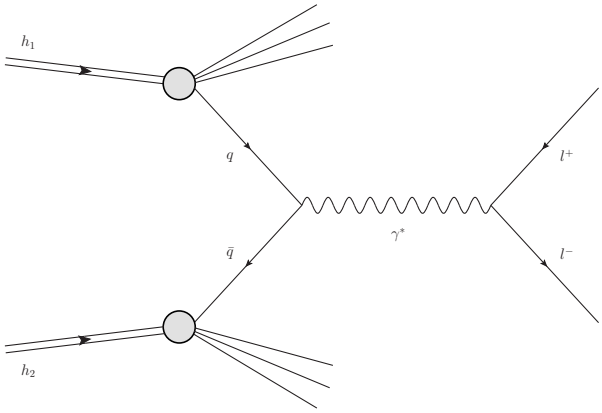

Figure 6.1: Drell-Yan dilepton production at leading order.

of high energy resummations at small x. They investigated this process in proton-proton scattering at the LHC with $\sqrt{s} = 14$ TeV. Their focus lied on the dipole formalism with saturation corrections, using the Golec-Biernat-Wüsthoff model [71, 72], or without them, making use of the Balitsky-Fadin-Kuraev-Lipatov (BFKL) approach at leading order (LO). Their investigations centered around the idea of what is the different twist content in each approach (see also their previous related work in [206]).

In the present chapter we shift the focus showing that it is possible to obtain a good description of the latest DY data for small values of the lepton pair masses when an unintegrated gluon density calculated within the next-to-leading order (NLO) BFKL formalism with collinear corrections is used. This shows that it is possible to obtain a correct description of HERA structure functions F_2 and F_L together with LHC DY data using a common approach based on the NLO BFKL formalism. Our calculation is particularly relevant in the low DY pair mass region, where we focus the discussion. The results here presented should also be compared to those in [207–210].

To be more precise, we study the production of a lepton-antilepton pair, L^+L^-, in proton-proton (pp) collisions as shown in Fig. 6.1 with notation

$$p(P_1) + p(P_2) \to L^+(l^+) + L^-(l^-) + X \tag{6.1}$$

where X indicates any inclusive secondary radiation. At leading order in the electroweak coupling this process is mediated by a virtual photon $\gamma^*(q)$ or a $Z^0(q)$ boson, where the vector boson momentum $q = l^+ + l^-$ carries a q_T transverse component. $M^2 \equiv q^2 > 0$ corresponds to the lepton pair invariant mass squared. The angular distributions of the lepton pair can be expressed in terms of four independent structure functions, $\mathcal{W}_{[\lambda]}$. The DY standard formulation [211] allows for a factorization between the lepton pair angular

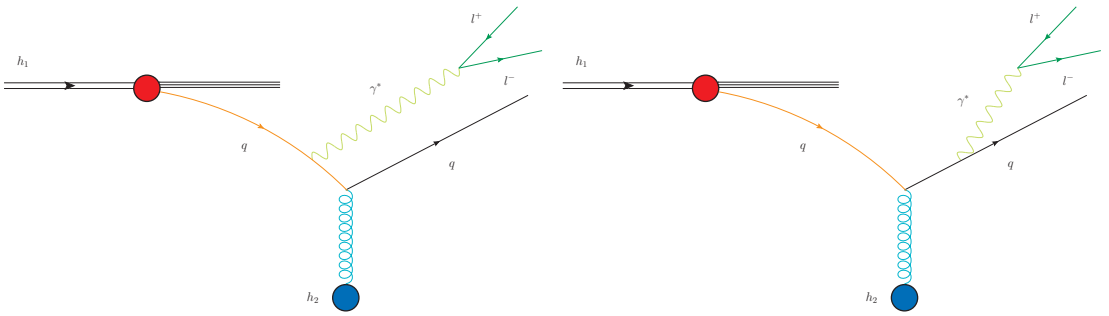

Figure 6.2: Compton scattering diagrams for DY dilepton forward production.

phase space $\mathrm{d}\vartheta^*\,\mathrm{d}\varphi^* \equiv \mathrm{d}\Omega_l^*$, where ϑ^* and φ^* are the polar and azimuthal angles of the lepton momentum vector in the dilepton center-of-mass frame, and the structure functions, defined as projections of the DY amplitudes on the exchanged boson.

In the present work we neglect the Z^0 contribution which is only relevant at higher M^2 (we will also show the experimental data points at the highest values of M^2 just to gauge the importance of the missing diagrams). The DY differential cross section hence reads

$$\frac{\mathrm{d}\sigma}{\mathrm{d}M\,\mathrm{d}\Omega_l^*\,\mathrm{d}x_F\,\mathrm{d}q_T} = \frac{\alpha^2 q_T}{(2\pi M)^3}\left[\left(1-\cos^2\vartheta^*\right)\mathcal{W}_L + \left(1+\cos^2\vartheta^*\right)\mathcal{W}_T + \left(\sin 2\vartheta^*\cos\varphi^*\right)\mathcal{W}_\Delta + \left(\sin^2\vartheta^*\cos 2\varphi^*\right)\mathcal{W}_{\Delta\Delta}\right], \tag{6.2}$$

where x_F stands for the Feynman variable representing the longitudinal momentum fraction from the initial-state hadron carried by the virtual photon, α is the electromagnetic coupling constant, $\mathcal{W}_L$ and $\mathcal{W}_T$ are structure functions for longitudinally and transversely polarized virtual photons, respectively, $\mathcal{W}_\Delta$ is the single-spin-flip structure function, and $\mathcal{W}_{\Delta\Delta}$ is the double-spin-flip one. The frame orientation is not unique and determines the form of the structure functions. In this work the choice of the Gottfried–Jackson frame [212], with the Z axis anti-parallel to the target's momentum and the Y axis orthogonal to the reaction plane, is employed.

In the high energy factorization approach, it is possible to write the structure functions as the convolution

$$\mathcal{W}_{[\lambda]} = \frac{2\pi}{3}\alpha_s(\mu_R)M^2\int_{x_F}^1 \frac{\mathrm{d}z}{z^2} f^*\left(\frac{x_F}{z},\mu_F\right)\int \frac{\mathrm{d}\kappa_T\mathrm{d}\phi_{\kappa_T}}{\left(\kappa_T^2\right)^2}\mathcal{G}(x_g,\kappa_T^2)\Phi_{[\lambda]}(q_T,\vec{\kappa}_T,z). \tag{6.3}$$

z is the longitudinal momentum fraction of the initial-state quark carried by the virtual photon, $\kappa_T \equiv |\vec{\kappa_T}|$ and $q_T \equiv |\vec{q_T}|$. We use a collinear parton distribution function, $f^*\left(x,\mu_F\right) = \sum_r f_r\left(x,\mu_F\right)$ which accounts for the incident u, d, s, c and b quarks and corresponding antiquarks with a high-x value (orange lines in Fig. 6.2).

We also have an unintegrated, transverse momentum dependent, gluon distribution function, $\mathcal{G}(x_g, \kappa_T^2)$, carrying all the information about the small-x gluon evolution (blue lines in Fig. 6.2), and the forward DY impact factors, $\Phi_{[\lambda]}(q_T, \vec{\kappa}_T, z)$, accounting for the $\gamma^* \to L^+L^-$ transition. The gluon longitudinal momentum fraction x_g follows from the forward DY kinematics in the $qg^* \to q\gamma^*$ channel, *i.e.* (with $s = (P_1 + P_2)^2$ being the center-of-mass energy squared)

$$x_g = \frac{M^2(1-z) + q_T^2 + z(\kappa_T^2 - 2\vec{\kappa}_T \cdot \vec{q}_T)}{s\, x_F\, (1-z)} \approx \frac{M^2(1-z) + q_T^2}{s\, x_F\, (1-z)}. \tag{6.4}$$

After this brief Introduction regarding the process of interest and our calculational set up, we now give some details related to the unintegrated gluon density used in our calculations and the structure of the forward impact factors. We then present our results and Summary.

6.1 Unintegrated gluon distribution and forward impact factors

The standard definition of the small-x transverse momentum dependent gluon distribution, better known as unintegrated gluon distribution, relies on the convolution between the universal BFKL gluon Green's function, which takes into account the resummation of high-energy logarithms, and the proton impact factor, which describes the coupling of the gluon Green's function to the proton. This proton impact factor is characterized by large transverse scales and therefore, being of non-perturbative nature, needs to be modeled.

We use the three-parameter model for the coupling of the gluon Green's function and the proton put forward in the study of deep inelastic scattering structure functions in [75, 76]. More recently, it has been used to investigate single-bottom quark production at the LHC [213], J/Ψ and Υ photoprotoduction [214] and ρ-meson leptoproduction at HERA [215]. In transverse momentum space, it simply reads

$$\Phi_p(q, Q_0^2) = \frac{\mathcal{C}}{2\pi\Gamma(\delta)} \left(\frac{q^2}{Q_0^2}\right)^{\delta} e^{-\frac{q^2}{Q_0^2}} \tag{6.5}$$

having a maximum at $p^2 = \delta Q_0^2$. The values of the parameters $Q_0 = 0.28$ GeV, $\delta = 8.4$ and $\mathcal{C} = 1.50$, were obtained from a fit to combined HERA data [75, 76] when the leading order photon impact factor was used. Since we are also using a leading order calculation for the vertex producing the DY pair, it is consistent to use the same set of parameters in our current analysis.

Combining Eq. (6.5) with the gluon Green's function, we obtain the following expression for the unintegrated gluon density:

$$\begin{aligned}\mathcal{G}(x,\kappa^2,\mu_H) = \int_{-\infty}^{\infty}\frac{d\nu}{2\pi^2}\,\mathscr{C}\,\frac{\Gamma(\delta-i\nu-\frac{1}{2})}{\Gamma(\delta)}\left(\frac{1}{x}\right)^{\chi(\frac{1}{2}+i\nu)}\left(\frac{\kappa^2}{Q_0^2}\right)^{\frac{1}{2}+i\nu}\times \\ \times\left\{1+\frac{\bar{\alpha}_s^2\beta_0\chi_0\left(\frac{1}{2}+i\nu\right)}{8N_c}\log\left(\frac{1}{x}\right)\left[-\psi\left(\delta-\frac{1}{2}-i\nu\right)-\log\frac{\kappa^2}{\mu_H^2}\right]\right\},\end{aligned} \tag{6.6}$$

with $\beta_0=\frac{11N_c-2N_f}{3}$ the first coefficient of the QCD β-function, $N_f=5$, $\bar{\alpha}_s\equiv N_c/\pi\alpha_s\left(\mu^2\right)$, and $\mu^2=\mu_H Q_0$. $\chi_0(\gamma)=2\psi(1)-\psi(\gamma)-\psi(1-\gamma)$, with $\gamma\equiv\frac{1}{2}+i\nu$, is the LO eigenvalue of the BFKL kernel and $\psi(z)=\Gamma'(z)/\Gamma(z)$. μ_H is a characteristic hard scale which can be set equal to the photon invariant mass, M. Finally, $\chi(\gamma)$ is the NLO eigenvalue of the BFKL kernel,

$$\chi(\gamma)=\bar{\alpha}_s\chi_0(\gamma)+\bar{\alpha}_s^2\chi_1(\gamma)-\frac{1}{2}\bar{\alpha}_s^2\chi_0'(\gamma)\chi_0(\gamma)+\chi_{RG}(\bar{\alpha}_s,\gamma), \tag{6.7}$$

with $\chi_1(\gamma)$ and $\chi_{RG}(\bar{\alpha}_s,\gamma)$ (which includes the collinear corrections resummed in the form of a Bessel function as calculated in [216]) given in Section 2 of Ref. [213], to which we refer for further details (also on the particular treatment of the running of the coupling).

For completeness, we now briefly write down the expressions for the forward dilepton impact factors used in our work. In κ_T-representation they can be computed combining Eq. (3.5) with Eqs. (3.12) and (3.13) of Ref. [206], and applying the relations given in Eqs. (3.24)-(3.27) of the same Reference, *i.e.*

$$\Phi_L(q_T,\vec{\kappa}_T,z)=\frac{2M^2(1-z)^2z^2((z\vec{\kappa}_T-2\vec{q}_T)\cdot\vec{\kappa}_T)^2}{[M^2(1-z)+q_T^2]^2[M^2(1-z)+(\vec{q}_T-z\vec{\kappa}_T)^2]^2}, \tag{6.8}$$

$$\begin{aligned}\Phi_T(q_T,\vec{\kappa}_T,z)=\frac{1+(1-z)^2}{2}\left[\frac{(q_T-z\kappa_x)^2-z^2\kappa_y^2}{[M^2(1-z)+(\vec{q}_T-z\vec{\kappa}_T)^2]^2}+\right. \\ \left.+\frac{q_T^2}{[M^2(1-z)+q_T^2]^2}+\frac{2q_T(z\kappa_x-q_T)}{[M^2(1-z)+q_T^2][M^2(1-z)+(\vec{q}_T-z\vec{\kappa}_T)^2]}\right],\end{aligned} \tag{6.9}$$

$$\begin{aligned}\Phi_\Delta(q_T,\vec{\kappa}_T,z)=\left(q_T(z\vec{\kappa}_T-2\vec{q}_T)\cdot\vec{\kappa}_T+\kappa_x(M^2(1-z)+q_T^2)\right)\times \\ \times\frac{M(2-z)(1-z)z^2(z\vec{\kappa}_T-2\vec{q}_T)\cdot\vec{\kappa}_T}{[M^2(1-z)+q_T^2]^2[M^2(1-z)+(\vec{q}_T-z\vec{\kappa}_T)^2]^2},\end{aligned} \tag{6.10}$$

$$\begin{aligned}\Phi_{\Delta\Delta}(q_T,\vec{\kappa}_T,z)=(z-1)\left[\frac{(q_T-z\kappa_x)^2-z^2\kappa_y^2}{[M^2(1-z)+(\vec{q}_T-z\vec{\kappa}_T)^2]^2}+\right. \\ \left.+\frac{q_T^2}{[M^2(1-z)+q_T^2]^2}+\frac{2q_T(z\kappa_x-q_T)}{[M^2(1-z)+q_T^2][M^2(1-z)+(\vec{q}_T-z\vec{\kappa}_T)^2]}\right],\end{aligned} \tag{6.11}$$

where $\kappa_x \equiv \kappa_T \cos\phi_{\kappa_T}$, $\kappa_y \equiv \kappa_T \sin\phi_{\kappa_T}$ and $\vec{q}_T \cdot \vec{\kappa_T} \equiv q_T \kappa_T \cos\phi_{\kappa_T}$.

Before moving forward to presenting our results together with the LHC data, let us indicate that, for comparison, we will present and compare our results with a LO BFKL model defined within the color dipole approach [217–220], which has also been used in the work of Motyka et al in [194]. Analogously to the formula given in Eq. (6.3), it is possible to write expressions for the helicity structure functions as the convolution

$$\mathcal{W}_{[\lambda]} = \int_{x_F}^{1} \mathrm{d}z\, f^*\left(\frac{x_F}{z}, \mu_F\right) \int_{\frac{1}{2}-i\infty}^{\frac{1}{2}+i\infty} \frac{\mathrm{d}\gamma}{2\pi i}\, \hat{\sigma}(\gamma) \left[\frac{z^2 \hat{Q}_0^2}{M^2(1-z)}\right]^{\gamma} \hat{\Phi}_{[\lambda]}(q_T, \gamma, z)\,, \tag{6.12}$$

where $f^*\left(\frac{x_F}{z}, \mu_F\right)$ is the collinear quark parton distribution functions defined right below Eq. (6.3), $\hat{\sigma}(\gamma)$ is the dipole proton cross section calculated in Mellin space, $\hat{Q}_0$ is the scale transform parameter and $\hat{\Phi}_{[\lambda]}(q_T, \gamma, z)$ are the Mellin-transformed impact factors, originally calculated in Ref. [206] (see Eqs. (3.32)-(3.35) of the same Reference for their analytic expressions). As a LO BFKL model for the dipole cross section we follow [194] and use

$$\hat{\sigma}(\gamma) \equiv \hat{\sigma}_{\mathrm{LL}}(\gamma) = -\hat{\sigma}_0\, \Gamma(-\gamma)\, e^{\bar{\alpha}_s \chi_0(\gamma) y}\,, \tag{6.13}$$

where $y = \log\left(\frac{x_A}{x_g}\right)$ with $x_A = 0.1$ and $x_g = \frac{M^2(1-z)+q_T^2}{s\, x_F (1-z)}$ is the evolution length in rapidity. The relevant parameters are fixed by a fit to the deep inelastic scattering data [221]: $\hat{Q}_0 = 0.51$ GeV, $\hat{\sigma}_0 = 17.04$ mb, $\bar{\alpha}_s = 0.087$, while running-coupling effects are neglected.

We now present the results of our calculations.

6.2 Results and comparison to data

We are interested in the study of the dependence on the dilepton invariant mass M of the forward Drell-Yan cross section (Eq. (6.2)):

$$\frac{\mathrm{d}\sigma(M)}{\mathrm{d}M} = \int \mathrm{d}\Omega_l^* \int \mathrm{d}x_F \int \mathrm{d}q_T\, \frac{\mathrm{d}\sigma}{\mathrm{d}M\, \mathrm{d}\Omega_l^*\, \mathrm{d}x_F\, \mathrm{d}q_T}\,. \tag{6.14}$$

We will also provide predictions for the total cross section averaged on bins in the M variable. In order to match the kinematical cuts on the dilepton phase space used by the LHCb collaboration [222] it is needed to perform a Lorentz boost from the dilepton frame to the collision center-of-mass frame. The corresponding boost parameters are

$$\gamma_{\mathrm{B}} = \frac{x_F \sqrt{s}}{2M} \beta^+\,, \quad \vec{v}_{\mathrm{B}} = -\left(\frac{\vec{q}_T}{\gamma_{\mathrm{B}} M}, \frac{\beta^-}{\beta^+}\right)_{x,y,z} \tag{6.15}$$

with $\beta^{\pm} = 1 \pm \frac{M^2+q_T^2}{s\,x_F^2}$. We can now give expressions for the lepton momenta in the collision frame:

$$l^{\pm} \equiv |\vec{l}^{\pm}| = E^{\pm} = \frac{\gamma_B M}{2}\left(1 \mp \vec{v}_B \cdot \vec{u}_{\Omega_l^*}\right), \tag{6.16}$$

$$l^{z,\pm} = \frac{M}{2}\left[\pm\cos\theta^* + \gamma_B \frac{\beta^-}{\beta^+}\left(1 \mp \frac{\vec{v}_B \cdot \vec{u}_{\Omega_l^*}}{1+\gamma_B^{-1}}\right)\right], \tag{6.17}$$

where $\vec{u}_{\Omega_l^*}$ is a unit vector pointing in the Ω_l^* direction. The scalar product $\vec{v}_{\rm B} \cdot \vec{u}_{\Omega_l^*}$ can be written in the form

$$\vec{v}_{\rm B} \cdot \vec{u}_{\Omega_l^*} = -\frac{\beta^-}{\beta^+}\cos\vartheta^* - \frac{q_T}{\gamma_{\rm B} M}\sin\vartheta^*\cos\varphi^* . \tag{6.18}$$

Considering the relation between the lepton transverse momentum $l_T^{\pm}$ and rapidity $\eta^{\pm}$ with the remaining relevant variables,

$$l_T^{\pm} \equiv |\vec{l}_T^{\pm}| = \left(l^{\pm}\right)^2 - \left(l^{z,\pm}\right)^2 \;,\; \eta^{\pm} = \operatorname{arctanh}\frac{l^{z,\pm}}{l^{\pm}}, \tag{6.19}$$

we have all the necessary ingredients needed to impose the kinematical cuts set by the LHCb collaboration [222], *i.e.*

$$2 < \eta^{\pm} < 4.5\,, \quad l^{\pm} > 10\ \text{GeV}\,, \quad \begin{cases} l_T^{\pm} > 3\ \text{GeV} & \text{if} \quad M \le 40\ \text{GeV} \\ l_T^{\pm} > 15\ \text{GeV} & \text{if} \quad M > 40\ \text{GeV} \end{cases} \tag{6.20}$$

with the dilepton invariant mass in the range $5.5\ \text{GeV} < M < 120\ \text{GeV}$. For comparison, we give predictions also in the ATLAS kinematics [196, 223], which, however, are constrained to more central rapidity ranges than the LHCb experiment. In the ATLAS configuration, we have

$$|\eta^{\pm}| < 2.4 \;,\; l_T^{\pm} > 6\ \text{GeV} \;,\; l_T^{+} > 9\ \text{GeV or } l_T^{-} > 9\ \text{GeV}, \tag{6.21}$$

with the dilepton invariant mass in the range $12\ \text{GeV} < M < 66\ \text{GeV}$. We expect our formalism to be more accurate when describing the LHCb data than the ATLAS data since it corresponds to a more forward kinematics.

We have used FORTRAN for our numerical analysis, in particular the `Vegas` integrator [175] as implemented in the `Cuba` library [176, 177] and specific `Cernlib` routines [224]. A two-loop running coupling with $\alpha_s(M_Z) = 0.11707$ and five active quark flavors was also chosen. The NLO `Mmht` 2014 sets [225] were used, as provided by the `Lhapdf` Interface 6.2.1 [226], to calculate the collinear quark parton distribution functions. In the calculation

of the unintegrated gluon density, the uncertainty stemming from the numerical multi-dimensional integration when combining Eqs. (6.2) and (6.14) with Eq. (6.3) or Eq. (6.12) was steadily held below 0.5%. The error bands of all the presented results were calculated by varying the factorization scale[1] in the range $M/4 \leq \mu_F \leq 4M$, while the renormalization scale μ_R was fixed to M.

We present our results in Fig. 6.3 where we show how, in the lower plot, the outcome of our calculations is very close to the LHCb data points in the full range of M values. In the same plot we also draw the line corresponding to the calculation in the dipole model approach with LO BFKL evolution and fixed running coupling, which lies well above the experiment results. For the sake of showing the universality of the model here presented, in the upper plot within the same figure, we reproduce the description given in [75, 76] for the Q^2 dependence of the energy growth of the F_2 HERA structure function of the proton at small values of Bjorken x when expressed in the form $F_2 \simeq x^{-\lambda(Q^2)}$. Since, for simplicity, we do not include Z-boson production diagrams we lie slightly below the data for larger values of the DY invariant mass M.

The equivalent comparison to ATLAS data is presented in Fig. 6.4, which, as we have already mentioned, does not allow for a very forward production of the DY pair. Nevertheless, we obtain a good description of the data, even though the uncertainty band associated to changes in the factorization scale is rather large. Lower values of this scale seem to be preferred by the data as extracted from both experiments.

Before presenting our Conclusions let us show the comparison of the LHCb data with the cross section averaged on dilepton invariant mass bins. These provides a somehow more fair matching with the experimental presentation of the results. This can be seen in Fig. 6.5.

[1] In Ref. [194] the factorization scale was set equal to the transverse mass of the exchanged boson, $\mu_F = M_T \equiv \sqrt{M^2 + q_T^2}$. We checked that the effect of using this choice with respect to ours is negligible.

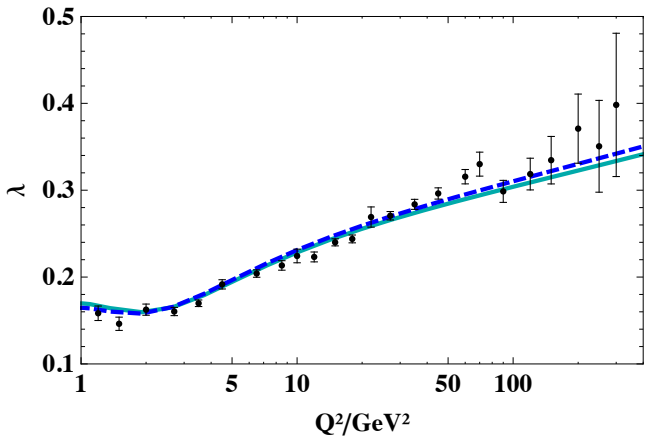

a) Fit of the effective intercept λ in $F_2 \simeq x^{-\lambda(Q^2)}$ for small x HERA data.

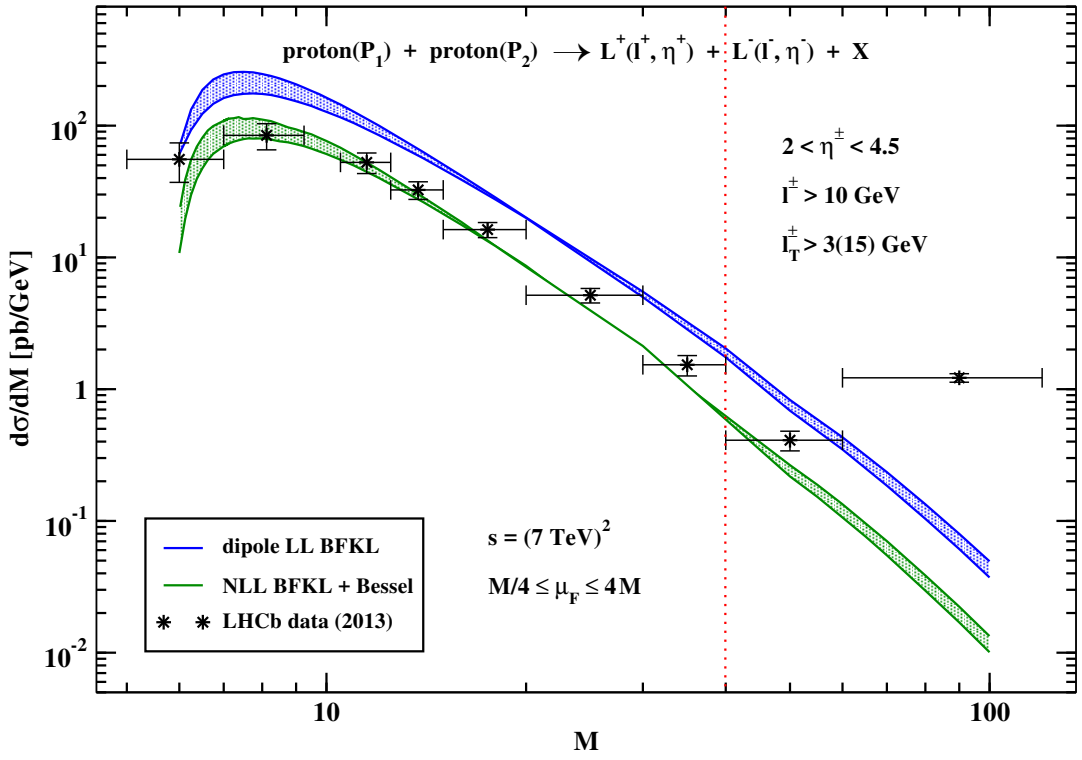

b) M dependence of the Drell-Yan differential cross section.

Figure 6.3: Comparing experimental data with higher-order BFKL predictions for two different colliders. First (top panel, plot from Ref. [75, 76]), the fit of the effective intercept λ of F_2 to HERA data [227]. Solid and dashed lines refer to the LO photon impact factor and a kinematically improved one, respectively. Then (bottom panel), the Drell-Yan differential cross section is given as a function of the dilepton invariant mass M. The NLO BFKL prediction with collinear corrections is compared with a LO dipole model and with LHCb data [222]. Uncertainty bands account for changes in the factorization scale in the range $M/4 \leq \mu_F \leq 4M$.

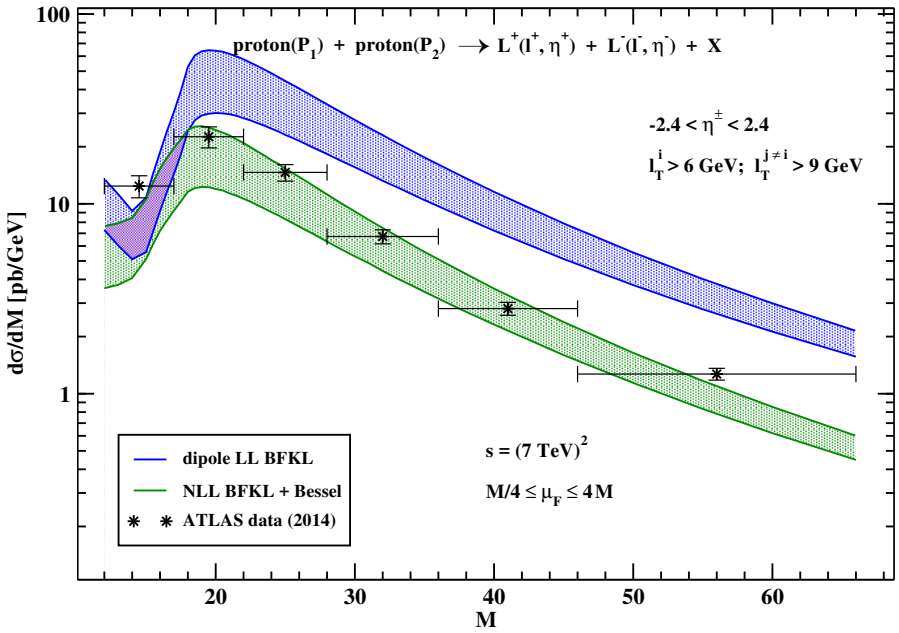

Figure 6.4: Matching ATLAS data [196, 223] with higher-order BFKL predictions. Uncertainty bands are given as the effect of allowing the factorization scale to be in the range $M/4 \leq \mu_F \leq 4M$.

6.3 Summary

Building up on previous work on forward production of Drell-Yan pairs at the LHC in [194], we propose to use the BFKL formalism at next-to-leading order with collinear corrections to describe the LHCb and ATLAS data. We make use of the idea of high energy factorization and show that the same unintegrated gluon density as obtained from a fit of HERA data at small values of Bjorken x provides a good description of the LHC data. This is an encouraging result from the point of view of the BFKL approach since this type of global description of different processes is expected from this framework. Nevertheless, the same data can be also described by a fixed order calculation and this observable needs to be pushed experimentally further to really test different theoretical calculations. This also includes the description of the data in [194] which makes use of saturation corrections. Future LHC data for Drell-Yan production in forward directions [129] will be very useful to gauge the need of high energy resummations in Quantum Field Theory.

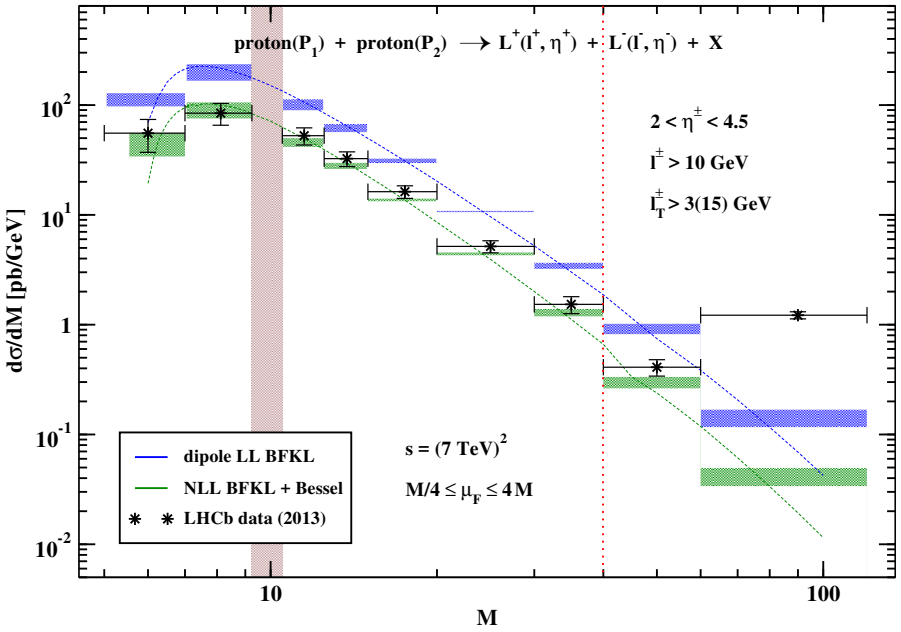

Figure 6.5: Differential Drell-Yan cross section averaged over bins of the dilepton invariant mass M. The NLO BFKL with collinear corrections prediction is compared with a LO dipole model calculation and with LHCb data [222]. Uncertainty bands account for changes in the factorization scale in the range $M/4 \leq \mu_F \leq 4M$. Dashed lines show the M dependence with $\mu_F = M$.

CHAPTER 7

CONCLUSIONS AND OUTLOOK

In the first Part of the Thesis we have explored the richness of BFKL phenomenology. The advent of the LHC has brought us the access to higher energies, the basic requirement to test high-energy resummations; and an previously unseen amount of data, which allows us to measure more exclusive observables with statistical confidence. Bearing that in mind, we have studied different observables at present LHC capabilities.

One problem when dealing with higher order corrections in the BFKL framework, is that the NLLA corrections to BFKL equation are considerably large, leading to instabilities in the perturbative expansion. There has been several proposals to reduce the effects of the non-resummed logarithms, as collinear improvements or different prescription to choose the renormalization scale. In Chapter 2, we have explored the possibility of introducing a rough constant cut-off in the rapidity differences among emitted mini jets in the final state. Previously, this idea was had been only tested in formal studies based on the asymptotic behavior of the gluon Green's function alone, which is not the case in present collider experiments. By comparing to current LHC data we have found that it is possible to get a reasonable global description of many different azimuthal angle correlations in dijet cross sections with a rapidity veto $b \gtrsim 1$. This value is far from previous studies, around $b \gtrsim 2$, and it depends on the actual rapidity difference. This shows how far we are from the asymptotic region at collider energies (of order 10 TeV) and give an estimate of the collider regions that need to be taken into account to accurately describe the experiments. A connection with the success of the BLM approach to set the renomalization scale can be make here, since it provides another way of setting the higher-order corrections by a

redefinition of the Landau pole. As a future way of testing the idea of the rapidity veto, it would be important to describe another observable using the values that we obtained in this fitting.

In the exploration of more exclusive observables, during Chapters 3 and 4 we have presented a first complete phenomenological study at LLA and NLLA of inclusive three-jet production at the LHC within the BFKL framework. While in Chapter 5 we extended the LLA results to the 4-jet production. Together with the usual two forward/backward jets present in Mueller-Navelet events, we ask for one/two additional hard jets in more central regions of rapidity. By demanding a strong ordering in rapidity among the jets, according to Multi Regge Kinematics, we generalized the Mueller-Navelet formalism to account for high-energy resummation effects. This allowed us to define new, suitable BFKL observables, sensitive to the azimuthal configurations of the tagged extra particles. We considered two colliding energies, $\sqrt{s} = 7, 13$ TeV and an asymmetric kinematic cut with respect to the transverse momentum of the forward (k_A) and backward (k_B) jets, compatible with the experimental studies performed so far by CMS in [135, 136]. The general conclusion is that the NLLA corrections are moderate and our proposed observables exhibit a good perturbative stability. Furthermore, we see that for a wide range of rapidities, the changes we notice when going from 7 TeV to 13 TeV are small which makes us confident that these generalized ratios pinpoint the crucial characteristics of the BFKL dynamics regarding the azimuthal behavior of the hard jets in inclusive three-jet production. For the 4-jets case, it is noteworthy that the plots for ratios we presented exhibit in some cases considerable change when the colliding energy increases from 7 to 13 TeV. This tells us that pre-asymptotic effects do play a role for the azimuthal ratios in inclusive four-jet production.

As a future and ongoing work, it will be very interesting to compare with possible predictions for these observables from fixed order analyses as well as from the BFKL inspired Monte-Carlo `BFKLex` [180–186, 189] and general-purpose Monte-Carlos tools. Most importantly though, we encourage experimental collaborations to consider an analysis of these observables using the existing and future LHC data. It would also serve as a very good test of models describing multiple interactions and to gauge how important those effects can be. In the future, there will be access to larger rapidity differences, thanks to the CASTOR detector, that probes rapidities up to 6.6, so predictions for this new kinematical set will be pursued.

In addition to that, we are investigating even more exclusive observables, based on describing the statistical features of the minijet radiation in between two Mueller-Navelet jets. The multiplicity of the events, and its distribution in azimuthal angle and transverse momentum, should be different in DGLAP and BFKL regimes, so comparing predictions

of BFKLex with general purpose Monte-Carlo event generators should shed light on the correct physics to describe high multiplicity events.

We finalized Part I of this Thesis moving to a different process, forward production of Drell-Yan pairs at the LHC. Building up on previous work on the same process in [194], we applied the BFKL formalism at NLLA to describe the LHCb and ATLAS data. In this case, we use collinear corrections as a way of resumming higher order corrections beyond NLLA. This process allowed us to test $k_\perp$ factorization at small-x, since we used the same unintegrated gluon density as obtained from a fit of HERA data, obtaining a good description of the LHC data, at much higher energies. This is an encouraging result, since it is a demonstration of the universality of the impact factors used in high-energy factorization. Nevertheless, the same data can be also described by a fixed order calculation and this observable needs to be pushed to higher energies to really discern between different theoretical descriptions. Future LHC data for Drell-Yan production in forward directions [129] will be very useful to gauge the need of high energy resummations in Quantum Field Theory.

Part II

Formal Aspects

CHAPTER 8

PRELIMINARIES

Quantum field theory was born due to need to unify special relativity and quantum mechanics and it was realized, after a long period full of experiments and theoretical developments, that it is an appropriate framework [228] to understand processes involving fundamental particles, taking the place of the S-matrix program of the 60's in the goal to understand strong interactions. Scattering amplitudes have been essential in the understanding of quantum field theories, playing a central role as they constitute the building blocks for the construction of scattering cross sections determining the probabilities for scattering processes to occur at particle colliders. Scattering amplitudes are usually calculated in the context of perturbative Quantum Field Theory: from the Lagrangian we obtain the Feynman rules of the theory (that are gauge dependent), then we sum over all contributing diagrams (to obtain a gauge independent expression) and integrate over the internal loop momenta. This procedure, that in principle is straightforward, is not an easy task (specially at loop level) and even numerical results required by high precision experiments need a large amount of work.

In the case of gauge interactions, that are crucial for our understanding of nature, even at tree level the traditional approach based on Feynman diagrams becomes rather cumbersome even for simple cases. A very well known example is the Parke-Taylor [229] formula for n-gluon maximally helicity violating (MHV) amplitudes at tree level, a very simple formula when expressed in convenient variables, although the number of Feynman diagrams contributing to it grows as $n!$. A reason for the complexity of the Feynman diagrams calculation is that demanding to have manifest locality and unitarity leads

to the introduction of gauge redundancies and intermediate off-shell states in internal propagators. On the contrary, the amplitude is gauge invariant and only involves on-shell degrees of freedom. Furthermore, amplitudes can show symmetries that are not present in the Lagrangian (nor in the Feynman rules), and that constraint the structure of the final amplitude once we have summed over all diagrams, but not of the individual diagrams structure, making these symmetries very difficult to realize before studying the amplitudes.

The Feynman diagrams approach combined with the use of computers to do the calculation has been very fruitful, but sometimes numerical evaluation of amplitudes written in terms of Feynman diagrams is so slow that it is not a practical method, so it is important to try to obtain compact formulae for the expressions involved or recursion relations that allow us to make use of previous calculations. The presence of spurious poles [230] that cancel once we have summed over all diagrams originates big numerical errors, so compact analytical expressions for the amplitudes are required in practical applications.

In the past decade an enormous progress has been made in the field of scattering amplitudes, coming on the scene new tools that go beyond the traditional approaches. An on-shell formalism that focus on the analytic structure of the final result leads, in a large class of theories, to impressive recursion relations and eludes gauge redundancies, using three-point amplitudes as building blocks. Spinor helicity variables, perfectly suited for massless particles, avoid working with polarization vectors and have transparent transformations under helicity transformations (little group of the Lorentz group). At loop level, generalized unitarity methods provide us a way of calculating amplitudes from products of tree-level on-shell amplitudes and a basis of scalar integrals. This connection between loop amplitudes and on-shell tree level amplitudes highlighted the usefulness of on-shell objects to draw new insights into the study of scattering amplitudes. A complete introduction to those methods can be found in [231].

The starting point of these new developments is the discovery of the formulas commonly called on-shell or Britto-Cachazo-Feng-Witten (BCFW) recursion relations [232]. In order to exploit the analyticity properties of the tree-level scattering amplitudes we can make a linear momentum shift in complexified momentum space, depending on one complex parameter and keeping the momentum conservation and on-shell constraints; this makes the amplitudes a function of one complex variable and the whole complex analysis machinery can be applied to it. For a special class of theories which we will describe later, this construction allows us to write the n-point tree level on-shell amplitude in terms of lower point tree level on-shell amplitudes, i.e., we have a recursion relation involving on-shell amplitudes only. Avoiding the use of off-shell amplitudes allows us to circumvent unphysical degrees of freedom associated with gauge redundancies and virtual particles,

keeping formulae simpler than with the Feynman diagram approach. A straightforward corollary of this is that these theories can be described in terms of the minimal on-shell amplitude, that are the building blocks with which we can reconstruct all tree-level amplitudes, there is a notion of *constructability*. For example, pure Yang-Mills tree-level amplitudes are entirely determined by the tree-point on-shell amplitude (with external complex momenta), and the 4-gluon vertex can be seen as another gauge redundancy.

At loop level the situation gets more involved. In principle, scattering amplitudes at loop level are ill-defined, they require a regularization scheme due to the so-called ultraviolet (UV) and infrared (IR) divergences. Also, the analytic structure of the S-matrix, seen as a function of the external momenta, includes new type of singularities with respect to the tree level ones, branch cuts appear in addition to the poles present at tree level. The *unitarity method* [233] started as a tool for one-loop calculations that takes advantage of the unitarity of the S-matrix and its singularities. Rather than an expansion in terms of Feynman diagrams including loops, the amplitude can be linearly expanded in a basis of "master" integrals with coefficients that are rational functions of the external momenta, as it was first realized by Passarino-Veltman [234]. Performing these master integrals, which contain all the branch-cut singularities, is the most difficult part of the calculation; but in that way they can be done once and for all and be tabulated. The remaining part is to obtain their coefficients, and this is where unitarity of the S-matrix comes into play. The unitarity cut of a one-loop amplitude is its discontinuity across the branch-cut in a kinematic region associated to a particular momentum channel, and using the unitarity of the S-matrix it can be related to the product of two tree-level amplitudes. In terms of Feynman diagrams the branch-cut discontinuity can be obtained putting two propagators within the loop on-shell or cutting them, these are the well-known Cutkosky rules [112]. Applying unitarity cuts in different channels the coefficients can be obtained, and the key point here is that they are quantities involving tree-level amplitudes. Generalizing this procedure by putting different numbers of propagators on-shell is what is called *generalized unitarity* [235], and it allows us to explore unphysical momentum channels where the use of complexified momenta is crucial.

In addition to the generalized unitarity methods, the BCFW recursion relation has been generalized to loop amplitudes. Strictly speaking, an all-loop generalization of the BCFW recursion relations for the *integrand* of amplitudes in $\mathcal{N} = 4$ SYM in the planar limit was introduced in [236], obtaining a recursive formula for the loop integrands with the usual loop-integration measure $\mathrm{d}^4 l$. Afterwards, it was discovered that the computation of on-shell diagrams can be done relating them to a mathematical structure known as the Grassmanian [237], that makes superconformal and dual superconformal symmetries

manifest. Within this new point of view, the integrand of MHV amplitudes to all-loops is automatically written as a product of d log's, a fact far from obvious from any other method of calculating scattering amplitudes. That d log form puts limits on the kind of singularities that can appear in the integrated amplitude. It has to be pointed out that these formulas only produce the integrand, but the integration, with a proper regularization procedure, is still an open problem.

The aim of these new methods is not only to be a competitor in the calculation race, but also to be applied and streamline phenomenological applications demand high precision results for events which demand a large number of particles in the Large Hadron Collider (LHC). Usually large theoretical uncertainties make difficult to compare the Standard Model predictions with experimental results due to the prohibitively lenghty calculations involved.

Also, hints from the simplicity of on-shell amplitudes can lead to a novel formulation of Quantum Field Theory, bringing new insights beyond scattering amplitudes, the perturbative level or overthrowing some of the basic principles in which the theory is based up to now. Gravity, which in principle seems to be completely unrelated, is deeply connected to Yang Mills theories via the color-kinematics duality [238], that makes possible to write perturbative scattering amplitudes for gravitons in terms of "double copies" of gluon amplitudes. Using this duality and generalized unitarity methods, it has been demonstrated [239] that, up to four loops, the UV behavior of $\mathcal{N} = 8$ SUGRA is as good as the $\mathcal{N} = 4$ SYM one, as opposed to the power-counting non-renormaliable nature of the theory. For the maximally sypersymmetric gauge theory in four dimensions, $\mathcal{N} = 4$ super Yang-Mills (SYM), an additional symmetry appear in the planar limit, the dual superconformal invariance discovered in [240]. Combined with the superconformal one leads to an unexpected Yangian symmetry. Although these properties are completely hidden at Lagrangian level, are made explicit with the use of new on-shell methods [237], that help understand them from a new point of view. Furthermore, principles as locality and unitarity are emergent concepts with the use of a new mathematical object, called the Amplituhedron as introduced in [241], to calculate scattering amplitudes of $\mathcal{N} = 4$ SYM in the planar limit. One can foresee that having a formalism where these principles are emergent can lead to a more fundamental description of physics that prepares us for the transition to a deeper underlying theory that describes quantum gravity, where those principles do not have to hold.

While these structures for *planar* $\mathcal{N} = 4$ SYM have been extensively discussed, the non-planar sector has been object of studies just more recently [242–247]. Even less is known outside the context of $\mathcal{N} = 4$ SYM, with the notable exception of the three-dimensional

ABJM theory [237, 248–251] and for $\mathcal{N} < 4$ SYM theories[1] [253]. In the latter case, the on-shell diagrammatics acquires new features: it is endowed with a *physical* decoration which encodes the helicities of the coherent states propagating along the edges of each on-shell diagrams. Such a decoration, which is represented as incoming/outgoing arrows for negative/positive helicity coherent states, induces directed paths along the edges (named helicity flows) of the diagrams which beautifully encode the singularity structure of a given on-shell process. Furthermore, the equivalence relations are now codified in terms of such helicity flows, while the permutations represent Ward identities among different on-shell processes. The helicity flows can form loops in a diagram: this corresponds to singularities (higher-order poles) which are completely absent in the maximally supersymmetric case and are associated to further structures in loop amplitudes, such as the UV divergences and the rational terms [253].

A complete introduction to those methods can be found in Refs. [231, 254, 255]. In this chapter we provide a general, and slightly superficial, introduction to these methods, mainly to establish the notation and give the non-expert reader a general idea of the methods used in the main core of Part II of this Thesis.

8.1 Color Ordering

In order to calculate gauge theory amplitudes one has to deal with, both kinematical and color degrees of freedom, with the consequent proliferation of indices. A strategy to avoid this problem is to specify the color of the particles as early as possible, leading us to color-ordered amplitudes, which are independent of color and simpler to calculate. To compute the full amplitude, we have to combine these simpler pieces, which are usually related by symmetries.

To disentangle the color and the kinematical degrees of freedom we have to find a basis spanning the color structures of scattering amplitudes at tree and loop level. For this we consider the case of the gauge group $SU(N_c)$, with N_c arbitrary, whose algebra is generated by the $N_c \times N_c$ traceless hermitian matrices usually denoted as T^a, with $a = 1, \ldots, N_c^2 - 1$. The generators and the structure constants f^{abc} are normalized as[2]

$$\mathrm{Tr}\left(T^a T^b\right) = \delta^{ab} \quad \left[T^a, T^b\right] = i\sqrt{2} f^{abc} T^c \,, \tag{8.1}$$

from which it follows that

$$f^{abc} = -\frac{i}{\sqrt{2}} \mathrm{Tr}\left(T^a T^b T^c - T^a T^c T^b\right) . \tag{8.2}$$

[1] For $\mathcal{N} < 4$ SYM theories, an on-shell treatment of the scattering amplitudes was discussed in [252].

[2] Note that this is not the common $\mathrm{Tr}\left(T^a T^b\right) = \frac{1}{2}\delta^{ab}$ normalization.

Gluon propagators have a color conserving δ^{ab} that produces contractions over adjoint indices, that can be performed using the Fierz identity

$$\sum_a \left(T^a\right)^{j_1}_{i_1}\left(T^a\right)^{j_2}_{i_2} = \delta^{j^2}_{i_1}\delta^{j^1}_{i_2} - \frac{1}{N_c}\delta^{j^1}_{i_1}\delta^{j^2}_{i_2}, \tag{8.3}$$

that can be easily proven extending the gauge group to $U(N_c) = U(1)\times SU(N_c)$, whose generators T^A with $A = 0, a$ form a basis of the $N_c \times N_c$ hermitian matrices and then satisfy a completeness relation

$$\sum_A \left(T^A\right)^{j_1}_{i_1}\left(T^A\right)^{j_2}_{i_2} = \delta^{j_2}_{i_1}\delta^{j_1}_{i_2}. \tag{8.4}$$

Moving the $A = 0$ term to the right hand side (8.3) is obtained.

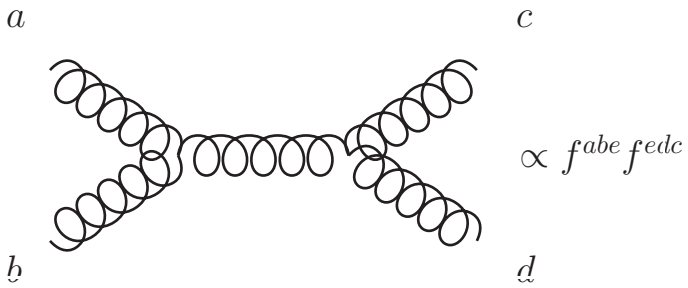

Figure 8.1: Feynman diagram contributing to the 4-gluon scattering in pure YM.

For example, for one of the diagrams corresponding to the 4-gluon amplitude of Fig. 8.1 we have

$$\begin{aligned} f^{abe}f^{edc} \propto \mathrm{Tr}\left(\left[T^a,T^b\right]T^e\right)\mathrm{Tr}\left(T^e\left[T^d,T^c\right]\right) = \\ = \mathrm{Tr}\left(\left[T^a,T^b\right]\left[T^d,T^c\right]\right) - \frac{1}{N_c}\mathrm{Tr}\left[T^a,T^b\right]\mathrm{Tr}\left[T^d,T^c\right]. \end{aligned} \tag{8.5}$$

In that case the terms with $1/N_c$ cancel out, but this is a general feature of the tree level pure YM amplitudes. To see this, we have to notice that this term would be absent if the gauge group were $U(N_c)$ instead of $SU(N_c)$, but this extra "photon" field does not couple to the gluons, so it does not contribute. With these considerations, it follows that at tree level all color factors combine into a sum of terms with only a single trace in each one.

At tree level, the gluon amplitudes have a color decomposition of the form

$$\mathscr{A}_n^{tree}(a,\varepsilon,p) = g^{n-2} \sum_{\sigma\in S_{n-1}} \mathrm{Tr}\left(T^{a_1}T^{\sigma(a_2)}\cdots T^{\sigma(a_n)}\right)\mathscr{A}_n(1,\sigma(2),\ldots,\sigma(n)), \tag{8.6}$$

where g is the coupling constant of the theory, a_i the color indices of the external gluons and the numbers inside $\mathscr{A}_n$ are a short notation for the momentum and helicity of the particles,i.e., only kinematical degrees of freedom.

The quantities $\mathscr{A}_n(1,\sigma(2),\ldots,\sigma(n))$, called *partial* or *color-ordered amplitudes*, are cyclically invariant due to the properties of the trace, only depend on kinematical arguments and, what makes them very useful, each of them is *gauge invariant*. When working with pure YM we will refer to these functions as the amplitude of the scattering. Color-ordered amplitudes are much simpler than the full amplitude, as they only receive contributions from a fixed cyclic ordering of the external gluons reducing the number of channels involved. This fact is very important when considering on-shell recursion relations. Furthermore, they have several properties that make the number of independent amplitudes less than the initial $(n-1)!$. $\sigma \in S_{n-1}$ One-loop amplitudes of gluons have additional double-trace terms. Their color decomposition is

$$\begin{aligned}\mathscr{A}_n^{1-loop} = \\ g^n N_c \left[\sum_{\sigma\in S_{n-1}} \mathrm{Tr}\left(T^{a_1}T^{\sigma(a_2)}\cdots T^{\sigma(a_n)}\right)\mathscr{A}_{n;1}(1,\sigma(2),\ldots,\sigma(n)) + \right. \\ \left. + \frac{1}{N_c}\sum_{i=2}^{[n/2]+1}\sum_{\sigma\in S_{n-1}} \mathrm{Tr}\left(T^{a_1}T^{\sigma(a_2)}\cdots T^{\sigma(a_{i-1})}\right)\mathrm{Tr}\left(T^{\sigma(a_i)}\cdots T^{\sigma(a_n)}\right)\mathscr{A}_{n;i}(1,\sigma(2),\ldots,\sigma(n))\right],\end{aligned} \tag{8.7}$$

where $[x]$ =Integer$[x]$. The partial amplitude $\mathscr{A}_{n;1}$ coming with the single-trace term is called leading-color or primitive partial amplitude, and the $\mathscr{A}_{n;i}$ are called subleading-color partial amplitudes. There are relationships among these partial amplitudes, so it is only necessary to calculate the leading-color partial amplitudes [256]. It is worth noting that in the planar limit ($N_c \to \infty$) the single trace term is leading. In the following we will only consider the planar limit of the theory, where the L-loop amplitude is usually written as [257]

$$\mathscr{A}_n^{(L)} = g^{n-2}\left[\frac{2e^{-\varepsilon\gamma}g^2N_c}{(4\pi)^{2-\varepsilon}}\right]^L \sum_{\sigma\in S_{n-1}} \mathrm{Tr}\left(T^{a_1}T^{\sigma(a_2)}\cdots T^{\sigma(a_n)}\right)A_n^{(L)}(1,\sigma(2),\ldots,\sigma(n)). \tag{8.8}$$

8.2 Spinor Helicity Notation

The spinor helicity formalism is highly useful for the description of scattering amplitudes of massless particles, providing an uniform description of the kinematical degrees of freedom

(momentum and polarization) for the states of all helicities. We can trade the use of polarization vectors (that suffer from gauge redundancies) for more diagrams written completely in terms of Weyl spinors. Although we are not covering massive particles, a beautiful extension of the spinor-helicity notation to massive particles was presented in Ref. [258]. In this Section we give a brief introduction, which will serve to present our conventions. A nice introduction to the formalism can be found in the excellent textbook [259].

To begin we can start with the momentum information, noting that the universal covering of the Lorentz group $SO(3,1)$ is isomorphic to $SL(2,\mathbb{C})$ we can map a Lorentz four-vector into a matrix with spinor indices, where the first index transforms as the fundamental representation of $SL(2,\mathbb{C})$, and the second one in the anti-fundamental representation. The translation is the following

$$p_\mu \to p_{a\dot{b}} \equiv \sigma^\mu_{a\dot{b}} p_\mu = \begin{pmatrix} p^0 - p^3 & -p^1 + ip^2 \\ -p^1 - ip^2 & p^0 + p^3 \end{pmatrix}_{a\dot{b}} , \tag{8.9}$$

where $\sigma^\mu_{a\dot{b}} = \left(\mathbb{1}_{a\dot{b}}, \vec{\sigma}_{a\dot{b}}\right)$ are the Pauli matrices. The matrix $p_{a\dot{b}}$ has null determinant due to the massless condition of p, and therefore it can be written as the product of two spinors λ_a and $\tilde{\lambda}_{\dot{b}}$ transforming respectively as the $(1/2,0)$ and $(0,1/2)$ representations of $SL(2,\mathbb{C})$.

$$p_{a\dot{b}} = \lambda_a \tilde{\lambda}_{\dot{b}} \Longleftrightarrow p^2 = 0 . \tag{8.10}$$

Requiring the four-momentum to be real imposes an hermiticity condition on $p_{a\dot{b}}$ that translates into the relation $(\lambda_a)^\star = \pm\tilde{\lambda}_{\dot{a}}$. An explicit realization of the spinors is

$$\lambda_a = \frac{e^{i\alpha}}{\sqrt{p^0+p^3}} \begin{pmatrix} -p^1 + ip^2 \\ p^0 + p^3 \end{pmatrix}_a , \quad \tilde{\lambda}_{\dot{a}} = \frac{e^{-i\alpha}}{\sqrt{p^0+p^3}} \begin{pmatrix} -p^1 - ip^2 \\ p^0 + p^3 \end{pmatrix}_{\dot{a}} , \tag{8.11}$$

that are defined up to an arbitrary phase and satisfy $(\lambda_a)^\star = sign(p^0)\tilde{\lambda}_{\dot{a}}$. If one extends the definition of the momenta into the complex plane, the universal covering of the Lorentz group is isomorphic to $SL(2,\mathbb{C}) \times SL(2,\mathbb{C})$, and then the spinors λ_a and $\tilde{\lambda}_{\dot{b}}$ are independent, transforming under a different copy of $SL(2,\mathbb{C})$ each.

Both representations of $SL(2,\mathbb{C})$ have Lorentz invariant inner products defined using the Levi-Civita symbols ϵ_{ab} and $\epsilon_{\dot{a}\dot{b}}$, for which we take the convention $\epsilon_{12} = 1 = \epsilon_{\dot{1}\dot{2}}$ and $\epsilon^{12} = -1 = \epsilon^{\dot{1}\dot{2}}$ and $\epsilon^{ab}\epsilon_{bc} = \delta^a_c$. Those are defined as[3]

$$\langle \lambda, \lambda' \rangle \equiv \epsilon^{ab}\lambda_a \lambda'_b = \lambda_a \lambda'^a \ , \ [\tilde{\lambda}, \tilde{\lambda}'] \equiv \epsilon^{\dot{a}\dot{b}} \tilde{\lambda}_{\dot{a}} \tilde{\lambda}'_{\dot{b}} = \tilde{\lambda}_{\dot{a}} \tilde{\lambda}'^{\dot{a}} . \tag{8.12}$$

[3] This convention is not standard and many authors use a different one.

Once we have defined the inner product we can lower and raise indices with the Levi-Civita symbol,

$$\lambda^a \equiv \epsilon^{ab}\lambda_b \Leftrightarrow \lambda_a \equiv \epsilon_{ab}\lambda^b\,, \tag{8.13}$$

which implies that the derivatives satisfy the opposite relationship, this is

$$\begin{aligned} \frac{\partial}{\partial\lambda_a} = \frac{\partial}{\partial\lambda^b}\epsilon^{ba} \Leftrightarrow \frac{\partial}{\partial\lambda^a} = \frac{\partial}{\partial\lambda_b}\epsilon_{ba}\,, \\ \partial^a = \partial_b\epsilon^{ba} \Leftrightarrow \partial_a = \partial^b\epsilon_{ba}\,, \end{aligned} \tag{8.14}$$

and we have the same relationships for $\tilde{\lambda}$.

The kinematical degrees of freedom of the scattering particles can be encoded in the pair of spinors $(\lambda^{(i)},\tilde{\lambda}^{(i)})$ and the helicities h_i, so the color-ordered amplitudes are functions of them $\mathscr{A}_n = \mathscr{A}_n(\lambda^{(i)},\tilde{\lambda}^{(i)},h_i)$. The spinors λ_a and $\tilde{\lambda}_{\dot{b}}$ carry helicity $-1/2$ and $1/2$ respectively, and the helicity operator of the particle i acts on the amplitude as

$$\hat{h}^{(i)}\mathscr{A}_n = \frac{1}{2}\left(-\lambda_a^{(i)}\frac{\partial}{\partial\lambda_a^{(i)}} + \tilde{\lambda}_{\dot{b}}^{(i)}\frac{\partial}{\partial\tilde{\lambda}_{\dot{b}}^{(i)}}\right)\mathscr{A}_n = h_i\mathscr{A}_n\,. \tag{8.15}$$

The invariance of the momentum $p_{a\dot{b}}$ under the rescaling $(\lambda,\tilde{\lambda})\to(t^{-1}\lambda,t\tilde{\lambda})$ can now be understood as the helicity is the generator of the little group of the Lorentz group for massless particles, since this rescaling is the finite transformation that has the helicity as infinitesimal generator. The finite transformation generated by Eq. 8.15 can also be understood as

$$\mathscr{A}_n\left(t_i^{-1}\lambda^{(i)},t_i\tilde{\lambda}^{(i)}\right) = \prod_{i=1}^{n} t_i^{2h_i}\mathscr{A}_n\left(\lambda^{(i)},\tilde{\lambda}^{(i)}\right). \tag{8.16}$$

The helicity covariance will be very important in order to fix the amplitudes from first principles, and also they serve as a fast crosscheck when performing calculations.

In order to relax the notation it is usually defined

$$\left\langle\lambda^{(i)},\lambda^{(j)}\right\rangle \equiv \langle ij\rangle\,,\quad [\tilde{\lambda}^{(i)},\tilde{\lambda}^{(j)}] \equiv [ij], \tag{8.17}$$

and we mention the following useful results.

$$s_{ij} \equiv (p^{(i)}+p^{(j)})^2 = 2p^{(i)}\cdot p^{(j)} = \langle ij\rangle[ij]. \tag{8.18}$$

The Schouten identity, that is similar for the conjugated spinors

$$\langle ij\rangle\langle kl\rangle + \langle ki\rangle\langle jl\rangle + \langle jk\rangle\langle il\rangle = 0\,. \tag{8.19}$$

And the momentum conservation in terms of spinors

$$\sum_i p^{(i)} = 0 \Longleftrightarrow \sum_i \langle ji\rangle [ik] = 0\,. \tag{8.20}$$

Finally, the polarization vectors $\varepsilon^{\mu}_{\pm}$ expressed in terms of the helicity spinors are written as

$$\varepsilon^{+,(i)}_{a\dot{b}} = -\sqrt{2}\frac{\mu^{(i)}_a \tilde{\lambda}^{(i)}_{\dot{b}}}{\langle \mu^{(i)}, \lambda^{(i)}\rangle}, \quad \varepsilon^{-,(i)}_{a\dot{b}} = \sqrt{2}\frac{\lambda^{(i)}_a \tilde{\mu}^{(i)}_{\dot{b}}}{\langle \lambda^{(i)}, \mu^{(i)}\rangle}\,, \tag{8.21}$$

where $\mu(\varepsilon^+)^2$ and $\tilde{\mu}^{(i)}$ are arbitrary reference spinors associated with the gauge invariance of the polarization vectors.

By acting with the helicity operator of equation (8.15) it is straightforward to see that they carry the correct helicity, *i.e.*, $\hat{h}^{(i)}\varepsilon^{\pm} = \pm 1\varepsilon^{\pm}$. The signs and $\sqrt{2}$ factors are included in order for the polarization vectors to satisfy the following conditions

$$(\varepsilon^+)^\star = \varepsilon^-, \quad \varepsilon^+ \cdot \varepsilon^- = -1\,. \tag{8.22}$$

And their form makes evident that:

$$(\varepsilon^+)^2 = (\varepsilon^-)^2 = 0, \quad 2p^{(i)} \cdot \varepsilon^{+,(i)} \propto [ii] = 0 = 2p^{(i)} \cdot \varepsilon^{-,(i)}\,. \tag{8.23}$$

Since we know that the amplitude can be written factorizing the polarization vectors as

$$\mathscr{A}_n\left(1^{h_1}, \cdots, n^{h_n}\right) = \prod_{i=1}^{n} \varepsilon^{h_i} \tilde{A}_n\left(p^{(1)}, \cdots, p^{(n)}\right), \tag{8.24}$$

we have a way of demonstrating that the helicity operator acts diagonally on it as $\hat{h}^{(i)}\mathscr{A}_n = h_i \mathscr{A}_n$. Where we have used the fact that the momenta do not transform under the little group.

8.3 BCFW Recursion Relations

Great advances have been achieved in Quantum Field Theory focusing on specific classes of observables. In the field of scattering amplitudes, on-shell objects have been found to play a fundamental role in the discovery of outstanding structures. In this work we are dealing with *massless particles* only, although some of the methods explored have been generalized to massive particles [260].

The idea of three-particle on-shell amplitudes as building blocks arises from the discovery of the on-shell or Britto-Cachazo-Feng-Witten (BCFW) recursion relations [232],

that can be applied to all the theories satisfying well defined requirements in the UV limit for complex momenta. This method exploits the power of complex analysis and ideas that can be traced back to the so called S-matrix program, in particular, the analyticity of the S-matrix. Therefore, the BCFW construction is an excellent tool, not only because it can be applied to a wide range of theories, but also because of the fact that it usually generates amplitudes in simple and compact forms.

The recursion relation is based on a linear momentum shift or momentum deformation in complexified momentum space $\left(p^{(i)} \in \mathbb{C}^d\right)$ depending on one complex variable $z \in \mathbb{C}$, but preserving both momentum conservation and the on-shell condition for every momenta. In general, it can be written as:

$$p^{(i)} \to p^{(i)}(z) = p^{(i)} - z \sum_{j=1}^{n} \alpha_{ij} q^{(j)} \tag{8.25}$$

where the coefficients α_{ij} and the momenta $q^{(j)} \in \mathbb{C}^d$ are constrained because of momentum conservation and the on-shell condition, in particular the $q^{(j)}$ must be light-like. Notice that the coefficients α_{ij} do not need to be all non-vanishing, allowing us to consider deformations of an arbitrary number of external momenta.

Let us work with the momentum-conservation stripped scattering amplitude $M\left(p^{(1)}, \ldots, p^{(n)}\right)$, which does not include the delta function imposing energy-momentum conservation. We have a complex function of external momenta, and after the deformation it is a meromorphic function of the complex parameter z, $M \to M(z)$. Considering the Feynman diagram representation of the amplitude we know that the only singularities of $M(z)$ come from its propagators which, at tree level, are all simple poles.

These considerations imply that, at *tree level* and if there is *no contribution of the pole at infinity*, the sum of all residues of the function $M(z)/z$ is zero, noticing that the residue at $z = 0$ is the original amplitude we obtain

$$M = M(0) = -\sum_{z_p} Res\left(\frac{M(z)}{z}\right)_{z=z_p} \tag{8.26}$$

where the z_p are the poles of the deformed amplitude $M(z)$.

Let us analyze the terms in this equation, $M(0)$ is our goal, the unshifted amplitude, while the other residues turn out to be factorization limits of the amplitude. Those limits break the amplitude into smaller pieces that, because the poles are where propagators go to zero, are *on-shell scattering amplitudes* with a lower number of external particles.

Let us consider the simplest deformation, where two momenta are shifted. We label them by (i) and (j), leaving the others unchanged

$$p^{(i)}(z) \equiv \hat{p}^{(i)} = p^{(i)} - zq, \;\; p^{(j)}(z) \equiv \hat{p}^{(j)} = p^{(j)} + zq \tag{8.27}$$

Momentum conservation clearly holds, and on-shell conditions impose

$$0 = p^{(i)} \cdot q = p^{(j)} \cdot q \Longrightarrow q = \lambda^{(i)}\tilde{\lambda}^{(j)} \text{ or } \lambda^{(j)}\tilde{\lambda}^{(i)} \tag{8.28}$$

having two solutions for q up to a constant factor that can be absorbed in z. Focusing in the first solution (the other is analogous), the spinors are deformed as

$$\tilde{\lambda}^{(i)}(z) = \tilde{\lambda}^{(i)} - z\tilde{\lambda}^{(j)}, \quad \lambda^{(j)}(z) = \lambda^{(j)} + z\lambda^{(i)} \tag{8.29}$$

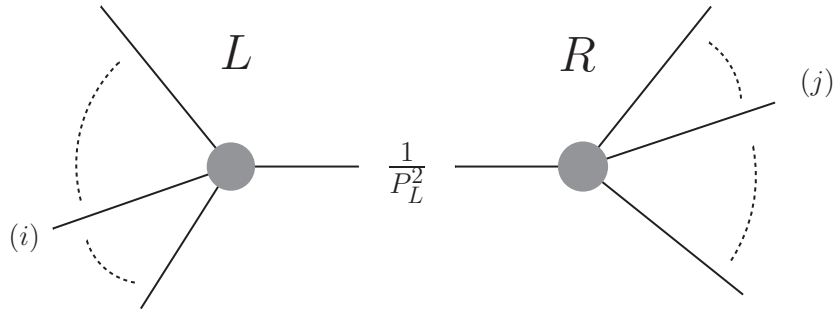

Figure 8.2: Diagram representing a term in the BCFW recursion relation. Each grey blob is an on-shell amplitude, particle (i) has to be on the left side, while particle (j) on the right side.

With the choice of this deformation we obtain a recursion relation involving the minimum number of terms, each one associated with a factorization channel containing either $p^{(i)}$ or $p^{(j)}$. Channels containing both deformed momenta are z independent because of $p^{(i)}(z) + p^{(j)}(z) = p^{(i)} + p^{(j)}$, and then cannot develop a pole. Then, the propagator can only depend on z if shifted particles (i) and (j) are on opposite sides. Let us call P_L the sum of momenta entering the propagator from the left,containing the particle (i). Finally, the pole can be calculated as

$$P_L(z_p)^2 = 0 = P_L^2 - 2z_p q \cdot P_L \Longrightarrow z_p = \frac{P_L^2}{2q \cdot P_L} \tag{8.30}$$

The residues in equation (8.26) are provided by the product of two tree-level on-shell amplitudes with fewer external states [232]. As the pole in the propagator is approached, the corresponding momentum goes on-shell and this channel dominates the others, factorizing in the following way

$$\lim_{z \to z_p} M(z) = \sum_{h,states} M_L(z_p) \frac{1}{(z - z_p)(-2q \cdot P_L)} M_R(z_p) + \mathcal{O}((z - z_p)^0) \tag{8.31}$$

where $M_L(z_p)$ and $M_R(z_p)$ are on-shell amplitudes calculated at the deformed (complex) momenta. The sum over helicities and states is there because we can have propagators of several particles and, for fermions or gauge bosons, the numerator of the propagator can be replaced by the polarization sum on-shell, as is guaranteed by unitarity.

Then Eq. (8.26) allows us to express the amplitude as

$$M = M(0) = \sum_{z_p,h,states} M_L(z_p)\frac{1}{P_L^2}M_R(z_p) \tag{8.32}$$

as is represented in Fig. 8.2.

In general, we can have different kind of particles (scalars, fermions, gauge bosons, ...), so in Eq. (8.32) the sum is not only over the poles or factorization channels, but also over all internal states (helicities, different particles, ...) that can propagate.

In pure YM theory, using color ordering, external states are labeled in a cyclic order, so the number of possible partitions L and R in the BCFW recursion relations is reduced considerably. If we pick adjacent particles to be deformed, the number of partitions is minimal, making this choice the most convenient in the general case. As we have said before, there is a non-trivial requirement for (8.32) to hold, that the residue of the pole at infinity vanishes, or equivalently, that $\lim_{|z|\to\infty} M(z) = 0$. In the same paper [232], BCFW proved that for the amplitude to vanish at infinite z once the deformation of equation (8.29) is applied, the helicities of particles i and j, (h_i, h_j) need to be $(+,+)$, $(-,-)$ or $(-,+)$. To get a recursion relation in the remaining case $(+,-)$ we have to exchange the roles of λ and $\tilde{\lambda}$, returning to one of the previous cases.

Let us make an explicit example of the application of this method to obtain a color-ordered 4-gluon MHV amplitude in pure YM, $A_4(1^-,2^-,3^+,4^+)$, where $i^\pm$ is a short notation to denote $(p^{(i)}, h_i)$. We can choose to deform particles 1 and 4 in the following way

$$\tilde{\lambda}^{(1)}(z) = \tilde{\lambda}^{(1)} - z\tilde{\lambda}^{(4)}, \quad \lambda^{(4)}(z) = \lambda^{(4)} + z\lambda^{(1)} \tag{8.33}$$

which consists of the allowed case $(-,+)$.

Since the minimal non-vanishing contribution comes when having three-particle amplitudes, and we have to respect color-ordering, there is only one partition contributing to the recursion relation, which is $L = 1^-, 2^-$ $R = 3^+, 4^+$. Furthermore, in the sum over helicities of the internal state, there is only one non-vanishing contribution, because $M_3(+,+,+)$ and $M_3(-,-,-)$ are both zero. Therefore, there is only one term in the recursion relation, depicted in Figure. 8.3.

The value of z at the pole is obtained putting the internal propagator on-shell

$$(p^{(1)}(z_p) + p^{(2)})^2 = 0 = (p^{(1)} + p^{(2)})^2 - 2z_p q\cdot(p^{(1)} + p^{(2)}) \Longrightarrow z_p = \frac{[12]}{[42]} \tag{8.34}$$

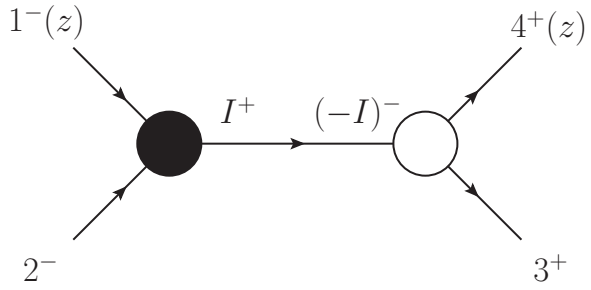

Figure 8.3: Diagram representing a term in the BCFW recursion relation. The incoming arrows represent a negative helicity state, while the outgoing arrow represent a positive helicity state. The color of the vertices follow conventions described in Section 8.6.

The three-particle amplitudes are calculated in Section 8.4, formulae (8.42) and (8.43). Applying the BCFW recursion relation (8.32) we obtain

$$A_4(1^-,2^-,3^+,4^+) = A_3(1^-(z),2^-,I^+)\frac{1}{(p^{(1)}+p^{(2)})^2}A_3((-I)^-,3^+,4^+(z)) = \tag{8.35}$$
$$= \frac{\langle 1(z)2\rangle^3}{\langle 2I\rangle\langle I1(z)\rangle}\frac{1}{\langle 12\rangle[12]}\frac{[34(z)]^3}{[4(z)(-I)][(-I)3]}$$

Using momentum conservation to determine the internal momentum $\lambda^{(I)}\tilde{\lambda}^{(I)}$, and simplifying the result we arrive at

$$A_4(1^-,2^-,3^+,4^+) = \frac{\langle 12\rangle^4}{\langle 12\rangle\langle 23\rangle\langle 34\rangle\langle 41\rangle} = \frac{[34]^4}{[12][23][34][41]} \tag{8.36}$$

which are the Parke-Taylor formulae for 4-gluon MHV and $\overline{\text{MHV}}$ amplitudes respectively, since in the special case of 4 gluons we can consider the amplitude MHV and $\overline{\text{MHV}}$ simultaneously.

The major point is that we have arrived to a recursive procedure where on-shell amplitudes are written only in terms of lower point amplitudes, which are evaluated in complex external momenta, but remain on-shell. Keeping ourself in the field of on-shell amplitudes allows us to circumvent all the unphysical degrees of freedom associated with gauge redundancies and virtual particles, and maintains the formulae in a simpler form. Although this construction was originally used and proved in pure Yang-Mills theory, they has been applied to obtain scattering amplitudes in QCD with massive fermions [261], string theory [262] and even gravity [263], where the traditional approach is extremely cumbersome due to the complexity of the Feynman rules of the theory.

To sum up, we need two ingredients for this recursion to work which are a linear momentum deformation preserving on-shell and momentum conservation conditions, and

the absence of the pole at infinity. The vanishing of the pole at infinity is where the details of the theory come in, and its symmetries are a crucial aspect. It is worth noting that this recursion relation provides a notion of constructability of a theory at tree level; continuing the recursive procedure all amplitudes can be expressed as products of a minimal set of on-shell amplitudes, which can be considered the building blocks of the theory. Usually this minimal blocks are the three-particle on-shell amplitudes, which vanish for real momenta. However, when going to complexified momenta they do not vanish, and what is crucial, they are fixed by Poincaré invariance [264]. Thus, any theory which admits an on-shell representation is totally determined by the information encoded in the three-particle on-shell amplitudes, in spite of the fact that for Yang-Mills theory the 4-particle vertex is crucial to maintain gauge invariance. This can be understood pointing out that in the on-shell approach every piece is separately gauge invariant, contrary to what happens in the framework of Feynman diagrams. However, there is a disadvantage in the BCFW representation of the amplitude, each term in the recursion relation presents spurious poles that cancel once all the terms are summed, this is the reason individual BCFW terms break locality.

8.4 The Three-particle Amplitude

The BCFW recursion relations lead us to focus on the study of the minimal on-shell scattering amplitude, that, as we will see, is the three-particle one. In principle, it seems that we do not have three-particle on-shell amplitudes for massless particles because

$$p^{(1)} + p^{(2)} + p^{(3)} = 0,\ (p^{(i)})^2 = 0 \Longrightarrow p^{(1)} \cdot p^{(2)} = p^{(1)} \cdot p^{(3)} = p^{(2)} \cdot p^{(3)} = 0\,. \tag{8.37}$$

All Mandelstam invariants vanish and there are no other Lorentz scalars available for real momenta the amplitude could depend on. The situation changes in the complexified momentum space, since the helicity spinors $\lambda^{(i)}$ and $\tilde{\lambda}^{(i)}$ are unrelated, each condition $p^{(i)} \cdot p^{(j)} = 0$ admits two independent solutions.

In terms of spinors

$$p^{(i)} \cdot p^{(j)} = 0 \Longleftrightarrow \langle ij \rangle [ij] = 0, \quad \forall i, j\,, \tag{8.38}$$

that it is solved if either $\lambda^{(1)} \propto \lambda^{(2)} \propto \lambda^{(3)}$ or $\tilde{\lambda}^{(1)} \propto \tilde{\lambda}^{(2)} \propto \tilde{\lambda}^{(3)}$. Thus, a three-particle on-shell amplitude for massless particles has the following structure

$$\mathscr{M}_3(\lambda, \tilde{\lambda}) = \delta^{2\times 2}\left(\sum_i \lambda^{(i)} \tilde{\lambda}^{(i)}\right) \left\{ M_3^H(\lambda) + M_3^A(\tilde{\lambda}) \right\}, \tag{8.39}$$

where $M_3^H(\lambda)$ and $M_3^A(\tilde{\lambda})$ are called holomorphic and anti-holomorphic contributions, respectively. This structure is satisfied to all orders in perturbation theory, since this result is based on momentum conservation and the massless condition of the particles involved.

Considering scattering amplitudes of particles with defined helicity $M_3(\lambda,\tilde{\lambda},h)$, they must be eigenfunctions of the helicity operator $\hat{h}^{(i)}$ for each particle i, so Eq. (8.15) implies

$$\left(\frac{1}{2}\lambda_a^{(i)}\frac{\partial}{\partial\lambda_a^{(i)}}+h_i\right)M_3^H=0,\quad\left(\frac{1}{2}\tilde{\lambda}_{\dot{b}}^{(i)}\frac{\partial}{\partial\tilde{\lambda}_{\dot{b}}^{(i)}}-h_i\right)M_3^A=0\,, \tag{8.40}$$

for each $i=1,2,3$.

The holomorphic and anti-holomorphic amplitudes can only depend on the Lorentz invariant contractions of spinors $\langle ij\rangle$ and $[ij]$ respectively, and equation (8.40) can be solved, providing a general expression for the on-shell three-particle amplitude with arbitrary helicities

$$\begin{aligned}\mathscr{M}_3(\lambda,\tilde{\lambda},h)=\delta^{2\times2}(\sum_i\lambda^{(i)}\tilde{\lambda}^{(i)})\times\\ \times\left\{\kappa^H\langle12\rangle^{d3}\langle23\rangle^{d1}\langle31\rangle^{d2}+\kappa^A[12]^{-d3}[23]^{-d1}[31]^{-d2}\right\},\end{aligned} \tag{8.41}$$

where $d_1=h_1-h_2-h_3$, $d_2=h_2-h_1-h_3$ and $d_3=h_3-h_1-h_2$.

Another requirement is that, as we have seen before, these amplitudes need to vanish when the momenta are taken to be real. In that case, we have that $\lambda^{(1)}\propto\lambda^{(2)}\propto\lambda^{(3)}$ and $\tilde{\lambda}^{(1)}\propto\tilde{\lambda}^{(2)}\propto\tilde{\lambda}^{(3)}$, so in order to avoid a singular behavior, the coupling constant of the holomorphic part κ^H should be zero for $d_1+d_2+d_3=-(h_1+h_2+h_3)<0$ and the anti-holomorphic one κ^A should vanish for $d_1+d_2+d_3=-(h_1+h_2+h_3)>0$. In the case $d_1+d_2+d_3=-(h_1+h_2+h_3)=0$ both the holomorphic and the anti-holomorphic parts can contribute.

To sum up, the minimal on-shell scattering amplitude of massless particles for complexified momenta is the three-particle amplitude, whose form is fixed by Poincaré invariance. For states whose helicities are such that $h_1+h_2+h_3\neq0$, the amplitude can be either holomorphic or anti-holomorphic, and has a fixed form in terms of contractions of spinors $\langle ij\rangle$ or $[ij]$.

Applying this to the case of pure YM we can obtain the 3-gluon color-ordered amplitudes (for complex momenta) up to a constant, that is the coupling constant of the theory. There are only two possible helicity configurations compatible with a dimesionless coupling constant [264]

$$\mathscr{A}_3^{MHV}(1^-,2^-,3^+)=\delta^{2\times2}(\sum_i\lambda^{(i)}\tilde{\lambda}^{(i)})\times\frac{\langle12\rangle^3}{\langle23\rangle\langle31\rangle}\,, \tag{8.42}$$

and

$$\mathcal{A}_3^{\overline{MHV}}(1^+,2^+,3^-) = \delta^{2\times 2}(\sum_i \lambda^{(i)}\tilde{\lambda}^{(i)}) \times \frac{[12]^3}{[23][31]}, \tag{8.43}$$

that are particular cases of the Parke-Taylor formula.

We have the three-particle amplitude and for each state an on-shell phase space, that is Lorentz invariant and explicitly eliminates the little group redundancies, which is defined as

$$\Omega = \sum_h \frac{d^2\lambda d^2\tilde{\lambda}}{\mathrm{Vol}\{GL(1)\}}. \tag{8.44}$$

It will be useful when defining on-shell diagrams to think on the amplitude as a differential form, so we include in its definition the phase space of the states

$$\mathcal{M}_3(i,j,k) \to \mathcal{M}_3(i,j,k)\Omega^{(i)}\Omega^{(j)}\Omega^{(k)}. \tag{8.45}$$

8.5 $\mathcal{N}$=4 Super Yang-Mills

Maximizing the amount of symmetry in a theory has been proven very useful and, supersymmetry, although not yet discovered in nature, is a very important idea in elementary particle physics. Supersymmetry proposes an extension of the Poincaré algebra with Grassmann odd generators relating fermionic and bosonic fields. Trying to extend pure YM, the simplest possibility ($\mathcal{N}=1$) adds a spin 1/2 Weyl fermion (the gluino) to every gluon. If we want to maintain renormalizability, the maximal amount of supersymmetry that we can have in a gauge theory is $\mathcal{N}=4$, and the resultant theory is called $\mathcal{N}=4$ Supersymmetric Yang-Mills ($\mathcal{N}=4$ SYM).

The particle content of the theory, considering $SU(N)$ as the gauge group is: a gluon with helicities $h=\pm 1$, 4 gluinos with helicities $h=\pm 1/2$ and 6 scalar particles with helicities $h=0$. As a consequence of sypersymmetry on-shell degrees of freedom are balanced between bosons and fermions: in that case we have 8 bosonic and 8 fermionic degrees of freedom. All states of the theory are connected via supersymmetry transformations and then they belong to the same representation of $SU(N)$, what distinguishes gluinos from quarks.

The theory has only two parameters, the rank of the gauge group N and the coupling constant g_{YM}. It is remarkable that $\mathcal{N}=4$ SYM is ultraviolet finite, g_{YM} is not renormalized at the quantum level; the conformal symmetry at tree-level survives the quantization without the presence of anomalies: $\mathcal{N}=4$ SYM is a conformal Quantum Field Theory. Nonetheless, scattering amplitudes are not free of divergences, radiative corrections suffer from infrared (IR) divergencies that need to be regularized.

Even if we were only interested in pure YM amplitudes, at tree-level both theories are equivalent, explaining this the simplicity and additional symmetries that tree-level gluon amplitudes manifest in pure YM. Also, $\mathcal{N}=4$ SYM theory is a much simpler than pure YM, serving as a toy model to study the later.

Supersymmetric theories can be described in a much simpler way enlarging the space-time to a superspace, where in addition to the space-time components, we have a Grassmann odd variable η_I, with $I=1,\dots,\mathcal{N}$ being the R-symmetry index. The $\mathcal{N}=4$ on-shell multiplet may be assembled into one on-shell superfield defined in that space. This natural construction already appears in the paper of Nair [265] and can be expanded into helicity states as follows

$$\begin{aligned}\left|\lambda,\tilde{\lambda};\eta\right\rangle = |-1\rangle + \eta_{I_1}\left|-\frac{1}{2}\right\rangle^{I_1} + \frac{1}{2!}\eta_{I_1}\eta_{I_2}|0\rangle^{I_1I_2} + \\ + \frac{1}{3!}\eta_{I_1}\eta_{I_2}\eta_{I_3}\epsilon^{I_1I_2I_3I_4}\left|\frac{1}{2}\right\rangle_{I_4} + \frac{1}{4!}\eta_{I_1}\eta_{I_2}\eta_{I_3}\eta_{I_4}\epsilon^{I_1I_2I_3I_4}|1\rangle\,,\end{aligned} \tag{8.46}$$

where the right-hand-side states depend on the momentum spinors λ and $\tilde{\lambda}$, and the number inside the ket denotes the helicity of the state. From this expression it is clear that we must assign helicity $h=-1/2$ to the Grassman variables η_I and that the superfield carries constant helicity $h=-1$ along all its terms.

If Q_{aI} and $\tilde{Q}^{\dot{a}I}$ are the supercharges, with a and $\dot{a}$ spinor indices, then the superfield in (8.46) is an eigenstate of the supercharges $\tilde{Q}^{\dot{a}I}$

$$\tilde{Q}_{\dot{a}I}\left|\lambda,\tilde{\lambda};\eta\right\rangle = \eta_I\tilde{\lambda}_{\dot{a}}\left|\lambda,\tilde{\lambda};\eta\right\rangle \tag{8.47}$$

Since Q_{aI}, $\tilde{Q}^{\dot{a}I}$ have a non-vanishing anticommutator, we can not diagonalize both of them simultaneously. We can make an analogous construction for the supercharges Q_{aI}, that is related to the previous one via a Grassmann-Fourier transformation

$$\left|\lambda,\tilde{\lambda};\tilde{\eta}\right\rangle = \int d^4e^{\eta\tilde{\eta}}\left|\lambda,\tilde{\lambda};\eta\right\rangle,\quad Q_{aI}\left|\lambda,\tilde{\lambda};\tilde{\eta}\right\rangle = \tilde{\eta}_I\lambda_a\left|\lambda,\tilde{\lambda};\tilde{\eta}\right\rangle, \tag{8.48}$$

where the expansion of $\left|\lambda,\tilde{\lambda};\tilde{\eta}\right\rangle$ in helicity defined states is like (8.46) interchanging the sign of the helicities:

$$\begin{aligned}\left|\lambda,\tilde{\lambda};\tilde{\eta}\right\rangle = |+1\rangle + \tilde{\eta}^{I_1}\left|\frac{1}{2}\right\rangle_{I_1} + \frac{1}{2!}\tilde{\eta}^{I_1}\tilde{\eta}^{I_2}|0\rangle_{I_1I_2} + \\ + \frac{1}{3!}\tilde{\eta}^{I_1}\tilde{\eta}^{I_2}\tilde{\eta}^{I_3}\epsilon_{I_1I_2I_3I_4}\left|-\frac{1}{2}\right\rangle^{I_4} + \frac{1}{4!}\tilde{\eta}^{I_1}\tilde{\eta}^{I_2}\tilde{\eta}^{I_3}\tilde{\eta}^{I_4}\epsilon_{I_1I_2I_3I_4}|-1\rangle\,.\end{aligned} \tag{8.49}$$

Once that states defined in the on-shell superspace are introduced, it is natural to consider color-ordered superamplitudes whose external legs are described by a point in

the super-momentum space $\{\lambda^{(i)},\tilde{\lambda}^{(i)},\eta^{(i)}\}$ or $\{\lambda^{(i)},\tilde{\lambda}^{(i)},\tilde{\eta}^{(i)}\}$. This prescription abridges all possible field amplitudes involving gluons, gluinos and scalars as external states into a single object, keeping the computations much shorter and making explicit the relations among them. In the supersymmetric case, we have a new variable the amplitudes depend on, and the helicity operator definition (8.15) must be extended to[4]:

$$\begin{aligned}\hat{h}^{(i)} &= \frac{1}{2}\left(-\lambda_a^{(i)}\frac{\partial}{\partial\lambda_a^{(i)}}+\tilde{\lambda}_{\dot{b}}^{(i)}\frac{\partial}{\partial\tilde{\lambda}_{\dot{b}}^{(i)}}+\tilde{\eta}^{(i)I}\frac{\partial}{\partial\tilde{\eta}^{(i)I}}-2\right)= \\ &= \frac{1}{2}\left(-\lambda_a^{(i)}\frac{\partial}{\partial\lambda_a^{(i)}}+\tilde{\lambda}_{\dot{b}}^{(i)}\frac{\partial}{\partial\tilde{\lambda}_{\dot{b}}^{(i)}}-\eta^{(i)I}\frac{\partial}{\partial\eta^{(i)I}}+2\right),\end{aligned} \tag{8.50}$$

this is in accordance with the fact that the momentum and supermomentum are left invariant under the little group rescaling $\left(t^{-1}\lambda,t\tilde{\lambda},t^{-1}\eta,t\tilde{\eta}\right)$.

As we will see in Sec. 8.5.1, using the variables $\left(\lambda,\tilde{\lambda},\eta\right)$ or $\left(\lambda,\tilde{\lambda},\tilde{\eta}\right)$, from all the generators of the super-conformal $\mathfrak{su}(2,2|4)$ symmetry algebra, only the momentum and one of the supercharges are multiplicative operators, while the rest are first order or second order differential operators. Then, there is an advantage if all external states are described either with η or $\tilde{\eta}$, without mixing them. Invariance under supersymmetry transformations generated by $\tilde{Q}^{\dot{a}I}$ lead to the following identity

$$\mathcal{M}(\eta)=e^{\tilde{\zeta}\sum_i\tilde{Q}_i}\mathcal{M}(\eta)=e^{\tilde{\zeta}\sum_i\eta^{(i)}\tilde{\lambda}^{(i)}}\mathcal{M}(\eta), \tag{8.51}$$

which tells us that all amplitudes must be proportional to a "supermomentum" conserving delta function $\delta^{2\times4}(\sum_i\eta^{(i)}\tilde{\lambda}^{(i)})$. This is completely parallel to the invariance of the amplitudes under translations, that leads to the momentum conserving delta function. The new condition is a direct consequence of supersymmetry and has to be taken into account when we extend the BCFW deformation to supersymmetric theories in order to respect supersymmetry.

Adding the supersymmetry considerations to the Poincaré invariance, the three-particle amplitudes are similarly fixed in $\mathcal{N}=4$ SYM [266]. Following the notation in (8.39), they acquire the form

$$\begin{aligned}M_3^H(\lambda,\tilde{\lambda},\eta) &= \frac{\delta^4(\langle12\rangle\eta^{(3)}+\langle31\rangle\eta^{(2)}+\langle23\rangle\eta^{(1)})}{\langle12\rangle\langle23\rangle\langle31\rangle}, \\ M_3^H(\lambda,\tilde{\lambda},\tilde{\eta}) &= \frac{\delta^{2\times4}(\sum_i\tilde{\eta}^{(i)}\lambda^{(i)})}{\langle12\rangle\langle23\rangle\langle31\rangle},\end{aligned} \tag{8.52}$$

[4]The convention for the helicity operator has been chosen to be equal to one half of the one defined in Sec. 5.1 in Ref. [231]. This has the property that superamplitudes are annihilated by the total helicity.

$$M_3^A(\lambda,\tilde{\lambda},\eta)=\frac{\delta^{2\times 4}(\sum_i \eta^{(i)}\tilde{\lambda}^{(i)})}{[12][23][31]}\,,$$
$$M_3^A(\lambda,\tilde{\lambda},\tilde{\eta})=\frac{\delta^{4}([12]\tilde{\eta}^{(3)}+[31]\tilde{\eta}^{(2)}+[23]\tilde{\eta}^{(1)})}{[12][23][31]}\,. \tag{8.53}$$

Again, we can define a super phase-space form for a given supersymmetric state, replacing the sum over helicities by a sum over all different particles in the multiplet and their helicities, which is compactly encoded as an integration over the Grassmann variable η or $\tilde{\eta}$. The generalization of Eq. (8.44) is

$$\Omega_\eta = d^{\mathcal{N}}\eta\frac{d^2\lambda d^2\tilde{\lambda}}{\mathrm{Vol}\{GL(1)\}},\quad \Omega_{\tilde{\eta}} = d^{\mathcal{N}}\tilde{\eta}\frac{d^2\lambda d^2\tilde{\lambda}}{\mathrm{Vol}\{GL(1)\}} \tag{8.54}$$

8.5.1 Superconformal symmetry of $\mathcal{N}$=4 SYM

First of all, let us recall the Poincarè and Conformal symmetry generators of the theory. For notational convenience, we are gonna discuss all the operators acting on one particle. Since we are dealing with local symmetries, the total generator is the sum over all the particles that are involved in the process. In the spinor-helicity space the momentum operator is a multiplicative operator

$$P^{a\dot{a}} = \lambda^a\tilde{\lambda}^{\dot{a}}\,, \tag{8.55}$$

which implies that our amplitude is annihilated by this operator is ensured in a distributional sense by the momentum-conserving delta function.

The Lorentz generators, which encode rotations and boosts, are translated into two symmetric tensors when they are projected into the spinor representation through $\sigma^{\mu\nu}_{ab}$ and $\bar{\sigma}^{\mu\nu}_{\dot{a}\dot{b}}$. They are first order differential operators given by[5]

$$M_{ab} = \lambda_{(a}\frac{\partial}{\partial\lambda^{b)}}\quad,\quad \tilde{M}_{\dot{a}\dot{b}} = \tilde{\lambda}_{(\dot{a}}\frac{\partial}{\partial\tilde{\lambda}^{\dot{b})}}\,, \tag{8.56}$$

where the invariance of the amplitudes with respect to angular momentum is manifest since the angle and square spinor brackets are invariant under its action.

From now on, we are going to use the following convention to denote the derivatives. We define $\frac{\partial}{\partial\lambda^a}\equiv\partial_a$, $\frac{\partial}{\partial\tilde{\lambda}^a}\equiv\partial_{\dot{a}}$ and $\frac{\partial}{\partial\tilde{\eta}^I}\equiv\partial_I$; where the type of index is sufficient to recognize the variable w.r.t. we are taking the derivative.

The dilatations, or scale transformations of the momentum, are written in the spinor-helicity space as

$$D=\frac{1}{2}\left(\lambda^a\partial_a+\tilde{\lambda}^{\dot{a}}\partial_{\dot{a}}\right)+1\,, \tag{8.57}$$

[5] We use the weight one convention for the symmetrization of tensors, *i.e.*, $A_{(ab)}\equiv\frac{1}{2}\left(A_{ab}+A_{ba}\right)$.

which reflects that the spinor variables have weight $\frac{1}{2}$ under dilatations. The constant factor 1 is chosen for the operator to annihilate MHV amplitudes.

We also have the special conformal transformations, which are realized as a second order differential operator

$$K_{a\dot{a}} = \partial_a \partial_{\dot{a}} \,. \tag{8.58}$$

The whole set of generators described so far $\{P^{a\dot{a}}, M_{ab}, \tilde{M}_{\dot{a}\dot{b}}, D, K_{a\dot{a}}\}$ generate the conformal group in four dimensions, $SO(2,4)$. Of course, this representation obeys the commutation relations of the conformal algebra $\mathfrak{so}(2,4)$, and the helicity operators defined in Eqs. 8.15 and 8.50 commute with all the generators, making the helicity a good quantum number.

The $\mathcal{N}=4$ SYM supersymmetry transformations are generated by the supercharges Q_{aI} and $\tilde{Q}^{\dot{a}I}$. By definition their anti-commutator gives the momentum operator

$$\left\{Q^{aI}, \tilde{Q}^{\dot{a}}_J\right\} = \delta^I_J P^{a\dot{a}} = \delta^I_J \lambda^a \tilde{\lambda}^{\dot{a}} \tag{8.59}$$

which is the basic commutation relation of supersymmetry. The natural representation in the $(\lambda, \tilde{\lambda}, \tilde{\eta})$ space is then

$$Q^{aI} = \lambda^a \tilde{\eta}^I \quad , \quad \tilde{Q}^{\dot{a}}_I = \tilde{\lambda}^{\dot{a}} \partial_I \,. \tag{8.60}$$

In addition to the supercharges, we have a global $SU(4)$ R-symmetry, which acts as internal rotations in the $\tilde{\eta}$ space. It is represented by the traceless operator

$$R^I{}_J = \tilde{\eta}^I \partial_J - \frac{1}{4} \delta^I_J \tilde{\eta}^K \partial_K \,. \tag{8.61}$$

When combining the special conformal transformations with the supercharges we obtain the conformal supersymmetry generators

$$\begin{aligned} \left[K_{a\dot{a}}, \tilde{Q}^{\dot{b}}_I\right] &= \delta^{\dot{b}}_{\dot{a}} S_{aI} \quad , \quad S_{aI} \equiv \partial_a \partial_I \,, \\ \left[K_{a\dot{a}}, Q^b_I\right] &= \delta^b_a \tilde{S}_{\dot{a}I} \quad , \quad \tilde{S}_{\dot{a}I} \equiv \partial_{\dot{a}} \tilde{\eta}_I \,, \end{aligned} \tag{8.62}$$

which consist of first and second order differential operators.

The *super* part of the algebra yields[6]

$$\begin{aligned} &[P^{a\dot{a}}, S_{bI}] = -\delta^a_b \tilde{Q}^{\dot{a}}_I \quad , \quad [P^{a\dot{a}}, \tilde{S}_{\dot{b}I}] = -\delta^{\dot{a}}_{\dot{b}} Q^a_I \,, \\ &\left\{Q^{aI}, \tilde{Q}^{\dot{a}}_J\right\} = \delta^I_J P^{a\dot{a}} \quad , \quad \left\{S_{aI}, \tilde{S}^J_{\dot{a}}\right\} = \delta^J_I K_{a\dot{a}} \,, \\ &\left\{Q^{aI}, S_{bJ}\right\} = \frac{1}{2} \delta^I_J M^a{}_b - \delta^a_b R^I{}_J + \frac{1}{2} \delta^I_J \delta^a_b (D - h) \,, \\ &\left\{\tilde{Q}^{\dot{a}}_I, \tilde{S}^J_{\dot{b}}\right\} = \frac{1}{2} \delta^J_I \tilde{M}^{\dot{a}}{}_{\dot{b}} + \delta^{\dot{a}}_{\dot{b}} R^J{}_I + \frac{1}{2} \delta^J_I \delta^{\dot{a}}_{\dot{b}} (D + h) \,, \end{aligned} \tag{8.63}$$

[6] The following relationship is useful to compute the commutation relations $2\lambda_a \partial_b = \lambda_{(a} \partial_{b)} + \epsilon_{ab} \left(\lambda^c \partial_c\right)$.

while the helicity operator defined in Eq. (8.50) constitutes a central charge of the algebra, since it commutes with all the generators. The helicity is defined in such a way that it vanishes on superamplitudes.

Let us summarize the generators of the superconformal algebra:

- $P^{a\dot{a}}$: 4 translations.
- M_{ab} and $\tilde{M}_{\dot{a}\dot{b}}$: 6 rotations and boosts.
- D: 1 dilatation.
- $K_{a\dot{a}}$: 4 special conformal transformations.
- Q^{aI} and $\tilde{Q}^{\dot{a}}_{I}$: 16 fermionic supersymmetry generators.
- $R^{I}{}_{J}$: 15 $SU(4)$ R-symmetry rotations, which are traceless.
- S_{aI} and $\tilde{S}^{I}_{\dot{a}}$: 16 fermionic conformal supersymmetry generators.

Considering all the generators, we have 32 fermionic and 30 bosonic generators, which constitute the graded superconformal $\mathfrak{psu}(2,2|4)$ algebra.

8.5.2 Twistor space

Once we have studied the superconformal algebra, there are two aspects of the space in which we are representing the amplitudes that are not convenient. On one hand, we have that the little group scaling of the variables is asymmetrical $\left(t^{-1}\lambda, t\tilde{\lambda}, t\tilde{\eta}\right)$. On the other hand, the representation of the superconformal generators is not uniform, *i.e.*, it contains operators with zero, one and two derivatives. Both issues can be solved by performing a 'Fourier transform' on the spinor variable λ^a. Let us define the amplitude in the twistor space as

$$\mathscr{A}_n\left(\mathscr{W}^{(i)}\right) \equiv \int \prod_{i=1}^{n} \mathrm{d}^2\lambda^{(i)}\, e^{i\tilde{\mu}_a^{(i)}\lambda^{a(i)}}\, \mathscr{A}_n\left(\lambda^{(i)}, \tilde{\lambda}^{(i)}, \tilde{\eta}^{(i)}\right), \tag{8.64}$$

where the new variables $\mathscr{W}^A = \left(\tilde{\mu}^a, \tilde{\lambda}^{\dot{a}}, \tilde{\eta}^I\right)$ are called *supertwistors*, and we have defined the collective index $A = (a, \dot{a}, I)$. The Fourier transform implies the following equivalences in going from the λ to the $\tilde{\mu}$ space

$$\begin{aligned} \lambda^a \to -i\frac{\partial}{\partial\tilde{\mu}_a} \quad &, \quad \tilde{\mu}_a \to i\frac{\partial}{\partial\lambda^a}\,, \\ \lambda_a \to i\frac{\partial}{\partial\tilde{\mu}^a} \quad &, \quad \tilde{\mu}^a \to -i\frac{\partial}{\partial\lambda_a}\,. \end{aligned} \tag{8.65}$$

The bosonic components of the supertwistor were first introduced by Penrose in Ref. [267] and then supersymmetrize in Ref. [268]. It is important to notice that now, under the little group, all the coordinates scale homogeneously, this is, $\mathcal{W}^{(i)} \to t_i \mathcal{W}^{(i)}$, so they can be defined projectively. The supertwistors are kinematical points defined in $\mathbb{CP}^{3|4}$.

Concerning the superconformal group, using supertwistors the generators can be written in a surprisingly simple form as

$$G_B^A = \mathcal{W}^A \frac{\partial}{\partial \mathcal{W}^B} - \frac{1}{4}\delta_B^A \mathcal{W}^C \frac{\partial}{\partial \mathcal{W}^C}, \tag{8.66}$$

where it is clear that we have linearize the transformations. Now the superconformal group acts on each supertwistor simply by rotating its components among themselves, while the second term imposes the traceless conditions on the two bosonic subgroups, $SU(2,2)$ and $SU(4)$. This last term simply weights the number of $\mathcal{W}$, so it can be ignored if the function is homogeneous of degree zero on this variable. As was pointed out before, in order to obtain the complete transformation, we have to sum the generator over all the external particles, since we are dealing with a local operator.

8.5.3 Supersymmetric BCFW recursion relations

In the case of supersymmetric theories the deformations (8.25) and (8.27) do not respect supersymmetry and, moreover, if we try to use these unnatural deformations the residue of the pole at infinity usually does not vanish. It is possible to define a supersymmetric extension of the BCFW deformations respecting the supermomentum conservation derived in equation (8.51), as it has been done in [236]

$$\tilde{\lambda}^{(i)}(z) = \tilde{\lambda}^{(i)} - z\tilde{\lambda}^{(j)}, \quad \lambda^{(j)}(z) = \lambda^{(j)} + z\lambda^{(i)}, \quad \eta^{(j)}(z) = \eta^{(j)} + z\eta^{(i)} \tag{8.67}$$

if we are working in the η representation, or

$$\tilde{\lambda}^{(i)}(z) = \tilde{\lambda}^{(i)} - z\tilde{\lambda}^{(j)}, \quad \lambda^{(j)}(z) = \lambda^{(j)} + z\lambda^{(i)}, \quad \tilde{\eta}^{(i)}(z) = \tilde{\eta}^{(i)} - z\tilde{\eta}^{(j)} \tag{8.68}$$

while working in the $\tilde{\eta}$ representation.

Maximal supersymmetry makes the good UV properties of the best-behaved high-spin amplitudes to be inherited by normally badly behaved lower-spin particles. In the case of $\mathcal{N} = 4$ SYM, under these deformations the complex UV behavior of the amplitudes is $\mathcal{O}(z^{-1})$, so there is no contribution of the pole at infinity.

The generalization of the BCFW recursion relation (8.32) to maximally supersymmetric theories is (with a similar formula for the $\tilde{\eta}$ representation)

$$M_n(\lambda, \tilde{\lambda}, \eta) = \sum_{z_p} \int \mathrm{d}^{\mathcal{N}}\eta^{int}\, M_L(z_p)\, \frac{1}{P_L^2} M_R(z_p) \tag{8.69}$$

where the η^{int} to be integrated is the associated with the propagator legs, and substitutes the sum over helicities and states in the non-supersymmetric case. As before, the lower-point amplitudes $M_L(z_p)$ and $M_R(z_p)$ has to be evaluated at the deformed points in superspace.

8.6 On-shell Diagrams

Once three-particle on-shell amplitudes, totally fixed by Poincaré invariance, are recognized as the building blocks of the theory at tree level, it is natural to build more complicated objects *gluing* them together to generate *on-shell diagrams*. In these on-shell diagrams there are no virtual particles involved, all the lines represent on-shell states and are gauge invariant, thus each of them is physically meaningful. In particular, $\mathcal{N} = 4$ SYM scattering amplitudes (the amplitude for tree level processes and the integrand for loop level ones) can be represented by on-shell diagrams, and the physical equivalences among them lead to different interpretations of the same process, totally hidden in the Feynman diagram representation.

In section 8.4 we have seen that every three particle amplitude can be either holomorphic ,where all the $\tilde{\lambda}$'s are proportional and the amplitude can only depend on the λ's, or antiholomorphic, where all the λ's are proportional and the amplitude can only depend on the $\tilde{\lambda}$'s. We will represent the holomorphic amplitude, including the phase-space of the particles involved, with a black three-point vertex, and the anti-holomorphic one with a white three-point vertex.

In pure Yang-Mills this amplitude is not cyclically symmetric and depends on the helicities of the external gluons, so we have to make this fact explicit in the diagram. As we are considering all the external momenta as incoming, we can represent the helicity of each particle with an arrow in the leg: if the arrow is incoming, the helicity is negative, and vice versa. These diagrams are shown in Fig. 8.4 and represent the amplitudes in equations (8.42) and (8.43) respectively, including the on-shell phase-space factors as in (8.45).

Having defined the vertices we have to join them. As we are dealing with on-shell diagrams, there are no virtual internal particles involved, and each internal line represents a sum over all possible particles which can be exchanged in the theory, integrating over the on-shell phase space of each - consisting of all possible helicities and on-shell momenta. If an internal particle carries momentum $p = \lambda\tilde{\lambda}$ and helicity h, then p flows into one vertex with helicity h and $(-p)$ into the other with opposite helicity, being consequent with momentum conservation and angular momentum conservation. This is done integrating

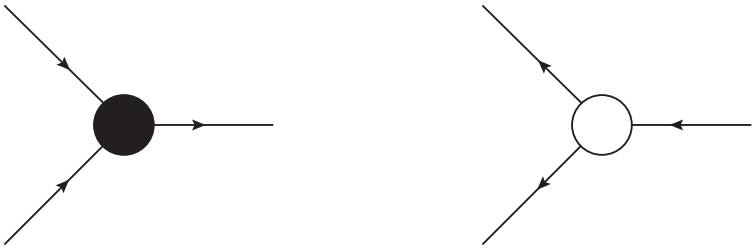

Figure 8.4: Three-particle amplitudes for pure YM theory. The black point vertex represent the holomorphic amplitude, while the white vertex the anti-holomorphic one. Incoming arrows represent states with negative helicity, if the arrow is outgoing the helicity is positive.

over the spinors λ and $\tilde{\lambda}$, modulo the $GL(1)$ redundancy of the little group (rescaling $\lambda \to t^{-1}\lambda$ and $\tilde{\lambda} \to t\tilde{\lambda}$), which gives a total of three degrees of freedom, as corresponds to an on-shell momentum. In terms of the diagram, and recalling that each vertex includes the on-shell phase-space forms of each particle, a line represents a δ-function eliminating one of the "repeated" phase-spaces and a integration over the on-shell degrees of freedom of the remaining phase-space form. In that way, an on-shell diagram will have only dependency on the external states degrees of freedom.

In maximally supersymmetric theories all helicity states are contained in a single superfield, so there is no need to distinguish among particular helicities of particles. As before, we represent with a black vertex the holomorphic amplitude and with a white vertex the anti-holomorphic one, since both of them are cyclically invariant as can be seen in Eqs. (8.52) and (8.53). We can represent them with the vertices in Fig. 8.5. As in the non-supersymmetric case vertices are forms defined as in (8.45), but with the super phase-space of Eq. (8.54).

Depending on the number of vertices and internal lines, we will have some number of momentum conserving δ-functions and integration variables corresponding to on-shell internal momenta, which can lead to three different cases. We may have just enough δ-functions to localize all the internal momenta, the on-shell diagram then represents an ordinary function of the external data, this has been called historically a *leading singularity*. If there are more δ-functions than the necessary to fix the internal momenta we will have extra momentum conserving δ-functions involving the external momenta, this object is called a *singularity* or to have singular support. If there are fewer δ-functions than the necessary to fix the internal momenta we will have free degrees of freedom leading to a *differential form*, wich we are free to integrate over any contour. If we also add the

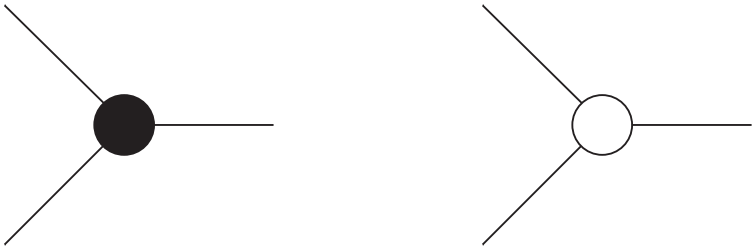

Figure 8.5: Three-particle amplitudes for maximally supersymmetric theories. The black point vertex represent the holomorphic amplitude, while the white vertex the anti-holomorphic one. These are not decorated with arrows because each external state contains all the helicity states of the theory.

on-shell phase space of the external lines we obtain a differential form defined on the space of external and internal on-shell momenta. All the possibilities an on-shell diagram can lead to are considered *on-shell forms* [237].

Let us write some simple examples of on-shell diagrams. As a first approach we can glue together two on-shell three-particle vertices, one holomorphic and the other anti-holomorphic, as can be seen in Fig. 8.6. The internal line carries momentum $p_{int} = p^{(1)} + p^{(2)} = -(p^{(3)} + p^{(4)})$, and must be on-shell, imposing a δ-function constraint on the external momenta, $\delta((p^{(1)} + p^{(2)})^2)$. This on-shell diagram represents a singularity.

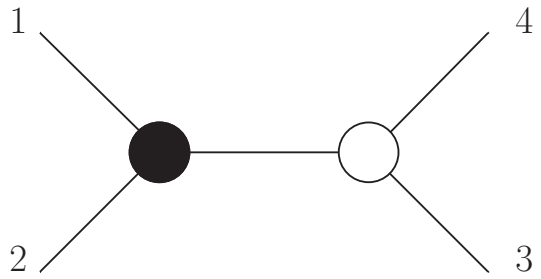

Figure 8.6: On-shell diagram formed by gluing two three-particle vertices. It represents a singularity because it imposes $(p^{(1)} + p^{(2)})^2 = 0 = (p^{(3)} + p^{(4)})^2$.

We can also join two vertices of the same kind, for example, holomorphic vertices. Because the vertices require the four external $\tilde{\lambda}$'s to be proportional, it makes no physical difference how they are connected. The same physical process can be represented using different channels, leading us to the definition of higher-point vertices which are symmetric among the external lines. This property is usually called *merger operation* and it is repre-

sented in Fig. 8.7. The merger operation can be seen as a contraction of two three-particle vertices into a four-particle vertex, and then expanding it along another channel, which can be very useful when it is contained in a bigger on-shell diagram to relate diagrams that in principle look different. This relationship is general and does not depend on the amount of supersymmetry of the YM theory.

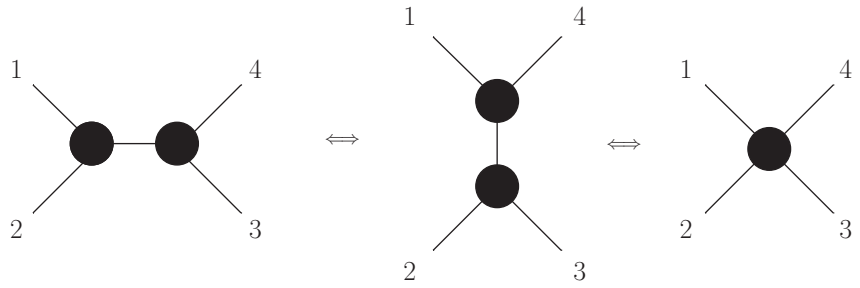

Figure 8.7: Merger operation on on-shell diagrams. Two (anti-) holomorphic vertices glued together make the four $\tilde{\lambda}$'s (λ's) proportional, thus the external legs can be joined through a different channel representing the same physical process.

Going a step further, we con join four vertices forming a square. If we do not want to impose any constraint on the external legs we have to alternate the type of consecutive vertices, as we have seen in the previous example. This leads us to two different possibilities, that are related by a permutation of the labels and indeed we will see that they are equivalent. Let us consider one of them and denote the internal momentum joining vertices i and j as $q^{(ij)}$, as can be seen in Fig. 8.8. Imposing the proportionality conditions for the holomorphic vertex at the upper-left corner and the anti-holomorphic at the lower-left corner, the momentum $q^{(12)}$ has to take the form

$$q^{(12)} = z\lambda^{(2)}\tilde{\lambda}^{(1)} \tag{8.70}$$

where z is a complex proportionality constant to be determined.

Imposing momentum conservation in vertices containing particles 1 and 2 we can determine $q^{(41)}$ and $q^{(23)}$ to be

$$\begin{aligned} q^{(41)} &= p^{(1)} + q^{(12)} = (\lambda^{(1)} + z\lambda^{(2)})\tilde{\lambda}^{(1)}, \\ q^{(23)} &= p^{(2)} - q^{(12)} = \lambda^{(2)}(\tilde{\lambda}^{(2)} - z\tilde{\lambda}^{(1)}) \end{aligned} \tag{8.71}$$

which are clearly on-shell, so there is nothing else to impose in their internal lines.

At this point is clear that momenta $q^{(41)}$ and $q^{(12)}$ are equivalent to the deformed momenta $p^{(1)}(z)$ and $p^{(2)}(z)$ of a BCFW-deformation, so this diagram is equivalent to the one

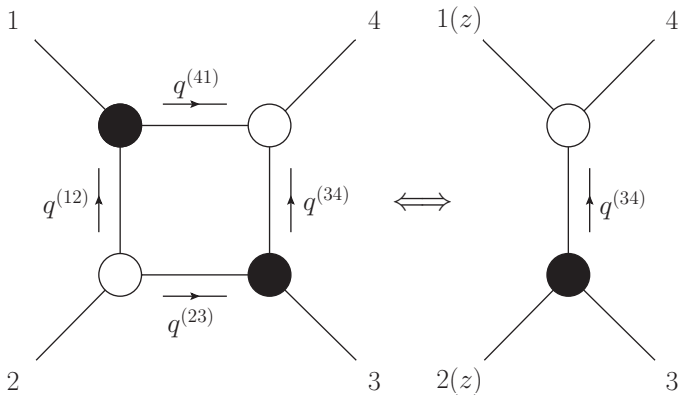

Figure 8.8: On-shell diagram with four external particles. This is the 4-point tree-level amplitude in $\mathcal{N}=4$ SYM and also in pure YM for particular helicities. Note the relation with the BCFW deformation.

in Fig. 8.6 with the degree of freedom z still unfixed. But this remaining diagram represents a singularity, that puts the internal momentum on-shell, fixing the z parameter with the on-shell condition $(q^{(34)})^2 = (p^{(2)}(z) + p^{(3)})^2 = 0$. This is nothing else than the representation of the 4-point tree-level amplitude via the BCFW recursion relations deforming particles (1) and (2), equivalent to the example of Fig. 8.3.

In the case of pure YM we have to check that the deformation has the correct complex-UV behavior in order for the diagram to represent the 4-point tree level amplitude, although a generalization to all cases will be carried out in Sec. 8.7, where we will not only consider on-shell diagrams describing amplitudes, but we will be interested in on-shell diagrams in general. If the $\mathcal{N}=4$ SYM case the deformation has to modify not only the momentum spinors, but also the Grassmann variables η (or $\tilde{\eta}$). This is indeed done by the super momentum-conserving δ-functions associated with each three-point amplitude, which imposes the correct value for η (or $\tilde{\eta}$) in the internal lines to be the deformation described in Eq.(8.67) (or (8.68)).

MHV tree-level scattering amplitudes in $\mathcal{N}=4$ SYM are cyclically symmetric, as it is clearly seen in the following formula demonstrated by Bianchi et al. in [269]

$$\mathcal{M}_n^{\text{MHV}}(\tilde{\eta}) = \frac{\delta^{2\times 2}(\sum_i \lambda^{(i)}\tilde{\lambda}^{(i)}) \times \delta^{2\times 4}(\sum_i \lambda^{(i)}\tilde{\eta}^{(i)})}{\langle 12\rangle \cdots \langle n1\rangle} \tag{8.72}$$

Since the on-shell form associated with the on-shell diagram of Fig. 8.8 is the 4-point tree level amplitude, we have demonstrate another equivalence relation for $\mathcal{N}=4$ SYM on-shell diagrams: the square move, depicted in 8.9. Both diagrams are related by a cyclic permutation of the external states, but they represent a cyclically invariant on-shell form,

then they are equivalent. This relationship will not hold in general when we consider $\mathcal{N} < 4$.

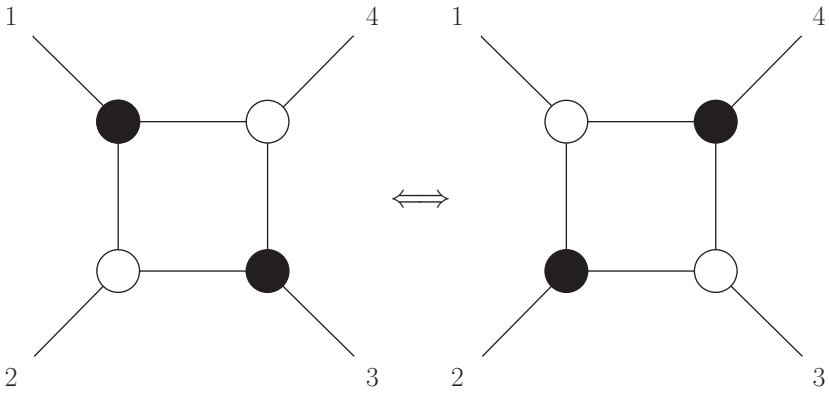

Figure 8.9: Square move in $\mathcal{N} = 4$ SYM. An on-shell diagram containing a square diagram with alternate white and black three-particle amplitudes is equivalent to the on shell diagram obtained by exchanging white and black three-particle amplitudes.

This last example can be generalized, yielding an important method to build in a simple way complicated diagrams from simpler ones: the *BCFW-Bridge* [237]. Starting from an on-shell diagram we can pick two external lines and attach to them a white and a black vertices joined by an internal line, like it is represented in Fig. 8.10. This has been referred as attaching a BCFW-bridge, and generates a new more complicated diagram from a simpler one. We have added two vertices and three internal lines, adding the corresponding on-shell phase space of the internal lines and localizing them with the momentum conserving δ-functions of the vertices we end with with one extra free parameter z, that remains free. The new on-shell form is related to the previous one through[7]

$$\hat{\mathcal{M}}_n(\lambda^{(i)},\tilde{\lambda}^{(i)},\lambda^{(j)},\tilde{\lambda}^{(j)}) = \frac{dz}{z}\mathcal{M}_n(\lambda^{(i)},\tilde{\lambda}^{(i)}-z\tilde{\lambda}^{(j)},\lambda^{(j)}+z\lambda^{(i)},\tilde{\lambda}^{(j)}) \tag{8.73}$$

in the non-supersymmetric case, and for the supersymmetric case

$$\hat{\mathcal{M}}_n(\lambda^{(i)},\tilde{\lambda}^{(i)},\lambda^{(j)},\tilde{\lambda}^{(j)},\eta^{(i)},\eta^{(j)}) = \frac{dz}{z}\mathcal{M}_n(\lambda^{(i)},\tilde{\lambda}^{(i)}-z\tilde{\lambda}^{(j)},\lambda^{(j)}+z\lambda^{(i)},\tilde{\lambda}^{(j)},\eta^{(i)},\eta^{(j)}+z\eta^{(i)}) \tag{8.74}$$

[7] We will explore in Sec. 8.7 what happens when we attach a BCFW bridge not respecting the UV behavior in $\mathcal{N} < 4$.

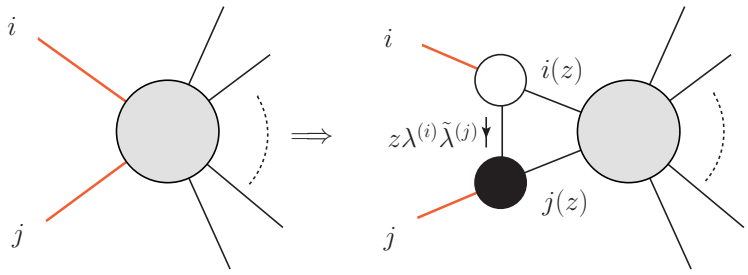

Figure 8.10: BCFW bridge applied to a generic on-shell diagram.

Successively attaching BCFW-bridges to a small set of simple diagrams very complex on-shell diagrams can be generated, relating the on-shell form complex diagrams with the on-shell form of simple diagrams evaluated at deformed (super)momentum.

8.7 On-shell Diagrams for $\mathcal{N} < 4$ SYM

Although on-shell diagrams have served as an incredibly useful tool to broaden out knowledge about QFTs in general, a great part of its results has focused just on planar $\mathcal{N} = 4$ SYM, while the exploration of the non-planar sector has been started in Refs. [242–245]. For the planar case, the analysis of loop integrals have shown that the theory is enriched with an additional symmetry, the dual conformal symmetry [257, 270]. Combining the conformal and dual conformal symmetries, the planar sector is endowed with the infinite dimensional Yangian symmetry [240]. Additionally, it is possible to establish an on-shell recursion relation at loop level, which relates the integrand of the L-loop amplitude to $(L-1)$-loop ones. This last property was discovered in Ref. [236] and we will discuss it in Sec. 8.9.2.

The existence of recursion relations at both tree and loop level, implies that all amplitudes are determined by the smallest non-trivial object to all orders in perturbation theory. This shows that we can describe physical observables bypassing the idea of a Lagrangian, while the Feynman diagrams are replaced by on-shell diagrams, whose states are always on-shell. Whereas individual on-shell diagrams generally break locality, the gluing procedure which allows to generate more complicated on-shell processes preserves the Yangian invariance [237]. The ability to evidence all the symmetries of the theory by the on-shell methods, which were hidden for long, is even more clear if one describes the amplitudes as an integral over the Grassmannian. An idea that arose in Refs. [271, 272] and we will introduce in Sec. 8.8.

In is interesting to explore if all these ideas, centered around building the observables without any reference to a Lagrangian and making as many structures manifest as possible, can be generalized to a broader class of theories. Since on-shell diagrams can be defined with no reference to a specific theory, it is a great idea to begin this project by studying on-shell diagrammatics and their related mathematical structures in less special theories. This work was initiated by Paolo Benincasa in Ref. [253], where on-shell diagrams for planar SYM, with $\mathcal{N} < 4$, were discussed in detail. In this Section we will only describe some basics results that will be useful in the rest of Part II, while suggesting the reader to study Ref. [253] for further details.

Except for the maximally supersymmetric case, where all the helicity states are contained in a single multiplet, in the theories with less amount of supersymmetry we have to deal with two multiplets, each of them carrying the gluons with + or − helicity. Then, we are going to generalize the states given in Sec. 8.5 to the $\mathcal{N} \leq 2$ case. The coherent states are now

$$\begin{aligned} \left|\lambda,\tilde{\lambda},\eta,-\right\rangle &= \sum_{s=0}^{\mathcal{N}} \frac{1}{s!}\left(\prod_{r=0}^{s}\eta_{I_r}\right)\left|\lambda,\tilde{\lambda},-(1-s/2)\right\rangle^{I_1\cdots I_s}, \\ \left|\lambda,\tilde{\lambda},\tilde{\eta},+\right\rangle &= \sum_{s=0}^{\mathcal{N}} \frac{1}{s!}\left(\prod_{r=0}^{s}\tilde{\eta}^{I_r}\right)\left|\lambda,\tilde{\lambda},+(1-s/2)\right\rangle_{I_1\cdots I_s}, \end{aligned} \tag{8.75}$$

where $\tilde{\eta}_I^{(i)}$ are the Grassmann variables through which the supersymmetric coherent states are defined ($I = 1,\dots\mathcal{N}$ is the $SU(\mathcal{N})$ index).

With such a representation, in which we have the η-representation for the negative helicity state, and the $\tilde{\eta}$-representation for the positive helicity state, the spin-1 state is contained in the zeroth order term in $\eta(\tilde{\eta})$. We can Fourier transform to express them in the conjugate representation as

$$\begin{aligned} \left|\lambda,\tilde{\lambda},\tilde{\eta},-\right\rangle &= \int \mathrm{d}^{\mathcal{N}}\eta\,\left|\lambda,\tilde{\lambda},\eta,-\right\rangle = \sum_{s=0}^{\mathcal{N}} \frac{1}{s!}\left(\prod_{r=0}^{s}\tilde{\eta}^{I_r}\right)\left|\lambda,\tilde{\lambda},-\left(1-\frac{\mathcal{N}-s}{2}\right)\right\rangle_{I_1\cdots I_s}, \\ \left|\lambda,\tilde{\lambda},\eta,+\right\rangle &= \int \mathrm{d}^{\mathcal{N}}\tilde{\eta}\,\left|\lambda,\tilde{\lambda},\tilde{\eta},+\right\rangle = \sum_{s=0}^{\mathcal{N}} \frac{1}{s!}\left(\prod_{r=0}^{s}\eta_{I_r}\right)\left|\lambda,\tilde{\lambda},+\left(1-\frac{\mathcal{N}-s}{2}\right)\right\rangle^{I_1\cdots I_s}. \end{aligned} \tag{8.76}$$

We can choose these coherent states as asymptotic states for our scattering process, and thus the amplitude will depend on η and $\tilde{\eta}$. A nice property to keep in mind is that η and $\tilde{\eta}$ scale under the little group as λ and $\tilde{\lambda}$, respectively. For example, using the $\tilde{\eta}$-representation for all the states, momentum conservation and super-momentum conservation imply that the amplitude can be stripped as

$$\mathcal{M}_n\left(\lambda,\tilde{\lambda},\eta\right) = \delta^{(2\times 2)}\left(\sum_{i=1}^{n}\lambda^{(i)}\tilde{\lambda}^{(i)}\right)\delta^{(2\times\mathcal{N})}\left(\sum_{i=1}^{n}\lambda^{(i)}\tilde{\eta}^{(i)}\right)M_n\left(\lambda,\tilde{\lambda},\eta\right), \tag{8.77}$$

in which the stripped amplitude M_n transforms under the action of the supersymmetric charge $\tilde{Q}$ via a shift in $\tilde{\eta}$.

As discussed in Section 8.4, the simplest objects we can use as building blocks to draw complex on-shell diagrams are the three-point amplitudes. More precisely, while for real momenta, invariance under space-time translations forces these objects to vanish, for complexified momenta there are two non-trivial solutions with support on the momentum-conserving sheet[8]. Taking the complexified Lorentz group as $SL(2,\mathbb{C})\times SL(2,\mathbb{C})$, the kinematic data can be encoded into spinorial variables $p_{a\dot{a}} = \lambda_a\tilde{\lambda}_{\dot{a}}$, with the two spinors transforming under different copies of $SL(2,\mathbb{C})$, and the two solutions identified by having either all the λ's or all the $\tilde{\lambda}$'s proportional to each other. The functional expression of each of these two solutions is fixed by Little group covariance, through the requirement that the amplitudes are eigenfunctions of the helicity operator

$$\begin{aligned}\mathscr{M}_3^A\left(1^+,2^+,3^-\right) =&\delta^{(2\times 2)}\left(\sum_{i=1}^3\lambda^{(i)}\tilde{\lambda}^{(i)}\right)\delta^{(1\times\mathscr{N})}\left(\sum_{i=1}^3[i+1,i-1]\tilde{\eta}^{(i)}\right)\frac{[1,2]^{4-\mathscr{N}}}{[1,2][2,3][3,1]}\,,\\ \mathscr{M}_3^H\left(1^-,2^-,3^+\right) =&\delta^{(2\times 2)}\left(\sum_{i=1}^3\lambda^{(i)}\tilde{\lambda}^{(i)}\right)\delta^{(2\times\mathscr{N})}\left(\sum_{i=1}^3\lambda^{(i)}\tilde{\eta}^{(i)}\right)\frac{\langle 1,2\rangle^{4-\mathscr{N}}}{\langle 1,2\rangle\langle 2,3\rangle\langle 3,1\rangle}\,.\end{aligned} \tag{8.78}$$

The three-particle amplitude, whose rational part just depends on the holomorphic Lorentz invariants $\langle i,j\rangle$, are defined on a support where all the $\tilde{\lambda}$'s are proportional to each other. The one whose rational part is just a function of the anti-holomorphic Lorentz invariants $[i,j]$, are instead defined on a support where all the λ's are proportional to each other.

As before, when included into on-shell diagrams, the amplitudes are considered to be forms [237] with the following replacement

$$\mathscr{M}_3(1,2,3)\to\mathscr{M}_3(1,2,3)\Omega^{(1)}\Omega^{(2)}\Omega^{(3)}\,, \tag{8.79}$$

where the measure for general $\mathscr{N}$ is

$$\Omega\equiv \mathrm{d}^{\mathscr{N}}\tilde{\eta}\,\frac{\mathrm{d}^2\lambda\,\mathrm{d}^2\tilde{\lambda}}{\mathrm{Vol}\{GL(1)\}}\,. \tag{8.80}$$

At a diagrammatic level, $\mathscr{M}_3^{(A)}$ and $\mathscr{M}_3^{(H)}$ are represented as a white and black trivalent nodes respectively, with the three lines departing from their centers representing the helicity of the multiplet state. In order to differentiate the helicity, we associate an incoming (outgoing) arrow to the external lines to represent a negative (positive) helicity multiplet,

[8] The three-particle amplitudes are also non-zero if we consider our space-time in $(2,2)$-signature. In this case, the Lorentz group is isomorphic to $SL(2,\mathbb{R})\times SL(2,\mathbb{R})$ and the two spinors in which a four-dimensional massless momentum can be decomposed transform under a different copy of $SL(2\mathbb{R})$ each.

as depicted in

(8.81)

$$\mathcal{M}_3^A\left(1^+,2^+,3^-\right) = \quad 3 = \frac{\delta^{(2\times 2)}\left(\lambda\cdot\tilde{\lambda}\right)\delta^{(1\times\mathcal{N})}\left(\alpha\cdot\tilde{\eta}\right)[1,2]^{4-\mathcal{N}}}{[1,2][2,3][3,1]},$$

$$\mathcal{M}_3^H\left(1^-,2^-,3^+\right) = \quad 3 = \frac{\delta^{(2\times 2)}\left(\lambda\cdot\tilde{\lambda}\right)\delta^{(2\times\mathcal{N})}\left(\lambda\cdot\tilde{\eta}\right)\langle 1,2\rangle^{4-\mathcal{N}}}{\langle 1,2\rangle\langle 2,3\rangle\langle 3,1\rangle},$$

where $\lambda\cdot\tilde{\lambda} \equiv \sum_i \lambda^{(i)}\tilde{\lambda}^{(i)}$, $\lambda\cdot\tilde{\eta} \equiv \sum_i \lambda^{(i)}\tilde{\eta}^{(i)}$, $\alpha\cdot\tilde{\eta} \equiv \sum_i [i-1,i]\tilde{\eta}^{(i)}$. The trivalent black (white) nodes represent the three-particle amplitudes with all the $\tilde{\lambda}$'s (λ's) proportional to each other.

Once we have establish the building blocks and the integration measure, we can combine them to study more complex on-shell diagrams. The most natural operation to be defined is the gluing of two general on-shell diagrams (or two three-point amplitudes o start), along one external leg each. Following Ref. [237], the natural prescription is to integrate over the super phase space of the glued legs imposing momentum conservation and summing over all the coherent states which can propagate, after using the delta functions we have

$$\mathcal{M}_{n_1+n_2} = \sum_{h=\pm}\int \mathrm{d}^{\mathcal{N}}\tilde{\eta}^{(P)}\,\frac{\mathrm{d}^2\lambda^{(P)}\,\mathrm{d}^2\tilde{\lambda}^{(P)}}{\mathrm{Vol}\{GL(1)\}}\mathcal{M}_{n_1+1}\left(-P,-h,\tilde{\eta}^{(P)}\right)\mathcal{M}_{n_2+1}\left(P,h,\tilde{\eta}^{(P)}\right) \tag{8.82}$$

Higher-degree on-shell forms can be systematically generated from a lower-degree one via the *BCFW bridge*: given an n-point on-shell p-form $\mathcal{M}_n^{(p)}$, one can single out two adjacent[9] external lines and connect them by gluing a *bridge* formed by two three-particle amplitudes of different type – the integration over the internal delta-functions leaves one degree of freedom unfixed, mapping the original n-point on-shell p-form $\mathcal{M}_n^{(p)}$ into an n-point on-shell $(p+1)$-form:

(8.83) $\mathcal{M}_n^{(p)} =$ $\quad\Longrightarrow\quad = dz\,\mu(z)\,\mathcal{M}_n^{(p)}(z) \equiv \mathcal{M}_n^{(p+1)},$

$i+1$ $\qquad$ i $\qquad\qquad$ $i+1$ $\qquad$ i

[9] It is actually possible to consider two non-adjacent lines. In this case, a planar on-shell diagram – which is embeddable into a disk – can me mapped into a non-planar one, which is instead embeddable into an higher genus Riemann surface [245].

with z being the unfixed degree of freedom, $\mu(z)$ is the measure associated to the bridge and $\mathscr{M}_n^{(p)}(z)$ is the BCFW-deformed p-form whose lines which have been single out (and which have now become internal) have momenta $p^{(i)}(z) = (\lambda^{(i)} + z\lambda^{(i+1)})\tilde{\lambda}^{(i)}$ and $p^{(i+1)}(z) = \lambda^{(i+1)}(\tilde{\lambda}^{(i+1)} - z\tilde{\lambda}^{(i)})$. Notice that the function expression of the measure $\mu(z)$ as well as of $\mathscr{M}_n^{(p)}$ and, thus, the $(p+1)$-form depend on the choice of the states which get BCFW-bridged. Thus the notation in the formula above needs to be understood as referring to a specific BCFW bridge.

The measure $\mu(z)$ depends on the helicity configuration of the BCFW bridge. Concretely, given a certain helicity configuration for the on-shell p-form $\mathscr{M}_n^{(p)}$, the BCFW bridge is added in such a way that the external states i and $i+1$ in the newly generated on-shell $(p+1)$-form still have the original helicity. However, in the internal edges now we need to sum all the possible helicity states which can propagate. If the direction of the helicity arrows from the external states into the deformed internal ones is preserved, than $\mu(z) = z^{-1}$, while if it is not $\mu(z) = z^{3-\mathscr{N}}$ [253]. This means that in the first case the original on-shell p-form is associated to the residue of the pole $z = 0$, while in the second case the on-shell p-form is mapped into another on-shell p-form with a different helicity configuration which is no longer associated to a residue at $z = 0$ given that such a pole is now absent (for $\mathscr{N} \leq 3$). Furthermore, in the latter case a multiple pole at infinity is introduced, which is a reflection of the change of the helicity arrow directions in the edges on which the BCFW bridge has been applied. Another way to think about this is that, if in the on-shell $(p+1)$-form (8.83) the helicity states of the particles labelled by $(i, i+1)$ is $(+,-)$ (*i.e.* the on-shell diagram shows an incoming arrow in the white node and an outgoing one in the black node), the helicities of the internal states are fixed and there is a *helicity flow* from the external lines towards the on-shell p-form: in this case the BCFW measure is $\mu(z) = z^{-1}$, and the bridge induces a BCFW-deformation on the internal p-form with no pole at infinity. If now, the external states $(i, i+1)$ have helicity $(-,+)$, different coherent states can propagate in the internal edges, generating a counter-clockwise helicity flow in one case and a clockwise one in the other case. The counter-clockwise helicity flow preserves the helicity states along the lines i and $i+1$, the related BCFW measure is again $\mu(z) = z^{-1}$ and the BCFW bridge induces a deformation on the p-form with a multiple pole at infinity. The clockwise flow instead does not preserve the helicities along the lines i and $i+1$, the related BCFW measure is now $\mu(z) = z^{3-\mathscr{N}}$ and the p-form which the BCFW bridge is attached has now a different helicity configuration. The helicity flows thus keep track of the singularities in an on-shell process: given a sub-diagram of the form of the right-hand-side of (8.83), the presence of a helicity flow guarantees that the bridge can be removed and that the diagram left corresponds to the residue of the related simple pole;

the presence of the helicity loops are instead a manifestation of the existence of higher order poles.

The decoration associated to the helicities therefore introduces a perfect orientation on the on-shell processes and it is a reflection of their singularity structure.

8.7.1 Equivalence classes and equivalence operations

When we build complicated on-shell processes by gluing several three-particle amplitudes, not all of them turns out to be inequivalent. As an example, let us take an on-shell process which has two black (white) nodes connected to each other along one line as a sub-diagram. These black (white) nodes have all the $\tilde{\lambda}$'s (λ's) proportional to each other, so that they can be equivalently merged together to form a four-valent black (white) node and expanded again along a different line into two three-valent black (white) node:

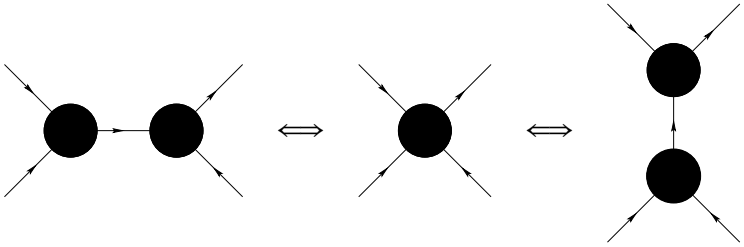

This equivalence operation goes under the name of *merger*: Any two diagrams which can be mapped into each other by merging together two nodes of the same type and expanding them along a different channel are equivalent. Importantly, this equivalence operation does not depend on the particular helicity configuration because it is just related to the proportionality relations among spinors of the same type.

Let us now consider a p-valent black (white) node with just incoming (outgoing) helicity arrows. Notice that in general it cannot be opened up into a tree-like configuration as in the merger operation just described. However, it can be open up into the sum of two p-gons with the two possible helicity loops:

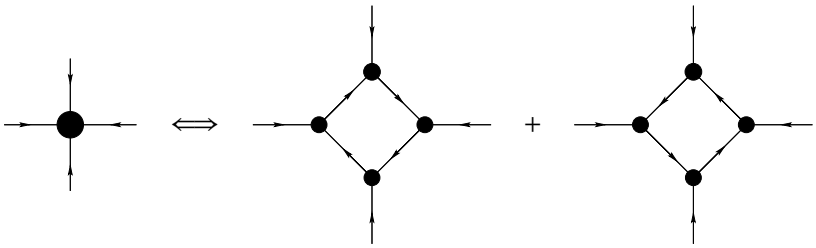

This operation is named *blow-up*. It is important to stress that this operation is possible if and only if the p-valent node has all the helicity arrows with the same direction. These

are the only cases given the relation outlined before between helicity flows and singularity structure of an on-shell diagram.

Let us now consider the on-shell diagram having the topology of a square with nodes (three-particle amplitudes) of alternating colour at the vertices. If the diagram is not decorated, the two possible ordering for alternating black/white nodes are actually equivalent: they contain exactly the same sub-diagrams. This means that a diagram having a square with alternating black and white nodes as a sub-diagram can be mapped into an equivalent diagram by exchanging the black and white nodes in the square. This equivalence operation is called *square move*. For the decorated diagrams, the requirement that the square diagram contains the same sub-diagrams means that the helicity flows are preserved. This turns out to be true just if the external helicity arrows with the same direction are adjacent

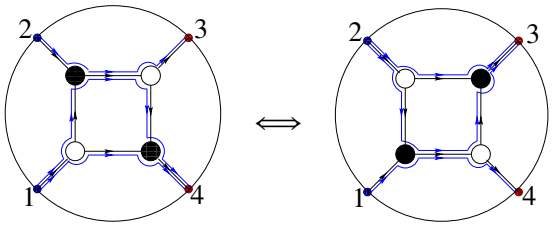

If instead the states with the same helicity are not adjacent, the helicity flow structure is sensibly different, with one of the two configuration allowing for both the multiplet to propagate in the internal lines generating helicity loops:

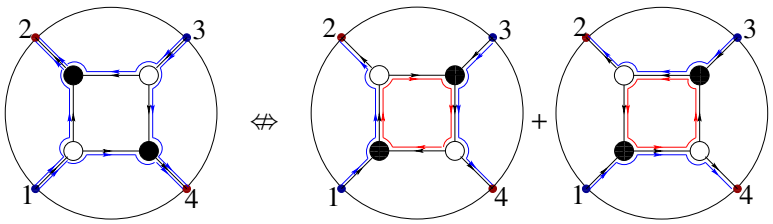

Therefore, the square move is an equivalence relation if and only if the on-shell box shows two states with the same helicity direction as adjacent.

All the equivalence relation above can be viewed under the light of permutations. Disregarding for a moment the helicity flows, if one assigns the directed paths $i \longrightarrow i-1$ to the black nodes and $i \longrightarrow i+1$ to the white nodes with the map $\sigma : \{n\} \longrightarrow \{2n\}$ such that $\sigma(i) \in [i, i+1]$ and the fixed points $\sigma(i) = i$ and $\sigma(i) = i+n$ corresponding to the black and white lollipop respectively, then a decorated permutation is assigned to each on-shell diagram and all the equivalence relations discussed above *do not* change the permutation. Thus, two equivalent on-shell diagrams belong to the same decorated permutation. Notice however that all the decorated on-shell box diagrams discussed above belong to the same

decorated permutation but, because of the different helicity flow structure, strictly speaking not all of them are equivalent. However, one can map them into each other by a helicity flow reversal operation [253]. Thus, the fact that all those diagrams belong to the same permutation means that they are related by Ward identities. If we associate a point to each helicity configuration and an edge to the helicity flow reversal, the resultant polytope represent the Ward identities relating different decorated on-shell diagrams

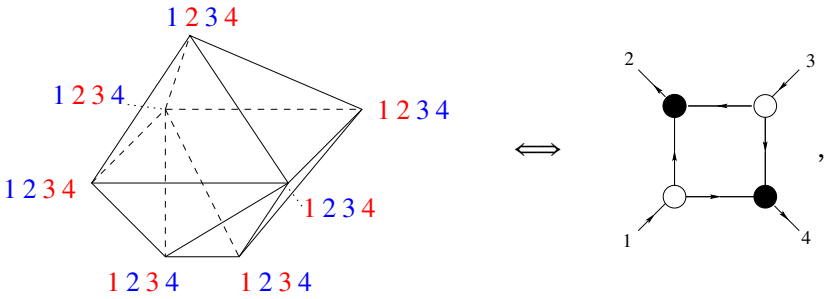

where the blue (red) labels indicate the incoming (outgoing) helicity arrows, while on the right it is represented the on-shell diagram which sits at the top vertex of the polytope. This diagram, as well as the ones sitting at the two lowest vertices, does not admit the square move equivalence relation, while the other four vertices of the polytope correspond to diagram which do admit such an equivalence relation. The polytope associated to on-shell boxes with exchanged white and black nodes can be obtained from the one above by contracting the two lowest vertices 1234 and expanding the top vertex 1234 into two.

The polytope above, together with the operation of contraction and expansion of the vertices with alternating colors for its labels, represents all the possible functions with ordering (1234) which can be defined on the top cell of the Grassmannian $Gr(2,4)$ and can be completely constructed via BCFW bridges.

Finally, there is a further operation which maps a given diagram into another diagram with one face less singling out one degree of freedom. It can be performed whenever a diagram has, as a sub-diagram, a black node and a white node connected through two edges forming a bubble. This diagrammatic operation goes under the name of *bubble reduction*. If the helicity arrows along these two lines have the same direction, than the bubble can be replaced by a single edge decorated with the same helicity arrow, factorising a $d\log$-form:

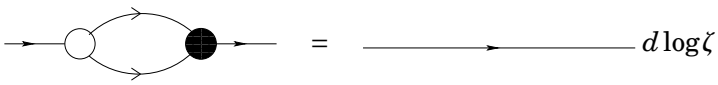

In this case just one coherent state is allowed to propagate. If instead both the two coherent states can run into the bubble, the diagram will show the two helicity loops signalising the appearance of a multiple pole. The bubble reduction can be still performed, factorizing a

different differential form than the $d\log$:

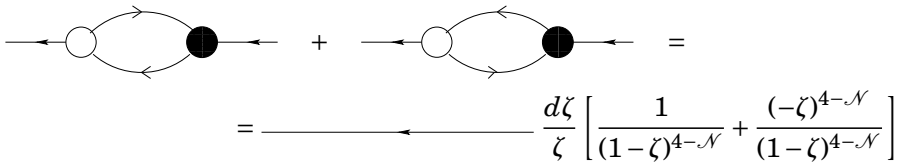

$$= \int \frac{d\zeta}{\zeta}\left[\frac{1}{(1-\zeta)^{4-\mathcal{N}}} + \frac{(-\zeta)^{4-\mathcal{N}}}{(1-\zeta)^{4-\mathcal{N}}}\right]$$

which, for $\mathcal{N} = 3$, reduces to the $d\log\zeta$ form as in the maximally supersymmetric case.

8.8 Grassmannian representation of $\mathcal{N}$=4 SYM on-shell diagrams

The computation of on-shell diagrams can be carried out in a more transparent way through the elements of an auxiliary mathematical structure, that has been studied by mathematicians over the past number of years, known as the Grassmanian [237]. Even though these building blocks can not be associated with local space-time processes, they make manifest the superconformal and dual superconformal symmetries (and consequently the infinite dimensional Yangian symmetry). An unsatisfying feature of this representation is that the way the building blocks have to be combined is dictated by imposing a particular singularity structure on the amplitude, this is, by imposing locality and unitarity.

A big step in the direction of showing locality and unitarity as emergent properties has been recently taken with the introduction of a new mathematical object in [241]: the Amplituhedron. It is a generalization of the positive Grassmanian and its “volume" is identified with scattering amplitudes (or its integrand at loop level) in planar $\mathcal{N} = 4$ SYM. While in the usual formulation of QFT locality and unitarity are first principles that lead to redundancies in order to maintain both; in this new framework, where avoiding these redundancies has been a guideline, both locality and unitarity emerges as a result of positive geometry.

In this section we will quickly review the basic definition of the Grassmannian and its properties[10].

The Grassmannian $Gr(k,n)$ is defined as the space of k-planes in n-dimensions intersecting at the origin. Any of its elements $C \in Gr(k,n)$ can be represented as a $k \times n$ matrix. Notice that the space spanned by the k rows is not changed by a $GL(k)$ transformation, so that the Grassmannian can be also defined as the space of $(k \times n)$ matrices modulo $GL(k)$ and, consequently, its dimension is $k(n-k)$.

[10] For a more exhaustive exposition see [237, 273–275]

The degrees of freedom of $C \in Gr(k,n)$ can be parametrised via the so-called Plücker coordinates, which are nothing but the set of maximal minors $\left\{\Delta_I, I \in \binom{[n]}{k}\right\}$. Of all these minors, just a subset of them is really independent: The Grassmannian is defined on the subspace of the Plücker embedding defined by the so-called Plücker relations

$$\begin{array}{ccc} Gr(k,n) & \longrightarrow & \mathbb{P}^{\binom{[n]}{k}-1} \\ C & \longrightarrow & [\Delta_I(C)]_{I\in\binom{[n]}{k}} \end{array}, \qquad \sum_{i=1}^{k+1}(-1)^{i-1}\Delta_{I_1\cup a_i}\Delta_{I_2\setminus a_i} = 0, \tag{8.84}$$

with I_1 and I_2 being respectively $(k-1)$- and $(k+1)$-element subsets of $[n]$ and $a_i \in I_2$. Importantly, the Plücker coordinates Δ_I's are $SL(k)$-invariant, so that an invariant way to parametrise an element of the Grassmannian is through ratios of the Plücker coordinates themselves, which is instead $GL(k)$-invariant. They allow to define affine charts $\Omega_I \equiv \{C \in Gr(k,n) | \Delta_I(C) \neq 0\}$, whose representative $C^\star$ is given by a matrix with the $(k\times k)$ identity $\mathbb{I}_{(k\times k)}$ placed in the columns I, and the collection of $\binom{n}{k}$ covers the whole $Gr(k,n)$. Choosing Ω_I such as $\Delta_I(C) \neq 0$ is the first non-zero Plücker coordinates in lexicographic order, then the Grassmannian is decomposed in the so-called Schubert cells, for which all the Plücker coordinate lexicographically larger than I are not constrained and thus can be zero or non-zero. The intersection of the Schubert cells $\Omega^{(i)}_{I_i}$ $(i = 1\dots n)$, with i labelling where the counting for the lexicographic order starts, defines a positroid stratum of $Gr(k,n)$. The locus in $Gr(k,n)$ characterised by having all the Plücker coordinates non-negative defines the so-called totally non-negative Grassmannian $Gr_{\geq 0}(k,n)$ [273] and its intersection with the positroid stratification defines a positroid cell. The positroid cell having all the Plücker coordinates non-zero is named top-cell, which is the highest dimensional cell. Furthermore, to each positroid stratification it is naturally associated a rational top-form which is characterised by logarithmic poles at the boundary and the absence of zeros, and it is $GL(k)$-invariant

$$\omega_{k,n} = \frac{d^{k\times n}C}{\text{Vol}\{GL(k)\}}\frac{1}{\Delta_{12\dots k}\Delta_{23\dots(k+1)}\dots\Delta_{n1\dots(k-1)}}. \tag{8.85}$$

The Grassmannian degrees of freedom can be nicely parametrised via the (undecorated) on-shell diagrams by either assigning a weight α_e to each edge e and fixing a perfect orientation with two (one) incoming arrows for the black (white) nodes, or by assigning a variable to each face into which the disc is divided by the diagram. In the first case, fixing a perfect orientation implies fixing the sources and sinks at the boundary of the disc. Then the entry c_{ij} of the Grassmannian representative matrix is given by the sum of the

products of the edge variables α's along all the paths from the source i to the sink j:

$$c_{ij} = -\sum_{\Gamma\in\{i\to j\}}\prod_{e\in\Gamma}\alpha_e \tag{8.86}$$

This definition leaves unfixed a $GL(1)$ for each vertex, which can be used to further set some of the edge variables to one. The edge variables can be actually chosen in such a way that all the minors $\Delta_I(C)$ are positive if they are themselves real and positive [237].

The relation between the entries of the matrix representative of the Grassmannian and the face variables is instead given (minus) the sum of the products of the variables associated to the faces which will be inside the paths from the source i to the sink j once they get closed clockwise:

$$c_{ij} = -\sum_{\Gamma\in\{i\to j\}}\prod_{f\in\hat{\Gamma}}(-f). \tag{8.87}$$

Again, not all the parameters turn out to be independent, rather they are linked by the relation $\prod(-f) = 1$, with the index of the product running over all the faces.

The choice of a given perfect orientation amounts to the choice of a coordinate patch which (partially) covers the Grassmannian. Any equivalence relation amounts to a change of coordinates in the same patch. Notice also that the parametrisation of the Grassmannian via the on-shell diagrams does not rely of any amplitude interpretation.

8.8.1 Describing kinematics with the Grassmannian

Up to now, we have given a formal description of the Grassmannian. Let us now proceed to give the geometrical picture of the Grassmannian representation of the kinematical data. When computing on-shell diagrams, we encounter that the most difficult part is to perform the phase space integral over the internal lines degrees of freedom. The obstacle in doing these integrals is that the momentum and supermomentum constraints are imposed as a second order polynomial, while coupling the different type of kinematical variables. The major advantage of using the Grassmannian to describe on-shell diagrams is that it describes the building blocks, the three particle amplitudes, decoupling the kinematical data. As we will see, the constraints appear linearly in delta functions.

In order to introduce the Grassmannian, we can first rethink the geometrical meaning of the momentum conservation constraint. Instead of thinking of the momentum spinors as a collection of n two component spinors $\lambda_a^{(i)}$ and $\tilde{\lambda}_{\dot{a}}^{(i)}$, each of them can be interpreted as 2 vectors in the n-dimensional *particle* space. The two vectors can be combined in a matrix,

Λ and $\tilde{\Lambda}$, that are defined as

$$\Lambda \equiv \begin{pmatrix} \lambda_1^{(1)} & \lambda_1^{(2)} & \cdots & \lambda_1^{(n)} \\ \lambda_2^{(1)} & \lambda_2^{(2)} & \cdots & \lambda_2^{(n)} \end{pmatrix} = \begin{pmatrix} \lambda_1 \\ \lambda_2 \end{pmatrix} = \begin{pmatrix} \lambda^{(1)} & \lambda^{(2)} & \cdots & \lambda^{(n)} \end{pmatrix}. \tag{8.88}$$

Let us now focus on the two row vectors of each of the matrices, that live in the n-dimensional space. Since Lorentz transformations act as $SL(2)\times SL(2)$ on the spinor indices, the 2-planes generated by Λ and $\tilde{\Lambda}$ are left invariant. Then, we should think in Λ and $\tilde{\Lambda}$ as two 2-planes that intersect in the origin of the n-dimensional space. In that picture, the momentum conservation constraint $\sum_{i=0}^{n} \lambda_a^{(i)} \tilde{\lambda}_{\dot{a}}^{(i)} = 0$ imposes that the planes are orthogonal to each other.

This geometrical understanding gives an alternative explanation to the three-particle solutions in spinor-helicity space, in which we have that all the $\lambda^{(i)}$ (or the $\tilde{\lambda}^{(i)}$) must be proportional. In the case of having three particles, Λ and $\tilde{\Lambda}$ must be two orthogonal 2-planes in 3 dimensions, which is not possible in general. The way out is that one of them is degenerate, this is, the two vectors defining it are proportional, and instead of having a 2-plane we have a 1-plane (a line). As an example, let us consider that we have 3 generic $\lambda^{(i)}$, so we can choose the line orthogonal to Λ to be

$$\Lambda^{\perp} = \begin{pmatrix} \langle 23\rangle & \langle 31\rangle & \langle 12\rangle \end{pmatrix}, \tag{8.89}$$

which satisfies $\Lambda^{\perp}\cdot\Lambda = 0$ using the Schouten identity. Now, momentum conservation implies that the $\tilde{\Lambda}$ plane must be spanned by $\Lambda^{\perp}$, so all the $\tilde{\lambda}^{(i)}$ must be proportional to each other. For example, we can choose

$$\tilde{\Lambda} = \begin{pmatrix} \tilde{\lambda}^{(1)} & \tilde{\lambda}^{(2)} & \tilde{\lambda}^{(3)} \end{pmatrix} = \begin{pmatrix} \langle 23\rangle & \langle 31\rangle & \langle 12\rangle \\ \langle 23\rangle & \langle 31\rangle & \langle 12\rangle \end{pmatrix}. \tag{8.90}$$

In order to linearize the orthogonality, or momentum conservation, constraint we introduce an auxiliary plane. Consider the k-plane C passing through the origin in the n-dimensional space. Automatically, we have $C^{\perp}$, which is the orthogonal $(n-k)$-plane. With this new object,which belongs to $Gr(k,n)$, the constraint is imposed with two linear constraints

$$\delta^{k\times 2}\left(C\cdot\tilde{\lambda}\right)\ ,\ \delta^{2\times(n-k)}\left(\lambda\cdot C^{\perp}\right), \tag{8.91}$$

enforcing that C is orthogonal to $\tilde{\Lambda}$, and that $C^{\perp}$ is orthogonal to Λ. That $C\cdot\tilde{\Lambda} = 0$ implies that $\tilde{\Lambda}$ must be contained in $C^{\perp}$. Similarly, since $\Lambda\cdot C^{\perp} = 0$, Λ must be contained in C. It follows that the two constraints together enforce momentum conservation. This argument

is impossible to apply when $k = 0, 1, n-1, n$, since C or $C^\perp$ would be a point or a line and they cannot span the kinematical variables.

When considering the supermomentum conservation condition, it follows exactly the same geometrical picture. Imposing that C is orthogonal to the $\mathcal{N}$ vectors of $\tilde{\eta}^{(i)}$, since C contains the Λ plane, we are enforcing automatically that $\sum_i \lambda_\alpha^{(i)} \tilde{\eta}_I^{(i)} = 0$. So we must have an additional delta function[11]

$$\delta^{k\times\mathcal{N}}\left(C\cdot\tilde{\eta}\right). \tag{8.92}$$

Unlike the other two type of variables, we have that the condition on λ is imposed making use of $C^\perp$ instead of C. This causes trouble, since we cannot choose an arbitrary representative of $C^\perp$ once we have fix a gauge for C, but we have to respect the global $GL(k)$ invariance of the Grassmannian. A nice solution is to work with the twistor variables, since we have that when the correct $C^\perp$ is used, it is satisfied

$$\delta^{k\times 2}\left(C\cdot\tilde{\mu}\right) = \int \prod_{i=1}^{n} \mathrm{d}^2\lambda^{(i)}\, e^{i\tilde{\mu}_a^{(i)}\lambda^{a(i)}}\, \delta^{2\times(n-k)}\left(\lambda\cdot C^\perp\right), \tag{8.93}$$

which allows to write all the constraints in a compact way

$$\delta^{k\times 4|k\times\mathcal{N}}\left(C\cdot\mathcal{W}\right) \equiv \delta^{k\times 2}\left(C\cdot\tilde{\mu}\right)\delta^{k\times 2}\left(C\cdot\tilde{\lambda}\right)\delta^{k\times\mathcal{N}}\left(C\cdot\tilde{\eta}\right). \tag{8.94}$$

8.8.2 Grassmannian representation of 3-particle amplitudes

In the 3-particle amplitudes, we know that apart of momentum conservation, we have that either the $\lambda^{(i)}$ or the $\tilde{\lambda}^{(i)}$ are parallel to each other. However, our representation of the on-shell diagram in terms of the amplitude does not make this important fact manifest. As we discussed earlier, this has a simple interpretation using the Grassmannian as an auxiliary object to impose the (super)momentum conservation constraints. Recovering the $\mathcal{N} = 4$ SYM amplitudes from Eqs. (8.52) and (8.53), let us start with the antiholomorphic vertex

$$\mathcal{M}_3^A(1,2,3) = \delta^{(2\times 2)}\left(\sum_{i=1}^{3}\lambda^{(i)}\tilde{\lambda}^{(i)}\right)\delta^{(1\times\mathcal{N})}\left(\sum_{i=1}^{3}[i+1,i-1]\tilde{\eta}^{(i)}\right)\frac{1}{[1,2][2,3][3,1]}. \tag{8.95}$$

We know that all the $\lambda^{(i)}$ are parallel, so they have to be spanned by a 1-dimensional plane. The condition $\lambda\cdot C^\perp = 0$ implies that λ is spanned by C, so $C \in Gr(1,3)$. Notice that the coefficients of the $\tilde{\eta}^{(i)}$ are the same as the factors in the denominator, and coincide

[11] Although we are working with $\mathcal{N} = 4$, we maintain $\mathcal{N}$ to exhibit the similarities with the $\mathcal{N} < 4$ case we are studying in Chapter 10.

with the plane orthogonal to $\tilde{\lambda}$, which is C, so we have all the ingredients to fix it, *i.e.*, $C = \Big([23] \quad [31] \quad [12]\Big)$. This, making the expression *gauge invariant* under the $GL(1)$ redundancy of the Grassmannian

$$\mathscr{M}_3^A(1,2,3) = \int \frac{\mathrm{d}^{1\times 3}C}{\mathrm{Vol}\{GL(1)\}} \frac{\delta^{(1\times\mathscr{N})}\big(C\cdot\tilde{\eta}\big)\,\delta^{(1\times 2)}\big(C\cdot\tilde{\lambda}\big)\,\delta^{(2\times 2)}\big(\lambda\cdot C^{\perp}\big)}{\Delta_1\Delta_2\Delta_3}, \tag{8.96}$$

where Δ_i is the i-th (1×1) minor of C. The delta function imposing $C\cdot\tilde{\lambda}=0$ sets, once we have fixed the gauge redundancy $C = \Big([23] \quad [31] \quad [12]\Big)$. The remaining delta functions simply become the momentum and supermomentum constraints.

Let us now study the holomorphic vertex

$$\mathscr{M}_3^H(1,2,3) = \delta^{(2\times 2)}\left(\sum_{i=1}^{3}\lambda^{(i)}\tilde{\lambda}^{(i)}\right)\delta^{(2\times\mathscr{N})}\left(\sum_{i=1}^{3}\lambda^{(i)}\tilde{\eta}^{(i)}\right)\frac{1}{\langle 1,2\rangle\langle 2,3\rangle\langle 3,1\rangle}. \tag{8.97}$$

In this case, we know that all the $\tilde{\lambda}^{(i)}$ are proportional to each other. Taking into account that they must be spanned by $C^{\perp}$, we have that $C\in Gr(2,3)$, and a gauge invariant expression is

$$\mathscr{M}_3^H(1,2,3) = \int \frac{\mathrm{d}^{2\times 3}C}{\mathrm{Vol}\{GL(2)\}} \frac{\delta^{(2\times\mathscr{N})}\big(C\cdot\tilde{\eta}\big)\,\delta^{(2\times 2)}\big(C\cdot\tilde{\lambda}\big)\,\delta^{(1\times 2)}\big(\lambda\cdot C^{\perp}\big)}{\Delta_{12}\Delta_{23}\Delta_{31}}. \tag{8.98}$$

The integral over C, once we fix the $GL(2)$ redundancy C has only 2 free parameters to integrate over. The constraint $\delta^{(1\times 2)}\big(\lambda\cdot C^{\perp}\big)$ localize the integral, while setting $C=\lambda$. The determinants of the (2×2) minors coincide with the angle brackets, and the remaining delta functions are nothing but the momentum and supermomentum conservation constraints.

8.9 A little excursion into Loops

8.9.1 Generalized Unitarity Method

The structure of amplitudes at loop-level is much more complicated than the tree-level one, because now they include both poles and branch-points. Like in the tree-level case, its pole structure can be exploited to develop methods to calculate amplitudes, taking advantage of the loop level branch cuts. It is generally easier to compute discontinuities along these branch cuts than performing the loop integration of the Feynman diagrams, and this can be done using the unitarity condition of the S-matrix.

The S-matrix operator can be written as $\hat{S} = \mathbb{1} + i\hat{T}$, with the operator $\hat{T}$ defining the scattering amplitude

$$\Big\langle p^{(j_1)},\ldots,p^{(j_m)}\Big|\, i\hat{T}\,\Big|p^{(i_1)},\ldots,p^{(i_n)}\Big\rangle = M_n\big(\big\{p^{(i_1)},\ldots,p^{(i_n)}\big\}\big)\to\big\{p^{(j_1)},\ldots,p^{(j_m)}\big\}\big) \tag{8.99}$$

The unitarity of the S-matrix translates into the condition

$$-i(\hat{T}-\hat{T}^\dagger)=\hat{T}^\dagger\hat{T}\,, \tag{8.100}$$

that can be expanded perturbatively in the coupling constant and, using the completeness relation of the Hilbert space, its right-hand-side shows an integration over the momenta of all possible intermediate states. In that way, the imaginary part of the loop amplitude, that is directly related to the discontinuity along the branch cuts, can be determined from the phase-space integrals of products of lower-order amplitudes, which are identified by restricting two internal propagators to be on-shell. The operations described before are encoded under the name of Cutkosky cutting rules presented in Ref. [112].

The idea now is expanding the loop amplitude, instead of in terms of the usual Feynman diagrams, in terms of a basis of scalar integrals, which are loop momentum integrals whose numerators do not have a tensor structure. The point is that the coefficients of this expansion are rational functions of the external momenta, and all the branch-point structure is encoded in the scalar integrals, that can be done once and for all and be tabulated. This was first done by Passarino-Veltman in Ref. [234] for the 1-loop case, turning out that the one-loop amplitude for an arbitrary number of external particles can be written as

$$M_n^{1-\text{loop}}=\sum_{i\in\mathscr{S}_4}\mathscr{C}_4^{(i)}I_4^{(i)}+\sum_{i\in\mathscr{S}_3}\mathscr{C}_3^{(i)}I_3^{(i)}+\sum_{i\in\mathscr{S}_2}\mathscr{C}_2^{(i)}I_2^{(i)}+\mathscr{R}^{(1)}\,, \tag{8.101}$$

where the I_m are scalar integrals with m internal propagators (like those appearing in a scalar ϕ^n theory), the coefficients $\mathscr{C}_m$ and $\mathscr{R}^{(1)}$ are rational functions of the external momenta and the sums $i\in\mathscr{S}_m$ are over all possible partitions of the external momenta in m groups. The absence of scalar integrals I_1 is due to that in dimensional regularization tadpoles vanish identically. For higher number of loops there is no general procedure to identify a basis, although Passarino-Veltman reduction techniques are applied to find them in each case.

Let us now describe *generalized unitarity methods*, while further details can be found in Refs. [235, 276, 277]. Once such an expansion is known, we need to compute the coefficients, that can be determined by unitarity through the computation of branch-cut discontinuities along all possible momentum channels. The idea behind generalized unitarity is to go beyond double cuts and to impose more constraints in order to have also cuts with a higher number of propagators on-shell. In a 4-dimensional space-time the maximum number of conditions that we can impose on a four-vector is four, but we need to complexify the momentum in order to guarantee the existence of a solution (via the fundamental theorem

of algebra); then there is possible to apply triple and quadruple cuts. Cutting k propagators we select all those Feynman diagrams on the left-hand-side and all scalar integrals on the right-hand-side presenting these internal propagators, allowing us to relate the coefficients of a particular number of scalar integrals with Feynman diagrams where propagators have been cut. It is worth noting that in 4 dimensions if we perform a 4-cut, on the right-hand-side only the box integrals contribute.

In practice, what it is done follows the reverse logic [266]. At the start, we perform all possible quadruple cuts and propose an ansatz for the amplitude in terms of only box integrals, matching the coefficients to reproduce the cuts. Having reproduced the quadruple cuts, we move towards the triple cuts. Our ansatz predicts some values for these cuts, since the scalar box integrals have non-vanishing triple cuts; if they agree with the triple cuts of the amplitude, we would be done. If not, we have to continue with the procedure including in the ansatz scalar triangle integrals. Then we perform double cuts, and if the result do not agree, we have to include also scalar bubble integrals. This construction reproduce the amplitude up to the rational terms, that are not constructible using unitarity cuts.

Conformal properties of maximally supersymmetric YM theories in the planar limit offer a simple way to identify a basis of scalar integrals for the loop amplitude [257], which usually consist of a generalization of the box integral of the Passarino-Veltman decomposition to arbitrary loops. In particular, the one and two-loop four-particle amplitudes amplitudes in planar $\mathcal{N}=4$ SYM, first calculated in [278] and [279], can be written, as it is done in [257], in the following form

$$\mathscr{A}_4^{(1)} = A_4^0 \times \left(-\frac{1}{2} s_{12} s_{41} I_4^{(1)}(s_{12}, s_{41})\right), \tag{8.102}$$

$$\mathscr{A}_4^{(2)} = A_4^0 \times \frac{1}{4} s_{12} s_{41} \left(s_{12} I_4^{(2)}(s_{12}, s_{41}) + s_{41} I_4^{(2)}(s_{41}, s_{12})\right), \tag{8.103}$$

where factors $-\frac{1}{2}$ and $\frac{1}{4}$ appear because of the normalization convention in equation (8.8). The integrals $I_4^{(L)}$ are scalar box integrals defined by

$$I_4^{(1)}(s_{12}, s_{41}) = -ie^{\varepsilon\gamma}\pi^{-d/2} \int \frac{d^4 l}{l^2 (l - p^{(1)})^2 (l + p^{(2)})^2 (l - p^{(1)} - p^{(4)})^2}, \tag{8.104}$$

and for the two-loop one

$$\begin{aligned} I_4^{(2)}(s_{12}, s_{41}) &= (-ie^{\varepsilon\gamma}\pi^{-d/2})^2 \times \\ &\times \int \frac{d^4 l\, d^4 q}{l^2 (l - p^{(1)})^2 (l + p^{(2)})^2 q^2 (q + p^{(4)})^2 (q - p^{(3)})^2 (l - q - p^{(1)} - p^{(4)})^2}. \end{aligned} \tag{8.105}$$

Up to convention factors both amplitudes can be represented as in Fig. 8.11 and Fig. 8.12.

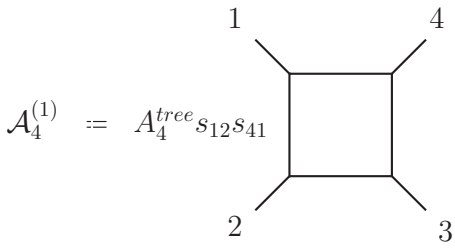

Figure 8.11: 4-particle 1-loop amplitude in $\mathcal{N}=4$ SYM in terms of scalar integrals.

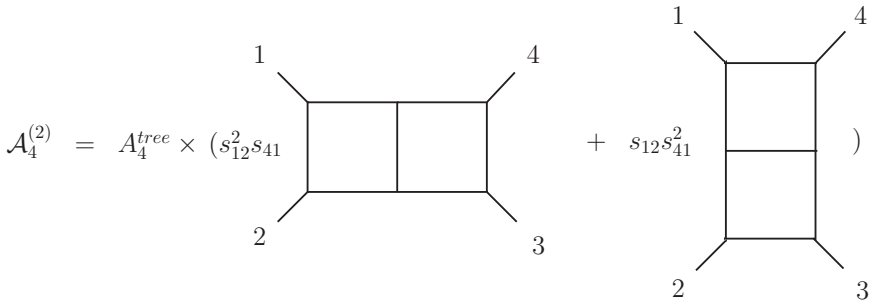

Figure 8.12: 4-particle 2-loop amplitude in $\mathcal{N}=4$ SYM in terms of scalar integrals.

8.9.2 BCFW Recursion Relations for Loop Amplitudes

Loop amplitudes have a complicated analytic structure, but the loop integrand is just a rational function with poles at the location of the propagators, much similar to tree amplitudes. Suppose we do a BCFW deformation on two external particles $p^{(i)}$ and $p^{(j)}$, we can deduce by looking at the Feynman diagrams expression that the loop integrand can develop two kinds of poles: poles in loop independent propagators or poles in propagators involving loop momentum. The residue of the former type of propagator corresponds to a factorization of the loop integrand into a product of two lower-loop integrands. The residue of the latter type of pole in an L-loop n-point integrand is not understood in general, but at least for planar $\mathcal{N}=4$ SYM it corresponds [280] to an (L-1)-loop (n+2)-point integrand with two adjacent legs evaluated in the forward limit, that corresponds to take

$$p^{(n+1)} = -p^{(n+2)} = q, \quad \text{with} \quad q^2 = 0 \ \text{ light-like}. \tag{8.106}$$

For a general theory, it is not clear how to define the loop integrand, since there are ambiguities such as the identification of *the* loop momenta, leading to different pole structures in the integrand, the presence of terms that vanish upon (a particular) regularized

integration or problems with singularities appearing when taking the forward limit. Those subtleties have been partially solved in non-supersymmetric theories [281] and completely solved in supersymmetric theories in the planar limit [236, 280].

As well as for tree-level amplitudes the knowledge of the singularities can lead to recursion relations relating the amplitude with lower-point amplitudes, in the case of loop level understanding all possible singularities that can appear in the loop integrand lead to an all-loop recursion relation for planar $\mathcal{N}=4$ SYM. The formula, represented in terms of on-shell diagrams, has been proven in [237] and it is depicted in Fig. 8.13.

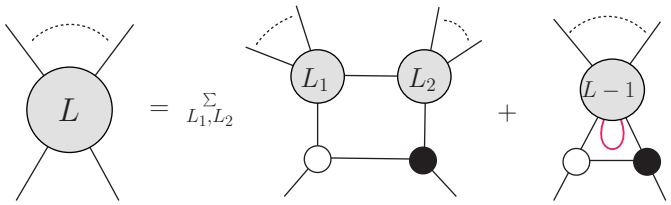

Figure 8.13: On-shell diagramatic formula for the all-loop recursion relation in planar $\mathcal{N}=4$ SYM.

Using the on-shell representation of the L-loop integrand given by that recursion relation in the same paper it is proven that all MHV amplitudes of planar $\mathcal{N}=4$ SYM can be written in a compact "$d\log$" form

$$\mathcal{A}_n^{\text{MHV},L} = A_n^{\text{MHV},0} \times \prod_{i=1}^{4L} d\log\zeta_i \,. \tag{8.107}$$

CHAPTER 9

ON A REGULARIZATION PRESCRIPTION FOR ON-SHELL FORMS

On-shell forms obtained from on-shell diagrams provide a representation of scattering amplitudes at tree level and, in the case of loop-level, of the *loop integrand*, that we later need to integrate properly.

A regularization scheme defined directly in terms of on-shell diagrams, without any reference to the standard off-shell momentum integration expressions, is needed if we want to understand scattering amplitudes fully in terms of these *recently developed* on-shell formalism. Without it, we need to be constantly mapping all the on-shell expressions to the standard off-shell expressions, requiring to work in both frameworks, what it is not very practical. In addition, we would be tied to traditional interpretations, being difficult to find new insights. A complementary description of scattering amplitudes completely in terms of on-shell forms would be highly satisfactory, with the possibility of opening of new ways to understand fundamental aspects of nature.

As we have been pointing during the work, the on-shell formalism depends crucially in the massless character of the external states and the dimensionality of space-time. Although there are ways of circumvent these restrictions [258, 282, 283], we are not considering them. Typical regularization procedures, as giving mass to the massless particle in order to avoid the IR divergences, or dimensional regularization where the space-time dimension is extended to complex values are not applicable here, at least if we want to keep using the mentioned methods. A regularization scheme called four-dimensional helicity (FDH) [284] keeps fixed the space-time dimension of the external states, only modifying the dimension of the loop momenta, but we want to avoid mentioning

any loop momentum, which is purely an off-shell concept.

We described in Ref. [6] a regularization procedure that does not spoil the requirements needed to apply spinor-helicity techniques, and it is completely defined in terms of the on-shell formalism point of view, via a suitable modification of the building blocks of the framework, the three-point amplitudes. Three-particle amplitudes, fixed by Poincaré invariance, depend on the helicities of the particles and the coupling constants of the theory; the idea of the regularization procedure is to *deform* these amplitudes by making an *unphysical* extension of the helicity space. This prescription can be applied to any on-shell diagram, so it is not restricted to maximally supersymmetric theories, allowing us to apply it even to theories with no supersymmetry, as pure YM.

For sake of simplicity, let us consider a theory whose coupling constants have all the same dimension, that we will impose to be fixed. Fixing the dimension of the coupling constants will constraint the helicity deformations that we can perform. Recall from Section 8.4 that the expressions of three-particle amplitudes with states of arbitrary helicity are

$$\begin{aligned}\mathscr{M}_3^H(\lambda,\tilde{\lambda},h) &= \delta^{2\times 2}(\sum_i \lambda^{(i)}\tilde{\lambda}^{(i)}) \times \left\{\kappa^H \langle 12\rangle^{d_3}\langle 23\rangle^{d_1}\langle 31\rangle^{d_2}\right\} \\ \mathscr{M}_3^A(\lambda,\tilde{\lambda},h) &= \delta^{2\times 2}(\sum_i \lambda^{(i)}\tilde{\lambda}^{(i)}) \times \left\{\kappa^A [12]^{-d_3}[23]^{-d_1}[31]^{-d_2}\right\}\end{aligned} \tag{9.1}$$

where $d_1 = h_1 - h_2 - h_3$, $d_2 = h_2 - h_1 - h_3$ and $d_3 = h_3 - h_1 - h_2$.

The dimension of the coupling constants is obtained taking into account that a cross-section has the dimension of an area. Thus, a n-particle amplitude has dimension $4-n$, that in the case of $n = 3$ lead to dimension 1 (without considering the momentum-conserving δ-function). The kinematic factors $\langle ij\rangle$ and $[ij]$ have dimension 1, as we saw in Section 8.2. All these considerations imply that $\left[\kappa^H\right] = 1+h$ and $\left[\kappa^A\right] = 1-h$, where $h = h_1+h_2+h_3$, so the allowed deformations have to keep h constant

$$h_i \longrightarrow h_i + \varepsilon_i, \quad \text{with} \quad \sum_i \varepsilon_i = 0 \quad (i = 1,2,3) \tag{9.2}$$

which is consistent with the fact that the (anti-)holomorphic amplitude is only defined for $h = h_1+h_2+h_3 < 0$ (> 0), since the deformations can not alter this condition.

The tree-particle amplitudes are transformed as

$$\begin{aligned}\mathscr{M}_3^H(\lambda,\tilde{\lambda},h) &\longrightarrow \mathscr{M}_3^{H,(d)}(\lambda,\tilde{\lambda},h,\varepsilon) = \langle 12\rangle^{e_3}\langle 23\rangle^{e_1}\langle 31\rangle^{e_2}\mathscr{M}_3^H(\lambda,\tilde{\lambda},h) \\ \mathscr{M}_3^A(\lambda,\tilde{\lambda},h) &\longrightarrow \mathscr{M}_3^{A,(d)}(\lambda,\tilde{\lambda},h,\varepsilon) = [12]^{-e_3}[23]^{-e_1}[31]^{-e_2}\mathscr{M}_3^A(\lambda,\tilde{\lambda},h)\end{aligned} \tag{9.3}$$

where $e_1 = \varepsilon_1 - \varepsilon_2 - \varepsilon_3$, $e_2 = \varepsilon_2 - \varepsilon_1 - \varepsilon_3$ and $e_3 = \varepsilon_3 - \varepsilon_1 - \varepsilon_2$. It is important to notice that even in the amplitudes are not equal for in pure Yang-Mills and in general $\mathscr{N}$ SYM, they

get deformed with the same factor when the regularization prescription is applied, making the regularization convenient to study theories with arbitrary $\mathcal{N}$.

These regularized three-particle amplitudes can be glued together in the same way as the normal ones and, because they are modified by a multiplicative factor, the resulting on-shell form is given by the unregularized on-shell form times a multiplicative factor depending on the kinematical data as well as the regularization parameters.

In the case of internal particles, characterized by an internal line connecting two blobs, the deformation parameter ε has opposite signs at the two end-points. By convention, we choose each internal line to have $+\varepsilon$ at the end-point belonging to the holomorphic amplitude and $-\varepsilon$ at the end-point belonging to the anti-holomorphic amplide. Notice that any deformed on-shell form built in that way satisfies

$$\sum_i \varepsilon_i = 0 \tag{9.4}$$

for the deformation parameters of all external states.

For example, the 4-particle tree-level amplitude, which is represented by an on-shell box alternating holomorphic and anti-holomorphic vertices, gets deformed as it is seen in Fig. 9.1. Where the multiplicative factor generated by the regularization is given by

$$\begin{aligned}\mathscr{F}(\lambda,\tilde{\lambda},\varepsilon) = \left(\frac{[12][41]}{[24]}\right)^{\varepsilon_1}\left(\frac{\langle 31\rangle}{\langle 12\rangle\langle 23\rangle}\right)^{\varepsilon_2}\left(\frac{[23][34]}{[42]}\right)^{\varepsilon_3}\left(\frac{\langle 13\rangle}{\langle 34\rangle\langle 41\rangle}\right)^{\varepsilon_4}\times \\ \times\left(\frac{-1}{s_{12}}\right)^{\varepsilon_{12}+\varepsilon_{34}}\left(\frac{-1}{s_{41}}\right)^{\varepsilon_{41}+\varepsilon_{23}}\end{aligned} \tag{9.5}$$

where $s_{ij} = (p^{(i)} + p^{(j)})^2$ are the Mandelstam variables.

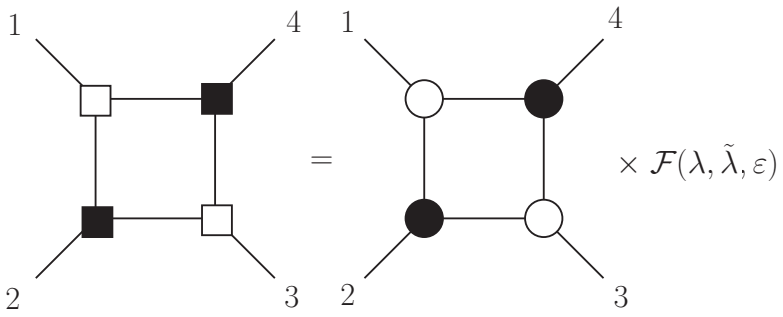

Figure 9.1: Regularized on-shell diagram corresponding to the 4-particle tree level amplitude. Regularized vertices are represented with squares.

Using condition (9.4) in each vertex we can write the ε_i in terms of the ε_{ij} (but not the opposite), leading to the following expression

$$\mathscr{F}(\lambda,\tilde{\lambda},\varepsilon)=\left(\frac{\langle 23\rangle}{\langle 13\rangle}\right)^{2\varepsilon_{12}}\left(\frac{[34]}{[24]}\right)^{2\varepsilon_{23}}\left(\frac{[23]}{[24]}\right)^{2\varepsilon_{34}}\left(\frac{\langle 34\rangle}{\langle 13\rangle}\right)^{2\varepsilon_{41}} \tag{9.6}$$

The aim of the regularization scheme is to regularize loop integrals, so what we need are on-shell forms representing loop integrands or, at least, a contribution to a loop integrand. The BCFW-bridge construction is very useful for that purpose, applying four inequivalent BCFW-bridges to the 4-point tree-level amplitude considered before we obtain an on-shell form with four degrees of freedom unfixed, which can be the ones parametrizing the loop.

Using the BCFW recursion relation at loop level and equivalence relations of on-shell diagrams in $\mathcal{N}=4$ SYM, it is proven in [237] that the full 1-loop amplitude for four particles in the planar limit is given by the on-shell form associated to the on-shell diagram of Fig. 9.2. As anticipated, this symmetric form of the on-shell diagram can be interpreted as four BCFW-bridges attached to the internal square, which is the four-particle tree-amplitude. For a generic theory it is not necessary the full integrand, but it can represent a contribution to it.

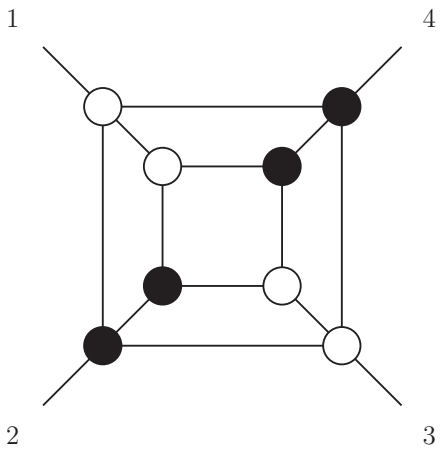

Figure 9.2: On-shell diagram representing the 4-particle 1-loop integrand in $\mathcal{N}=4$ SYM.

Under the regularization prescription, we have to take in account how formulae (8.73) and (8.74) change in order to use the BCFW-bridge construction. As we have mentioned before, we have to consider only the multiplicative deformation factor for each blob in the diagram, in that case one of each kind. To fix the notation for the deformation parameters of the internal particles, let us consider the diagram of Fig. 9.3. We will denote by $\hat{\varepsilon}_i$, $\hat{\varepsilon}_j$

the deformation parameters of the internal lines associated with $i(z)$ and $j(z)$ respectively, with the plus sign at the end-point entering the big square. For the internal line with momentum $z\lambda^{(i)}\tilde{\lambda}^{(j)}$ we keep the usual convention, we will denote by ε_{ij} the deformation parameter, with the plus sign at the end-point attached to the black vertex. To sum up, the states entering the white vertex have regularization parameters $(\varepsilon_1, -\hat{\varepsilon}_1, -\varepsilon_{ij})$, while those entering the black vertex have parameters $(\varepsilon_2, -\hat{\varepsilon}_2, \varepsilon_{ij})$.

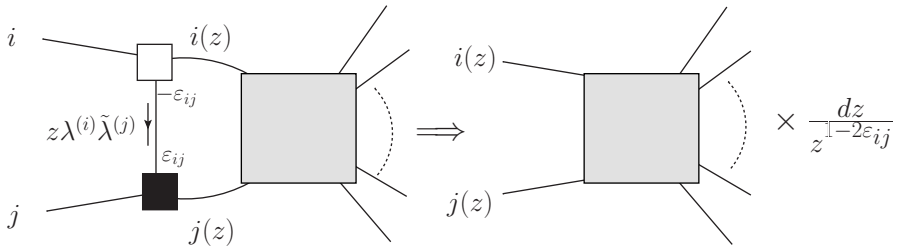

Figure 9.3: On-shell diagram representing the regularized version of the BCFW-bridge.

After some algebra we obtain the following formula for the deformation factor

$$\mathscr{F}_B(\lambda,\tilde{\lambda},\varepsilon) = \left(-s_{ij}\right)^{-\varepsilon_{ij}} (z[ij])^{\varepsilon_i-\hat{\varepsilon}_i} (-z\langle ij\rangle)^{\hat{\varepsilon}_j-\varepsilon_j} \tag{9.7}$$

that can be simplified using the constraints on the regularization parameters

$$\mathscr{F}_B(\lambda,\tilde{\lambda},\varepsilon) = z^{2(\varepsilon_1-\hat{\varepsilon}_1)} = z^{2\varepsilon_{ij}} \tag{9.8}$$

that only depends on the regularization parameter of the internal bridge momentum.

We have the required ingredients to calculate the regularized version of the one-loop on-shell diagram of Fig. 9.2. First, the number of independent regularization parameters is in that case 8: corresponding to 4 external particles, 12 states flowing in the internal lines and 8 vertices. We can pick as independent parameters the four ε associated with the four BCFW bridges, that we will denote by ε_{ij}, as in Fig. 9.3. Once we have applied the BCFW-bridge simplification we are left with the diagram of Fig. 9.1, where the external states are now the deformed momenta depending on four complex variables that we will call z_{ij}, using the same notation as for the ε_{ij}.

The deformed tree-level amplitude is easily obtained using equation (9.6), where the regularization parameters associated with the internal lines of the tree-level on-shell box are denoted by $\bar{\varepsilon}_{ij}$, completing the required number of independent regularization parameters. That lead as to the following formula for the regularized planar $\mathcal{N}=4$ SYM

1-loop integrand

$$\begin{aligned}\mathscr{A}_4^{(1),(d)}(\lambda,\tilde{\lambda},\eta,\varepsilon) &= \mathscr{A}_4^{tree}(\lambda,\tilde{\lambda},\eta)\times \\ &\times\left(\frac{\langle 23\rangle}{\langle 13\rangle}\right)^{2(\varepsilon_{12}+\bar{\varepsilon}_{12})}\left(\frac{[34]}{[24]}\right)^{2(\varepsilon_{23}+\bar{\varepsilon}_{23})}\left(\frac{[23]}{[24]}\right)^{2(\varepsilon_{34}+\bar{\varepsilon}_{34})}\left(\frac{\langle 34\rangle}{\langle 13\rangle}\right)^{2(\varepsilon_{41}+\bar{\varepsilon}_{41})}\times \\ &\times\prod_{ij} d\hat{z}_{ij}\hat{z}_{ij}^{-1+2\varepsilon_{ij}}\left(1+\hat{z}_{ij}\right)^{-1+2\bar{\varepsilon}_{ij}}\end{aligned} \tag{9.9}$$

where the $\hat{z}_{ij}$ are obtained rescaling the z_{ij} to be helicity blind. The integrand is easily related to the integrand of the Euler's Beta function, that it is well-defined if $\mathrm{Re}\left(\varepsilon_{ij}\right)>0$ and $\mathrm{Re}\left(1-2\varepsilon_{ij}-2\bar{\varepsilon}_{ij}\right)>0$.

It is worth noting that taking the limit in which the regularization parameters vanish, the integrand can be written in a compact "dlog" form, as it was mentioned in Section 8.9.2,

$$\mathscr{A}_4^{(1)}(\lambda,\tilde{\lambda},\eta,\varepsilon) = \mathscr{A}_4^{tree}(\lambda,\tilde{\lambda},\eta)\times\prod_{ij} d\log\frac{\hat{z}_{ij}}{1+\hat{z}_{ij}} \tag{9.10}$$

that makes natural to define new variables ζ_{ij} related to the helicity-blind $\hat{z}_{ij}$ via

$$\zeta_{ij}\equiv\frac{\hat{z}_{ij}}{1+\hat{z}_{ij}} \tag{9.11}$$

in terms of these new variables the integrand of the one-loop amplitude can be written, up to ζ independent factors, as

$$\Omega_4(\zeta,\varepsilon)\equiv\prod_{ij} d\zeta_{ij}\zeta_{ij}^{2\varepsilon_{ij}-1}\left(1-\zeta_{ij}\right)^{-2(\varepsilon_{ij}+\bar{\varepsilon}_{ij})} \tag{9.12}$$

Some comments are now in order. Firstly, setting all the parameters to zero, one obtains the $\bigwedge_{i=1}^{4} d(\log\zeta_{i,i+1})$ form for the above integrand, as it should be for UV-finite contributions. Secondly, the $\Omega_4(\zeta)$ in Eq. (9.12) can be seen as a four-form with branch points at $\zeta_{i,i+1}=0,\infty,1$. Thus, the introduction of our helicity deformations opens up the poles naturally present in the integrand producing branch cuts as well as new singularities ($\zeta_{i,i+1}=1$) not present in the undeformed integrand. The 4-form Ω_4 can be thought of as a holomorphic multi-valued 4-form on the complement of a branch locus in $\mathbb{C}^4$. In order to extract physical information from Rq. (9.12), one has to identify the correct integration path and how to correctly treat the branch locus.

9.1 The Integration Contour at one-loop

We have determined the on-shell form describing the regularized one-loop amplitude in planar $\mathcal{N}=4$ SYM, but in order to obtain the amplitude we need to identify the integration

contour that lead to the one-loop amplitude in Lorentzian signature. The main goal is to build up a first-principle criterion which determines the appropriate contour of integration depending on the quantity we want to calculate: the amplitude in Lorentzian or in $SO(2,2)$ signature, a leading singularity or another physical quantity at loop-level.

The form to be integrated does not have any dependence on the kinematics, then all kinematical information has to be encoded in the integration contour. As we have mentioned earlier, the choice of the contour integration determines the physical quantity one is computing, and even the signature in which we are working.

A general criterion to identify the contours of integration has not been found yet, and there is no physical interpretation of the on-shell form degrees of freedom that can lead to a possible contour. However, it is possible to obtain restrictions on the contour of integration relating the ζ_{ij} variables to the traditional off-shell loop momentum, that we know how to integrate.

In order to establish the connection let us recall that the one-loop integral can be written in terms of the scalar box integral, as in equation (8.104). Up to convention factors the amplitude is given by

$$\mathscr{A}_4^{(1)} = \mathscr{A}_4^{tree} s_{12} s_{41} \int d^4 l \frac{1}{l^2 (l - p^{(1)})^2 (l + p^{(2)})^2 (l - p^{(4)} - p^{(1)})^2} \tag{9.13}$$

For notational convenience, we will define

$$I_{\text{box}} = \int d^4 l \frac{1}{l^2 (l - p^{(1)})^2 (l + p^{(2)})^2 (l - p^{(4)} - p^{(1)})^2} \tag{9.14}$$

It is convenient to introduce a momentum variable for each internal leg. Let us denote the internal momentum joining the vertices containing particles i and j by l_{ij}, so they are related to the previous quantities by

$$l_{12} \equiv l, \quad l_{23} \equiv -(l + p^{(2)}), \quad l_{34} \equiv l - p^{(4)} - p^{(1)}, \quad l_{41} \equiv p^{(1)} - l \tag{9.15}$$

leading to a more symmetrical expression of the integral (9.14)

$$\begin{aligned} I_{\text{box}} = \prod_{ij} \int \frac{d^4 l_{ij}}{l_{ij}^2} \delta^4(p^{(1)} - l_{12} - l_{41}) \delta^4(p^{(2)} + l_{12} + l_{23}) \times \\ \times \delta^4(p^{(3)} - l_{23} - l_{34}) \delta^4(p^{(4)} + l_{41} + l_{34}) \end{aligned} \tag{9.16}$$

To make contact with the on-shell formalism we parametrize each of-shell momentum l_{ij} as a sum of two light-like vectors

$$l_{ij} \equiv \mu_{ij} + z_{ij} q_{ij}, \quad \mu_{ij}^2 = 0 = q_{ij}^2, \quad z_{ij} \in \mathbb{C} \tag{9.17}$$

where the q_{ij} are fixed momentum, to be chosen at convenience. This change of variables lead to the following Jacobian factor

$$\frac{d^4 l_{ij}}{l_{ij}^2} = \frac{dz_{ij}}{z_{ij}} d^4\mu_{ij}\delta(\mu_{ij}^2) \tag{9.18}$$

that makes explicit the on-shell nature of the μ_{ij} momenta.

We can write the $p^{(i)}$ entirely in terms of the μ_{ij} defining deformed momenta $p^{(i)}(z)$ in analogy with the BCFW-bridge representation of the one-loop amplitude. The deformation is given by

$$\begin{aligned} p^{(1)}(z) &\equiv p^{(1)} - z_{41}q_{41} - z_{12}q_{12}, \quad p^{(2)}(z) \equiv p^{(2)} + z_{12}q_{12} + z_{23}q_{23} \\ p^{(3)}(z) &\equiv p^{(3)} - z_{23}q_{23} - z_{34}q_{34}, \quad p^{(4)}(z) \equiv p^{(4)} + z_{34}q_{34} + z_{41}q_{41} \end{aligned} \tag{9.19}$$

Choosing μ_{12} as a reference internal on-shell momentum we can rewrite the integral as

$$\begin{aligned} I_{\text{box}} = \delta^4(\sum_i p^{(i)}) \prod_{ij} \int \frac{dz_{ij}}{z_{ij}} \int d^4\mu_{12}\, \delta\left(\mu_{12}^2\right) \delta\left((\mu_{12} - p^{(1)}(z))^2\right) \times \\ \times \delta\left((\mu_{12} + p^{(2)}(z))^2\right) \delta\left((\mu_{12} - p^{(4)}(z) - p^{(1)}(z))^2\right) \end{aligned} \tag{9.20}$$

where it can be seen that the δ-functions put on-shell the internal propagators of box integrals, but with deformed external momenta.

If we want to maintain the BCFW-deformation analogy we have to choose all q_{ij} in such a way that the deformed momenta remain on-shell, up to proportionality factors that would be absorbed in the z_{ij} there are only two possibilities

$$\begin{gathered} (q_{12}, q_{23}, q_{34}, q_{41}) = (\lambda^{(1)}\tilde{\lambda}^{(2)}, \lambda^{(3)}\tilde{\lambda}^{(2)}, \lambda^{(3)}\tilde{\lambda}^{(4)}, \lambda^{(1)}\tilde{\lambda}^{(4)}) \\ \text{or} \\ (q_{12}, q_{23}, q_{34}, q_{41}) = (\lambda^{(2)}\tilde{\lambda}^{(1)}, \lambda^{(2)}\tilde{\lambda}^{(3)}, \lambda^{(4)}\tilde{\lambda}^{(3)}, \lambda^{(4)}\tilde{\lambda}^{(1)}) \end{gathered} \tag{9.21}$$

It is worth noting that both deformations naturally appear when considering the on-shell diagram of Fig. 9.2 as four BCFW-bridges applied to the tree-level amplitude. Both deformations are related by the application of square moves to the diagram.

Taking into account that all $p^{(i)}(z)$ are on-shell the integration over μ_{12} can be carried out to give the following expression for the one-loop amplitude

$$\mathscr{A}_4^{(1)} = \mathscr{A}_4^{tree} \prod_{ij} \int \frac{dz_{ij}}{z_{ij}} \frac{s_{12}s_{41}}{s_{12}(z)s_{41}(z)} \tag{9.22}$$

Using the same rescaling to define helicity-blind variables $\hat{z}_{ij}$ we obtain

$$\mathscr{A}_4^{(1)} = \mathscr{A}_4^{tree} \prod_{ij} \int \frac{d\hat{z}_{ij}}{\hat{z}_{ij}(1+\hat{z}_{ij})} = A_4^{tree} \prod_{ij} \int d\log\zeta_{ij} \tag{9.23}$$

that is exactly equal to equation (9.10), establishing the connection between the ζ_{ij} variables and the loop momentum. First, we have to determine μ_{12} in terms of the external deformed momenta. Imposing the four on-shell conditions of equation (9.20) there are two solutions, one of them leading to a z-independent momentum l and the other, if we choose the first option in equation (9.21), to

$$l = \frac{\langle 14(z)\rangle}{\langle 2(z)4(z)\rangle}\lambda^{(2)}(z)\tilde{\lambda}^{(1)}(z) + z_{12}\lambda^{(1)}\tilde{\lambda}^{(2)} \tag{9.24}$$

To obtain a relation between the variables l^0, l^1, l^2, l^3 and the z_{ij} (or the ζ_{ij}), we write the momentum l in the following basis of spinors

$$l = \gamma_{11}\lambda^{(1)}\tilde{\lambda}^{(1)} + \frac{[14]}{[24]}\gamma_{12}\lambda^{(1)}\tilde{\lambda}^{(2)} + \frac{[24]}{[14]}\gamma_{21}\lambda^{(2)}\tilde{\lambda}^{(1)} + \gamma_{22}\lambda^{(2)}\tilde{\lambda}^{(2)} \tag{9.25}$$

The reality condition for the loop momentum l in Lorentzian signature translates into the following conditions for the γ_{ij} variables

$$\gamma_{11}, \gamma_{22} \in \mathbb{R}, \quad \gamma_{12} \in \mathbb{C}, \quad s_{41}\bar{\gamma}_{12} = s_{13}\gamma_{21} \tag{9.26}$$

and after some tedious algebra they can be related to the ζ_{ij} variables

$$\begin{aligned}
\zeta_{12} &= \frac{\gamma_{11}\gamma_{22} - \gamma_{12}\gamma_{21}}{\gamma_{11}\gamma_{22} - \gamma_{12}\gamma_{21} + \gamma_{21}} \\
\zeta_{23} &= \frac{\gamma_{11}\gamma_{22} - \gamma_{12}\gamma_{21} + \gamma_{11}}{\gamma_{11}\gamma_{22} - \gamma_{12}\gamma_{21} + \gamma_{21}} \\
\zeta_{34} &= \frac{\gamma_{11}\gamma_{22} - \gamma_{12}\gamma_{21} + \gamma_{21} + \frac{s_{41}}{s_{12}}\left(1 + \gamma_{21} + \gamma_{22} - \gamma_{11} - \gamma_{12}\right)}{\gamma_{11}\gamma_{22} - \gamma_{12}\gamma_{21} + \gamma_{21}} \\
\zeta_{41} &= \frac{\gamma_{11}\gamma_{22} - \gamma_{12}\gamma_{21} - \gamma_{22}}{\gamma_{11}\gamma_{22} - \gamma_{12}\gamma_{21} + \gamma_{21}}
\end{aligned} \tag{9.27}$$

In that form, the ζ_{ij} variables have a common denominator, which is a complex number, but their numerators are all real numbers, as can be checked using the reality conditions of equation (9.26). There is also a representation of the ζ_{ij} variables that makes these properties manifest, from the previous relations it is easy to demonstrate that

$$\begin{aligned}
\zeta_{12} &= \frac{l^2}{(l-l')^2}, \qquad \zeta_{23} = \frac{(l+p^{(2)})^2}{(l-l')^2} \\
\zeta_{34} &= \frac{(l-p^{(4)}-p^{(1)})^2}{(l-l')^2}, \quad \zeta_{41} = \frac{(l-p^{(1)})^2}{(l-l')^2}
\end{aligned} \tag{9.28}$$

where the complex momentum l' is equal to $\frac{[14]}{[24]}\lambda^{(1)}\tilde{\lambda}^{(2)}$.

The relations among the γ_{ij} derived from the reality condition of the momentum l lead to conditions among the ζ_{ij}, that can be written in a simple symmetrical form. These

constraints define a submanifold of $\mathbb{C}^4$ that we will consider as the integration contour of the one-loop amplitude in Lorentzian signature

$$\Gamma_{\text{Lor}} = \left\{ \vec{\zeta} \in \mathbb{C}^4 \,/\, s_{12}\zeta_{12}\zeta_{34} + s_{41}\zeta_{41}\zeta_{23} = -s_{13}\frac{\zeta_{12}}{\bar{\zeta}_{12}} = \cdots = -s_{13}\frac{\zeta_{41}}{\bar{\zeta}_{41}} \right\} \tag{9.29}$$

The conditions defining Γ_{Lor} imply that any ratio between the ζ's is real, as well as products of the type $\zeta_{i,i+1}\bar{\zeta}_{j,j+1}$. Another condition, not independent of the others, is the symmetrical relation

$$s_{12}\bar{\zeta}_{12}\zeta_{34} + s_{41}\zeta_{23}\bar{\zeta}_{41} = -u \tag{9.30}$$

in which every term is real.

In the Lorentz signature there are four IR singularities, which in the ζ_{ij} variables are located at the points there three of the variables goes to zero while the other one goes to infinity, satisfying the condition of equation (9.30). We then have

$$\begin{aligned} &\zeta_{12} \longrightarrow \begin{cases} 0 \\ \\ \infty \end{cases}, \quad \zeta_{34} \longrightarrow \begin{cases} \infty \\ \\ 0 \end{cases}, \quad (\zeta_{23}, \zeta_{41}) \longrightarrow (0,0), \quad \bar{\zeta}_{12}\zeta_{34} = -\frac{u}{s}, \\ &\zeta_{41} \longrightarrow \begin{cases} 0 \\ \\ \infty \end{cases}, \quad \zeta_{23} \longrightarrow \begin{cases} \infty \\ \\ 0 \end{cases}, \quad (\zeta_{12}, \zeta_{34}) \longrightarrow (0,0), \quad \bar{\zeta}_{41}\zeta_{23} = -\frac{u}{t}, \end{aligned} \tag{9.31}$$

9.1.1 General Structure of the Integrals

Instead of the "$d\log$" form, regularized on-shell forms will lead in a general theory, for the one loop case, to a expression of the form

$$\omega_4(\zeta) = \prod_{i=1}^{4} d\zeta_{i,i+1}\, \zeta_{i,i+1}^{\mathfrak{a}_{i,i+1}(\varepsilon)-1} \left(1-\zeta_{i,i+1}\right)^{\mathfrak{b}_{i,i+1}(\varepsilon)-1} \tag{9.32}$$

where $\mathfrak{a}_{i,i+1}(\varepsilon)$ and $\mathfrak{b}_{i,i+1}(\varepsilon)$ are linear combinations of the deformation parameters. Thus, the regularization procedure transforms the poles naturally present in the integrand producing a branch-points structure.

This form presents branch points at $\zeta_{i,i+1} = 0, \infty, 1$. Branch points at 0 and ∞ are related to singularities in the IR, while branch points at $\zeta_{i,i+1} = 1$ represent possible singularities in the UV. Notice that on-shell diagrams associated to UV-finite quantities, as the $\mathcal{N} = 4$ SYM 1-loop on-shell form, are characterized by the fact that when the regulators are set to zero it is $\mathfrak{b}_{i,i+1}(\varepsilon) = 1$. The branch-points at $\zeta_{i,i+1} = 1$ disappear when regulators are set to zero without leaving any pole.

While working in the complement of the branch locus of ω_4 in $\mathbb{C}^4$, it is an holomorphic but multivalued 4-form, and it can be integrated there without "theoretical" problems. In order to obtain physical quantities as the amplitude, one has to identify the corresponding integration contour, being specially careful with the branch locus. The integration path has to dictate how to go around the branch points. It is important to stress out that the shape of the branch locus also depends on the contour of integration, because it constraints the submanifold of $\mathbb{C}^4$ where the integration takes place. Therefore, the branch locus encode physical information, for example the residue at the point $\{\zeta_{i,i+1} = 0, \forall i\}$ provides the leading singularity of the amplitude.

To discuss how to deal with the branch points, let us work with a toy model. Instead of studying the 4-form of equation (9.32), we will consider the simplest case possible, a one dimensional version of it

$$\omega_1(\zeta) = d\zeta \zeta^{\mathfrak{a}-1}(1-\zeta)^{\mathfrak{b}-1} \tag{9.33}$$

For general values of $\mathfrak{a}$ and $\mathfrak{b}$ this form has branch points at $\zeta = 0, \infty, 1$. As an example, let us integrate ω_1 over the interval $[0,1]$. If $\mathrm{Re}(\mathfrak{a}) > 0$ and $\mathrm{Re}(\mathfrak{b}) > 0$, the solution is simply the Euler's Beta function $\mathrm{B}(\mathfrak{a},\mathfrak{b})$, but these conditions are not satisfied in general. The definition of the integral can be analytically continued in $\mathfrak{a}$ and $\mathfrak{b}$ while having a finite expression regularizing the integral, i.e., we want an expression that is finite for arbitrary values of $\mathfrak{a}$ and $\mathfrak{b}$ while returning $\mathrm{B}(\mathfrak{a},\mathfrak{b})$ when $\mathrm{Re}(\mathfrak{a}) > 0$ and $\mathrm{Re}(\mathfrak{b}) > 0$.

This can be done for $\mathfrak{a}, \mathfrak{b} \notin \mathbb{Z}$, considering the branch in which the one-form is single valued in the lower-half plane, through the following *twisted cycle* [285]

$$\Delta = \frac{1}{e^{2\pi i \mathfrak{a}} - 1} S^{(1)}_{\delta}(0) + [\delta, 1-\delta] - \frac{1}{e^{2\pi i \mathfrak{b}} - 1} S^{(1)}_{\delta}(1) \tag{9.34}$$

where $S^{(1)}_{\delta}(p)$ is a counter-clockwise circle of radius δ around the point p.

In general, one can regularize the integration over an interval passing through more than two branch-points generalizing the previous twisted cycle. Keeping the branch in with ω_1 is single-valued in the lower-half plane, one can take a counter-clockwise circle of radius δ for each branch-point (with the corresponding phase factors) and summing the contributions of the intervals between all the pairs of consecutive branch-points.

Regularizing these kind of integrals encircling the branch points lead to expressions where the singular behavior gets factored out. In our toy example, if we want to regularize the integral over the real segment $[x,1]$ with $0 < x < 1$ using a contour that starts just below x, encircles the branch-point $\zeta = 1$ counter-clockwise and returns to x (above the real

line) one gets

$$\int_x^1 d\zeta \zeta^{\mathfrak{a}-1}(1-\zeta)^{\mathfrak{b}-1} \longrightarrow \frac{1}{2i\sin\pi\mathfrak{b}} \int_\gamma d\zeta \zeta^{\mathfrak{a}-1}(1-\zeta)^{\mathfrak{b}-1} \tag{9.35}$$

with $\mathfrak{b} \notin \mathbb{Z}$. The integral is now well-defined for arbitrary values of $\mathfrak{b}$, and the singular behavior when $\mathfrak{b}$ approaches integer values has been explicitly factored out.

In the case of the integral of ω_1 over the real segment $[0,1]$ a well known regularization can be done using a Pochhammer contour [286]. It consist of a proper closed path (it returns to the same point of the Riemmann surface) encircling the point $\zeta = 0$ in the counter-clockwise direction, then $\zeta = 1$ counter-clockwise, after that circling $\zeta = 1$ and $\zeta = 0$ clockwise, finishing in the same point that it started. The integral along this contour is regular for arbitrary values of $\mathfrak{a}$ and $\mathfrak{b}$, and it allows us to define the analytic continuation of the Beta function to $\mathfrak{a}, \mathfrak{b} \in \mathbb{C}$. In that way the singular behavior factorizes out

$$\int_0^1 d\zeta \zeta^{\mathfrak{a}-1}(1-\zeta)^{\mathfrak{b}-1} \longrightarrow -\frac{e^{-i\pi(\mathfrak{a}+\mathfrak{b})}}{4\sin\pi\mathfrak{a}\sin\pi\mathfrak{b}} \oint_{\gamma_P} d\zeta \zeta^{\mathfrak{a}-1}(1-\zeta)^{\mathfrak{b}-1} \tag{9.36}$$

Let us consider now a slightly more complicated case by considering the exterior product of two ω_1's

$$\omega_2(\zeta_1,\zeta_2) \equiv \omega_1(\zeta_1) \wedge \omega_1(\zeta_2) \tag{9.37}$$

integrated along a toy contour defined by

$$\Gamma = \left\{ \vec{\zeta} \in \mathbb{C} \,/\, \zeta_1\zeta_2 = -a\frac{\zeta_1}{\bar{\zeta}_1} = -a\frac{\zeta_2}{\bar{\zeta}_2} \right\} \tag{9.38}$$

In the subspace defined by Γ we can write ζ_2 in terms of $\bar{\zeta}_1$, so the integration leads to the following expression

$$\begin{aligned} \int_\Gamma \omega_2 &= (-a)^{\mathfrak{a}_2} \int_{\bar{\zeta}_1=\zeta_1^\star} d\zeta_1 d\bar{\zeta}_1 \zeta_1^{\mathfrak{a}_1-1}(1-\zeta_1)^{\mathfrak{b}_1-1}\left(\bar{\zeta}_1\right)^{-\mathfrak{a}_2-1}\left(1+\frac{a}{\bar{\zeta}_1}\right)^{\mathfrak{b}_2-1} = \\ &= 2(-a)^{\mathfrak{a}_2} \int_{|w|} dw w^{\mathfrak{a}_1+\mathfrak{a}_2-1} \int_{\mathbb{R}_+} d\rho \rho^{\mathfrak{a}_1-\mathfrak{a}_2-\mathfrak{b}_2}\left(1-w\rho\right)^{\mathfrak{b}_1-1}\left(\rho+aw\right)^{\mathfrak{b}_2-1} \end{aligned} \tag{9.39}$$

where in the first line the integral is written in terms of the variables ζ_1 and $\bar{\zeta}_1$, with the integration contour defined by imposing that the variables are related by complex conjugation. In the second line we have used polar coordinates $\zeta_1 = \rho w$, where w is the phase and ρ the radius. It is important to remember that conditions in Γ define the maximum available integration domain, that in general does not have to match with the integration contour.

If we consider the integral in the variables ζ_1 and $\bar{\zeta}_1$, in order for the integral to be well-defined the contour has avoid the branch-points of the two-form. These are located at $\zeta_1 = \{0, 1, \infty\}$ and $\bar{\zeta}_1 = \{0, -a, \infty\}$. One can take a Pochhammer contour which encircles 0 and 1 for ζ_1, while it encircles 0 and $-a$ for $\bar{\zeta}_1$, projected into the real sheet $\bar{\zeta}_1 = \zeta_1^\star$. This explicitly factors out expressions like in equation (9.36), showing poles when the parameters $\mathfrak{a}_i$ and $\mathfrak{b}_i$ are taken to be integers.

Considering the representation in terms of ρ and w the branch locus is defined by the conditions

$$\{w = 0, \infty\,;\, \rho = 0, +\infty\,;\, 1 - w\rho = 0\,;\, \rho + a\omega = 0\} \tag{9.40}$$

In principle, we would be interested in a domain satisfying the conditions $|w| = 1$ and $\rho \in \mathbb{R}_+$. If we want to integrate ρ over the whole $\mathbb{R}_+$ we can perform its integral first, regularizing it taking a Pochhammer contour around the branch-points $\rho = 0, \infty$. Then, the branch-point given by $(\rho, w) = (1, 1)$ will be treated by the integration over w.

In the more general case we will have a p-form such as

$$\omega_p(\zeta_i, \mathfrak{a}_i, \mathfrak{b}_j) = \prod_{i=1}^{p} d\zeta_i\, \zeta_i^{\mathfrak{a}_i - 1} \prod_{j=1}^{m} \left[P_j(\{\zeta_i\})\right]^{\mathfrak{b}_j - 1} \tag{9.41}$$

with $P_j(\{\zeta_i\})$ being polynomials of arbitrary order in all variables $\{\zeta_i\}$, i.e., the variables do not have to decouple, as we have seen in the 2 dimensional examples. Furthermore, let us consider the variables ζ_i to be real. This kind of expression can appear when we restrict the original form to the integration contour.

The branch locus is determined by the points $\zeta_i = 0, \infty$ as well as the conditions $P_j(\{\zeta_i\}) = 0$. Such conditions decompose the space $(\mathbb{R} \cup \{\infty\})^p$ into bounded chambers, where we can define twisted cycles constructed by gluing together suitable one-dimensional twisted cycles [285]. The integral of ω_p over these twisted cycles turn out to be well-defined for $\mathfrak{a}_i, \mathfrak{b}_j \in (\mathbb{C} \setminus \mathbb{Z})$ and for $\mathrm{Re}(\mathfrak{a}_i), \mathrm{Re}(\mathfrak{b}_j) > 0$.

9.1.2 Structure of the One-Loop Integral

Let us return to our main problem, the integration of the four-form (9.32) in the case of the four-particle one-loop $\mathcal{N} = 4$ SYM that we have obtained in (9.12).

In order to suitably parametrize the Lorentz-sheet, it is convenient to perform the following change of variables

$$\zeta_{23} = x\sqrt{\frac{\zeta_{12}}{\bar{\zeta}_{12}}}, \quad \zeta_{41} = y\sqrt{\frac{\zeta_{12}}{\bar{\zeta}_{12}}}, \quad x, y \in \mathbb{R} \tag{9.42}$$

so that the integral of the four-form ω_4 can be written as

$$
\begin{aligned}
I_4 = &\left(-\frac{u}{s}\right)^{2\varepsilon_{34}} \oint_{\bar{\zeta}_{12}=\zeta_{12}^{\star}} d\zeta_{12} d\bar{\zeta}_{12} \zeta_{12}^{2\varepsilon_{12}+\varepsilon_{23}+\varepsilon_{41}-1} \bar{\zeta}_{12}^{-2\varepsilon_{34}-\varepsilon_{23}-\varepsilon_{41}-1} (1-\zeta_{12})^{-2(\varepsilon_{12}+\bar{\varepsilon}_{12})} \\
&\int dx\, x^{2\varepsilon_{23}-1} \left(1-x\sqrt{\frac{\zeta_{12}}{\bar{\zeta}_{12}}}\right)^{-2(\varepsilon_{23}+\bar{\varepsilon}_{23})} \int dy\, y^{2\varepsilon_{41}-1} \left(1-y\sqrt{\frac{\zeta_{12}}{\bar{\zeta}_{12}}}\right)^{-2(\varepsilon_{41}+\bar{\varepsilon}_{41})} \\
&\left(1+\frac{t}{u}xy\right)^{2\varepsilon_{34}-1} \left[1+\frac{u}{s}\frac{1}{\bar{\zeta}_{12}}\left(1+\frac{t}{u}xy\right)\right]^{-2(\varepsilon_{34}+\bar{\varepsilon}_{34})}
\end{aligned}
\tag{9.43}
$$

The variables ζ_{12} and $\bar{\zeta}_{12}$ can be considered as independent and then integrated on the sheet for which they are related by complex conjugation.

Let us analyze the integral (9.43) in the IR-region by taking$(\zeta_{12},\bar{\zeta}_{12}) \longrightarrow (0,0)$. The integral is reduced to

$$
\begin{aligned}
I_4|_{\mathrm{IR}} = &\left(-\frac{u}{s}\right)^{2\varepsilon_{34}} \oint_{\bar{\zeta}_{12}=\zeta_{12}^{\star}} d\zeta_{12} d\bar{\zeta}_{12} \zeta_{12}^{2\varepsilon_{12}+\varepsilon_{23}+\varepsilon_{41}-1} \bar{\zeta}_{12}^{-2\varepsilon_{34}-\varepsilon_{23}-\varepsilon_{41}-1} \\
&\int dx\, x^{2\varepsilon_{23}-1} (1-x)^{-2(\varepsilon_{23}+\bar{\varepsilon}_{23})} \\
&\int dy\, y^{2\varepsilon_{41}-1} (1-y)^{-2(\varepsilon_{41}+\bar{\varepsilon}_{41})} \left(1+\frac{t}{u}xy\right)^{-2\bar{\varepsilon}_{34}-1},
\end{aligned}
\tag{9.44}
$$

where the integral over the complex variables $\zeta_{12},\bar{\zeta}_{12}$ is taken over a contour encircling zero and returns the discontinuity along the cut departing from zero. Notice that the integrals in the real variables x, y do not explicitly depend on ζ_{12} or $\hat{\zeta}_{12}$. Let us focus on them. Notice that the branch locus is defined by

$$
\left\{x = 0, 1, \infty;\ y = 0, 1, \infty;\ 1+\frac{t}{u}xy = 0\right\}. \tag{9.45}
$$

It is easy to see that the two-dimensional plane $\mathbb{R}^2$ gets divided into several chambers. Furthermore, if we restrict to the domain for which both x, y run from 0 to 1, such a domain can be a single bounded chamber or gets divided into two depending on the value of $-u/t$ (one obtains a single bounded chamber if either $-u/t$ is negative or $-u/t \in]0,1[$) It is interesting to notice that if we ask $\bar{\varepsilon}_{34} = -\bar{\varepsilon}_{23} = \bar{\varepsilon}_{41}$, this integral has the structure of a Gaussian hypergeometric function, while for generic parameters one obtains the generalized hypergeometric function ${}_3F_2$. One can get around the issue of the structure of the bounded chambers by either performing the integrals in a particular kinematical regime and then define suitably an analytic continuation or rewriting the last term in the integral(9.44) as a Mellin-Barnes integral

$$
(A+B)^{-\lambda} = \frac{1}{\Gamma(\lambda)}\frac{1}{2\pi i}\int_{-i\infty}^{+i\infty} d\sigma\, \Gamma(\lambda+\sigma)\Gamma(-\sigma)\frac{B^{\sigma}}{A^{\lambda+\sigma}} \tag{9.46}
$$

where, as usual, the integration path is chosen in such a way that all the poles given by the Γ function with argument $\ldots + \sigma = 0$ are located on its left, while the ones given by the Γ function with argument $\ldots - \sigma = 0$ are on its right.

In any case, extending x and y to the complex plane and taking a Pochhammer contour around both 0 and 1, or even just a contour which starts form one and encircles zero counter-clockwise (this can be always done given that the powers of $(1-x)$ and $(1-y)$ have the structure $1-2(\varepsilon+\bar{\varepsilon})-1$ and thus one can always consider $\text{Re}\{1-2(\varepsilon+\bar{\varepsilon})\} > 0$), one obtains well-defined integrals with overall coefficients of type $\Gamma(2\varepsilon_{23})\Gamma(2\varepsilon_{41})$. Once we take the limit for $\varepsilon, \bar{\varepsilon} \longrightarrow 0$, these overall factors provide the behaviour $1/(4\varepsilon_{23}\varepsilon_{41})$.

Two comments are now in order. First, once we consider the other bounded chambers defined by (9.45), it is easy to see that no further source of singularities (of order ε^{-2} or higher) emerges as the deformation parameters are taken to zero. Secondly, if we compare our parametrization of the one-loop degrees of freedom through $\{\zeta_{12}, \bar{\zeta}_{12}, x, y\}$ with the standard off-shell loop momentum, we can easily see that the limit $(\zeta_{12}, \bar{\zeta}_{12}) \longrightarrow (0,0)$ is exactly the IR-limit for the loop-momentum choosen as running from particle-1 to particle-2, while the points $x = 0$ and $y = 0$ correspond to the soft loop momentum becoming collinear with $p^{(1)}$ and $p^{(2)}$, which is exactly the source of the IR-singularities.

One can obtain the other three IR singularities, by changing how the Lorentzian-sheet is implemented in the integration, which simply amount to a relabelling of the change of variables (9.42) and thus in the integral (9.43).

9.2 Towards the two-loop contour

Since the all-loop MHV amplitudes in planar $\mathcal{N} = 4$ SYM can be written in a "dlog" form, all the kinematical information is encoded in the contour integration. It order to know if there is any relation between the amplitude at one-loop and two-loops for the same number of particles, we need to compare their integration contours.

The two-loop case introduces several complications respecting the one-loop case. Instead of having one scalar box integral, now the amplitude has to be written in terms of two scalar integrals that separately break the cyclical symmetry of the full amplitude. Applying the same method as for the one-loop case, each integral will lead to an integration contour defined by algebraic equations of their integration variables, making the combination of contours a non-trivial task, since we are dealing with high-dimensional subspaces of $\mathbb{C}^8$.

Focusing in one of the two integrals

$$A_4^{tree} \int d^4l d^4q \frac{\delta^4(\sum p_i) s_{12} s_{41}^2}{l^2 (l+p^{(1)})^2 (l-p^{(4)})^2 (l-q+p^{(1)}+p^{(2)})^2 q^2 (q+p^{(3)})^2 (q-p^{(2)})^2} \tag{9.47}$$

It can be written using the same procedure as

$$A_4^{tree}\delta^4(\sum p_i)I_{\text{box}}^{(2)} \tag{9.48}$$

where

$$I_{\text{box}}^{(2)} \equiv \prod_{i=1}^{4}\int \frac{dw_{i,i+1}}{w_{i,i+1}}\frac{dz_{i,i+1}}{z_{i,i+1}}\frac{s_{12}s_{41}s_{41}}{s_{12}(z,w)s_{41}(w)s_{41}(z)} \tag{9.49}$$

The deformed momenta are now

$$p_1(z) = p_1 - z_{12}k_{12} - z_{41}k_{41}\;\; p_1(w) = p_1 - w_{12}q_{12} - w_{41}q_{41}$$

$$p_1(z,w) = p_1 - z_{12}k_{12} - z_{41}k_{41} - w_{12}q_{12} - w_{41}q_{41} \tag{9.50}$$

with analogous definitions for the rest of variables following the conventions in (9.19).

Imposing that the deformed particles remain on-shell lead to constraints on q_{ij} and k_{ij}, the easiest choice leading to a related on-shell diagram is obtained setting $q_{ij} = k_{ij}\;\forall\; i,j$, and one of the options of equation (9.21). As in the one-loop case, let us pick the first option, that leads to

$$\begin{aligned} I_{\text{box}}^{(2)} = \prod_{i=1}^{4}\int \frac{d\hat{w}_{i,i+1}}{\hat{w}_{i,i+1}}\frac{d\hat{z}_{i,i+1}}{\hat{z}_{i,i+1}}\frac{1}{(1+\hat{z}_{12})(1+\hat{z}_{34})(1+\hat{w}_{12})(1+\hat{w}_{34})}\times \\ \times\frac{1}{(1+\hat{z}_{23}+\hat{w}_{23})(1+\hat{z}_{41}+\hat{w}_{41})} \end{aligned} \tag{9.51}$$

Although the variables (12) and (34) are already in the wanted '$d\log$" form, an additional change of variables for variables (23) and (41) is needed. We will define a new set of variables that keep intact variables (12), (34) but change (23) and (41) in the following way[1]

$$\begin{aligned} \tilde{w}_{41} = \hat{w}_{41},\quad \tilde{z}_{41} = \frac{\hat{z}_{41}}{1+\hat{w}_{41}} \\ \tilde{z}_{23} = \hat{z}_{23},\quad \tilde{w}_{23} = \frac{\hat{w}_{23}}{1+\hat{z}_{23}} \end{aligned} \tag{9.52}$$

Using these new variables the integrand has the desired form

$$\begin{aligned} I_{\text{box}}^{(2)} &= \prod_{i=1}^{4}\int d\log\frac{\tilde{w}_{i,i+1}}{1+\tilde{w}_{i,i+1}}d\log\frac{\tilde{z}_{i,i+1}}{1+\tilde{z}_{i,i+1}} \\ &\equiv \prod_{i=1}^{4}\int d\log\zeta_{i,i+1}d\log\eta_{i,i+1} \end{aligned} \tag{9.53}$$

[1]At this step, we can change either $z_{i,i+1}$ or $w_{i,i+1}$ for each $i = 2,4$, leading to the same result. The choice has to be made when imposing the reality conditions for the loop momenta, noticing that one of the options simplifies the expressions much more than the other.

This expression, with the same deformation parameters for the momenta and using a simple change of variables like in equation (9.52), can be obtained from the on-shell diagram depicted in Fig. 9.4, that is the trivial generalization of Fig. 9.2 to two loops.

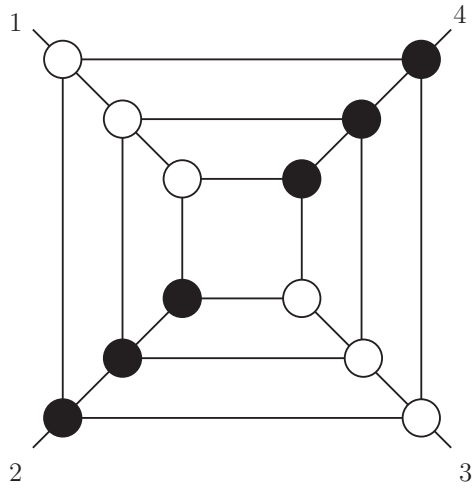

Figure 9.4: On-shell diagram related to the 4-particle 2-loop integrand in $\mathcal{N}=4$ SYM.

The loop-momenta can be written in terms of variables z and w as

$$l = -\frac{(p^{(1)}(z,w)+p^{(2)}(z,w))^2}{\langle 4(w)|p^{(1)}(z,w)+p^{(2)}(z,w)|1(w)]}\lambda^{(4)}(w)\tilde{\lambda}^{(1)}(w) - w_{41}\lambda^{(1)}\tilde{\lambda}^{(4)} \tag{9.54}$$

$$q = -\frac{(p^{(1)}(z)+p^{(2)}(z)+l)^2}{\langle 2(z)|p^{(1)}(z)+l|3(z)]}\lambda^{(2)}(z)\tilde{\lambda}^{(3)}(z) - z_{23}\lambda^{(3)}\tilde{\lambda}^{(2)} \tag{9.55}$$

where the quantity $\langle i|q|j]$ is linear in the momentum q and, for a light-like momentum $q=\lambda\tilde{\lambda}$, the quantity is equal to $\langle i\lambda\rangle[\tilde{\lambda}j]$. The momentum l depends on both groups of variables, the z's and the w's, and the momentum q depends on the momentum l. At that point it is clear that both groups of variables are tightly entangled, making the two-loop case much more difficult than the one-loop case.

In spite of the entanglement between the variables in the loop momenta, some of them behaves as in the one-loop case. The unentangled variables are $\zeta_{12},\zeta_{34},\zeta_{41},\eta_{12},\eta_{23}$ and η_{34}, that maintain the property of having a real numerator and a common complex denominator,

one for each group of variables. They are related to the off-shell momenta by

$$\begin{aligned}
\zeta_{12} &= \frac{(l+p^{(1)})^2}{(l-l')^2}, \qquad & \zeta_{34} &= \frac{(l-p^{(4)})^2}{(l-l')^2} \\
\zeta_{41} &= -\frac{l^2}{(l-l')^2} & & \\
\eta_{12} &= \frac{(q-p^{(2)})^2}{(q-q')^2}, \qquad & \eta_{23} &= \frac{q^2}{(q-q')^2} \\
\eta_{34} &= \frac{(q+p^{(3)})^2}{(q-q')^2} &&
\end{aligned} \tag{9.56}$$

where $l' = \frac{[12]}{[24]}\lambda^{(1)}\tilde{\lambda}^{(4)}$ and $q' = -\frac{[34]}{[24]}\lambda^{(3)}\tilde{\lambda}^{(2)}$. Taking the ratio between two variables of the same group (not considering ζ_{23} nor η_{41}) we obtain real quantities, as in the one-loop case.

The conditions that relate all variables are now

$$\begin{aligned}
\frac{1}{\zeta_{41}}\left[\frac{s_{12}}{s_{13}}(1-\zeta_{12})(1-\zeta_{34})(1-\eta_{41}) + \frac{s_{41}}{s_{13}}(1-\zeta_{41})(1-\zeta_{23})(1-\eta_{23})\right] = \\
= \frac{1}{|\tilde{w}_{41}|^2} + \frac{s_{12}}{s_{13}}(1-\frac{\zeta_{12}}{\zeta_{41}})(1-\frac{\zeta_{34}}{\zeta_{41}})
\end{aligned} \tag{9.57}$$

$$\frac{1}{\eta_{23}}\frac{N}{D} = \frac{1}{|\tilde{z}_{23}|^2} + \frac{s_{12}}{s_{13}}(1-\frac{\eta_{12}}{\eta_{23}})(1-\frac{\eta_{34}}{\eta_{23}}) \tag{9.58}$$

where the auxiliary quantities N and D are

$$\begin{aligned}
N = &-\left[\frac{s_{12}}{s_{13}}(1-\zeta_{12})(1-\zeta_{34})(1-\eta_{41}) + \frac{s_{41}}{s_{13}}(1-\zeta_{41})(1-\zeta_{23})(1-\eta_{23})\right] \times \\
&\times \left[\frac{s_{12}}{s_{13}}(1-\eta_{12})(1-\eta_{34}) + \frac{s_{41}}{s_{13}}(1-\eta_{41})(1-\eta_{23})(1-\zeta_{41})\right] + \\
&+ (1-\eta_{41})\left[\frac{s_{12}}{s_{13}}(1-\eta_{12})(1-\zeta_{34}) + \frac{s_{41}}{s_{13}}(1-\zeta_{41})(1-\eta_{23})\right] \times \\
&\times \left[\frac{s_{12}}{s_{13}}(1-\zeta_{12})(1-\eta_{34}) + \frac{s_{41}}{s_{13}}(1-\zeta_{41})(1-\eta_{23})\right]
\end{aligned} \tag{9.59}$$

and

$$D = 2\frac{s_{12}}{s_{13}}(1-\zeta_{12})(1-\zeta_{34})(1-\eta_{41}) + \frac{s_{41}}{s_{13}}(1-\zeta_{41})(1-\zeta_{23})(2-\eta_{23}) \tag{9.60}$$

As it is seen, the relations involved are much more complicated for two-loops. There is no hint of simplicity nor of cyclic symmetry,that it is not expected in that case, because we are breaking it in the intermediate steps. Without having a much simpler expression for the reality conditions, joining the subspaces defined by the constraints of each of the two

integrals seems hopeless. Then, it would be desirable to find a more symmetric expression for the Lorentz sheet.

However, our way of proceeding serves just to have an idea of what the Lorenzt-sheet can be, and indeed it is not a feasible procedure for arbitrary number of loops. Thus, a first principle approach is still needed and necessary.

9.3 Summary

In this chapter we propose a general (theory-independent) scheme for regularizing on-shell forms, which allows to have well-defined integrals on the Lorentz sheet. Our idea comes from two basic considerations. First, the fundamental objects for the on-shell representation of a scattering amplitude are the three-particle ones, whose coupling constant dimensionality $[\kappa]$ allows to classify theories. The dimension of the three-particle coupling constant depends on the helicities, so that fixing it restricts the possible states which can interact in a given three-particle amplitude. Secondly, the on-shell construction breaks locality at intermediate steps, *i.e.* a single on-shell diagram can show poles which are not in the amplitude it contributes to. With these considerations in mind, we propose to perform a deformation of the helicity space on the three-particle amplitudes, in such a way that its dimensionality is not changed. This constraint allows us to keep a four-dimensional framework as well as to remain in a given class of theories at fixed $[\kappa]$ but extending it to *unphysical* values of the helicities. As a consequence of this extension, locality gets broken. A regularization scheme typically breaks some features of a theory, which is the price one has to pay to be able to have well-defined quantities. Given that, at least at intermediate steps, the on-shell construction breaks locality, it can be more suitable in such a framework to introduce a regularization scheme which performs such a breaking (in a controlled way), rather than giving up any other feature or symmetry. We discuss the locality breaking in our scheme, arguing that it allows to associate the relevant physical quantities to poles in the parameter space. More precisely, even at tree level, one can read off the collinear behavior of an amplitude as well as the underformed on-shell diagrams from poles in the deformation parameter space. It is interesting that at integrand level, our deformation maps the four-form $\bigwedge_{i=1}^{4} d(\log\zeta_{i,i+1})$ into another four-form which is nothing but the integrand of the Euler beta-function, even if then the integration contour Γ complicates the branch cut structure, it would be interesting to exploit the power of the hypergeometric function theory to have a cleaner and somehow more natural way to treat the integration and the branch locus.

In order to perform the integration directly in the *on-shell variables* we needed to find a

contour of integration implementing the Lorentz sheet. We proceded by inspection but still we do not have a general, first principle critirium to define such contours. Finding such a criterium, with the hope of extending it to higher loops, still remains an open question, even if we consider instructive to have shown both the shape of the Lorentz sheet from the on-shell perspective and have performed directly the integration.

CHAPTER 10

GRASSMANNIAN FOR $\mathcal{N} < 4$ SYM

Once we have described the great success of on-shell diagrams and the Grassmannian formalism in $\mathcal{N} = 4$ SYM, allowing to uncover symmetries as the Yangian, or to establish an all-loop recursion formula for the integrand.

In this Chapter, we continue the investigation of the on-shell diagrammatics and the related mathematical structures for less/no-supersymmetric Yang-Mills theories in the planar sector, that was started in Ref. [253]. In particular, we focus on the possibility of associating an *auxiliary* Grassmannian to the on-shell processes along similar lines of what happens in the maximally supersymmetric case. In particular, we focus on its relation with the structure of varieties on the Grassmannian. The decoration of the on-shell diagrams, which physically keeps tracks of the helicity of the coherent states propagating along their edges, defines new on-shell functions on the Grassmannian and can introduce novel higher-order singularities, which graphically are reflected into the presence of helicity loops in the diagrams. These new structures turn out to have similar features as in the non-planar case: the related higher-codimension varieties are identified by either the vanishing of one (or more) Plücker coordinates involving at least two non-adjacent columns, or new relations among Plücker coordinates. A distinctive feature is that the functions living on these higher-codimenson varieties can be thought of distributionally as having support on derivative delta-functions. After a general discussion, we explore in some detail the structures of the on-shell functions on $Gr(2,4)$ and $Gr(3,6)$ on which the residue theorem allows to obtain a plethora of identities among them.

A property of the Grassmannian integral is its invariance under $GL(k)$-transformations.

In the maximally supersymmetric case this is guaranteed by the fact that both the Grassmannian form and the kinematic support turn out to be separately $GL(k)$-invariant. This is no-longer true for $\mathcal{N}<4$. However, the decoration induces a further function of the Plücker coordinates which complete the integrand, satisfying the required invariance. Concretely, also in this case, an on-shell diagram corresponds to a particular stratification of the Grassmannian, with integral representation given by:

$$\mathcal{M}_{k,n}^{(OD)} = \int_{\Pi} \frac{d^{k\times n}C}{\text{Vol}\{GL(k)\}} \frac{\delta^{(4k|k\mathcal{N})}(C\cdot\mathcal{W})\,\Delta_{s_1\dots s_k}^{4-\mathcal{N}}}{\Delta_{i_1\dots i_k}\Delta_{i_2\dots i_{k+1}}\dots\Delta_{i_{n-k+1}\dots i_n}\Delta_{i_{n-k+2}\dots i_n i_1}} \left[\mathfrak{h}\left(\frac{\Delta_I}{\Delta_J}\right)\right]^{4-\mathcal{N}}, \tag{10.1}$$

where the kinematic data $\mathcal{W}$ are represented in twistor space, the Δ's are the maximal minors of C (the indices $s_1,\dots s_k$ represents the helicity sources, *i.e.* the columns of C related to the coherent states with negative helicity), and $\mathfrak{h}$ is a rational function of the maximal minors. More precisely, $\mathfrak{h}$ turns out to be both invariant under little group transformations and $GL(k)$-invariant, given that it is a function of the ratios of the Plücker coordinates.

The structure in (10.1) can be easily obtained by gluing the trivalent nodes, with such a procedure determining also the functional form of $\mathfrak{h}(\Delta_I/\Delta_J)$. The presence of a helicity loop in the on-shell diagrams is reflected in the structure of $\mathfrak{h}$ through the presence of a non-planar pole. The on-shell function related to the codimension-1 variety identified by such a pole can be seen as having support on a derivative delta-function.

We will discuss this new structures in relation to both the top-varieties and the higher-codimension ones, and discuss new relations among the on-shell functions that beautifully the Grassmann representation encodes, with specific examples for $Gr(2,4)$ and $Gr(3,6)$.

The Chapter is organised as follows. Section 10.1 is devoted to a general discussion of the features of the Grassmannian integrals for on-shell processes in the cases where the supersymmetry is not maximal. Section 10.2 contains a detailed analysis of the new structures emerging in our context, with a particular focus on $Gr(2,4)$. Interestingly, the residue theorem on $Gr(2,4)$ returns two classes of identities, one of which corresponds to the equivalence between two different BCFW representations while the other one provides an equivalence relation between the on-shell diagram with a helicity loop and a *non-planar* diagram. In Section 10.3 we discuss the structure on-shell functions on $Gr(3,6)$. Notably, new poles appear, whose location imposes a relation among the Plücker coordinates keeping them all non-zero. In momentum space such a relation turns out to have two solutions, both of which need to be considered (see Appendix C.2).

10.1 Decorated On-Shell Diagrams and the Grassmannian

The undecorated on-shell diagrams can be naturally associated to the total non-negative Grassmannian [237]. In this section we will discuss the Grassmannian formulation for amplitudes in $\mathcal{N} < 4$ SYM theories.

On-shell processes can be seen as an integral over the Grassmannian (partially) localized on some kinematic support:

$$\mathcal{M}_{k,n}^{(\mathrm{OD})} = \int_{\Pi} \omega_{k,n}(C)\, \mathscr{F}^{(4k|k\mathcal{N})}(\delta)\, f(\Delta(C)), \tag{10.2}$$

where $\omega_{k,n}$ is the canonical top form defined in Eq. (8.85), that we repeat here for clarity

$$\omega_{k,n} = \frac{d^{k\times n}C}{\mathrm{Vol}\{GL(k)\}} \frac{1}{\Delta_{12\ldots k}\Delta_{23\ldots(k+1)}\ldots\Delta_{n1\ldots(k-1)}}, \tag{10.3}$$

and $\mathscr{F}^{(4k|k\mathcal{N})}(\delta)$ is the kinematic support, whose explicit expression depends on the space where the kinematics is defined. Finally, the function $f(\Delta)$ of the Plücker coordinates Δ guarantees that the integrand transform properly under $C \longrightarrow tC$. For concreteness, we will consider for the time being the kinematics either defined in momentum space or in twistor space:

$$\begin{aligned} \mathscr{F}^{(4k|k\mathcal{N})}(\delta)\big|_{(\lambda,\tilde{\lambda})} &= \delta^{(2\times(n-k))}\left(\lambda\cdot C^{\perp}\right)\delta^{(2\times k)}\left(C\cdot\tilde{\lambda}\right)\delta^{(k\times\mathcal{N})}\left(C\cdot\tilde{\eta}\right), \\ \mathscr{F}^{(4k|k\mathcal{N})}(\delta)\big|_{\mathscr{W}} &= \delta^{(4k|k\mathcal{N})}(C\cdot\mathscr{W}), \end{aligned} \tag{10.4}$$

where $C^{\perp}$ in the first line is the orthogonal complement of C defined by $C\cdot C^{\perp}=0$, while $\mathscr{W}\equiv(\tilde{\mu},\tilde{\lambda},\tilde{\eta})^{\mathrm{T}}$ encodes the kinematics in twistor space, and $\tilde{\mu}$ is defined through the twistor transform $\int d^{2\times n}\, e^{i\lambda\cdot\tilde{\mu}}$. The k-plane C is thus orthogonal to the 2-plane $\tilde{\lambda}$ (and contains the 2-plane λ) in momentum space, while it is orthogonal to $\mathscr{W}$ in twistor space. Notice that the δ-functions localize $2n-4$ degrees of freedom of C, so that the cells of the Grassmannian with exactly $2n-4$ degrees of freedom correspond to rational functions of the kinematic data (up to the momentum conserving delta-function support), while lower cells will have some δ-function support and higher cells will be some differential form. Notice that the top cell, which has $k(n-k)$ dimensions is fully localized just in the $k=2$ and $k=n-2$ case, *i.e.* in the MHV and M$\bar{\text{H}}$V sectors. In twistor space one actually has distribution constraining the twistor data.

Let us now consider the external kinematic data in twistor space, so that the generic form for an on-shell diagram can be written as

$$\mathcal{M}_{k,n}^{(\mathrm{OD})} = \int_{\Pi} \omega_{k,n}\, \delta^{(4k|k\mathcal{N})}(C\cdot\mathscr{W})\, f(\Delta). \tag{10.5}$$

A way to constrain the function $f(\Delta)$ is the requirement that the integrand is invariant under the transformation $C \longrightarrow tC$. While the top form $\omega_{k,n}$ is indeed invariant under such a transformation, the maximal minors Δ_I are mapped into $t^k\Delta_I$, while the twistor space δ-function provide a factor $t^{-k(4-\mathcal{N})}$. Thus, in order for the integrand to be invariant, the function $f(\Delta)$ needs to transform as: $f(\Delta) \longrightarrow f(t^k\Delta) = t^{k(4-\mathcal{N})}f(\Delta)$, *i.e.* it needs to transform as a maximal minor with some power. Its general structure therefore becomes

$$f(\Delta) = \Delta^{4-\mathcal{N}}_{s_1\ldots s_k}\mathfrak{f}\left(\frac{\Delta_I}{\Delta_J}\right), \tag{10.6}$$

where the indices $s_1,\ldots,s_k$ indicates the sources of the helicity arrows in the decorated on-shell diagrammatics, while $\mathfrak{f}(\Delta_I/\Delta_J)$ is just a function of ratios of the Plücker coordinates. The little group covariance also implies that $\mathfrak{f}$ needs to be invariant under a little group transformation. On the Grassmannian such a transformation can be seen as just the rescaling of a given column of C: $c^{(i)} \longrightarrow t_i\, c^{(i)}$. Thus, in order for $\mathfrak{f}$ to be invariant under the little group, it needs to be a (sum of) ratio(s) of the Plücker coordinates such that numerators and denominators have the same indices but shuffled. Notice that, being a function of ratios of Plücker coordinates, $\mathfrak{f}$ introduces new (higher order) singularities, breaking the general logarithmic structure at the boundary.

Finally, coming to the parametrisation of the Grassmannian, even if in principle one could keep using whichever parametrisation coming from assigning a perfect orientation to the undecorated counterpart, the helicity arrows provide a physical perfect orientation which becomes the preferred way to parametrise $C \in Gr(k,n)$ given that makes the physical structure related to the helicity flows manifest. With this choice, irrespectively of the type (edge or face) of the variables that one can use, the Plücker coordinates related to the sources only is set to one.

For future reference, let us write here the explicit Grassmannian form for the three-particle building blocks:

(10.7)

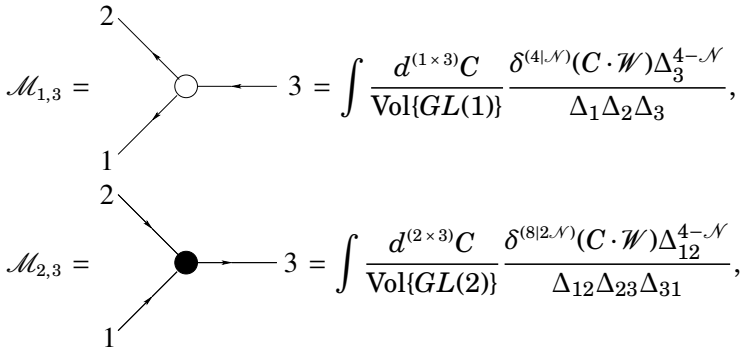

where the Grassmannian measure (the top form) $\omega_{k,3}$ has been explicitly written. Notice that the two functions defining these three-point objects, $\delta^{(4k|k\mathcal{N})}(C\cdot\mathscr{W})\Delta_I^{4-\mathcal{N}}$, are defined

on the top cell of $G(k,3)$. Furthermore, $\mathfrak{f} = 1$ is the only possible function which is $GL(k)$-invariant and has the correct little group behaviour at the same time. As a last comment, notice that any higher-point on-shell diagram, being built gluing three-particle amplitude is characterised by $\mathfrak{f} = [\mathfrak{h}(\Delta_I/\Delta_J)]^{4-\mathcal{N}}$, where the function $\mathfrak{h}$ is a ratio of two sums of products of Plucker coordinates such that the indices in the numerator and denominators are the same but reshuffled. This particular form of the function $\mathfrak{f}$ is due to the presence of $\Delta^{4-\mathcal{N}}$ in the numerator of the Grassmannian integrand of all the three-particle amplitudes: when a number of three-particle amplitudes get glued, the on-shell diagram generated in this way will contain a function with power $4-\mathcal{N}$, which is f appearing in equation (10.5). Stripping-off the Plucker coordinate having just indices corresponding to sources, as in equation (10.6), one gets $\mathfrak{f}$ as $\mathfrak{h}^{4-\mathcal{N}}$.

10.2 Amplitudes, Singularities and the Grassmannian

In the previous section we discussed the general structure of decorated on-shell diagrams as defined by the usual delta-functions times a rational function of the Plücker coordinates. Their general form is constrained by the little group covariance and the invariance under $GL(k)$ transformations, and it can be computed by the usual amalgamation and projection operations on the three-particle amplitudes (10.7). The appearance of such a rational function introduces new singularities, which will be the main subject of this section.

As a first step, let us build the Grassmannian representation for the decorated on-shell boxes with non-adjacent sources. The starting point is the following singularity diagram

(10.8)
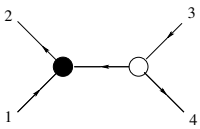

$$= \int \frac{d^{(2\times 4)}C}{\mathrm{Vol}\{GL(2)\}} \frac{\delta^{(8|2\mathcal{N})}(C\cdot\mathcal{W})\delta(\Delta_{34})\Delta_{13}^{4-\mathcal{N}}}{\Delta_{12}\Delta_{23}\Delta_{41}},$$

from which the on-shell boxes can be constructed via a BCFW bridge, whose degree of freedom gets localized by the δ-function support in (10.8). Concretely, the on-shell box with no internal helicity loops is obtained by applying a BCFW to (10.8) in the $(4,1)$-channel:

(10.9)
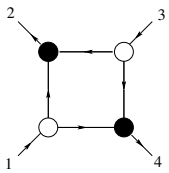

$$= \int \frac{dz}{z} \int \frac{d^{(2\times 4)}C}{\mathrm{Vol}\{GL(2)\}} \frac{\delta^{(8|2\mathcal{N})}(C\cdot\mathcal{W})\delta(\Delta_{34}-z\Delta_{13})\Delta_{13}^{4-\mathcal{N}}}{\Delta_{12}\Delta_{23}\Delta_{41}} =$$
$$= \int \frac{d^{(2\times 4)}C}{\mathrm{Vol}\{GL(2)\}} \frac{\delta^{(8|2\mathcal{N})}(C\cdot\mathcal{W})\Delta_{13}^{4-\mathcal{N}}}{\Delta_{12}\Delta_{23}\Delta_{34}\Delta_{41}},$$

while adding a BCFW bridge in the (2,3)-channel returns the on-shell boxes with the internal helicity loops:

(10.10)

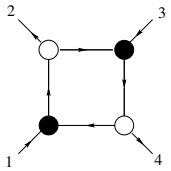

$$= \int \frac{dz}{z} \int \frac{d^{(2\times 4)}C}{\text{Vol}\{GL(2)\}} \frac{\delta^{(8|2\mathcal{N})}(C\cdot\mathcal{W})\delta(\Delta_{34}+z\Delta_{24})(\Delta_{13}+z\Delta_{12})^{4-\mathcal{N}}}{\Delta_{12}\Delta_{23}\Delta_{41}} =$$

$$= \int \frac{d^{(2\times 4)}C}{\text{Vol}\{GL(2)\}} \frac{\delta^{(8|2\mathcal{N})}(C\cdot\mathcal{W})\Delta_{13}^{4-\mathcal{N}}}{\Delta_{12}\Delta_{23}\Delta_{34}\Delta_{41}} \left(\frac{\Delta_{23}\Delta_{14}}{\Delta_{13}\Delta_{24}}\right)^{4-\mathcal{N}},$$

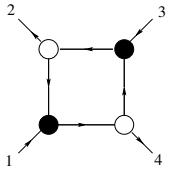

$$= \int dz\, z^{3-\mathcal{N}} \int \frac{d^{(2\times 4)}C}{\text{Vol}\{GL(2)\}} \frac{\delta^{(8|2\mathcal{N})}(C\cdot\mathcal{W})\delta(\Delta_{34}+z\Delta_{24})\Delta_{12}^{4-\mathcal{N}}}{\Delta_{12}\Delta_{23}\Delta_{41}} =$$

$$= \int \frac{d^{(2\times 4)}C}{\text{Vol}\{GL(2)\}} \frac{\delta^{(8|2\mathcal{N})}(C\cdot\mathcal{W})\Delta_{13}^{4-\mathcal{N}}}{\Delta_{12}\Delta_{23}\Delta_{34}\Delta_{41}} \left(\frac{\Delta_{12}\Delta_{34}}{\Delta_{13}\Delta_{24}}\right)^{4-\mathcal{N}}.$$

Notice that in the second diagram one needs to take into account a Jacobian related to the change in the helicities of the states which the BCFW bridge is applied on: This is related to the fact that the BCFW bridge introduces a new multiple pole at infinity and, consequently, the singularity (10.8) is not part of the boundary of the second diagram in (10.10). The Grassmannian expressions (10.9) and (10.10) have the exact structure as predicted in (10.5) and (10.6) from $GL(2)$-invariance and little group covariance. Actually in the present cases, even the form of $\mathfrak{h}(\Delta_I/\Delta_J)$ can be exactly predicted directly from the on-shell diagrams. More precisely, the helicity flows encode the information about the singularity structure of the on-shell diagrams. For the on-shell box (10.9), the helicity flow structure guarantees that all the four sub-diagrams have exactly the same helicity configuration as the full-diagram: all of them belongs to the boundary of the on-shell box and thus represent its singularities. In other words, all the strata defined by $\Delta_{i,i+1}=0$ encode the singularity information of the amplitude. Consequently, $\mathfrak{h}(\Delta_I/\Delta_J)$ cannot have in the numerator any of the minors formed by two consecutive columns of C and the only function which can fulfil the requirement of invariance under both $GL(2)$ and little group transformations is 1.

Considering the two diagrams with helicity loops, the helicity flow structure shows that just two sub-diagrams really belongs to the boundary of each of the on-shell diagrams. These two diagrams correspond to the two complex factorisations in a given channel (the s-channel for the first on-shell box in (10.10), and the t-channel for the second one). In other words, on the Grassmannian the decorated on-shell boxes have just two poles of the form $\Delta_{i,i+1}=0$. Consequently, the function $\mathfrak{h}(\Delta_I/\Delta_J)$ needs to suppress the other two

possible singularities, so that its numerator can correspond only to $\Delta_{23}\Delta_{14}$ in the on-shell box with clockwise helicity loop and $\Delta_{12}\Delta_{34}$ in the on-shell diagram with counter-clockwise helicity loop. Then, the little group invariance allows the denominator to be only $\Delta_{13}\Delta_{24}$ in both cases. Having this extra singularity corresponds to the presence of the helicity loops in the diagrammatics.

Notice also that summing the two on-shell boxes in (10.10) for $\mathcal{N}=3$ and using the Plücker identities, one obtains (10.9), which represents the four-particle amplitude at tree-level.

Finally, let us keep focusing on the diagrams with the helicity loops. As mentioned earlier, these on-shell diagrams have higher order singularities which are graphically identified via the helicity loops themselves. The residue related to this higher-order pole can be also diagrammatically identified by following the helicity flows. Concretely,

(10.11)

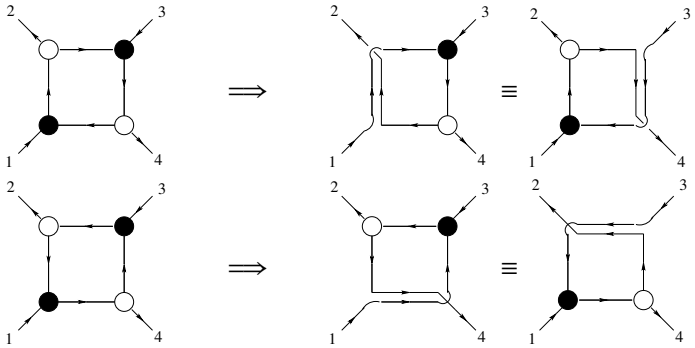

which are u-channel singularities with support on a $(3-\mathcal{N})$-derivative delta-function:

(10.12)

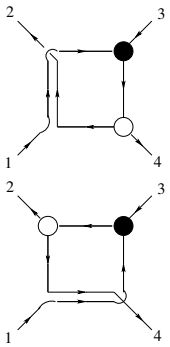

$$= \int \frac{d^{(2\times 4)}C}{\text{Vol}\{GL(2)\}} \frac{\delta^{(2\times 4|2\times\mathcal{N})}(C\cdot\mathcal{W})(\Delta_{23}\Delta_{41})^{3-\mathcal{N}}}{\Delta_{34}\Delta_{21}}\delta^{(3-\mathcal{N})}(\Delta_{24}),$$

$$= \int \frac{d^{(2\times 4)}C}{\text{Vol}\{GL(2)\}} \frac{\delta^{(2\times 4|2\times\mathcal{N})}(C\cdot\mathcal{W})(\Delta_{12}\Delta_{34})^{3-\mathcal{N}}}{\Delta_{23}\Delta_{14}}\delta^{(3-\mathcal{N})}(\Delta_{24}),$$

where, contrarily to the notation used so far, the apex in the last delta function indicates the number of derivatives on the δ-function[1]. Notice that the two lines in (10.12) differ

[1] More precisely, the apex of the δ-function in (10.12) includes a factor $(-1)^{(3-\mathcal{N})}/(3-\mathcal{N})!$, so that:

$$\delta^{(3-\mathcal{N})}(x) \stackrel{\text{def}}{=} \frac{(-1)^{3-\mathcal{N}}}{(3-\mathcal{N})!}\left(\frac{d}{dx}\right)^{3-\mathcal{N}}\delta(x).$$

just in their lexicographic order ($2<1<3<4$ in the first line and $4<2<3<1$) if it is seen still as a embedded in a disk, while it can be equivalently seen as a non-planar diagram if we embed it into an annulus. As shown in [245], a given on-shell diagram can be equivalently embedded into different surfaces, the embedding not being a property of the diagrams themselves.

A comment is now in order. The natural direct construction of the singularity diagrams in (10.11) would be via the gluing of a black and a white nodes, which would return an object with support on $\delta(\Delta_{24})$. However, for the ones we are dealing with now, this is strictly true in the $\mathcal{N}=3$ case only. Furthermore, all the on-shell diagrams constructed by gluing black and white nodes live on δ-function supports or on a constant support. Objects with support on distributions which are derivative of δ-functions can be naturally defined from higher dimensional *planar* diagrams with helicity loops, as we just saw, and they correspond to residues of (higher order) poles involving Plücker coordinates made out of non-adjacent columns, without the need of setting any other Plücker coordinate to zero. In a sense, they are *non-planar* objects with support on a derivative δ-function. In the present context, the presence of non-planar looking structures can be only due to the presence of some higher order poles in the higher dimensional diagram. Furthermore, they can be seen as *unwinding* a helicity loop. The presence of factors such as the ones in the round brackets with power $3-\mathcal{N}$ are needed for both preserving the $GL(k)$-invariance of the integrand and for having the correct little group behaviour, and their specific form is related to the direction of the helicity loop (which determines how it can be unwinded) – indeed, all this comes naturally from the computation of the higher order residue, but it can be understood on these more general grounds. Thus, along all the Chapter, any non-planar diagram will be understood as either having support on a derivative delta-function or having a higher-order pole and a constant support (it depends on its dimensionality), and it will be represented in a way that makes manifest which and how a helicity loop has been unwinded. Indeed, this is not completely satisfactory given that the proposed association between diagrams and functions with support on derivative δ-function makes sense just when we go from a higher dimensional object to a lower one, while it is still not clear how to construct them from lower dimensional quantities. However, starting from the higher-order singularities (10.12), it is possible to construct the 0-forms (10.11) via a BCFW bridge: applying a BCFW bridge in the s-channel to the higher order singularity in the first line of (10.12), one obtains the on-shell box with clockwise helicity loop, a BCFW bridge in the t-channel to the one in the second line of (10.12) returns the on-shell box with counter-clockwise helicity loop. More precisely, these BCFW-bridges on the higher-order singularities return diagrams which are *equivalent* to the on-shell boxes with helicity loops.

Such an equivalence can be demonstrated via a residue theorem, as we will show in the subsection 10.2.1.

Indeed these higher order non-planar structures are present in the Grassmannian $Gr(k,n)$ for any $k \geq 2$ and any $n \geq 4$. In the $k = 2$ sector, as the case we just discussed, these structures are related to higher order poles of type $\Delta_{i,i+2} = 0$, *i.e.* they are identified by a single Plücker coordinate vanishing. As soon as we move away from this sector, new poles appear. More precisely, depending on the helicity arrow configurations, these higher order poles can either be located at $\Delta_{i_1\dots i_k} = 0$ or when some special relation within the Plücker coordinates is satisfied, as we will show in Section 10.3. This is exactly what happens for non-planar on-shell diagrams in $\mathcal{N} = 4$ SYM [245, 246], which is interpreted as a signature of the impossibility of expressing all the leading singularities as linear combination of the planar ones [237, 245]. In the present case, the interpretation is quite different: they are a signature of the inequivalence between the two leading singularities in a given channel (which also reflects in the general non-validity of the square move) and thus of the existence of sub-leading singularities which cannot be expressed in terms of the leading ones. This is what lies behind the failure of representing an amplitude in terms of standard on-shell diagrams under any BCFW recursion. These on-shell diagrams with higher-order δ-function support allow to complete such recursions and realise, as discussed in Appendix C.1, a direct link to the new singularities which arise in the on-shell $4L$-forms representing the L-loop integrand [253].

10.2.1 Identities on $Gr(2,4)$

Let us now consider the on-shell 1-form which is obtained by applying a BCFW bridge to the on-shell box (10.9) in the following fashion

(10.13)

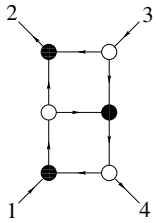

$$= \frac{dz'}{z'} \int \frac{d^{(2\times 4)}C}{\mathrm{Vol}\{GL(2)\}} \frac{\delta^{(8|2\mathcal{N})}(C\cdot\mathcal{W})(\Delta_{13}-z'\Delta_{34})^{4-\mathcal{N}}}{(\Delta_{12}-z'\Delta_{24})\Delta_{23}\Delta_{34}\Delta_{41}},$$

where the lower box shows a clockwise helicity loop. In principle we would need to sum over the two possible helicity loops. However, for the present discussion we will just focus for the time being on the diagram in (10.13). If we integrate such a 1-form over the Riemann sphere, the residue theorem returns a relation between the original diagram (the residue of the pole at $z = 0$, which corresponds to diagrammatically remove the lower horizontal line in the left-hand-side. of (10.13)), the residue of the pole at $z = \Delta_{12}/\Delta_{23}$, which corresponds

to remove the upper horizontal line leaving an on-shell box with a clockwise helicity loop and finally the residue of the multiple pole at infinity. Let us focus on the latter and compute its residue explicitly. First, notice that the on-shell one-form (10.13) can be also parametrised as

(10.14) 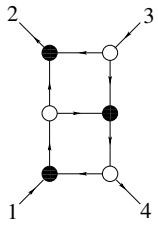

$$= \frac{dz}{z}\int \frac{d^{(2\times 4)}C}{\text{Vol}\{GL(2)\}}\frac{\delta^{(8|2\mathcal{N})}(C\cdot\mathcal{W})\Delta_{13}^{4-\mathcal{N}}}{(\Delta_{12}+z\Delta_{13})\Delta_{23}\Delta_{34}\Delta_{41}}\left[\frac{\Delta_{23}\Delta_{41}}{\Delta_{13}(\Delta_{24}+z\Delta_{34})}\right]^{4-\mathcal{N}},$$

so that the multiple pole at infinity is mapped into a multiple pole at $z=-\Delta_{24}/\Delta_{34}$. The parametrisation (10.14) is obtained by applying a standard BCFW bridge in the $(2,3)$-channel ($c_2 \longrightarrow c_2+zc_3$) to the on-shell box with a clockwise helicity loop and it is related to the previous one in (10.13) via a Möbius transformation [253]. As discussed in the previous subsection, such a pole corresponds to taking collinear two non-adjacent particles but has support on a $(3-\mathcal{N})$-derivative delta-function.

Thus, the integration of the on-shell one-form (10.14) over the full Riemann sphere returns the following identity:

(10.15) $0 =$ 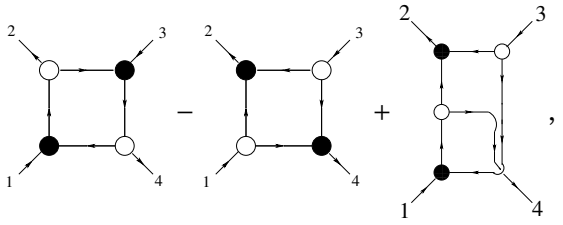

,

where

(10.16) 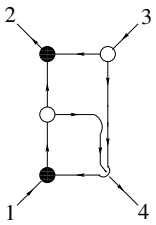

$$= \int \frac{d^{2\times 4}C}{\text{Vol}\{GL(2)\}}\frac{\delta^{(8|2\mathcal{N})}(C\cdot\mathcal{W})\Delta_{13}^{4-\mathcal{N}}}{\Delta_{14}\Delta_{42}\Delta_{23}\Delta_{31}}\sum_{r=0}^{3-\mathcal{N}}\left(\frac{\Delta_{14}\Delta_{23}}{\Delta_{13}\Delta_{24}}\right)^r$$

which correspond exactly to the four-particle amplitude with lexicographic order $1<4<2<3$ just for the case $\mathcal{N}=3$.

The one-form (10.14) with counter-clockwise helicity loops has two poles in z, one at 0 (whose residue is the on-shell box with counter-clockwise helicity loop) and the multiple pole at $z=-\Delta_{24}/\Delta_{34}$. Consequently, the identity obtained by integrating this one-form over

the Riemann sphere establishes the equivalence between the on-shell box with counter-clockwise helicity loop and (higher order) on-shell box with ordering (1423):

(10.17)

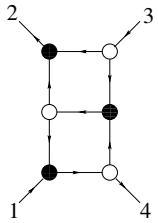

$$= \frac{dz}{z}\int \frac{d^{(2\times 4)}C}{\text{Vol}\{GL(2)\}}\,\frac{\delta^{(8|2\mathcal{N})}(C\cdot\mathcal{W})\Delta_{13}^{4-\mathcal{N}}}{(\Delta_{12}+z\Delta_{13})\Delta_{23}\Delta_{34}\Delta_{41}}\left[\frac{(\Delta_{12}+z\Delta_{13})\Delta_{34}}{\Delta_{13}(\Delta_{24}+z\Delta_{34})}\right]^{4-\mathcal{N}},$$

$\Downarrow$

$0 =$

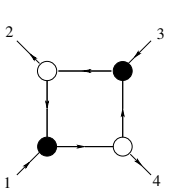

$+$

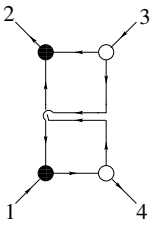

If one applies a BCFW bridge in the $(3,4)$-channel to the on-shell boxes with internal helicity loops, one obtains the same identities but with the label exchanges $2 \longleftrightarrow 4$ and $1 \longleftrightarrow 3$. Let us stress here that, in principle, the two non-planar-like diagrams in (10.14) and (10.17) are *in principle* topologically equivalent. What marks the difference between the two diagrams are the way the legs are winded, which here keeps track of the origin of the diagram, *i.e.* one comes from opening up a clockwise helicity loop while the other one from a counter-clockwise helicity loop.

Finally, notice that, just in the $\mathcal{N} = 3$, the pole associated to the helicity loop is a simple pole and its residue is exactly (up to a sign) the four-particle amplitude with a different ordering, which depends on the orientation on the loop. Such an identity is given by a residue theorem of the type of (10.17).

10.3 On-shell functions on $Gr(3,6)$

Let us focus on the simplest non-trivial example which is given by $Gr(3,6)$. In the planar sector, there is a unique top cell which the following undecorated bipartite diagram is associated to

(10.18)

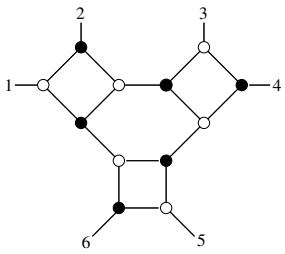

$$\longleftrightarrow \omega_{3,6} \equiv \frac{d^{(3\times 6)}C}{\text{Vol}\{GL(3)\}}\,\frac{1}{\Delta_{123}\Delta_{234}\Delta_{345}\Delta_{456}\Delta_{561}\Delta_{612}}.$$

Through equivalence relations such as square-moves and mergers, the diagram drawn above can be mapped into other equivalent diagrams. However, once these diagrams get decorated with helicity arrows (which are fixed for the external lines) they generate inequivalent on-shell functions, which can share at most a subset of simple poles and in general differ for the location of the multiple pole. For definiteness, let us choose the external helicity arrows to have alternating directions – all the other configurations in the NMHV sector can be obtained via the helicity flow reversal operation. In general, the (super)-momentum conserving δ-functions fix all the degrees of freedom of the Grassmannian but one which can be used to obtain identities among on-shell diagrams of codimension-1 by integrating it over the Riemann sphere.

10.3.1 Poles and non-Plücker relations

The on-shell function returned by the very same diagram in (10.18) with such a choice shows helicity loops in the central hexagon only and thus just one higher order pole:

(10.19)

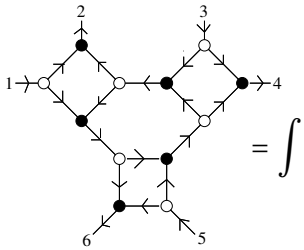

$$= \int \frac{d^{(3\times 6)}C}{\text{Vol}\{GL(3)\}} \frac{\delta^{(3\times 4|3\mathcal{N})}(C\cdot\mathcal{W})}{\Delta_{123}\Delta_{234}\Delta_{345}\Delta_{456}\Delta_{561}\Delta_{612}} \left[\frac{\Delta_{134}\Delta_{356}\Delta_{512}}{\Delta_{346}\Delta_{512}-\Delta_{345}\Delta_{612}}\right]^{4-\mathcal{N}}$$

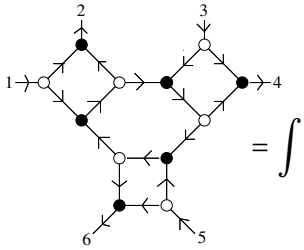

$$= \int \frac{d^{(3\times 6)}C}{\text{Vol}\{GL(3)\}} \frac{\delta^{(3\times 4|3\mathcal{N})}(C\cdot\mathcal{W})}{\Delta_{123}\Delta_{234}\Delta_{345}\Delta_{456}\Delta_{561}\Delta_{612}} \left[\frac{\Delta_{123}\Delta_{345}\Delta_{561}}{\Delta_{346}\Delta_{512}-\Delta_{345}\Delta_{612}}\right]^{4-\mathcal{N}}$$

Notice that in the diagram with counter-clockwise helicity loop in the first line, no equivalence move holds: the on-shell function on the right-hand-side in the first line is uniquely associated to this perfect orientation. The helicity flows define all the possible *removable edges*, which coincide with taking residues in the on-shell functions: and edge is said to be removable if no helicity flow is broken by such an operation. All the simple poles are related to the boundary measurements from the top form. Taking the residues at $\Delta_{123}=0$, $\Delta_{345}=0$ and $\Delta_{561}=0$ corresponds to remove one of the edges shared between the internal hexagon and one of the boxes. However, notice that the helicity flows allow to remove such edges just in the first diagram in (10.19). Indeed, this is reflected into the

Grassmannian representation which shows, for the second line of (10.19), a numerator proportional to $\Delta_{123}\Delta_{345}\Delta_{561}$.

In the first diagrams, instead, when one takes these type of residues the higher order pole disappears. Diagrammatically, this is a reflection of the disappearance of the internal helicity loop when any of these edges gets removed:

(10.20)

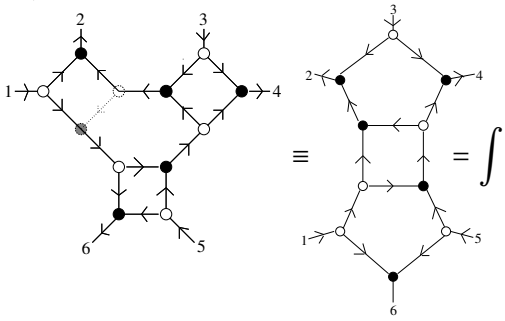

$$\equiv$$

$$= \int \frac{d^{(3\times 6)}C}{\text{Vol}\{GL(3)\}} \frac{\delta^{(3\times 4|3\mathcal{N})}(C\cdot\mathcal{W})\,\Delta_{135}^{4-\mathcal{N}}}{\Delta_{123}\Delta_{234}\Delta_{345}\Delta_{456}\Delta_{612}}\delta(\Delta_{561})$$

The other two residues can be obtained from (10.20) by shifting the labels: $i \longrightarrow i \mp 2$.

The other three poles $\{\Delta_{234}=0,\Delta_{456}=0,\Delta_{612}=0\}$ of the top form $\omega_{3,6}$ are actually poles of the full integrand and their residues diagrammatically correspond to remove the outer edge of one of the boxes. The resulting diagrams still show an internal helicity loop and thus their Grassmannian representation still show a higher order pole:

(10.21)

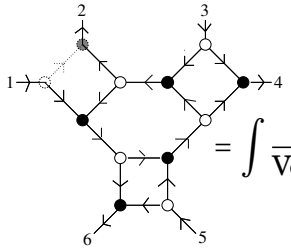

$$= \int \frac{d^{(3\times 6)}C}{\text{Vol}\{GL(3)\}} \frac{\delta^{(3\times 4|3\mathcal{N})}(C\cdot\mathcal{W})}{\Delta_{123}\Delta_{345}\Delta_{456}\Delta_{561}\Delta_{612}} \left[\frac{\Delta_{356}\Delta_{512}}{\Delta_{256}}\right]^{4-\mathcal{N}} \delta(\Delta_{234}),$$

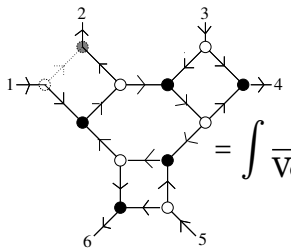

$$= \int \frac{d^{(3\times 6)}C}{\text{Vol}\{GL(3)\}} \frac{\delta^{(3\times 4|3\mathcal{N})}(C\cdot\mathcal{W})}{\Delta_{123}\Delta_{345}\Delta_{456}\Delta_{561}\Delta_{612}} \left[\frac{\Delta_{123}\Delta_{345}\Delta_{561}}{\Delta_{134}\Delta_{256}}\right]^{4-\mathcal{N}} \delta(\Delta_{234}),$$

where now the higher order pole has the more standard form of a single Plücker coordinate vanishing. From the expression above, it seems that there are actually two of such type of poles. However, it is easy to check that $\Delta_{134}=0$ is not actually a singular point of the integrand[2] and, thus, the higher order pole is localized at $\Delta_{256}=0$.

[2]Notice that in the subcell $\Delta_{234}=0$, the identity $\Delta_{123}\Delta_{345}=\Delta_{134}\Delta_{235}$ holds, from which the statement

Finally, let us discuss the new structures which characterise the decorated diagrammatics and reflects into the appearance of new poles. In particular, for the on-shell functions in (10.19), the location of such poles is no longer given by a single Plücker coordinate vanishing, rather by a relation among some of them. For the case at hand (10.19), it consists of

$$0 = \Delta_{346}\Delta_{512} - \Delta_{345}\Delta_{612} \equiv \Delta_{134}\Delta_{562} - \Delta_{234}\Delta_{561} \equiv \Delta_{124}\Delta_{563} - \Delta_{123}\Delta_{456}, \tag{10.22}$$

where the last two expressions have been obtained via Plücker relations. Geometrically, it means that, looking at the columns of $C \in Gr(3,6)$ as points in $\mathbb{C}^3$, the points 3 and 4 become collinear with the point identified by the intersection of the straight line determined by the points $(1,2)$ with the one passing through $(5,6)$:

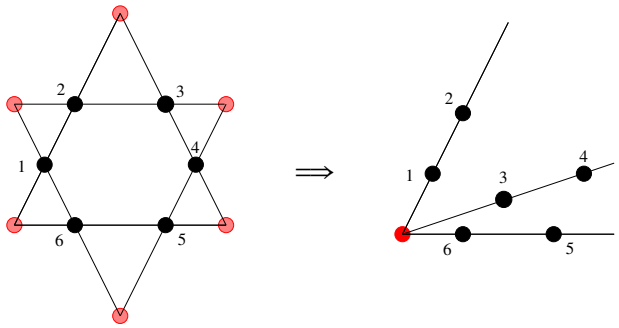

where in shaded red nodes on the left hand side are the points in $\mathbb{C}^3$ identified by the intersection of (at least) two straight lines passing through two consecutive points, while the right-hand side represents the geometry which realises the non-Plücker constraint (10.22), with three of the red points in the left-hand-side collapsing into one which lies simultaneously on the three straight lines identified by the pairs of points $(1,2)$, $(3,4)$ and $(5,6)$. Identifying the intersection between the lines $\{(12),(34)\}$, $\{(34),(56)\}$ and $\{(56),(12)\}$ as $\mathfrak{a}$, $\mathfrak{b}$ and $\mathfrak{c}$ respectively, this singularity can be indicated as $0 = \Delta_{12\mathfrak{b}} = \Delta_{34\mathfrak{c}} = \Delta_{56\mathfrak{a}}$.

As we emphasised at the beginning, this type of singularity is a feature of a non-planar diagrams, and thus it is not a surprise that the on-shell diagram with support on $\delta^{(3-\mathcal{N})}(\Delta_{34\mathfrak{c}})$ is genuinely non-planar:

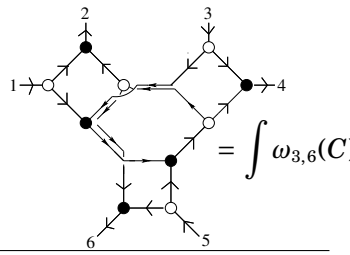

$$= \int \omega_{3,6}(C)\delta^{(3\times 4|3\times\mathcal{N})}(C\cdot\mathcal{W})(\Delta_{134}\Delta_{356}\Delta_{512})^{(4-\mathcal{N})}\delta^{(3-\mathcal{N})}(\Delta_{34\mathfrak{c}}). \tag{10.23}$$

that $\Delta_{134} = 0$ is not a pole follows. This identity can be obtained by rewriting the column c_4 as a linear combination of c_2 and c_3, as implied by $\Delta_{234} = 0$.

where $\Delta_{34c} \equiv \Delta_{346}\Delta_{512} - \Delta_{345}\Delta_{612}$.

10.3.2 Standard non-planar-like pole

Let us now consider the undecorated diagram (10.18) but with the lower box with white and black node exchanged and let us decorate the external edges with exactly the same choice as above. There are three possible helicity arrow assignment for the internal edges:

(10.24)

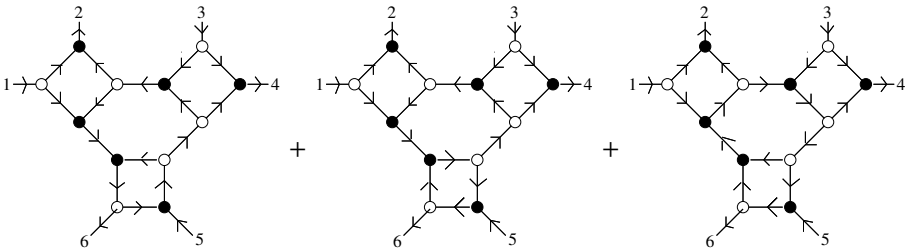

The first and the third diagrams have a single helicity loop (in the lower box and in the inner hexagon respectively), while the second one shows a helicity flow in both the lower box and the inner hexagon whose orientation is opposite with respect to the one in the other diagrams. Notice that the third diagram is equivalent to the second one discussed in the previous section upon square move, which holds for the lower box only. For the first two diagrams, the only equivalence move possible is the merger.

The presence of the helicity loop in the outer sub-diagram, as in the first and second diagrams (10.24), indicates that the related higher order pole is located at $\Delta_{ijk} = 0$, while its presence in the inner sub-diagrams is an indication that the location of the related singularity is given by a special relation among Plücker coordinates, as in the example discussed in the previous section. Notice that the second diagram has both type of helicity loop and, hence, it shows both type of singularities.

The explicit expressions for the on-shell functions on $Gr(3,6)$ represented by the first two diagrams in (10.24) (the one for the third diagram is given in the second line of (10.19))

are given by

(10.25)

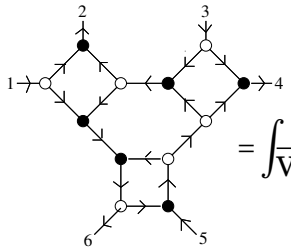

$$= \int \frac{d^{(3\times 6)}C}{\mathrm{Vol}\{GL(3)\}} \frac{\delta^{(3\times 4|3\times\mathcal{N})}(C\cdot\mathcal{W})}{\Delta_{123}\Delta_{234}\Delta_{345}\Delta_{456}\Delta_{561}\Delta_{612}} \left[\frac{\Delta_{134}\Delta_{356}}{\Delta_{346}}\right]^{4-\mathcal{N}}$$

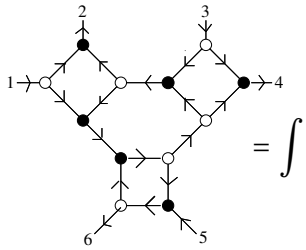

$$= \int \frac{d^{(3\times 6)}C}{\mathrm{Vol}\{GL(3)\}} \frac{\delta^{(3\times 4|3\times\mathcal{N})}(C\cdot\mathcal{W})\,\Delta_{612}^{4-\mathcal{N}}}{\Delta_{123}\Delta_{234}\Delta_{345}\Delta_{456}\Delta_{561}\Delta_{612}} \times$$

$$\times \left[\frac{\Delta_{345}}{\Delta_{346}} \frac{\Delta_{134}\Delta_{356}}{\Delta_{346}\Delta_{512}-\Delta_{345}\Delta_{612}}\right]^{4-\mathcal{N}}.$$

As predicted, they share a higher order pole, located at $\Delta_{346}=0$, whose residue can be diagrammatically depicted by unwinding the helicity loop according to its direction, as seen in Section 10.2:

(10.26)

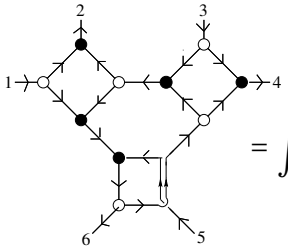

$$= \int \frac{d^{(3\times 6)}C}{\mathrm{Vol}\{GL(3)\}} \frac{\delta^{(3\times 4|3\times\mathcal{N})}(C\cdot\mathcal{W})\,(\Delta_{134}\Delta_{356})^{4-\mathcal{N}}}{\Delta_{123}\Delta_{234}\Delta_{345}\Delta_{456}\Delta_{561}\Delta_{612}} \delta^{(3-\mathcal{N})}(\Delta_{346})$$

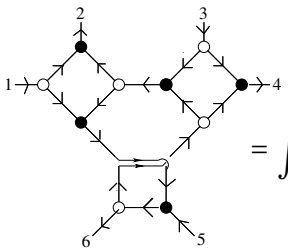

$$= \int \frac{d^{(3\times 6)}C}{\mathrm{Vol}\{GL(3)\}} \frac{\delta^{(12|3\mathcal{N})}(C\cdot\mathcal{W})(\Delta_{612}\Delta_{345})^{4-\mathcal{N}}}{\Delta_{123}\Delta_{234}\Delta_{345}\Delta_{456}\Delta_{561}\Delta_{612}} \times$$

$$\times \left[\frac{\Delta_{134}\Delta_{356}}{\Delta_{346}\Delta_{512}-\Delta_{345}\Delta_{612}}\right]^{4-\mathcal{N}} \delta^{(3-\mathcal{N})}(\Delta_{346})$$

10.3.3 Identities among on-shell diagrams

As seen for the $Gr(2,4)$ case, also on $Gr(3,6)$ the residue theorem returns a set of identities among on-shell functions. In this case, the (super)-momentum conserving delta-functions

are able to fix eight out of the nine degrees of freedom of the top-cell and, therefore, the free parameter can be used as integration variable. The integration over the Riemann sphere, because of Cauchy's theorem, tells us that the sum over all the residues needs to vanish. As a first example, let us consider the on-shell function in the first line of (10.25):

(10.27)

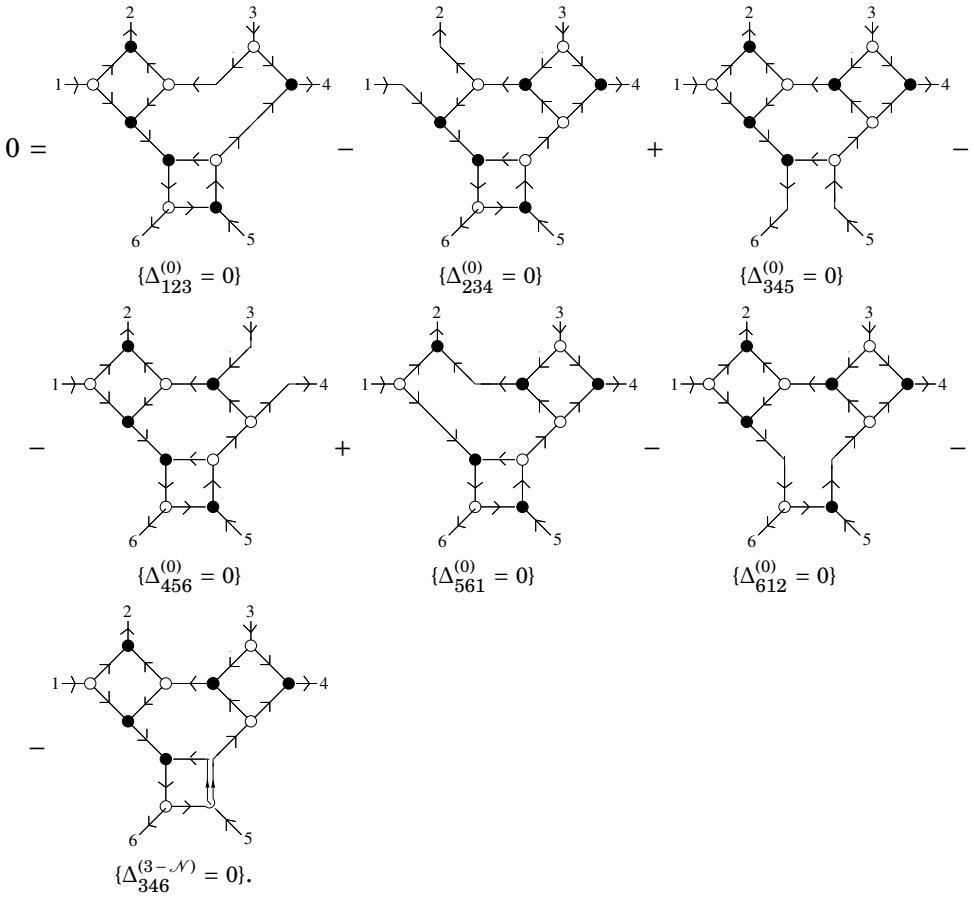

In the identity above, the label $\{\Delta^{(m)}_{ijk} = 0\}$ below each decorated on-shell diagram identifies the $\delta^{(m)}$-support where each of them lives – let us stress again that in all the cases these on-shell diagrams identify on-shell functions which live in the sub-cell $\Delta_{ijk} = 0$ of $Gr(3,6)$.

Let us move on to the most interesting case given by the on-shell function in the first

line of (10.19). The identity coming from the residue theorem is given by:

$$0 = \quad - \quad + \quad - \quad - \quad + \quad - \quad - \quad - \tag{10.28}$$

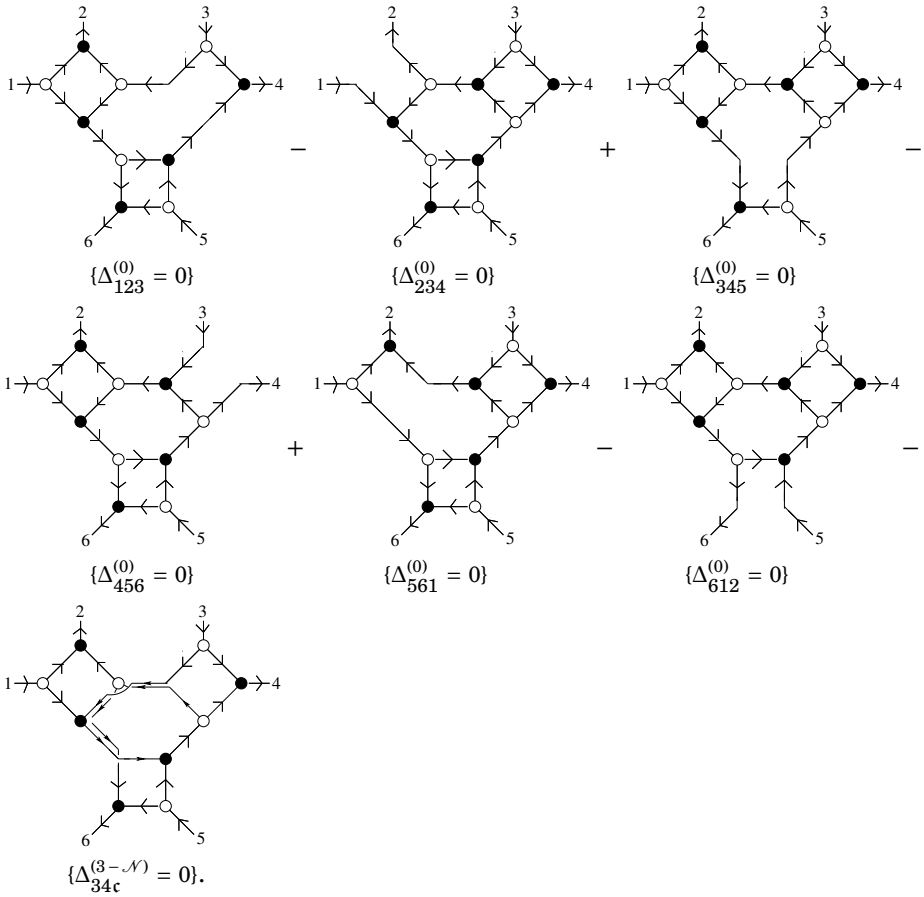

Very interestingly, notice that the sum of the diagrams corresponding to the residues in $\{\Delta_{123}=0,\Delta_{345}=0,\Delta_{561}=0\}$ is a representation of the tree-level 6-particle amplitude with helicity configuration $(-,+,-,+,-,+)$. The identity (10.28) then provides another representation for such an amplitude, which involves diagrams with non-planar structures. Importantly, this representation does not come from the recursion which a BCFW bridge on any of the pairs $\{(1,2),(3,4),(5,6)\}$ with helicity loop would generate.

10.4 Summary

In this Chapter, we discussed the Grassmannian representation for on-shell processes. The richness of the structure appears immediately because of the presence of new poles which are typically a feature of non-planar diagrams. They are multiple poles, except in $\mathcal{N}=3$ SYM whose individual diagrams show a very close structure with the non-planar diagrams in $\mathcal{N}=4$ SYM. These new singularities are associated to the helicity loops which can

appear in the on-shell diagrams, and can be identified either by the vanishing of a single Plücker coordinate involving at least two non-adjacent columns (*e.g* in $Gr(2,4)$), or as a non-Plücker relation (*e.g.* $Gr(3,6)$). The on-shell diagrams can be thought of as generalised functions on the Grassmannian, with the ones which live on the on-shell variety defined by a non-planar conditions having support on a derivative delta-function.

We extensively discussed the on-shell functions on $Gr(2,4)$ and $Gr(3,6)$. In both cases, this formulation allows to obtain several identities among on-shell functions defined on codimension-0 and codimension-1 varieties for $Gr(2,4)$ and $Gr(3,6)$ respectively. More precisely, on $Gr(2,4)$ it is possible to identify two classes of such identities: The first one provides the equivalence between two different BCFW representations of the four-particle amplitude, with the explicit on-shell function for the contribution related to the multiple pole; The second one establishes an equivalence between the on-shell diagrams with helicity loops and non-planar functions.

On $Gr(3,6)$, the residue theorem allows to obtain a plethora of identities among the on-shell functions on a codimension-1 variety, the most interesting of which provides a new representation for the NMHV six-particle amplitude with helicity configuration $(-,+,-,+,-,+)$: Notice that such a representation, in terms of individual diagrams, is not the one that would be obtained by simply generating the amplitude recursively (with boundary term) using a BCFW bridge with a helicity loop – It can be indeed recast into it but applying several other identities among on-shell functions.

On the top-cell of $Gr(3,6)$, the delta-functions containing the kinematic data fix all the degrees of freedom of the Grassmannian but one. Analysing the non-Plücker relations in momentum space in terms of such a parameter, one discovers that such relations are second-order algebraic equations. Thus the correct on-shell function living on the sheet identified by a non-Plücker relation, is obtained by summing over both the solutions.

To conclude, in this work we have worked out, for the first time, the implications of reducing the supersymmetry amount in the on-shell diagrams connection to the Grassmannian formalism. Furthermore, We have revealed a new connection between between the planar on-shell diagrams with helicity loops and non-planar functions.

CHAPTER 11

CONCLUSIONS AND OUTLOOK

In this Part II of the Thesis, we take the very first steps towards both, developing a regularization theory suitable for on-shell forms and the generalization of the Grassmannian formalism to theories with less supersymmetry than $\mathcal{N}=4$ SYM.

The first part of this project has been to define a regularization scheme suitable for on-shell forms, not restricting ourselves to any particular theory. It has been done deforming the helicity of each particle in the on-shell diagram (internal and externals) to take arbitrary complex values, while maintaining the dimensions of the coupling constants fixed. In order to make a connection between the BCFW recursion relation to all-loops integrands and the amplitudes, we need to integrate the differential forms. An appropriate regularization prescription must tame the UV and IR singularities, which in the special case of $\mathcal{N}=4$ SYM the IR ones are the only ones present. We have tested the regularization prescription on on-shell forms contributing to planar $\mathcal{N}=4$ loop amplitudes, that can be written (when not regularized) as a product of $\mathrm{d}\log\zeta_i$'s. Using these variables we have an universal on-shell form, from where we need to extract physical quantities as the scattering amplitude, being all the information encoded in the integration contour. Thus the major problem is not regularizing the integrand (that it is not an trivial task), but to understand the contour where the form has to be integrated along. Instead of finding the integration contour from a first-principle approach, since we do not know how to do that, we have attacked the problem connecting the on-shell form variables to the usual off-shell momentum degrees of freedom. In that way we have been able to restrict the space of on-shell degrees of freedom, that initially is $\mathbb{C}^4$ to a submanifold of (real) dimension 4, as

it should be. But it is still not clear if the amplitude is given by integrating the on-shell form along the whole submanifold or only in a region of it. Another problem we have encounter is that the regularized integrands transform the initial poles into branch-points, complicating the analytical structure of the on-shell form. Since the integration contour can pass trough these branch-points we also need a prescription to regularize the integrals, we have done it analytically continuing the integrals in such a way that the singularities explicitly factor out. We have been able to understand some of these branch points in terms of physical singularities (the IR and UV limits of the amplitude), so an open possibility is that the correct integration contour is encoded in the branch-point structure.

In the future, it would be interesting to directly work in $SO(2,2)$ signature, instead of working in Lorentzian one, as it has been done here. The advantage of working in signature $SO(2,2)$ is that each momentum is represented by two independent real spinors, while in Lorenz signature we need two complex spinors related by complex conjugation. This is directly related with the relationships among the degrees of freedom that define the on-shell forms and, therefore, with the integration contour that defines the integrated loop amplitude. For example, in the one-loop case, it is much easier to work in a part of $\mathbb{R}^4$ than in a 4 dimensional hypersurface embedded in $\mathbb{C}^4$.

On the other hand, the on-shell diagrammatics allows to define a theory, at least perturbatively, from first principles without any reference to a pre-existent Lagrangian and just in terms of observables, making manifest structures of theory that are completely hidden in the most traditional approach of Quantum Field Theory. This approach has been extensively explored in the context of maximally supersymmetric Yang-Mills theory, whose properties can be translated in geometrical terms. What turns out to be very interesting is the relation between the on-shell diagrams and mathematical structures such as permutations, the positive Grassmannian and cluster algebras.

A general question that we have started addressing in the present work is whether much of the mathematical structure unveiled for $\mathcal{N} = 4$ SYM survives for more general theories. Indeed the procedure for constructing on-shell processes is not theory dependent: the three-particle amplitudes (the nodes of the diagrams) are fixed by Poincaré invariance for arbitrary helicity configurations, and the gluing of these objects just amounts to integrate out the degrees of freedom along the edges which gets glued. Thus, the question is not really whether it is possible to build on-shell diagrams for more general theories, rather which information about the theory they encode, given that, in these cases, it is not clear the direct relation between on-shell diagrams and the amplitudes.

The less/no-supersymmetric Yang-Mills theories offer a good arena for addressing these issues: They can be thought of as the next-to-simplest examples because, on one

side, at least a class of diagrams have a direct physical interpretation, and on the other side they offer a richer structure (*e.g* UV divergences and rational terms at loop level). In the same direction, a discussion about on-shell diagrams in gravity has been recently pursued [287, 288]. The richness of the structure in $\mathcal{N} < 4$ SYM appears immediately because of the presence of new poles which are typically a feature of non-planar diagrams. They are multiple poles, except in $\mathcal{N} = 3$ SYM whose individual diagrams show a very close structure with the non-planar diagrams in $\mathcal{N} = 4$ SYM. These new singularities are associated to the helicity loops which can appear in the on-shell diagrams. This work represents a first step towards a deeper understanding on the geometry of decorated on-shell diagrams for $\mathcal{N} < 4$ SYM theories, and several questions remains open. The first one indeed is related to the possibility of a systematic survey of these non-planar (higher-order) structures for $Gr(k,n)$ as well as of the identities among the on-shell functions on $Gr(k,n)$. Secondly, in the maximally supersymmetric case, the positive-preserving diffeomorphisms on $Gr_{\geq 0}(k,n)$ are related to the Yangian symmetry. In the present context, it is a fair question to ask whether the diffeomorphisms on $Gr(k,n)$ encode some (so far) hidden symmetry. Furthermore, even if there is no real notion of positivity, it would be interesting to check whether there is a general criterium to fix the signs, as it occurs in the non-planar sector of $\mathcal{N} = 4$ SYM. Finally, it would be interesting to explore the possibility to have an amplituhedron formulation, along similar lines of what happens in the maximally supersymmetric cases [241, 289–297], and how the new structures are encoded in this geometry.

Part III

Conclusiones finales en español

Primera parte

En la primera parte de la tesis hemos explorado la riqueza de la fenomenología derivada del formalismo BFKL. Con la llegada del LHC se ha tenido acceso a energías más altas, que es el requerimiento básico de las resumaciones de alta energía, y a una cantidad de datos no vista hasta la fecha, lo que permite medir observables más exclusivos con significancia estadística. Con esto en mente hemos desarrollado el estudio de diferentes observables a las energías que permite alcanzar el LHC en la actualidad.

Cuando tratamos de introducir correcciones de órdenes más alto a la ecuación BFKL se observa que éstas son considerablemente grandes, lo que acarrea inestabilidades en la expansión en teoría de perturbaciones. Para reducir el efecto de los logaritmos no tenidos en cuenta se han propuesto diversos métodos, como pueden ser las mejoras colineales o el uso de diferentes prescripciones para escoger la escala de renormalización. En el Capítulo 2 se ha explorado la posibilidad de introducir un valor mínimo a la diferencia en rapidez de las emisiones consecutivas en el estado final. Hasta la fecha esta idea solamente se había estudiado formalmente considerando el comportamiento asintótico de la función de Green de forma aislada, lo que no corresponde de forma exacta a la situación dada en los experimentos de colisión de partículas. Teniendo todo en cuenta, es posible describir de forma razonable los datos del LHC, obteniendo una descripción global de las diferentes correlaciones en ángulo azimutal en Mueller-Navelet *jets* usando un veto en rapidez $b \gtrsim 1$. Este valor dista mucho de los estudios mencionados anteriormente, en los que se obtenía un valor de $b \gtrsim 2$, y en este caso tiene dependencia en la diferencia en rapidez entre los *jets* medidos. Esto da una estimación de cuán lejos estamos de la región asintótica en las energías accesibles actualmente (del orden de 10 TeV) y nos da una estimación del tamaño de las regiones colineales que necesitan ser tenidas en cuenta para describir de forma adecuada los experimentos. También podemos conectar con otra forma de fijar las correcciones de órdenes más alto, la prescripción BLM. Según esta descripción, éstas se fijan con una redefinición del polo de Landau en la *constante* de acoplamiento fuerte. En el

futuro es importante hacer comprobaciones más exigentes de la idea de introducir un veto en rapidez, y para ello se puede aplicar los valores obtenidos en este estudio para hacer predicciones en otros observables.

En los Capítulos 3 y 4 se ha presentado el primer estudio fenomenológico completo de la producción inclusiva de tres *jets* en el LHC dentro del marco BFKL, realizando los cálculos en la aproximación LLA y también a NLLA. Luego hemos extendido el análisis a la producción de cuatro *jets* en la aproximación LLA en el Capítulo 5. En estos observables, además de los típicos dos *jets* muy cercanos al eje de colisión que se miden en los eventos de Mueller-Navelet, se requiere la medida de un (o dos en el caso de 4 *jets*) *jet* con momento transverso grande en regiones centrales de rapidez. Otro requisito para poder aplicar el formalismo de BFKL es que los *jets* medidos tengan una separación en rapidez apreciable, de manera que satisfagan los requerimientos de la cinemática *Multi-Regge*. Con estos ingredientes podemos generalizar el formalismo desarrollado para estudiar eventos de Mueller-Navelet a estos nuevos procesos, y definir nuevos observables que son sensibles a efectos BFKL en los que se estudian las configuraciones en ángulo azimutal del estado final. En todos los casos hemos estudiado los procesos en un régimen cinemático compatible con los estudios experimentales llevados a cabo hasta la fecha por la colaboración CMS en [135, 136]. Las energías del centro de masas han sido $\sqrt{s} = 7,13$ TeV y hemos aplicado cortes simétricos y asimétricos en los momentos transversos de los *jets* delantero (k_A) y trasero (k_B). La conclusión general es que las correcciones de orden NLLA son moderadas y los observables propuestos gozan de estabilidad bajo correcciones perturbativas. Además, cuando cambiamos la energía de 7 a 13 TeV los cambios en los observables son muy pequeños para un rango amplio de rapidez, lo que corrobora la idea de que los cocientes generalizados son un buen observable para exhibir las características de la dinámica BFKL en cuanto a el comportamiento en ángulo azimutal en el caso de la producción de tres *jets*. Cuando consideramos cuatro *jets* podemos destacar que las gráficas de los observables si difieren con el cambio de la energía, diciéndonos que hay efectos preasintóticos jugando un rol importante en este caso.

Con una visión hacia proyectos futuros, y algunos aún desarrollándose en el presente, sería muy interesante comparar las predicciones de los observables que hemos propuesto con las de otros marcos teóricos, como pueden ser análisis sin incluir resumaciones (conocidos como *fixed-order*), simuladores de eventos del tipo Monte-Carlo, o incluso el generados de Monte-Carlo inspirado en la ecuación BFKL, llamado `BFKLex` [180–186, 189]. Aunque lo más importante, como en toda ciencia, es incentivar a las colaboraciones experimentales a hacer una medida de los observables con los datos del LHC que hay disponibles, y los que vendrán en un futuro próximo. El análisis experimental también servirá como

comprobación para modelos que describen la interacción múltiple y podría medir cómo de importantes son estos efectos. En un futuro tendremos acceso a diferencias en rapidez aún mayores, gracias al detector CASTOR que puede medir estados finales hasta rapideces de valor 6.6. Por supuesto, análisis de los observables para la cinemática que puede medir CASTOR se llevarán a cabo, ya que los efectos tipo BFKL serán mas notables.

A parte de lo detallado anteriormente, estamos llevando a cabo la investigación de observables aún más exclusivos, basados en el estudio estadístico de la radiación de *minijets* que se produce entre los dos *jets* tipo Mueller-Navelet. Tanto la multiplicidad de los eventos, como las distribuciones en ángulo azimutal o momento transverso deben ser diferentes en los regímenes de DGLAP y BFKL, con lo que una comparación de las predicciones de `BFKLex` con simuladores Monte-Carlo de propósito general puede iluminar la senda hacia una descripción correcta de eventos con gran multiplicidad.

Concluimos la primera parte de la tesis cambiando a un proceso diferente, la producción de pares Drell-Yan muy cerca del eje de colisión en el LHC. Trabajando sobre estudios previos sobre el mismo proceso que se pueden encontrar en [194], hemos aplicado el formalismo BFKL en la aproximación NLLA para describir datos de LHCb y ATLAS. En este caso hemos usado correcciones colineales para fijar las correcciones a órdenes más altos de NLLA. Una ventaja de este proceso es que nos permite poner a prueba la factorización $k_\perp$ a baja fracción de momento longitudinal x, ya que hemos usado la misma densidad gluónica no integrada que fue obtenida de un ajuste a datos de HERA, resultando en una buena descripción de datos del LHC, en los que la energía es mucho mayor. Este resultado es muy prometedor, ya que es una demostración de la universalidad del factor de impacto usado en la factorización de altas energías. Sin embargo, es justo puntualizar que los mismos datos se pueden describir usando cálculos sin resumación tipo BFKL (cálculos a *fixed-order*), por lo que es necesario ir a energías aún más altas para discernir entre las diferentes descripciones teóricas. En un futuro cercano, la medida de eventos para este proceso en el LHC [129] será muy útil para sopesar la necesidad de resumación BFKL en Teorías Cuánticas de Campos.

Segunda parte

En la parte II de la tesis tomamos los primeros pasos hacia el desarrollo de una teoría de regularización adaptada a formas diferenciales *on-shell* y, además, la generalización del formalismo Grassmanniano a teorías con menos supersumetría que $\mathcal{N} = 4$ SYM.

En la primera parte del proyecto hemos definido el esquema de regularización directamente sobre las formas *on-shell*, siendo el mecanismo válido para cualquier teoría. La

regularización consiste en deformar el valor de helicidad de cada partícula que aparece en el diagrama *on-shell* para tomar valores complejos arbitrarios, con la condición de mantener la dimensión de la constante de acoplo fijada en dicha deformación. Para poder conectar la relación recursiva BCFW a todos los órdenes, que nos da una representación del integrando de la amplitud, con la Amplitud de Dispersión necesitamos integrar la forma diferencial. Una prescripción de regularización apropiada debe dar sentido a las divergencias IR y UV, que en el caso especial de $\mathcal{N} = 4$ SYM sólo las de tipo IR están presentes. Se ha comprobado la regularización sobre formas *on-shell* que contribuyen a amplitudes a nivel de *loop* del sector *planar* de $\mathcal{N} = 4$ SYM, que pueden escribirse (en su forma no regularizada) como un producto $\mathrm{d}\log\zeta_i$'s. Con el uso de estas variables obtenemos una forma diferencial universal, de la que se pueden extraer cantidades físicas como la Amplitud de Dispersión, y dónde toda la información está ahora codificada en el contorno de integración. Nos encontramos entonces con que el mayor problema no es regularizar el integrando (aunque esta tarea no es trivial), sino entender el contorno sobre el que la forma ha de ser integrado. Como no sabemos como encontrar el contorno de integración desde primeros principios, hemos atacado el problema conectando las variables de la forma *on-shell* con los grados de libertad del momento *off-shell* que aparece en la integral a nivel de *loop*. Mediante esta relación se ha restringido el espacio de los grados de libertad *on-shell*, que en principio viven en $\mathbb{C}^4$, a una subvariedad de dimensión (real) cuatro, como es de esperar. Pero queda aún claro que la amplitud venga dada por la integración sobre toda la subvariedad, o sólo una región de ésta. Otro problema con el que nos hemos encontrado es que la regularización transforma los polos iniciales en puntos de ramificación, complicando la estructura analítica de la forma diferencial. Como el contorno de integración puede pasar a través de los puntos de ramificación, necesitamos una prescripción sobre cómo regularizar dichas contribuciones. Esto se ha conseguido continuando analíticamente las integrales de una forma en la que las singularidades factorizan fueran de la integral, y se hacen explícitas. Hemos sido capaces de entender que algunos puntos de ramificación corresponden a singularidades físicas (las singularidades IR y UV de la amplitud), con lo que deja abierta la posibilidad de que el contorno esté codificado en la estructura de puntos de ramificación.

En un futuro, sería interesante trabajar directamente en la signatura $SO(2,2)$, en lugar de trabajar en la de Lorentz, como se ha hecho aquí. La ventaja de esto es que cada momento *on-shell* viene representado por dos espinores reales e independientes, mientras que en la signatura de Lorentz necesitamos dos espinores complejos que están ligados por ser complejos conjugados. Esto está directamente asociado con los grados de libertad necesarios para definir la forma diferencial *on-shell*, y por lo tanto con el contorno de integración que define la amplitud integrada. Por ejemplo, en el caso de 1-*loop*, facilita

mucho la tarea trabajar en una subvariedad de $\mathbb{R}^4$ que en una subvariedad de dimensión 4 embebida en $\mathbb{C}^4$.

Por otro lado los diagramas *on-shell* permiten definir una teoría, en la región perturbativa, desde primeros principios sin referencia alguna a un Lagrangiano y solamente haciendo referencia a observables físicos. Esto pone de manifiesto estructuras que están completamente ocultas in los marcos más tradicionales de la Teoría Cuántica de Campos. Este enfoque ha sido explorado en el contexto de la teoría Yang-Mills máximamente supersimétrica, cuyas propiedades se han podido traducir a términos geométricos. Se han llegado, por ejemplo, a relaciones muy interesantes entre diagramas *on-shell* y estructuras matemáticas como permutaciones, el Grassmanniano positivo y *cluster-algebras*.

La pregunta que hemos empezado a responder en este trabajo ha sido cuánto de todas estas estructuras matemáticas encontradas en $\mathcal{N} = 4$ SYM sobreviven cuando pasamos a teorías más generales. Tenemos que el proceso para construir procesos *on-shell* no depende de la teoría: las amplitudes a tres puntos (que son los nodos de los diagramas) están fijados por la invarianza Poincaré y las simetrías de la teoría, y la unión de estos ladrillos consiste en integrar los grados de libertad de las uniones entre nodos. Entonces, la pregunta no es si se pueden construir diagramas *on-shell* para teorías generales, sino qué información de la teoría están codificando, ya que en general no hay una relación directa entre estos diagramas y las Amplitudes de Dispersión.

La reducción de supersimetría partiendo desde $\mathcal{N} = 4$ SYM ofrece un campo de pruebas ideal para responder a las preguntas formuladas anteriormente ya que por un lado, sabemos que una parte de los diagramas tienen interpretación física directa y, por otra, la estructura ofrecida es mucho más rica al aparecer divergencias UV y términos racionales a nivel de *loop*. En una dirección similar se han realizado estudios recientemente para teorías de gravedad por otros autores [287, 288]. La riqueza de estructuras en teorías $\mathcal{N} < 4$ SYM aparece de forma inmediata por la presencia de nuevos polos que son típicos de diagramas no *planares*. Son polos de orden alto, excepto en el caso de $\mathcal{N} = 3$ SYM que para diagramas individuales tienen una estructura similar a la de los diagramas no *planares* de $\mathcal{N} = 4$ SYM. Estas nuevas singularidades están asociadas a los bucles en helicidad que aparecen en los diagramas *on-shell*. Este trabajo supone un primer paso para un entendimiento más profundo de la geometría de los diagramas *on-shell* decorados para $\mathcal{N} < 4$ SYM, y deja cuestiones abiertas. La primera está relacionada con la posibilidad de un estudio sistemático de las estructuras no *planares* (de order más alto) en el Grassmanniano $Gr(k,n)$, así como las relaciones entre las diferentes funciones definidas sobre él. La segunda cuestión abierta está relacionada con la simetrías del Grassmanniano, en el caso máximamente supersimétrico los difeomorfismos que preservan la positividad en $Gr_{\geq 0}(k,n)$

están relacionados con la simetría Yangian. En este contexto, es natural preguntarse si los difeomorfismos sobre $Gr(k,n)$ están codificando alguna simetría por ahora oculta. Además, aún si no queda ninguna noción de positividad, sería interesante comprobar si hay algún criterio general para fijar los signos, como ocurre en el sector no *planar* de $\mathcal{N}=4$ SYM. Para concluir, queda estudiar si hay posibilidad de tener una formulación en términos del Amplituhedro, en líneas similares a las de caso máximamente supersimétrico que se han explorado en [241, 289–297], y cómo las nuevas estructuras están codificadas en esta geometría.

APPENDIX A

NLO EIGENVECTORS AND NLO IMPACT FACTOR

A.1 Normalization of the eigenvectors

(A.1) $$\langle \vec{q}_A | \, \vec{q}_B \rangle = \delta^2(\vec{q}_A - \vec{q}_B) \ , \ \mathbb{1} = \int \mathrm{d}^2\vec{q} \, |\vec{q}\rangle \langle \vec{q}|$$

(A.2) $$\langle n,\nu \big| \, m,\mu \rangle = \delta\left(\nu-\mu\right)\delta_{nm} \ , \ \mathbb{1} = \sum_n \int \mathrm{d}\nu \, |n,\nu\rangle \langle n,\nu|$$

(A.3) $$\langle H_{n,\nu} \big| \, H_{m,\mu} \rangle = \delta\left(\nu-\mu\right)\delta_{nm} + \mathcal{O}\left(\bar{\alpha}^2_{\mu_R}\right) \ , \ \mathbb{1} = \sum_n \int \mathrm{d}\nu \, \big|H_{n,\nu}\big\rangle \big\langle H_{n,\nu}\big| + \mathcal{O}\left(\bar{\alpha}^2_{\mu_R}\right)$$

(A.4) $$\langle \vec{q}| \, n,\nu\rangle = \frac{1}{\pi\sqrt{2}} \left(\vec{q}^{\,2}\right)^{i\nu-\frac{1}{2}} e^{in\theta}$$

(A.5) $$\big\langle \vec{q}\big| \, H_{n,\nu}\big\rangle = \frac{1}{\pi\sqrt{2}} \left(\vec{q}^{\,2}\right)^{i\nu-\frac{1}{2}} e^{in\theta} \left[1 + \bar{\alpha}_{\mu_R}\beta_2 \log\frac{\vec{q}^{\,2}}{\mu_R^2}\left(A(n,\nu)\log\frac{\vec{q}^{\,2}}{\mu_R^2} + B(n,\nu)\right)\right]$$

where $A(n,\nu) = \frac{i}{2}\frac{\chi_0(n,\nu)}{\chi_0'(n,\nu)}$ and $B(n,\nu) = \frac{1}{2}\frac{\partial}{\partial\nu}\frac{\chi_0(n,\nu)}{\chi_0'(n,\nu)}$. The prime indicates a derivative with respect to ν and the integrals over ν must be regulated at $\nu = 0$ treating the eigenfunctions as distributions, and applying the principal value prescription to the pole.

A.2 NLO Impact factor

We have used the NLO impact factor calculated in [145], being aware that their definition of γ, $\gamma_{I.P.} = -\frac{1}{2} + i\nu$, is different from ours, $\gamma = \frac{1}{2} + i\nu$. Also, some simplifications were done converting the hypergeometric functions into incomplete Beta functions. We remind that the effective PDF is defined as $f^\star(x_J) \equiv \frac{N_C}{C_F} f_g(x_J) + \sum_{i=q,\bar{q}} f_i(x_J)$. Also, the impact factor satisfies the expected property $\phi_1(n,\gamma,\omega,J) = \phi_1(-n,\gamma,\omega,J)$. Its expression can be written as following[1]

(A.6)

$$\begin{aligned}
&\phi_1(n,\gamma,\omega,J) = \\
&= \frac{f_q(x_J,\mu_F)}{2C_A f^\star(x_J,\mu_F)} \left\{ C_q + 2(C_F - C_A)\log(1-x_J)^2 + C_F(x_J^2 + 2x_J + 4\log(1-x_J))\log\frac{k_J}{R\mu_F} \right\} + \\
&\quad + \frac{f_g(x_J,\mu_F)}{2C_F f^\star(x_J,\mu_F)} \left\{ C_g + 4N_C\beta_2 \log\frac{2k_J}{R\mu_F} + 2C_A \log(1-x_J)(2\log\frac{k_J}{R\mu_F} + \chi_0(n,\gamma)) \right\} + \\
&\quad + \frac{1}{4}\left\{ \psi'(\frac{n}{2}+1-\gamma) - \psi'(\frac{n}{2}+\gamma) - \chi_0(n,\gamma)^2 \right\} + \frac{1}{2C_A f^\star(x_J,\mu_F)} \int_{x_J}^1 \mathrm{d}\zeta\, \Phi_{int}(\zeta,n,\gamma,\omega,J),
\end{aligned}$$

where we have defined the following constant factors

$$C_q = \left(\frac{85}{18} + \frac{\pi^2}{2}\right) C_A - \left(\frac{9}{2} + \frac{\pi^2}{3} - 3\log 2\right) C_F - \frac{5}{9} N_F, \tag{A.7}$$

$$C_g = \left(\frac{1}{12} + \frac{\pi^2}{6}\right) C_A - \frac{1}{12} N_F, \tag{A.8}$$

and the expression under the integral sign is given by

[1] The input J in the impact factor Φ stands for all the variables associated to the jet J: $k_J, x_J, \mu_F, \mu_R, R$, being R the radius associated with the jet reconstruction algorithm.

$$
\begin{aligned}
&\Phi_{int}(\zeta,n,\gamma,\omega,J)= \\
&=-\frac{\zeta^{-\omega+\gamma-\frac{n}{2}}}{2C_F\bar{\zeta}\zeta^2}\left\{\left[2C_A f_g\left(\frac{x_J}{\zeta},\mu_F\right)\left(C_A\left(1-\zeta\bar{\zeta}\right)^2+N_F T_R\zeta\bar{\zeta}\left(\zeta^2+\bar{\zeta}^2\right)\right)+\right.\right. \\
&\left.+C_F f_q\left(\frac{x_J}{\zeta},\mu_F\right)\left(2C_F\zeta\left(1+\zeta^2\right)+C_A(1-2\zeta)\left(2-\zeta+\zeta^2\right)\right)\right] \\
&\left[B_\zeta\left(\frac{n}{2}+1-\gamma,0\right)+\zeta^n\left(B_\zeta\left(-\frac{n}{2}+1-\gamma,0\right)+B_\zeta\left(\frac{n}{2}+\gamma,0\right)+B_\zeta\left(-\frac{n}{2}+\gamma,0\right)\right)\right]\Big\}+ \\
&+\frac{2\zeta^{-\omega}}{C_F\bar{\zeta}\zeta^2}f_g\left(\frac{x_J}{\zeta},\mu_F\right)\left\{C_F N_F\zeta^2\bar{\zeta}^2+2\log\frac{k_J}{\mu_F}\left[C_A^2\left(1-\zeta\bar{\zeta}\right)^2+T_R C_F N_F\zeta\bar{\zeta}\left(\zeta^2\bar{\zeta}^2\right)\right]-\right. \\
&-2C_A\zeta^{2\gamma}\log\left(\bar{\zeta}R\right)\left[C_A\left(1-\zeta\bar{\zeta}\right)^2+N_F T_R\zeta\bar{\zeta}\left(\zeta^2\bar{\zeta}^2\right)\right]+ \\
&\left.+\chi_0(n,\gamma)\left[C_A\left(1-\zeta\bar{\zeta}\right)^2\left(1+\zeta^{2\gamma}\right)+N_F T_R\zeta\bar{\zeta}\left(1-2\zeta\bar{\zeta}\right)\left(C_F+\zeta^{2\gamma}C_A\right)\right]\right\}+ \\
&+\frac{\zeta^{-\omega}}{\bar{\zeta}\zeta^2}f_q\left(\frac{x_J}{\zeta},\mu_F\right)\left\{\zeta\bar{\zeta}\left(C_A\zeta+C_F\bar{\zeta}\right)+2\log\frac{k_J}{\mu_F}\left[C_A\bar{\zeta}\left(2-2\zeta+\zeta^2\right)+C_F\zeta\left(1+\zeta^2\right)\right]-\right. \\
&-2C_F\zeta^{2\gamma}\left(2-3\zeta\bar{\zeta}\right)\log\left(\bar{\zeta}R\right) \\
&\left.+\chi_0(n,\gamma)\left[C_A\bar{\zeta}\left(2-2\zeta+\zeta^2\right)+C_F\left(\zeta\left(1+\zeta^2\right)+\zeta^{2\gamma}\left(2-3\zeta\bar{\zeta}\right)\right)\right]\right\}- \\
&-\frac{2}{C_F\bar{\zeta}}\left\{C_A^2 f_g\left(\frac{x}{\zeta},\mu_F\right)\left[2\log\frac{k_J}{R\mu_F}+\chi_0(n,\gamma)\right]+\right. \\
&\left.\left.+C_F f_q\left(\frac{x}{\zeta},\mu_F\right)\left[C_F\left(1+\zeta^2\right)\log\frac{k_J}{R\mu_F}+C_A\chi_0(n,\gamma)+2(C_F-C_A)\log\bar{\zeta}\right]\right\}
\end{aligned}
\tag{A.9}
$$

where $\bar{\zeta}=1-\zeta$, $T_R=\frac{1}{2}$, $C_F=\frac{N_C^2-1}{2N_C}$ and $C_A=N_C$, the number of colors. The incomplete Beta function is defined as $B_\zeta(a,b)=\int_0^\zeta \mathrm{d}x\, x^{a-1}(1-x)^{b-1}$.

APPENDIX B

'CUTTING' THE BFKL LADDER

We show now how Eq. (4.20) is derived. A simple manipulation using Dirac's notation lets us express the GGF as

$$\begin{aligned}
\varphi\left(\vec{k}_A,\vec{k}_B,Y\right) &= \int \frac{\mathrm{d}\omega}{2\pi i} e^{\omega Y} \left\langle \vec{k}_A \middle| \varphi_\omega \middle| \vec{k}_A \right\rangle = \\
&= \sum_n \int \mathrm{d}\nu \int \frac{\mathrm{d}\omega}{2\pi i} e^{\omega Y} \left\langle \vec{k}_A \middle| \frac{\mathbb{1}}{\omega\mathbb{1}-\mathscr{K}} \middle| n,\nu \right\rangle \left\langle n,\nu \middle| \vec{k}_B \right\rangle = \\
&= \sum_n \int \mathrm{d}\nu \int \frac{\mathrm{d}\omega}{2\pi i} \frac{e^{\omega Y}}{\omega-\chi(n,\nu)} \left\langle \vec{k}_A \middle| n,\nu \right\rangle \left\langle n,\nu \middle| \vec{k}_B \right\rangle = \\
&= \sum_n \int \mathrm{d}\nu\, e^{\chi(n,\nu)Y} \left\langle \vec{k}_A \middle| n,\nu \right\rangle \left\langle n,\nu \middle| \vec{k}_B \right\rangle .
\end{aligned} \tag{B.1}$$

With the previous equality, it is straightforward to demonstrate the relationship we are looking for

$$\begin{aligned}
&\int \mathrm{d}^2\vec{k}\, \varphi\left(\vec{k}_A,\vec{k},Y-y\right)\varphi\left(\vec{k},\vec{k}_B,y\right) = \\
&= \int \mathrm{d}^2\vec{k} \int \frac{\mathrm{d}\omega}{2\pi i} e^{\omega(Y-y)} \left\langle \vec{k}_A \middle| \varphi_\omega \middle| \vec{k} \right\rangle \int \frac{\mathrm{d}\omega'}{2\pi i} e^{\omega' y} \left\langle \vec{k} \middle| \varphi_{\omega'} \middle| \vec{k}_B \right\rangle = \\
&= \int \frac{\mathrm{d}\omega}{2\pi i} \frac{\mathrm{d}\omega'}{2\pi i} e^{\omega(Y-y)} e^{\omega' y} \left\langle \vec{k}_A \middle| \varphi_\omega \varphi_{\omega'} \middle| \vec{k}_B \right\rangle = \\
&= \sum_n \int \mathrm{d}\nu \int \frac{\mathrm{d}\omega}{2\pi i} \frac{\mathrm{d}\omega'}{2\pi i} \frac{e^{\omega(Y-y)}}{\omega-\chi(n,\nu)} \frac{e^{\omega' y}}{\omega'-\chi(n,\nu)} \left\langle \vec{k}_A \middle| n,\nu \right\rangle \left\langle n,\nu \middle| \vec{k}_B \right\rangle = \\
&= \sum_n \int \mathrm{d}\nu\, e^{\chi(n,\nu)Y} \left\langle \vec{k}_A \middle| n,\nu \right\rangle \left\langle n,\nu \middle| \vec{k}_B \right\rangle = \varphi\left(\vec{k}_A,\vec{k}_B,Y\right).
\end{aligned} \tag{B.2}$$

The relation in Eq. (B.2) is remarkable because it holds for any intermediate rapidity y. Is is important to notice that for this relationship to be fulfilled, no other $\vec{k}$-dependent factor should appear apart of the integration measure.

APPENDIX C

ON THE STRUCTURE ON THE 1-LOOP INTEGRAND

C.1 On the structure on the 1-loop integrand

The identities discussed in Section 10.2.1 relate on-shell functions defined on the top-cell of $Gr(2,4)$ with a given choice for the external sources/sinks to an on-shell function defined again on the top-cell of $Gr(2,4)$ but with a different ordering. They can be useful to rewrite the on-shell 4-forms, which are related to the constructible part of the one-loop integrand [253], in such a way that that the $d\log$ part and the part which contains higher order poles get split:

(C.1)

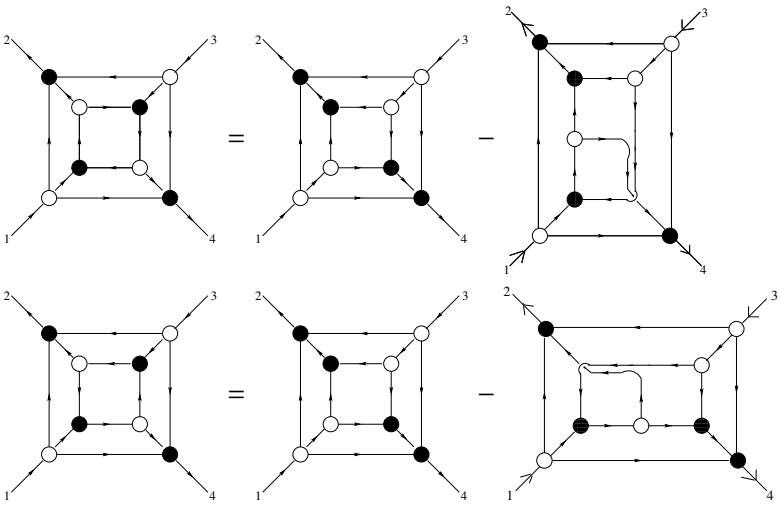

The first diagram in the right-hand-side of both lines correspond to the purely $d\log$ contribution: using the merger equivalence relation and the bubble reduction, it can be written as the on-shell box which corresponds to the four-particle amplitude at tree level times four $d\log$'s. The other contributions contain a new higher order pole located at $\Delta_{24}(z)$. Actually, the expression in (10.16) is a geometric sequence (truncated at order $4-\mathcal{N}$) in $\Delta_{24}(z)$. As shown in [253], upon summation between the two contribution of this type in the two lines in (C.1), $\mathcal{N}=1,2$ SYM theories contain terms with single and double poles in $\Delta_{24}(z)$, while $\mathcal{N}=0$ theory shows poles up to order 4. The terms with a simple pole correspond to triangle integrands, while the ones with double poles to bubble integrands [253]. The presence of higher order poles for $\mathcal{N}=0$ is a signature of the presence extra information, which is related to the rational contribution of the Passarino-Veltman reduction.

C.2 Non-planar poles in momentum space

In Section 10.3 we saw that on-shell functions on the top-cell of $Gr(3,6)$ can show (higher order) poles which are typical of non-planar diagrams. In particular, a class of such poles do not correspond to any Plücker coordinate vanishing but rather it imposes relations among them. In this section we examine again the on-shell function of Section 10.3.1 with such a pole in momentum-space. Its expression on the twistor-space Grassmannian is given by the first line of (10.19), and we will write it here for convenience in the momentum-space Grassmannian:

(C.2)
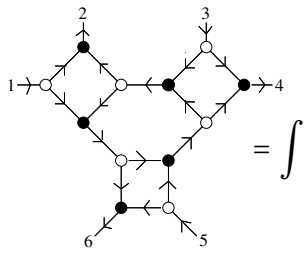

$$= \int \frac{d^{(3\times 6)}C}{\mathrm{Vol}\{GL(3)\}} \frac{\delta^{(2\times 3)}\left(\lambda\cdot C^{\perp}\right)\delta^{(2\times 3}\left(C\cdot\tilde{\lambda}\right)\delta^{(3\times\mathcal{N})}\left(C\cdot\tilde{\eta}\right)}{\Delta_{123}\Delta_{234}\Delta_{345}\Delta_{456}\Delta_{561}\Delta_{612}}\times$$

$$\times\left[\frac{\Delta_{134}\Delta_{356}\Delta_{512}}{\Delta_{346}\Delta_{512}-\Delta_{345}\Delta_{612}}\right]^{4-\mathcal{N}}$$

The residue of the higher order pole is represented by a non-planar on-shell diagram:

(C.3)
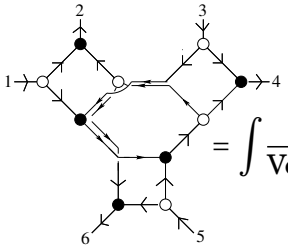

$$= \int \frac{d^{(3\times 6)}C}{\mathrm{Vol}\{GL(3)\}} \frac{\delta^{(2\times 3)}\left(\lambda\cdot C^{\perp}\right)\delta^{(2\times 3)}\left(C\cdot\tilde{\lambda}\right)\delta^{(3\times\mathcal{N})}\left(C\cdot\tilde{\eta}\right)}{\Delta_{123}\Delta_{234}\Delta_{345}\Delta_{456}\Delta_{561}\Delta_{612}}\times$$

$$\times\left(\Delta_{134}\Delta_{356}\Delta_{512}\right)^{(4-\mathcal{N})}\delta^{(3-\mathcal{N})}\left(\Delta_{346}\Delta_{512}-\Delta_{345}\Delta_{612}\right).$$

As we already mentioned in the main text of the paper, the momentum-conserving delta-functions fix 8 out of the 9 parameter of $Gr(3,6)$. Let us choose the following representative for C:

$$C^{\star} = \begin{pmatrix} \lambda_1^{(1)} & \lambda_1^{(2)} & \lambda_1^{(3)} & \lambda_1^{(4)} & \lambda_1^{(5)} & \lambda_1^{(6)} \\ \lambda_2^{(1)} & \lambda_2^{(2)} & \lambda_2^{(3)} & \lambda_2^{(4)} & \lambda_2^{(5)} & \lambda_2^{(6)} \\ 0 & z[4,6] & 0 & [5,6]-z[2,6] & [6,4] & [4,5]-z[4,6] \end{pmatrix} \tag{C.4}$$

with z being the unfixed parameter of $Gr(3,6)$. It is straightforward to see that the location of the higher-order pole is given by a second-order algebraic equation in the free parameter z:

$$0 = \Delta_{346}\Delta_{512}-\Delta_{345}\Delta_{612} = [6,5(z)]\langle 1,2\rangle\langle 3|5(z)+6|4]-z[6,4]\langle 3|1+2(z)|5(z)+6|1\rangle, \tag{C.5}$$

where $\lambda^{(2)}(z)\equiv\lambda^{(2)}+z\lambda^{(5)}$ and $\tilde{\lambda}^{(5)}(z)\equiv\tilde{\lambda}^{(5)}-z\tilde{\lambda}^{(2)}$. Therefore, in order to correctly compute the residue of this pole, one needs to sum up over both the solutions of (C.5). Notice that the form of these solutions is $z_{\pm}=a\pm\sqrt{b}$, with a and b being rational functions of the Lorentz invariants. At a generic point in momentum space, the function b is not a perfect square and the individual residues at $z=z_{\pm}$ are no longer meromorphic functions. However, the square-roots cancel upon summation of the two terms, returning a meromorphic function as it should, and which is represented by the decorated on-shell diagram on the left-hand-side of (C.3).

BIBLIOGRAPHY

[1] F. Caporale, F. Celiberto, G. Chachamis, D. G. Gómez, and A. S. Vera, "Inclusive dijet hadroproduction with a rapidity veto constraint," *Nuclear Physics B* (2018) , 1806.06309 [hep-ph]. http://www.sciencedirect.com/science/article/pii/S0550321318302499.
i, xvii

[2] F. Caporale, F. G. Celiberto, G. Chachamis, D. Gordo Gomez, and A. Sabio Vera, "BFKL Azimuthal Imprints in Inclusive Three-jet Production at 7 and 13 TeV," *Nucl. Phys.* **B910** (2016) 374–386, arXiv:1603.07785 [hep-ph].
i, xvii, 106, 138

[3] F. Caporale, F. G. Celiberto, G. Chachamis, D. G. Gomez, and A. Sabio Vera, "Stability of Azimuthal-angle Observables under Higher Order Corrections in Inclusive Three-jet Production," *Phys. Rev.* **D95** no. 7, (2017) 074007, arXiv:1612.05428 [hep-ph].
i, xvii

[4] F. Caporale, F. G. Celiberto, G. Chachamis, D. Gordo Gomez, and A. Sabio Vera, "Inclusive Four-jet Production at 7 and 13 TeV: Azimuthal Profile in Multi-Regge Kinematics," *Eur. Phys. J.* **C77** no. 1, (2017) 5, arXiv:1606.00574 [hep-ph].
i, xvii, 92

[5] F. G. Celiberto, D. Gordo Gómez, and A. Sabio Vera, "Forward Drell-Yan production at the LHC in the BFKL formalism with collinear corrections," arXiv:1808.09511 [hep-ph].
i, xvii

[6] P. Benincasa, E. Conde, and D. Gordo, "On the Regularization of On-Shell Diagrams," arXiv:1411.7987 [hep-th].
i, xviii, 214

[7] P. Benincasa and D. Gordo, "On-shell diagrams and the geometry of planar $\mathcal{N} < 4$ SYM theories," *JHEP* **11** (2017) 192, arXiv:1609.01923 [hep-th].
i, xviii

[8] F. Caporale, F. G. Celiberto, D. Gordo Gomez, A. Sabio Vera, and G. Chachamis, "Multi-jet production in the high energy limit at LHC," in *25th Low-x Meeting (Low-x 2017) Bari, Italy, June 13-17, 2017*.
2017.
arXiv:1801.00014 [hep-ph].
ii

[9] F. Deganutti, D. Gordo Gomez, T. Raben, and C. Royon, "Pomeron Physics at the LHC," *EPJ Web Conf.* **172** (2018) 06006, arXiv:1711.07514 [hep-ph].

[10] G. Chachamis, F. Caporale, F. G. Celiberto, D. Gordo Gomez, and A. Sabio Vera, "Azimuthal-angle Observables in Inclusive Three-jet Production," *PoS* **DIS2017** (2018) 067, arXiv:1709.02649 [hep-ph].

[11] F. Caporale, F. G. Celiberto, G. Chachamis, D. Gordo Gómez, and A. Sabio Vera, "Probing the BFKL dynamics in inclusive three jet production at the LHC," *EPJ Web Conf.* **164** (2017) 07027, arXiv:1612.02771 [hep-ph].

[12] F. Caporale, F. G. Celiberto, G. Chachamis, D. G. Gomez, and A. Sabio Vera, "Inclusive three- and four-jet production in multi-Regge kinematics at the LHC," *AIP Conf. Proc.* **1819** no. 1, (2017) 060009, arXiv:1611.04813 [hep-ph].

[13] G. Chachamis, F. Caporale, F. Celiberto, D. Gomez Gordo, and A. Sabio Vera, "Inclusive three jet production at the LHC for 7 and 13 TeV collision energies," *PoS* **DIS2016** (2016) 178.

[14] F. Caporale, F. G. Celiberto, G. Chachamis, D. Gordo Gomez, B. Murdaca, and A. Sabio Vera, "High energy effects in multi-jet production at LHC," in *24th Low-x Meeting (Low-x 2016) Gyongyos, Hungary, June 6-10, 2016*.
2016.
arXiv:1610.04765 [hep-ph].

[15] G. Chachamis, F. Caporale, F. G. Celiberto, D. G. Gomez, and A. Sabio Vera, "Inclusive three jet production at the LHC at 7 and 13 TeV collision energies,"
2016.
arXiv:1610.01342 [hep-ph].
ii

[16] H. Fritzsch, M. Gell-Mann, and H. Leutwyler, "Advantages of the Color Octet Gluon Picture," *Phys. Lett.* **47B** (1973) 365–368.
3

[17] S. Weinberg, "Nonabelian Gauge Theories of the Strong Interactions," *Phys. Rev. Lett.* **31** (1973) 494–497.

[18] D. J. Gross and F. Wilczek, "Ultraviolet Behavior of Nonabelian Gauge Theories," *Phys. Rev. Lett.* **30** (1973) 1343–1346. [,271(1973)].
3, 4

[19] M. Gell-Mann, "A Schematic Model of Baryons and Mesons," *Phys. Lett.* **8** (1964) 214–215.
3

[20] G. Zweig, "An SU(3) model for strong interaction symmetry and its breaking. Version 1,".

[21] G. Zweig, "An SU(3) model for strong interaction symmetry and its breaking. Version 2," in *DEVELOPMENTS IN THE QUARK THEORY OF HADRONS. VOL. 1. 1964 - 1978*, D. Lichtenberg and S. P. Rosen, eds., pp. 22–101.
1964.
3

[22] J. D. Bjorken, "Asymptotic Sum Rules at Infinite Momentum," *Phys. Rev.* **179** (1969) 1547–1553.
3

[23] G. F. Chew, *S-matrix theory of strong interactions; a lecture note and reprint volume.* W.A. Benjamin, New York, 1961.
4

[24] G. F. Chew, "The Analytic S-Matrix: A Basis for Nuclear Democracy," *W.A. Benjamin Inc.* (1966) .

[25] R. J. Eden, P. V. Landshoff, D. I. Olive, and J. C. Polkinghorne, *The analytic S-matrix*. Cambridge Univ. Press, Cambridge, 1966.
4

[26] G. 't Hooft, "Remarks after Symanzik's Presentation," *In Korthals-Altes, C. P. (Ed) Renormalization of Yang - Mills fields and applications to particle physics* (1972) .
4

[27] H. D. Politzer, "Reliable Perturbative Results for Strong Interactions?," *Phys. Rev. Lett.* **30** (1973) 1346–1349. [,274(1973)].
4

[28] G. 't Hooft and M. J. G. Veltman, "Regularization and Renormalization of Gauge Fields," *Nucl. Phys.* **B44** (1972) 189–213.
4, 5

[29] C. G. Bollini and J. J. Giambiagi, "Lowest order divergent graphs in nu-dimensional space," *Phys. Lett.* **40B** (1972) 566–568.
5

[30] S. Coleman, "Notes from Sidney Coleman's Physics 253a: Quantum Field Theory," arXiv:1110.5013 [physics.ed-ph].
5, 7

[31] S. Weinberg, *The Quantum theory of fields. Vol. 1: Foundations*. Cambridge University Press, 2005.
5, 33

[32] S. Coleman, *Aspects of Symmetry*. Cambridge University Press, Cambridge, U.K., 1985.
6

[33] M. Srednicki, *Quantum field theory*. Cambridge University Press, 2007.
7

[34] **Particle Data Group** Collaboration, C. Patrignani *et al.*, "Review of Particle Physics," *Chin. Phys.* **C40** no. 10, (2016) 100001.
9, 10, 28, 29

[35] T. van Ritbergen, J. A. M. Vermaseren, and S. A. Larin, "The Four loop beta function in quantum chromodynamics," *Phys. Lett.* **B400** (1997) 379–384, arXiv:hep-ph/9701390 [hep-ph].
10

[36] M. Czakon, "The Four-loop QCD beta-function and anomalous dimensions," *Nucl. Phys.* **B710** (2005) 485–498, arXiv:hep-ph/0411261 [hep-ph].
10

[37] F. Herzog, B. Ruijl, T. Ueda, J. A. M. Vermaseren, and A. Vogt, "The five-loop beta function of Yang-Mills theory with fermions," *JHEP* **02** (2017) 090, arXiv:1701.01404 [hep-ph].
10

[38] T. Appelquist and J. Carazzone, "Infrared Singularities and Massive Fields," *Phys. Rev.* **D11** (1975) 2856.
10

[39] A. V. Manohar, "Introduction to Effective Field Theories," in *Les Houches summer school: EFT in Particle Physics and Cosmology Les Houches, Chamonix Valley, France, July 3-28, 2017*. 2018. arXiv:1804.05863 [hep-ph].
10

[40] B. Delamotte, "A Hint of renormalization," *Am. J. Phys.* **72** (2004) 170–184, arXiv:hep-th/0212049 [hep-th].
10

[41] W. Celmaster and R. J. Gonsalves, "The Renormalization Prescription Dependence of the QCD Coupling Constant," *Phys. Rev.* **D20** (1979) 1420.
12, 109

[42] S. Pokorski, *Gauge Field Theories*.
Cambridge University Press, 2005.
http://www.cambridge.org/uk/catalogue/catalogue.asp?isbn=0521265371.
12

[43] J. C. Collins, D. E. Soper, and G. F. Sterman, "Factorization of Hard Processes in QCD," *Adv. Ser. Direct. High Energy Phys.* **5** (1989) 1–91, arXiv:hep-ph/0409313 [hep-ph].
13, 15

[44] F. Bloch and A. Nordsieck, "Note on the Radiation Field of the electron," *Phys. Rev.* **52** (1937) 54–59.
14

[45] T. Kinoshita, "Mass singularities of Feynman amplitudes," *J. Math. Phys.* **3** (1962) 650–677.
14

[46] T. D. Lee and M. Nauenberg, "Degenerate Systems and Mass Singularities," *Phys. Rev.* **133** (1964) B1549–B1562. [,25(1964)].
14

[47] V. N. Gribov and L. N. Lipatov, "Deep inelastic e p scattering in perturbation theory," *Sov. J. Nucl. Phys.* **15** (1972) 438–450. [Yad. Fiz.15,781(1972)].
15, 52

[48] L. N. Lipatov, "The parton model and perturbation theory," *Sov. J. Nucl. Phys.* **20** (1975) 94–102. [Yad. Fiz.20,181(1974)].

[49] G. Altarelli and G. Parisi, "Asymptotic Freedom in Parton Language," *Nucl. Phys.* **B126** (1977) 298–318.
52

[50] Y. L. Dokshitzer, "Calculation of the Structure Functions for Deep Inelastic Scattering and e+ e- Annihilation by Perturbation Theory in Quantum Chromodynamics.," *Sov. Phys. JETP* **46** (1977) 641–653. [Zh. Eksp. Teor. Fiz.73,1216(1977)].
15, 52

[51] **Particle Data Group** Collaboration, C. Patrignani *et al.*, "Review of Particle Physics. Structure functions," *Chin. Phys.* **C40** no. 10, (2016) 100001. http://pdg.lbl.gov/2018/reviews/rpp2018-rev-structure-function-figs.pdf.
19

[52] J. D. Bjorken and E. A. Paschos, "Inelastic Electron Proton and gamma Proton Scattering, and the Structure of the Nucleon," *Phys. Rev.* **185** (1969) 1975–1982.
19, 21

[53] R. P. Feynman, "Very high-energy collisions of hadrons," *Phys. Rev. Lett.* **23** (1969) 1415–1417. [,494(1969)].
19

[54] W. K. H. Panofsky, "Electromagnetic interactions: low Q^2 electrodynamics: elastic and inelastic electron (and muon) scattering," in *Proc. of Int. Conf. on High-Energy Physics, Vienna, 1968. Geneva, CERN, 1968. p. 23-39*, pp. 23–39. 1968.
http://www-public.slac.stanford.edu/sciDoc/docMeta.aspx?slacPubNumber=SLAC-PUB-0502.
19

[55] J. Collins, "Foundations of perturbative QCD," *Camb. Monogr. Part. Phys. Nucl. Phys. Cosmol.* **32** (2011) 1–624.
20

[56] C. G. Callan, Jr. and D. J. Gross, "High-energy electroproduction and the constitution of the electric current," *Phys. Rev. Lett.* **22** (1969) 156–159.
21

[57] H. Lehmann, K. Symanzik, and W. Zimmermann, "On the formulation of quantized field theories," *Nuovo Cim.* **1** (1955) 205–225.
21

[58] G. Altarelli, R. K. Ellis, and G. Martinelli, "Large Perturbative Corrections to the Drell-Yan Process in QCD," *Nucl. Phys.* **B157** (1979) 461–497.
23

[59] R. K. Ellis, W. J. Stirling, and B. R. Webber, "QCD and collider physics," *Camb. Monogr. Part. Phys. Nucl. Phys. Cosmol.* **8** (1996) 1–435.
27, 28

[60] A. De Rujula, S. L. Glashow, H. D. Politzer, S. B. Treiman, F. Wilczek, and A. Zee, "Possible NonRegge Behavior of Electroproduction Structure Functions," *Phys. Rev.* **D10** (1974) 1649.
31

[61] L. N. Lipatov, "Reggeization of the Vector Meson and the Vacuum Singularity in Nonabelian Gauge Theories," *Sov. J. Nucl. Phys.* **23** (1976) 338–345. [Yad. Fiz.23,642(1976)].
33, 41, 54, 62

[62] E. A. Kuraev, L. N. Lipatov, and V. S. Fadin, "The Pomeranchuk Singularity in Nonabelian Gauge Theories," *Sov. Phys. JETP* **45** (1977) 199–204. [Zh. Eksp. Teor. Fiz.72,377(1977)].

[63] I. I. Balitsky and L. N. Lipatov, "The Pomeranchuk Singularity in Quantum Chromodynamics," *Sov. J. Nucl. Phys.* **28** (1978) 822–829. [Yad. Fiz.28,1597(1978)].
33, 41, 54, 62

[64] V. Barone and E. Predazzi, *High-Energy Particle Diffraction*, vol. v.565 of *Texts and Monographs in Physics*.
Springer-Verlag, Berlin Heidelberg, 2002.
http://www-spires.fnal.gov/spires/find/books/www?cl=QC794.6.C6B37::2002.
35, 36, 41

[65] S. Catani, M. Ciafaloni, and F. Hautmann, "Gluon contributions to small x heavy flavor production," *Phys. Lett.* **B242** (1990) 97–102.
34

[66] S. Catani, M. Ciafaloni, and F. Hautmann, "High-energy factorization and small x heavy flavor production," *Nucl. Phys.* **B366** (1991) 135–188.
34

[67] V. S. Fadin and L. N. Lipatov, "BFKL pomeron in the next-to-leading approximation," *Phys. Lett.* **B429** (1998) 127–134, arXiv:hep-ph/9802290 [hep-ph].
36, 41, 54, 62

[68] M. Ciafaloni, "Energy scale and coherence effects in small x equations," *Phys. Lett.* **B429** (1998) 363–368, arXiv:hep-ph/9801322 [hep-ph].
36, 93, 105

[69] M. Ciafaloni and G. Camici, "Energy scale(s) and next-to-leading BFKL equation," *Phys. Lett.* **B430** (1998) 349–354, arXiv:hep-ph/9803389 [hep-ph].
36, 41, 54, 62

[70] **Small x** Collaboration, B. Andersson *et al.*, "Small x phenomenology: Summary and status," *Eur. Phys. J.* **C25** (2002) 77–101, arXiv:hep-ph/0204115 [hep-ph].
37

[71] K. J. Golec-Biernat and M. Wusthoff, "Saturation in diffractive deep inelastic scattering," *Phys. Rev.* **D60** (1999) 114023, arXiv:hep-ph/9903358 [hep-ph].
37, 40, 148

[72] K. J. Golec-Biernat and M. Wusthoff, "Saturation effects in deep inelastic scattering at low Q^2 and its implications on diffraction," *Phys. Rev.* **D59** (1998) 014017, arXiv:hep-ph/9807513 [hep-ph].
37, 148

[73] M. G. Ryskin and Yu. M. Shabelski, "The Role of screening corrections in small x behavior of structure functions," *Z. Phys.* **C66** (1995) 151–155. [Yad. Fiz.58,1884(1995)].
38

[74] J. Kwiecinski, A. D. Martin, and A. M. Stasto, "A Unified BFKL and GLAP description of F2 data," *Phys. Rev.* **D56** (1997) 3991–4006, arXiv:hep-ph/9703445 [hep-ph].
38

[75] M. Hentschinski, A. Sabio Vera, and C. Salas, "Hard to Soft Pomeron Transition in Small-x Deep Inelastic Scattering Data Using Optimal Renormalization," *Phys. Rev. Lett.* **110** no. 4, (2013) 041601, arXiv:1209.1353 [hep-ph].
38, 58, 147, 150, 154, 155

[76] M. Hentschinski, A. Sabio Vera, and C. Salas, "F_2 and F_L at small x using a collinearly improved BFKL resummation," *Phys. Rev.* **D87** no. 7, (2013) 076005, arXiv:1301.5283 [hep-ph].
38, 58, 147, 150, 154, 155

[77] G. P. Salam, "A Resummation of large subleading corrections at small x," *JHEP* **07** (1998) 019, arXiv:hep-ph/9806482 [hep-ph].
38, 60, 61

[78] J. Blumlein, "On the k(T) dependent gluon density of the proton," in *Deep inelastic scattering and QCD. Proceedings, Workshop, Paris, France, April 24-28, 1995*, pp. 265–268. 1995.
arXiv:hep-ph/9506403 [hep-ph].
http://www-library.desy.de/cgi-bin/showprep.pl?desy95-121.
38

[79] M. A. Kimber, A. D. Martin, and M. G. Ryskin, "Unintegrated parton distributions," *Phys. Rev.* **D63** (2001) 114027, arXiv:hep-ph/0101348 [hep-ph].
38

[80] H. Jung, "CCFM prediction on forward jets and F(2): Parton level predictions and a new hadron level Monte Carlo generator CASCADE," in *Monte Carlo generators for HERA physics. Proceedings, Workshop, Hamburg, Germany, 1998-1999*, pp. 75–90. 1998.
arXiv:hep-ph/9908497 [hep-ph].
38

[81] H. Jung and G. P. Salam, "Hadronic final state predictions from CCFM: The Hadron level Monte Carlo generator CASCADE," *Eur. Phys. J.* **C19** (2001) 351–360, arXiv:hep-ph/0012143 [hep-ph].
38

[82] B. Foster, "Low x physics," *Phil. Trans. Roy. Soc. Lond.* **A359** (2001) 325–378, arXiv:hep-ex/0008069 [hep-ex].
39

[83] M. Ciafaloni, "Coherence Effects in Initial Jets at Small Q^2/s," *Nucl. Phys.* **B296** (1988) 49–74.
38

[84] S. Catani, F. Fiorani, and G. Marchesini, "QCD Coherence in Initial State Radiation," *Phys. Lett.* **B234** (1990) 339–345.

[85] S. Catani, F. Fiorani, and G. Marchesini, "Small x Behavior of Initial State Radiation in Perturbative QCD," *Nucl. Phys.* **B336** (1990) 18–85.
38

[86] J. Kwiecinski, A. D. Martin, and P. J. Sutton, "The gluon distribution at small x obtained from a unified evolution equation," *Phys. Rev.* **D52** (1995) 1445–1458, arXiv:hep-ph/9503266 [hep-ph].
38

[87] E. Levin, "The Pomeron: Yesterday, today and tomorrow," in *Proceedings, 3rd Gleb Wataghin School on High-energy Phenomenology: Campinas, Brasil, July 11-16 1994*, pp. 0158–261. 1994.
arXiv:hep-ph/9503399 [hep-ph].
39

[88] I. Balitsky, "Operator expansion for high-energy scattering," *Nucl. Phys.* **B463** (1996) 99–160, arXiv:hep-ph/9509348 [hep-ph].
40

[89] Y. V. Kovchegov, "Small x F(2) structure function of a nucleus including multiple pomeron exchanges," *Phys. Rev.* **D60** (1999) 034008, arXiv:hep-ph/9901281 [hep-ph].
40

[90] A. H. Mueller, "Soft gluons in the infinite momentum wave function and the BFKL pomeron," *Nucl. Phys.* **B415** (1994) 373–385.
40, 41

[91] H. Mäntysaari, *Scattering off the Color Glass Condensate*.

PhD thesis, Jyvaskyla U., 2015.
arXiv:1506.07313 [hep-ph].
40

[92] A. M. Stasto, K. J. Golec-Biernat, and J. Kwiecinski, "Geometric scaling for the total gamma* p cross-section in the low x region," *Phys. Rev. Lett.* **86** (2001) 596–599, arXiv:hep-ph/0007192 [hep-ph].
40

[93] E. Iancu, *Physics of the Color Glass Condensate*.
PhD thesis, Saclay, 2005.
http://ipht.cea.fr/Docspht//search/article.php?IDA=9767.
40

[94] F. Gelis, E. Iancu, J. Jalilian-Marian, and R. Venugopalan, "The Color Glass Condensate," *Ann. Rev. Nucl. Part. Sci.* **60** (2010) 463–489, arXiv:1002.0333 [hep-ph].
40

[95] J. Jalilian-Marian, A. Kovner, L. D. McLerran, and H. Weigert, "The Intrinsic glue distribution at very small x," *Phys. Rev.* **D55** (1997) 5414–5428, arXiv:hep-ph/9606337 [hep-ph].
40

[96] J. Jalilian-Marian, A. Kovner, A. Leonidov, and H. Weigert, "The BFKL equation from the Wilson renormalization group," *Nucl. Phys.* **B504** (1997) 415–431, arXiv:hep-ph/9701284 [hep-ph].

[97] J. Jalilian-Marian, A. Kovner, and H. Weigert, "The Wilson renormalization group for low x physics: Gluon evolution at finite parton density," *Phys. Rev.* **D59** (1998) 014015, arXiv:hep-ph/9709432 [hep-ph].
40

[98] J. R. Forshaw and D. A. Ross, *Quantum Chromodynamics and the Pomeron*.
Cambridge Lecture Notes in Physics. Cambridge University Press, 1997.
41, 46, 50

[99] M. Gell-Mann and M. L. Goldberger, "Elementary Particles of Conventional Field Theory as Regge Poles," *Phys. Rev. Lett.* **9** no. 6, (1962) 275–277.
41

[100] M. Gell-Mann, M. L. Goldberger, F. E. Low, and F. Zachariasen, "Elementary particles of conventional field theory as regge poles - II," *Phys. Lett.* **4** no. 5, (1963) 265–267.

[101] M. Gell-Mann, M. L. Goldberger, F. E. Low, V. Singh, and F. Zachariasen, "Elementary Particles of Conventional Field Theory as Regge Poles. IV," *Phys. Rev.* **133** (1964) B161–B174.

[102] M. Gell-Mann, M. Goldberger, F. Low, E. Marx, and F. Zachariasen, "Elementary Particles of Conventional Field Theory as Regge Poles. III," *Phys. Rev.* **133** no. 1B, (1964) B145–B160.
41

[103] S. Mandelstam, "Non-Regge Terms in the Vector-Spinor Theory," *Phys. Rev.* **137** (1965) B949–B954.
41

[104] V. S. Fadin, E. A. Kuraev, and L. N. Lipatov, "On the Pomeranchuk Singularity in Asymptotically Free Theories," *Phys. Lett.* **60B** (1975) 50–52.
41, 54, 62

[105] E. A. Kuraev, L. N. Lipatov, and V. S. Fadin, "Multi - Reggeon Processes in the Yang-Mills Theory," *Sov. Phys. JETP* **44** (1976) 443–450. [Zh. Eksp. Teor. Fiz.71,840(1976)].
54, 62

[106] M. T. Grisaru, H. J. Schnitzer, and H.-S. Tsao, "Reggeization of elementary particles in renormalizable gauge theories - vectors and spinors," *Phys. Rev.* **D8** (1973) 4498–4509.

[107] M. T. Grisaru, H. J. Schnitzer, and H.-S. Tsao, "Reggeization of yang-mills gauge mesons in theories with a spontaneously broken symmetry," *Phys. Rev. Lett.* **30** (1973) 811–814.
41

[108] V. S. Fadin and V. E. Sherman, "Fermion Reggeization in Nonabelian Calibration Theories," *Pisma Zh. Eksp. Teor. Fiz.* **23** (1976) 599–602.
41

[109] V. S. Fadin and V. E. Sherman, "Processes Involving Fermion Exchange in Nonabelian Gauge Theories," *Zh. Eksp. Teor. Fiz.* **72** (1977) 1640–1658.

[110] A. V. Bogdan, V. Del Duca, V. S. Fadin, and E. W. N. Glover, "The Quark Regge trajectory at two loops," *JHEP* **03** (2002) 032, arXiv:hep-ph/0201240 [hep-ph].

[111] M. I. Kotsky, L. N. Lipatov, A. Principe, and M. I. Vyazovsky, "Radiative corrections to the quark gluon Reggeized quark vertex in QCD," *Nucl. Phys.* **B648** (2003) 277–292, arXiv:hep-ph/0207169 [hep-ph].
41

[112] R. E. Cutkosky, "Singularities and discontinuities of Feynman amplitudes," *J. Math. Phys.* **1** (1960) 429–433.
43, 167, 208

[113] A. H. Mueller and H. Navelet, "An Inclusive Minijet Cross-Section and the Bare Pomeron in QCD," *Nucl. Phys.* **B282** (1987) 727–744.
51, 57

[114] V. Del Duca and C. R. Schmidt, "Dijet production at large rapidity intervals," *Phys. Rev.* **D49** (1994) 4510–4516, arXiv:hep-ph/9311290 [hep-ph].
51, 57

[115] W. J. Stirling, "Production of jet pairs at large relative rapidity in hadron hadron collisions as a probe of the perturbative pomeron," *Nucl. Phys.* **B423** (1994) 56–79, arXiv:hep-ph/9401266 [hep-ph].
57

[116] L. H. Orr and W. J. Stirling, "Dijet production at hadron hadron colliders in the BFKL approach," *Phys. Rev.* **D56** (1997) 5875–5884, arXiv:hep-ph/9706529 [hep-ph].

[117] J. Kwiecinski, A. D. Martin, L. Motyka, and J. Outhwaite, "Azimuthal decorrelation of forward and backward jets at the Tevatron," *Phys. Lett.* **B514** (2001) 355–360, arXiv:hep-ph/0105039 [hep-ph].

[118] **Small x** Collaboration, J. R. Andersen *et al.*, "Small x Phenomenology: Summary of the 3rd Lund Small x Workshop in 2004," *Eur. Phys. J.* **C48** (2006) 53–105, arXiv:hep-ph/0604189 [hep-ph].

[119] A. De Roeck *et al.*, "From the LHC to Future Colliders," *Eur. Phys. J.* **C66** (2010) 525–583, arXiv:0909.3240 [hep-ph].

[120] M. Angioni, G. Chachamis, J. D. Madrigal, and A. Sabio Vera, "Dijet Production at Large Rapidity Separation in N=4 SYM," *Phys. Rev. Lett.* **107** (2011) 191601, arXiv:1106.6172 [hep-th].

[121] F. Caporale, B. Murdaca, A. Sabio Vera, and C. Salas, "Scale choice and collinear contributions to Mueller-Navelet jets at LHC energies," *Nucl. Phys.* **B875** (2013) 134–151, arXiv:1305.4620 [hep-ph].
97, 110

[122] F. Caporale, D. Yu. Ivanov, B. Murdaca, and A. Papa, "Mueller-Navelet small-cone jets at LHC in next-to-leading BFKL," *Nucl. Phys.* **B877** (2013) 73–94, arXiv:1211.7225 [hep-ph].
53

[123] C. Marquet and C. Royon, "Azimuthal decorrelation of Mueller-Navelet jets at the Tevatron and the LHC," *Phys. Rev.* **D79** (2009) 034028, arXiv:0704.3409 [hep-ph].

[124] D. Colferai, F. Schwennsen, L. Szymanowski, and S. Wallon, "Mueller-Navelet jets at LHC - complete NLL BFKL calculation," *JHEP* **12** (2010) 026, arXiv:1002.1365 [hep-ph].

[125] B. Ducloue, L. Szymanowski, and S. Wallon, "Confronting Mueller-Navelet jets in NLL BFKL with LHC experiments at 7 TeV," *JHEP* **05** (2013) 096, arXiv:1302.7012 [hep-ph].
67, 98, 113, 145

[126] B. Ducloue, L. Szymanowski, and S. Wallon, "Violation of energy-momentum conservation in Mueller-Navelet jets production," *Phys. Lett.* **B738** (2014) 311–316, arXiv:1407.6593 [hep-ph].

[127] A. H. Mueller, L. Szymanowski, S. Wallon, B.-W. Xiao, and F. Yuan, "Sudakov Resummations in Mueller-Navelet Dijet Production," *JHEP* **03** (2016) 096, arXiv:1512.07127 [hep-ph].

[128] G. Chachamis, "BFKL phenomenology," in *New Trends in High-Energy Physics and QCD Natal, Rio Grande do Norte, Brazil, October 21-November 6, 2014*.
2015.
arXiv:1512.04430 [hep-ph].
http://inspirehep.net/record/1409541/files/arXiv:1512.04430.pdf.

[129] **LHC Forward Physics Working Group** Collaboration, K. Akiba *et al.*, "LHC Forward Physics," *J. Phys.* **G43** (2016) 110201, arXiv:1611.05079 [hep-ph].
51, 156, 161, 261

[130] B. Ducloue, L. Szymanowski, and S. Wallon, "Evidence for high-energy resummation effects in Mueller-Navelet jets at the LHC," *Phys. Rev. Lett.* **112** (2014) 082003, arXiv:1309.3229 [hep-ph].
51, 60, 82, 109

[131] F. Caporale, D. Yu. Ivanov, B. Murdaca, and A. Papa, "Mueller-Navelet jets in next-to-leading order BFKL: theory versus experiment," *Eur. Phys. J.* **C74** no. 10, (2014) 3084, arXiv:1407.8431 [hep-ph]. [Erratum: Eur. Phys. J.C75,no.11,535(2015)].
67, 68, 109

[132] F. Caporale, D. Yu. Ivanov, B. Murdaca, and A. Papa, "Brodsky-Lepage-Mackenzie optimal renormalization scale setting for semihard processes," *Phys. Rev.* **D91** no. 11, (2015) 114009, arXiv:1504.06471 [hep-ph].

[133] F. G. Celiberto, D. Yu. Ivanov, B. Murdaca, and A. Papa, "Mueller–Navelet Jets at LHC: BFKL Versus High-Energy DGLAP," *Eur. Phys. J.* **C75** no. 6, (2015) 292, arXiv:1504.08233 [hep-ph].
98, 113, 145

[134] F. G. Celiberto, D. Yu. Ivanov, B. Murdaca, and A. Papa, "Mueller–Navelet jets at 13 TeV LHC: dependence on dynamic constraints in the central rapidity region," *Eur. Phys. J.* **C76** no. 4, (2016) 224, arXiv:1601.07847 [hep-ph].
51, 60, 107

[135] **CMS** Collaboration, CMS Collaboration, "Azimuthal angle decorrelations of jets widely separated in rapidity in pp collisions at sqrts = 7 TeV," *CMS-FSQ-12-002* (2013) .
51, 60, 61, 67, 68, 82, 90, 104, 160, 260

[136] **CMS** Collaboration, V. Khachatryan *et al.*, "Azimuthal decorrelation of jets widely separated in rapidity in pp collisions at $\sqrt{s} = 7$ TeV," *JHEP* **08** (2016) 139, arXiv:1601.06713 [hep-ex].
51, 60, 61, 67, 68, 82, 90, 104, 106, 160, 260

[137] F. Caporale, A. Papa, and A. Sabio Vera, "Collinear improvement of the BFKL kernel in the electroproduction of two light vector mesons," *Eur. Phys. J.* **C53** (2008) 525–532, arXiv:0707.4100 [hep-ph].
53

[138] L. N. Lipatov, "The Bare Pomeron in Quantum Chromodynamics," *Sov. Phys. JETP* **63** (1986) 904–912. [Zh. Eksp. Teor. Fiz.90,1536(1986)].
54

[139] A. V. Kotikov and L. N. Lipatov, "NLO corrections to the BFKL equation in QCD and in supersymmetric gauge theories," *Nucl. Phys.* **B582** (2000) 19–43, arXiv:hep-ph/0004008 [hep-ph].
54, 55, 63

[140] G. A. Chirilli and Y. V. Kovchegov, "Solution of the NLO BFKL Equation and a Strategy for Solving the All-Order BFKL Equation," *JHEP* **06** (2013) 055, arXiv:1305.1924 [hep-ph].
55, 56, 63

[141] G. A. Chirilli and Y. V. Kovchegov, "$\gamma^*\gamma^*$ Cross Section at NLO and Properties of the BFKL Evolution at Higher Orders," *JHEP* **05** (2014) 099, arXiv:1403.3384 [hep-ph]. [Erratum: JHEP08,075(2015)].
55, 63

[142] J. Bartels, D. Colferai, and G. P. Vacca, "The NLO jet vertex for Mueller-Navelet and forward jets: The Quark part," *Eur. Phys. J.* **C24** (2002) 83–99, arXiv:hep-ph/0112283 [hep-ph].
55, 93, 105, 128

[143] J. Bartels, D. Colferai, and G. P. Vacca, "The NLO jet vertex for Mueller-Navelet and forward jets: The Gluon part," *Eur. Phys. J.* **C29** (2003) 235–249, arXiv:hep-ph/0206290 [hep-ph].
55, 93, 105, 128

[144] F. Caporale, D. Yu. Ivanov, B. Murdaca, A. Papa, and A. Perri, "The next-to-leading order jet vertex for Mueller-Navelet and forward jets revisited," *JHEP* **02** (2012) 101, arXiv:1112.3752 [hep-ph].
55

[145] D. Yu. Ivanov and A. Papa, "The next-to-leading order forward jet vertex in the small-cone approximation," *JHEP* **05** (2012) 086, arXiv:1202.1082 [hep-ph].
55, 63, 266

[146] M. Furman, "Study of a Nonleading QCD Correction to Hadron Calorimeter Reactions," *Nucl. Phys.* **B197** (1982) 413–445.
55

[147] S. Catani, Y. L. Dokshitzer, M. H. Seymour, and B. R. Webber, "Longitudinally invariant K_t clustering algorithms for hadron hadron collisions," *Nucl. Phys.* **B406** (1993) 187–224.
55

[148] S. D. Ellis, Z. Kunszt, and D. E. Soper, "One-jet inclusive cross section at order α_s^3. gluons only," *Phys. Rev. D* **40** (Oct, 1989) 2188–2222. https://link.aps.org/doi/10.1103/PhysRevD.40.2188.
55

[149] D. Colferai and A. Niccoli, "The NLO jet vertex in the small-cone approximation for kt and cone algorithms," *JHEP* **04** (2015) 071, arXiv:1501.07442 [hep-ph].
55, 68

[150] B. L. Combridge and C. J. Maxwell, "Untangling Large p(T) Hadronic Reactions," *Nucl. Phys.* **B239** (1984) 429–458.
56, 63

[151] A. Sabio Vera and F. Schwennsen, "The Azimuthal decorrelation of jets widely separated in rapidity as a test of the BFKL kernel," *Nucl. Phys.* **B776** (2007) 170–186, arXiv:hep-ph/0702158 [HEP-PH].
57, 58, 59, 64, 87, 135

[152] A. Sabio Vera, "The Effect of NLO conformal spins in azimuthal angle decorrelation of jet pairs," *Nucl. Phys.* **B746** (2006) 1–14, arXiv:hep-ph/0602250 [hep-ph].
58, 59, 87, 135

[153] S. J. Brodsky, G. P. Lepage, and P. B. Mackenzie, "On the Elimination of Scale Ambiguities in Perturbative Quantum Chromodynamics," *Phys. Rev.* **D28** (1983) 228.
60, 109

[154] C. R. Schmidt, "Rapidity separation dependence and the large next-to-leading corrections to the BFKL equation," *Phys. Rev.* **D60** (1999) 074003, arXiv:hep-ph/9901397 [hep-ph].
60, 64, 65

[155] J. R. Forshaw, D. A. Ross, and A. Sabio Vera, "Rapidity veto effects in the NLO BFKL equation," *Phys. Lett.* **B455** (1999) 273–282, arXiv:hep-ph/9903390 [hep-ph].
61, 65

[156] D. A. Ross and A. Sabio Vera, "The Effect of a Rapidity Gap Veto on the Discrete BFKL Pomeron," *Phys. Lett.* **B760** (2016) 428–431, arXiv:1605.00692 [hep-ph].
61

[157] G. Chachamis, M. Lublinsky, and A. Sabio Vera, "Higher order effects in non linear evolution from a veto in rapidities," *Nucl. Phys.* **A748** (2005) 649–663, arXiv:hep-ph/0408333 [hep-ph].
61

[158] R. Enberg, "Traveling waves and the renormalization group improved Balitsky-Kovchegov equation," *Phys. Rev.* **D75** (2007) 014012, arXiv:hep-ph/0612005 [hep-ph].
61

[159] **ATLAS** Collaboration, G. Aad *et al.*, "Measurement of dijet production with a veto on additional central jet activity in pp collisions at $\sqrt{s} = 7$ TeV using the ATLAS detector," *JHEP* **09** (2011) 053, arXiv:1107.1641 [hep-ex].
67

[160] D. Colferai, F. Deganutti, and A. Niccoli, "Improved theoretical description of Mueller-Navelet jets at LHC," in *25th Low-x Meeting (Low-x 2017) Bari, Italy, June 13-17, 2017*.
2017.
arXiv:1709.10370 [hep-ph].
https://inspirehep.net/record/1627887/files/arXiv:1709.10370.pdf.
68

[161] A. D. Martin, W. J. Stirling, R. S. Thorne, and G. Watt, "Parton distributions for the LHC," *Eur. Phys. J.* **C63** (2009) 189–285, arXiv:0901.0002 [hep-ph].
68, 98, 111, 137

[162] C. R. Schmidt, "A Monte Carlo solution to the BFKL equation," *Phys. Rev. Lett.* **78** (1997) 4531–4535, arXiv:hep-ph/9612454 [hep-ph].
83

[163] F. Caporale, G. Chachamis, B. Murdaca, and A. Sabio Vera, "Balitsky-Fadin-Kuraev-Lipatov Predictions for Inclusive Three Jet Production at the LHC," *Phys. Rev. Lett.* **116** no. 1, (2016) 012001, arXiv:1508.07711 [hep-ph].
91, 95, 104, 107, 118

[164] F. Caporale, F. G. Celiberto, G. Chachamis, and A. Sabio Vera, "Multi-Regge kinematics and azimuthal angle observables for inclusive four-jet production," *Eur. Phys. J.* **C76** no. 3, (2016) 165, arXiv:1512.03364 [hep-ph].
92, 95, 128, 145

[165] H. Jung, M. Kraemer, A. V. Lipatov, and N. P. Zotov, "Investigation of beauty production and parton shower effects at LHC," *Phys. Rev.* **D85** (2012) 034035, arXiv:1111.1942 [hep-ph].
92, 128

[166] S. P. Baranov, A. V. Lipatov, M. A. Malyshev, A. M. Snigirev, and N. P. Zotov, "Associated $W^{\pm}D^{(*)}$ production at the LHC and prospects to observe double parton interactions," *Phys. Lett.* **B746** (2015) 100–103, arXiv:1503.06080 [hep-ph].

[167] R. Maciuła and A. Szczurek, "Searching for and exploring double-parton scattering effects in four-jet production at the LHC," *Phys. Lett.* **B749** (2015) 57–62, arXiv:1503.08022 [hep-ph].

[168] R. Maciula and A. Szczurek, "Double-parton scattering contribution to production of jet pairs with large rapidity separation at the LHC," *Phys. Rev.* **D90** no. 1, (2014) 014022, arXiv:1403.2595 [hep-ph].

[169] K. Kutak, R. Maciula, M. Serino, A. Szczurek, and A. van Hameren, "Four-jet production in single- and double-parton scattering within high-energy factorization," *JHEP* **04** (2016) 175, arXiv:1602.06814 [hep-ph].
92

[170] B. Ducloué, L. Szymanowski, and S. Wallon, "Evaluating the double parton scattering contribution to Mueller-Navelet jets production at the LHC," *Phys. Rev.* **D92** no. 7, (2015) 076002, arXiv:1507.04735 [hep-ph].
92, 128

[171] F. Caporale, D. Y. Ivanov, B. Murdaca, A. Papa, and A. Perri, "NLO forward jet vertex," arXiv:1212.0487 [hep-ph]. [AIP Conf. Proc.1523,282(2012)].
93, 95, 105, 128, 134

[172] V. S. Fadin, R. Fiore, M. I. Kotsky, and A. Papa, "The Gluon impact factors," *Phys. Rev.* **D61** (2000) 094005, arXiv:hep-ph/9908264 [hep-ph].

[173] V. S. Fadin, R. Fiore, M. I. Kotsky, and A. Papa, "The Quark impact factors," *Phys. Rev.* **D61** (2000) 094006, arXiv:hep-ph/9908265 [hep-ph].
128

[174] M. Ciafaloni and D. Colferai, "K factorization and impact factors at next-to-leading level," *Nucl. Phys.* **B538** (1999) 187–214, arXiv:hep-ph/9806350 [hep-ph].
93, 105

[175] G. P. Lepage, "A New Algorithm for Adaptive Multidimensional Integration," *J. Comput. Phys.* **27** (1978) 192.
98, 111, 137, 153

[176] T. Hahn, "CUBA: A Library for multidimensional numerical integration," *Comput. Phys. Commun.* **168** (2005) 78–95, arXiv:hep-ph/0404043 [hep-ph].
98, 111, 137, 153

[177] T. Hahn, "Concurrent Cuba," *J. Phys. Conf. Ser.* **608** no. 1, (2015) 012066, arXiv:1408.6373 [physics.comp-ph].
98, 111, 137, 153

[178] R. Piessens, E. de Doncker-Kapenga, and C. W. Ueberhuber, *Quadpack. A subroutine package for automatic integration*.
1983.
98, 111, 137

[179] W. J. Cody, A. J. Strecok, and H. C. Thacher, "Chebyshev approximations for the psi function," *Mathematics of Computation* **27** no. 121, (Jan, 1973) 123–123. https://doi.org/10.1090/s0025-5718-1973-0326986-3.
98, 111, 137

[180] G. Chachamis, M. Deak, A. S. Vera, and P. Stephens, "A Comparative study of small x Monte Carlos with and without QCD coherence effects," *Nucl. Phys.* **B849** (2011) 28–44, arXiv:1102.1890 [hep-ph].
104, 125, 145, 160, 260

[181] G. Chachamis and A. Sabio Vera, "The Colour Octet Representation of the Non-Forward BFKL Green Function," *Phys. Lett.* **B709** (2012) 301–308, arXiv:1112.4162 [hep-th].

[182] G. Chachamis and A. S. Vera, "The NLO N =4 SUSY BFKL Green function in the adjoint representation," *Phys. Lett.* **B717** (2012) 458–461, arXiv:1206.3140 [hep-th].

[183] G. Chachamis, A. Sabio Vera, and C. Salas, "Bootstrap and momentum transfer dependence in small x evolution equations," *Phys. Rev.* **D87** no. 1, (2013) 016007, arXiv:1211.6332 [hep-ph].

[184] F. Caporale, G. Chachamis, J. D. Madrigal, B. Murdaca, and A. Sabio Vera, "A study of the diffusion pattern in N = 4 SYM at high energies," *Phys. Lett.* **B724** (2013) 127–132, arXiv:1305.1474 [hep-th].

[185] G. Chachamis and A. Sabio Vera, "Monte Carlo study of double logarithms in the small x region," *Phys. Rev.* **D93** no. 7, (2016) 074004, arXiv:1511.03548 [hep-ph].

[186] G. Chachamis and A. Sabio Vera, "The high-energy radiation pattern from BFKLex with double-log collinear contributions," *JHEP* **02** (2016) 064, arXiv:1512.03603 [hep-ph].
104, 125, 145, 160, 260

[187] F. G. Celiberto, D. Yu. Ivanov, B. Murdaca, and A. Papa, "Dihadron production at the LHC: full next-to-leading BFKL calculation," *Eur. Phys. J.* **C77** no. 6, (2017) 382, arXiv:1701.05077 [hep-ph].
107

[188] A. D. Bolognino, F. G. Celiberto, D. Yu. Ivanov, M. A. Mohammed, Mohammed, and A. Papa, "Hadron-jet correlations in high-energy hadronic collisions at the LHC," arXiv:1808.05483 [hep-ph].
107

[189] G. Chachamis and A. Sabio Vera, "Solution of the Bartels-Kwiecinski-Praszalowicz equation via Monte Carlo integration," *Phys. Rev.* **D94** no. 3, (2016) 034019, arXiv:1606.07349 [hep-ph].
125, 160, 260

[190] **CMS** Collaboration, S. Chatrchyan *et al.*, "Measurement of four-jet production in proton-proton collisions at $\sqrt{s} = 7$ TeV," *Phys. Rev.* **D89** no. 9, (2014) 092010, arXiv:1312.6440 [hep-ex].
128

[191] **ATLAS** Collaboration, G. Aad *et al.*, "Measurement of four-jet differential cross sections in $\sqrt{s} = 8$ TeV proton-proton collisions using the ATLAS detector," *JHEP* **12** (2015) 105, arXiv:1509.07335 [hep-ex].

[192] **ATLAS** Collaboration, M. Aaboud *et al.*, "Study of hard double-parton scattering in four-jet events in pp collisions at $\sqrt{s} = 7$ TeV with the ATLAS experiment," *JHEP* **11** (2016) 110, arXiv:1608.01857 [hep-ex].
128

[193] K. Kutak, R. Maciuła, M. Serino, A. Szczurek, and A. van Hameren, "Search for optimal conditions for exploring double-parton scattering in four-jet production: k_t-factorization approach," *Phys. Rev.* **D94** no. 1, (2016) 014019, arXiv:1605.08240 [hep-ph].
128

[194] D. Brzeminski, L. Motyka, M. Sadzikowski, and T. Stebel, "Twist decomposition of Drell-Yan structure functions: phenomenological implications," *JHEP* **01** (2017) 005, arXiv:1611.04449 [hep-ph].
147, 152, 154, 156, 161, 261

[195] S. D. Drell and T.-M. Yan, "Massive Lepton Pair Production in Hadron-Hadron Collisions at High-Energies," *Phys. Rev. Lett.* **25** (1970) 316–320. [Erratum: Phys. Rev. Lett.25,902(1970)].
147

[196] **ATLAS** Collaboration, G. Aad *et al.*, "Measurement of the low-mass Drell-Yan differential cross section at $\sqrt{s}$ = 7 TeV using the ATLAS detector," *JHEP* **06** (2014) 112, arXiv:1404.1212 [hep-ex].
153, 156

[197] **CMS** Collaboration, V. Khachatryan *et al.*, "Measurements of differential and double-differential Drell-Yan cross sections in proton-proton collisions at 8 TeV," *Eur. Phys. J.* **C75** no. 4, (2015) 147, arXiv:1412.1115 [hep-ex].

[198] **ATLAS** Collaboration, G. Aad *et al.*, "Measurement of the Z/γ^* boson transverse momentum distribution in pp collisions at $\sqrt{s}$ = 7 TeV with the ATLAS detector," *JHEP* **09** (2014) 145, arXiv:1406.3660 [hep-ex].

[199] **CMS** Collaboration, V. Khachatryan *et al.*, "Measurement of the Z boson differential cross section in transverse momentum and rapidity in proton–proton collisions at 8 TeV," *Phys. Lett.* **B749** (2015) 187–209, arXiv:1504.03511 [hep-ex].

[200] **CMS** Collaboration, V. Khachatryan *et al.*, "Angular coefficients of Z bosons produced in pp collisions at $\sqrt{s}$ = 8 TeV and decaying to $\mu^+\mu^-$ as a function of transverse momentum and rapidity," *Phys. Lett.* **B750** (2015) 154–175, arXiv:1504.03512 [hep-ex].

[201] **LHCb** Collaboration, R. Aaij *et al.*, "Measurement of the forward Z boson production cross-section in pp collisions at $\sqrt{s}$ = 7 TeV," *JHEP* **08** (2015) 039, arXiv:1505.07024 [hep-ex].

[202] **LHCb** Collaboration, R. Aaij *et al.*, "Measurement of forward W and Z boson production in pp collisions at $\sqrt{s}$ = 8 TeV," *JHEP* **01** (2016) 155, arXiv:1511.08039 [hep-ex].

[203] **ATLAS** Collaboration, G. Aad *et al.*, "Measurement of the angular coefficients in Z-boson events using electron and muon pairs from data taken at $\sqrt{s}$ = 8 TeV with the ATLAS detector," *JHEP* **08** (2016) 159, arXiv:1606.00689 [hep-ex].
147

[204] **LHCb** Collaboration, J. Anderson, "Constraints on low-x PDFs from Drell Yan processes, and first studies of exclusive dimuon production with the LHCb experiment," in

Proceedings, 40th International Symposium on Multiparticle Dynamics (ISMD 2010): Antwerp, Belgium, September 21-25, 2010, pp. 227–232.
2010.
147

[205] J. Bartels, "Private discussions with jochen bartels on this process over many years." Private discussions.
147

[206] L. Motyka, M. Sadzikowski, and T. Stebel, "Twist expansion of Drell-Yan structure functions in color dipole approach," *JHEP* **05** (2015) 087, arXiv:1412.4675 [hep-ph].
148, 151, 152

[207] K. Golec-Biernat, E. Lewandowska, and A. M. Stasto, "Drell-Yan process at forward rapidity at the LHC," *Phys. Rev.* **D82** (2010) 094010, arXiv:1008.2652 [hep-ph].
148

[208] M. B. G. Ducati, M. T. Griep, and M. V. T. Machado, "Study on the low mass Drell-Yan production at the CERN LHC within the dipole formalism," *Phys. Rev.* **D89** no. 3, (2014) 034022, arXiv:1307.6882 [hep-ph].

[209] W. Schäfer and A. Szczurek, "Low mass Drell-Yan production of lepton pairs at forward directions at the LHC: a hybrid approach," *Phys. Rev.* **D93** no. 7, (2016) 074014, arXiv:1602.06740 [hep-ph].

[210] B. Ducloué, "Nuclear modification of forward Drell-Yan production at the LHC," *Phys. Rev.* **D96** no. 9, (2017) 094014, arXiv:1701.08730 [hep-ph].
148

[211] C. S. Lam and W.-K. Tung, "A Systematic Approach to Inclusive Lepton Pair Production in Hadronic Collisions," *Phys. Rev.* **D18** (1978) 2447.
148

[212] K. Gottfried and J. D. Jackson, "On the Connection between production mechanism and decay of resonances at high-energies," *Nuovo Cim.* **33** (1964) 309–330.
149

[213] G. Chachamis, M. Deák, M. Hentschinski, G. Rodrigo, and A. Sabio Vera, "Single bottom quark production in $k_\perp$-factorisation," *JHEP* **09** (2015) 123, arXiv:1507.05778 [hep-ph].
150, 151

[214] I. Bautista, A. Fernandez Tellez, and M. Hentschinski, "BFKL evolution and the growth with energy of exclusive J/ψ and Υ photoproduction cross sections," *Phys. Rev.* **D94** no. 5, (2016) 054002, arXiv:1607.05203 [hep-ph].

150

[215] A. D. Bolognino, F. G. Celiberto, D. Yu. Ivanov, and A. Papa, "Unintegrated gluon distribution from forward polarized ρ-electroproduction," arXiv:1808.02395 [hep-ph].
150

[216] A. Sabio Vera, "An 'All-poles' approximation to collinear resummations in the Regge limit of perturbative QCD," *Nucl. Phys.* **B722** (2005) 65–80, arXiv:hep-ph/0505128 [hep-ph].
151

[217] N. N. Nikolaev and B. G. Zakharov, "Color transparency and scaling properties of nuclear shadowing in deep inelastic scattering," *Z. Phys.* **C49** (1991) 607–618. [,733(1990)].
152

[218] S. J. Brodsky, A. Hebecker, and E. Quack, "The Drell-Yan process and factorization in impact parameter space," *Phys. Rev.* **D55** (1997) 2584–2590, arXiv:hep-ph/9609384 [hep-ph].

[219] B. Z. Kopeliovich, J. Raufeisen, and A. V. Tarasov, "The Color dipole picture of the Drell-Yan process," *Phys. Lett.* **B503** (2001) 91–98, arXiv:hep-ph/0012035 [hep-ph].

[220] B. Z. Kopeliovich, J. Raufeisen, A. V. Tarasov, and M. B. Johnson, "Nuclear effects in the Drell-Yan process at very high-energies," *Phys. Rev.* **C67** (2003) 014903, arXiv:hep-ph/0110221 [hep-ph].
152

[221] L. Motyka and M. Sadzikowski, "Twist decomposition of proton structure from BFKL and BK amplitudes," *Acta Phys. Polon.* **B45** no. 11, (2014) 2079, arXiv:1411.7774 [hep-ph].
152

[222] **LHCb** Collaboration, "Inclusive low mass Drell-Yan production in the forward region at $\sqrt{s}$ = 7 TeV,".
152, 153, 155, 157

[223] E. Piccaro, *Measurement of the low mass Drell-Yan cross section in the di-muon channel in proton-proton collisions at $\sqrt{s}$ = 7 TeV with the ATLAS detector*.
PhD thesis, Queen Mary, U. of London, 2012-08-21.
153, 156

[224] CERNLIB, "Cernlib homepage," 2018.
http://cernlib.web.cern.ch/cernlib.
153

[225] L. A. Harland-Lang, A. D. Martin, P. Motylinski, and R. S. Thorne, "Parton distributions in the LHC era: MMHT 2014 PDFs," *Eur. Phys. J.* **C75** no. 5, (2015) 204, arXiv:1412.3989 [hep-ph].
153

[226] A. Buckley, J. Ferrando, S. Lloyd, K. Nordström, B. Page, M. Rüfenacht, M. Schönherr, and G. Watt, "LHAPDF6: parton density access in the LHC precision era," *Eur. Phys. J.* **C75** (2015) 132, arXiv:1412.7420 [hep-ph].
153

[227] **ZEUS, H1** Collaboration, F. D. Aaron *et al.*, "Combined Measurement and QCD Analysis of the Inclusive e+- p Scattering Cross Sections at HERA," *JHEP* **01** (2010) 109, arXiv:0911.0884 [hep-ex].
155

[228] S. Weinberg, "What is quantum field theory, and what did we think it is?," arXiv:hep-th/9702027 [hep-th].
165

[229] S. J. Parke and T. R. Taylor, "An Amplitude for n Gluon Scattering," *Phys. Rev. Lett.* **56** (1986) 2459.
165

[230] A. Hodges, "Eliminating spurious poles from gauge-theoretic amplitudes," *JHEP* **1305** (2013) 135, arXiv:0905.1473 [hep-th].
166

[231] H. Elvang and Y.-t. Huang, "Scattering Amplitudes," arXiv:1308.1697 [hep-th].
166, 169, 183

[232] R. Britto, F. Cachazo, B. Feng, and E. Witten, "Direct proof of tree-level recursion relation in Yang-Mills theory," *Phys.Rev.Lett.* **94** (2005) 181602, arXiv:hep-th/0501052 [hep-th].
166, 174, 176, 177

[233] Z. Bern, L. J. Dixon, D. C. Dunbar, and D. A. Kosower, "Fusing gauge theory tree amplitudes into loop amplitudes," *Nucl.Phys.* **B435** (1995) 59–101, arXiv:hep-ph/9409265 [hep-ph].
167

[234] G. Passarino and M. Veltman, "One Loop Corrections for e+ e- Annihilation Into mu+ mu- in the Weinberg Model," *Nucl.Phys.* **B160** (1979) 151.
167, 208

[235] R. Britto, F. Cachazo, and B. Feng, "Generalized unitarity and one-loop amplitudes in N=4 super-Yang-Mills," *Nucl.Phys.* **B725** (2005) 275–305, arXiv:hep-th/0412103 [hep-th].
167, 208

[236] N. Arkani-Hamed, J. L. Bourjaily, F. Cachazo, S. Caron-Huot, and J. Trnka, "The All-Loop Integrand For Scattering Amplitudes in Planar N=4 SYM," *JHEP* **1101** (2011) 041, arXiv:1008.2958 [hep-th].
167, 187, 194, 211

[237] N. Arkani-Hamed, J. L. Bourjaily, F. Cachazo, A. B. Goncharov, A. Postnikov, *et al.*, "Scattering Amplitudes and the Positive Grassmannian," arXiv:1212.5605 [hep-th].
167, 168, 169, 190, 193, 194, 196, 197, 202, 204, 211, 216, 235, 241

[238] Z. Bern, J. Carrasco, and H. Johansson, "New relations for gauge theory amplitudes," *Phys. Rev.* **D78** (2008) 085011, arXiv:0805.3993 [hep-th].
168

[239] Z. Bern, J. J. Carrasco, L. J. Dixon, H. Johansson, and R. Roiban, "Amplitudes and Ultraviolet Behavior of N = 8 Supergravity," *Fortsch.Phys.* **59** (2011) 561–578, arXiv:1103.1848 [hep-th].
168

[240] J. M. Drummond, J. M. Henn, and J. Plefka, "Yangian symmetry of scattering amplitudes in N=4 super Yang-Mills theory," *JHEP* **0905** (2009) 046, arXiv:0902.2987 [hep-th].
168, 194

[241] N. Arkani-Hamed and J. Trnka, "The Amplituhedron," *JHEP* **1410** (2014) 30, arXiv:1312.2007 [hep-th].
168, 202, 255, 264

[242] B. Chen, G. Chen, Y.-K. E. Cheung, Y. Li, R. Xie, *et al.*, "Nonplanar On-shell Diagrams and Leading Singularities of Scattering Amplitudes," arXiv:1411.3889 [hep-th].
168, 194

[243] N. Arkani-Hamed, J. L. Bourjaily, F. Cachazo, A. Postnikov, and J. Trnka, "On-Shell Structures of MHV Amplitudes Beyond the Planar Limit," arXiv:1412.8475 [hep-th].

[244] Z. Bern, E. Herrmann, S. Litsey, J. Stankowicz, and J. Trnka, "Logarithmic Singularities and Maximally Supersymmetric Amplitudes," *JHEP* **1506** (2015) 202, arXiv:1412.8584 [hep-th].

[245] S. Franco, D. Galloni, B. Penante, and C. Wen, "Non-Planar On-Shell Diagrams," arXiv:1502.02034 [hep-th].
194, 197, 240, 241

[246] J. L. Bourjaily, S. Franco, D. Galloni, and C. Wen, "Stratifying On-Shell Cluster Varieties: the Geometry of Non-Planar On-Shell Diagrams," arXiv:1607.01781 [hep-th].
241

[247] R. Frassek and D. Meidinger, "Yangian-type symmetries of non-planar leading singularities," *JHEP* **05** (2016) 110, arXiv:1603.00088 [hep-th].
168

[248] Y.-T. Huang and C. Wen, "ABJM amplitudes and the positive orthogonal grassmannian," *JHEP* **1402** (2014) 104, arXiv:1309.3252 [hep-th].
169

[249] J. Kim and S. Lee, "Positroid Stratification of Orthogonal Grassmannian and ABJM Amplitudes," *JHEP* **1409** (2014) 085, arXiv:1402.1119 [hep-th].

[250] Y.-t. Huang, C. Wen, and D. Xie, "The Positive orthogonal Grassmannian and loop amplitudes of ABJM," *J.Phys.* **A47** no. 47, (2014) 474008, arXiv:1402.1479 [hep-th].

[251] H. Elvang, Y.-t. Huang, C. Keeler, T. Lam, T. M. Olson, *et al.*, "Grassmannians for scattering amplitudes in 4d $\mathcal{N} = 4$ SYM and 3d ABJM," *JHEP* **1412** (2014) 181, arXiv:1410.0621 [hep-th].
169

[252] H. Elvang, Y.-t. Huang, and C. Peng, "On-shell superamplitudes in N<4 SYM," *JHEP* **09** (2011) 031, arXiv:1102.4843 [hep-th].
169

[253] P. Benincasa, "On-shell diagrammatics and the perturbative structure of planar gauge theories," arXiv:1510.03642 [hep-th].
169, 195, 198, 201, 233, 241, 242, 271, 272

[254] L. J. Dixon, "Scattering amplitudes: the most perfect microscopic structures in the universe," *J.Phys.* **A44** (2011) 454001, arXiv:1105.0771 [hep-th].
169

[255] J. M. Henn and J. C. Plefka, "Scattering Amplitudes in Gauge Theories," *Lect. Notes Phys.* **883** (2014) pp.1–195.
169

[256] Z. Bern and D. A. Kosower, "Color decomposition of one loop amplitudes in gauge theories," *Nucl.Phys.* **B362** (1991) 389–448.
171

[257] Z. Bern, M. Czakon, L. J. Dixon, D. A. Kosower, and V. A. Smirnov, "The Four-Loop Planar Amplitude and Cusp Anomalous Dimension in Maximally Supersymmetric Yang-Mills Theory," *Phys.Rev.* **D75** (2007) 085010, arXiv:hep-th/0610248 [hep-th].
171, 194, 209

[258] N. Arkani-Hamed, T.-C. Huang, and Y.-t. Huang, "Scattering Amplitudes For All Masses and Spins," arXiv:1709.04891 [hep-th].
172, 213

[259] M. D. Schwartz, *Quantum Field Theory and the Standard Model*. Cambridge University Press, 2014. http://www.cambridge.org/us/academic/subjects/physics/theoretical-physics-and-mathematical-physics/quantum-field-theory-and-standard-model.
172

[260] S. Badger, E. N. Glover, V. Khoze, and P. Svrcek, "Recursion relations for gauge theory amplitudes with massive particles," *JHEP* **0507** (2005) 025, arXiv:hep-th/0504159 [hep-th].
174

[261] K. Ozeren and W. Stirling, "Scattering amplitudes with massive fermions using BCFW recursion," *Eur.Phys.J.* **C48** (2006) 159–168, arXiv:hep-ph/0603071 [hep-ph].
178

[262] R. H. Boels, D. Marmiroli, and N. A. Obers, "On-shell Recursion in String Theory," *JHEP* **1010** (2010) 034, arXiv:1002.5029 [hep-th].
178

[263] F. Cachazo and P. Svrcek, "Tree level recursion relations in general relativity," arXiv:hep-th/0502160 [hep-th].
178

[264] P. Benincasa, "New structures in scattering amplitudes: a review," *Int.J.Mod.Phys.* **A29** no. 5, (2014) 1430005, arXiv:1312.5583 [hep-th].
179, 180

[265] V. Nair, "A Current Algebra for Some Gauge Theory Amplitudes," *Phys.Lett.* **B214** (1988) 215.
182

[266] N. Arkani-Hamed, F. Cachazo, and J. Kaplan, "What is the Simplest Quantum Field Theory?," *JHEP* **1009** (2010) 016, arXiv:0808.1446 [hep-th].
183, 209

[267] R. Penrose, "Twistor algebra," *Journal of Mathematical Physics* **8** no. 2, (Feb, 1967) 345–366. https://doi.org/10.1063/1.1705200.
187

[268] A. Ferber, "Supertwistors and Conformal Supersymmetry," *Nucl. Phys.* **B132** (1978) 55–64.
187

[269] M. Bianchi, H. Elvang, and D. Z. Freedman, "Generating Tree Amplitudes in N=4 SYM and N = 8 SG," *JHEP* **09** (2008) 063, arXiv:0805.0757 [hep-th].
192

[270] J. Drummond, J. Henn, V. Smirnov, and E. Sokatchev, "Magic identities for conformal four-point integrals," *JHEP* **0701** (2007) 064, arXiv:hep-th/0607160 [hep-th].
194

[271] L. Mason and D. Skinner, "Dual Superconformal Invariance, Momentum Twistors and Grassmannians," *JHEP* **0911** (2009) 045, arXiv:0909.0250 [hep-th].
194

[272] N. Arkani-Hamed, F. Cachazo, and C. Cheung, "The Grassmannian origin of dual superconformal invariance," *JHEP* **1003** (2010) 036, arXiv:0909.0483 [hep-th].
194

[273] A. Postnikov, "Total positivity, Grassmannians, and networks," arXiv:math/0609764 [math.CO].
202, 203

[274] S. Franco, D. Galloni, and A. Mariotti, "The Geometry of On-Shell Diagrams," *JHEP* **1408** (2014) 038, arXiv:1310.3820 [hep-th].

[275] T. Lam, "Totally nonnegative Grassmannian and Grassmann polytopes," arXiv:1506.00603 [math.CO].
202

[276] Z. Bern, L. J. Dixon, D. C. Dunbar, and D. A. Kosower, "One loop n point gauge theory amplitudes, unitarity and collinear limits," *Nucl.Phys.* **B425** (1994) 217–260, arXiv:hep-ph/9403226 [hep-ph].
208

[277] Z. Bern and Y.-t. Huang, "Basics of Generalized Unitarity," *J.Phys.* **A44** (2011) 454003, arXiv:1103.1869 [hep-th].
208

[278] M. B. Green, J. H. Schwarz, and L. Brink, "N=4 Yang-Mills and N=8 Supergravity as Limits of String Theories," *Nucl.Phys.* **B198** (1982) 474–492.
209

[279] Z. Bern, J. Rozowsky, and B. Yan, "Two loop four gluon amplitudes in N=4 superYang-Mills," *Phys.Lett.* **B401** (1997) 273–282, arXiv:hep-ph/9702424 [hep-ph].
209

[280] S. Caron-Huot, "Loops and trees," *JHEP* **1105** (2011) 080, arXiv:1007.3224 [hep-ph].
210, 211

[281] H. Elvang, D. Z. Freedman, and M. Kiermaier, "Integrands for QCD rational terms and N=4 SYM from massive CSW rules," *JHEP* **1206** (2012) 015, arXiv:1111.0635 [hep-th].
211

[282] C. Cheung and D. O'Connell, "Amplitudes and Spinor-Helicity in Six Dimensions," *JHEP* **0907** (2009) 075, arXiv:0902.0981 [hep-th].
213

[283] S. Davies, "One-Loop QCD and Higgs to Partons Processes Using Six-Dimensional Helicity and Generalized Unitarity," *Phys.Rev.* **D84** (2011) 094016, arXiv:1108.0398 [hep-ph].
213

[284] Z. Bern, A. De Freitas, L. J. Dixon, and H. Wong, "Supersymmetric regularization, two loop QCD amplitudes and coupling shifts," *Phys.Rev.* **D66** (2002) 085002, arXiv:hep-ph/0202271 [hep-ph].
213

[285] K. AOMOTO, *Theory of Hypergeometric Functions*.
Springer, 2011.
http://amazon.com/o/ASIN/B00EZ180NE/.
223, 225

[286] E. T. Whittaker and G. N. Watson, *A Course of Modern Analysis*.
Watchmaker Publishing, 2, 2012.
http://amazon.com/o/ASIN/1603864547/.
224

[287] P. Heslop and A. E. Lipstein, "On-shell diagrams for $\mathcal{N}$ = 8 supergravity amplitudes," *JHEP* **06** (2016) 069, arXiv:1604.03046 [hep-th].
255, 263

[288] E. Herrmann and J. Trnka, "Gravity On-shell Diagrams," arXiv:1604.03479 [hep-th].
255, 263

[289] N. Arkani-Hamed and J. Trnka, "Into the Amplituhedron," *JHEP* **1412** (2014) 182, arXiv:1312.7878 [hep-th].
255, 264

[290] Y. Bai and S. He, "The Amplituhedron from Momentum Twistor Diagrams," *JHEP* **1502** (2015) 065, arXiv:1408.2459 [hep-th].

[291] S. Franco, D. Galloni, A. Mariotti, and J. Trnka, "Anatomy of the Amplituhedron," *JHEP* **1503** (2015) 128, arXiv:1408.3410 [hep-th].

[292] T. Lam, "Amplituhedron cells and Stanley symmetric functions," *Commun. Math. Phys.* **343** no. 3, (2016) 1025–1037, arXiv:1408.5531 [math.AG].

[293] N. Arkani-Hamed, A. Hodges, and J. Trnka, "Positive Amplitudes In The Amplituhedron," arXiv:1412.8478 [hep-th].

[294] Y. Bai, S. He, and T. Lam, "The Amplituhedron and the One-loop Grassmannian Measure," *JHEP* **01** (2016) 112, arXiv:1510.03553 [hep-th].

[295] L. Ferro, T. Lukowski, A. Orta, and M. Parisi, "Towards the Amplituhedron Volume," *JHEP* **03** (2016) 014, arXiv:1512.04954 [hep-th].

[296] Z. Bern, E. Herrmann, S. Litsey, J. Stankowicz, and J. Trnka, "Evidence for a Nonplanar Amplituhedron," *JHEP* **06** (2016) 098, arXiv:1512.08591 [hep-th].

[297] D. Galloni, "Positivity Sectors and the Amplituhedron," arXiv:1601.02639 [hep-th].
255, 264